Synthesis, spectroscopic characterization and investigation of the oxidation behavior of intermetallic aluminum compounds

DISSERTATION

zur Erlangung des Grades

des Doktors der Naturwissenschaften

der Naturwissenschaftlich-Technischen Fakultät

der Universität des Saarlandes

vorgelegt von

Elias C. J. Gießelmann

Saarbrücken

2025

Tag des Kolloquiums:	09.01.2026
Dekan:	Prof. Dr.-Ing. Dirk Bähre
Berichterstatter:	Priv.-Doz. Dr. Oliver Janka
	Prof. Dr.-Ing. Frank Mücklich
	Prof. Dr. Holger Kohlmann
Vorsitz:	Prof. Dr. Gregor Jung
Akad. Mitglied:	Dr. Andreas Rammo

Danksagung

Ich bedanke mich bei Herr Prof. Dr. Guido Kickelbick für die umgehende Bereiterklärung diese Arbeit zu finanzieren, mich in seine Arbeitsgruppe aufzunehmen, die Freiheit bei der Auswahl der bearbeiteten Themen sowie den wissenschaftlichen Input in vielen Gesprächen und beim Finalisieren der Publikationen.

PD Dr. Oliver Janka kann ich gar nicht genug danken für die exzellente Betreuung, seine angenehme Art, die geteilte Begeisterung und Inspiration sowie die Fülle an vermitteltem Wissen für das Fach Chemie in all seinen Facetten. Danke für alles, was ich über die vergangenen Jahre von dir lernen durfte.

Herrn Prof. Dr.-Ing. Frank Mücklich und Herrn Prof. Dr. Holger Kohlmann danke ich für die Bereiterklärung die weiteren Gutachten zu dieser Arbeit zu verfassen.

Ich danke dem gesamten vierten Stockwerk, namentlich allen aktiven und ehemaligen Mitgliedern der Arbeitsgruppe Kickelbick, Janka, Schäfer und natürlich auch der Gruppe Kautenburger für die allzeit hilfsbereite und angenehme Arbeitsatmosphäre.

Des Weiteren möchte ich mich bedanken:

- Bei allen Studierenden, die bei mir eine Vertiefungsarbeit (Lukas Schank, Jessica Lambert, Cedric Kloos, Robin Völkers, Marcel Miodek) oder ein Praktikum (Israa El-Saudi) absolviert haben, und damit meine Forschung vorangebracht haben.
- Allen Kooperationspartnern, die Messungen für diese Arbeit durchgeführt haben, darunter
    - Den Mitgliedern der Arbeitsgruppe von Prof. Dr. Rainer Pöttgen, namentlich Lars Schumacher, Jasper Baldauf, Aylin Koldemir und Joshua Wiethölter, sowie bei ihm selbst, für alle Messungen der Mößbauer-Spektren und Aufnahme der physikalischen Eigenschaftsmessungen, sowie Hilfestellungen bei Einkristall- und Strukturlösungsfragen
    - Dr. Christoph Pauly für die TEM und Dr. Stefan Engel, sowie Jörg Schmauch für die SEM/EDX Messungen am INM
    - Lukas Rüthing und Prof. Dr. Jörn Schmedt auf der Günne für die Messung der MQ/MAS Festkörper NMR Spektren

- Johannes Volpini und Prof. Dr. Hubert Huppertz für die schöne Zeit bei meinem ersten Hirschegg-Festkörperseminar sowie Unterstützung und weiteren Input beim Anfertigen der Publikation zum Oxidaionsverhalten von $CaAl_2$
- Prof. Dr. Yuemei Zhang, Weronika Kostusiak, Prof. Dr. Samir Matar und PD Dr. Oliver Janka für die Durchführung und Interpretation quantenchemischer Rechnungen zu unseren Verbindungen
- Dr. Petra Herbeck-Engel für die Durchführung der Messungen und Interpretation der Raman-Spektren
- Dr. Kristina Brix und apl. Prof. Dr. Ralf Kautenburger für die Analyse einiger Verbindungen mittels ICP-MS
- Prof. Dr. Horst P. Beck für seinen wissenschaftlichen Rat und Input
- Dr. Michael Zimmer für die Einarbeitung in die Thematik Festkörper-NMR
- Dr. Bernd Morgenstern und PD Dr. Oliver Janka für die Hilfe bei Einkristallmessungen und Auswertung der Daten, dazu auch ein großes Dankeschön an Dipl. Ing. Jutta Kösters aus der Gruppe von Prof. Dr. Rainer Pöttgen

Zuletzt möchte ich einigen Personen abseits des Wissenschaftlichen danken.

Beginnen möchte ich nochmal mit Oliver Janka. Danke für die Einblicke, die ich durch dich auf nationalen und internationalen Konferenzen erwerben durfte, sowie die wunderbare Zeit, die wir im Anschluss an die Konferenzen gemeinsam im Urlaub verbracht haben. Ein großer Dank auch an deine Frau Yvonne mit der wir zusammen einen unvergesslichen Kalifornien-Urlaub voller Insidertipps verbracht haben.

Unter allen Arbeitskollegen stachen über die vergangenen drei Jahre einige Personen, die den Alltag vor allem durch ihren Humor versüßt haben, heraus. Ein großes Dankeschön an Jessica Lambert und im Besonderen an Aylin Feuerstein.

Vor der Promotion war das Studium. Während diesem hat mich Yannic Curto tagtäglich begleitet. Danke, dass wir uns gegenseitig immer unterstützt und gepusht haben.

Danke an meinen besten Freund Phillip Baus und meine Schwester Elena, dafür, dass ihr mich schon seit Kindertagen begleitet und Teil meines Lebens seid.

Fast der letzte Dank geht an meine Eltern, Susanne und Marcel. Eine bessere Unterstützung als die Eure könnte ich mir nicht wünschen.

Ich habe ein ganzes Pharmaziestudium mit dir durchgehalten und Du mit mir ein Chemiestudium und diese ganze Arbeit hier – vom ersten bis zum letzten Tag. An jedem einzelnen davon warst du für mich da, hast mich motiviert, mich aufgebaut, mit mir gelacht und gefeiert.

Melina, danke für einfach alles.

Abstract

Intermetallic compounds not only play a crucial role in everyday life, since they appear in various applications ranging from communication devices, superconducting materials as well as high corrosion resistant materials. They are also of high interest with respect to fundamental research regarding their huge variety of structural chemistry just to name one example. Within this thesis, studies about intermetallic compounds combining aluminum with alkaline earth, rare earth and early transition metals were conducted. The focus was set on their synthesis, structure determination or validation using X-ray diffraction methods. Different aspects of the compounds were elucidated using spectroscopic methods such as solid state NMR, physical property measurements and DFT calculations. From a structural point of view a focus was applied on Laves phases, solid solutions within these structure types and finally the Frank-Kasper phases. In the second part the question whether it is possible to use intermetallic aluminum compounds as precursors for oxidation reactions (limited to the chalcogenides) was investigated. The oxidation behavior of many compounds of the general formula $AEAl_x$ (AE = Ca, Sr, Ba) and $REAl_2$ (*RE* = Sc, Y, La, Eu, Yb,) was investigated using various synthetic methods. Reactions using selenium and sulfur gave phase pure compounds that could be analyzed using the methods stated above.

Kurzzusammenfassung

Intermetallische Verbindungen spielen nicht nur im täglichen Leben eine wichtige Rolle. Sie kommen in verschiedenen Anwendungen von Kommunikation über supraleitende Materialien bis hin zu korrosionsresistenten Werkstoffen vor. Für die Grundlagenforschung sind sie von großem Interesse, da sie, nur um ein Beispiel zu nennen, eine immens vielfältige Strukturchemie aufweisen. Im Rahmen dieser Arbeit wurden Studien über intermetallische Verbindungen von Aluminium mit Erdalkali-, Seltenerd- und frühen Übergangsmetallen durchgeführt. Der Schwerpunkt lag dabei auf ihrer Synthese, Strukturbestimmung oder Validierung mittels Röntgenbeugungsmethoden. Die Verbindungen wurden, falls möglich, mit spektroskopischen Methoden wie Festkörper-NMR, physikalischen Eigenschaftsmessungen und DFT-Rechnungen untersucht. Aus struktureller Sicht lag der Schwerpunkt auf Laves Phasen, festen Lösungen innerhalb dieser Strukturtypen und den Frank-Kasper Phasen. Im zweiten Teil wurde der in der Literatur nur wenig untersuchten Frage nachgegangen, ob es möglich ist, intermetallische Aluminiumverbindungen als Vorstufe für Oxidationsreaktionen zu verwenden (beschränkt auf die Chalkogenide). Das Oxidationsverhalten vieler Verbindungen der allgemeinen Formel *AE*Al_x (*AE* = Ca, Sr, Ba) und *RE*Al_2 (*RE* = Sc, Y, La, Eu, Yb,) wurde untersucht. Die Reaktionen mit Selen und Schwefel ergaben phasenreine Verbindungen, die mit den oben genannten Methoden analysiert werden konnten.

Abbreviations

DFT	Density Functional Theory
EDX	Energy dispersive X-ray analysis
LOBSTER	Local-Orbital Basis Suite Towards Electronic-Structure Reconstruction
MAS	Magic angle spinning
NMR	Nuclear magnetic resonance
PXRD	Powder X-ray diffraction
SCXRD	Single-crystal X-ray diffraction
SEM	Scanning electron microscopy
STA	Simultaneous thermal analysis
TEM	Transmission electron microscopy
VASP	Vienna ab initio program package

List of all publications

The following list provides a chronological overview of all peer-reviewed publications containing contributions by Elias C. J. Gießelmann, including all publications that appeared before the start of the doctoral thesis (numbers 1 and 2).

22 T. Straub, **E. C. J. Gießelmann**, G. Kickelbick, Mechanochemical Activation and Sodium Intercalation in the $NaTi_2(PO_4)_3$ NASICON Structure, Manuscript submitted to *RSC Mechanochem*.

21 A. Michaely, **E. C. J. Gießelmann**, G. Kickelbick, Mechanochemical Defect Engineering of Nb_2O_5: Influence of $LiBH_4$ and $NaBH_4$ Reduction on Structure and Photocatalysis, *Solids* **2025**, *6*, 26-38. DOI: doi.org/10.3390/solids6020026

20 **E. C. J. Gießelmann**, L. Ruck, S. Engel, B. Morgenstern, L. Schumacher, G. Kickelbick, O. Janka, Hf_6Al_7 and $Hf_{4.44(1)}Nb_{1.56(1)}Al_7$ – The first fully ordered main group metal containing W_6Fe_7 type compound and its ternary coloring variant, *Z. Anorg. Allg. Chem.* **2025**, *651*, e202500044. DOI: doi.org/10.1002/zaac.202500044

19 **E. C. J. Gießelmann**, L. Schumacher, S. F. Matar, S. Engel, G. Kickelbick, O. Janka, Systematic investigations of the solid solution $Zr(V_{1-x}Al_x)_2$ adopting the Laves phase structure, *Chem. Eur. J.* **2025**, *31*, e202404248. DOI: doi.org/10.1002/chem.202404248

18 **E. C. J. Gießelmann**, S. Engel, S. Pohl, M. Briesenick, L. P. Rüthing, C. Kloos, A. Koldemir, L. Schumacher, J. Wiethölter, J. Schmedt auf der Günne, G. Kickelbick, O. Janka, Rapid synthesis of a green emitting phosphor by sulfidation of intermetallic $EuAl_2$ and its use in a hybrid material, *Chem. Mater.* **2025**, *37*, 97-108. DOI: doi.org/10.1021/acs.chemmater.4c02093

17 **E. C. J. Gießelmann**, G. Kickelbick, O. Janka, Changing the reaction pathway of the $CaAl_2$ oxidation using ball milling, *Dalton Trans.* **2025**, *54,* 1173-1181. DOI: doi.org/10.1039/D4DT02459A

16 A. Feuerstein, T. Rittner, B. Boßmann, **E. C. J. Gießelmann**, J. Schu, B. Morgenstern, M. Gallei, A. Schäfer: Synthesis and Properties of Symmetrical and Asymmetrical Polyferrocenylmethylenes *Chem. Eur. J.* **2025**, *31*, e202404283. DOI: doi.org/10.1002/chem.202404283

15 S. Engel, **E. C. J. Gießelmann**, L. Schumacher, Y. Zhang, F. Müller, O. Janka, Synthesis, Magnetic and NMR spectroscopic properties of the MAl$_5$Pt$_3$ series (M = Ca, Y, La-Nd, Sm-Er), *Dalton Trans.* **2024**, *53*, 12176-12188. DOI: doi.org/10.1039/D4DT01296H

14 M. Radzieowski, **E. C. J. Gießelmann**, S. Engel, O. Janka, Structure, Physical and 27Al NMR Spectroscopic Properties of the Missing Members of the Equiatomic REAlRh (RE = Sm, Tb, Dy, Er, and Lu) series, *Z. Naturforsch. B* **2024**, *79*, 459-467. DOI: doi.org/10.1515/znb-2024-0053

13 I.-A. Bischoff, S. Danés, P. Thoni, B. Morgenstern, D. M. Andrada, C. Müller, J. Lambert, **E. C. J. Gießelmann**, M. Zimmer, A. Schäfer, A lithium-aluminium heterobimetallic dimetallocene, *Nat. Chem.* **2024**, *16*, 1093-1100. DOI: doi.org/10.1038/s41557-024-01531-y

12 **E. C. J. Gießelmann**, S. Engel, J. Baldauf, J. Kösters, S. F. Matar, G. Kickelbick, O. Janka, Searching for Laves Phase Superstructures: Structural and ^{27}Al NMR Spectroscopic Investigations in the Hf−V−Al System, *Inorg. Chem.* **2024**, *63*, 8180-8193. DOI: doi.org/10.1021/acs.inorgchem.4c00391

11 S. Engel, **E. C. J. Gießelmann**, M. K. Reimann, R. Pöttgen, O. Janka, On the ytterbium valence and the physical properties in selected intermetallic phases, *ACS Organic & Inorganic Au* **2024**, *4*, 188-222. DOI: doi.org/10.1021/acsorginorgau.3c00054

10 **E. C. J. Gießelmann**, S. Engel, J. G. Volpini, H. Huppertz, G. Kickelbick, O. Janka, Mechanistic Studies on the Formation of Ternary Oxides by Thermal Oxidation of the Cubic Laves Phase CaAl$_2$, *Inorg. Chem. Front.* **2024**, *11*, 286-297. DOI: doi.org/10.1039/d3qi01604h

9 **E. C. J. Gießelmann**, R. Pöttgen, O. Janka, Laves phases: superstructures induced by coloring and distortions, *Z. Allg. Anorg. Chem.* **2023**, *649*, e202300109. DOI: doi.org/10.1002/zaac.202300109

8 **E. C. J. Gießelmann**, S. Engel, I. El Saudi, L. Schumacher, M. Radzieowski, J. M. Gerdes, O. Janka, On the RE_2TiAl$_3$ (RE = Y, Gd-Tm, Lu) series – the first aluminum representatives of the rhombohedral Mg$_2$Ni$_3$Si type structure, *Solids* **2023**, *4*, 166-180. DOI: doi.org/10.3390/solids4030011

7 **E. C. J. Gießelmann**, M. Radzieowski, S. F. Matar, O. Janka, Formation of the Sub-Oxide $Sc_4Au_2O_{1-x}$ and Drastically Negative ^{27}Al NMR Shift in Sc_2Al, *Inorg. Chem.* **2023**, *62*, 9602-9617. DOI: doi.org/10.1021/acs.inorgchem.3c01097

6 S. Engel, **E. C. J. Gießelmann**, R. Pöttgen, O. Janka, Trivalent Europium – A scarce case in intermetallics, *Rev. Inorg. Chem.* **2023**, *43*, 571-582. DOI: doi.org/10.1515/revic-2023-0003

5 A. Michaely, O. Janka, **E. C. J. Gießelmann**, R. Haberkorn, H. T. A. Wiedemann, C. W. M. Kay, G. Kickelbick, Black Titania and Niobia within Ten Minutes – Mechanochemical Reduction of Metal Oxides with Alkali Metal Hydrides, *Chem. Eur. J.* **2023**, *29*, e202300223. DOI: doi.org/10.1002/chem.202300223

4 **E. C. J. Gießelmann**, S. Engel, W. Kostusiak, Y. Zhang, P. Herbeck-Engel, G. Kickelbick, O. Janka, Raman and NMR Spectroscopic and Theoretical Investigations of the Cubic Laves-Phases $REAl_2$ (*RE* = Sc, Y, La, Yb, Lu), *Dalton Trans.* **2023**, *52*, 3391-3402. DOI: doi.org/10.1039/D3DT00141E

3 S. Engel, **E. C. J. Gießelmann**, L. E. Schank, G. Heymann, K. Brix, R. Kautenburger, H. P. Beck, O. Janka, Theoretical and ^{27}Al NMR Spectroscopic Investigations of Binary Intermetallic Alkaline-Earth Aluminides, *Inorg. Chem.* **2023**, *62*, 4260-4271. DOI: doi.org/10.1021/acs.inorgchem.2c04391

2 **E. Gießelmann**, R. S. Touzani, B. Morgenstern, O. Janka, Synthesis, crystal and electronic structure of $CaNi_2Al_8$, *Z. Naturforsch. B* **2021**, *76*, 659-668. DOI: doi.org/10.1515/znb-2021-0105

1 H. P. Beck, M. Zhou, P. Hasanovic, **E. Gießelmann**, M. Springborg, Course on the Use of DFT Calculations to Improve Understanding of Phase Diagrams in Solid-State Chemistry, *J. Chem. Edu.* **2021**, *98*, 3207-3217. DOI: doi.org/10.1021/acs.jchemed.1c00510

Table of content

1 Motivation

The research area on intermetallic compounds plays a crucial role in many everyday life applications and brings together material scientists, physicists and of course chemists.

The latter are interested, sometimes fascinated and sometimes desperate about the unmanageable variety of structures that can be formed by combining two, three or more metals. To investigate all facets of these compounds, methods for structure determination such as X-ray diffraction on powders and single crystals, spectroscopic investigations such as solid state nuclear magnetic resonance, X-ray absorption or fluorescence and Mössbauer spectroscopy as well as quantum-chemical DFT-based calculations using the program packages VASP and LOBSTER, just to name examples, are used. Solid state physicists are always searching for new interesting physical phenomena found in intermetallic compounds, such as magnetic ordering, superconductivity, thermoelectric behavior, heavy-fermion behavior, the Kondo effect, charge density waves and many more. Finally, material scientists are fascinated by extraordinary mechanical properties (e.g. high tensile strength) combined with low density as well as ultrahigh thermal stability found in alloys or intermetallic compounds, that qualifies them for use in highly corrosive environments.

Examples for intermetallic compounds in various applications are the superconductor Nb_3Sn used in NMR and MRI instruments,[1] the permanent magnets $SmCo_5$,[2] Sm_2Co_{17},[3] and $Nd_2Fe_{14}B$,[4] the magnetocaloric compound $Gd_5Si_2Ge_2$[5] or $Yb_{14}MnSb_{11}$[6] which is a highly interesting thermoelectric material. The explorative syntheses in the system Mn-Al led to the discovery of aperiodic materials followed by many more quasicrystalline compounds; all formed by the combination of solely metallic elements.[7, 8]

Intermetallic compounds can be formed by almost every combination of two metals in the periodic table (exceptions confirm a rule). A comprehensive overview sorting intermetallic compounds and their structures by the main (group) element, respectively the network builder, is given in a recent textbook by Pöttgen and Johrendt.[8] An overview focusing on the most important rare earth element containing compounds is given in the chapter by Janka and Pöttgen in “Rare Earth chemistry”.[9] Further aspects of intermetallic compounds can be found in other textbooks.[10-12] Moreover, various review articles addressing different families of compounds can be found in literature.[13-18] This work sets a focus on intermetallic compounds containing aluminum as the main element and usually the only p-block element.

When it comes to real life applications, aluminum intermetallics (or alloys) are interesting since aluminum belongs to the light elements/metals and therefore forms light-weight materials. Element combinations that are the most prominent ones are with Ni or Ti, namely NiAl and Ni_3Al,[19, 20] as well as TiAl and Ti_3Al,[21] which show high stability and good mechanical properties. For the tuning of specific properties, additional metals can be incorporated. An additional benefit is the low cost of aluminum.[22, 23]

The variety in structural chemistry of aluminum containing binary and ternary compounds is overwhelming. Aluminum forms binary compounds with almost all metallic elements, one clear exception is found for the alkaline metals, except for lithium. When it comes to ternary compounds the same applies with the addition that all metals can form ternary compounds containing aluminum. The variety of structures becomes unmanageable. Therefore, databases like the Pearson's Crystal Data database become an important tool for solid state chemists.[24] Many of the above-mentioned properties and phenomena apply to compounds with aluminum. Therefore, explorative synthesis is necessary to fill gaps within science. If isostructural series are identified by changing the additional elements, it is possible to compare the structural and/or spectroscopic properties. For this thesis a focus was put on intermetallic compounds with aluminum combined with two early transition metals or combined with one rare earth metal and a transition metal (mainly groups IV & V).

Besides the interesting structures and properties of aluminum intermetallics, this dissertation also deals with the oxidation behavior of these compounds and wants to extend the knowledge on the usage of these materials as potential precursor materials for non-metallic (oxides, sulfides etc.) products. This topic has only been scarcely investigated in literature, although a strong focus was set on the corrosion behavior with regards to applications.

Aluminum is an element with a high oxophilicity under high temperatures resulting in passivating surface layers that qualify the materials for the application in high corrosive environments.[25] This is the case, for example, with the above-mentioned combination of aluminum and the noble metal nickel.[19] For the case of Ti and Al the resulting oxides highly depend on the conditions like atmosphere and temperature, however, in many cases undesired TiO_2 is formed. If e.g. Nb or Cr is added to the phase, the oxidation products and kinetics can change dramatically.[21]

From a chemical point of view, the question of whether a binary aluminum compound can be used for the selective synthesis of oxidation products is extremely interesting. Reactions that

do not lead to the desired or expected product can provide insights into the reaction pathways through analysis of the products obtained. The investigation of the influence of various reaction parameters can probably be applied to other systems.

2 Introduction

2.1 On the existence, structural chemistry and interesting properties of selected important intermetallic (aluminum) compounds

The focus, or rather the starting point, of this work are (mostly binary) aluminum compounds containing either alkaline earth metals (*AE* = Ca-Ba), rare earth metals (*RE* = Sc, Y, La-Nd, Sm-Lu) or the early transition metals of group IV (Ti-Hf). These seemed to be a good starting point for investigating the oxidation behavior. Moreover, ternary compounds of these given elements with an additional early transition metal (group V-VI) were investigated. The late transition metals of groups VIII-XI are only sporadically used and therefore shall not be discussed in detail. The following section is intended to give a comprehensive and not even nearly complete overview of the existence of important intermetallic compounds with different compositions; to explain the structure types and point out some interesting findings already reported in the literature.

This overview is important for the following work for two reasons. On the one hand, series of compounds adopting the same composition and/or structure enable systematic investigation of either spectroscopic properties or the oxidation behavior. On the other hand, it enables systematic studies for the finding of new multinary compounds.

2.1.1 Laves phases and their superstructures

When discussing the above-mentioned combinations of metals with aluminum, a discussion of the Laves phases is unavoidable. The so-called Laves phases (named after the crystallographer Fritz Laves)[26, 27] adopt three structure types namely cubic $MgCu_2$ ($Fd\bar{3}m$),[28] as well as hexagonal $MgZn_2$[29, 30] and $MgNi_2$ (both $P6_3/mmc$).[31, 32] They belong to a larger family of compounds called Frank-Kasper phases, which will be explained a little in section 2.1.2. The three basis structure types have in common that they show the same composition of AB_2 with the element *A* being larger (atomic radius) than *B*. For the discussion, *B* is considered as a network forming element, while *A* remains in the voids, respectively cavities, of the network. The optimal theoretical atomic radii ratio can be calculated to $r_A/r_B \approx 1.225$, while a broad spread of this ratio from ~1.1 to ~1.7 is found. More and detailed information on the applications and properties can be found in an extensive review by Leineweber.[33] A review article published during the process of this thesis set a focus on the structural variety of the superstructures that can be derived from the Laves phases (*vide infra*).[34]

All three structures have in common, that the connection mode of the B-atoms is identical. They form empty tetrahedra, which are connected in different modes. The Laves phases can also be considered as tetrahedrally closest-packed structures. The tetrahedra are either only connected *via* the corners ($MgCu_2$ type) or they form an empty trigonal bipyramid or a trigonal antiprism around a central *B*-atom ($MgZn_2$ type). The $MgNi_2$ type can be understood as an intergrowth, in which both connection modes are present. The three prototypes are shown in Figure 1.

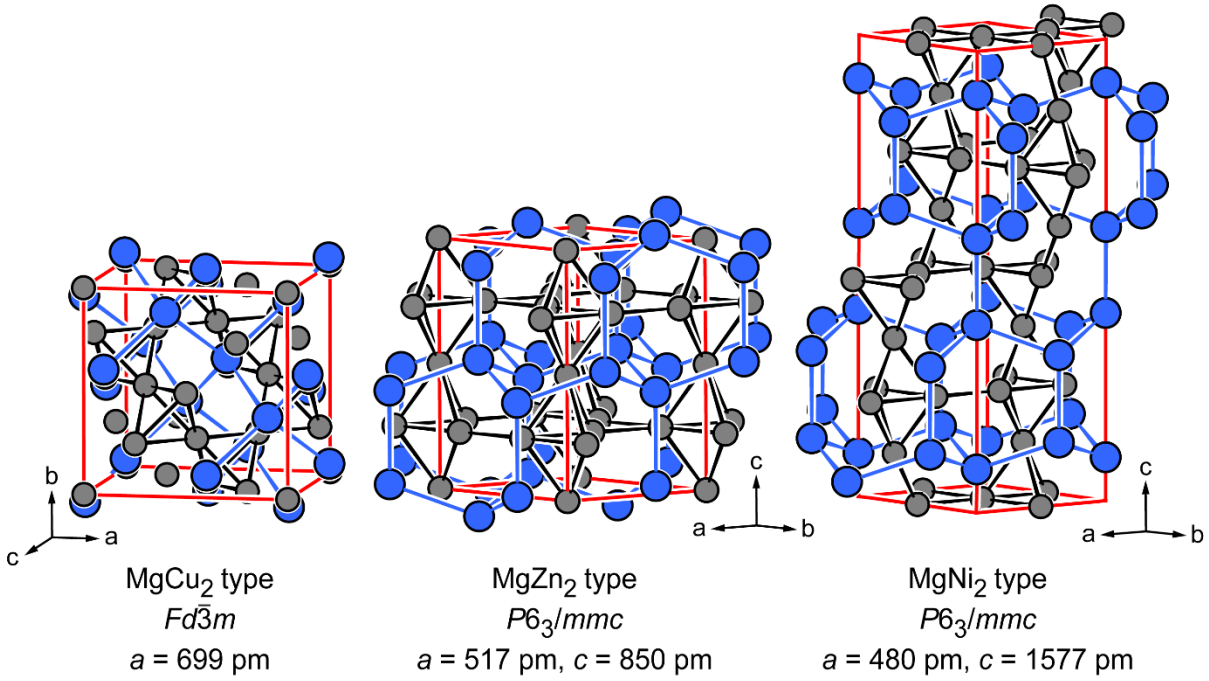

Figure 1. Crystal structures of the three prototypes of the Laves phases. The network building atom *B* (Cu, Zn, Ni) is shown as grey spheres, while the Mg atoms (cavities) are colored blue.

The importance of the Laves phases in aluminum chemistry is illustrated in Figure 2. All rare earth elements (Sc, Y, La-Nd, Sm-Lu) as well as Ca and U form the compounds MAl_2 adopting the $MgCu_2$ structure type as usually most stable phase under normal conditions.[24] For Sr, Ba and Th, these phases are reported as high-pressure compounds.[35, 36] Under ambient conditions, Hf and Zr crystallize in the hexagonal $MgZn_2$ structure type.[37, 38] "$MgAl_2$" is reported as an off-stoichiometry and metastable phase with mixed site occupancies of Mg and Al on the Zn positions of $MgZn_2$.[39]

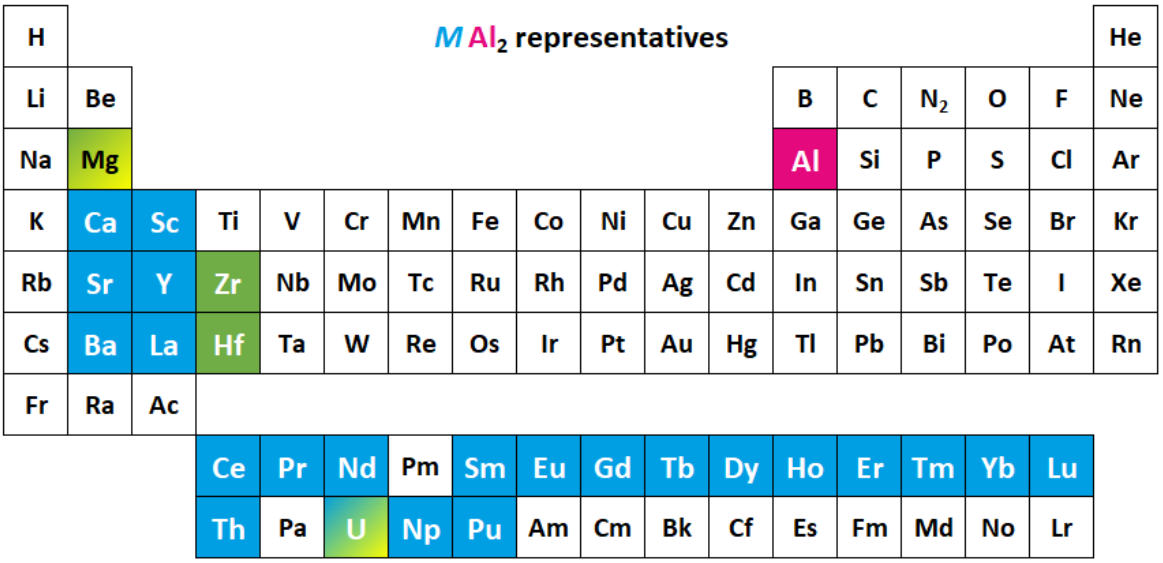

Figure 2. Existence of the three Laves phases for the general formula MAl_2. $MgCu_2$ type compounds are colored blue, $MgZn_2$ type green and $MgNi_2$ type yellow. Multiple colors indicate polymorphism.[24]

An interesting point here is the absence of binary Laves phase type compounds with the surrounding elements of aluminum (e.g. B, Ga, Si, Ge) in the p-block as *B* element. For most other main group elements, no binary compounds adopting the Laves phase structures are known, except for some lead and bismuth compounds as well as non-intermetallic high-pressure phases of nitrogen, hydrogen and noble gases, such as $NeHe_2$,[40] stressing the closest-packed structure for two given atoms of different sizee realized in these structures.

A distribution of the observed ratio of the atomic radii becomes immediately clear when looking at Figure 2. With e.g. r_{atom}(Sc) = 161, r_{atom} (La) = 188 and r_{atom}(Al) = 143 pm, it becomes clear that small deviations in the optimal geometry are allowed in the gain of most likely electronic stabilization which can be the main reason for the formation of these structure types then.[41]

Interestingly, for many combinations of early transition metals the Laves phase exists; examples for this are e.g. ZrV_2 and HfV_2 or MCr_2 (*M* = Ti, Zr, Hf, Ta, Nb).[42] For many systems it is moreover the only binary compound known. This again shows their remarkable stability and importance for structural chemistry of the early transition metals as well. Some of these compounds show interesting properties, for example superconductivity in HfV_2 below T_C = 9.6 K.[43] This compound also shows an interesting phase transition at low temperatures, which leads to another large field of structural chemistry. More binary distortions variants as well as ternary coloring and puckering variants can be derived from the highly symmetric structures of the Laves phases. The already mentioned HfV_2 undergoes a phase transition to the distorted

YMn_2 ($I4_1/amd$) type and then to the orthorhombic UMn_2 (*Imma*) type.[44] This structural relationship can be expressed in a group-subgroup scheme following the Bärnighausen formalism.[45-48] For structures that are related to the cubic Laves phase, this scheme is shown in Figure 3. It indicates the reduction of symmetry leading to different space groups as well as the transformations of the unit cell. Indices *k* and *t* stand for *klassengleiche*, respectively *translationengleiche* transition. The discussed phases can be found in the right part of the scheme.

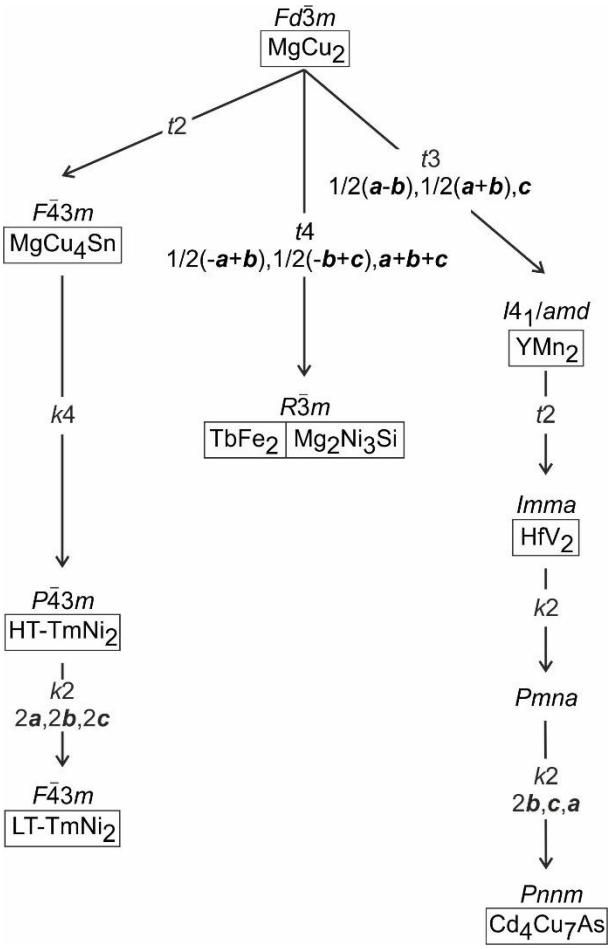

Figure 3. Group-subgroup scheme in the Bärnighausen formalism for the $MgCu_2$ superstructures. The indices for the *klassengleiche* (*k*) and *translationengleiche* (*t*) symmetry reductions and the unit cell transformations are given. Reprinted from *Z. Anorg. Allg. Chem.* **2023**, *649*, e202300109, published under CC BY-NC-ND 4.0. Copyright 2025 WILEY-VCH.

As can already be seen in Figure 3, the discussed example is only one of the many structure types that can be derived from the three basic Laves phase structures. To stress this structural variety, some of these structures and some important representatives will be discussed in the following.

The easiest ternary compound that can be derived starting from $MgZn_2$ is the ternary coloring variant of $MgZn_2$. Since this structure has two different Zn positions in a 3:1 ratio (Wyckoff positions 6*h* and 2*a*), coloring allows for the formation of compounds without the loss of symmetry. The prototype for this is the Mg_2Cu_3Si type structure ($P6_3/mmc$).[49] Many aluminum compounds such as Ce_2RuAl_3,[50] U_2Cu_3Al,[51] the series RE_2TAl_3 (*RE* = Y, La-Nd, Sm, Gd–Lu and *T* = Ru, Rh, Ir),[52] the gallium compounds U_2Fe_3Ga,[53] Eu_2IrGa_3[54] or the germanide Mn_2Co_3Ge[55] are reported. The same composition cannot be formed starting from the cubic Laves phase $MgCu_2$ without the loss of symmetry. However, a *translationengleiche* symmetry reduction of index 4 leads to the trigonal crystal system and space group $R\bar{3}m$ allowing for coloring and the formation of the Mg_2Ni_3Si (respectively $TbFe_2$) type structure, as expressed in the middle path of Figure 3.[56, 57] Here, the gallium representatives RE_2Rh_3Ga (*RE* = Y, La-Nd, Sm, Gd-Er),[58] the silicides RE_2Rh_3Si (*RE* = Ce, Pr, Er)[59, 60] or the germanide Ca_2Pd_3Ge[61] are known. Another possibility is the formation of the cubic Al_2Mo_3C type structure ($P4_132$).[62] Here, for example, the aluminum auride Na_2Au_3Al is reported.[63]

When looking at this list of compounds (which is not intended to be a complete list by all means), one interesting observation can be made. While the most compounds reported follow the general formula M_2T_3X with *X* being Ga, Ge or Si, the Al representatives tend to form the corresponding antitypes, with respect to the transition metal. This observation can be made at quite some points in literature. Exceptions confirm a trend. Some examples are e.g. the YNi_5Si_3 prototype (*Pnma*), for which all aluminum compounds reported show the main group element rich antitype such as the MPt_3Al_5 (*M* = Ca, Y, La–Nd, Sm–Er) series[64, 65] or $Eu_2Ni_8Si_3$ and $Sr_2Al_8Pt_3$.[66]

URe_2 (*Cmcm*) is an orthorhombic distortion variant of $MgZn_2$.[67] The coloring of this compound leads to Mg_2MnGa_3[68] or Mg_2NiGa_3.[69] Staying with binary distortion variants, from the cubic Laves phase the two polymorphs of $TmNi_2$, adopting the cubic space groups $P\bar{4}3m$ and $F\bar{4}3m$, can be derived *via* two consecutive structural transformations.[70] The transformation from cubic $MgCu_2$ to tetragonal YMn_2 ($I4_1/amd$)[71] down to orthorhombic UMn_2 type structure (*Imma*),[72] which is realized for e.g. HfV_2 at low temperatures, has already been mentioned.[44] Further symmetry reduction leads to the so far only known compound adopting this structure, orthorhombic Cd_4Cu_7As (*Pnnm*).[73]

Compounds close to the equiatomic compositions are the reported gallium compounds $RE_6Ir_5Ga_7$ (*RE* = Sc, Y, Nd, Sm, Gd–Lu)[74] and aluminum representatives $RE_6T_5Al_7$ (*RE* = Sc,

Y, Ce-Nd, Sm, Gd-Lu, T = Ru, Ir)[74] adopting the $Yb_6Ir_5Ga_7$ type structure ($P6_3/mcm$).[75] If a compound is not fully ordered, one would expect a statistical mixing within, for example, the $MgZn_2$ structure type. The finding of the mixed site occupancy in compounds like $Nb_{6.4}Ir_4Al_{7.6}$ shows that site occupancy accompanied by symmetry changes are possible.[76]

Lastly, the structures of $MnCu_4In$ ($P6_3mc$)[77] and $MgCu_4Sn$ ($F\bar{4}3m$),[78] one of the very few variants in which a splitting of the positions of the *A* atoms leaving the composition $A(C_{1-x}B_x)_2$ accompanied by different coloring are reported. The structural transformation for the latter is shown in the left part of Figure 3. Many isostructural compounds have been reported. [79-82] Some examples for the discussed structure types are summarized in Figure 4.

Two interesting things that clearly motivate further work on these types of compounds are that their structural variety is not fully explored yet and the formation of distinct structures with certain element combinations is not predictable in any way. It was further explained that the existence of the binary Laves phases involving main group elements is limited to aluminum. However, the discussion of all ternary variants clearly shows that in the ternary system these structures can be formed by almost all metallic elements of the periodic table. And even this limitation is only partially true, since the Laves phases also come up in compounds involving non- or semimetals like the discussed Cd_4Cu_7As (*Pnnm*)[73] or in the phosphides Mg_2Ni_3P (Mg_2Ni_3Si type, $R\bar{3}m$).[83]

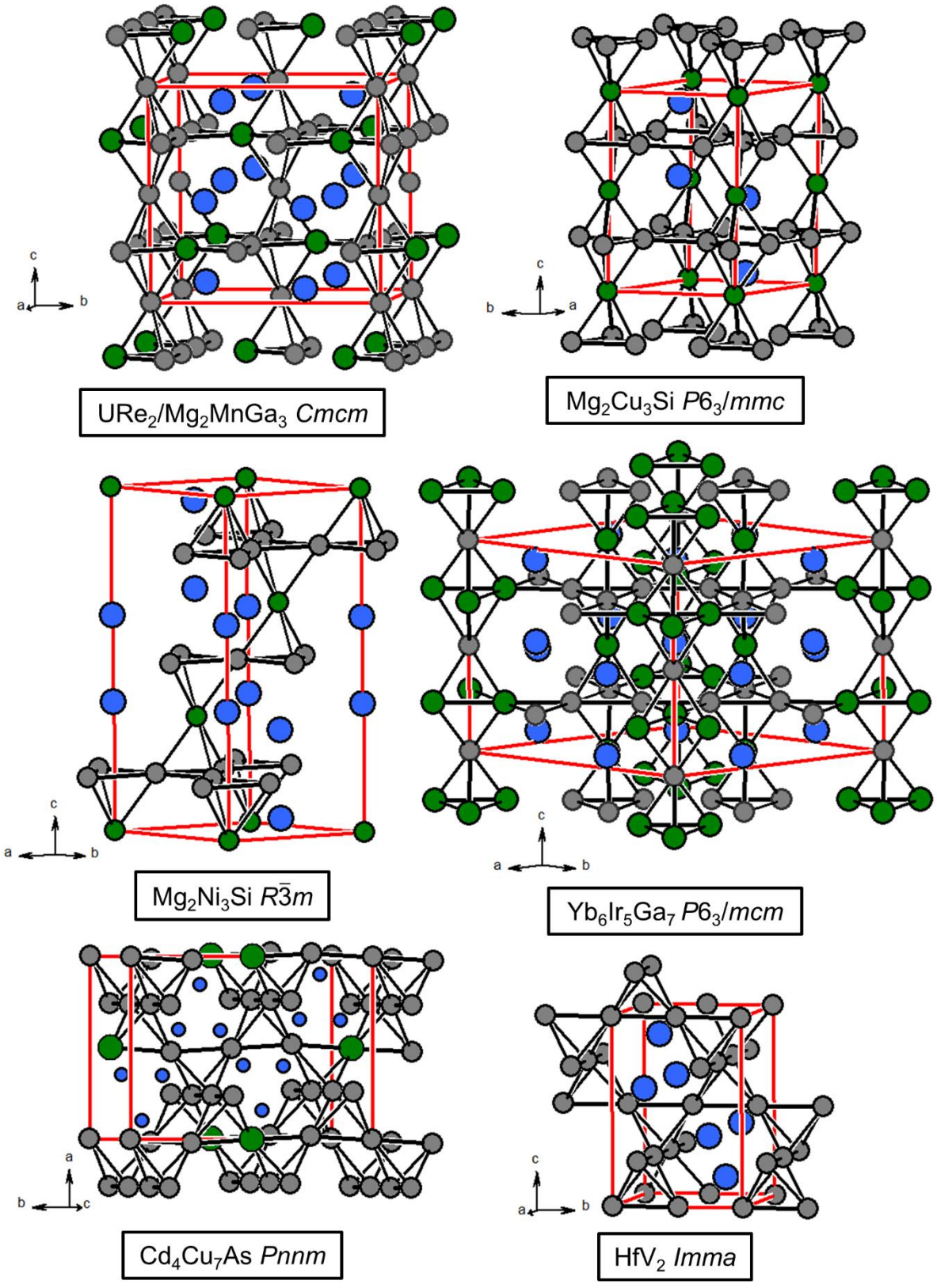

Figure 4. Structural examples for the compounds discussed in this section. The network of the condensed tetrahedra is emphasized. The cavity atoms are depicted as blue spheres, while the network atoms are shown as grey and green spheres.

2.1.2 Frank-Kasper phases

As already mentioned, the Laves phases belong to a larger family of structural familiar compounds, namely the "so-called" Frank-Kasper phases, named after the two scientists, F. C. Frank and J. S. Kasper, that introduced the concept of topological closest packing.[84, 85]

For the closest packing of equally sized spheres the cubic closest packing (*ccp*, $Fm\bar{3}m$) and the hexagonal closest packing (*hcp*, $P6_3/mmc$) are the preferred structure types, which have an optimal space filling of 74.05 %. These structures are adopted by many metallic elements, such as Al, Cu and Au as examples for *ccp* and Mg, Zn or Sc and Y as selected examples for *hcp*. From these structures many examples of coloring variants can be derived. Within these structures the highest possible coordination number that can occur is 12. It is realized as either a cuboctahedron (*ccp*) or anticuboctahedron (*hcp*), both shown in Figure 5. Another possibility for the same coordination number is an icosahedron, which is not found in the closest packing of equally sized spheres. However, Frank and Kasper found that this coordination environment is often found in more complex structures together with three other coordination environments of the coordination numbers (CN) 14, 15 and 16. The Frank-Kasper phases are complex phases of at least two elements with different sizes for which only these four coordination environments are realized. These four coordination environments have in common, that they have only triangular faces in contrast to the *ccp* and *hcp* structures in which still rectangles are present. They are called topological densest structures.

One example has already been discussed with the Laves phases being by far the most prominent Frank-Kasper phases. The coordination environment is shown in Figure 5 for the example of $ScAl_2$ adopting the $MgCu_2$ structure type. Here, only the coordination numbers 12 and 16 are present. The different combinations of these coordination environments lead to a high variety of compounds, with totally different elements and compositions. Besides the Laves phases other important structure types, such as the already mentioned prominent superconductor Nb_3Sn, also are Frank-Kasper phases. The coordination environments here are 14 ($Nb@Sn_4Nb_{10}$) and 12 ($Sn@Nb_{12}$). Other examples are β-Mg_2Al_3,[86, 87] the σ-phase as well as the *P*- and *R*-phases.[84]

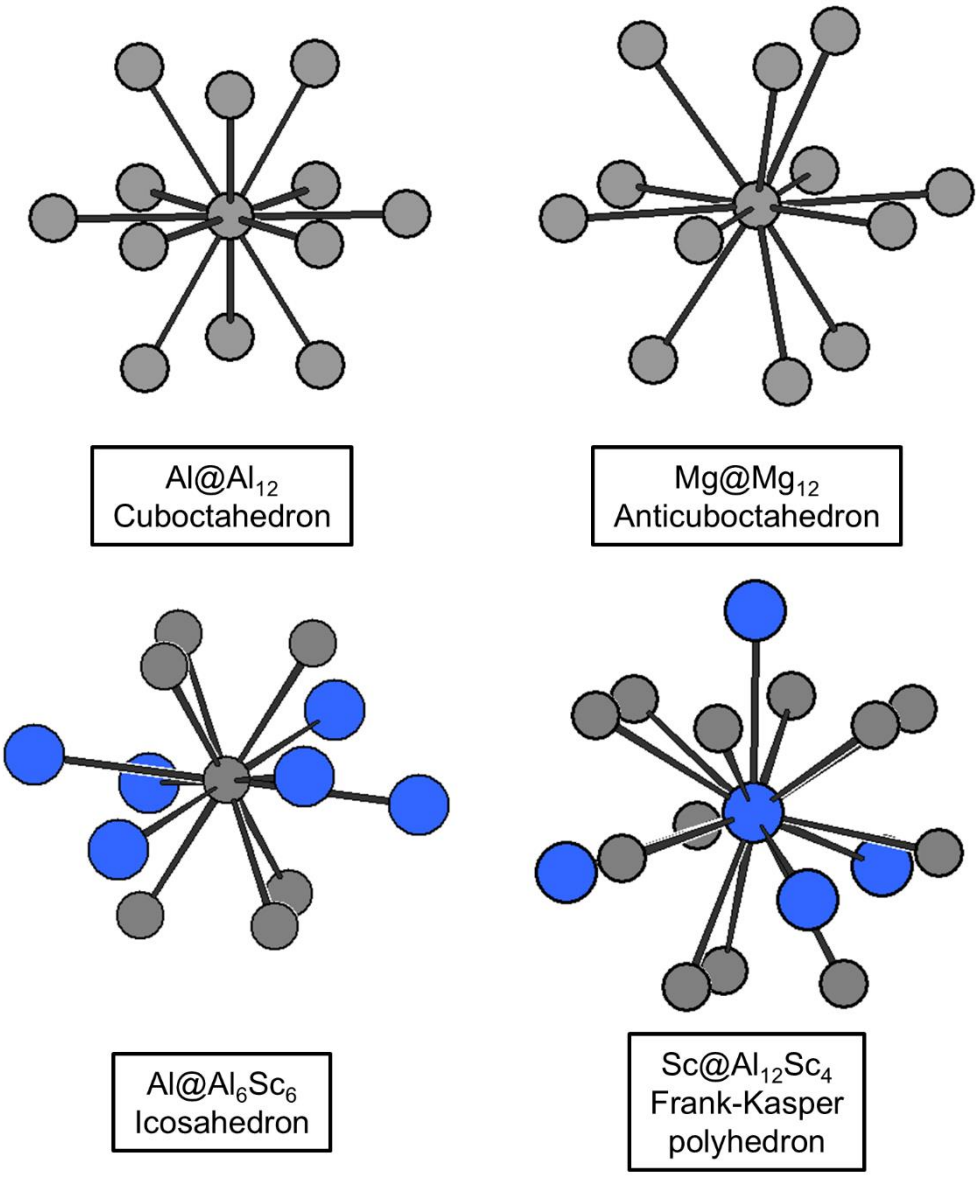

Figure 5. Different coordination environments in the closest packing (*hcp* and *ccp*) vs. the Frank Kasper polyhedra for CN = 12 and 16.

Lastly, two structure types shall be mentioned in a little more detail; the Zr_4Al_3 structure type (*P*6/*mmm*),[88] which is adopted by Zr and Hf in combination with aluminum.[89] These are the only two binary examples for this structure type. Aluminum is coordinated in an icosahedral fashion ($Al@Al_4Zr_8$), while two Zr atoms are surrounded by a 14 ($Zr1@Al_6Zr_8$) and 15 ($Zr2@Al_6Zr_9$) atoms forming the remaining two Frank-Kasper polyhedron. The so-called μ-phase, W_6Fe_7 type ($R\bar{3}m$),[90] is an interesting example for the appearance of all Frank-Kasper polyhedral, within the same structure. Binary examples for this structure are Nb_6Zn_7[91] or nominal Nb_6Ni_7 and Ta_6Ni_7,[92] both reported with mixed site occupancies. For aluminum, many ternary disordered compounds with mixed site occupancies are reported, e.g. in the systems Zr–

Cu–Al or Hf–Ag–Al.[93] The structure of the W_6Fe_7 structure type represented by the respective coordination polyhedral is shown in Figure 6.

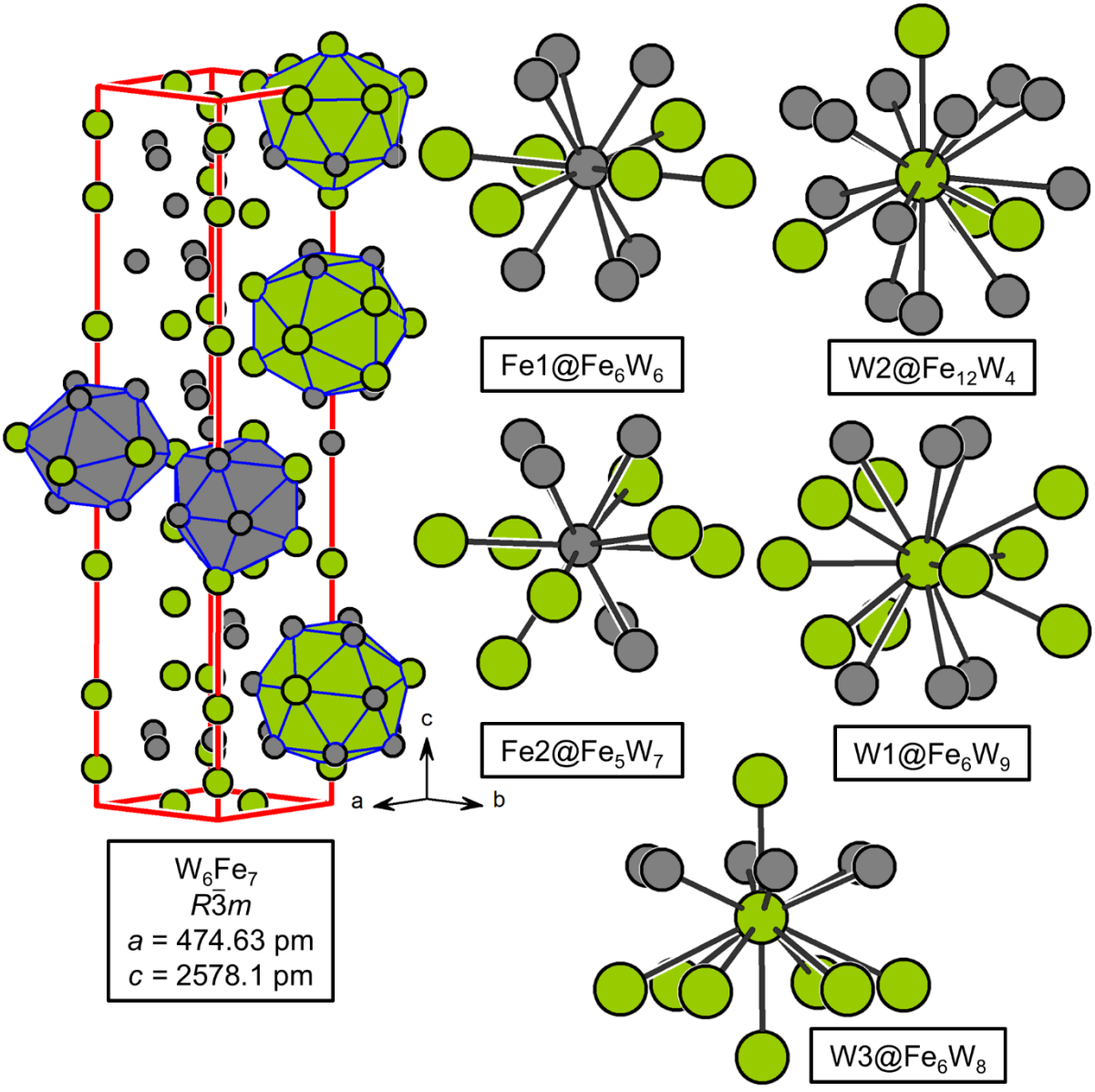

Figure 6. Unit cell and crystallographic environments of the five atoms in the W_6Fe_7 type. All Frank Kasper polyhedra are present. W and Fe are represented as green, respectively grey, spheres.

2.1.3 Other important binary structure types in intermetallic aluminum chemistry

Interestingly, besides the already discussed Laves phases, it is hard to identify families of binary compounds that adopt the same structure type and are that prominent in aluminum chemistry. It is, however, at least possible to identify some prominent compositions.

Sticking with the composition of the Laves phases; when looking at Figure 2, it is quite puzzling that titanium is the only element from all the relevant ones that does not form the Laves phase. The formed compound $TiAl_2$ adopts the $HfGa_2$ type structure ($I4_1/amd$).[94] With this structure type also metastable $MgAl_2$ was reported.[95] The compound $SrAl_2$, which is the ambient pressure variant, undergoes a phase transition to $MgCu_2$ type under high pressures. It adopts the KHg_2 type (*Imma*) and is the only binary aluminum compound to exist in that specific structure.[96] This is comparable to the Ba compound which also forms cubic $BaAl_2$ only at high pressures. In contrast to $SrAl_2$ a stable "$BaAl_2$" formed under ambient conditions does not exist. Instead, a complex structure with the nominal composition $Ba_{21}Al_{40}$ (own type $P31m$) could be identified. This structure is strongly related to the hexagonal $MgNi_2$ type.[97]

When further looking at the alkaline earth metals, as well as Europium, the only isostructural family of compounds exists for the composition MAl_4 (M = Ca, Sr, Ba and Eu), adopting the $BaAl_4$ structure type.[98-101] It has to be mentioned that the Ca compound adopts a monoclinic distorted variant at room temperature and undergoes a phase transition to the tetragonal phase at 443 K.[102] For the rare earth metals La, Ce-Nd and Sm a phase being isostructural was postulated but later corrected to the composition RE_3Al_{11} adopting the La_3Al_{11} type (*Immm*).[103]

As already stated, identifying other compositions that are often found is easy when looking at the system *M*–Al (*M* = *RE*, Ti-Hf, V-Ta). However, here no example with large families of isostructural compounds can be identified anymore. The occurrence of the Laves phases for so many elements is outstanding.

A composition that is often found has the general formula 1:3 or vice versa. For the general formula MAl_3 compounds with M = Sc-La, Ti-Hf, V-Ta and all lanthanoids (except for Eu) are listed in the Pearson's Crystal Data database.[24] The main structure types are the Cu_3Au structure type ($Pm\bar{3}m$),[104] which is a coloring variant of the cubic closest packing. And the hexagonal Mg_3Cd (Ni_3Sn) structure type ($P6_3/mmc$), which is a stacking variant of the hexagonal closest packing.[105] For the elements of groups IV-V, the dominant structure types

are the tetragonal $TiAl_3$ and $ZrAl_3$ (both $I4/mmm$),[106, 107] being superstructures of the cubic closest packing.

The aluminum poor counterpart M_3Al only exists for some examples such as M = Y, La, Ti, Zr, V, Nb, Ce-Nd and Tb. Here, still the structure types Cu_3Au and Ni_3Sn are the most prominent ones next to the Cr_3Si type ($Pm\bar{3}n$), which is adopted by the V and Nb compound.[94]

Lastly the equiatomic composition shall be mentioned. Sc is the only example to only adopt the CsCl ($Pm\bar{3}m$) structure type.[108] An equiatomic compound exists for all rare earth elements, except for Nd, Yb and Lu. Besides other, the DyAl type structure ($Pbcm$) is the most prominent one.[109] Y, La as well as Ti-Hf compounds exist but do, however, form multiple different structure types.[24] The compound EuAl (own type, $Pmmn$) is the only representative of its own structure type so far.[110]

2.1.4 Ternary compounds

This section is supposed to give a short overview on the few structures of ternary compounds that are known for the combination of mainly elements that are colored in Figure 2, being group II-IV metals as well as the lanthanoids, in combination with other transition metals, mostly of group IV-VI. The reason that group IV is mentioned twice here, is that titanium mostly shows different behavior compared to Zr and Hf. In this context, it must be mentioned, that many reports on solid solutions realized for example in the elemental structures, the Laves phases or the $ThMn_{12}$ type ($I4/mmm$)[111] are reported regarding these element combinations.[24] However, this is not the main interest here.

The two main prototypes that have to be mentioned here are the cubic $CeCr_2Al_{20}$ ($Fd\bar{3}m$)[112] and the hexagonal $Ho_6Mo_4Al_{43}$($P6_3/mcm$).[113] The occurrence of the first one alongside with interesting physical phenomena has been reviewed recently.[114] The $CeCr_2Al_{20}$ structure type can be understood as a ternary coloring variant of $ZrZn_{22}$.[115] A second example for this is the $Mg_2Cr_3Al_{18}$ type structure[116] of which several representatives are reported, all following the formula $Mg_2T_3Al_{18}$ (T = Ti, V, Mn).[117, 118] The structure itself is highly interesting since it is strongly related to the cubic Laves phase, not only because they share the same space group. The network formed by the $CeCr_2$ substructure is identical to the atoms in $MgCu_2$. This network is stuffed with 20 more atoms, leading to extremely long Ce-Ce distances (<500 pm). However, the coordination polyhedra remain the same. Cr is surrounded by 12, whereas Ce is surrounded by 16 aluminum atoms in the manner of an icosahedron and a 16 Frank-Kasper polyhedron (Figure 7). The coordination environment of the aluminum atoms is described by

bi-capped hexagonal and pentagonal prisms. Al1 is surrounded by 12 aluminum atoms and two capping cerium atoms (Al1@$Al_{12}Ce_2$). For Al2, ten aluminum atoms are arranged as pentagonal prism capped with two chromium atoms (Al2@$Al_{10}Cr_2$). For Al3, a mixture is observed. The pentagonal prism of ten aluminum atoms is capped with one cerium and chromium atom (Al3@$Al_{10}CrCe$).

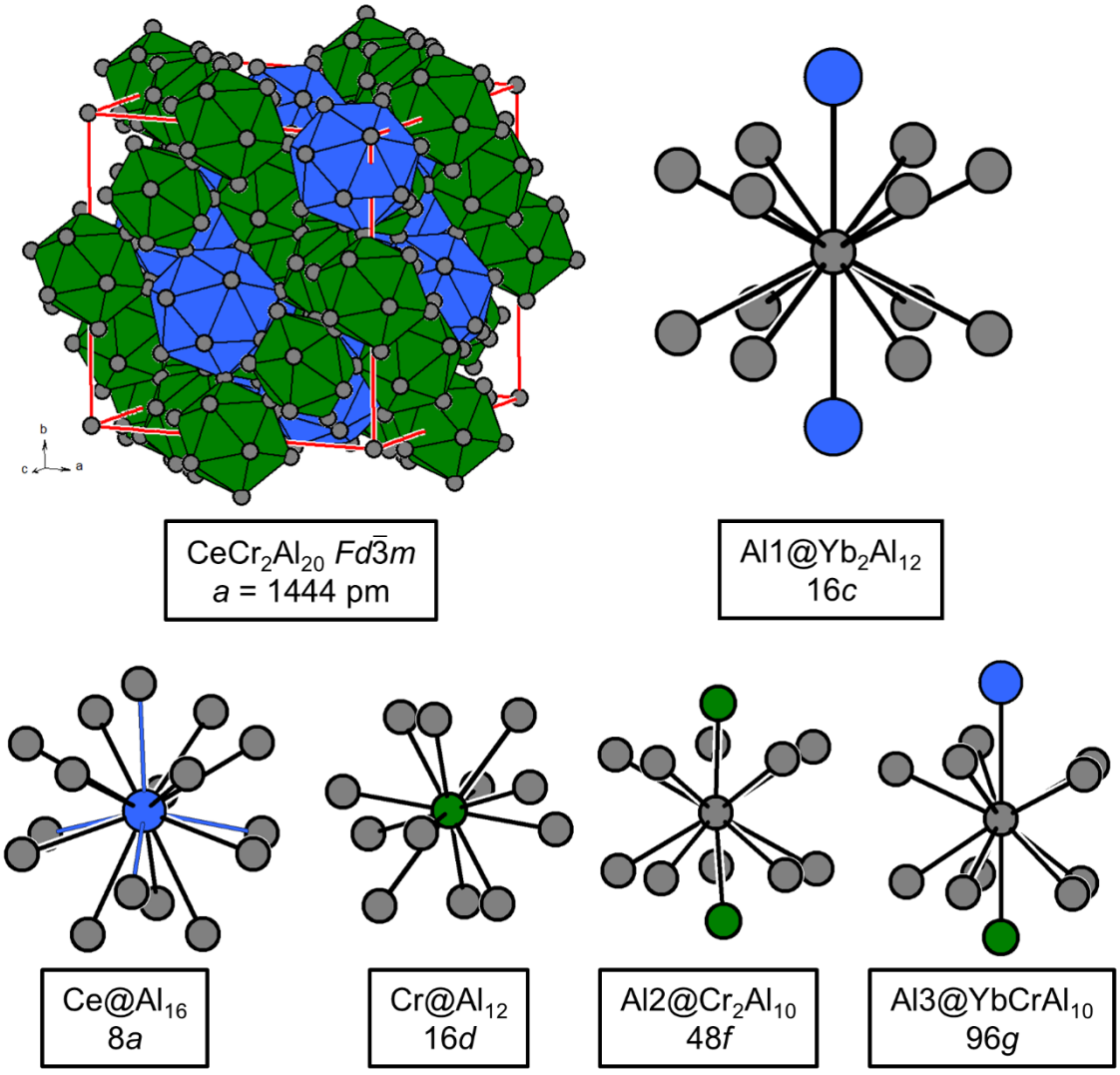

Figure 7. Unit cell and coordination environments of the $CeCr_2Al_{20}$ structure type.[112, 114]

This structure type is formed by the main group elements aluminum but also many zinc and cadmium compounds are known. Focusing on the aluminum case, it is highly interesting that for the general formula RET_2Al_{20} (*RE* = Sc, Y, La-Nd, Sm-Lu) only compounds with *T* being an early transition metal (*T* = Ti, V-Ta, Cr-W and Mn) are known. For *T* = Ti-Mo, Ca compounds are also reported. In comparison for RET_2Zn_{20} and RET_2Cd_{20} (*RE* = Sc, Y, La-Nd, Sm-Lu), only compounds with *T* = Fe-Os, Co-Ir and Ni are known. In the case of the Zn compounds also compounds like $ZrCr_2Zn_{20}$ or $HfCo_2Zn_{20}$ are known. Many of these

compounds were investigated towards the formation of solid solutions, their magnetic and spectroscopic properties as well as superconductivity, which is observed for many compounds at low temperatures.[114] Lastly, the only two magnesium representatives *RE*Ni_2Mg_{20} with *RE* = Pr and Nd shall be discussed. They are reported to crystallize in a tetragonal subgroup $I4_1/amd$, which can be derived from $CeCr_2Al_{20}$ by a *translationengleiche* transition.[119]

For the $Ho_6Mo_4Al_{43}$ type series compounds like $Y_6T_4Al_{43}$ (T = Ti, Nb, Ta, Cr, Mo W) or single representative $Ca_6W_4Al_{43}$[120] exist. Many other combinations involving rare earth elements are reported and can be found in the Pearson's Crystal Data database.[24]

As already stated, these two extremely aluminum rich structures are the only representatives relevant for these element combinations so far. Within the context, one can mention the tetragonal $YbMo_2Al_4$ structure type (*I*4/*mmm*),[121] which has been reported for the series *RE*Mo_2Al_4 (RE = Y, Gd-Lu),[121, 122] as well as the tetragonal $CaCr_2Al_{10}$ (*I*4/*mmm*)[123] type structure. Here, only a few compounds are described such as the prototype compound as the only Cr compound and many group VII compounds such as *RE*Mn_2Al_{10} (*RE* = Y, La-Nd, Sm, Gd-Dy) and *RE*Re_2Al_{10} (*RE* = Ce, Pr, Sm).[124]

When selectively picking a three-component system, the absence of many examples of ternary ordered structures is quite surprising. Looking at the system Zr–V–Al, for example no ordered compounds are reported. Here, only solid solutions of V and Al are known in the $MgZn_2$, respectively the $MgCu_2$, structure with the general formula $Zr(V_{1-x}Al_x)_2$[125, 126] or within the cubic closest packing, respectively the Cu_3Au structure.[127] When looking at the surrounding elements of aluminum in the periodic table many ternary ordered compounds appear such as gallium compounds $Zr_3V_2Ga_4$ (own type, *Pnma*),[128] ZrV_2Ga_4 ($YbMo_2Al_4$ type, *I*4/*mmm*),[117] the silicide ZrVSi (PbFCl / MnAlGe type, *P*4/*nmm*)[129] and the germanides $Zr_2V_3Ge_4$ ($Zr_2Nb_3Ge_4$ type, *Pnma*)[130] and ZrVGe (UGeTe type, *I*4/*mmm*).[131]

Another out of many examples is the system Sc–V–Al, for which sole compound ScV_2Al_{20} adopting the already explained $CeCr_2Al_{20}$ structure is known.[132] When looking at the surrounding elements again, the gallium compound ScV_2Ga_4,[117] the silicide and germanides $Sc_2V_3Si_4$ and respective germanide $Sc_2V_3Ge_4$[133] or the stannides ScV_6Sn_6 that recently got attention due to a charge density wave.[134] In contrast to this is, for example, the system Yb–Ti–Al for which the two compounds $YbTi_2Al_{20}$[135] and $Yb_6Ti_4Al_{43}$[136] exist, however, no compounds of Yb, Ti and the surrounding *p*-block elements are reported.[24]

The list of compounds that do and do not exist could be continued endlessly; however, this short introduction should have conveyed a fascination for the complexity of intermetallic compounds and encourage further research on this topic.

2.2 The oxidation of intermetallic compounds and alloys

This chapter gives a short overview of the literature work that has been done on the oxidation behavior of intermetallic compounds and alloys. The first section contains a brief overview of the main principles in corrosion of alloys and intermetallic compounds. Due to the high technological interest in selected systems for application, the literature studies are uncountable. The second part provides an overview of studies that were conducted to find different synthetic routes to new materials, that were either not accessible by reaction of the elements or to discover new reaction pathways. Selected examples that have used the concept of oxidizing an intermetallic precursor to get to ideally phase-pure products are described.

Aluminum based alloys and intermetallic compounds are interesting for several applications due to low specific weight and density combined with remarkable mechanical properties, excellent oxidation (corrosion) resistance and low fabrication temperatures. This results in applications such as architecture or automative sector. The most prominent examples are alloys based on either Cu, Mg, Fe, Ti or Ni in combination with Al. Either alloying or coating can be used.[23, 25]

It is known that elemental aluminum is passivated with a layer of alumina (thickness between 0.005-0.01 mm depending on the conditions) even at room temperature. Other metals occurring in the aluminum will be incorporated into this oxide layer, which can lead to mixed oxides. When multiple metals are involved, it becomes clear that it is likely that one element is oxidized first.[25] As stated above, the parameters that influence the oxidation resistance of a material show an immense variety. The main points are the temperature, the composition of the material and/or the coating as well as the oxidizing medium and its concentration.[25, 137]

Taking a look at the compositions of alloys, a key property must be that the oxide that is formed at first instance (on the surface) shows high stability and low diffusivity. Then the material is passivated and protected against further oxidation. This is e.g. the case for Al_2O_3, SiO_2 or Cr_2O_3. It must be mentioned that Cr_2O_3 evaporates at high temperatures as CrO_3 limiting the application environments.[138] Moreover, the stability of the formed oxide on the metal surface below plays a crucial role. Examples for this are the incorporation (or coating) of aluminum into nickel (β-NiAl and γ-Ni_3Al) or $MoSi_2$ which is used in heating elements. If this

clear difference in the stability of selective oxide formation is not given, as for the system of titanium and aluminum (Ti_3Al and TiAl), the processes involved become more complicated. If an element is only added as a "dopant" (small amounts) it plays a crucial role, whether the amount is sufficient for passivating the whole surface with sufficient thickness of the more active metal oxide, otherwise, mixed oxides can be formed.[137]

Another parameter that plays a crucial role is the adhesion of the passivating layer to the metal surface. For the system $NbAl_3$ it has been shown that under a small layer of Al_2O_3, the intermetallic compound Nb_2Al is formed, which leads to a cracking of the alumina surface layer. The formation of mixed oxide $AlNbO_4$ and Nb_2O_5 in various layers has been proven to be highly temperature dependent. This effect can be overcome by adding elemental aluminum on the grain boundaries. Then solely the formation of Al_2O_3 is observed. The depletion of $NbAl_3$ to Nb_2Al formed on the metal-oxide surface was not observed. It has been shown that all processes also show a temperature dependence.[139]

Going back to the highly prominent system Ni-Al. Extensive investigations have been carried out to analyze the procedures of oxidation for the two most prominent example (β-NiAl and γ-Ni_3Al). It has been shown that small incorporations of rare earth elements or zirconium, for example, improve the adhesion of the formed surface oxide to the metal. However, the oxidation behavior of both alloys differs due to the different compositions. For the Ni rich Ni_3Al the formation of $NiAl_2O_4$ and Al_2O_3 was observed, while on NiAl only alumina was observed.[20] In extensive computational supported studies the structure of this thin film was analyzed.[19] Embedding Cr into NiAl results in the formation of Al_2O_3, Cr_2O_3 or solid solutions of both oxides highly depending on morphology and temperature. Interestingly, the use of Mo leads to a total loss of corrosion stability due to volatile oxide formation. PXRD analysis revealed the remaining compounds as $Al_2Mo_3O_{12}$ and $NiMo_4$.[140]

Besides the system Ni–Al, alloys of titanium and aluminum, namely γ-TiAl (and Ti_3Al) have extensively been studied and reviewed.[138, 141, 142] They show remarkable mechanical properties combined with light-weight and low cost of the two metal main components. The oxidation behavior, however, differs mainly from the system Ni-Al and other transition metals such as Fe or Co.[138] While for many of these systems it is sufficient to mix (or coat) the materials with Al or Si, which form the protective oxides, this is not straightforward for titanium. This is due to the comparable tendency of formation of Al_2O_3 and TiO on the metal surface, which is the limiting factor. TiO_2 as final product shows negative influence on the

oxidation behavior and is not favored. The formation of one oxide over the other depends highly on the activities of the metals, the oxygen partial pressure and the exact composition of the alloy. The system is even more complex due to the possibility of nitride formation by titanium.[138] The oxidation behavior can be influenced by many elements like Mo, Cr but also C, Si or Y_2O_3. The latter gave exceptional oxidation resistance due to the formation of $Y_2Ti_2O_7$ which decreases undesired TiO_2 formation.[143]

To conclude, one could extend the number of systems and examples endlessly. The corrosion/oxidation behavior of metals, alloys and intermetallic compounds is a huge field of research and technology. The oxidation behavior of metallic materials highly depends on the composition, structure on the surface, external conditions such as oxidizing medium and temperature. The best systems for applications rely on the formation of thin layers of ultra stable low diffusivity oxides such as alumina or SiO_2. This however is the counterpart of what is described within the next chapter, in which literature examples are presented that use the concept of oxidation reactions to obtain phase pure or unknown compounds, by reaction of the whole material.

2.2.1 The use of intermetallic compounds as precursor materials

In the 1960's, Hoppe and coworkers reported on the synthesis of cubic and hexagonal $NaTlO_2$ starting from the Zintl phase NaTl. It was further possible to identify $LiInO_2$ and $KTlO_2$ using the same route. The authors state that the reaction worked better than combining the respective oxidic precursors (Li_2CO_3/In_2O_3 or Na_2O_2/Tl_2O_3).[144-146] The question of what could be the outcome if a compound containing a noble metal and a base metal is oxidized was answered by Hoppe and coworkers, who investigated the oxidation of CsAu. It was postulated that either the formation of the base metal oxides and the elemental noble metal occurs, or the formation of the ternary oxide immediately happens. By the oxidation approach they could form CsAuO, which oxidizes further to $CsAuO_2$ when heated to 672 K. However, the product always showed trace amounts of elemental gold and was unstable in water.[147] Several attempts to obtain the high temperature superconductor $YBa_2Cu_3O_7$[148] or related compounds such as $Tl_2Ba_2CaCu_2O_8$[149] and $Bi_2Sr_2CaCu_2O_x$[150] were successfully applied in the 1990's. Either reactions were performed under oxygen flow or with defined amounts of oxygen using the thermal decomposition of PbO_2 into PbO and 1/2 O_2.[149]

In the late 1990's, Jung and coworkers published many investigations on the oxidation products of alloys that were obtained and structurally characterized. However, in these works

it is stated that the precursor was a multi-phase sample (some components identified), the alloys could not be pulverized due to their ductility and were used as pieces. Single crystals of $(Al_{0.5}Ga_{0.5})CuOAsO_4$ were obtained after the reaction of an Al/Ga/Cu/As alloy with the composition $Al_{0.5}Ga_{0.5}CuAs$. The authors state that the precursor was characterized, however an inhomogeneous mixture was identified. The same applies after oxidation reaction; within the mixture the authors could identify $CuGa_2O_4$ and $Cu_4O(AsO_4)_2$ beside the single crystals of the newly identified phase.[151] $Tl_2Cu^{I}AsO_4$ was identified as an intermediate phase when oxidizing alloys with the general compositions TlCuAs and $TlCu_2As$ at low temperatures.[152] Under increased reaction temperatures the product $Tl[Cu^{II}AsO_4]$ could be identified as well as the isostructural $Tl[Cu^{II}PO_4]$, when starting with TlCuP alloys.[153] In an analogous way the intermediate mixed valent compound $TlCu^{I}Cu^{II}P_2O_7$ could be identified.[154] For the same elements with different starting composition also the oxide phosphate $Cu_4O(PO_4)_2$ was identified.[155] Other compounds described in these studies are e.g. $CuInOPO_4$,[156] $CuInOVO_4$,[157] $TlCu_5O(VO_4)_3$[158] or $TlNi_4(PO_4)_3$, $Tl_4Ni_7(PO_4)_6$ and $Tl_2Ni_4(P_2O_7)(PO_4)_2$ which were all identified starting with an alloy of the composition $TlNi_2P$ depending on the respective reaction temperature.[159]

The huge variety of structures, compositions (sometimes independent from the starting composition) and valence states (when looking at the Cu atoms within the compounds) shows the potential of this reaction pathway. However, it shall be mentioned that within these studies the precursor was not fully characterized nor was the product mixture of the reactions fully investigated. The focus was clearly set on the growth of single crystals on the surface of the metallic starting material.

This is different for some more recent studies. Mosel and coworkers reported on the phase-pure formation of Eu_2GeS_4 starting with the phase-pure Zintl phase Eu_2Ge, based on X-ray analysis. ^{151}Eu Mößbauer spectroscopic investigations and magnetic measurements proved the presence of only divalent Europium after sulfidation.[160] Grin, Armbrüster and coworkers have worked intensively on the processes involved when $CaAg_2$ (KHg_2 type) is used for catalytic applications, namely ethylene epoxidation. By using SEM/EDX and powder X-ray analysis, it was proven that highly crystalline $CaAg_2$ produces Ca rich oxidic phases (CaO) and a silver enriched intermetallic phase Ca_2Ag_7 and finally elemental Ag.[161] The group of Hoch and coworkers reported on the use of highly crystalline LiGa as a precursor. The corresponding oxide, $LiGaO_2$ and the corresponding sulfide $LiGaS_2$ were obtained straightforward and structurally characterized. $LiGa_5O_8$ was identified as intermediate phase. However, for the

reaction with nitrogen a mixture of GaN and Li_3GaN_2 was identified.[162] One example for a nitride that could be synthesized successfully is the $Sr_{0.99}Eu_{0.01}AlSiN_3$ starting with $Sr_{0.99}Eu_{0.01}AlSi$. The compound shows an intense orange-red emission corresponding to Eu^{2+}. Product formation is reported to depend on the nitrogen pressure.[163]

With all previously discussed studies about the use of intermetallic precursors, finally work related to aluminum chemistry shall be discussed. Eisenmann and Schäfer synthesized and determined the structures of many ternary sulfides and selenides of group II elements in combination with group XIII elements. For the synthesis of orthorhombic $CaAl_2S_4$ and $SrAl_2S_4$ (both *Fddd*), they explicitly state that a stoichiometric premelting of the alkaline earth metal and aluminum (respectively Ga/In) was used before reacting with the correct amount of sulfur due to the highly exothermal reaction (explosive character) when starting from the elements.[164] The isostructural compounds $CaGa_2S_4$, $SrGa_2S_4$ and $BaIn_2S_4$[164] as well as the cubic ($Pa\bar{3}$) $BaAl_2S_4$ and $BaGa_2S_4$[165] and the compound $BaAl_4S_7$[166] were obtained by the same method. This was not the case for the selenides $CaAl_2Se_4$ and $SrAl_2Se_4$ which could be obtained by the reaction of the elements.[167]

3 Methods

This chapter is supposed to give an overview about the utilized analytical methods, such as diffraction methods, spectroscopy, physical property measurements and quantum chemical calculations, that can be used to shine light on the nature of not only intermetallic compounds but basically every kind of solid material. All methods for the synthesis of the materials as well as thermal analysis are explained in the following chapter.

Diffraction-based techniques such as powder diffraction and single-crystal X-ray (or neutron) diffraction are the methods of choice for analyzing the structures of crystalline compounds. Powder analysis can also be used to make statements about phase compositions, for microstructure analysis and quantitative phase analysis to determine the phase fractions of the present crystalline compounds. Depending on the results obtained and the nature of the compounds, the structural findings can be supported or extended by performing different further analyses. Within this work, solid state Nuclear Magnetic Resonance (NMR), Mößbauer and Raman spectroscopic studies as well as physical property measurements (magnetism and heat capacity) were conducted. Density Functional Theory (DFT) based quantum-chemical calculations using the Vienna ab initio program package (VASP) enabled the extraction of different parameters using the Local-Orbital Basis Suite Towards Electronic-Structure Reconstruction (LOBSTER).

3.1 X-ray diffraction methods

X-ray diffraction is the universal method of choice for the work on crystalline materials, either performed on a single crystal to do a detailed structure determination or done on a powdered sample (usually in combination with Rietveld refinement) to either confirm a structure, do quantitative phase analysis, determine the different phase compositions or extract microstructural parameters. Examples of the usage of these techniques are found in a huge number of (but not limited to) publications dealing with inorganic solid state materials. The principles shortly discussed here, have been examined in many textbooks.[168, 169]

As the names indicate, the requirements on a sample for the performance are different, since for powder X-ray diffraction (PXRD) a fine-grained powder, depending on the elements in quantities of 20-50 mg, while for the analysis of single crystals the name says it all; well-shaped single crystals are necessary.

The common ground is the interaction of crystalline solids with X-ray radiation, which is expressed in equation 1, the Bragg equation. Here, d is the distance of the *hkl*-layers in the structure, λ the wavelength, θ the diffraction angle and n the diffraction order.

$$2d \sin\theta = n\lambda \qquad (1)$$

It describes when constructive interference of the diffracted radiation is observed. Since the distances in inorganic materials (d-values) are in the same order of magnitude as the X-ray radiation used it is possible to utilize it for structure determination. The most common X-ray sources are either Cu (λ = 1.5418 Å) or Mo (λ = 0.7107 Å) anodes.

The Bragg equation gives information about the geometrical requirements to observe constructive interference of the diffracted radiation. If one calculates the so-called squared Bragg equations one can determine the lattice parameters of a system directly, if the symmetry is known. The simplest example, for the cubic crystal system, is given in equation 2. Here, the lattice parameter a is the only degree of freedom.

$$(\sin\theta)^2 = \frac{\lambda^2}{4a^2}\,[h^2 + k^2 + l^2] \qquad (2)$$

By only taking geometrical considerations of a crystal into account one can also determine the systematic absences of reflections, which result in the centering of the lattice. Details on the rules to select the respective *hkl*-values can be found in literature.[168, 169]

Besides the occurrence and the position of a Bragg reflection, which can be calculated by solely taking symmetry and geometry of the unit cell into account, the question the chemist is most interested in is the exact position and nature of an atom within a crystal structure. For this analysis multiple factors must be considered, which are called atomic scattering factors (or form factors), thermal displacement factors and finally the structure factors.

Atoms interact with X-rays in such a way that the incident X-ray beam is coherently diffracted by the electrons, not the nuclei, without the loss of energy. This is called Thompson scattering and the basis for the analysis of diffractograms. It shall be mentioned that incoherent scattering, which is accompanied by the loss of energy of the incident beam also exists. This is called Compton scattering. But this only plays a major role when materials containing mainly light elements are investigated. Details about the determination of the atomic factors shall not be discussed here. For all atoms these are tabulated in the *International Tables for X-Ray Crystallography* – Volume B and implemented in the widely used analysis tools for the evaluation of both powder and single-crystal analysis.[170] The most important consequences

that are needed for the interpretation of diffraction data are that light elements are harder to detect in X-ray diffraction experiments and the fact that the atomic form factors strongly decrease for high diffraction angles. Therefore, the intensity at high angles 2θ is normally quite low.

For real samples, a correction term for these atomic form factors is necessary. All calculations about the atomic scattering factors consider the spatial extension of the electron hull of a given atom, but do not consider that the atoms within a crystal structure move around their center of gravity due to thermal vibration. Therefore, the electron density of a given atom is not fixed at one certain point but is smeared out over a distinct volume. Since the thermal vibration of an atom is temperature dependent, this correction is expressed as a temperature factor. In a refinement these can be calculated as isotropically, assuming a spherical movement of an atom, however, often anisotropic values are used describing the motion as ellipsoid.

By going to a three-dimensional unit cell, taking all atoms and their respective positions within the unit cell into account it is then possible to calculate a so-called structure factor F. With this it is possible to calculate the position and the intensity of any given *hkl*-reflection. All structure refinement relies on the comparison of the calculated F_{calc} and observed structure factor F_{obs}.

3.1.1 Powder X-ray diffraction and Rietveld refinement

As already explained, the requirement for the performance of PXRD analysis is that the material can be ground to a fine powder to reduce the crystallite size, avoid effects of preferred orientation and provide a homogeneous sample. This can usually be done for any sample and is much easier than obtaining single crystals. It should be noted that it is also possible to measure thin films or polished samples, which are not powdered. The refinement of the data using the Rietveld method is a crucial analysis technique, which has been done after every synthesis discussed in this thesis. It is a widely applied method to confirm crystal structures, if a structural model is available, or to check the outcome of a synthesis. Data analysis with regards to structure determination cannot be done that easily. Small structures can be completely solved if, for example, they are isostructural to already known compounds. It is sometimes possible to refine a powder diffractogram using an *hkl*-phase to get a possible symmetry and unit cell, without any chemical information (indexing).

The Rietveld method is a powerful tool to extract other data from a powder diffractogram.[171, 172] Besides structural confirmation, lattice parameters can be calculated with high accuracy alongside information about strain and average crystallite sizes, since an average of many crystallites is taken. This is a difference to single-crystal analysis (*vide infra*). For good quality PXRD data atomic positions, mixed site-occupancies and isotropic temperature factors can be considered and examined. Further information that can then be obtained is the sample but not structure dependent analysis of the microstructure such as the crystallite size and the strain. Finally, quantitative phase analysis, which can also be done by the Rietveld method, is a powerful tool that can be used when all phases present in a sample can be identified. This provides information about the phase contributions of a mixture of solid materials. And it is possible to determine the amount of impurities. For this, a detailed determination of the fundamental parameters is necessary. This is done by the measurement of standards such as elemental Si, Al_2O_3 or LaB_6. The quality of the refinement can be presented as it is done for the refinement of single-crystal structures (*vide infra*). The intensity profile of the measured one-dimensional powder diffractogram is compared to the calculated intensity profile. In contrast to the presentation of single-crystal data it is not common to give the R_p-value (equation 3), but rather R_{wp} being the weighted *R*-value or the *GOF* (Goodness of fit) are used. The calculation of the R_{wp} is equivalent to the *wR*2 value given for single-crystal data. Equations for *wR*2 and GOF are discussed in the following section (equations 5 and 6). Usually, the difference profile between measurement and calculation is shown.

$$R_P = \frac{\sum||I_{obs}|-|I_{calc}||}{|I_{obs}|} \quad (3)$$

The sample holders that can be used are shown in Figure 8. For larger quantities, stainless steel sample holders can be used. Here it is extremely important that that all the available space is filled with powder, while the "so-called" zero-background sample holders made from single crystalline silicon enable measurements with extremely low amounts of sample. Powder X-ray diffraction can also be performed under non-ambient conditions. For air-sensitive samples, a closed system using a dome, which is prepared in an argon filled glovebox can be used.

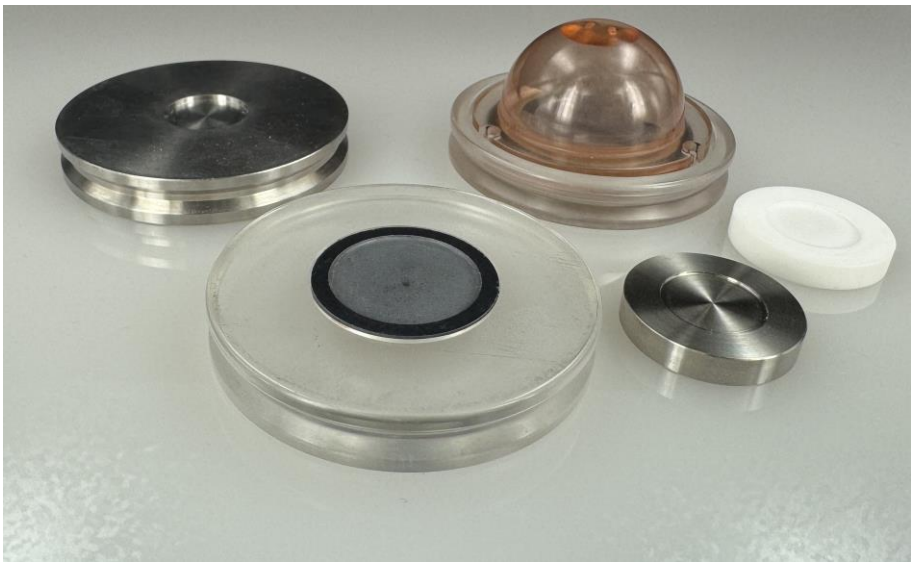

Figure 8. Sample holders for PXRD measurements, from *left* to *right*: stainless-steel for large quantities, zero-background sample holders for small amounts, zero-background sample holder capped with a dome for measurements under inert gas atmosphere and smaller sample holder for the non-ambient chambers made of stainless steel and MACOR®.

Temperature-dependent PXRD can be used as an in-situ method in two ways, one possibility is to heat up or cool down samples under an inert atmosphere. Here, possible phase transitions can be observed, for example, for the already discussed HfV_2 or $Eu_2Pt_5Al_{16}$. Another possibility is the heating under reactive atmosphere such as air, oxygen or hydrogen. In this thesis mainly a XRK 900 (Anton Paar GmbH, Graz, Austria) with a maximum temperature of 1173 K was used. Samples holders can be either made of stainless steel or MACOR®. Before a measurement, a correction of the height sample displacement must be done using silicon as a standard material to exclude all effects of thermal extension of the sample holder and chamber. For the measurement, usually heating steps of 50 or 100 K were used. After 10 minutes of equilibration at a given temperature the measurement of about 1 h was started. The temperature program was repeated in cycles. The mentioned temperature chamber as well as the special sample holders, which are also made of stainless steel or MACOR®, are shown in Figure 9.

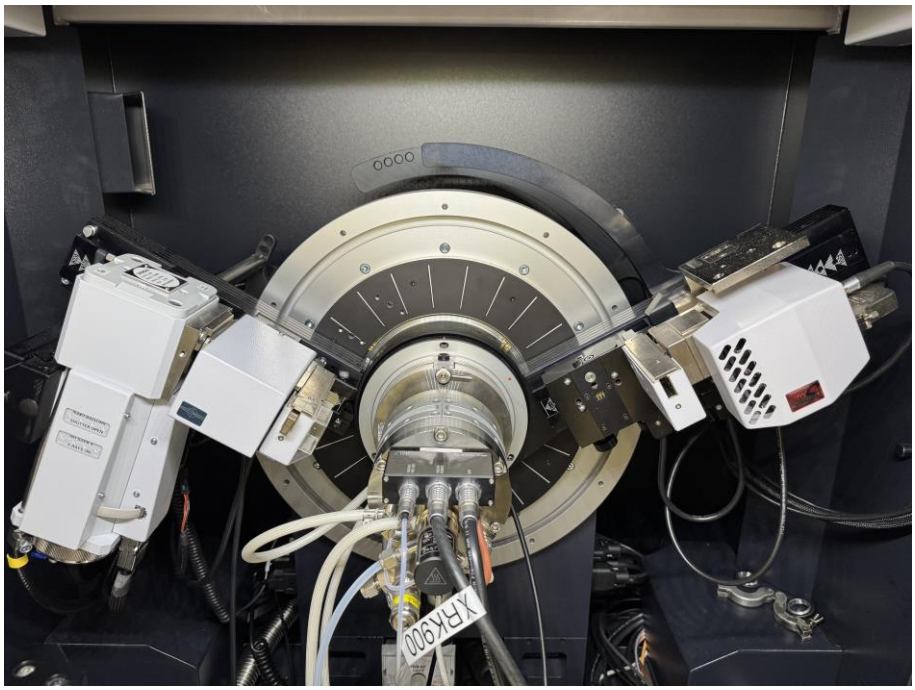

Figure 9. Picture of the XRK900 non-ambient temperature chamber for PXRD measurements at temperatures up to 1173 K.

The measurements discussed in this thesis were performed either on a D8-A25-Advance diffractometer (Bruker, Karlsruhe, Germany) in Bragg-Brentano θ-θ-geometry (goniometer radius 280 mm) or an X'Pert MPD diffractometer (PANalytical, Almelo, Netherlands) in Bragg-Brentano θ-θ-geometry (goniometer radius 240 mm). Both are operating with non-monochromatic Cu $K\alpha_{1,2}$-radiation (λ = 154.0596 and 154.4425 pm). Diffraction patterns were usually recorded between 6 and 130° 2θ with a step size of 0.013° and a total scan time of 1-2 h. A 12 µm Ni foil working as K_β filter and a variable divergence slit were mounted at the primary beam side. On the Bruker instrument, a LYNXEYE detector with 192 channels was used at the secondary beam side, and on the PANalytical instrument, a PIXcel1D detector was used at the secondary beam side. The recorded data was evaluated using the Bruker TOPAS 5.0 software[173] using the fundamental parameter approach and the Rietveld method.[171, 172]

3.1.2 Single-Crystal X-ray diffraction analysis

As already discussed, the analysis of powdered samples can be used as a crystallographic tool to confirm crystal structures or even solve them, if a good structure model and high-quality data are available. It can provide a reasonable determination of the atomic coordinates, mixed site-occupancies or the microstructure of a given sample. However, it is mostly used for quantitative phase analysis. But for a detailed structure determination powder X-ray diffraction is not the method of choice for several reasons. Within the one-dimensional data set, the three-dimensional information of the reflections are not present anymore. That can lead to a strong overlap of different reflections, which makes indexing as well as a clear matching of intensities difficult. As a result, some space groups belonging to the same crystal class cannot be differentiated. If single crystals of a material can be grown a better determination of the structure, even without having an input structure, can be provided. A major drawback of the technique is that good single crystals are not always available.

Single crystals must be pre-selected in a sample; for intermetallic compounds only an incident light microscope can be used, since the material is never transparent. The situation is different for e.g. most molecular crystals, or the chalcogenides discussed in this thesis. Here, a transmission light microscope using polarized light can be used for the selection. Examples of well-shaped intermetallic single crystals are shown in Figure 10.

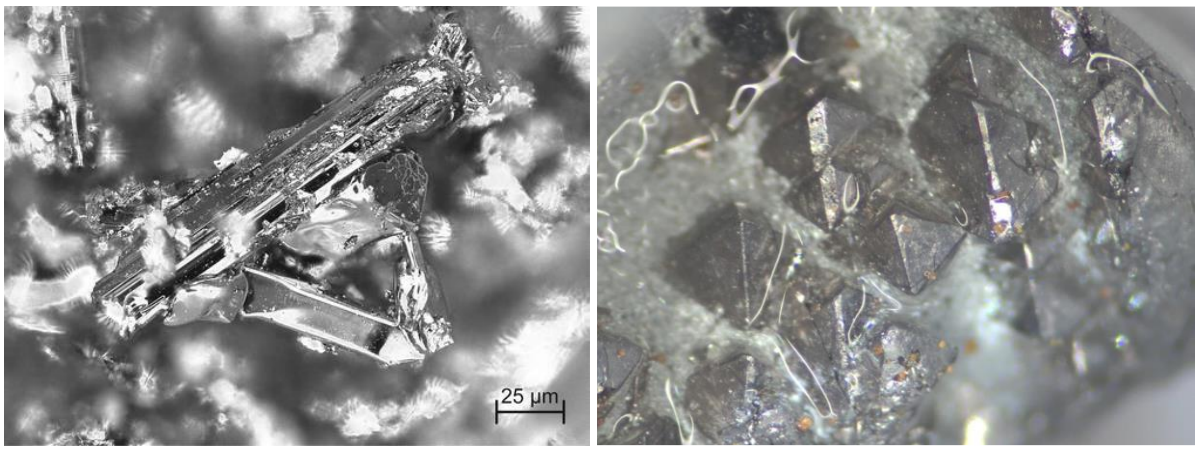

Figure 10. Examples for nicely grown single crystals of (*left*) intermetallic compounds of $Ba_3Pt_4Al_4$[174] grown from the elements ("Reprinted with permission from *Inorg. Chem.* **2015**, *54*, 10785. Copyright 2025 American Chemical Society.") and (*right*) LaV_2Al_{20} obtained after flux synthesis following the synthetic strategy of [175].

Crystals can be glued to a glass fibers using beeswax, which is softened using a soldering iron, or by a so-called loop system. Air-sensitive samples can be kept under oil and when selected directly be transferred to the diffractometer.

The samples presented in this thesis were either measured on a Bruker X8 APEX2 Nonius k-CCD or a Bruker D8 Venture diffractometer, both operating with graphite monochromated Mo $K\alpha_1$ (λ = 71.073 pm) radiation. Multi-scan absorption corrections using the Bruker SadABS datapackage[176] were applied to the data sets. Alternatively, measurements were performed on a Synergy-S diffractometer (Rigaku, Neu-Isenburg, Germany), operating with monochromatic Mo $K\alpha_1$ (λ = 0.71073 Å) radiation. Multi-scan absorption corrections and scaling using the Crysalis program package[177] were applied to the data sets. The crystal structures were solved and refined using either SUPERFLIP[178] and JANA2006;[179, 180] or by direct methods using SHELXT[181] and refined by full matrix least squares calculations on F^2 (SHELXL2018),[182] part of the SHELX program package,[183] in the graphical user interface ShelXle.[184] Structural drawings were generated with Diamond 4[185] and edited with Adobe Illustrator CS6 or MS PowerPoint. The details on the respective measurements and refinements are always given at the respective places in the form of a comprehensive table.

When reporting the result of structural refinement, it has already been stated that a comparison between the calculated and the observed structure factor is given. This is called the residual factor or *R*-value. It is calculated by equation 4.

$$R = \frac{\sum||F_{obs}|-|F_{calc}||}{|F_{obs}|} \qquad (4)$$

This value is usually given as a percentage, so it must be multiplied with 100. It should be lower than ~10 %. This calculation does not give any information about the data considered. One can give a weighted *R*-value called *wR*2 which then considers only the data collected with a sufficient high intensity, e.g. $F \geq 3\sigma(F)$. These are calculated according to equation 5.

$$wR2 = \sqrt{\frac{\sum w((F_{obs})^2-(F_{calc})^2)^2}{\sum w(F_{obs})^2}} \qquad (5)$$

Another possibility to express the quality of the refined structure is the goodness of fit (*GOF*) parameter (equation 6) which also takes the number of parameters *n* and the number of measured reflections *m* into account.

$$GOF = \frac{\sum w\left((F_{obs})^2-(F_{calc})^2\right)^2}{m-n} \qquad (6)$$

3.2 Spectroscopic Methods

3.2.1 Solid state Nuclear Magnetic Resonance – Background

(Solid state) Nuclear Magnetic Resonance (NMR) spectroscopy is a widely used technique for structure determination or validation in all aspects of chemistry. For molecular chemists, proton (^{1}H) solution NMR is the most powerful tool due to the high sensitivity, high resonance frequency and almost 100% abundance of the ^{1}H nucleus and the fact that high-quality spectra with narrow lines can be measured within seconds. The situation is different for the solid state, especially for inorganic solid state chemistry. Here, many contributions to line broadening come into play that are neglectable in solution. A detailed description of these effects is given in a review along the example of the ^{13}C solid state NMR investigation of Glycin, as well as a detailed comparison to solution NMR. The fundamental physical principles of solid state NMR are summarized in many textbooks and review articles. Therefore, here only the most important theoretical background as well as some examples are discussed.[186]

Within this thesis, the application of ^{27}Al NMR is by far the most applied nucleus. Therefore, the principles shall be discussed in this example. For every nucleus having a half-integer spin >1/2, such as ^{7}Li, ^{9}Be ^{11}B, ^{23}Na or ^{45}Sc the principles are the same.[187-189]

The basis of an NMR experiment is that a nucleus must have a spin ≠ 0. Examples for nuclei without spin are ^{12}C and ^{28}Si. The spin of the nucleus is accompanied by a splitting of the Zeeman energy levels when an external magnetic field B_0 is applied. For the case of the ^{27}Al nucleus this is shown in Figure 11. Due to the spin of I = 5/2 six energy levels exist, which results in five possible transitions.

The basis of the NMR experiment is that this energy splitting depends on other contributions that slightly affect the size of this splitting. This is expressed in equation 7. Here, ω is the frequency, at which a resonance is observed; γ is the gyromagnetic ratio, a nucleus specific constant (γ(Al) = 6.976 × 10^{7} rad s^{-1} T^{-1}). B_{int} is a sum of local fields at a specific nucleus that slightly affect the position of the resonance. In the case of ^{27}Al the resonance frequency at ~9.4 T is at 104.5 MHz.[187]

$$\omega = \gamma\,(B_0 + B_{int}) \qquad (7)$$

For the case of the spin I = 5/2 nucleus ^{27}Al the main contribution to the change of the Zeemann levels is the quadrupolar interaction or more precisely the interaction of the quadrupolar moment of the nucleus with the electric field gradient (EFG). This quadrupolar

splitting, which is demonstrated for first and second order perturbation, is shown in the energy diagram in Figure 11. It becomes clear that the central transition does not change when only first order effects are considered. However, for sufficiently large interactions the central transition is also affected. Other contributions to the signal are the anisotropy of the magnetic shielding and the dipole coupling to surrounding nuclei. These anisotropies can be reduced by applying a technique called magic-angle spinning (MAS). When the sample is rotated with an angle of 54.7° respective to the external magnetic field the first order effects are eliminated. Within this work, usually rotation frequencies of 8 to 13 kHz are used. Nowadays frequencies up to 100 kHz are possible.[190] Analysis of the resulting spectra is described in the following. The quadrupolar interaction is usually the most dominant part when measuring in the solid state.

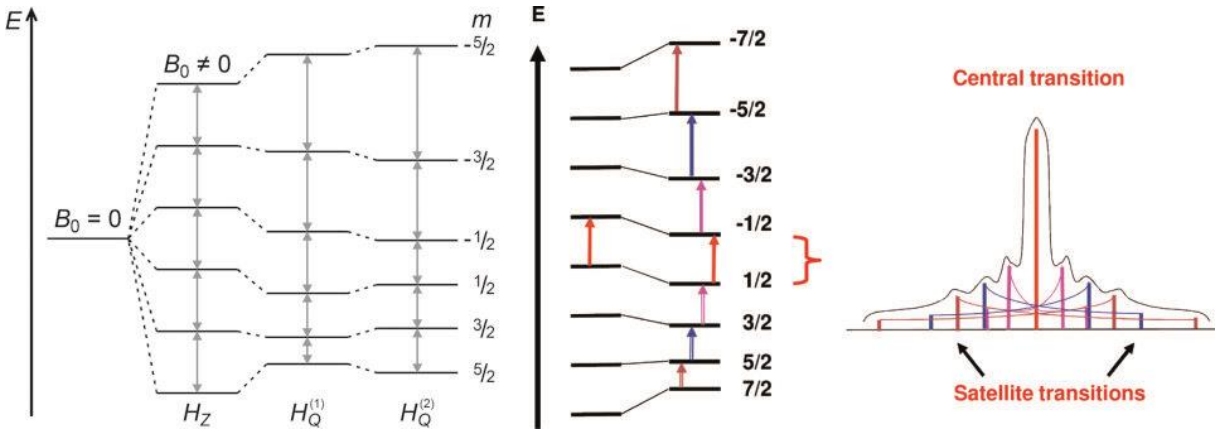

Figure 11. Zeemann splitting of (*left*) a ^{27}Al nucleus with the respective splitting of the quadrupolar interaction and (*right*) for ^{45}Sc together with the respective lines that create the satellite transitions. Reprinted with permission from *Acc. Chem. Res.* **2017**, *50*, 1459. Copyright 2025 American Chemical Society. Reprinted with permission from *Z. Anorg. Allg. Chem.* **2010**, *636*, 2232. Copyright 2025 WILEY-VCH.

The so called EFG (electric field gradient) tensor is characterized by the two quadrupolar parameters, namely the quadrupolar coupling constant C_Q (within the range of usually 0-10 MHz) and the asymmetry parameter η_Q ($0 \leq \eta_Q \leq 1$). These parameters are essential for structure validation, since these can be calculated using quantum mechanical calculations for the respective atoms within a crystal structure.

Figure 12 illustrates how these two parameters affect the spectrum and can be determined from the same. On the right a simulation of a spectrum for a small C_Q (< 5 MHz) parameter is depicted. One relatively sharp, usually symmetric and intense central transition $|+1/2> \leftrightarrow |-1/2>$ is observed together with a broad spinning sideband manifold originating from the satellite transitions $|\pm1/2> \leftrightarrow |\pm3/2>$ and $|\pm3/2> \leftrightarrow |\pm5/2>$. As one can see in Figure 12, the intensity pattern of the spinning sideband manifolds one can estimate the value of η_Q. Since C_Q gives information about the magnitude of the quadrupolar interaction, the range in which

rotational sidebands are observed gives rise to this parameter. Although one must care about the excitation bandwidth of the respective spectrometer. Therefore, this analysis cannot always be applied and is limited to small values of C_Q (<5 MHz). As already mentioned for larger interactions the central transition becomes also affected, as MAS cannot average out all anisotropic effects. Figure 12 (left) shows the anisotropic broadening that is observed for the central transition. It highly depends on the asymmetrical parameter. The width is determined by C_Q.

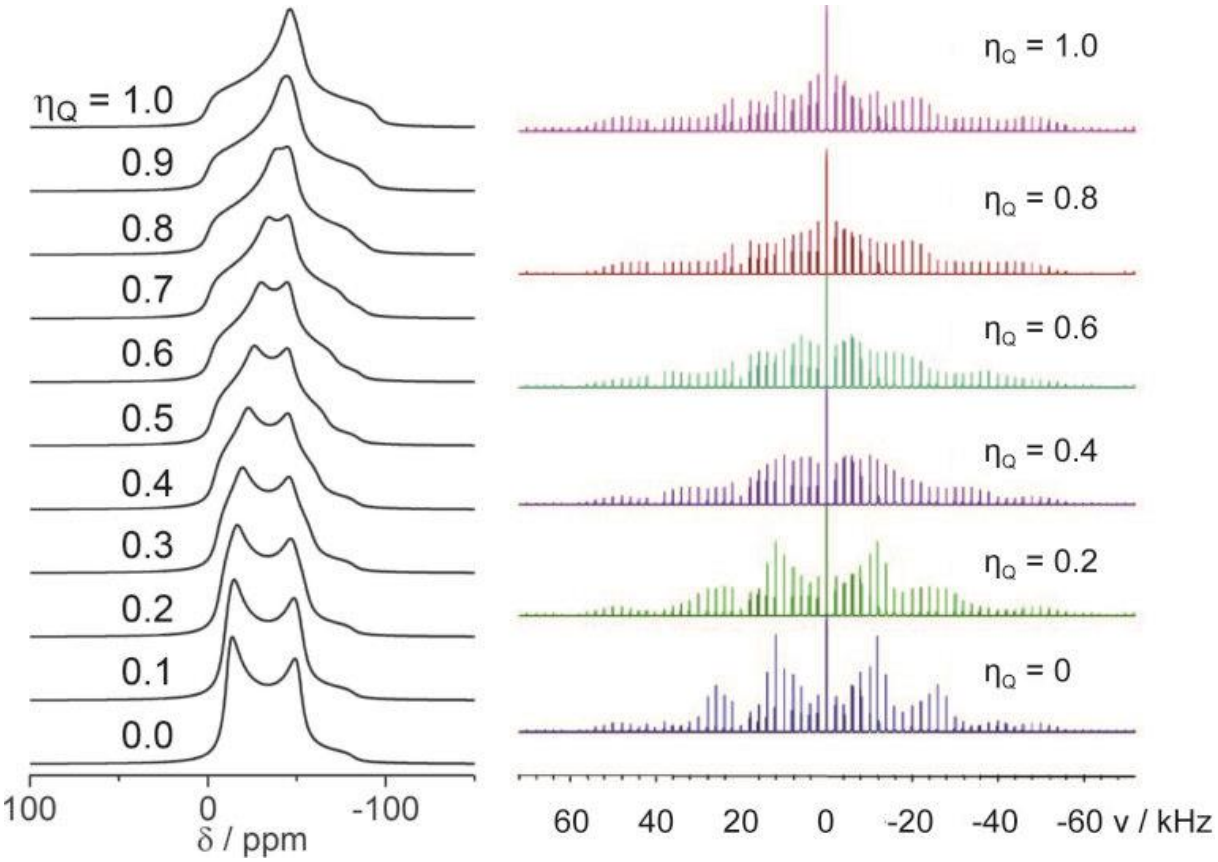

Figure 12. (*left*) Simulation of the second order perturbation line shape in dependence of η_Q. (*right*) Simulated intensity pattern of the spinning sideband manifold for different values of η_Q when small quadrupolar splitting is present (first order). Reprinted with permission from *Acc. Chem. Res.* **2017**, *50*, 1459. Copyright 2025 American Chemical Society. Reprinted with permission from *Z. Anorg. Allg. Chem.* **2010**, *636*, 2232. Copyright 2025 WILEY-VCH.

Another piece of information that can be obtained from the spectra, which is highly interesting for intermetallic compounds, is the position of the resonance frequency of the central transition. This is the sum of the magnetic shielding contribution δ_{ms} and a negative term involving the second order quadrupolar interactions. By measuring at two different magnetic field strengths, it is therefore possible to determine C_Q and η_Q, however, this was not done within this thesis. Details on that can be found in literature.[187]

More interesting are the different contributions to the magnetic shielding parameter. It is the sum of many contributions, which is expressed in equations 8 and 9.

$$\delta_{ms} = \delta_{CS} + \delta_{Curie} + \delta_{K} \quad (8)$$

$$\delta_{ms} = \delta_{dia} + \delta_{orb} + \delta_{Curie} + \delta_{K} \quad (9)$$

For the most compounds (non-metallic) the term chemical shift (δ_{CS}) is the most important contribution being the sum of diamagnetic interaction of paired electrons (δ_{dia}) and the part of the orbital angular momentum (δ_{orb}). The term δ_{Curie} refers to paramagnetic samples, in which unpaired electrons are present. The main contribution to the resonance shift observed in (inter)metallic systems is the so-called Knight shift (δ_K), which originates from the interaction of the nucleus with the conduction electrons close to the Fermi-level E_F. The resulting shifts can be quite large, e.g. resulting in a resonance shift of elemental aluminum at around 1640 ppm.

Details on the experiments for the solid state NMR spectra are given with the respective samples. In general, the measurements were performed on a Bruker Avance III 400 WB device. Spectra were recorded using the Bruker TopSpin[191] software and analyzed using the Dmfit[192] software package. For the measurements of metallic compounds, it is necessary to dilute the powder using an NMR inactive substance such as NaCl or KCl to prevent heating of the sample under the MAS conditions. The ground powder was loaded into ZrO_2 rotos (diameter 4 mm). The spectra of $CaAl_2S_4$ and $SrAl_2S_4$ were recorded and evaluated in cooperation with Lukas Rüthing and Prof. Dr. Jörn Schmedt auf der Günne from the University of Siegen.

3.2.2 Solid state Nuclear Magnetic Resonance – Examples

Going from theory to practical applications, selected examples in which solid state NMR was applied to intermetallic systems shall be discussed. It must be mentioned that the application of NMR is limited to diamagnetic or Pauli-paramagnetic compounds. Usually these are compounds with the group II and IV elements and the diamagnetic rare earth atoms Sc, Y, La, Lu. Divalent Yb compounds can also be investigated. For all other rare earth elements spectra are usually heavily broadened due to the high magnetic moment and cannot be measured.

As a first example, the structure validation of $Ba_3Pt_4Al_4$ shall be discussed. It crystallizes in its own structure type (space group *Cmcm*) with lattice parameters of a = 1073.07(3), b = 812.30(3), c = 1182.69(3) pm.[174] The ^{27}Al solid state NMR spectrum (recorded at B_0 = 9.4 T and a MAS frequency of 30 kHz) together with the most important structural motif is shown in Figure 13. It contains a distorted cube shaped building block with alternating corners of Pt and Al. As labelled in Figure 13 there are two different Al sites present. The spectrum clearly shows two sharp central transitions at 1031, and 762 ppm accompanied with a wide sideband spinning manifold. Upon analysis of the structure, one observes a more asymmetric coordination environment for the Al2 site, since the deviation from the optimal angle within the tetrahedra is larger than for Al1. This is also stressed by the calculation of the C_Q parameters using DFT methods. A site assignment and therefore structure validation was possible since the spinning sideband manifold belonging to the signal at 1031 ppm extends over a broader range and is therefore linked to a higher quadrupolar constant.

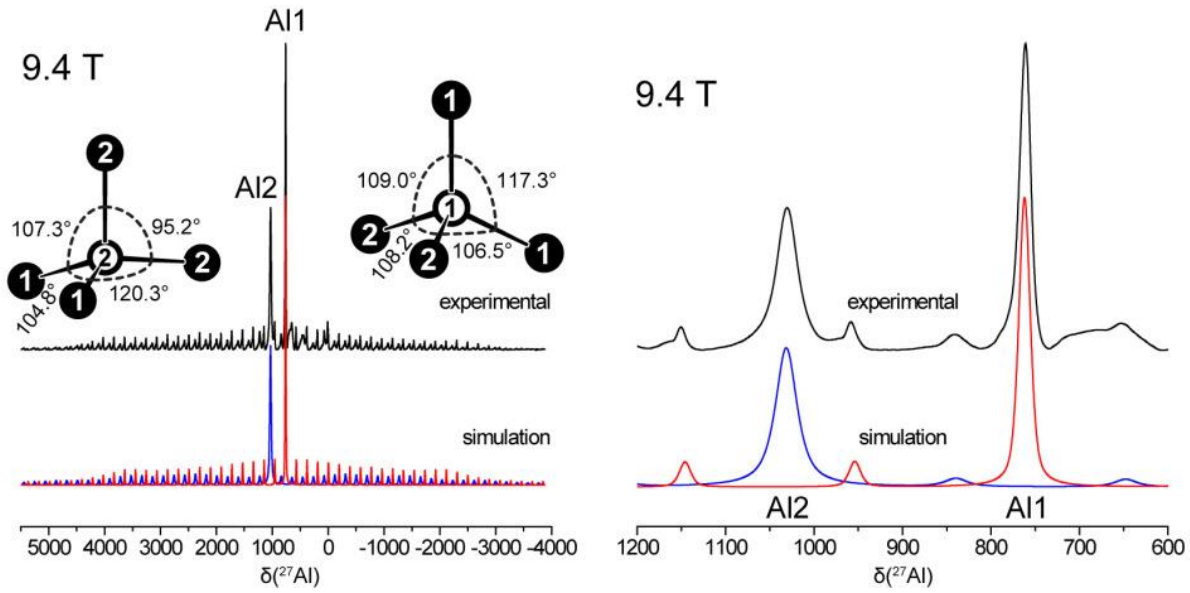

Figure 13. (*left*) Full and (*right*) enlarged section of the ^{27}Al NMR spectrum of the compound $Ba_3Pt_4Al_4$. Adapted with permission from *Inorg. Chem.* **2015**, *54*, 10785. Copyright 2025 American Chemical Society.

As already explained in equation 9, different contributions of the observed NMR shifts exist, whereas in intermetallic compounds the Knight shift is the main contribution. In studies of aluminum compounds, it was tried to find correlations of the observed shift. This is so far also only possible for isostructural series of aluminum compounds.

The left part of Figure 14 shows this for the series of $MgCu_2$ type compounds with the general formula $REAl_2$ (*RE* = Y, La and Lu). This has been correlated with the calculated *s*-electron density at the Fermi level E_F. This is the major contribution to the Knight shift.[193]

In a different study of the ternary series $RETAl_2$ (*RE* = Sc, Y, La, Lu; *T* = Ni, Pd, Pt), it was shown that the observed shift could be calculated by increments, similar to ^{1}H solution NMR spectra. Different elements change the surrounding of the aluminum nucleus, therefore change the electronic situation at the Al nucleus, which therefore changes the observed shift. As one can see in Figure 14 a good agreement was observed. However, identifying this large family of isostructural compounds is rare in literature.[194] It was also possible to set up this increment approach for the quadrupolar parameters, however a common correlation of the observed shift and the C_Q value with regard to the elements involved was not possible. The authors state that this is due to the fact that the Knight shift and the EFG parameters C_Q have different origins, which are differently affected by the substituting elements. The Knight shift is a local probe of the *s*-electron density at the Fermi level E_F, while the EFG tensor depends on all electrons and their distribution as well as local geometric distortion.

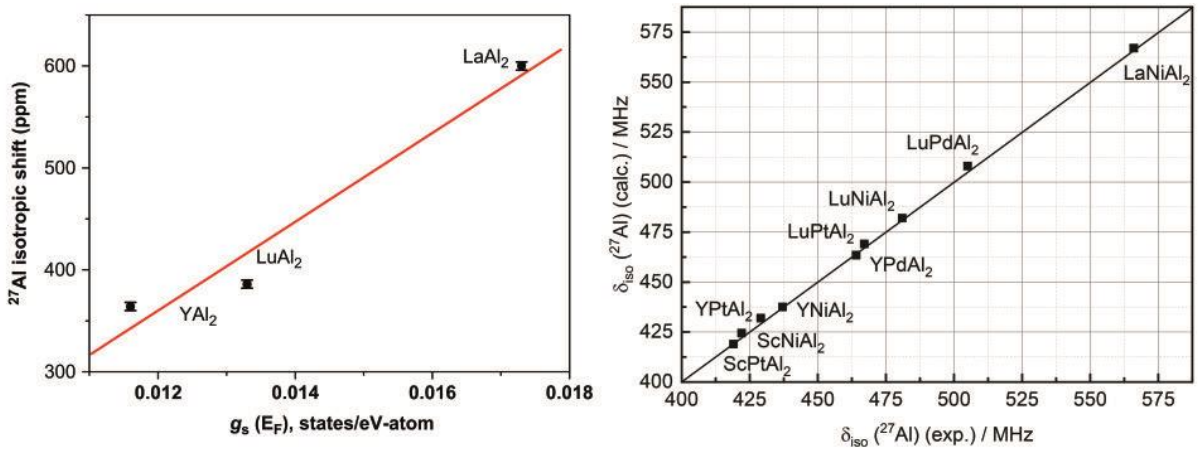

Figure 14. (*left*) Dependence of the observed ^{27}Al NMR shift in dependence of the *s*-electron density for the series *RE*Al$_2$ (*RE* = Y, La, Lu) and (*right*) an incremental approach to predict the Knight shift in the series *MT*Al$_2$. Reprinted from *Solid State Nucl. Magn. Reson.* **2012**, *41*, 28. C.C. Yuan, Y.-F. Yang, X.K. Xi, J. Cui, J.F. Xiang, Solid state ^{27}Al NMR investigation of Knight shift tensors of *Ln*Al$_2$ (*Ln*=Y, La and Lu) and correlation with DFT calculations, Copyright 2025, with permission from Elsevier. Reprinted with permission from *Inorg. Chem.* **2019**, *58*, 7010. Copyright 2025 American Chemical Society.

Lastly the example of Na_2Au_3Al from the literature shall be discussed. This compound has already been mentioned as a representative of the Al_2Mo_3C type ($P4_132$), being a superstructure that can be derived from the cubic Laves phase.

Figure 15 (*left*) shows the ^{27}Al MAS spectra for the ordered compound Na_2Au_3Al at three different magnetic field strengths. The full spectrum could nicely be simulated by assuming an ordered component, which shows severe quadrupolar broadening due to second order perturbation. This results in the asymmetric line shape of the central transition. The further red curve indicates a disordered solid solution, which is in parts formed in the samples.

The red spectra again show the ordered sample (*top right*) and two members of the solid solution with the nominal composition $Na_2Au_{4-x}Al_x$ (x = 0.5, 0.75). The disorder of the phase is clearly shown in the spectra, in which only a featureless broad line is visible. A comparable trend is visible when looking at the ^{23}Na spectra recorded for the three samples. The interested reader is referred to the original work.[63] Moreover, the work also nicely shows two spectra that are nearly not affected by quadrupolar interactions. Due to their high symmetry the spectra of the endmembers ^{23}NaAu$_2$ (MgCu$_2$ type) and Au^{27}Al$_2$ (CaF$_2$ type, $Fm\bar{3}m$) show sharp central transitions only accompanied by less than five visible spinning sidebands.[63]

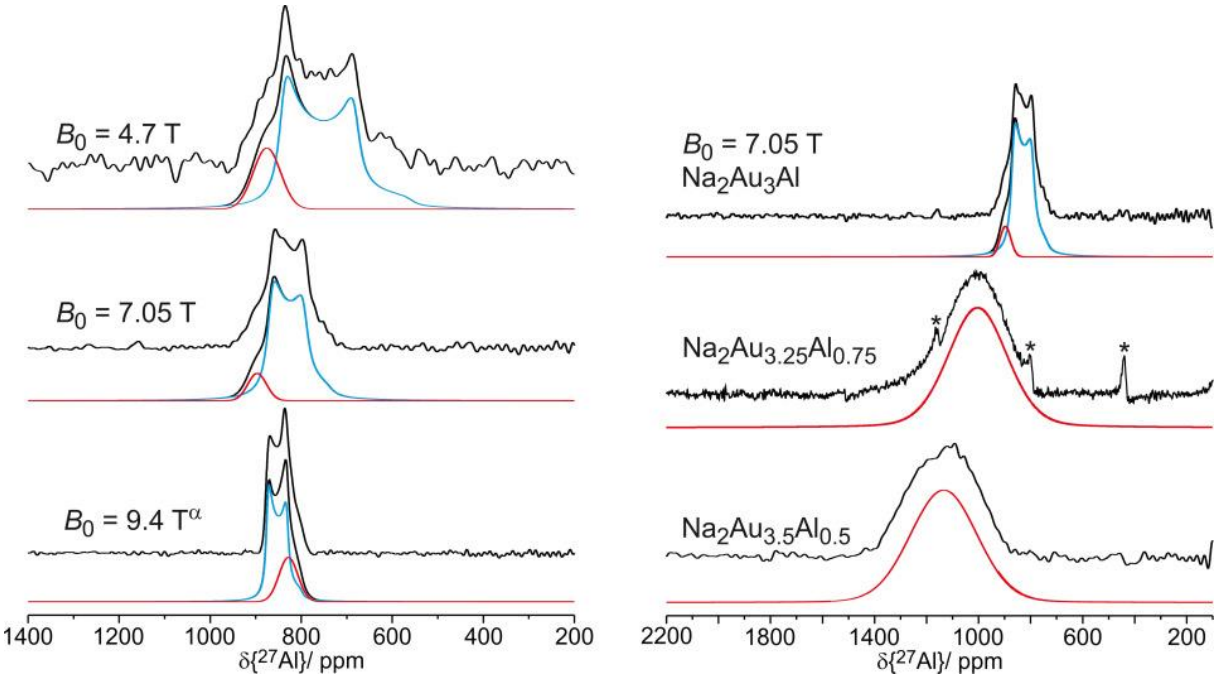

Figure 15. ^{27}Al solid state NMR spectra of (*left*) the compound Na_2Au_3Al and (*right*) off-stoichiometric solid solutions. Adapted with permission from *Inorg. Chem.* **2017**, *56*, 1919. Copyright 2025 American Chemical Society.

3.2.3 Mößbauer spectroscopic investigations

This spectroscopic method, named after its explorer Rudolf Mößbauer, also involves the nucleus but not in a way that the spin states but the energy levels of the nucleus itself are targeted. These transitions are in the range of γ-radiation. The source of the radiation is usually produced by the decay of isotopes of the same element, that shall be investigated. Examples for this are e.g. ^{57}Co/Rh or $Ca^{119m}SnO_3$. The decay of these isotopes is recoilless, so the emission is highly monochromate γ-radiation. For the measurement of ^{151}Eu, a ^{151}Sm:EuF_3 source is used.

Since the energy levels of the nucleus within a sample can be slightly changed in comparison to the source, shifts in the energy can occur. In order to address these energy differences, one uses the Doppler effect. The source is moved with a defined velocity towards or away from the sample (saw-tooth pattern), resulting in a change in energy. In the spectrum of a Mößbauer spectroscopic investigation, usually this shift is shown. If source and sample are identical, one observes an absorbance signal at 0 mm s^{-1}. The shift, however, depends on the electron density and distribution around the nucleus and is therefore called *isomeric shift* in analogy to NMR spectroscopy.[169] Therefore, one can observe severe differences in the Mößbauer resonances depending on the valence state of the nucleus e.g. Fe^{2+}/Fe^{3+} or the difference between Eu^{2+} and Eu^{3+} (*vide infra*).

Besides the position of the signal, the splitting of the signal is of interest. It appears due to quadrupolar splitting, if a nucleus with a spin $I > 1/2$ is investigated as well as magnetic ordering phenomena can be observed. This is called magnetic hyperfine Zeeman splitting and appears if the nucleus is placed into a magnetic field. This can be due to intrinsic magnetism induced due to an applied external magnetic field or by ferro-, ferri- or antiferromagnetism. In the case of the latter, a splitting below the ordering temperature is observed.

It shall be mentioned that Mößbauer spectroscopic investigations can be applied to many nuclei, such as ^{57}Fe, ^{119}Sn, ^{121}Sb,^{151}Eu and ^{170}Yb. Within this thesis only ^{151}Eu plays a role, therefore it shall be discussed in more detail.

Figure 16 sums up the different values for isomeric shifts observed in a Mößbauer spectroscopic experiment. One can clearly see that the valence state of the Eu atoms plays a crucial role for the observed shift. It plays moreover a crucial role, if the sample investigated is metallic or non-metallic, which simply reflects the fact that the overall electron density significantly influences the observed isomeric shift. Details on different valence states, static and dynamic valance states can be found in detail in another review article on Eu intermetallic compounds published during this thesis[195] or in review articles and handbooks on Mößbauer spectroscopic investigations.[196-199]

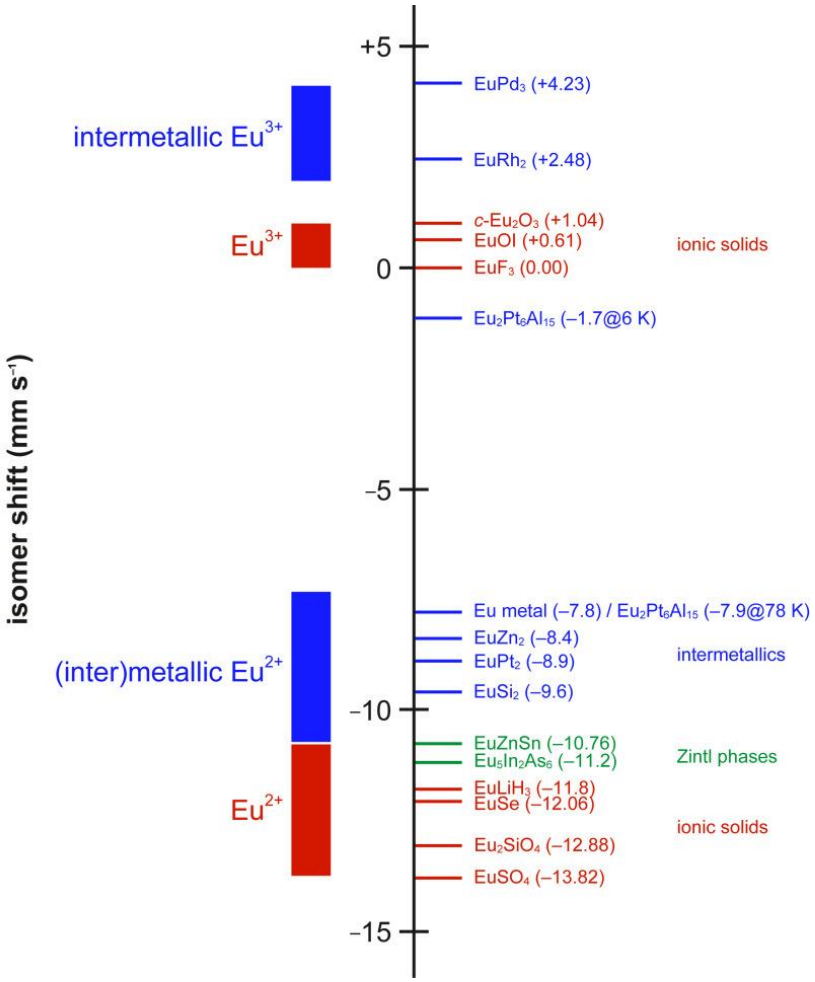

Figure 16. Mößbauer shift range for the ^{151}Eu isotope in different inorganic compounds. Adapted from *Rev. Inorg. Chem.* **2023**, *43*, 571.

One examples that nicely shows the use of Mößbauer spectroscopic investigations is given with the example of $Eu_2Pt_6Al_{16}$. It crystallizes in an orthorhombic (3+1)D commensurately modulated structure ($Sc_2Pt_6Al_{15}$ type) with space group *Cmcm* (α,0,0)0s0 ($\alpha = 2/3$). The compound showed an anomaly within the magnetic susceptibility curves that could not be explained straightforwardly. However, the combination of temperature dependent PXRD and Mößbauer spectroscopic investigations clearly proofed the change in the valence state of the Eu atoms. The spectra at 78, 40 and 6 K are shown in Figure 17 (*left*). Beginning with the 78 K spectrum, one signal with an isomeric shift with δ = –7.93(3) mm s^{-1} is observed. For the simulation a quadrupolar splitting energy of 2.5 mm s^{-1} was used for all spectra. Upon cooling a second species appears, as can be seen in the spectrum at 40 K, showing the presence of both Eu^{2+} and Eu^{3+} according to the observed isomeric shifts. Finally at 6 K, only a signal at δ = –1.71(3) mm s^{-1} is visible. Upon heating and cooling the spectra are all reproducible, clearly underlining the reversible change in the valence state of the Eu atoms. The absence of any hyperfine splitting further shows that no magnetic ordering is present. This is different for the

isostructural Ga compound $Eu_2Pt_6Ga_{15}$. The conducted ^{151}Eu Mößbauer spectroscopic investigations are shown in Figure 17 (*right*). Over the whole temperature range divalent Eu is present. Below the Neel temperature T_N = 13.1 K a strong hyperfine splitting with a high value of B_{hf} = 34.7 T is observed.[200]

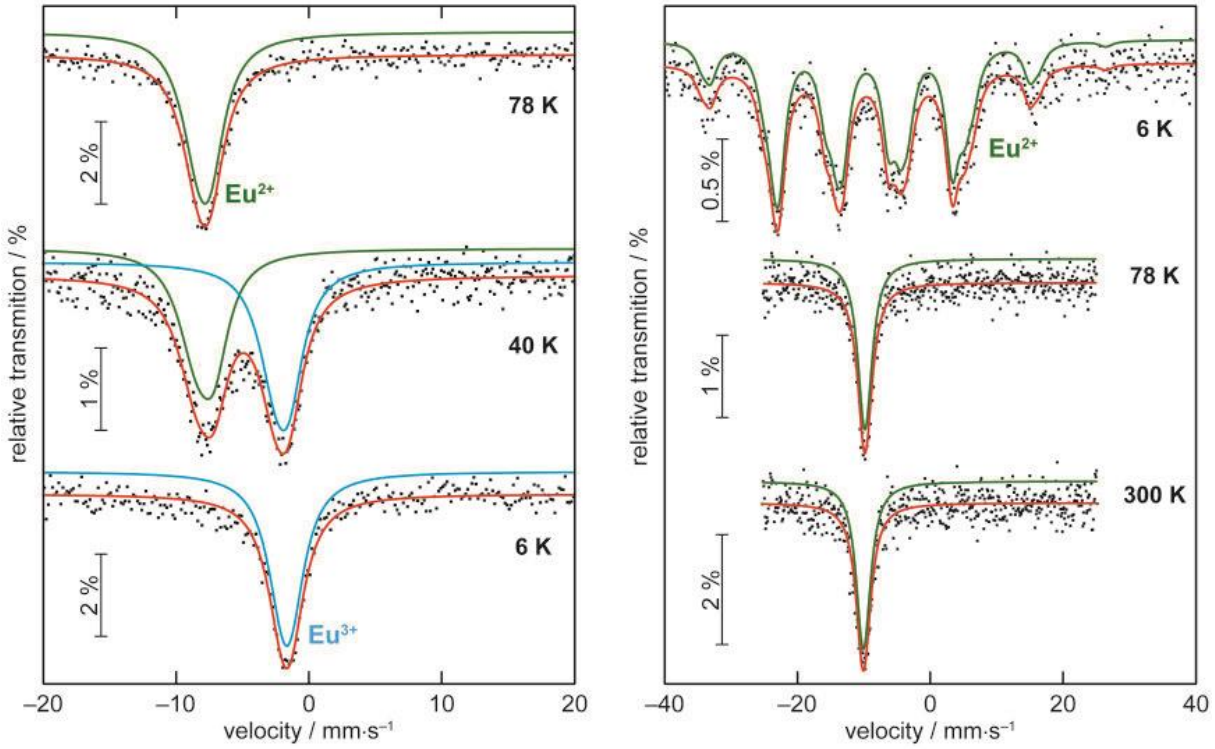

Figure 17. Temperature dependent Mößbauer spectra of (*left*) $Eu_2Pt_6Al_{15}$ and (*right*) the corresponding Ga compound. Adapted with permission from *J. Am. Chem. Soc.* **2018**, *140*, 8950. Copyright 2025 American Chemical Society.

The ^{151}Eu Mößbauer spectroscopic measurements conducted within the scope of this thesis were performed by Aylin Koldemir and Joshua Wiethölter at the University of Münster. Details of the experimental setup can be found in the respective chapter (5.4.2).

3.2.4 Raman spectroscopy

Raman spectroscopy is a technique that involves the vibrations of usually functional groups or specific bonds in molecules. It is closely related to infrared spectroscopy (IR), but unlike IR spectroscopy, it does not require a change in the transition dipole moment, but rather a change in the polarization of the respective vibration. An experiment is done by irradiating a sample with highly monochromatic light. In contrast to other spectroscopic techniques, the method is a non-resonant method. The energy of the incident radiation does not have the same wavelength as the excited transition, which is why this is a scattering technique in which vibrational

transitions take place within the sample. One observes either Stokes or anti-Stokes bands in the spectrum, which are shifted by a certain energy compared to the used excitation light.[169]

Raman spectroscopy is a technique which is rarely used to investigate intermetallic compounds and therefore only some interesting examples shall be discussed here. Examples found in literature are the isostructural series REAl$_2$ (RE = La, Ce, Eu, Gd, Tb, Dy and Yb)[201] the solid solution (Sm$_{1-x}$Gd$_x$)Al$_2$ with x = 0, 0.01 and 0.02[202] as well as the gold and platinum compounds adopting the cubic CaF_2 structure type AuX_2 (X = Al, Ga and In)[203] and $PtGa_2$.[204]

The measurements shown within this thesis were performed by Dr. Petra Herbeck-Engel at INM Saarbrücken. Details of the experimental setup can be found with the respective measurements (5.1.1).

3.2.5 SEM/EDX

Electron microscopy is a powerful tool for the analysis of solids. It is based on the different interaction and penetration depth of high energy electrons of different domains of a solid sample. Electron microscopes can be used in transmission mode, then called *transmission electron microscopy* (TEM). Sample requirements for this are that thin films or foils can be produced, or the sample thickness can be reduced (e.g. by Ar ion milling), as otherwise penetration of electrons through a sample to a detector is not possible. It has a very low resolution limit and is therefore capable of imagining the exact surroundings of an atom. Structure analysis can also be performed *via* electron diffraction.[169]

Another possibility, and the one used in this thesis, is scanning electron microscopy (SEM). Here the sample is measured in reflection geometry. SEM is usually combined with energy dispersive X-ray spectroscopy (EDX). It can be used as an imaging technique taking pictures analyzing surface morphology of a sample and quantifying the elemental composition of a sample.[205, 206]

A sample is targeted with high energy electrons with an acceleration voltage between 5 and 30 kV. Following the same principle as for the generation of X-rays, every element within a sample emits characteristic X-ray radiation. As the name indicates, the detector of an EDX, also known as EDS, device differentiates between the different energies of the emitted radiation. After calibration it is therefore possible to quantify the elemental composition at certain points of the sample. With a standard device, however, this is not possible in an unlimited way. The lower limit, when it comes to elements, is sodium, which can be measured. For lighter elements

other techniques (e.g. Auger and electron energy loss spectroscopy) can be used. Moreover, sample preparation plays a crucial role for the accuracy of the values obtained. It is possible to work with powdered samples, however, small deviations in height can cause deviating results. Samples are usually covered with gold to avoid a charging of the surface. For (inter)metallic investigations it is more common to work with polished melting beads. Within this thesis and also in literature, it is used as a standard method to determine and confirm the elemental composition of samples.[169]

The measurements within this thesis were performed by Dr. Stefan Engel and Jörg Schmauch. Details of the experimental setup can be found in the respective publications. For all investigations powdered samples were used.

3.3 Physical property measurements

Magnetism is just one of the interesting properties when it comes to intermetallic compounds, or solid materials, in general. One can just think of the already mentioned strong permanent magnet $Nd_2Fe_{14}B$.[4] This chapter is intended to give an overview of the most common observations. All principles and expected results are summarized in excellent textbooks.[8, 207, 208] Examples for measurements of magnetism for intermetallic compounds are found at various points in literature.

Magnetic properties of a sample can readily be measured in a large temperature range by using a MPMS (Magnetic Property Measurement System) or PPMS (Physical Property Measurement System). The magnetic susceptibility can be measured as a function of temperature or magnetic field strength. For the first measurement, the difference between zero-field-cooled and field-cooled (ZFC/FC) is often important. It depends on the time, respectively the temperature, at which the external magnetic field is turned on. Usually, magnetic field strengths of 100 Oe are used for the ZFC/FC measurements, in addition, ZFC measurements at higher magnetic fields (10 kOe) are conducted. When the magnetic field varies but the temperature is held constant, the measurement is called a magnetization isotherm. All investigations within this thesis have been carried out by the group of Prof. Dr. Rainer Pöttgen at the University of Münster by Lars Schumacher and Jasper Baldauf. Details on sample preparation and experimental parameters can be found in the respective publications.

Most of the elements involved in the discussion in section 2, including elements belonging to group II and IV of the periodic table and the rare earth atoms Sc, Y, La and Lu are diamagnetic. Since only paired electrons are present, no permanent magnetic moment should

be observed. However, in metallic systems unpaired electrons from paramagnetic impurities and the paramagnetism caused by the interaction of conduction electrons with the magnetic field, called Pauli-paramagnetism, can cause a response in magnetic measurements. A usual measurement of the magnetic susceptibility in dependence of the temperature shows a negative susceptibility which is temperature independent. For metallic compounds, sometimes a temperature independent small positive susceptibility is observed due to the above-mentioned Pauli-paramagnetic behavior. In this case, one speaks of the fact that the intrinsic Pauli paramagnetic overcompensates the intrinsic diamagnetism. This can lead to either positive susceptibility or a susceptibility close to zero even for diamagnetic systems. Another feature, which is sometimes observed, is the small rise of the susceptibility of dia- or Pauli-paramagnetic compounds at temperatures below 25 K. This is often due to traces of Curie-paramagnetic impurities.[8, 209]

When (magnetic) transition metals or rare earth elements are present in compounds having unpaired *d*- or *f*-electrons, magnetic moments can behave differently. One possibility is Curie-paramagnetic behavior. The magnetic moments align in an applied external magnetic field but do not interact with each other. The temperature dependence of magnetic susceptibility follows the Curie (for only paramagnetic substances) or Curie-Weiss Law (for antiferro-, ferro- or ferrimagnetic substances in their paramagnetic temperature region) expressed in Equations 10 and 11. χ is the magnetic susceptibility, C the Curie constant and θ_P the paramagnetic Curie temperature, sometimes also labeled Weiss constant. For compounds in which the temperature independent Pauli-paramagnetism is present, the so-called modified Curie-Weiss law (Equation 12) should be used. It includes a temperature independent constant called χ_0. With increasing temperature, the magnetic moments tend to dissipate orientation more often resulting in less susceptibility. With these three equations one can determine the magnetization of a sample by analyzing the measured (inverse) susceptibility as a function of temperature.

$$\chi = \frac{C}{T} \tag{10}$$

$$\chi = \frac{C}{T-\theta_P} \tag{11}$$

$$\chi = \frac{C}{T-\theta_P} + \chi_0 \tag{12}$$

In that case, two interesting anomalies have been mentioned before. It can happen that below certain temperatures the magnetic moments spontaneously align parallel or anti-parallel. This is called ferro- (for parallel moments) or antiferromagnetic (for antiparallel moments).

This results in anomalies within the temperature dependent susceptibility curves. The respective temperatures at which ordering is observed are called Curie temperature T_C for ferromagnetic materials and Néel temperature T_N for antiferromagnetic materials. The latter case has already been discussed in section 3.2.3 for the compound $Eu_2Pt_6Ga_{15}$ with a T_N = 13.1 K.[200]

Lastly, one must mention the phenomenon of superconductivity, which was first discovered in several metals.[210] When a material enters a superconducting state, it has no electrical resistivity and acts as a perfect diamagnet. The transition temperature below which superconductivity can be observed is called the critical temperature T_C. This effect can also be present in intermetallic compounds; it has already been mentioned for HfV_2 (T_C = 9.6 K)[43] or Nb_3Sn (T_C = 18 K),[1] which is used as a superconductor in many applications. Within a measurement of the magnetic susceptibility this can be seen as the sudden appearance of strong diamagnetism, indicated by a negative susceptibility. Due to the so-called Meissner effect in a superconducting material, all magnetic field is pushed out of the sample. Another characteristic of a superconductor is the critical magnetic field strength H_{crit} at which the superconducting state is not stable anymore. Depending on the behavior of the superconducting state in an applied external magnetic field, one can differentiate between type I and II superconductors.

3.4 Quantum-chemical calculations using VASP and LOBSTER

Besides experimental methods to analyze structure and properties of a solid material that have been described so far, quantum-chemical calculations based on mainly density functional theory (DFT) can be used to obtain various information about any crystalline solid compound (either metallic or oxidic (valence-precise) in character). Review articles and books addressing basic concepts are found in many places in literature.[211, 212] A comprehensive example is given in a recent textbook by Dronskowski.[213]

Within this chapter, only the most important concepts together with the actual use for the questions asked within this thesis are discussed. The quantum chemical calculations within this thesis were done by many different collaborators, namely Prof. Dr. Yuemei Zhang, Prof. Dr. Samir F. Matar, Prof. Dr. Horst P. Beck and PD Dr. Oliver Janka. The details on the parameters used for the calculations can be found in the respective publications.

The calculations for solid crystalline materials used within this thesis are based on the projector augmented wave (PAW) method introduced by Blöchl,[214, 215] which is implemented in the Vienna ab initio simulation package (VASP).[216, 217] An alternative available program is Quantum ESPRESSO.[218]

The basics of the calculations go back on the theorem of Bloch for calculations of a periodic material.[219] This results in wave functions that can be considered as periodic plane waves. An infinite translational periodic material is described as a small finite unit, which is defined by the *k*-spacing and is called the Brillouin zone. An optimization of this *k*-spacing can be done by using the approach by Monkhorst, for example.[220] The aforementioned work of Blöchl introduced the most effective way to describe the pseudopotentials used in calculations. By that, it is not necessary to consider all electrons of all nuclei present; only the valence electrons are considered, while the other electrons and the nucleus are considered as pseudopotential. More details on the topic can be found in literature. In the following, the actual information that can be obtained to analyze chemical structures is briefly summarized.

As a result of a calculation, one obtains (hopefully) an optimized structure of the system and by that the total energy of a compound. This can give information about the stability of certain structures for the same composition, for example. It is moreover possible to analyze the stabilities of compounds (at 0 K) when the total energies are compared to the elements or binary compounds. This is expressed in a so-called convex-hull diagram.[221, 222]

Another piece of information that can readily be obtained and has been used at various points in literature is the determination of the relevant solid state NMR quadrupolar parameters. It is not possible to calculate the shift of the NMR signal, however, as mentioned the quadrupolar constant C_Q and the asymmetry parameter η_Q can be calculated and used for further simulation of the spectra.[174, 187] This function is implemented in VASP and can readily be used when the quadrupolar moment of the respective nuclei is given.[223]

For the deeper analysis of solid compounds DFT based calculations are very helpful to get a better understanding of the charge distribution, electron density at the Fermi level and the bonding situation. In many cases a Bader analysis of the compounds is done, giving the respective charge of the nuclei. In the case of intermetallics, this often results in partially positive or negative atoms.[224-226] Addressing the bonding situation, it is further possible to extract an ELF (Electron localization function)[227] analysis. The program package developed by the Dronskoswki group at RWTH Aachen called LOBSTER[228-232] (Local Orbital Basis Suite Towards Electronic-Structure Reconstruction) allows for the fast analysis of Mulliken and Loewdin charges[233] and COBI (Crystal Orbital Bond Index) values which indicate the bond strength.[234] The integrated COBI – ICOBI – corresponds to the covalent bond order, usually adopting values between 0 and 1 in solid state materials. An ICOBI close to 0 indicates only

ionic (as for example in NaCl) or no interactions (for large distances between the atoms), for diamond an ICOBI of 0.95 was identified indicating a covalent single bond. Within SiO_2 a value of 0.76 was calculated showing the partially ionic and covalent character.[234]

4 Experimental

Since a detailed description of the experiments including the synthetic approach as well as the characterization is always given with the respective publications, the following chapter is supposed to give a general overview of the variety of experimental conditions that can be used for the synthesis of intermetallic compounds as well as the oxidation of the same.

4.1 Used chemicals

This first chapter is supposed to give the used metals or other chemicals for the synthesis done within this work. Table 1 sums up all chemicals used within this work, listed with the respective purity and supplier. Most metals were delivered in dendritic shape, as pellets or chunks. For the use of these in the arc furnace, they were all cut into smaller pieces enabling a better homogenization in the melt. The chalcogenides were used as fine powders. The alkaline earth metals Ca-Ba as well as the rare earth elements La, Ce and Eu as well as elemental manganese were stored in an argon filled glove box.

Table 1. Used chemicals, given with supplier, purity and appearance used within this work.

Chemical	Appearance	Purity / %	Supplier
Aluminum	pieces (2.5 mm)	99,99	Koch chemicals
	foil	99.5	Alujet
Magnesium	swarf	98	Sigma Aldrich
Calcium	pieces	99.5	chemPUR
Strontium	bar	99	Sigma Aldrich
Barium	pieces	99.95	Onyxmet
Scandium	pieces (dendritic)	99.98	Onyxmet
Yttrium	pieces (dendritic)	99.99	Onyxmet
Lanthanum	pieces	99.95	Onyxmet
Titanium	dendritic (electrolytic)	99.9	Onyxmet
Zirconium	crystal bar	99.9	Onyxmet
Hafnium	crystal bar	99.9	Onyxmet
Vanadium	pellets	99.9	Onyxmet
Niobium	pellets	99.95	Onyxmet
Tantalum	pellets	99.95	Onyxmet
Chromium	pieces (electrolytic)	99.99	Onyxmet
Molybdenum	pellets	99.95	Onyxmet
Tungsten	pellets (evaporation)	99.95	Onyxmet
Manganese	pieces (purified with SiO_2)	–	self-made
Iron	pieces	99.97	Onyxmet
Nickel	wire	99.98	chemPUR
	swarf	–	Riedel-de Haën
Palladium	rods	99.95	Onyxmet
Platinum	pieces	99.9	Agosi AG

	pellets	99.95	Onyxmet
Silver	pellets	99.99	Onyxmet
Gold	foil	99.9	Agosi
	shots	99.95	abcr
Silicon	pieces	99.99	chemPUR
Germanium	pieces	99.999	Onyxmet
Tin	pieces	–	Carl Roth
Cerium	pieces	99.9	Onyxmet
Europium	pieces	99.9	Onyxmet
Gadolinium	pieces	99.99	Smart Elements
Terbium	pieces	99.95	Onyxmet
Dysprosium	pieces	99.95	Smart Elements
Holmium	pieces	99	Smart Elements
Erbium	pieces	99.99	Onyxmet
Thulium	pieces (chips)	99.9	Smart Elements
Ytterbium	pieces	99.99	Smart Elements
Lutetium	pieces	99.95	Onyxmet
Bariumperoxide	powder	99.99	abcr
Sulfur	powder	99.95	chemPUR
Selenium	powder	99.7	abcr
Tellurium	powder	98	Merck

4.2 Synthesis of intermetallic compounds in the arc furnace

The principle of an electric arc furnace is that a material heats up because it functions as a resistor while it is incorporated into a circuit. The circuit to the material is obtained by an electric arc because a small gap of inert gas is left between the electrode and the sample, which prevents a reaction of the electrode with the material. The starting materials (here mainly the elements) are placed in a water-cooled crucible which acts as counter electrode closing the circuit. With that, an arc furnace is of course limited to materials which have sufficient electric conductivity. Heating of ceramics e.g. is not possible.

For the synthesis of intermetallic compounds, the use of an arc furnace is by far the fastest and most effective method, if the starting materials are suitable. It can be also used for the making and closing of metal ampoules of the refractory metals such as Nb, Ta or W. The limitation of the arc furnace is that only materials with rather high boiling point or low vapor pressure in the liquid state are suitable for a direct synthesis. Zn and Mg e.g. cannot be reacted in an arc furnace in any useful way due to direct evaporation, pointing out one obvious disadvantage of the setup; temperature control is not possible. For the other alkaline earth metals, Ca to Ba, it depends on the used amounts of the elements. In case of aluminum, a workaround is using aluminum foil, which is wrapped around the other elements and therefore can prevent evaporation since the reaction to the intermetallic compound happens before the alkaline earth element can vaporize. The same applies for the divalent rare earth metals Yb and Eu. Here, however, closed metal ampoules have shown to be way more advantageous. An upper limit of the melting point is not given, since temperatures way above 3000 K can be achieved melting even Ta or W (3269 respectively 3680 K).[41] Since in this thesis aluminum was present as the main component in most syntheses this is not necessary since Al melts at 660 °C and then readily reacts with the remaining elements.

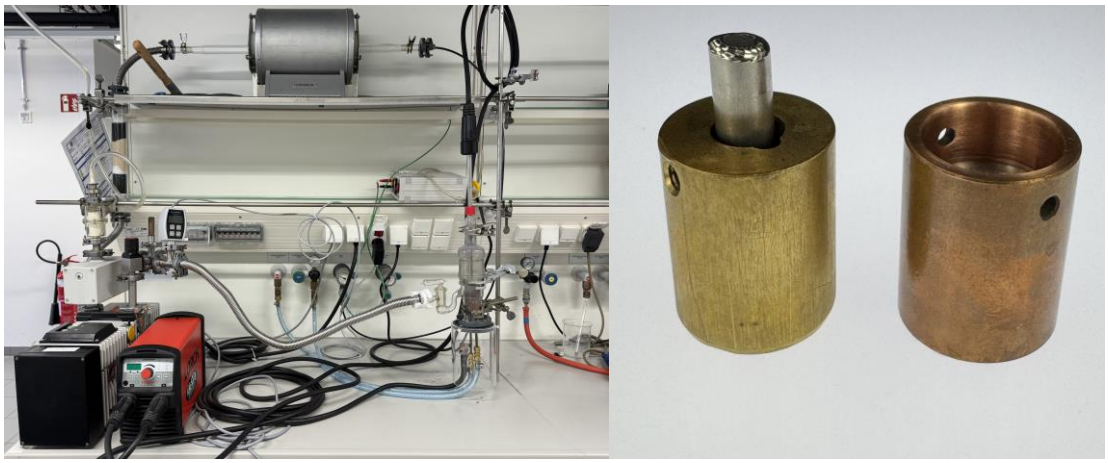

Figure 18. (*left*) Picture of the used arc furnace setup and (*right*) the home-made copper crucibles as well as the brass insert for the use of metal ampoules.

Figure 18 (*left*) shows a picture of the setup used for the synthesis of intermetallic compounds. Details on the design reported by Pöttgen, Gulden and Simon can be found in literature.[235] The home-built furnace contains a welding generator (Lorch, HandyTIG 180 DC) equipped with a ceria stabilized tungsten electrode. The counter electrode is a water-cooled hearth in which either a home-made copper crucible containing the elements or a brass insert for metal ampoules can be placed, both depicted in Figure 18 (*right*). The oven is closed by a three-component build made of silica. One is a ball cut on which the electrode is fixed but still enables movement of the electrode. This is attached to a piece with a large cut which is not closed to avoid working in a closed system (potential overpressure release possible) and the bottom piece which closes the oven and is moreover attached to a vacuum pump and argon. The argon is purified over Ti sponge (99.95 %, Alfa Aesar), which is placed in an oven at 873 K and moreover purified over molecular sieve and silica gel. Before use, the sample chamber was evacuated at least four times and backfilled with argon. As working pressure for the melting 800 mbar (±30 mbar) was used. For reactions, a power output of 30 A was used. For the melting of Nb and Ta ampoules this power was increased up to 45 A.

4.3 Container materials for annealing and synthesis

Since in this thesis most of the compounds deal with metals that can easily be handled in the arc furnace, this device was used for an initial reaction of the metals. To enhance crystallinity, homogeneity or to get to phase pure compounds, additional annealing is necessary in many cases. One easy possibility is the usage of silica ampoules. The obtained melting bead or pieces of it can be sealed in silica ampoules under vacuum. For this a so-called Stock apparatus was used. Silica tubes obtained from proQuarz (Mainz, Germany) were used and melted to ampoules with a variety of diameters and wall thicknesses of at least 1 mm. Direct synthesis in silica ampoules starting with the elements is not a suitable technique because highly oxophilic elements such as aluminum would react with the glass wall and break the ampoule. Nevertheless, for intermetallic compounds prepared by arc-melting, the use of silica ampoules works nicely. In cases in which side reactions with the glass wall are observed, even by the melting beads, either corundum or metal (Nb or Ta) crucibles can be placed inside a glass ampoule and prevent this reaction. It is also possible to put the elements inside these crucibles and perform reactions inside glass ampoules. As already described above, reactions involving elements with low boiling points, respectively high vapor pressures are better performed in fully closed metal ampoules. The metal ampoules used within this work were produced from either Nb or Ta pipes (WHS Sondermetalle) which were cut to a length of 3-5 cm. Sheet metal (WHS Sondermetalle) was used for the lids. Closing of the ampoules was done with the arc furnace. The corundum crucibles were obtained either from KYOCERA Fineceramics Europe GmbH (Mannheim, Germany) or THEPRO (Heinsberg, Germany). Lastly, carbon crucibles shall be mentioned as another possible container material. Here, either glassy carbon or graphite crucibles can be used. For the reaction of the intermetallic compounds with the chalcogenides S, Se and Te graphitized silica ampoules proved to be quite effective. For this, a small layer of graphite is deposited at the inner wall of the ampoule. This is achieved by the pyrolysis of small amounts of acetone. An advantage of this technique is that one avoids the incorporation of oxidic impurities which can happen in corundum crucibles. Oxidation reactions under air or oxygen were performed in porcelain (likely to be a mixture of Al_2O_3, SiO_2 and MgO) boats, simply because one can use higher masses while also having a large surface compared to small corundum crucibles alongside the advantage of using them in horizontal tube furnaces (*vide infra*). All described container materials are shown in Figure 19.

Figure 19. Container materials used within this thesis. From *left* to *right*: Silica ampoules; alumina and graphite crucibles for synthesis and annealing; niobium crucibles, sheet and tubes that can be closed to ampoules; porcelain boats in different sizes; small alumina crucibles which are used for thermal analysis.

4.4 Annealing and oxidation reactions in muffle furnaces

As explained before, glass ampoules were commonly used within this work. The closed silica ampoules were placed inside a resistance muffle furnace with a temperature controller. Samples can be heated with given heating rates, usually between 25-400 K h^{-1} kept at temperatures between 873-1473 K for dwelling times between 10 hours up to 40 days and cooled to room temperature with rates of usually 2-20 K h^{-1} or furnace cooling if slow cooling processes are not necessary. The advantages of muffle furnaces are that one can easily heat multiple samples at the same time, set the temperature precisely and enable slow to very slow cooling rates for crystallization if necessary. Besides annealing and reactions in closed ampoules oxidation reactions with air as reactive gas were also performed in muffle furnaces using the samples in either corundum crucibles or porcelain boats. Within this work either Nabertherm 11/HR (Lilienthal/Bremen, Germany) or Carbolite Gero CWF 3016 (Neuhausen, Germany) muffle furnaces were used.

4.5 High frequency induction system

Besides heating in the described classic muffle furnaces, also the use of high-frequency induction systems is possible. Heating of the sample is based on the resistivity of metals when placed in an electromagnetic field. They start heating due to the induced current within the material. The system used within this work (Typ TIG 5/300, Hüttinger Elektronik, Freiburg, Germany) is shown in Figure 20. A home-built water-cooled sample chamber can be attached to a vacuum pump and inert gas.[236] The Ar used in this system is also purified over Ti sponge at 873 K, molecular sieve and silica gel. Water cooling is necessary to prevent heating of the glassware and subsequent reactions with the container materials. Inside the sample chamber either a corundum crucible, a metal ampoule (or crucible) or carbon-based crucibles can be placed. Induction furnaces can either be used for synthesis (use of the element pieces), annealing of the melting beads after arc-melting or pressed pellets from ground intermetallic powder. When a ceramic crucible is used the heating is only based on the intrinsic heating of the intermetallic material. Metal and carbon crucibles heat up much faster than the sample due to their higher mass. In that case, the sample is heated indirectly at first. Reactions are usually done under flowing Ar, annealing under static Ar atmosphere. Besides that, it is also possible to anneal an arc-melted bead in a closed glass ampoule. The ampoule is put in an attachment which can also water-cool the ampoule from the outside in a way that the melting bead is placed in the center of the coil.[236] Upon heating the sample, “snipping” on the top of the ampoule, which must point out of the attachment, will create a sound due to the clicking of the melting bead inside the glass ampoule. When the temperature is high enough the clicking gets muffled based on the softening of the material, indicating that the sample is close to its melting point. With that technique one can anneal samples slightly below the melting point without knowing it precisely.

Figure 20. Picture of the (*left*) high-frequency generator, (*middle*) a vacuum pump attached to the (*right*) water-cooled reaction chamber for the insertion of alumina or metal crucibles and glass ampoules.

An advantage of the induction system is the incredibly fast homogeneous heating of a sample. Reactions can be done within minutes. Two disadvantages are that the temperature cannot be controlled precisely, and no controlled cooling is possible. The temperature can only be visually controlled (in the present system) based on black body radiation, furthermore the temperatures inside e.g. metal ampoules cannot be measured. It is also not possible to do a precise cooling of the samples since an external control to regulate the output power does not exist for the used system.

For the oxidation of intermetallic compounds, one could possibly think of attaching reactive gas to the sample chamber which was not done yet. But experiments were done using the induction system for heating pressed pellets of an intermetallic sample under vacuum. Opening the valve to air exposed the samples to oxygen at already elevated temperatures, neglecting possible effects of heating rates.

4.6 Oxidation reactions of intermetallic compounds

4.6.1 STA – A combination of thermogravimetric analysis and differential scanning calorimetry

One possibility for the oxidation reaction of intermetallic compounds is the use of a so-called STA (Simultaneous Thermal Analyis) device. A sample, which is placed in a corundum crucible can be heated under oxygen/argon atmosphere while the mass difference and heat flow against a reference is measured. These measurements generate results that are interesting in multiple ways. On the one hand, one can gather information about how much mass the samples gain when reacting with oxygen, on the other hand the heat flow gives information about the character of the occurring reaction (exo- or endothermic) alongside how intense the change in temperature is. Lastly, the obtained powder can of course be analyzed with PXRD revealing the formed phases. The setup used within this thesis was a TGA/DSC 1 Star HT/1600 system from Mettler Toledo (Columbus, OH, USA). Sample quantities range between 10-30 mg. Crucibles (usually 150 µL) are also shown in Figure 19.

4.6.2 Tube furnace with reactive gas

The above-mentioned possibilities of oxidation reactions of intermetallic compounds have the problem that the gas atmosphere cannot be controlled, since in muffle furnaces air is still present and no gas flow is present. Moreover, oxidation reactions in the STA setup only allow for low sample quantities. Therefore, a home-built system consisting of a tube furnace alongside a gas control unit was implemented, allowing for the use of porcelain boats in which more material can be oxidized. The installed flowmeters allow for controlled gas flow rates of oxygen or in theory any other reactive gas. To exclude all effects of air or moisture, the argon used to flush the device is also purified over Ti sponge at 873 K. The setup together with the flow meters is shown in Figure 21. Finally, the use of a combination of a reactive gas with argon or pure reactive gas is possible.

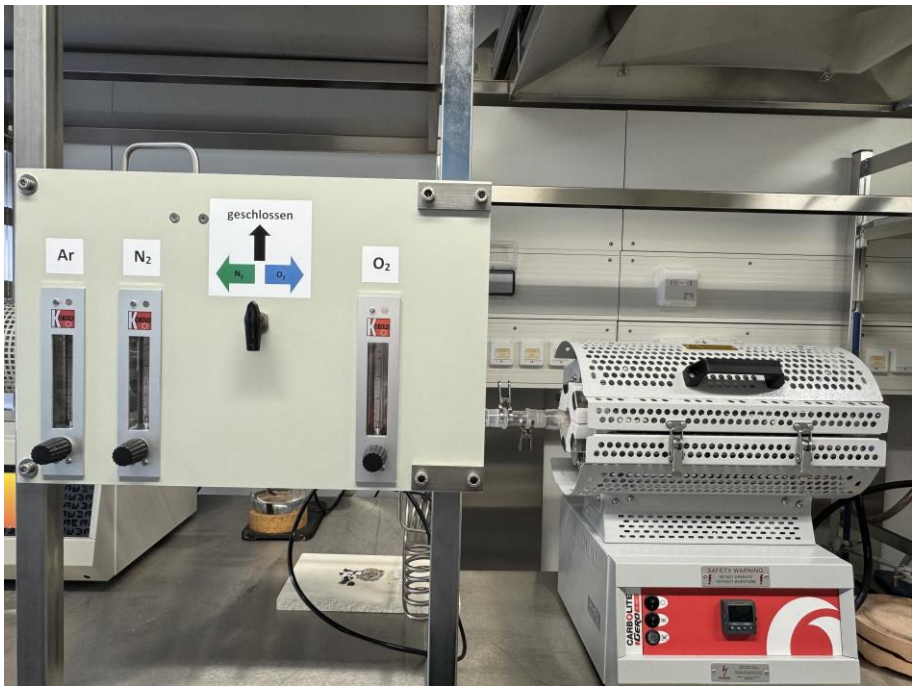

Figure 21. Tube furnace setup, which was used in this thesis. It can be run with either purified inert or reactive gas together with flowmeters to control the gas flow.

5 Results and discussion

The results in this thesis will be presented in four separate parts. Chapters 5.1 and 5.2 contain studies solely about intermetallic compounds, their synthesis, structural, spectroscopic and magnetic characterization, whereas the results of the first chapter have already been published in peer-reviewed scientific journals. The second chapter deals with unpublished results, which are presented in the way of a monography. The same applies for chapters 5.4 and 5.5 in which all results investigating the oxidation behavior of intermetallic compounds as well as their use as precursor materials are presented. In between, a small intermezzo between the two big acts, namely chapter 5.3, contains the results of a study of both worlds. During systematic investigations of an intermetallic solid solution, a still intermetallic sub-oxide was discovered.

In the first work an isostructural series of known binary aluminum compounds was synthesized and further investigated by spectroscopic methods, mainly ^{27}Al solid state NMR. This has been done due to the lack of comprehensive studies about the spectroscopic properties of such a series. The following publications deal with results found during exploratory synthesis of ternary aluminum compounds with either two early transition metals or one rare earth element and one early transition metal. Here the first compounds with the Mg_2Ni_3Si structure type with Al were found for the series RE_2TiAl_3 (RE = Y, Gd-Tm, Lu). Staying with the Laves phase structure types a detailed investigation of the solid solution $Hf(V_{1-x}Al_x)_2$, using powder and single-crystal XRD as well as solid state NMR experiments, SEM/EDX and where possible magnetic property measurements, was done. This study revealed a new superstructure of the hexagonal Laves phase $MgZn_2$, crystallizing in the trigonal crystal system with space group $P\bar{3}m1$ and the composition Hf_4VAl_7. This symmetry-reduced structure shows a small homogeneity range. These findings motivated new experiments in many directions leading to a similar detailed investigation of the solid solution $Zr(V_{1-x}Al_x)_2$ as well as finding more compounds adopting the newly discovered Hf_4VAl_7 structure type leading to the discovery of binary Hf_6Al_7 and a reinvestigation of ternary $Hf_4Nb_2Al_7$.

The second chapter summarizes unpublished results starting with attempts to find more compounds with the Hf_4VAl_7 structure type based on the approach of exchanging V leading to different results depending on the chosen transition metal. Furthermore, the formation of the compound ZrV_2Al_4, which adopts the tetragonal $YbMo_2Al_4$, after long annealing times is reported. Furthermore, a study about the synthesis and magnetic characterization of selected

members of the solid solution $Gd(Fe_{1-x}Al_x)_2$ is shown. A single-crystal analysis of a quaternary substitution compound of $YbTi_2Al_{20}$ substituted with Sn is given and finally, a study showing the synthesis and investigation of the local order or disorder in the compounds with the general formula RE_2Si_2Al (RE = Sc, Y, Lu) using ^{27}Al, ^{29}Si and ^{45}Sc solid state NMR is reported.

The third chapter contains a combination of both topics of this thesis due to an unexpected finding. While investigating the solid solution $Sc_2(Au_{1-x}Al_x)$, which was investigated by solid state NMR on one hand the instability towards air/humidity of the endmember Sc_2Au was investigated, which is interesting since Sc is a stable metal at room temperature. Moreover, during these investigations, the cubic sub-oxide $Sc_4Au_2O_{1-x}$ was discovered where oxygen stabilizes "Sc_2Au".

In the fourth chapter two separate publications sum up the oxidation behavior of the cubic Laves phase $CaAl_2$, which was carefully investigated, using different oxidation conditions, as well as high-energy ball milling. When switching the oxidation reagent from oxygen (air) to sulfur phase pure samples of the compounds MAl_2S_4 (M = Ca, Sr, Eu) could easily be obtained, spectroscopically characterized (NMR and Mößbauer) and embedded into a polysiloxane generating a luminescent hybrid material.

Finally, the fifth chapter shows further results about the oxidation chemistry of selected binary intermetallic aluminides. The oxidation behavior and product formation of the already discussed series of the $REAl_2$ (RE = Sc, Y, La, Eu, Yb), $AEAl_4$ (AE = Ca, Sr, Ba) as well as $SrAl_2$ and $Ba_{21}Al_{40}$ was investigated due to their availability and comparability. Based on intermetallic precursors the compound $CaAl_2Se_4$ could be synthesized and analyzed using SCXRD resulting in a correct description of the structure, which was not available in literature. The compounds $YbAl_2S_4$ and $YbAl_2Se_4$ which were lacking a structure description in literature could also be investigated. Leaving group II and rare earth elements, finally, the oxidation behavior of the hexagonal Laves phase $HfAl_2$ was investigated using in-situ PXRD.

5.1 Synthesis and spectroscopic investigations of intermetallic compounds (published)

5.1.1 Systematic studies of ^{27}Al solid state NMR spectroscopy on two isostructural series MAl$_2$ (M = Ca, Sr, Sc, Y, La, Yb, Lu) and AEAl$_4$ (AE = Ca, Sr, Ba)

Published as two articles:

Raman and NMR spectroscopic and theoretical investigations of the cubic laves-phases *RE*Al$_2$ (*RE* = Sc, Y, La, Yb, Lu)

Elias C. J. Gießelmann, Stefan Engel, Weronika Kostusiak, Yuemei Zhang, Petra Herbeck-Engel, Guido Kickelbick and Oliver Janka, *Dalton Trans.* **2023**, *52*, 3391.

https://doi.org/10.1039/d3dt00141e

Contribution of the authors to the manuscript

Supervision of this project was done by PD Dr. Oliver Janka. Elias C. J. Gießelmann did most of the synthetic work, the measurement and evaluation of the solid state NMR data and provided an initial draft of the manuscript. Dr. Stefan Engel assisted with the synthesis of YbAl$_2$ in a sealed metal ampoule. Weronika Kostusiak and Prof. Dr. Yuemei Zhang did the quantum mechanical calculations and wrote the respective parts in the manuscript. Dr. Petra Herbeck-Engel did the measurement and evaluation of the Raman spectroscopy measurement. The manuscript was finalized by PD Dr. Oliver Janka and Prof. Dr. Guido Kickelbick

Theoretical and ^{27}Al NMR Spectroscopic Investigations of Binary Intermetallic Alkaline-Earth Aluminides

Stefan Engel, Elias C. J. Gießelmann, Lukas E. Schank, Gunter Heymann, Kristina Brix, Ralf Kautenburger, Horst Philipp Beck, and Oliver Janka, *Inorg. Chem.* **2023**, *62*, 4260.

https://doi.org/10.1021/acs.inorgchem.2c04391

Contribution of the authors to the manuscript

Synthesis was done by Dr. Stefan Engel and Lukas Schank during his internship. High-pressure synthesis was done by assoz. Prof. Dr. Gunter Heymann. Dr. Kristina Brix and apl.

Prof. Dr. Ralf Kautenburger did the ICP-MS measurement and analysis. DFT calculations were performed by Prof. Dr. Horst P. Beck. The manuscript was finalized by PD Dr. Oliver Janka. Elias C. J. Gießelmann did the preparation, measurement and evaluation of the solid state NMR data, as well in parts the evaluation of the quantum mechanical data and wrote the respective parts in the manuscript. Therefore, only the solid state NMR data will be discussed in detail in the following. Other details about the compounds can be found in the publication, which is not incorporated here.

Summary

When looking into the literature on intermetallics, it becomes evident that systematic studies combining synthesis and spectroscopy on isostructural compounds are quite rare. This might be since isostructural series of multiple compounds, in which only one element is exchanged, are not often to be found. Especially for solid state NMR spectroscopic investigations, series of the rare earth atoms are unsuitable, as only compounds containing the closed-shell rare-earth elements can be investigated.

One excellent example for this is the series of binary aluminides $M\mathrm{Al_2}$ (M = Ca, Sr, Sc, Y, La, Lu, Yb) which all adopt the cubic $\mathrm{MgCu_2}$ type ($Fd\bar{3}m$). Another example is the series of the compounds $AE\mathrm{Al_4}$ (AE = Ca, Sr, Ba). Here, the Ca compound adopts the monoclinic $\mathrm{CaGa_4}$ ($C2/m$) structure type at ambient conditions. It undergoes a phase transition to the tetragonal $\mathrm{BaAl_4}$ structure type ($I4/mmm$). The Sr and Ba compound crystallize in this tetragonal structure at ambient conditions. However, despite the fact that $\mathrm{CaAl_4}$ adopts a different structure type at room temperature, the low and the high-temperature polymorphs are structurally closely related and therefore still comparable.

The synthesis and structural characterization of the above-mentioned aluminides of the alkaline earth metals were investigated by Stefan Engel. Furthermore, the structural relationship of the high and low temperature phase of $\mathrm{CaAl_4}$ as well as quantum chemical considerations of the stability of these compounds were conducted in the publication cited above. Here, only the NMR spectroscopic investigations on these compounds shall be discussed.

The compounds $AE\mathrm{Al_4}$ with AE = Ca, Sr, Ba have two crystallographically independent Al sites in the crystal structure. Therefore, one expects them to show two distinct signals within a ^{27}Al solid state NMR spectrum. Recorded ^{27}Al single-pulse excitation spectra for these compounds are shown in Figure 22.

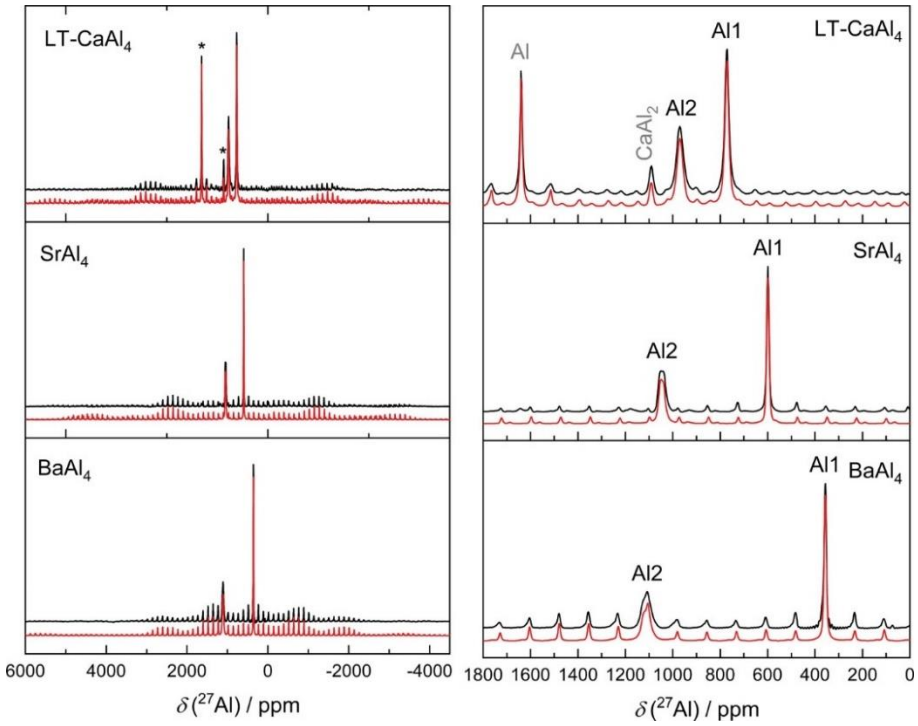

Figure 22. ^{27}Al solid state MAS NMR spectra of monoclinic $CaAl_4$ ($CaGa_4$ type, *top*), $SrAl_4$ (*middle*) and $BaAl_4$ (both $BaAl_4$ type, *bottom*). (*left*) Full spectra and (*right*) zoomed regions on the central transitions. Adapted with permission from *Inorg. Chem.* **2023**, *62*, 4260. Copyright 2025 American Chemical Society.

Details about the refinement, the starting values obtained from DFT calculations as well as a comparison of the extracted data to literature known values can be found in the publication given above. Here, it should simply be summarized that the analysis of the obtained spectra could nicely be done. The values obtained for the Sr and Ba compound were in good accordance with the literature.[98] The spectrum for the $CaAl_4$ compound shows the impurities of elemental Al and $CaAl_2$ ($MgCu_2$ type), which could also be identified in the powder X-ray diffractograms. A correlation of the obtained shifts of the resonance frequency of the two central transitions could be made within this work. It was pointed out that the Knight shift of the respective Al site shows a correlation with the calculated Bader charges for each Al site, when compared to the respective electronegativity difference of the alkaline earth metal to aluminum. While in the series from Ca to Ba the charge on the Al1 site becomes less negative, the negative charge of the Al2 site increases. The observed resonance frequency shifts show exactly the opposite trend. This is already visible in the spectra shown above, in which the two signals of the Al sites drift apart when going from Ca to Ba.

Within the above-mentioned work, the compounds $CaAl_2$ and $SrAl_2$ were synthesized by Stefan Engel. $CaAl_2$ adopts the cubic $MgCu_2$ type, as does the high-pressure modification of $SrAl_2$ synthesized by Gunther Heymann. The ambient pressure phase adopts the KHg_2 type

(*Imma*). All three were also investigated by solid state NMR spectroscopy. The spectra are shown in Figure 23.

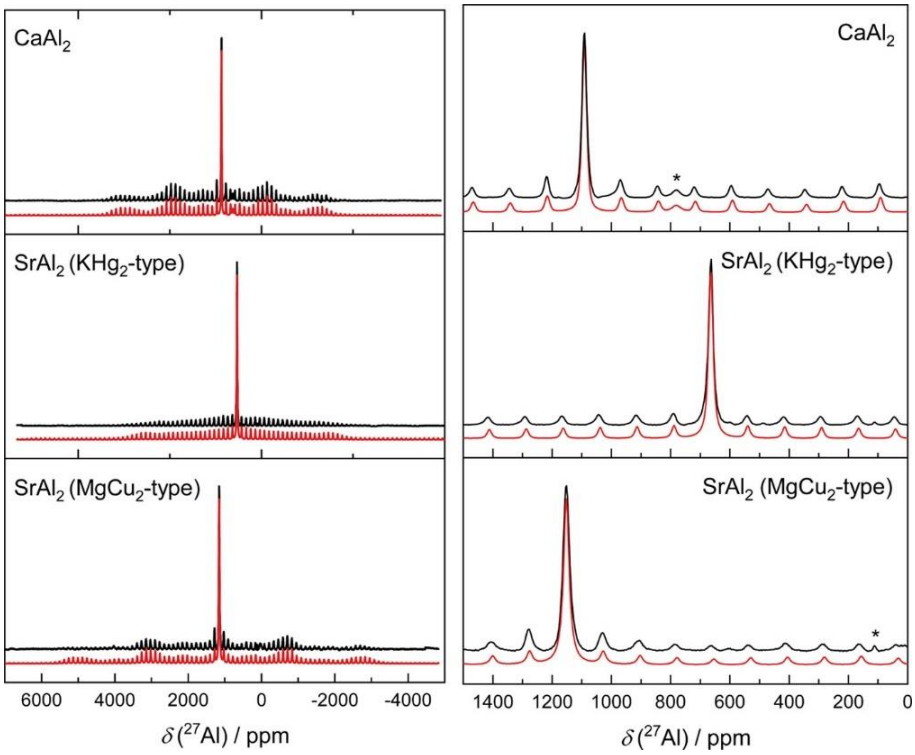

Figure 23. ^{27}Al solid state MAS NMR spectra of $CaAl_2$ ($MgCu_2$ type, *top*), $SrAl_2$ (KHg_2 type, *middle*) and $SrAl_2$ ($MgCu_2$ type, *bottom*). (*left*) Full spectra and (*right*) zoomed regions on the central transitions. Adapted with permission from *Inorg. Chem.* **2023**, *62*, 4260. Copyright 2025 American Chemical Society.

Interestingly, although the composition is the same for NP- and HP-$SrAl_2$, the structural differences lead to a dramatic change of the observed resonance shift of about ~480 ppm.

To sum up this first part, all synthesized aluminides could be characterized using ^{27}Al solid state NMR spectroscopy. The spectra could be fitted reasonably good using starting values obtained from DFT calculations. All spectra confirm the crystal structures of the binary phases and the impurities in the sample of $CaAl_4$, as identified by Rietveld refinement of the powder X-ray diffractograms.

In another parallel work, the isostructural series *RE*Al_2 with *RE* being the diamagnetic (closed shell) elements *RE* = Sc, Y, La, Yb, Lu was synthesized followed by a systematic study of these compounds using ^{27}Al and ^{45}Sc solid state NMR, Raman spectroscopy as well as DFT calculations. All the results are summed up in the publication on the following pages. The literature known phases could be synthesized phase pure based on X-ray powder analysis. Solid state NMR spectra for these compounds were in parts known to literature. In this work, they were set in context, as was the measurement of the missing compound $ScAl_2$. Here, also a ^{45}Sc

solid state NMR spectrum could be measured and nicely fitted due to the high symmetry of the structure. A significant impact on the spectrum of $LuAl_2$ was observed by annealing the sample, namely a significantly reduced line width of the central transition.

In addition, the symmetry of the cubic Laves phases makes it possible to measure Raman spectroscopy with these compounds. Here, literature known data for La, Yb and Lu could be confirmed and extended for the data of the Sc and Y compounds.

DFT calculations of the Bader charges for the discussed compounds showed a negative charge for the Al atoms confirming the term aluminides. Analysis of the electron localization functions revealed electron density between Al atoms showing covalent bonding interactions, while interactions between the rare earth atoms and aluminum are rather weakly covalent to moderate ionic.

Based on the extracted *s*-electron density at the Fermi-level E_F, a correlation of the observed resonance shifts can be done. This is given in Figure 13 of the attached manuscript. It is clearly visible that a correlation only makes sense when comparing the clearly trivalent rare earth atoms. The divalent (or more correctly intermediate valent) Yb compound is not in line with the others. Therefore, Figure 24 (left) shows the combination of a combined plot with all measured resonance shifts of the MAl_2 species as a function of the calculated *s*-electron density at the Fermi level. Values for the Ca and Sr compound were calculated after publication. In addition to the ELF analysis presented in the manuscript, a quantitative analysis using LOBSTER was performed to investigate bonding in the $REAl_2$ series. Results are shown in the right part of Figure 24. The ICOBI values for the Al–Al bonds, which are an indicator for the bond strength/covalency were calculated. They show that the increase in the Al–Al distances is likely to be a combination of a size effect of the rare earth atom but also the bonding plays a crucial role. Short distances in the Sc compound match a higher ICOBI value in comparison to the La compound. However, the Lu (with a full f-electron shell) and Yb as divalent metal do not fit in the order of the remaining compounds, with the ICOBI in $YbAl_2$ being the highest calculated for the series. The analysis for the NMR parameters as well as for the bonding situation is not straightforward here.

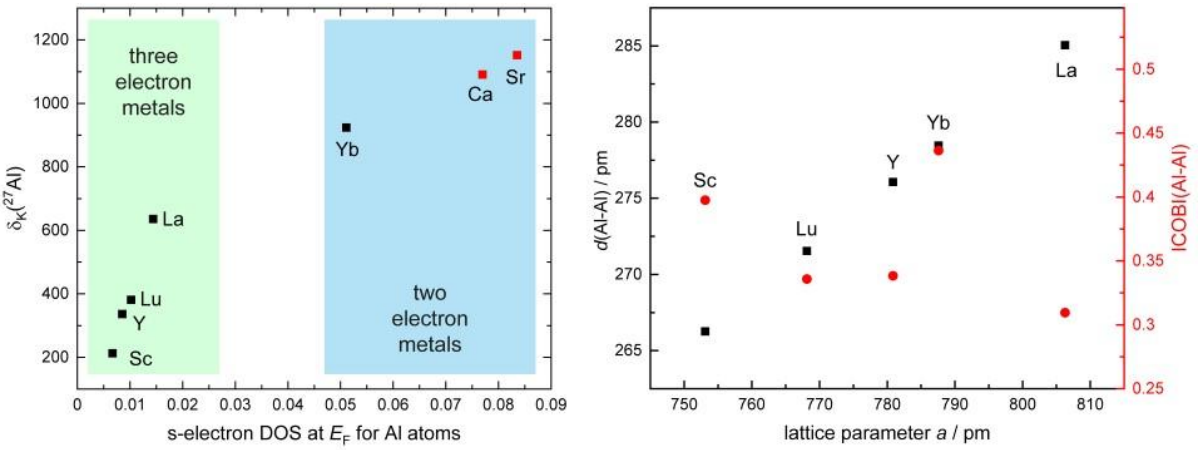

Figure 24. Additional Quantum chemical data and comparisons for the binary series MAl$_2$; (*left*) Compiled calculated *s*-electron density at the Fermi Level and the observed ^{27}Al solid state NMR shifts of all non-magnetic (diamagnetic) members of the series MAl$_2$; (*right*) Calculated ICOBI values in comparison to lattice parameters and resulting Al–Al distances in the series REAl$_2$.

Dalton Transactions

ROYAL SOCIETY OF CHEMISTRY

PAPER

View Article Online
View Journal | View Issue

Check for updates

Cite this: *Dalton Trans.*, 2023, **52**, 3391

Raman and NMR spectroscopic and theoretical investigations of the cubic laves-phases $REAl_2$ (RE = Sc, Y, La, Yb, Lu)†

Elias C. J. Gießelmann, [a] Stefan Engel, [a] Weronika Kostusiak,[b,c] Yuemei Zhang, [b] Petra Herbeck-Engel,[d] Guido Kickelbick [a] and Oliver Janka *[a]

Received 16th January 2023,
Accepted 9th February 2023

DOI: 10.1039/d3dt00141e

rsc.li/dalton

The cubic Laves-phase aluminides $REAl_2$ with RE = Sc, Y, La, Yb and Lu were prepared from the elements by arc-melting or using refractory metal ampoules and induction heating. They all crystallize in the cubic crystal system with space group $Fd\bar{3}m$ and adopt the $MgCu_2$ type structure. The title compounds were characterized by powder X-ray diffraction and spectroscopically investigated using Raman and ^{27}Al and in the case of $ScAl_2$ by ^{45}Sc solid-state MAS NMR. In both, the Raman and NMR spectra, the aluminides exhibit only one signal due to the crystal structure. DFT calculations were used to calculate Bader charges illustrating the charge transfer in these compounds along with NMR parameters and densities of states. Finally, the bonding situation was assessed by means of ELF calculations rendering these compounds aluminides with positively charged $RE^{\delta+}$ cations embedded in an $[Al_2]^{\delta-}$ polyanion.

1 Introduction

Intermetallic aluminium compounds are an interesting class of materials, since they play a major role in the formation of high-strength aluminium alloys formed during precipitation hardening.[1,2] In Mg–Cu–Al alloys for example, the so-called *S*-phase ($MgCuAl_2$, *Cmcm*) forms during annealing.[3–5] When searching the Pearson database,[6] it becomes evident that Al forms binary compounds with almost every other element in the periodic table. Exceptions are the alkali-metals Na and heavier (Li compounds do exist), Cd and Hg, In and Tl as well as Pm and most of the actinides. The latter ones, however, are probably unknown due to a lack of accessibility. Amongst these, the alkaline-earth, group 3 and rare-earth metals and some of the actinides form compounds with the general formula MAl_2 (Ca–Ba, Sc, Y, La–Nd, Sm–Lu, Th, U–Pu[7–13]) which adopt the cubic Laves-phase structure type $MgCu_2$ ($Fd\bar{3}m$). Having numerous isostructural compounds at hand enables the investigation of *e.g.* physical properties like their wear- and corrosion-resistance, their magnetic or superconductive, their low-temperature behaviour or their hydrogen storage capabilities also in dependence of the constituent elements.[14–17] When drawing back to the MAl_2 compounds, the compounds differ with respect to their unit cell parameter, but both crystallographic sites are special positions (M on 8*b* (3/8, 3/8, 3/8); Al on 16*c* (0,0,0)). Therefore, the sizes of the respective M atoms at least partially influence the lattice parameters. However, the elements differ significantly with respect to their electronegativities, and their valence electron configuration. In all cases, the Al atoms are more electronegative than the M atoms rendering these compounds aluminides. While the alkaline-earth atoms can supply a maximum of two electrons, elements of group 3 and the rare-earth atoms can supply up to three electrons. Exception of this rule are Eu and Yb, which are two electron metals in their elemental form.[18,19] This in turn leads to differences in the respective negative charges on the Al atoms in the binary MAl_2 compounds.

Solid-state Nuclear Magnetic Resonance (NMR) spectroscopy is a strong, site specific method for the characterization of compounds containing NMR active nuclei and known and used for several decades. Having 100% natural abundance the ^{27}Al nucleus (I = 5/2) is an excellent candidate for NMR spectroscopic experiments, however, a medium-sized nuclear electric quadrupole moment ($e_Q = 0.15 \times 10^{-28}$ m^2) and a moderately high gyromagnetic ratio ($\gamma = 6.976 \times 10^7$ rad T^{-1} s^{-1}) can complicate the interpretation of its spectra.[20,21] Still, ^{27}Al (MAS-)NMR is nowadays a widely established technique for structural characterization in different material classes.[22–26]

[a]*Inorganic Solid-State Chemistry, Saarland University, Campus C4.1, 66123 Saarbrücken, Germany. E-mail: oliver.janka@uni-saarland.de*
[b]*Department of Chemistry and Physics, Warren Wilson College, Swannanoa, NC, 28778, USA*
[c]*Department of Chemistry, University of Wroclaw, F. Joliot-Curie 14, 50-383 Wroclaw, Poland*
[d]*INM Leibniz Institute for New Materials, Campus D2.2, 66123 Saarbrücken, Germany*

†Electronic supplementary information (ESI) available: Additional powder X-ray data, individual ^{27}Al NMR spectra. See DOI: https://doi.org/10.1039/d3dt00141e

Especially in the last twenty years it has been established as a versatile method for additional characterization of intermetallic compounds.[27] And although this class of compounds has metallic character, the method can be used to gain a plethora of information such as validation of crystallographic structures, local environments, solid solutions and more. And although many ternary compounds have been characterized by NMR (*e.g.* the equiatomic ScTAl compounds,[28] the ScT_2Al Heusler phases,[29] the gold compounds Na_2Au_3Al,[30] AEAuX,[31] $AEAu_2Al_2$,[32] or the platinides $Ba_3Pt_4Al_4$[33] or $Sr_2Pt_3Al_8$[34]) there is a significant lack of comparing studies about a larger group of isostructural compounds. As examples for the latter, the $MTAl_2$[35,36] or the $RE_{10}TAl_3$ series[37] should be mentioned.

Here, a combining study on the rare-earth aluminides $REAl_2$ for the elements Sc, Y, La, Yb and Lu is presented. These aluminides are Pauli-paramagnetic (no localized magnetic moments, only conduction electrons) and exhibit only one crystallographic Al site, rendering them ideal candidates for systematic ^{27}Al NMR studies. Individual studies on some of the compounds have already been reported before,[38–41] however, a comparing work of the ^{27}Al NMR data is missing and $ScAl_2$ has not been characterized before. For this compound, in addition to ^{27}Al also ^{45}Sc NMR data could be obtained. Raman spectroscopic investigations were conducted on all prepared samples, which help to understand these compounds even further. Additionally, quantum-chemical calculations were carried out to help with the interpretation of the NMR data and to calculate Bader charges which can be used to analyse the anionic character of the $[Al_2]^{\delta-}$ network. The bonding situation was assessed using the electron localization function ELF.

2 Experimental

2.1 Synthesis

Aluminium pellets (99.99%, Onyxmet), scandium (99.98%; Onyxmet), yttrium (99.99%; Onyxmet), lanthanum (99.95%, Onyxmet), ytterbium (99.95%, Onyxmet) and lutetium (99.95%; Onyxmet) chunks were used for the reported syntheses. Lanthanum pieces were stored under an argon atmosphere, surface contaminations on the pieces were removed mechanically in an argon filled glovebox. The elements were weighed in the ideal stochiometric ratio of RE : Al = 1 : 2 and subsequently arc-melted in water-cooled copper crucibles in an argon atmosphere of about 800 mbar.[42] The argon gas was purified over a titanium sponge (873 K), molecular sieve and silica gel prior to the use. The obtained buttons were remelted four to five times to improve the homogeneity. Powdered as-cast $LuAl_2$ was loaded into a corundum crucible which was sealed in an evacuated silica tube and annealed at 1073 K for 48 h followed by cooling to RT within 48 h. The other samples were used without any further heat treatment. The ytterbium compound was synthesized in an arc-welded niobium ampoule[43] due to the low boiling point of ytterbium metal (1496 K[18]). The Nb ampoule was heated for 2 h to approximately 1200 K in an induction furnace (Trumpf Hüttinger, Truheat HF 5010) under argon atmosphere. All samples show metallic lustre, ground powders are grey and stable in air over months.

2.2 X-ray diffraction

Powder X-ray diffraction (PXRD) patterns of the pulverized samples were recorded at room temperature on a D8-A25-Advance diffractometer (Bruker, Karlsruhe, Germany) in Bragg Brentano θ-θ-geometry (goniometer radius 280 mm) with Cu K_α-radiation (λ = 154.0596 pm). A 12 μm Ni foil working as K_β filter and a variable divergence slit were mounted at the primary beam side. A LYNXEYE detector with 192 channels was used at the secondary beam side. Experiments were carried out in a 2θ range of 6–130° with a step size of 0.013° and a total scan time of 1 h. The recorded data was evaluated using the Bruker TOPAS 5.0 software.[44]

2.3 Solid-state NMR

^{27}Al and ^{45}Sc solid-state NMR spectra were recorded using a Bruker Avance III 400 WB spectrometer at 104.31 and 97.24 MHz using magic-angle spinning (MAS) conditions. The samples were used as fine powders. To reduce density and electrical conductivity, samples were mixed with dried sodium chloride in a 1 : 9 ratio. The diluted samples were loaded into a cylindrical ZrO_2 rotor with a diameter of 4 mm and spun at the magic angle with 13 kHz. All experiments conducted were single-pulse with a typical pulse length of 0.83 μs and a relaxation delay of 1 s. Resonance shifts were referenced to 1 molar $AlCl_3$ and $ScCl_3$ solutions in H_2O. The NMR spectra were recorded using the Bruker Topspin software,[45] the analysis was performed with the help of the DMFit software.[46]

2.4 Raman measurements

For the acquisition of the Raman spectra, a Raman microscope LabRAM HR Evolution HORIBA Jobin Yvon A (Longmujeau, France) equipped with 532 and 633 nm Lasers (Melles Griot, IDEX Optics and Photonics, Albuquerque, USA) and an 1800 lines mm^{-1} grating and a 100er LWD objective was used.

2.5 Theoretical calculations

Density functional theory (DFT) calculations of the $REAl_2$ series (RE = Sc, Y, La, Yb, Lu) were performed using the projector augmented wave method (PAW) of Blöchl[47,48] coded in the Vienna *ab initio* simulation package (VASP).[49,50] All VASP calculations employed the generalized gradient approximation (GGA) with exchange and correlation treated by Perdew–Burke–Enzerhof (PBE).[51] The cut-off energy for the plane wave calculations was set to 500 eV and the Brillouin zone integration was carried out using 9 × 9 × 9 k-point meshes. NMR parameters were evaluated through the field gradient tensor calculations in VASP with the nuclear quadrupole moment of 146.6 mb for ^{27}Al and −220 mb for ^{45}Sc. The Bader charge analysis was based on VASP calculations with subsequent calculations using the Bader program developed by the Henkelman group.[52–54] Chemical bonding was explored *via* Electron

Localization Functions (ELF)[55,56] obtained from the VASP calculations.

3 Results and discussion

3.1 Synthesis & X-ray diffraction

Phase pure samples, according to powder X-ray diffraction experiments, for all five rare-earth elements were obtained as described above. The diffraction patterns are shown in Fig. 1. The lattice parameters for the cubic compounds prepared in this work and from the literature are summarized in Table 1. As expected, the lattice parameters decrease with decreasing ionic radius[57,58] of the rare-earth atoms and show an almost linear trend as it is expected due to the lanthanide contraction (Fig. 2). Exceptions from this trend are observed for $EuAl_2$ and $YbAl_2$. While the Eu atoms in $EuAl_2$ exhibit a stable divalent state,[59] $YbAl_2$ was shown to be intermediate valent with a valence close to +2.4 at 300 K.[60,61] Since both Eu^{2+} and Yb^{2+} are significantly larger compared to their trivalent counterparts ($r(Eu^{2+})$ = 125 pm *vs.* $r(Eu^{3+})$ = 107 pm and $r(Yb^{2+})$ = 114 pm *vs.* $r(Yb^{3+})$ = 99 pm; all given for CN = 8 [57,58]), signficantly enlarged unit cells are observed for these two compounds.

A more detailed analysis of the diffraction patterns indicates that all samples contain a certain degree of strain since

Table 1 Lattice parameters, determined by Rietveld analysis from the recorded PXRD patterns of the cubic Laves-phases ($MgCu_2$ type, $Fd\bar{3}m$) and from the literature

Compound	*a*/pm	Ref.
$ScAl_2$	757.98(1)	This work
$ScAl_2$	758.0	62
YAl_2	786.29(1)	This work
YAl_2	786.0	12
$LaAl_2$	814.85(1)	This work
$LaAl_2$	816.9	63
$CeAl_2$	809.0	63
$PrAl_2$	803.5	11
$NdAl_2$	799.9	11
$SmAl_2$	794.3	11
$EuAl_2$	812.5	64
$GdAl_2$	790.0	13
$TbAl_2$	786.7	13
$DyAl_2$	784.0	13
$HoAl_2$	781.3	13
$ErAl_2$	779.5	13
$TmAl_2$	778.0	64
$YbAl_2$	788.36(1)	This work
$YbAl_2$	787.7	64
$LuAl_2$	774.37(1)	This work
$LuAl_2$ – annealed	774.24(1)	This work
$LuAl_2$	774.2	64

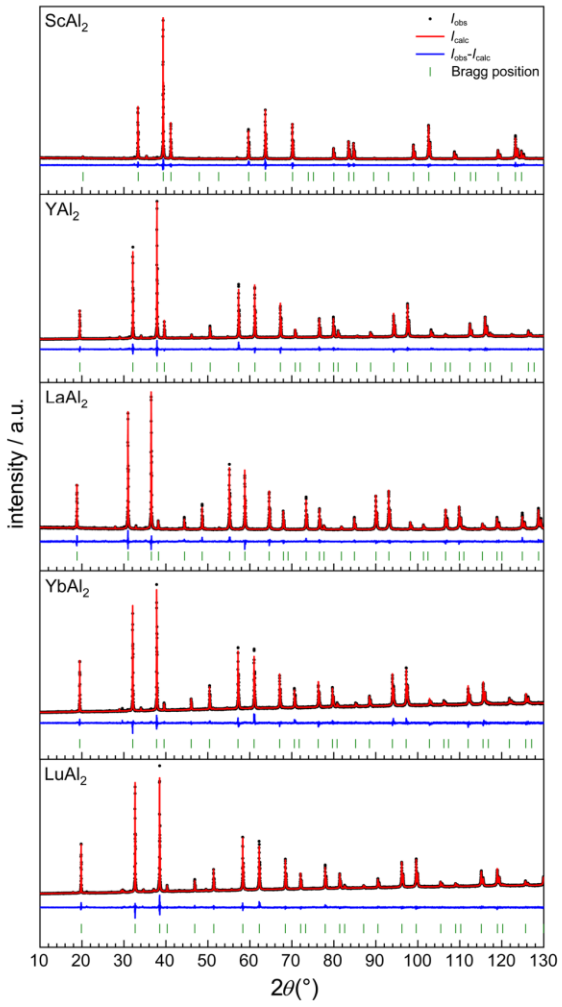

Fig. 1 Powder X-ray diffraction pattern of the $REAl_2$ compounds (RE = Sc, Y, La, Yb and Lu; top to bottom) crystallizing in the cubic $MgCu_2$ type structure ($Fd\bar{3}m$). The experimental data is shown as black dots, the fit as red line and the difference in blue. The green ticks indicate the Bragg positions.

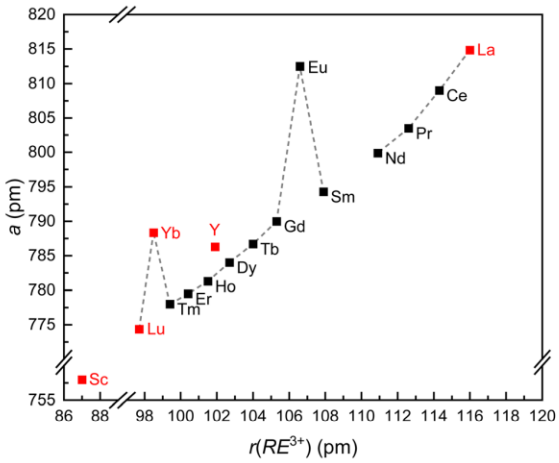

Fig. 2 Lattice parameters of the $REAl_2$ compounds (RE = Sc, Y, La–Nd, Sm–Lu) crystallizing in the cubic $MgCu_2$ type structure ($Fd\bar{3}m$) plotted *versus* their respective ionic radius for CN = 8.

A more detailed analysis of the diffraction patterns indicates that all samples contain a certain degree of strain since

they were used without annealing. The largest strain is observed for the samples of YAl_2 and $LuAl_2$, while $ScAl_2$ for example shows almost no strain. The work of Yuan and coworkers reported,[38] that a thermal treatment of the $LuAl_2$ sample improves the qualitity of the NMR spectrum with respect to the line broadening and assymmetry of the central transition line shape, however, the resonance frequency and the quadrupolar coupling are not affected. This might indicate that their initial sample also contained certain amounts of strain. Subsequently, the as-cast $LuAl_2$ sample from this work was annealed for 48 h at 1073 K, which led to a significant decrease of the strain.

3.2 Crystal chemistry

The $REAl_2$ members (RE = Sc, Y, La, Yb, Lu) all crystallize in the cubic crystal system with space group $Fd\bar{3}m$ and adopt the so-called cubic Laves-phase ($MgCu_2$ type). The structure contains one RE and one Al site, with the Al atoms forming empty Al_4 tetrahedra that are connected to other tetrahedra *via* all atoms forming a network (Fig. 3, left). The RE atoms reside in the cavities of this framework. When looking at the arrangement of the RE atoms, an arrangement similar to cubic diamond can be observed. In the following paragraph, the structure will be briefly discussed using $ScAl_2$ as example. The Al atoms are surrounded by six Al and six Sc atoms in the shape of a compressed icosahedron (Fig. 3, right). The Al atoms form two opposing triangular faces while the six Sc atoms are located near the equatorial plane, forming an undulating six-membered ring. The Sc atoms exhibit a coordination number of 16 arranged as Frank-Kasper polyhedron ($Sc@Sc_4Al_{12}$; Fig. 3, middle). Due to the high site symmetries (Sc: 8*b*, $\bar{4}3m$; Al: 16*c*, $.\bar{3}m$) and the symmetric coordination environment, one can derive that the asymmetry parameters η_Q for all ^{27}Al and the ^{45}Sc NMR spectra should be zero. At the same time, the nuclei of both Sc and Al exhibit a quadrupole moment. Therefore, the quadrupolar interaction of both nuclei is expected to be observed in their respective NMR spectra.

3.3 Solid State NMR spectroscopy

All five ^{27}Al MAS spectra recorded with single-pulse excitation experiments are shown in Fig. 4 (left). As described in the previous section, one resonance originating from one crystallographically independent Al site in the crystal structure is expected. All spectra show one sharp central line, originating from the $|+1/2> \leftrightarrow |-1/2>$ transition. All of them also show a wide spinning side band manifold caused by the $|\pm1/2> \leftrightarrow |\pm3/2>$ and $|\pm3/2> \leftrightarrow |\pm5/2>$ transitions, which are observable due to quadrupolar interactions. All resonance lines are significantly shifted compared to an aqueous solution of Al^{3+} within a range of 200 up to 950 ppm. This is caused by the interaction of the magnetic moment of the active ^{27}Al nuclei, the same is true for ^{45}Sc, with the conduction electrons of the metallic material. This is known as the Knight shift. To analyse the spectra, in a first step all central transitions were fitted with simple Gaussian-Lorentz lines. As can be seen on the right part of Fig. 4, all line shapes can be described with a Gaussian-Lorentz fit in a satisfying fashion. However, in the spectra of YAl_2, $LuAl_2$ and $YbAl_2$ the central transition shows a broad half-width and anisotropy with a shoulder on the left side.

Table 2 summarizes the relevant experimentally determined NMR parameters along with the ones from the DFT calculations. For some cases (RE = Y, La) the spectra could be simulated quite well using the values from DFT calculations. In these cases, the C_Q parameters were not refined. Due to the cubic symmetry of the structure, the asymmetry parameter η_Q must be zero, which agrees with the result of the DFT calculations. From the resonance shifts δ gained by fitting the data, the Knight shift contribution δ_K can be calculated using the NMR parameters from the DFT calculations as described in the literature.[27,65] Since all other contributions are small, they can be neglected as the Knight part dominates.

For all spectra the theoretical values of C_Q obtained from DFT calculations were used to simulate the spectra in the first place. In the cases of Sc, Yb and Lu the theoretical values did not match the experimental spectra well, here a better fit was

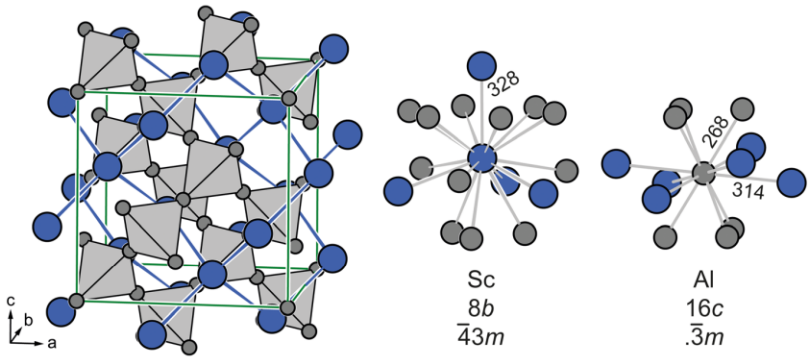

Fig. 3 (left) Unit cell of $ScAl_2$ ($MgCu_2$ type, $Fd\bar{3}m$) and coordination environments of the (middle) Sc (blue) and (right) Al (grey) atoms. Wyckoff positions and site symmetries as well as interatomic distances (in pm) are given.

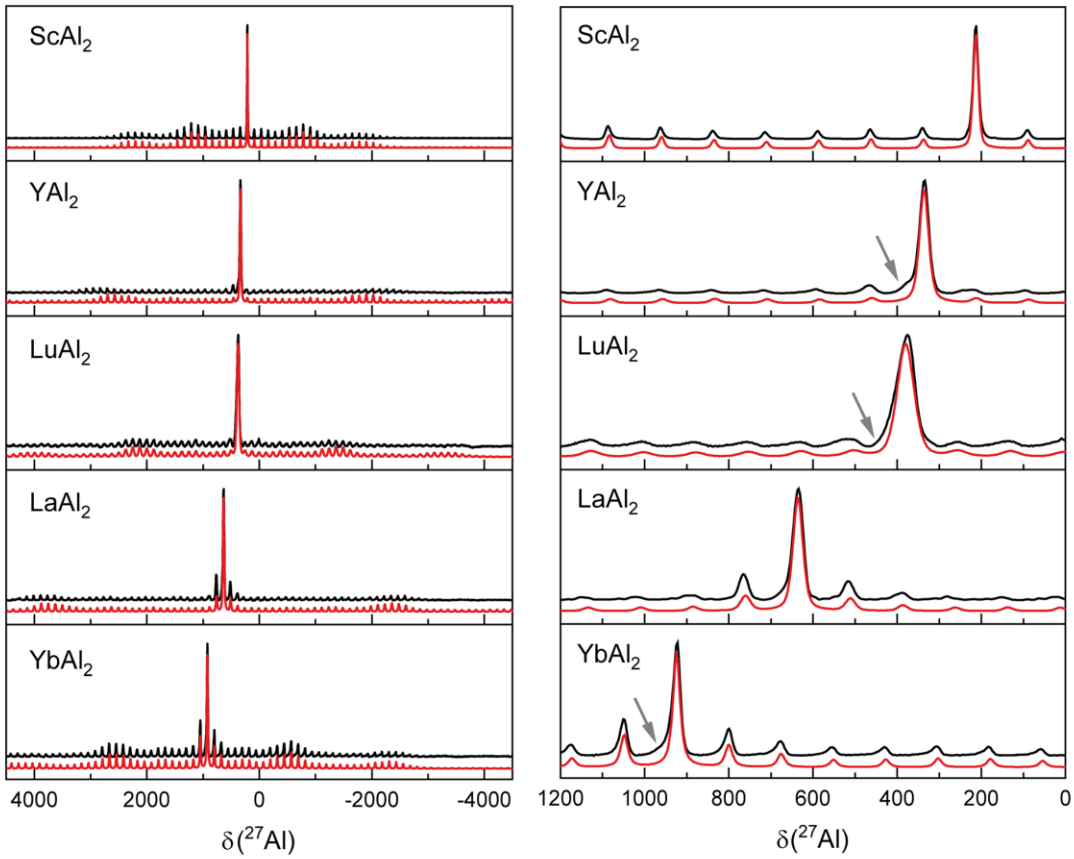

Fig. 4 ^{27}Al solid state MAS NMR spectra (black) of the $REAl_2$ compounds (RE = Sc, Y, La, Yb, Lu) with simulations (red) of the central transition and the rotational sideband manifold (left). On the right site the central transition of each spectrum is shown. The asymmetric broadening is indicated by grey arrows.

Table 2 ^{27}Al and ^{45}Sc NMR parameters for the measured $REAl_2$ compounds (RE = Sc, Y, La, Yb and Lu). Isotropic shift δ (±1 ppm), knight shift contribution δ_K, nuclear electric quadrupole coupling constants C_Q (±0.05 MHz), electric field gradient asymmetry parameters η_Q (±0.05), chemical shift anisotropy (dCS parameter) (±5 ppm) and degrees of Gaussian (*vs.* Lorentzian) character of the central MAS signal

Compound		δ/ppm	δ_K/ppm	$C_{Q,theo}$/kHz	$C_{Q,exp}$/kHz	G/L	dCS/ppm	Lit.
$ScAl_2$	^{27}Al	213	213	884	1618	0.53	43	This work
	^{45}Sc	2279	2279	0	92	0	−22	This work
YAl_2	^{27}Al	336	343	3466		0.49	−17	This work
	^{27}Al	364					30	38
$LaAl_2$	^{27}Al	636	648	4626		0.53	−108	This work
	^{27}Al	600			4630/5139		0	38–40
$YbAl_2$	^{27}Al	924	926	2072	2488	0.21	−188	This work
	^{27}Al	1100			2300/2580			39 and 41
$LuAl_2$	^{27}Al	379	381	2034	2794	0.65	−14	This work
	^{27}Al	386			2840		48/32	38

found using the DMFit simulation program.[46] Fig. 5 (left) exemplarily shows the ^{27}Al MAS spectrum for $YbAl_2$, where the intensity profile simulated based on the DFT-calculated C_Q does not match to the recorded spectrum, while Fig. 5 (right) shows the results from the fit. For quadrupolar coupling constants >3 MHz it is more difficult up to impossible to determine the C_Q parameter *via* the analysis of the experimental sideband spinning pattern because it extends over a too large spectral region which exceeds the available spectral bandwidth.[33] At the same time, it also becomes clear that a determination of C_Q from the line shape of the central transition is not possible because it is featureless and can be described well

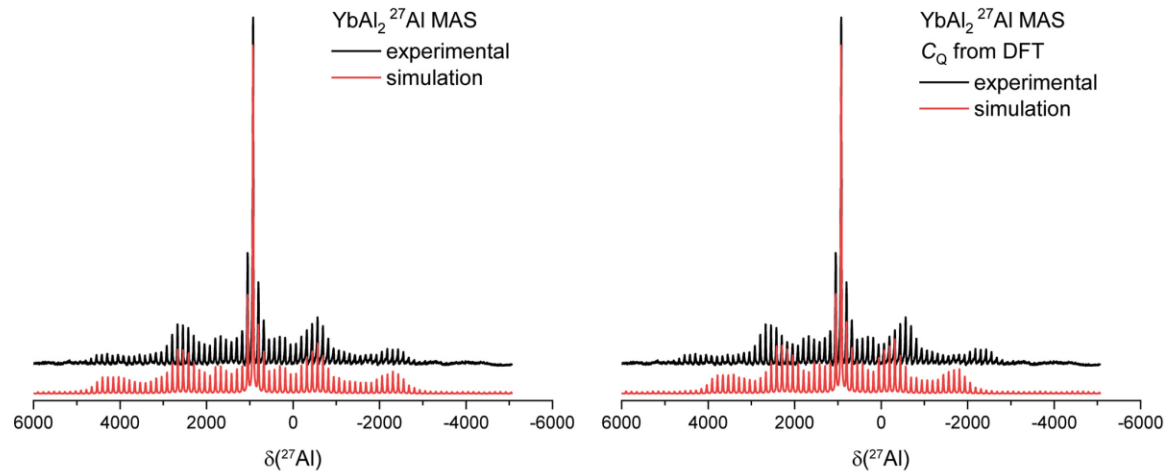

Fig. 5 ^{27}Al MAS spectrum of $YbAl_2$ fitted with an experimental determined value of C_Q (left) *versus* the C_Q value obtained by DFT calculations (right).

with a Gaussian-Lorentz simulation (Fig. 5). This is also the case for the La and Y compounds. Here, the quadrupolar coupling parameters obtained *via* DFT calculations were used and no refinement was performed. Finally, one can observe that the spinning sideband pattern intensities are asymmetric to the central transition. This indicates that chemical shift anisotropy (CSA) is present.

It should be noted that the samples of YAl_2, $YbAl_2$ and $LuAl_2$ show a shoulder to the left side of the central transition. Similar asymmetric line broadening of the central transition of the YAl_2 and $LuAl_2$ spectra is also observed in the literature.[38] That observation is consistent with the fact that significant strain is observed in the PXRD patterns for all compounds (*vide supra*). To overcome the influence of strain within the structure, the arc-melted sample of $LuAl_2$ was exemplarily heat treated and reinvestigated by NMR. It should be mentioned that the influence of annealing was already investigated in the literature.[38] Fig. 6 shows a comparison of the ^{27}Al MAS spectra of as-cast $LuAl_2$ and after annealing. It can be observed that the anisotropically broadened central transition is still present, but the line width of the transition gets smaller (by a factor of 2) after the thermal treatment. This observation is in line with the reduction in strain in the PXRD pattern.

The ^{27}Al and ^{45}Sc spectra of $ScAl_2$ are shown in Fig. 7. For the ^{45}Sc MAS NMR also one sharp central line, originating from the $|+1/2> \leftrightarrow |-1/2>$ transition is observed, a potential spinning side band manifold is caused by the $|\pm1/2> \leftrightarrow |\pm3/2>$, $|\pm3/2> \leftrightarrow |\pm5/2>$ and $|\pm5/2> \leftrightarrow |\pm7/2>$ transitions, which are observable due to quadrupolar interactions.[66] The DFT calculations on $ScAl_2$ suggest a C_Q and η_Q of zero, but simulations of the observed spinning sideband manifold give a rather small value of C_Q = 92 kHz. A possible explanation for the difference between experiment and theory in this case could be that the DFT calculations are performed with a non-defective, perfect structure, which is not true for as synthesized compounds.

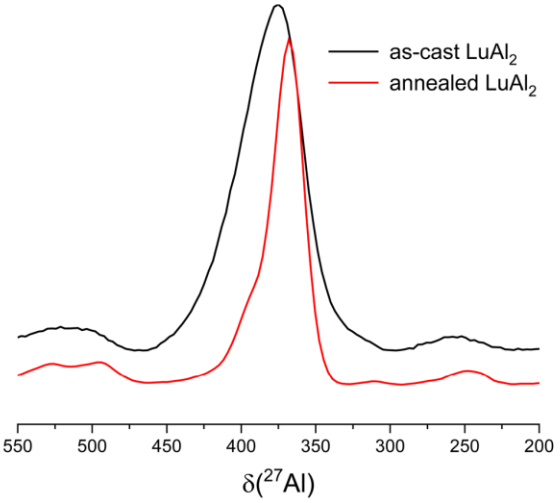

Fig. 6 Comparison of the central transition in the ^{27}Al MAS spectra of as-cast (black) and annealed (red) $LuAl_2$.

Here disorder and strain can play a significant role. And even if $ScAl_2$ exhibits a rather small strain as refined from the powder X-ray diffraction data, NMR as a local probe can visualize even these small influences. This observation can also explain, why the calculated C_Q parameters in most cases are smaller than the experimental values (Table 2). The same is true for the ^{27}Al MAS spectrum for $ScAl_2$, here the experimental C_Q value is double the size of the theoretical one (Table 2), similar to what has been observed for $YbAl_2$ (*vide supra*).

Of these five compounds, YAl_2, $LaAl_2$, $YbAl_2$ and $LuAl_2$ have already been investigated by ^{27}Al NMR investigations.[38–41] For these, a full characterization, along with partial quantum chemical investigations has been conducted and the results

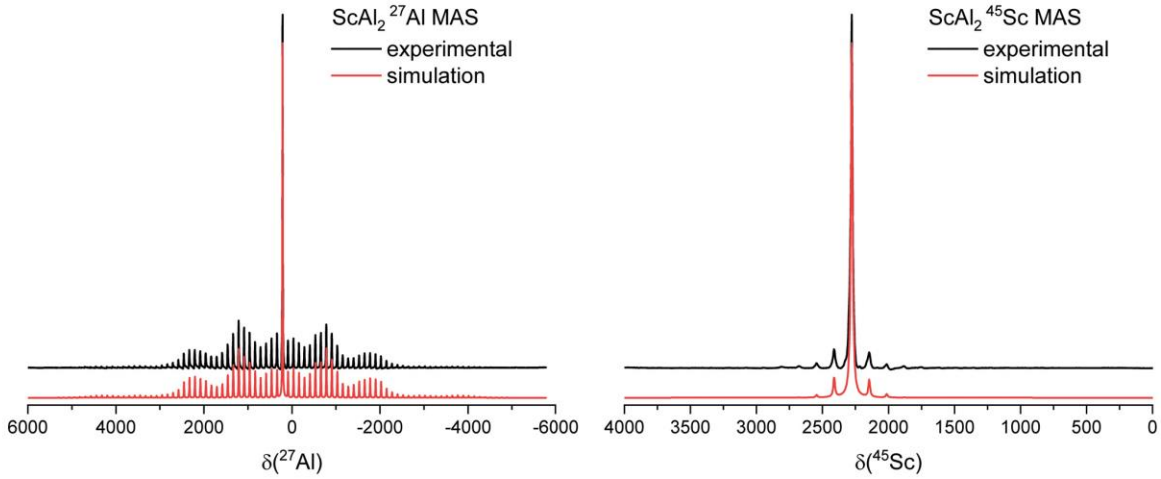

Fig. 7 ^{27}Al (left) and ^{45}Sc (right) MAS spectrum of $ScAl_2$ (black) along with the fitted spectra (red).

from the literature have been compiled in Table 2 along with the results of this study. The resonance shifts of the central transitions are in good (YAl_2 and $LuAl_2$) to fair ($LaAl_2$) agreement with the ones reported by Yuan *et al.*,[38] while the quadrupolar coupling constants C_Q are a good match. For $YbAl_2$, only the quadrupolar coupling constants C_Q had been reported before by Jaccarino[39] and Barnes,[41] which is in good agreement with the results reported here. In contrast, for $ScAl_2$, no investigations regarding the resonance shift and the quadrupolar coupling have been reported. Here, only the Knight shift contribution and an estimate of the s-electron densities have been reported.[67]

3.4 Raman spectroscopy

Raman spectroscopic measurements of the title compounds have been conducted using crystallites of the polycrystalline

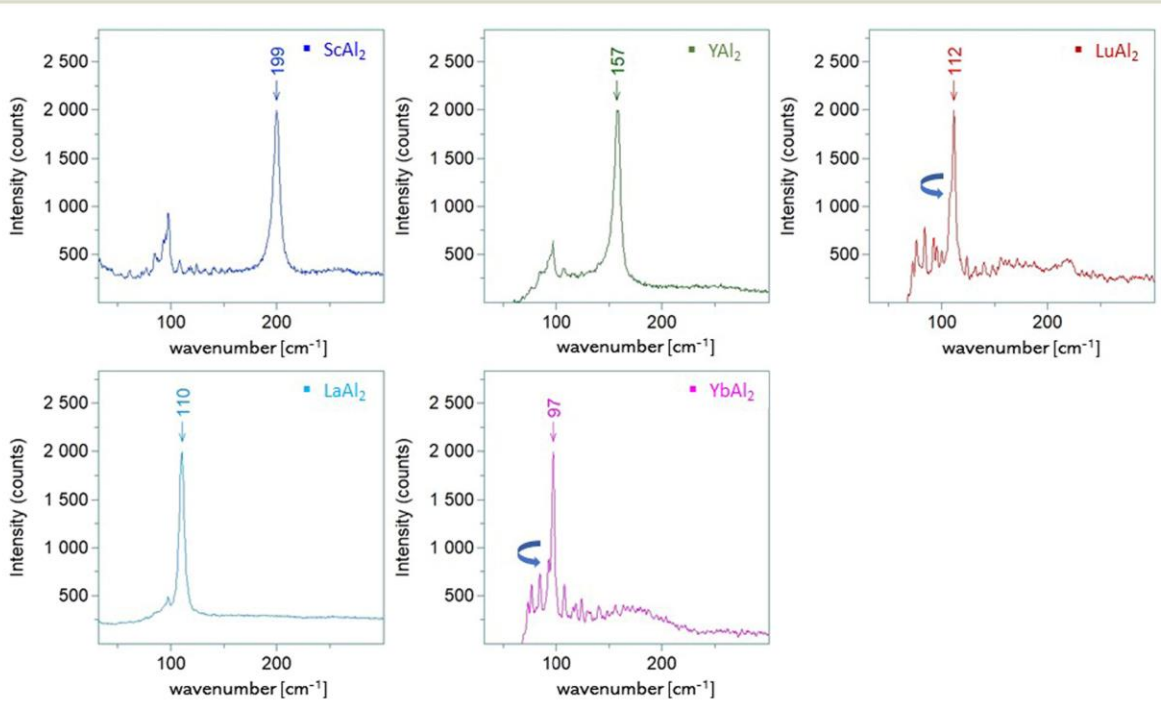

Fig. 8 Raman spectra of $REAl_2$ (RE = Sc, Y, Lu, La, Yb), the arrows mark the shoulders at RE = Lu, Yb.

Table 3 Raman bands of $REAl_2$ compounds, measurements conducted in this study are the average of 6 measurements, respectively, at room temperature

RE	Position T_{2g}/cm^{-1}	FWHM/cm^{-1}	Reference	Position T_{2g}/cm^{-1}	FWHM/cm^{-1}	Ref.
Sc	198–199	6.3	This work			
Y	157–160	5.4	This work			
Gd				118	4	68
Dy				117	5	68
Sm				115		69
Lu	111–112	3.4	This work			
	108 (shoulder)	3.8	This work			
La	110–112	4.9	This work	112	5	68
Ce				109	7	68
Yb	96–97	2.7	This work	95	10	68
Eu				96	4	68

FWHM: Full width at half maximum.

sample under a Raman microscope 532 nm and 633 nm laser excitation. All five compounds show one band in the measured range of 10 to 900 cm^{-1} (Fig. 8) originating from the respective intermetallic compound. The bands around 100 cm^{-1} could be assigned to water. According to the investigations of Güntherodt *et al.*,[68] the Γ_{25}' (T_{2g}) Raman-active mode in the cubic Laves-phase is caused by the rare-earth atoms (8*b* site) with their diamond-type arrangement. They investigated different $REAl_2$ compounds (RE = La, Ce, Eu, Gd, Dy, Yb) and observed modes with peak maxima ranging from 95 for $YbAl_2$ to 118 cm^{-1} for $GdAl_2$ (Table 3). Their data could be confirmed for the cases of $LaAl_2$, $YbAl_2$ and $LuAl_2$ and furthermore extended by the measurements of $ScAl_2$ and YAl_2 with maxima at 199 and 157–160 cm^{-1} and half-width values of 6 and 5 cm^{-1}, respectively. The positions for $LaAl_2$ and $YbAl_2$ as well as half-widths for $LuAl_2$ agree with the ones in the literature.[68] A striking feature, however, is that $EuAl_2$ and $YbAl_2$ exhibit by far the lowest wavenumbers. This nicely correlates with their formal oxidation state being divalent ($EuAl_2$) and intermediate valent ($YbAl_2$). The amplitudes of the $YbAl_2$ oscillation are weak; the cause could be the superposition with water vibrations as well as the intermediate valence state. $YbAl_2$ shows an asymmetric broadening of the band in direction to smaller wavenumbers and Güntherodt *et al.*, observed a half width of 10 cm^{-1}.[68] Analogously, a shoulder at 108 cm^{-1} was detected for $LuAl_2$ next to the main band at 112 cm^{-1}. Since here no intermediate valence behaviour is possible, this feature might be caused by the significant strain in the material.

Like with the NMR resonances, the Raman bands observed for the different $REAl_2$ members show significant differences. When the Raman bands are plotted *versus* the unit cell parameter *a* (Fig. 9), two trends are observed. For the members of group 3, the Raman bands shift almost linearly within the group from Sc (200 cm^{-1}) to Y (158 cm^{-1}) to La (110 cm^{-1}). In contrast, within the lanthanide series there are only small variations, with the exceptions of $EuAl_2$ and $YbAl_2$. The latter, however, exhibit divalent Eu^{2+} or intermediate valent $Yb^{2.4+}$ cations, hence, the unusually large lattice parameters and low

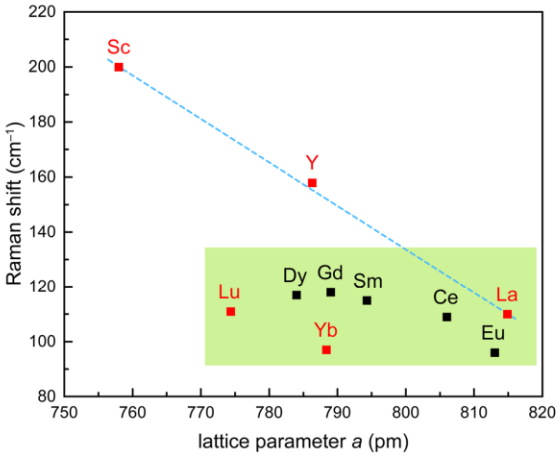

Fig. 9 Raman shifts plotted *versus* the lattice parameters of the $REAl_2$ compounds. The almost linear trend within group 3 is highlighted by the blue dashed line. The lanthanide compounds are highlighted by the green box.

Raman shifts. The differences could be explained by the electron configurations. While Sc, Y and La are rather transition metals, the other elements are f-elements and exhibit electron configurations of [Xe] 4f^n with $n \geq 1$.

3.5 Quantum chemistry

The electronic structures of the title compounds were analysed using density functional theory (DFT) calculations. The electron density of states (DOS) curves of $REAl_2$ (RE = Sc, Y, La, Yb, Lu) and the partial s-electron DOS (p-DOS) of the Al atoms in each compound are plotted in Fig. 10. There is a substantial density of states at the Fermi level for all five compounds, indicating metallic behaviour, in line with the silvery shiny metallic appearance. The calculated Bader effective charges for $REAl_2$ (RE = Sc, Y, La, Yb, Lu) are listed in Table 4. In all five compounds, the RE atoms have positive, while the Al atoms have negative charges, rendering them aluminides. The

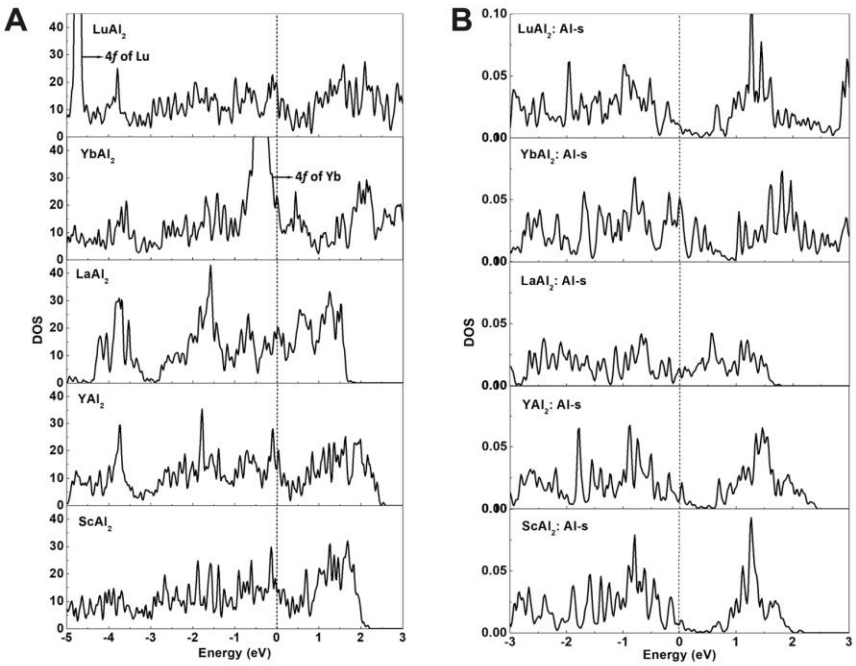

Fig. 10 (A) Total density of states and (B) Al s-electron partial density of states (per Al atom) of $REAl_2$ (RE = Sc, Y, La, Yb, Lu) from non-spin-polarized DFT calculations, dotted line indicates Fermi level.

Table 4 Bader charges and s-electron densities (DOS per Al atom, states/eV) of the Al atoms at the Fermi level in the $REAl_2$ series (RE = Sc, Y, La, Yb, Lu) obtained from non-spin-polarized DFT calculations

$REAl_2$	$ScAl_2$	YAl_2	$LaAl_2$	$YbAl_2$	$LuAl_2$
Charge on RE	+1.23	+1.25	+0.97	+1.08	+1.14
Charge on Al	−0.61	−0.62	−0.48	−0.54	−0.57
DOS per Al atom	0.00670	0.00851	0.0144	0.0511	0.0102

effective charges on the RE atoms are significantly smaller than +3 indicating weak ionic bonding between the $RE^{\delta+}$ cations and the $[Al_2]^{\delta-}$ polyanionic network. When looking at the trend of the Pauling electronegativities (EN)[18] (Sc: χ = 1.36; Y: χ = 1.22; La: χ = 1.1; Yb: χ = 1.1; Lu: χ = 1.27) one would expect larger positive effective charges of La and Yb, compared to Sc, Y and Lu, contrary to the Bader charges (Table 4). To

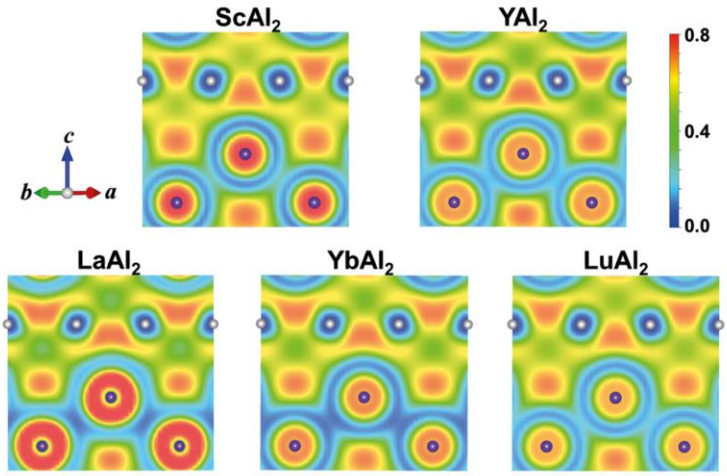

Fig. 11 Electron localization function (ELF) plots of the (110) plane for $REAl_2$ (RE = Sc, Y, La, Yb, Lu). Purple and grey spheres represent RE and Al atoms, respectively.

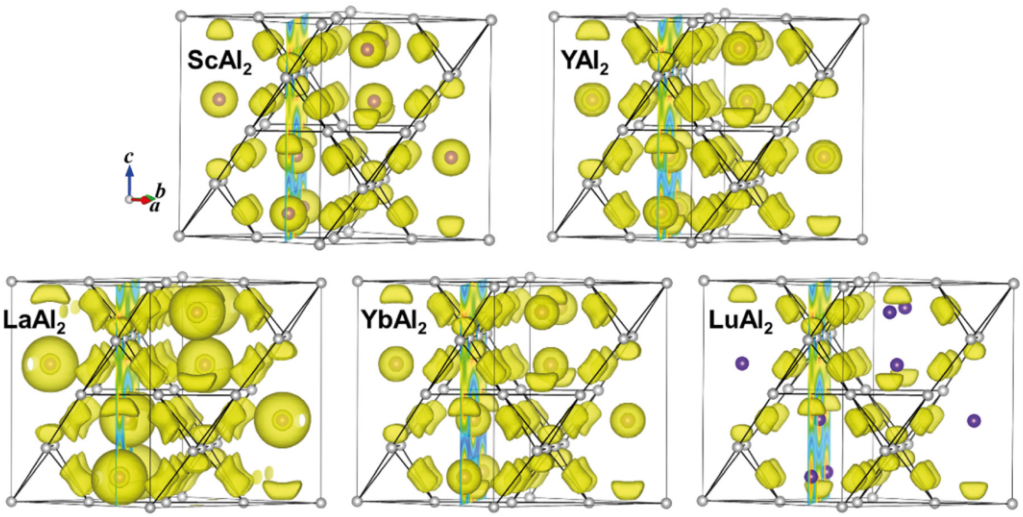

Fig. 12 Electron localization functions (ELF) plots for $REAl_2$ (RE = Sc, Y, La, Yb, Lu) at iso-surface level of 0.70. Purple and grey spheres represent RE and Al atoms, respectively.

better understand the chemical bonding in $REAl_2$, electron localization functions have been examined and the results are shown in Fig. 11 and 12. Fig. 11 shows a high electron localization between nearest neighbour Al atoms, signalling covalent Al–Al interactions, which form the $[Al_2]^{\delta-}$ network. This is also supported by the iso-surface plotted in Fig. 12. It is worth noting that the electron localization is not evenly distributed around the Al–Al bond but prefers the side of bond facing the RE atom, which may be caused by the orbital overlap between Al and the RE atoms indicating partial multi-centre bonding. There is a high electron localization between La (or Yb) and the Al atoms in $LaAl_2$ (or $YbAl_2$), indicating stronger La–Al (Yb–Al) covalent interactions (weaker ionic interactions respectively) compared to those in $ScAl_2$, YAl_2 and $LuAl_2$, providing an explanation for the small effective positive charges on La (or Yb), however, being in contrast with the EN. It is possible that the 5d orbitals in $LaAl_2$ can overlap more with Al s/p orbitals, resulting in stronger covalent La–Al interactions, or, as suggest before, multi-centre bonding takes place. For $YbAl_2$, based on the DOS in Fig. 10, the 4f orbital is right below the Fermi level, which might contribute to the Yb–Al orbital overlap and leading to strong Yb–Al covalent interactions. In addition, Yb is a so-called two-electron metal, despite Sc, Y, La and Lu being three-electron metals. Therefore, a reduced Bader charge on the Yb atoms is expected from this point of view. However, $YbAl_2$ is an intermediate valent compound[60,61] and exhibits partial Yb^{3+} character, making the bonding situation even more complicated.

Fig. 13 finally shows the correlation between the s-electron DOS of the Al atoms at the Fermi level plotted *versus* the calculated Knight shift contribution δ_K. As for the Raman measurements, also a correlation between the two and three electron metals can be observed. In $YbAl_2$, a significantly, almost by a factor of 10, larger s-electron DOS at E_F is observed leading to a dramatic shift in the ^{27}Al NMR signal. Within the close-shell compounds, an almost linear increase of the Knight shift δ_K *versus* the s-electron DOS is visible.

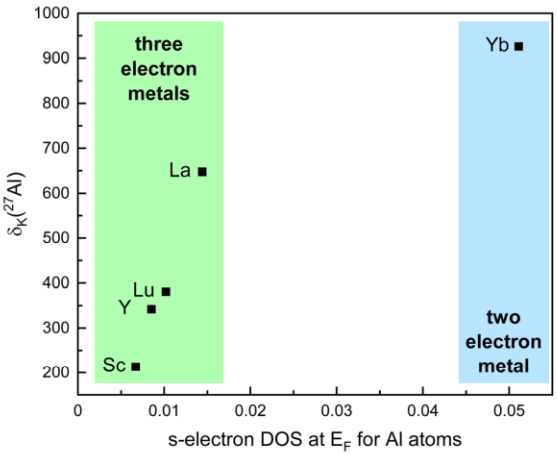

Fig. 13 Al atom s-electron pDOS at E_F plotted *versus* δ_K. The green and blue boxes indicate the formally two and three electron metals.

4 Conclusion

The close-shell rare-earth aluminides $REAl_2$ with RE = Sc, Y, La and Lu as well as intermediate valent $YbAl_2$ (all cubic $MgCu_2$ type) were synthesized from the elements and structu-

rally characterized by powder X-ray diffraction. All compounds are X-ray pure; however, significant strain could be observed for the Y, Yb and Lu compounds. Annealing of $LuAl_2$ decreased the strain. ^{27}Al solid-state MAS NMR spectra were recorded for all compounds and in addition, ^{45}Sc solid-state MAS NMR spectroscopic investigations for $ScAl_2$ were conducted. All ^{27}Al spectra exhibit a single central transition, in line with one crystallographic Al site, the same is true for the ^{45}Sc spectrum. However, in agreement with the PXRD investigations, the main transitions of YAl_2, $YbAl_2$ and $LuAl_2$ show an asymmetry which is probably caused by the strain of the material. Comparing investigations of annealed $LuAl_2$ show a significantly sharper signal. The spectra were fitted using NMR parameters obtained from quantum-chemical calculations, however, not for all compounds the calculated values are in line with the experimentally observed ones, again caused by the internal strain. Raman spectra collected of all title compounds also show the strain inherent to the material. A comparison of the Raman shifts with respect to the structural data shows that the shift in the Raman signals can be explained by the variations in the interatomic distances and the electronic situation of the respective RE element. Finally, the bonding situation within the $REAl_2$ members was assessed using Bader charge calculations and electron localization function (ELF). Bader charges clearly indicate the formation of aluminides due to the negatively charged $[Al_2]^{\delta-}$ framework, in line with the Pauling electronegativities. The peculiarities in the Bader charges can be attributed to the oxidation state of the RE atoms and a multicentre bond formation. A comparison of the s-electron density at E_F with the Knight shift contribution to the ^{27}Al NMR resonance shows a linear dependency for the close-shell atoms, Yb, however, differs, due to the intermediate valence state.

Author contributions

All authors have accepted responsibility for the entire content of this submitted manuscript and approved the submission.

Conflicts of interest

The authors declare no conflicts of interest regarding this article.

Acknowledgements

Instrumentation and technical assistance for this work were provided by the Service Center X-ray Diffraction, with financial support from Saarland University and German Science Foundation (project number INST 256/349-1) and by the Service Center NMR with financial support from Saarland University and German Research Foundation DFG. We thank the San Diego Supercomputer Center (SDSC) for providing computing resources. Funding has been provided by the Deutsche Forschungsgemeinschaft DFG (JA 1891-10-1).

References

1 O. Janka, Metallic light-weight alloys: Al, Ti, Mg, in *Applied Inorganic Chemistry*, ed. R. Pöttgen, T. Jüstel and C. Strassert, De Gruyter, 2022, pp. 158–173.
2 F. Ostermann, *Anwendungstechnologie Aluminium*, Springer Vieweg, Berlin, Heidelberg, 2014.
3 R. Kilaas, V. Radmilovic and U. Dahmen, *Mater. Res. Soc. Symp. Proc.*, 2001, **589**, 273–278.
4 B. Heying, R.-D. Hoffmann and R. Pöttgen, *Z. Naturforsch.*, 2005, **60b**, 491–494.
5 S. J. Andersen, C. D. Marioara, J. Friis, S. Wenner and R. Holmestad, *Adv. Phys.: X*, 2018, **3**, 1479984.
6 P. Villars and K. Cenzual, *Pearson's Crystal Data: Crystal Structure Database for Inorganic Compounds*, ASM International®, Materials Park, Ohio, USA, 2023.
7 H. Nowotny, E. Wormnes and A. Mohrnheim, *Z. Metallkd.*, 1940, **32**, 39–42.
8 R. E. Rundle and A. S. Wilson, *Acta Crystallogr.*, 1949, **2**, 148–150.
9 O. J. C. Runnalls, *JOM*, 1953, **5**, 1460–1462.
10 O. J. C. Runnalls, *Can. J. Chem.*, 1956, **34**, 133–145.
11 A. Iandelli, *Natl. Phys. Lab. (U. K.), Symp.*, 1951, 3F2–3F11.
12 V. B. Compton and B. T. Matthias, *Acta Crystallogr.*, 1959, **12**, 651–654.
13 J. H. Wernick and S. Geller, *Trans. Metall. Soc. AIME*, 1960, **218**, 866–868.
14 F. Stein and A. Leineweber, *J. Mater. Sci.*, 2021, **56**, 5321–5427.
15 E. Bauer, E. Gratz and G. Adam, *J. Phys. F: Met. Phys.*, 1986, **16**, 493.
16 A. T. Burkov, M. Vedernikov and E. Gratz, *Physica B Condens. Matter*, 1992, **176**, 263–274.
17 A. K. Pathak, D. Paudyal, K. A. Gschneidner and V. K. Pecharsky, *J. Appl. Phys.*, 2014, **115**, 17E109.
18 J. Emsley, *The Elements*, Clarendon Press, Oxford University Press, Oxford, New York, 1998.
19 J. Donohue, *The Structures of the Elements*, Wiley, New York, 1974.
20 R. K. Harris, E. D. Becker, S. M. Cabral de Menezes, P. Granger, R. E. Hoffman and K. W. Zilm, *Pure Appl. Chem.*, 2008, **80**, 59–84.
21 N. J. Stone, *At. Data Nucl. Data Tables*, 2016, **112**, 1–28.
22 A. Putnis, *Phys. Chem. Miner.*, 1996, **23**, 247–247.
23 M. Haouas, F. Taulelle and C. Martineau, *Prog. Nucl. Magn. Reson. Spectrosc.*, 2016, **95**, 11–36.
24 A. T. Bell, *Colloids Surf., A*, 1999, **158A**, 221–234.
25 G. Engelhardt, Characterization of Zeolite Catalysts and Related Materials by Multinuclear Solid-State NMR Spectroscopy, In *Surface Science: Principles and Current Applications*, ed. R. J. MacDonald, E. C. Taglauer and

K. R. Wandelt, Springer Berlin Heidelberg, Berlin, Heidelberg, 1996, pp. 321–330.
26 A. L. Blumenfeld and J. J. Fripiat, *Magn. Reson. Chem.*, 1999, **37**, S118–S125.
27 C. Benndorf, H. Eckert and O. Janka, *Acc. Chem. Res.*, 2017, **50**, 1459–1467.
28 M. Radzieowski, C. Benndorf, S. Haverkamp, H. Eckert and O. Janka, *Z. Naturforsch.*, 2016, **71b**, 553–566.
29 C. Benndorf, O. Niehaus, H. Eckert and O. Janka, *Z. Anorg. Allg. Chem.*, 2015, 168–175.
30 F. Stegemann, C. Benndorf, Y. Zhang, M. Bartsch, H. Zacharias, B. P. T. Fokwa, H. Eckert and O. Janka, *Inorg. Chem.*, 2017, **56**, 1919–1931.
31 C. Benndorf, F. Stegemann, S. Seidel, L. Schubert, M. Bartsch, H. Zacharias, B. Mausolf, F. Haarmann, H. Eckert, R. Pöttgen and O. Janka, *Chem. – Eur. J.*, 2017, **23**, 4187–4196.
32 F. Stegemann, C. Benndorf, Y. Zhang, M. Bartsch, H. Zacharias, B. P. T. Fokwa, H. Eckert and O. Janka, *Z. Anorg. Allg. Chem.*, 2017, **643**, 1379–1390.
33 F. Stegemann, C. Benndorf, T. Bartsch, R. S. Touzani, M. Bartsch, H. Zacharias, B. P. T. Fokwa, H. Eckert and O. Janka, *Inorg. Chem.*, 2015, **54**, 10785–10793.
34 F. Stegemann, T. Block, S. Klenner, Y. Zhang, B. P. T. Fokwa, C. Doerenkamp, H. Eckert and O. Janka, *Eur. J. Inorg. Chem.*, 2021, **2021**, 3832–3845.
35 F. Stegemann, T. Block, S. Klenner, Y. Zhang, B. P. T. Fokwa, A. Timmer, H. Mönig, C. Doerenkamp, H. Eckert and O. Janka, *Chem. – Eur. J.*, 2019, **25**, 10735–10747.
36 M. Radzieowski, F. Stegemann, C. Doerenkamp, S. F. Matar, H. Eckert, C. Dosche, G. Wittstock and O. Janka, *Inorg. Chem.*, 2019, **58**, 7010–7025.
37 C. Benndorf, H. Eckert and O. Janka, *Dalton Trans.*, 2017, **46**, 1083–1092.
38 C. C. Yuan, Y. F. Yang, X. K. Xi, J. Cui and J. F. Xiang, *Solid State Nucl. Magn. Reson.*, 2012, **41**, 28–31.
39 V. Jaccarino, B. T. Matthias, M. Peter, H. Suhl and J. H. Wernick, *Phys. Rev. Lett.*, 1960, **5**, 251–253.
40 K. Betsuyaku and H. Harima, *J. Magn. Magn. Mater.*, 2001, **226–230**, 199–201.
41 R. G. Barnes, W. H. Jones and T. P. Graham, *Phys. Rev. Lett.*, 1961, **6**, 221–223.
42 R. Pöttgen, T. Gulden and A. Simon, *GIT Labor-Fachz.*, 1999, **43**, 133–136.
43 R. Pöttgen, A. Lang, R.-D. Hoffmann, B. Künnen, G. Kotzyba, R. Müllmann, B. D. Mosel and C. Rosenhahn, *Z. Kristallogr.*, 1999, **214**, 143–150.
44 Bruker AXS Inc., *Topas, Version 5*, Karlsruhe, Germany, 2014.
45 Bruker Corp., *Topspin, Version 2.1*, Karlsruhe, 2008.
46 D. Massiot, F. Fayon, M. Capron, I. King, S. Le Calvé, B. Alonso, J.-O. Durand, B. Bujoli, Z. Gan and G. Hoatson, *Magn. Reson. Chem.*, 2002, **40**, 70–76.
47 P. E. Blöchl, *Phys. Rev. B*, 1994, **50**, 17953–17979.
48 G. Kresse and D. Joubert, *Phys. Rev. B*, 1999, **59**, 1758–1775.
49 G. Kresse and J. Furthmüller, *Phys. Rev. B*, 1996, **54**, 11169–11186.
50 G. Kresse and J. Furthmüller, *Comput. Mater. Sci.*, 1996, **6**, 15–50.
51 J. P. Perdew, K. Burke and M. Ernzerhof, *Phys. Rev. Lett.*, 1996, **77**, 3865–3868.
52 E. Sanville, S. D. Kenny, R. Smith and G. Henkelman, *J. Comput. Chem.*, 2007, **28**, 899–908.
53 G. Henkelman, A. Arnaldsson and H. Jónsson, *Comput. Mater. Sci.*, 2006, **36**, 354–360.
54 W. Tang, E. Sanville and G. Henkelman, *J. Phys.: Condens. Matter*, 2009, **21**, 084204.
55 A. Savin, R. Nesper, S. Wengert and T. F. Fässler, *Angew. Chem.*, 1997, **109**, 1892–1918.
56 B. Silvi and A. Savin, *Nature*, 1994, **371**, 683–686.
57 R. D. Shannon, *Acta Crystallogr.*, 1976, **A32**, 751.
58 R. D. Shannon and C. T. Prewitt, *Acta Crystallogr.*, 1969, **B25**, 925.
59 A. Gleissner, W. Potzel, J. Moser and G. M. Kalvius, *Phys. Rev. Lett.*, 1993, **70**, 2032–2035.
60 A. Iandelli and A. Palenzona, *J. Less-Common Met.*, 1972, **29**, 293–297.
61 E. E. Havinga, K. H. J. Buschow and H. J. van Daal, *Solid State Commun.*, 1973, **13**, 621–627.
62 V. N. Rechkin, L. K. Lamikhov and T. I. Samsonova, *Sov. Phys. Crystallogr.*, 1964, **9**, 325–327.
63 H. N. Nowotny, *Z. Metallkd.*, 1942, **34**, 22–24.
64 S. E. Haszko, *Trans. Metall. Soc. AIME*, 1960, **218**, 958.
65 S. Engel, E. C. J. Gießelmann, L. E. Schank, G. Heymann, K. Brix, R. Kautenburger, H. P. Beck and O. Janka, *Inorg. Chem.*, 2023, DOI: **10.1021/acs.inorgchem.2c04391**.
66 H. Eckert and R. Pöttgen, *Z. Anorg. Allg. Chem.*, 2010, **636**, 2232–2243.
67 E. P. Chock, R. A. B. Devine, S. A. Dodds, R. Orbach and L. Tippie, *J. Phys. F: Met. Phys.*, 1977, **7**, 1097–1102.
68 G. Güntherodt, A. Jayaraman, G. Batlogg, M. Croft and E. Melczer, *Phys. Rev. Lett.*, 1983, **51**, 2330–2332.
69 J. Su and C. Zhu, *Mater. Res. Bull.*, 2003, **38**, 2025–2029.

5.1.2 On the RE_2TiAl_3 (RE = Y, Gd–Tm, Lu) Series—The First Aluminum Representatives of the Rhombohedral Mg_2Ni_3Si Type Structure

Published as an article (under CC BY):

Elias C. J. Gießelmann, Stefan Engel, Israa M. El Saudi, Lars Schumacher, Mathis Radzieowski, Josef Maximilian Gerdes and Oliver Janka, *Solids*, **2023**, *4*, 166.

https://www.mdpi.com/2673-6497/4/3/11

Contribution of the authors to the manuscript (as published in the manuscript)

Conceptualization, O.J.; methodology, E.C.J.G., S.E., M.R., J.M.G. and L.S.; analysis, E.C.J.G., S.E., I.M.E., L.S. and O.J.; investigation, E.C.J.G., S.E., I.M.E., M.R., J.M.G. and L.S.; writing—original draft preparation, E.C.J.G. and M.R.; writing—review and editing, E.C.J.G. and O.J.; visualization, E.C.J.G.; supervision, O.J.; project administration, O.J.; funding acquisition, O.J.

Parts of the synthesis and preparation, physical property measurements as well as X-ray diffraction results (powder and single-crystal) have been reported in the dissertation of Mathis Radzieowski entitled “Darstellung, Kristallchemie, physikalische und spektroskopische Eigenschaften intermetallischer Aluminiumverbindungen sowie bi- und ternärer Zintl-Phasen” at University of Münster in 2020.[237]

The contribution of Elias C. J. Gießelmann was the repetition of the experiments and further explorative synthesis as well as additional magnetic characterization in collaboration with Lars Schumacher and finalization of the manuscript.

Summary

The series of ternary compounds RE_2TiAl_3 (RE = Y, Gd-Tm, Lu) could be synthesized as the first aluminum compounds of the rhombohedral distortion variant of the cubic Laves phase. Their existence is so far highly interesting as they differ significantly from all other known main group compounds (*p*-block elements) in this structure type. As the prototype indicates, compounds that adopt this structure type usually show the main group element as the minor component with a ratio to the transition metal of 3:1. As explained in the introduction, examples for these are the gallium compounds RE_2Rh_3Ga (RE = Y, La–Nd, Sm, Gd–Er), the silicides RE_2Rh_3Si (RE = Ce, Pr, Er), the germanides Ca_2Pd_3Ge and the phosphide Mg_2Ni_3P. When taking only the network building elements into account, the new series can be understood as an

antitype. It is moreover highly interesting because the only two structure types known before with these element combinations were the extremely Al-rich $CeCr_2Al_{20}$ and $Ho_6Mo_4Al_{43}$ structure types described in the introduction.

The compounds were synthesized by arc-melting followed by additional annealing and analyzed using PXRD. The Y, Gd and Tb compounds were structurally characterized by single-crystal XRD analysis. The lattice parameters and the unit cell volume show the expected correlation with the respective ionic radii of the trivalent rare earth atoms. Within the publication, the attempt to synthesize the La compound is discussed, which in case of success would have opened the question of whether the series can be expanded towards all early, large, rare earth elements. Here, results showed that the formation of the pure binary cubic Laves phases in combination with other byproducts are favored under the synthetic conditions chosen. Due to X-ray pure samples the magnetic properties were measured revealing diamagnetism for Y and Lu as well as Curie-paramagnetism for the other compounds alongside antiferromagnetic ordering below $T_N = 26$ K for example for Gd_2TiAl_3.

solids

MDPI

Article

On the RE_2TiAl_3 (RE = Y, Gd–Tm, Lu) Series—The First Aluminum Representatives of the Rhombohedral Mg_2Ni_3Si Type Structure

Elias C. J. Gießelmann [1], Stefan Engel [1], Israa M. El Saudi [1], Lars Schumacher [2], Mathis Radzieowski [2], Josef Maximilian Gerdes [2] and Oliver Janka [1,*]

[1] Anorganische Festkörperchemie, Universität des Saarlandes, Campus C4.1, 66386 Saarbrücken, Germany
[2] Institut für Anorganische und Analytische Chemie, Universität Münster, Corrensstrasse 28/30, 48149 Münster, Germany
* Correspondence: oliver.janka@uni-saarland.de; Tel.: +49-681-302-70665

Abstract: Several ternary rare-earth metals containing titanium aluminum intermetallics in the RE_2TiAl_3 series (RE = Y, Gd–Lu) have been synthesized from the elements using arc-melting techniques. All compounds crystallize in the trigonal crystal system with rhombohedral space group $R\bar{3}m$ (Z = 3) and lattice parameters ranging between a = 582–570 and c = 1353–1358 pm. They adopt the Mg_2Ni_3Si-type structure, which is an ordered superstructure of the cubic Laves phase $MgCu_2$ and has been observed for Al intermetallics for the first time. Tetrahedral [$TiAl_3$] entities that are connected over all corners form a network where the empty [$TiAl_3$] tetrahedra exhibit a full Ti/Al ordering based on the single crystal results. The Al atoms are arranged into 6^3 Kagomé nets, while the Ti atoms connect these nets over the triangular units. In the cavities of this three-dimensional arrangement, the RE cations can be found forming a distorted diamond-type substructure. Magnetic measurements revealed that Y_2TiAl_3 and Lu_2TiAl_3 are Pauli paramagnetic substances, in line with the metallic character. The other compounds exhibit paramagnetism with antiferromagnetic ordering at a maximum Néel temperature of T_N = 26.1(1) K for Gd_2TiAl_3.

Keywords: intermetallics; rare-earth elements; titanium; aluminum; physical properties

Citation: Gießelmann, E.C.J.; Engel, S.; El Saudi, I.M.; Schumacher, L.; Radzieowski, M.; Gerdes, J.M.; Janka, O. On the RE_2TiAl_3 (RE = Y, Gd–Tm, Lu) Series—The First Aluminum Representatives of the Rhombohedral Mg_2Ni_3Si Type Structure. *Solids* **2023**, *4*, 166–180. https://doi.org/10.3390/solids4030011

Academic Editor: Timothy J. Prior

Received: 2 June 2023
Revised: 21 June 2023
Accepted: 28 June 2023
Published: 5 July 2023

1. Introduction

The Laves phases of general composition AB_2, named after Fritz Laves, belong to the most prominent structure types in the field of intermetallic compounds [1–3]. The Pearson database [4] lists over 4000 (pseudo) binary compounds in the cubic $MgCu_2$ ($Fd\bar{3}m$) or the hexagonal $MgZn_2$ and $MgNi_2$ (both $P6_3/mmc$)-type structures [5]. The majority of these compounds contain a rare-earth element; therefore, the magnetic properties of these materials have been studied in great detail [6]. Their structures usually do not show larger homogeneity ranges and can be regarded as packing dominated as illustrated by the fact that, for example, $NeHe_2$ [7] and $ArNe_2$ [8] can be observed under high-pressure conditions and adopt the $MgZn_2$-type structure. Moreover, $Ar(H_2)_2$ was reported to form the hexagonal Laves phase at high pressure [9], while $Xe(N_2)_2$ adopts the cubic $MgCu_2$-type structure [10]. The ideal size ratio of the constituent elements A and B is $r_A/r_B = (3/2)^{1/2} \approx 1.225$. In all three binary Laves phases, the B atoms form empty B_4 tetrahedra that exhibit different connectivities, always forming a network, with the A atoms in the respective cavities. In the $MgCu_2$-type structure, however, only corner-sharing Cu_4 tetrahedra are present; in the $MgZn_2$-type structure, two tetrahedra are connected over a common face, and the remaining corners are used to form strands [001]. Finally, in $MgNi_2$, both connection modes can be found. In addition to these basic types, different (highly complex) stacking variants have been reported [11]. Based on these binary structure types, ordered ternary compounds can be derived. The Mg_2Cu_3Si ($P6_3/mmc$)-type structure [12],

for example, allows for an ordering on the two crystallographic Zn sites of the hexagonal $MgZn_2$-type structure. Besides the prototype, aluminum compounds (e.g., Ce_2RuAl_3 [13], the RE_2TAl_3 series with *RE* = Y, La–Nd, Sm, Gd–Lu and *T* = Ru, Rh, Ir [14], U_2Cu_3Al [15] or the solid solution $Ti_2Ni_{1-x}Al_{3+x}$ [16]) along with gallides (U_2Fe_3Ga [17], Eu_2IrGa_3 [18], $Nb_2Cu_{1.1}Ga_{2.9}$ [19], and $Ho_2Ru_2Ga_2$ [20]), silicides (e.g., the Sc_2T_3Si and Ti_2T_3Si series with *T* = Cr, Mn, Fe, Co, and Ni [21–23]), and germanides (U_2T_3Ge series with T = Mn, Fe, Co [24–27], Mn_2Cu_3Ge [28], and Mn_2Co_3Ge [29]) have been reported. The cubic $MgCu_4Sn$-type structure ($F\bar{4}3m$) [30] is a ternary ordered variant of the cubic $MgCu_2$ type, where magnesium/tin ordering takes place on the former Mg site. Exemplarily, the rare-earth-containing series *RE*Ni_4In (*RE* = Sc, Y, La–Nd, Sm, Gd–Tm) [31], *RE*Ni_4Au (*RE* = Sc, Y, Gd–Lu) [32,33], *RE*Cu_4Ag (*RE* = La–Nd, Sm, Gd–Tm) [34], and *RE*Cu_4Au (*RE* = Gd–Er) [35] should be mentioned. Furthermore, $Yb_6Ir_5Ga_7$ [36] represents a $\sqrt{3} \times \sqrt{3}$ superstructure of the hexagonal $MgZn_2$-type structure, allowing for a coloration of the tetrahedral strands of the prototype. To date, the iridium gallides $RE_6Ir_5Ga_7$ (*RE* = Sc, Y, Nd, Sm, Gd–Lu) [36,37] and the $RE_6T_5Al_7$ series (*RE* = Sc, Y, Ce–Nd, Sm, Gd–Lu, *T* = Ru, Ir) [38] have been reported. Finally, a rhombohedral ordered variant of the $MgCu_2$ type is observed for the Mg_2Ni_3Si ($R\bar{3}m$) type structure [39], realized, e.g., for the gallides RE_2Rh_3Ga (*RE* = Y, La–Nd, Sm, Gd–Er) [40], the silicides RE_2Rh_3Si (*RE* = Ce, Pr, Er) [41–43] and U_2Ru_3Si [44], or the germanides RE_2T_3Ge (*RE* = Y, Pr, Sm, Er) [41,45], U_2Ru_3Ge [44], and Ca_2Pd_3Ge [46]. More information on superstructures of the Laves phases can be found in a recent review article [47].

With respect to application, titanium and aluminum-based materials are of great interest since they belong to the group of light-weight alloys [48]. Therefore, the binary phase diagram Ti/Al is probably one of the best investigated ones [49–53]. Several binary intermetallics have been identified in this system, of which $TiAl_2$ and $TiAl_3$ are too brittle to be of technical importance; however, α_2-Ti_3Al and γ-TiAl are of crucial importance to the field of titanium-based alloys [54,55].

Here, we report on the synthesis and structural and magnetic characterization of the RE_2TiAl_3 series (*RE* = Y, Gd–Tm, Lu), the first aluminum intermetallics adopting the rhombohedral Mg_2Ni_3Si-type structure. However, as seen for many aluminum series, they form an *anti*-type arrangement within the network in comparison to the [Ni_3Si] one, that is, the prototype.

2. Materials and Methods

Synthesis: The compounds of the RE_2TiAl_3 (*RE* = Y, Gd–Tm, Lu) series were synthesized by arc-melting the elements, using rare-earth ingots (Onyxmet, 99.9%), titanium chips (Onyxmet, 99.9%), and aluminum turnings (Onyxmet, 99.99%). All starting materials were weighed in the ideal stoichiometry of 2:1:3 (*RE*:Ti:Al). The reactants were arc-melted under an argon atmosphere of about 800 mbar [56]. The obtained buttons were remelted several times to increase the homogeneity. All samples were weighed after arc-melting; the mass loss is <0.5%. The samples were subsequently enclosed in evacuated quartz tubes and annealed in a second step (923 or 1123 K, 7 to 12 d) to increase their overall phase purity and homogeneity. The Tm_2TiAl_3 sample was transferred to an Al_2O_3 crucible and annealed for 3 h in an induction furnace (Trumpf Hüttinger, TruHeat 5010, Freiburg, Germany). The annealing led to X-ray pure samples, suitable for physical property measurements. All samples obtained by these processes show metallic luster and are stable under ambient conditions over months.

SEM-EDX data: Semiquantitative EDX analyses of the bulk samples were conducted on a JEOL 7000F (Jeol, Freising, Germany) equipped with an EDAX Genesis 2000 EDX detector (EDAX, Unterschleissheim, Germany). Investigations of the single crystals were conducted on a Zeiss Evo MA10 (Zeiss, Jena, Germany) scanning electron microscope with an Oxford Instrument EDX detector using REF_3, TiO_2, and Al_2O_3 as internal standards. The crystals used for the structure determination were measured on their glass fibers in the variable pressure (VP) mode of the instrument under 60 Pa N_2 atmosphere.

X-Ray diffraction: The annealed polycrystalline samples were analyzed by powder X-ray diffraction. Powder X-ray diffraction (PXRD) patterns of the pulverized samples were recorded at room temperature on a D8-A25-Advance diffractometer (Bruker, Karlsruhe, Germany) in Bragg–Brentano θ-θ-geometry (goniometer radius 280 mm) with Cu Kα-radiation (λ = 154.0596 pm). A 12 µm Ni foil working as K_β filter and a variable divergence slit were mounted at the primary beam side. A LYNXEYE detector with 192 channels was used at the secondary beam side. Experiments were carried out in a 2θ range of 6 to 130° with a step size of 0.013° and a total scan time of 1 h.

Small fragments of the annealed and crushed samples of Y_2TiAl_3, Gd_2TiAl_3, and Tb_2TiAl_3 were glued to thin quartz fibers using beeswax. The crystallite quality was checked by Laue photographs on a Buerger precession camera (white molybdenum radiation; imaging plate system, Fujifilm, BAS-READER 1800, Minato, Japan). Intensity data sets of suitable single crystals were collected at room temperature, either on an IPDS-II (graphite-monochromatized Mo$K\alpha$ radiation; λ = 0.71073 pm; oscillation mode) or on a Bruker D8 Venture diffractometer (graphite-monochromatized Mo$K\alpha$ radiation; λ = 0.71073 pm) equipped with a μ-focus source.

CCDCs 1939725-1939727 contain the supplementary crystallographic data for this paper. The data can be obtained free of charge from The Cambridge Crystallographic Data Centre via www.ccdc.cam.ac.uk/structures.

Physical property measurements*:* Annealed pieces of the respective X-ray pure RE_2TiAl_3 (*RE* = Y, Gd–Tm, Lu) samples were attached to the sample holder rod of a Vibrating Sample Magnetometer (VSM) using Kapton foil for measuring the magnetization *M*(*H*,*T*) in a Quantum Design (San Diego, CA, USA) Physical Property Measurement System (PPMS). All samples were investigated in the temperature range of 2.5–300 K with applied external magnetic fields of up to 80 kOe.

3. Results and Discussion

3.1. Structure Refinement

The obtained single crystal data sets showed a rhombohedral lattice; space group $R\bar{3}m$ was found to be correct during the structure refinement. Isotypism to the Mg_2Ni_3Si-type structure was evident from both single crystal and powder X-ray diffraction experiments. Starting values for the structure refinement were obtained using the SuperFlip [57] program package, implemented in Jana2006 [58,59]. All atomic positions and anisotropic displacement parameters were subsequently refined, again using Jana2006. Occupancy parameters of all crystallographic sites were individually refined in separate series of least-squares refinements to check for the correct composition. No mixing, especially of Ti and Al, was observed. The final difference Fourier syntheses were contourless. Details on the measurements, refined atomic parameters, displacement parameters, and interatomic distances can be found in Tables 1–4.

3.2. SEM-EDX Data

EDX investigations of the bulk samples were carried out exemplarily on Er_2TiAl_3, Tm_2TiAl_3, and Lu_2TiAl_3. The experimentally determined averaged element ratios (Table 5) were obtained from five spot measurements and one area measurement and are in good agreement with the ideal compositions. The crystals of Y_2TiAl_3, Gd_2TiAl_3, and Tb_2TiAl_3 measured on the diffractometer were analyzed semi-quantitatively using a SEM in combination with EDX (Table 5). No impurity elements heavier than sodium (detection limit of the instrument) were observed. The experimentally determined averaged element ratios were obtained from five spot measurements and are in good agreement with the ideal compositions. Differences originate from the conchoidal fractures of the crystallites and the non-perfect perpendicular orientation of the crystals to the beam.

3.3. Crystal Chemistry

The rare-earth compounds of the RE_2TiAl_3 series (RE = Y, Gd–Tm, Lu) crystallize in the trigonal Mg_2Ni_3Si-type structure with space group $R\bar{3}m$ and Z = 3. The lattice parameters and unit cell volumes (Table 6) decrease from the gadolinium to the lutetium compound, as expected due to the lanthanide contraction (Figure 1, Table 6). Y_2TiAl_3 exhibits lattice parameters similar to those of Tb_2TiAl_3, in line with the comparable ionic radii of the trivalent cations (Y^{3+}: 106 pm; Tb^{3+} 104 pm; CN = 8 [60]). In Figure 2, a comparison of the Rietveld fit of the experimental diffraction pattern of Y_2TiAl_3 using the trigonal Mg_2Ni_3Si type and the cubic $MgCu_2$-type structure is shown. The rhombohedral distortion is easily visible in the diffraction patterns due to the splitting of the reflections (Figures S1–S6, Tables S1–S6).

Table 1. Crystallographic data and structure refinement information for Y_2TiAl_3, Gd_2TiAl_3, and Tb_2TiAl_3, space group $R\bar{3}m$, Z = 3, Mg_2Ni_3Si type determined from single crystal X-ray diffraction data. All data sets were collected at room temperature.

Formula	**Y_2TiAl_3**	**Gd_2TiAl_3**	**Tb_2TiAl_3**
CCDC number	1939725	1939727	1939726
Molar mass, g mol^{-1}	306.6	443.3	446.7
Lattice parameters		see Table 6	
Density calc., g cm^{-3}	4.04	5.77	5.90
Crystal size, µm	50 × 40 × 35	30 × 25 × 10	40 × 40 × 20
Diffractometer	IPDS-II	IPDS-II	Bruker CCD
Wavelength; λ, pm	Mo$K\alpha$; 71.073	Mo$K\alpha$; 71.073	Mo$K\alpha$; 71.073
Transmission ratio (min/max)	0.2943/0.4102	0.5295/0.7673	0.3054/0.5561
Detector distance, mm	60	70	40
Exposure time, min	10	30	0.167
Integr. param. A, B, EMS	14.0; −1.0; 0.030	16.0; –4.0; 0.030	–
F(000), e	417	567	573
Range in hkl	±9; −8, +9, ±21	±8; ±8, ±20	±7; ±8, −17, +20
θ_{min}, θ_{max}, deg	4.4/34.9	4.4/33.3	4.4/32.0
Linear absorption coeff., mm^{-1}	24.7	27.6	29.7
Total no. of reflections	2889	1579	826
Independent reflections/R_{int}	229/0.0510	212/0.0696	190/0.0143
Reflections with $I \geq 3\sigma(I)/R_\sigma$	191/0.0168	175/0.0275	181/0.0122
Data/parameters	229/11	212/11	190/11
$R1/wR2$ for $I \geq 3\sigma(I)$	0.0177/0.0357	0.0208/0.0214	0.0105/0.0259
$R1/wR2$ for all data	0.0286/0.0393	0.0317/0.0221	0.0111/0.0260
Goodness-of-fit on F^2	1.23	1.16	1.03
Extinction scheme		Lorentzian isotropic [61]	
Extinction coefficient	160(50)	58(19)	350(20)
Diff. Fourier residues /e$^-$ Å^{-3}	−1.32/+1.01	−1.81/+1.40	−0.37/+1.06

The following discussion of the crystal structure and the interatomic distances is based on the single crystal data obtained for Y_2TiAl_3. As the crystal structure (Figure 3) can be derived from the cubic Laves phase ($MgCu_2$ type, $Fd\bar{3}m$), the structural relationship is fairly obvious. A group–subgroup scheme according to the Bärnighausen formalism for the structural relationship of $CeRh_2$ and Ce_2Rh_3Ga has been provided in the literature [40]. As in the $MgCu_2$-type structure, only two crystallographic positions are occupied (Mg on 8*a*, 0,0,0; Cu on 16*c*, 3/8, 3/8, 3/8) and no distinct ordering is possible. A *translationengleiche* transition of index 4 leads to the structure of Mg_2Ni_3Si in the rhombohedral crystal system and space group $R\bar{3}m$. This allows for a decoupling of the lattice parameters along with the possibility of atomic ordering (16*c* splits into 3*a* and 9*d*). In addition, Mg atoms (6*c*) gain a free z parameter allowing the adjustment of interatomic distances. A recent review article [47] summarizes the information on the superstructures of Laves phases.

Table 2. Atom positions and equivalent isotropic displacement parameters (pm^2) for Y_2TiAl_3, Gd_2TiAl_3, and Tb_2TiAl_3 determined from single crystal X-ray diffraction data. U_{eq} is defined as one-third of the trace of the orthogonalized U_{ij} tensor.

Atom	Wyckoff Position	x	y	z	U_{eq}
Y_2TiAl_3					
Y	6*c*	0	0	0.37244(4)	89(1)
Ti	3*a*	0	0	0	75(2)
Al	9*d*	1/2	0	1/2	88(3)
Gd_2TiAl_3					
Gd	6*c*	0	0	0.37333(3)	81(1)
Ti	3*a*	0	0	0	67(5)
Al	9*d*	1/2	0	1/2	84(7)
Tb_2TiAl_3					
Tb	6*c*	0	0	0.37348(1)	64(1)
Ti	3*a*	0	0	0	54(2)
Al	9*d*	1/2	0	1/2	69(3)

Table 3. Anisotropic displacement parameters (pm^2) for Y_2TiAl_3, Gd_2TiAl_3, and Tb_2TiAl_3 determined from single crystal X-ray diffraction data. Coefficients U_{ij} of the anisotropic displacement factor tensor of the atoms are defined by $-2\pi^2[(ha^*)^2U_{11} + \ldots + 2hka^*b^*U_{12}]$.

Atom	U_{11}	U_{22}	U_{33}	U_{12}	U_{13}	U_{23}
Y_2TiAl_3						
Y	86(2)	U_{11}	94(2)	43(1)	0	U_{13}
Ti	79(3)	U_{11}	66(4)	40(1)	0	U_{13}
Al	84(3)	86(4)	95(5)	43(2)	5(2)	10(1)
Gd_2TiAl_3						
Gd	79(2)	U_{11}	84(2)	40(1)	0	U_{13}
Ti	74(5)	U_{11}	54(9)	37(3)	0	U_{13}
Al	77(6)	80(11)	95(10)	40(5)	4(6)	8(13)
Tb_2TiAl_3						
Tb	62(1)	U_{11}	69(1)	31(1)	0	U_{13}
Ti	55(3)	U_{11}	52(4)	28(1)	0	U_{13}
Al	74(3)	68(5)	64(4)	34(2)	2(2)	5(3)

Table 4. Interatomic distances (pm) for Y_2TiAl_3, Gd_2TiAl_3, and Tb_2TiAl_3 determined from single crystal X-ray diffraction data. All distances of the first coordination spheres are listed. All standard uncertainties were less than 0.1 pm.

Y_2TiAl_3				**Gd_2TiAl_3**				**Tb_2TiAl_3**			
Y:	3	Al	323.1	Gd:	3	Al	325.4	Tb:	3	Al	324.1
	3	Ti	332.3		6	Al	333.1		6	Al	331.3
	6	Al	332.4		3	Ti	333.8		3	Ti	332.1
	3	Y	344.7		1	Gd	344.1		1	Tb	342.2
	1	Y	345.1		3	Gd	346.8		3	Tb	345.1
Ti:	6	Al	278.8	Ti:	6	Al	279.9	Ti:	6	Al	278.6
	6	Y	332.3		6	Gd	333.8		6	Tb	332.1
Al:	2	Ti	278.8	Al:	2	Ti	279.9	Al:	2	Ti	278.6
	4	Al	284.1		4	Al	285.2		4	Al	283.7
	2	Y	323.1		2	Gd	325.4		2	Tb	324.1
	4	Y	332.4		4	Gd	333.1		4	Tb	331.3

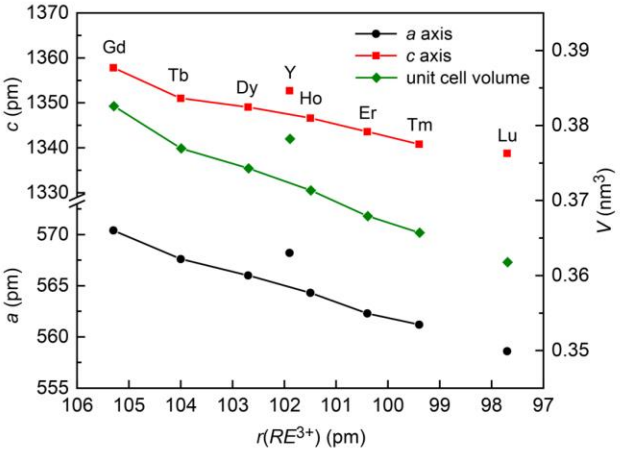

Figure 1. Trigonal lattice parameters and unit cell volumes of the RE_2TiAl_3 (*RE* = Y, Gd–Tm, Lu) series (Mg_2Ni_3Si type) plotted versus the ionic radii of the trivalent RE^{3+} cations. The connection between the data points is a guide to the eye.

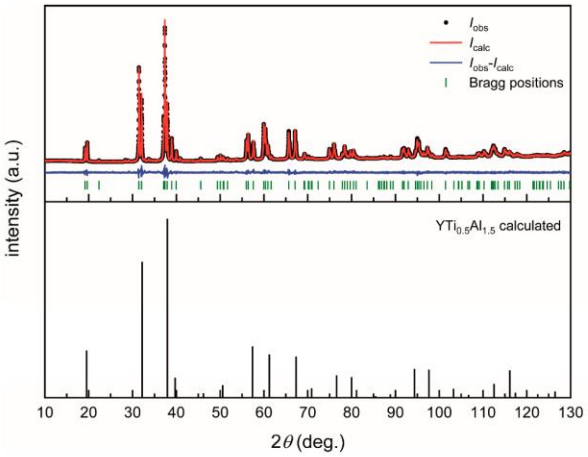

Figure 2. Rietveld refinement of Y_2TiAl_3 (**top**) in the trigonal Mg_2Ni_3Si-type structure in comparison with (**bottom**) the cubic $MgCu_2$-type structure.

Table 5. SEM-EDX data of the rhombohedral RE_2TiAl_3 series. Standard deviations are ±2 at.-%.

Compound	*RE* (at.-%)	Ti (at.-%)	Al (at.-%)
Ideal composition	33.3	16.7	50.0
Single crystal data			
Y_2TiAl_3	36	16	48
Gd_2TiAl_3	34	16	50
Bulk sample data			
Er_2TiAl_3	36	14	50
Tm_2TiAl_3	32	16	52
Lu_2TiAl_3	37	15	48

Table 6. Lattice parameters of the rhombohedral RE_2TiAl_3 series (RE = Y, Gd–Tm, Lu), space group $R\bar{3}m$, $Z = 3$, Mg_2Ni_3Si type, determined by powder X-ray diffraction. ^{P} denotes powder data, ^{SC} single crystal data.

Compound	a (pm)	c (pm)	V (nm^3)
Y_2TiAl_3 ^{P}	568.29(4)	1353.0(1)	0.3784
Y_2TiAl_3 ^{SC}	568.22(7)	1352.9(2)	0.3783
Gd_2TiAl_3 ^{P}	569.81(5)	1359.6(2)	0.3823
Gd_2TiAl_3 ^{SC}	570.45(5)	1358.0(1)	0.3827
Tb_2TiAl_3 ^{P}	567.55(6)	1351.0(3)	0.3769
Tb_2TiAl_3 ^{SC}	567.39(6)	1352.4(2)	0.3771
Dy_2TiAl_3 ^{P}	565.90(6)	1349.1(2)	0.3742
Ho_2TiAl_3 ^{P}	564.86(3)	1347.5(1)	0.3723
Er_2TiAl_3 ^{P}	563.10(3)	1344.3(1)	0.3691
Tm_2TiAl_3 ^{P}	559.61(9)	1341.3(3)	0.3638
Lu_2TiAl_3 ^{P}	558.37(4)	1338.2(1)	0.3613

The tetrahedral entities in the cubic structure type are connected over all corners, forming a network, however, by only one crystallographic position. In rhombohedral Y_2TiAl_3, a splitting of this single position takes places, allowing full Ti/Al ordering in the empty [$TiAl_3$] tetrahedra. The Al atoms form 6^3 Kagomé nets, while the Ti atoms connect these nets over the triangles. In the cavities of this three-dimensional arrangement, the RE cations can be found. They form a distorted cubic diamond-type substructure, as highlighted in Figure 3. The coordination environments of the Ti and Al atoms are depicted in Figure 4. In the network, Ti–Al distances of 279 pm can be found, longer than the sum of the covalent radii (Ti + Al = 132 + 125 = 257 pm [60]), suggesting moderate bonding interactions. In the binary compounds TiAl (tetragonal CuAu type, $P4/mmm$ [62]) and Ti_3Al (hexagonal Mg_3Cd type, $P6_3/mmc$ [63]), interatomic distances of 283 and 286 + 289 pm are observed, respectively, while in the only thus far known ternary compound $Y_6Ti_4Al_{43}$ (hexagonal $Ho_6Mo_4Al_{43}$ type, $P6_3/mcm$ [64]), Ti–Al distances of 259–287 pm are found. The Y atoms in Y_2TiAl_3 are surrounded by 16 atoms in the shape of a Frank–Kasper polyhedra [65,66] according to $Y@Al_9Y_4Ti_3$ (Figure 4, top), while Ti and Al both exhibit icosahedra coordination environments (Figure 4, middle and bottom). The Ti atoms are surrounded octahedrally by the Al atoms along with six Y atoms ($Y@Al_6Y_6$), the Al atoms by four Al, two Ti, and six Y atoms ($Al@Al_4Ti_2Y_6$). The Y–Ti distances are 332 pm, while the Y–Al distances range between 323 and 332 pm, suggesting rather weak interactions when compared to the sum of the covalent radii (Y + Ti = 162 + 132 = 294 pm; Y + Al = 162 + 125 = 287 pm [60]). In YAl_2 (cubic $MgCu_2$ type, $Fd\bar{3}m$ [67,68]), heteroatomic Y–Al distances of 325 pm can be observed, which suggest rather low interactions. Since no binary phases in the system Y/Ti exist; only the comparison with $Y_6Ti_4Al_{43}$ [64] is possible. The shortest Y–Ti distance is 354 pm, also suggesting very weak to no bonding interactions, while Y–Al distances between 308 and 344 pm are observed. In Y_2TiAl_3, two different Y–Y distances (344.7 and 345.2 pm) are observed, due to the distortion of the cubic $MgCu_2$-type structure. In cubic YAl_2 [67,68], only one distance of 340 pm is found.

Attempts to extend the series of the RE_2TiAl_3 compounds to the larger elements (RE = La-Nd, Sm, Eu) were not successful. For the lanthanum compound, a synthesis under the same conditions as described above resulted in a mixture of the binary compounds $LaAl_2$ ($MgCu_2$ type), LaAl (CeAl type) and elemental titanium (Mg type). The refined powder pattern is shown in Figure S7 (Table S7).

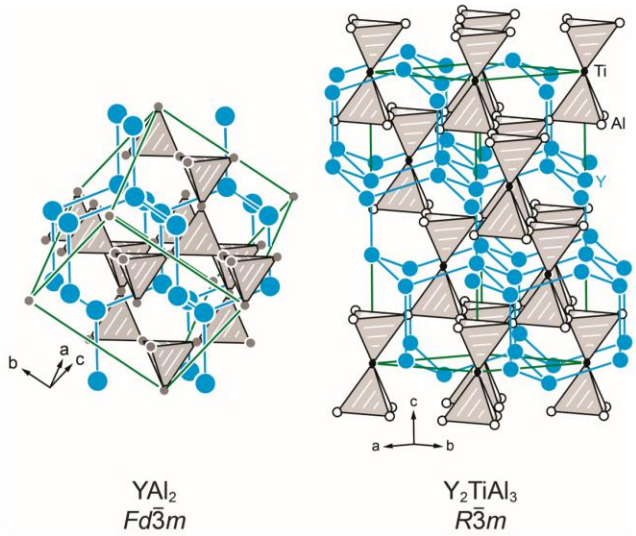

Figure 3. Unit cells of YAl_2 (**left**) and Y_2TiAl_3 (**right**). Yttrium, titanium, and aluminum atoms are depicted as blue, black, and open white circles, respectively. The empty $[Al_4]$ and $[TiAl_3]$ tetrahedra in YAl_2 and Y_2TiAl_3 and the diamond-related substructure formed by the Y atoms are highlighted.

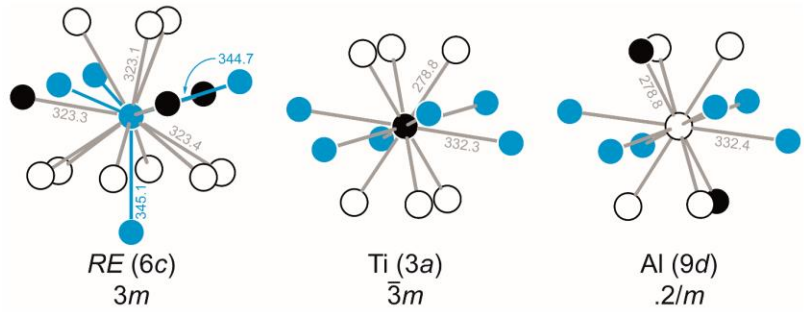

Figure 4. Coordination environments surrounding the Y, Ti, and Al atoms in the crystal structure of Y_2TiAl_3. Yttrium, titanium, and aluminum atoms are depicted as blue, black, and open white circles, respectively. Wyckoff sites, site symmetries, and interatomic distances (in pm) are given.

3.4. Physical Properties

The physical properties of the RE_2TiAl_3 series (Table 7; *RE* = Y, Gd–Tm, Lu) were determined by susceptibility and magnetization experiments. While Y_2TiAl_3 and Lu_2TiAl_3 exhibit Pauli paramagnetism, in line with their metallic character and the absence of (unpaired) *f*-electrons, all other compounds are paramagnetic. The temperature dependence of the magnetic susceptibility of Y_2TiAl_3 and Lu_2TiAl_3 is depicted in Figure 5. The susceptibility exhibits positive values over the whole investigated temperature region and reaches $\chi(300\ \mathrm{K}) = +2.48(1) \times 10^{-4}$ emu mol^{-1} (Y_2TiAl_3) and $\chi(300\ \mathrm{K}) = +2.14(1) \times 10^{-4}$ emu mol^{-1} (Lu_2TiAl_3), indicating that the Pauli paramagnetism overcompensates the intrinsic diamagnetism.

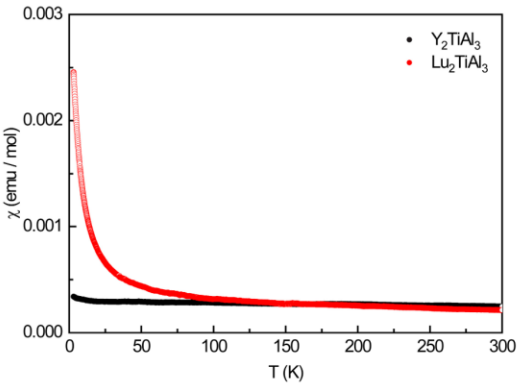

Figure 5. Temperature dependence of the magnetic susceptibility of Y_2TiAl_3 (black) and Lu_2TiAl_3 (red) measured with an applied external field of 10 kOe.

The magnetic data of Gd_2TiAl_3 is depicted in Figure 6. The ZFC (zero-field-cooled) investigations at high field (10 kOe) were conducted in the temperature range of 3–300 K and are shown in the top panel. From the inverse susceptibility, the effective magnetic moment was determined to μ_{eff} = 7.89(1) μ_B, well in line with the theoretical moment of $\mu_{eff,calc}$ = 7.94 μ_B for a free Gd^{3+} cation. The paramagnetic Curie temperature is θ_P = +20.8(1) K, indicating dominant ferromagnetic interactions in the paramagnetic temperature regime. From the low-field 100 Oe ZFC/FC (zero-field-cooled/field-cooled) measurements, an antiferromagnetic ordering was derived with a Néel temperature of T_N = 26.1(1) K. The rather strong bifurcation, along with the high residual magnetization, however, indicates that the investigated sample could contain ferromagnetic impurities. Samples of the same composition but from different batches exhibit a similar behavior. Therefore, homogeneity ranges within the samples are suspected. One impurity might be $GdAl_2$ [69], which exhibits ferromagnetic ordering below T_C = 170 K. Therefore, pure $GdAl_2$ cannot be the impurity but the solid solution $GdTi_xAl_{2-x}$ could be responsible for the magnetic behavior. Since these compounds crystallize in the cubic $MgCu_2$-type structure, trace impurities are invisible in the powder X-ray patterns, since the reflections overlap with those of rhombohedral Gd_2TiAl_3 (Figure 2). However, since ferromagnetic transitions are significantly stronger compared to antiferromagnetic ones (factor 1000 to 10,000), only traces of the respective impurity can be present. The magnetization isotherms (Figure 6, bottom) finally exhibit a steep increase already at low magnetic fields. This is an additional indication of the presence of ferromagnetic impurities. The 50 and 100 K isotherms are linear, as expected for a paramagnetic material; those measured at 3 and 10 K show a very weak curvature that could indicate an upcoming spin-reorientation at even higher fields. The comparatively low saturation magnetization of μ_{sat} = 3.98(1) μ_B reached at 3 K and 80 kOe also underlines a strong antiferromagnetic ground state. Similar effects have been observed, e.g., for $GdPtGe_2$ [70] or $Gd_3Pt_4Ge_6$ [71]. Usually, Gd intermetallics reach (nearly) the theoretical full saturation magnetization $\mu_{sat,theo}$ = 7 μB according to $g_J \times J$, as seen, e.g., for $GdAl_2$ [72], Gd_3Al_2 [72], Gd_2RhAl_3 [14], or $GdPt_6Al_3$ [73].

Er_2TiAl_3 could be obtained in nearly pure form; the magnetic data are depicted in Figure 7. The effective magnetic moment was determined to be μ_{eff} = 9.73(1) μ_B and is slightly enhanced compared to the theoretical moment of $\mu_{eff,calc}$ = 9.58 μ_B for a free Er^{3+} cation; the paramagnetic Curie temperature is θ_P = −6.5(1) K, indicating antiferromagnetic interactions in the paramagnetic temperature regime. An antiferromagnetic ordering was derived from the low-field zero-field-cooled measurements (Figure 7, middle) with a Néel temperature of T_N = 17.6(1) K; however, again a bifurcation is visible, suggesting traces of ferromagnetic impurities. The magnetization isotherms (Figure 7, bottom) at 50 and 100 K isotherms are linear, as expected for a paramagnetic material; the ones measured at 3 and 10 K show an S-shape with a curvature that indicates a spin-reorientation at a critical field

of H_{crit} = 20.7(5) kOe, determined by the derived value of the 3 K isotherm. The saturation magnetization of μ_{sat} = 4.46(1) μ_B reaches 3 K and 80 kOe, which is below the expected value of $\mu_{sat,theo}$ = 9 μ_B according to $g_J \times J$.

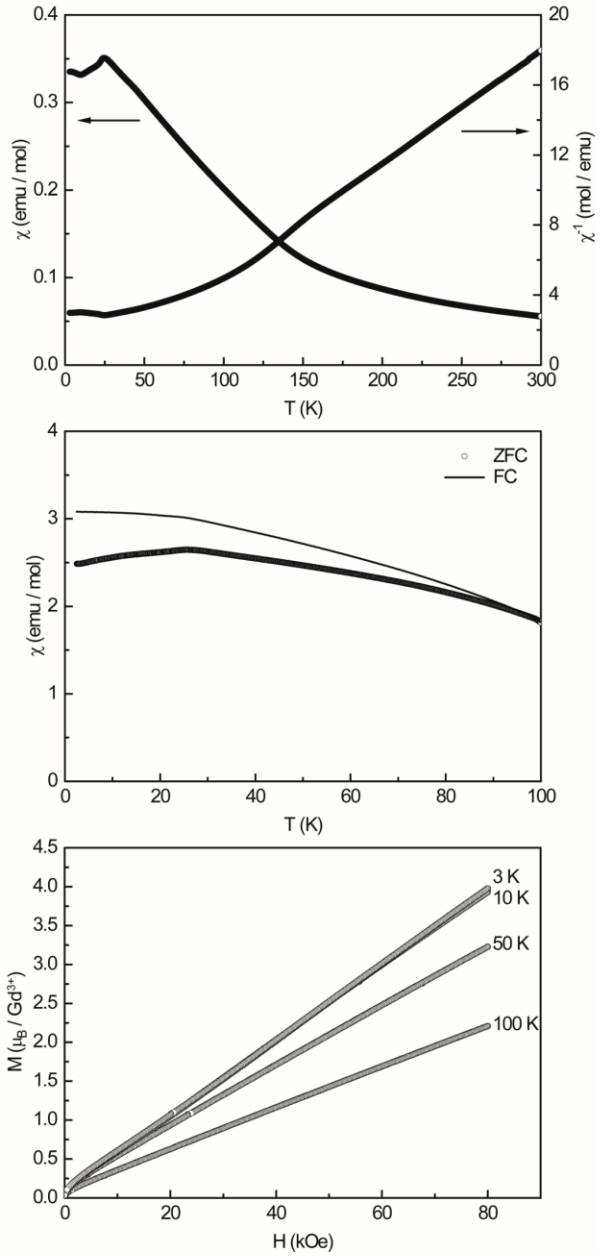

Figure 6. Magnetic data of Gd_2TiAl_3. (**top**) Temperature dependence of the magnetic and inverse magnetic susceptibility (χ and χ^{-1} data) measured with an applied external field of 10 kOe; (**middle**) zero-field-cooled/field-cooled (ZFC/FC) measurements measured with an applied external field of 100 Oe; (**bottom**) magnetization isotherms recorded at 3, 10, 50, and 100 K.

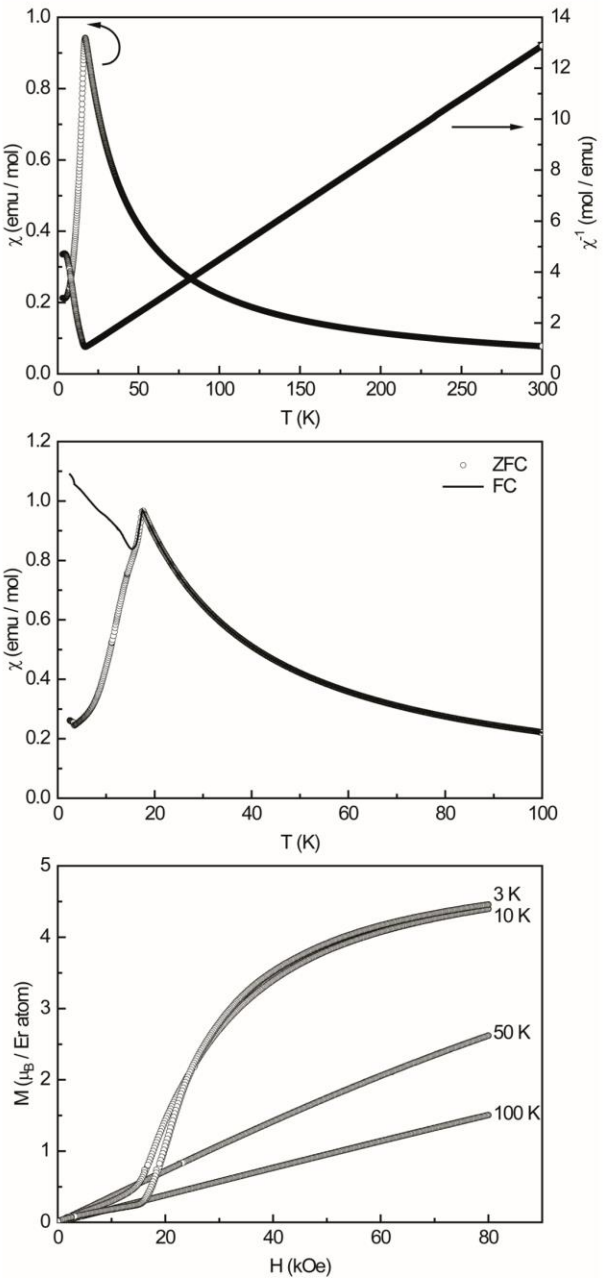

Figure 7. Magnetic data of Er_2TiAl_3. (**top**) Temperature dependence of the magnetic and inverse magnetic susceptibility (χ and χ^{-1} data) measured with an applied external field of 10 kOe; (**middle**) zero-field-cooled/field-cooled (ZFC/FC) measurements measured with an applied external field of 100 Oe; (**bottom**) magnetization isotherms recorded at 3, 10, 50, and 100 K.

Table 7. Physical properties of the RE_2TiAl_3 (*RE* = Y, Gd–Tm; Lu) series: T_N, Néel temperature; μ_{exp}, experimental magnetic moment; μ_{eff}, effective magnetic moment; θ_P, paramagnetic Curie temperature; μ_{sat}, experimental saturation magnetization; $g_J \times J$, theoretical saturation magnetization.

Compound	T_N (K)	μ_{exp} (μ_B)	μ_{eff} (μ_B)	θ_P (K)	μ_{sat} (μ_B per RE^{3+})	$g_J \times J$ (μ_B per RE^{3+})
Y_2TiAl_3	Pauli-paramagnetic, non-superconducting, χ(300 K) = +2.48(1) × 10^{-4} emu mol^{-1}					
Gd_2TiAl_3	26.1(1)	7.98(1)	7.94	+20.8(1)	3.98(1)	7
Tb_2TiAl_3	24.0(1)	10.04(1)	9.72	+31.7(1)	3.58(1)	9
Dy_2TiAl_3	26.1(1)	11.14(1)	10.65	−0.29(1)	7.98(1)	10
Ho_2TiAl_3	10.3(1)	10.85(1)	10.61	+0.72(1)	7.36(1)	10
Er_2TiAl_3	17.6(1)	9.73(1)	9.58	−6.5(1)	4.46(1)	9
Tm_2TiAl_3	10.8(1)	7.69(1)	7.61	−7.3(1)	3.46(1)	7
Lu_2TiAl_3	Pauli-paramagnetic, non-superconducting, χ(300 K) = +2.14(1) × 10^{-4} emu mol^{-1}					

4. Conclusions

In this paper, we present the synthesis as well as structural and magnetic characterization of the RE_2TiAl_3 series with *RE* = Y, Gd–Tm, and Lu. These compounds adopt the rhombohedral Mg_2Ni_3Si-type structure and are the first representations in the field of aluminum intermetallics. The crystal structures of Y_2TiAl_3, Gd_2TiAl_3, and Tb_2TiAl_3 have been refined from single crystal X-ray diffraction data and clearly indicate the formation of the rhombohedral structure. Powder X-ray diffraction experiments underline this observation as the diffraction patterns exhibit the expected splitting of reflections based on the transition from the cubic to the rhombohedral crystal system. Powder patterns of selected members of the series have been refined using the Rietveld method. All compounds have been characterized by magnetic susceptibility and magnetization experiments. While Y_2TiAl_3 and Lu_2TiAl_3 exhibit a nearly temperature independent behavior in line with the expected Pauli paramagnetism, the other compounds of the series show a stable trivalent oxidation state of the rare-earth atoms. All compounds exhibit antiferromagnetic transitions at lower temperatures; however, sometimes traces of ferromagnetic impurities can be observed. These originate from impurities that crystallize in the cubic $MgCu_2$-type structure and have to be considered solid solutions according to $RETi_xAl_{2-x}$. Even small traces of these compounds provide visible features in the magnetic data since ferromagnetic transitions are significantly stronger than antiferromagnetic ones. An identification of these impurities is impossible since their reflections overlap with those of the rhombohedral main phase. Finally, the valence electron concentration (VEC) also shows an intriguing feature. The title compounds exhibit a VEC of 19 e^- (2× $3e^-$ + $4e^-$ + 3× $3e^-$), while all other compounds that adopt the Mg_2Ni_3Si-type structure, including the prototype itself, exhibit VECs between 36 and 39. The stability of the aluminum representatives will be investigated by quantum-chemical calculations in the future.

Supplementary Materials: The following supporting information can be downloaded at: https://www.mdpi.com/article/10.3390/solids4030011/s1, Figure S1: Rietveld refinement of Y_2TiAl_3; Figure S2: Rietveld refinement of Dy_2TiAl_3; Figure S3: Rietveld refinement of Ho_2TiAl_3; Figure S4: Rietveld refinement of Er_2TiAl_3; Figure S5: Rietveld refinement of Tm_2TiAl_3; Figure S6: Rietveld refinement of Lu_2TiAl_3; Figure S7: Rietveld refinement of nominal La_2TiAl_3; Table S1: Rietveld refinement of Y_2TiAl_3; Table S2: Rietveld refinement of Dy_2TiAl_3; Table S3: Rietveld refinement of Ho_2TiAl_3; Table S4: Rietveld refinement of Er_2TiAl_3; Table S5: Rietveld refinement of Tm_2TiAl_3; Table S6: Rietveld refinement of Lu_2TiAl_3; Table S7: Rietveld refinement of nominal La_2TiAl_3.

Author Contributions: Conceptualization, O.J.; methodology, E.C.J.G., S.E., M.R., J.M.G. and L.S.; analysis, E.C.J.G., S.E., I.M.E., L.S. and O.J.; investigation, E.C.J.G., S.E., I.M.E., M.R., J.M.G. and L.S.; writing—original draft preparation, E.C.J.G. and M.R.; writing—review and editing, E.C.J.G. and O.J.; visualization, E.C.J.G.; supervision, O.J.; project administration, O.J.; funding acquisition, O.J. All authors have read and agreed to the published version of the manuscript.

Funding: This research was funded by the German Research Foundation DFG, grant numbers JA 1891-10-1 and INST 256/349-1.

Data Availability Statement: CCDCs 1939725-1939727 contain the supplementary crystallographic data for this paper. The data can be obtained free of charge from The Cambridge Crystallographic Data Centre via www.ccdc.cam.ac.uk/structures.

Acknowledgments: We thank Rolf-Dieter Hoffmann and Jutta Kösters for the collection of the single crystal intensity data and Jörg Schmauch for the help with the SEM/EDX investigations. Instrumentation and technical assistance for this work were provided by the Service Center X-ray Diffraction, with financial support from Saarland University and the German Science Foundation (project number INST 256/349-1).

Conflicts of Interest: The authors declare no conflict of interest.

References

1. Paufler, P.; Gustav, E.R. Schulze's pioneering work on Laves phases. *Z. Kristallogr.* **2006**, *221*, 311. [CrossRef]
2. Fischer, W.; Fritz, H. Laves—An ideal for generations. *Z. Kristallogr.* **2006**, *221*, 305. [CrossRef]
3. Parthé, E.; Fritz, H. Laves—100 years young. *Z. Kristallogr.* **2006**, *221*, 301. [CrossRef]
4. Villars, P.; Cenzual, K. (Eds.) *Pearson's Crystal Data: Crystal Structure Database for Inorganic Compounds*; (release 2022/23); ASM International®: Materials Park, OH, USA, 2023.
5. Laves, F.; Witte, H. Der Einfluß von Valenzelektronen auf die Kristallstruktur ternärer Magnesiumlegierungen. *Metallwirtsch. Metallwiss. Metalltech.* **1936**, *15*, 840–842.
6. Gschneidner, K.A., Jr.; Pecharsky, V.K. Binary rare earth Laves phases—An overview. *Z. Kristallogr.* **2006**, *221*, 375–381. [CrossRef]
7. Fukui, H.; Hirao, N.; Ohishi, Y.; Baron, A.Q.R. Compressional behavior of solid $NeHe_2$ up to 90 GPa. *J. Phys. Condens. Matter* **2010**, *22*, 095401. [CrossRef] [PubMed]
8. Dewaele, A.; Rosa, A.D.; Guignot, N. Argon-neon binary diagram and $ArNe_2$ Laves phase. *J. Chem. Phys.* **2019**, *151*, 124708. [CrossRef]
9. Ji, C.; Goncharov, A.F.; Shukla, V.; Jena, N.K.; Popov, D.; Li, B.; Wang, J.; Meng, Y.; Prakapenka, V.B.; Smith, J.S.; et al. Stability of $Ar(H_2)_2$ to 358 GPa. *Proc. Natl. Acad. Sci. USA* **2017**, *114*, 3596–3600. [CrossRef]
10. Laniel, D.; Weck, G.; Loubeyre, P. $Xe(N_2)_2$ compound to 150 GPa: Reluctance to the formation of a xenon nitride. *Phys. Rev. B* **2016**, *94*, 174109. [CrossRef]
11. Komura, Y.; Kitano, Y. Long-period stacking variants and their electron-concentration dependence in the Mg-base Friauf-Laves phases. *Acta Crystallogr.* **1977**, *B33*, 2496–2501. [CrossRef]
12. Witte, H. Untersuchungen im System Magnesium-Kupfer-Silicium mit besonderer Berücksichtigung des Schnittes $MgCu_2$-$MgSi_2$. *Z. Angew. Mineral.* **1938**, *1*, 255–268.
13. Mishra, T.; Hoffmann, R.-D.; Schwickert, C.; Pöttgen, R. Structure Refinement and Magnetic Properties of Ce_2RuAl_3 and a Group-Subgroup Scheme for $Ce_5Ru_3Al_2$. *Z. Naturforsch.* **2011**, *66b*, 771–776. [CrossRef]
14. Eustermann, F.; Stegemann, F.; Gausebeck, S.; Janka, O. Structural and Magnetic Investigations of the Pseudo Ternary RE_2TAl_3 series (*RE* = Sc, Y, La–Nd, Sm, Gd–Lu; *T* = Ru, Rh, Ir)—Size Dependent Formation of Two Different Structure Types. *Z. Naturforsch.* **2018**, *73b*, 819–830. [CrossRef]
15. Blazina, Z.; Ban, Z. The Crystal Structures of U_2Cu_3Al and $UCuAl_2$, and their Relationship with Some Other Phases in the System U-Cu-Al. *Z. Naturforsch.* **1981**, *35b*, 1162–1165.
16. Huneau, B.; Rogl, P.; Zeng, K.; Schmid-Fetzer, R.; Bohn, M.; Bauer, J. The ternary system Al–Ni–Ti Part I: Isothermal section at 900 °C; Experimental investigation and thermodynamic calculation. *Intermetallics* **1999**, *7*, 1337–1345. [CrossRef]
17. Zelinskii, A.V.; Fedorchuk, A.O.; Zelinska, O.Y. Synthesis and crystal structure of the compounds $UMn_{1.43}Ga_{0.57}$ and U_2Fe_3Ga. *Visn. Lviv. Derzh. Univ. Ser. Khim.* **2013**, *54*, 92–97.
18. Sichevych, O.; Prots, Y.; Schnelle, W.; Schmidt, M.; Grin, Y. Crystal structure of dieuropium trigallium iridium, Eu_2Ga_3Ir. *Z. Kristallogr. NCS* **2006**, *221*, 263–264. [CrossRef]
19. Mykhalichko, O.; Gladyshevskii, E.I.; Hlukhyy, V.; Fässler, T.F. Synthesis and crystal structure of the compound $Nb_2Cu_{1.10}Ga_{2.90}$. *Visn. Lviv. Derzh. Univ. Ser. Khim.* **2009**, *50*, 89–93.
20. Myakush, O.R.; Fedorchuk, A.A. Crystal structure and electrical properties of HoRuGa compound. *Visn. Lviv. Derzh. Univ. Ser. Khim.* **2004**, *44*, 62–66.
21. Yan, X.L.; Chen, X.-Q.; Grytsiv, A.; Witusiewicz, V.T.; Rogl, P.; Podloucky, R.; Giester, G. On the ternary Laves phases $\{Sc,Ti\}_2M_3Si$ (*M* = Cr, Mn, Fe, Co, Ni) with $MgZn_2$-type. *J. Alloys Compd.* **2007**, *429*, 10–18. [CrossRef]
22. Kotur, B.Y. Crystal structure of Sc_2M_3Si (where *M* = Fe, Co, Ni) compounds. *Dopov. Akad. Nauk Ukr. RSR* **1977**, *A39*, 164–165.
23. Bardos, D.I.; Gupta, K.P.; Beck, P.A. Ternary Laves Phases with Transition Elements and Silicon. *Trans. Metall. Soc. AIME* **1961**, *221*, 1087–1088.
24. Henriques, M.S.; Berthebaud, D.; Lignie, A.; El Sayah, Z.; Moussa, C.; Tougait, O.; Havela, L.; Gonçalves, A.P. Isothermal section of the ternary phase diagram U–Fe–Ge at 900 °C and its new intermetallic phases. *J. Alloys Compd.* **2015**, *639*, 224–234. [CrossRef]

25. Hoffmann, R.-D.; Pöttgen, R.; Chevalier, B.; Gaudin, E.; Matar, S.F. The ternary germanides UMnGe and U_2Mn_3Ge. *Solid State Sci.* **2013**, *21*, 73–80. [CrossRef]
26. Soudé, A.; Tougait, O.; Pasturel, M.; Kaczorowski, D.; Noël, H.; Roisnel, T. Characterization of the novel intermetallic compounds U_2Co_3Ge, $U_6Co_{12}Ge_4$ and $U_6Co_{12}Ge_4C$. *J. Alloys Compd.* **2011**, *509*, 5447–5452. [CrossRef]
27. Henriques, M.S.; Tougait, O.; Noel, H.; Pereira, L.C.J.; Waerenborgh, J.C.; Gonçalves, A.P. Evidence of uranium magnetic ordering on U_2Fe_3Ge. *Solid State Commun.* **2008**, *148*, 159–162. [CrossRef]
28. Teslyuk, M.Y.; Gladyshevskii, E.I. Crystal structure of $MnCu_{1.5}Ge_{0.5}$ ternary compound. *Visn. Lviv. Derzh. Univ. Ser. Khim.* **1963**, *6*, 42–45.
29. Kuz'ma, Y.B.; Gladyshevskii, E.I. Crystal structure of the compound Mn_2Co_3Ge. *Dopov. Akad. Nauk Ukr. RSR* **1963**, *A25*, 205–208.
30. Gladyshevskii, E.I.; Krypyakevych, P.I.; Teslyuk, M.Y. Crystal structure of the ternary phase Cu_4MgSn. *Dokl. Akad. Nauk. SSSR* **1952**, *85*, 81–84.
31. Zaremba, V.I.; Baranyak, V.M.; Kalychak, Y.M. Crystal structure of the RNi_4In compounds. *Visn. Lviv. Derzh. Univ. Ser. Khim.* **1984**, *25*, 18–19.
32. Felner, I. Magnetic properties of $RAuNi_4$ rare earth compounds. *Solid State Commun.* **1977**, *21*, 267–268. [CrossRef]
33. Dwight, A.E. Crystal structure of $RENi_4Au$ compounds and unitcell constants in the YCo_5-YNi_5-YCu_5 series. *J. Less-Common Met.* **1975**, *43*, 117–120. [CrossRef]
34. Takeshita, T.; Malik, S.K.; Wallace, W.E. Crystal structure of RCu_4Ag and RCu_4Al (R = Rare Earth) intermetallic compounds. *J. Solid State Chem.* **1978**, *23*, 225–229. [CrossRef]
35. Kaneko, T.; Arai, S.; Abe, S.; Kamigaki, K. Magnetic properties of cubic $RAuCu_4$ (R = Gd, Tb, Dy, Ho and Er) intermetallic compounds. *J. Phys. Soc. Jpn.* **1986**, *55*, 4441–4447. [CrossRef]
36. Seidel, S.; Pöttgen, R. $Yb_6Ir_5Ga_7$—A $MgZn_2$ Superstructure. *Z. Anorg. Allg. Chem.* **2017**, *643*, 261–265. [CrossRef]
37. Eustermann, F.; Pominov, A.; Pöttgen, R. Rare Earth (*RE*) Gallides with Closely Related Compositions: *RE*IrGa and $RE_6Ir_5Ga_7$. *Z. Anorg. Allg. Chem.* **2018**, *644*, 1297–1303. [CrossRef]
38. Eustermann, F.; Stegemann, F.; Radzieowski, M.; Janka, O. Intermetallic $RE_6T_5Al_7$ Phases (*RE* = Sc, Y, Ce–Nd, Sm, Gd–Lu, T = Ru, Ir)—Diversity in their Magnetic, Magnetocaloric and Critical Properties. *Inorg. Chem.* **2019**, *58*, 16211–16226. [CrossRef]
39. Noréus, D.; Eriksson, L.; Göthe, L.; Werner, P.E. Structure determination of Mg_2SiNi_3. *J. Less-Common Met.* **1985**, *107*, 345–349. [CrossRef]
40. Seidel, S.; Janka, O.; Benndorf, C.; Mausolf, B.; Haarmann, F.; Eckert, H.; Heletta, L.; Pöttgen, R. Ternary rhombohedral Laves phases RE_2Rh_3Ga (*RE* = Y, La–Nd, Sm, Gd–Er). *Z. Naturforsch.* **2017**, *72b*, 289–303. [CrossRef]
41. Cenzual, K.; Chabot, B.; Parthé, E. Y_2Rh_3Ge, a rhombohedral substitution variant of the $MgCu_2$ type. *J. Solid State Chem.* **1987**, *70*, 229–234. [CrossRef]
42. Lipatov, A.; Gribanov, A.; Grytsiv, A.; Safronov, S.; Rogl, P.; Rousnyak, J.; Seropegin, Y.; Giester, G. The ternary system cerium–rhodium–silicon. *J. Solid State Chem.* **2010**, *183*, 829–843. [CrossRef]
43. Kaczorowski, D.; Lipatov, A.; Gribanov, A.; Seropegin, Y. Low-temperature magnetic and electrical transport properties of some ternary Ce–Rh–Si compounds. *J. Alloys Compd.* **2011**, *509*, 6518–6521. [CrossRef]
44. Vernière, A.; Lejay, P.; Bordet, P.; Chenavas, J.; Brison, J.P.; Haen, P.; Boucherle, J.X. Crystal structures and physical properties of some new ternary compounds U_2T_3X (T = Ru, Os; X = Si, Ge). *J. Alloys Compd.* **1994**, *209*, 251–255. [CrossRef]
45. Morozkin, A.V. New ternary compounds in the Sm–Rh–Ge system. *J. Alloys Compd.* **2004**, *385*, L1–L2. [CrossRef]
46. Doverbratt, I.; Ponou, S.; Lidin, S. Ca_2Pd_3Ge, a new fully ordered ternary Laves phase structure. *J. Solid State Chem.* **2013**, *197*, 312–316. [CrossRef]
47. Gießelmann, E.; Pöttgen, R.; Janka, O. Laves phases: Superstructures induced by coloring and distortions. *Z. Anorg. Allg. Chem.* **2023**, e202300109. [CrossRef]
48. Janka, O. *Metallic Light-Weight Alloys: Al, Ti, Mg*; Pöttgen, R., Jüstel, T., Strassert, C., Eds.; De Gruyter: Berlin, Germany; Boston, MA, USA, 2022.
49. Massalski, T.B.; Okamoto, H.; Subramanian, P.R.; Kacprzak, L. *Binary Alloy Phase Diagrams*, 2nd ed.; ASM International: Materials Park, OH, USA, 1990.
50. Okamoto, H. Al-Ti (aluminum-titanium). *J. Phase Equilibria* **1993**, *14*, 120–121. [CrossRef]
51. Raghavan, V. Al-Ti-V (Aluminum-Titanium-Vanadium). *J. Phase Equilibria Diffus.* **2005**, *26*, 276–279. [CrossRef]
52. Batalu, D.; Coşmeleaţă, G.; Aloman, A. Critical analysis of the Ti-Al phase diagrams. *U.P.B. Sci. Bull. Ser. B* **2006**, *68*, 77–90.
53. Schuster, J.C.; Palm, M. Reassessment of the binary Aluminum-Titanium phase diagram. *J. Phase Equilibria Diffus.* **2006**, *27*, 255–277. [CrossRef]
54. Peters, M.; Hemptenmacher, J.; Kumpfert, J.; Leyens, C. *Structure and Properties of Titanium and Titanium Alloys in Titanium and Titanium Alloys: Fundamentals and Applications*; Wiley-VCH Verlag GmbH: Weinheim, Germany, 2003.
55. Sauthoff, G. *Intermetallics in Ullmann's Encyclopedia of Industrial Chemistry*; Wiley-VCH Verlag GmbH: Weinheim, Germany, 2012.
56. Pöttgen, R.; Gulden, T.; Simon, A. Miniaturisierte Lichtbogenapperatur für den Laborbedarf. *GIT Labor-Fachz.* **1999**, *43*, 133–136.
57. Palatinus, L.; Chapuis, G. SUPERFLIP—A computer program for the solution of crystal structures by charge flipping in arbitrary dimensions. *J. Appl. Crystallogr.* **2007**, *40*, 786–790. [CrossRef]
58. Petříček, V.; Dušek, M.; Palatinus, L. (Eds.) *The Crystallographic Computing System*; JANA 2006; Institute of Physics of the Czech Academy of Sciences: Praha, Czech Republic, 2006.

59. Petříček, V.; Dušek, M.; Palatinus, L. Crystallographic Computing System JANA2006: General features. *Z. Kristallogr.* **2014**, *229*, 345–352. [CrossRef]
60. Emsley, J. *The Elements*; Clarendon Press: Oxford, UK; Oxford University Press: New York, NY, USA, 1998.
61. Becker, P.J.; Coppens, P. Extinction within the limit of validity of the Darwin transfer equations. I. General formalism for primary and secondary extinction and their applications to spherical crystals. *Acta Crystallogr.* **1974**, *A30*, 129–147. [CrossRef]
62. Duwez, P.E.; Taylor, J.L. Crystal Structure of TiAl. *Trans. Am. Inst. Min. Metall. Pet. Eng.* **1952**, *194*, 70–71. [CrossRef]
63. Ence, E.; Margolin, H. Compounds in the Titanium-Rich Region of the Ti-Al System. *Trans. Am. Inst. Min. Metall. Pet. Eng.* **1957**, *209*, 484–485. [CrossRef]
64. Niemann, S.; Jeitschko, W. Ternary aluminides $A_6T_4Al_{43}$ with A = Y, Nd, Sm, Gd-Lu, Th, U and T = Cr, Mo, W. *Z. Metallkd.* **1994**, *85*, 345–349.
65. Frank, F.C.; Kasper, J.S. Complex alloy structures regarded as sphere packings. II. Analysis and classification of representative structures. *Acta Crystallogr.* **1959**, *12*, 483–499. [CrossRef]
66. Frank, F.C.; Kasper, J.S. Complex alloy structures regarded as sphere packings. I. Definitions and basic principles. *Acta Crystallogr.* **1958**, *11*, 184–190. [CrossRef]
67. Compton, V.B.; Matthias, B.T. Laves phase compounds of rare earths and hafnium with noble metals. *Acta Crystallogr.* **1959**, *12*, 651–654. [CrossRef]
68. Gießelmann, E.C.J.; Engel, S.; Kostusiak, W.; Zhang, Y.; Herbeck-Engel, P.; Kickelbick, G.; Janka, O. Raman and NMR spectroscopic and theoretical investigations of the cubic Laves-phases $REAl_2$ (RE = Sc, Y, La, Yb, Lu). *Dalton Trans.* **2023**, *52*, 3391–3402. [CrossRef] [PubMed]
69. Zhou, G.F.; Bakker, H. Mechanically induced structural and magnetic changes in the $GdAl_2$ Laves phase. *Phys. Rev. B* **1995**, *52*, 9437–9445. [CrossRef] [PubMed]
70. Janka, O.; Hoffmann, R.D.; Heying, B.; Pöttgen, R. Structural phase transitions in $YPtGe_2$ and $GdPtGe_2$. *Dalton Trans.* **2018**, *47*, 6075–6088. [CrossRef] [PubMed]
71. Eustermann, F.; Eilers-Rethwisch, M.; Renner, K.; Hoffmann, R.-D.; Pöttgen, R.; Janka, O. Magnetic properties of the germanides $RE_3Pt_4Ge_6$ (RE = Y, Pr, Nd, Sm, Gd–Dy). *Z. Naturforsch.* **2017**, *72b*, 855–864. [CrossRef]
72. Staliński, B.; Pokrzywnicki, S. Magnetic Properties of Gadolinium-Aluminium Intermetallic Compounds. *Phys. Status Solidi B* **1966**, *14*, K157–K160. [CrossRef]
73. Eustermann, F.; Stegemann, F.; Renner, K.; Janka, O. Platinum Triangles in the Pt/Al Framework of the Intermetallic $REPt_6Al_3$ (RE = Ce-Nd, Sm, Gd, Tb) Series. *Z. Anorg. Allg. Chem.* **2017**, *643*, 1836–1843. [CrossRef]

5.1.3 Searching for Laves Phase Superstructures: Structural and ^{27}Al NMR Spectroscopic Investigations in the Hf−V−Al System

Published as an article:

Elias C. J. Gießelmann, Stefan Engel, Jasper Baldauf, Jutta Kösters, Samir F. Matar, Guido Kickelbick and Oliver Janka, *Inorg. Chem.* **2024**, *63*, 8180.

https://doi.org/10.1021/acs.inorgchem.4c00391

Contributions of the authors to this manuscript

Elias C. J. Gießelmann conducted the synthetic work, the evaluation of the PXRD measurements, measured the solid state NMR spectra and provided an initial draft of the manuscript. PD Dr. Oliver Janka and Dipl.-Ing. Jutta Kösters helped with the measurement and evaluation of the SCXRD data. Dr. Stefan Engel collected the SEM/EDX data, Jasper Baldauf did the magnetic characterization as well as the heat capacity measurement. Prof. Dr. Samir Matar did the quantum chemical calculations. Prof. Dr. Guido Kickelbick and PD Dr. Oliver Janka supervised the work and finalized the manuscript.

Summary

Inspired by the literature studies about Laves phases described in sections 2.1.1 and 5.7.2, our attention was drawn to the ternary system Hf–V–Al, especially the solid solution $Hf(V_{1-x}Al_x)_2$. The Pearson's Crystal Data database [24] does not list any entry for the ternary system, while the binary phase diagram Hf–Al shows many different combinations of the two elements. The Hf–V system only shows the phase HfV_2, adopting cubic $MgCu_2$ structure. Upon cooling, this compound undergoes two phase transitions to tetragonal YMn_2 ($I4_1/amd$) and finally to the orthorhombic UMn_2 (*Imma*) which becomes a superconductor at around 9 K.[44, 238]

The full solid solution $Hf(V_{1-x}Al_x)_2$ for $0 \leq x \leq 1$ was synthesized and for many compositions the x was chosen according to the known ternary ordering variants of Laves phases discussed in the introduction. Despite these, also other values for x were selected. Analysis showed a small two-phase region for low values of x. Pure cubic samples were only obtained for $x \leq 0.05$. Although no formation of ternary ordered compounds were observed in the PXRD analysis, selected samples were investigated by solid state ^{27}Al NMR spectroscopy. This is necessary

because, for example, the formation of the coloring variant of $MgZn_2$ namely Mg_2Cu_3Si, can be difficult to detect by diffraction methods due to the small difference in the atomic form factors of V and Al. Solid state NMR as local probe would clearly indicate whether structural ordering was present in the sample. While in all other spectra only a very broad signal was observed, the samples with the nominal composition $Hf(V_{0.125}Al_{0.875})_2$ (Hf_4VAl_7) showed a sharp signal qualifying this compound for a more detailed analysis using SCXRD. The single-crystal data proved the formation of a superstructure with reduced symmetry with all reflections of the reduced symmetry being invisible in the PXRD data. The newly discovered ordering variant shows a small homogeneity range before the samples crystallize again as a solid solution in the $MgZn_2$ structure type.

Selected samples of the hexagonal solid solution showed Pauli-paramagnetic behavior. HfV_2 showed superconductivity at the critical temperature T_C reported in literature. Small substitution by Al, keeping the cubic $MgCu_2$ structure, showed a significant lowering of the critical temperature by 1.3 K.

Inorganic Chemistry

pubs.acs.org/IC Article

Searching for Laves Phase Superstructures: Structural and ^{27}Al NMR Spectroscopic Investigations in the Hf−V−Al System

Elias C. J. Gießelmann, Stefan Engel, Jasper Baldauf, Jutta Kösters, Samir F. Matar, Guido Kickelbick, and Oliver Janka*

Cite This: *Inorg. Chem.* 2024, 63, 8180−8193 Read Online

ACCESS | Metrics & More | Article Recommendations | Supporting Information

ABSTRACT: Laves phases exhibit a plethora of different structures and a multitude of physical properties. Investigations in the ternary system Hf−V−Al led to the discovery of numerous members of the solid solution $Hf(V_{1-x}Al_x)_2$, which adopt the hexagonal $MgZn_2$ type (C14) for medium to high amounts of Al (x = 0.2−1) and the cubic $MgCu_2$ type (C15) for small Al amounts (x = 0.05−0.1). While all members exhibit Pauli-paramagnetic behavior due to the absence of localized magnetic moments, the V-rich cubic member $Hf(V_{0.95}Al_{0.05})_2$ additionally exhibits a superconducting state below T_C = 7.6(1) K. All synthesized compounds were characterized by powder X-ray diffraction, and selected samples were furthermore investigated by ^{27}Al solid-state magic-angle spinning (MAS) NMR. $HfAl_2$ exhibits two Al resonances, one rather sharp and one significantly broadened signal, in line with the crystal structure and respective coordination environments. The members of the solid solution exhibit extremely broadened resonances due to the mixing of V and Al on the same crystallographic sites. For nominal $Hf(V_{0.125}Al_{0.875})_2$, however, two distinct sharp NMR signals were observed. This contrasts with the description of a solid solution. Therefore, single-crystal X-ray studies were conducted, showing that $Hf(V_{0.125}Al_{0.875})_2$ really is an ordered compound with the sum formula Hf_4VAl_7 ($P\bar{3}m1$), which exhibits an, thus far, unknown superstructure of $MgZn_2$.

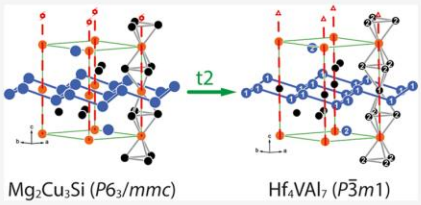

INTRODUCTION

Laves phases, named after the German mineralogist Fritz H. Laves,[1−3] are an important class of compounds, from both structural and property point of view. In the case of the original binary Laves phases, they all have the general composition AB_2, and three prototypes are known: the two hexagonal variants $MgZn_2$ (C14)[4,5] and $MgNi_2$ (C36)[6,7] (both space group type $P6_3/mmc$)[8] and the cubic $MgCu_2$ (C15, $Fd\bar{3}m$) type.[9] On the occasion of Laves' 100th birthday, a special issue was published (Z. Kristallogr. **2006**, 221, issues 5−7) including eulogies on Laves work[1,2,10] and summarizing different aspects of the work on Laves phases.[11−15]

Recently, we reported on the ^{27}Al NMR spectroscopic properties of the cubic MAl_2 phases[16,17] as well as on a new series of rare-earth-based Laves phases with the composition RE_2TiAl_3 (RE = Y, Gd−Tm, Lu).[18] The striking feature of the latter is that these compounds are the first aluminum-based representatives that adopt the rhombohedral Mg_2Ni_3Si type structure ($R\bar{3}m$), which can be derived from the cubic Laves phase. In contrast, the ternary rare-earth aluminum Laves phases of the late transition metals RE_2TAl_3 (RE = Sc, Y, La−Nd, Sm, Gd−Lu; T = Ru, Rh, Ir) adopt the Mg_2Cu_3Si type structure ($P6_3/mmc$), which is a coloring variant of the $MgZn_2$ type.[19] Finally, also some aluminum representatives of the $Yb_6Ir_5Ga_7$ type structure[20] ($P6_3/mcm$, superstructure of $MgZn_2$) could be synthesized and characterized by our group.[21]

Based on these and other recent results, we summarized the structural and crystal chemistry of Laves phases[22] and the Mo_3Al_2C type compounds[23] with a special focus on superstructure formation and discussed the crystal-chemical peculiarities based on group−subgroup relations. During the search in the Pearson database,[24] it became clear that the majority of the binary MAl_2 phases adopts the cubic $MgCu_2$ type structure (M = Ca−Ba, Sc, Y, La−Nd, Sm−Lu, Th, U−Pu),[17,25−34] while the hexagonal $MgZn_2$ type is only realized for $ZrAl_2$ and $HfAl_2$.[35,36] Interestingly, on examination of the respective ternary systems, no compounds have been reported in the Hf−V−Al system. Therefore, this system was selected for Laves phase investigations. Further interest was sparked as HfV_2 adopts the $MgCu_2$ type structure; therefore, the existence ranges of the two prototypes in the solid solution $Hf(V_{1-x}Al_x)_2$ can be investigated, and the formation of potential superstructures can be probed. Potential candidates are Mg_2Cu_3Si ($P6_3/mmc$),[37] a coloring variant of $MgZn_2$; orthorhombic Mg_2MnGa_3 ($Cmcm$),[38] a superstructure of $MgZn_2$/a coloring variant of URe_2; Mg_2Ni_3Si ($R\bar{3}m$)[39] and Na_2Au_3Al ($P4_132$),[40] both

Received: January 29, 2024
Revised: March 12, 2024
Accepted: March 14, 2024
Published: April 23, 2024

https://doi.org/10.1021/acs.inorgchem.4c00391
Inorg. Chem. 2024, 63, 8180−8193

Table 1. Lattice Parameters, Refined from Powder X-ray Diffraction, of the Solid Solution $Hf(V_{1-x}Al_x)_2$ for $x = 0-1$ and $Hf_4V_{1+y}Al_{7-y}$ for $y = 0$ and 0.13 As Well As Literature Values[a]

nominal	x_{theo}/y_{theo}	x_{ref}/y_{ref}	pot. superstructure	observed prototype	a (pm) composition	c (pm)	V (nm^3)
$HfAl_2$[36]	1	1		$MgZn_2$	528.8	873.9	0.2116
$HfAl_2$[b]	1	1		$MgZn_2$	524.1	867.4	0.2063
$Hf(V_{0.05}Al_{0.95})_2$[b]	0.95	0.98(2)		$MgZn_2$	525.2	865.0	0.2066
$Hf(V_{0.083}Al_{0.917})_2$[b]	0.917	0.90(2)		$MgZn_2$	526.3	862.1	0.2068
Hf_4VAl_7[b]	0	0[c]	Cd_4Cu_7As ($Pnnm$)[41]	Hf_4VAl_7	527.5	859.6	0.2071
$Hf(V_{0.167}Al_{0.833})_2$[b]	0.833	0.93(2)		$MgZn_2$	527.6	861.7	0.2078
$Hf_4V_{1.13}Al_{6.87}$	0.13	0.13[c]		Hf_4VAl_7	527.6	861.7	0.2078
$Hf(V_{0.25}Al_{0.75})_2$[b]	0.75	0.70(2)	Mg_2Cu_3Si ($P6_3/mcm$)[37] Mg_2MnGa_3 ($Cmcm$)[38] Mg_2Ni_3Si ($R\bar{3}m$)[39] Na_2Au_3Al ($P4_132$)[40]	$MgZn_2$	528.0	859.0	0.2074
$Hf(V_{0.33}Al_{0.67})_2$[b]	0.67	0.65(2)		$MgZn_2$	527.7	860.3	0.2074
$Hf(V_{0.417}Al_{0.583})_2$[b]	0.583	0.65(2)	$Yb_6Ir_5Ga_7$ ($P6_3/mcm$)[20]	$MgZn_2$	527.2	860.6	0.2072
$Hf(V_{0.5}Al_{0.5})_2$[b]	0.5	0.55(2)		$MgZn_2$	526.8	860.3	0.2067
$Hf(V_{0583}Al_{0.417})_2$[b]	0.417	0.50(2)	$Yb_6Ir_5Ga_7$ ($P6_3/mcm$)[20]	$MgZn_2$	526.0	859.4	0.2059
$Hf(V_{0.67}Al_{0.33})_2$[b]	0.33	0.41(2)		$MgZn_2$	525.5	858.4	0.2053
$Hf(V_{0.75}Al_{0.25})_2$[b]	0.25	0.27(2)	Mg_2Cu_3Si ($P6_3/mcm$)[37] Mg_2MnGa_3 ($Cmcm$)[38] Mg_2Ni_3Si ($R\bar{3}m$)[39] Na_2Au_3Al ($P4_132$)[40]	$MgZn_2$	524.7	856.5	0.2043
$Hf(V_{0.8}Al_{0.2})_2$[b]	0.2	0.24(2)		$MgZn_2$	524.5	855.4	0.2038
$Hf(V_{0.875}Al_{0.125})_2$[b]	0.125	0.20(2)	Cd_4Cu_7As ($Pnnm$)[41]	$MgZn_2$	524.3	852.6	0.2030
		0.02(2)		$MgCu_2$	741.6	a	0.4078
$Hf(V_{0.9}Al_{0.1})_2$[b]	0.1	0.17(2)		$MgZn_2$	523.9	851.3	0.2024
		0.02(2)		$MgCu_2$	740.2	a	0.4055
$Hf(V_{0.95}Al_{0.05})_2$[b]	0.05	0.10(2)		$MgCu_2$	740.7	a	0.4064
HfV_2[b]	0	0		$MgCu_2$	738.8	a	0.4032
HfV_2[50]	0	0		$MgCu_2$	741.2	a	0.4072

[a]The standard deviations for the lattice parameters are ±0.1 pm or smaller. [b]This work. [c]Value fixed to single-crystal data.

Table 2. Atom Positions and Site Occupancy Factors for Solid Solution $Hf(V_{1-x}Al_x)_2$ for $x = 0-1$[a]

compound	structure type	z (Hf)	x (M1)	M1: occ (Al)/occ (V)	M2: occ (Al)/occ (V)
$HfAl_2$[b]	$MgZn_2$	0.56447(8)	0.1710(4)	1/0	1/0
$Hf(V_{0.05}Al_{0.95})_2$[b]	$MgZn_2$	0.56236(6)	0.1744(2)	1/0[c]	0.90(1)/0.10(1)
$Hf(V_{0.083}Al_{0.917})_2$[b]	$MgZn_2$	0.56013(9)	0.1698(5)	0.93(1)/0.07(1)	0.47(1)/0.53(1)
$Hf(V_{0.25}Al_{0.75})_2$[b]	$MgZn_2$	0.56438(5)	0.1698(2)	0.63(1)/0.37(1)	0.91(1)/0.09(1)
$Hf(V_{0.33}Al_{0.67})_2$[b]	$MgZn_2$	0.56411(6)	0.1730(2)	0.7(1)/0.3(1)	0.85(1)/0.15(1)
$Hf(V_{0.417}Al_{0.583})_2$[b]	$MgZn_2$	0.56433(5)	0.1704(1)	0.56(1)/0.44(1)	0.93(1)/0.07(1)
$Hf(V_{0.5}Al_{0.5})_2$[b]	$MgZn_2$	0.56370(6)	0.1714(2)	0.46(1)/0.54(1)	0.81(1)/0.19(1)
$Hf(V_{0583}Al_{0.417})_2$[b]	$MgZn_2$	0.56381(5)	0.1702(2)	0.40(1)/0.60(1)	0.79(1)/0.21(1)
$Hf(V_{0.67}Al_{0.33})_2$[b]	$MgZn_2$	0.56332(4)	0.1698(1)	0.31(1)/0.69(1)	0.72(1)/0.28(1)
$Hf(V_{0.75}Al_{0.25})_2$[b]	$MgZn_2$	0.56308(4)	0.1716(1)	0.18(1)/0.82(1)	0.53(1)/0.47(1)
$Hf(V_{0.8}Al_{0.2})_2$[b]	$MgZn_2$	0.56361(8)	0.1711(2)	0.12(1)/0.88(1)	0.59(1)/0.41(1)
$Hf(V_{0.875}Al_{0.125})_2$[b]	$MgZn_2$	0.56243(10)	0.1707(3)	0.18(1)/0.82(1)	0.25(1)/0.75(1)
	$MgCu_2$	3/8	0	0.02(1)/0.98(1)	
$Hf(V_{0.9}Al_{0.1})_2$[b]	$MgZn_2$	0.5628(2)	0.1703(4)	0.22(1)/0.78(1)	0.03(1)/0.97(1)
	$MgCu_2$	3/8	0	0.02(1)/0.98(1)	
$Hf(V_{0.95}Al_{0.05})_2$[b]	$MgCu_2$	3/8	0	0.1(1)/0.9(1)	
HfV_2[b]	$MgCu_2$	3/8	0	0/1[c]	

[a]For the $MgZn_2$ type compounds: Hf on 4f (1/3, 2/3, z); M1 on 6h (x, 2x, 1/4); and M2 on 2a (0, 0, 0). For the $MgCu_2$ type compounds: Hf on 8b (3/8, 3/8, 3/8) and M1 on 16c (0, 0, 0). [b]This work. [c]Occupation at 1 during free refinement and fixed during subsequent refinement.

superstructure variants of $MgCu_2$; $Yb_6Ir_5Ga_7$ ($P6_3/mcm$),[20] a $\sqrt{2}a \times \sqrt{2}a$ superstructure of $MgZn_2$; as well as Cd_4Cu_7As ($Pnnm$),[41] an orthorhombic superstructure of $MgCu_2$. Finally, the synthesized systems can be investigated by ^{27}Al NMR spectroscopy, which was shown to be a valid technique for structure validation,[40,42,43] as well as magnetic susceptibility measurements, which is, at least, interesting for the $MgCu_2$ type compounds, since HfV_2 exhibits superconductivity below T_C = 9.57 K.[44]

https://doi.org/10.1021/acs.inorgchem.4c00391
Inorg. Chem. 2024, 63, 8180−8193

Table 3. Atom Positions and Site Occupancy Factors for Nominal Hf_4VAl_7 and $Hf_4V_{1.34}Al_{6.66}$[a]

compound	structure type	z(Hf1)	z(Hf2)	x(Al2)	z(Al2)
Hf_4VAl_7	Hf_4VAl_7	0.55728(6)	0.05998(8)	0.1694(3)	0.2405(4)
$Hf_4V_{1.34}Al_{6.66}$	Hf_4VAl_7	0.56333(7)	0.05778(7)	0.1671(4)	0.2466(5)

[a]The atom positions are Hf1 on 2*d* (1/3, 2/3, *z*); Hf2 on 2*d* (2/3, 1/3, *z*); V on 1*a* (0, 0, 0); Al1 on 1*b* (0, 0, 1/2); and Al2 on 6*i* (*x*, 2*x*, *z*).

Table 4. Crystallographic Data and Structure Refinement for Nominal $Hf(V_{0.083}Al_{0.917})_2$ and $Hf(V_{0.417}Al_{0.583})_2$ (Both $P6_3/mmc$, $Z = 4$, $MgZn_2$ Type) and Hf_4VAl_7 and $Hf_4V_{1.13}Al_{6.87}$ (Both $P\bar{3}m1$, $Z = 1$, Own Type)[a]

CSD number		2325587	2325589	2325590	2325588
nominal composition		$Hf(V_{0.083}Al_{0.917})_2$	$Hf(V_{0.125}Al_{0.875})_2$	$Hf(V_{0.167}Al_{0.833})_2$	$Hf(V_{0.417}Al_{0.583})_2$
refined composition		$Hf(V_{0.08(1)}Al_{0.92(1)})_2$	Hf_4VAl_7	$Hf_4V_{1.13(1)}Al_{6.87(1)}$	$Hf(V_{0.42(1)}Al_{0.58(1)})_2$
structure type		$MgZn_2$	Hf_4VAl_7	Hf_4VAl_7	$MgZn_2$
lattice parameters	*a* (pm)	524.91(1)	527.07(6)	526.42(2)	526.66(2)
	c (pm)	860.90(3)	857.73(12)	857.08(3)	859.85(4)
	V (nm^3)	0.2054	0.2064	0.2057	0.2065
molar mass, g mol^{-1}		236.5	953.8	957.0	252.6
density calcd, g cm^{-3}		7.65	7.68	7.73	8.12
crystal size, μm		65 × 50 × 35	55 × 35 × 30	50 × 55 × 40	45 × 40 × 30
detector distance, mm		40	40	40	40
exposure time, s		20	20	20	20
range in *hkl*		$-8 \le h \le +7$	$-7 \le h \le +7$	$-6 \le h \le +7$	$-9 \le h \le +9$
		$-7 \le k \le +8$	$-7 \le k \le +7$	$-7 \le k \le +7$	$-9 \le k \le +9$
		$-13 \le l \le +13$	$-12 \le l \le +12$	$-12 \le l \le +12$	$-14 \le l \le +14$
θ_{min}, θ_{max}, deg		4.48, 33.18	4.47, 30.28	2.38, 30.31	4.47, 38.61
linear absorption coeff., mm^{-1}		51.8	51.9	52.2	54.1
no. of reflections		3776	8996	6060	5238
R_{int}/R_σ		0.0306/0.0108	0.0389/0.0107	0.0335/0.0102	0.0482/0.0204
no. of independent reflections		177	278	279	258
reflections used [$I \ge 3\sigma(I)$]		165	250	269	217
F(000), e		399	402	403	426
*R*1/w*R*2 for $I \ge 3\sigma(I)$		0.0138/0.0492	0.0114/0.0249	0.0121/0.0325	0.0168/0.0365
*R*1/w*R*2 for all data		0.0167/0.0503	0.0093/0.0240	0.0127/0.0330	0.0216/0.0379
data/parameters		177/12	278/19	279/20	258/13
goodness-of-fit on F^2		1.87	0.90	1.24	1.09
extinction coefficient		64(17)	47(7)	182(13)	64(10)
twin fraction			0.434(3)	0.467(3)	
diff. Fourier residues (e^- $Å^{-3}$)		+3.03/−2.77	+0.84/−1.22	+2.01/−2.87	+2.01/−1.67

[a]Twinning for the Hf_4VAl_7 type structures was according to ($\bar{1}$ 0 0, 0 $\bar{1}$ 0, 0 0 1).

EXPERIMENTAL SECTION

Synthesis. Starting materials for the synthesis of the end members $HfAl_2$ and HfV_2 as well as the solid solution $Hf(V_{1-x}Al_x)_2$ were pieces of hafnium, vanadium, and aluminum, all purchased from Onyxmet (Olsztyn, Poland) with stated purities higher than 99.9%. For the synthesis of $HfAl_2$ and HfV_2 as well as the solid solution $Hf(V_{1-x}Al_x)_2$ with x = 0.95, 0.917, 0.875, 0.833, 0.75, 0.667, 0.583, 0.5, 0.417, 0.333, 0.25, 0.2, 0.125, 0.1, and 0.05, stoichiometric amounts of the elements were used. In all cases, the starting materials were arc-melted[45] in a custom-build arc-melting apparatus in a water-cooled copper hearth under 800 mbar argon pressure. The argon gas was purified with titanium sponge (873 K), molecular sieves, and silica gel. The obtained buttons were remelted several times to ensure phase pure samples with high homogeneity. The as-cast buttons were sealed in fused silica ampules and annealed in muffle furnaces. Corundum crucibles were used for some samples. They were heated to 1123 K within 6 h and then kept at this temperature for 12 days, followed by cooling to 623 K with a rate of 5 K min^{-1}. Subsequently, the oven was switched off and the mixture cooled to room temperature. Alternatively, the as-cast beads were placed in the water-cooled sample chamber of a high-frequency furnace (Typ TIG 5/300, Hüttinger Elektronik, Freiburg, Germany),[46] heated to approximately 1173 K, and kept at this temperature for 2 h before cooling to room temperature. The annealing led to X-ray pure samples; the specimens are stable in air over months and show metallic luster; ground samples are gray.

Powder X-ray Diffraction. The pulverized samples of $HfAl_2$, HfV_2, as well as all members of the solid solution $Hf(Al_{1-x}V_x)_2$ were investigated by powder X-ray diffraction experiments at room temperature either on a D8-A25-Advance diffractometer (Bruker, Karlsruhe, Germany) in Bragg−Brentano θ–θ-geometry (goniometer radius 280 mm) with Cu $K\alpha$-radiation (λ = 154.0596 pm) or on a X'Pert MPD diffractometer (PANalytical, Almelo, Netherlands) in Bragg−Brentano θ–θ-geometry (goniometer radius 240 mm) with Cu $K\alpha$-radiation (λ = 154.0596 pm). On both instruments, diffraction patterns were recorded between 6 and 130° 2θ with a step size of 0.013° and a total scan time of 1 h. A 12 μm Ni foil working as a $K\beta$ filter and a variable divergence slit were mounted at the primary beam side. On the Bruker instrument, a LYNXEYE detector with 192 channels was used at the secondary beam side, and on the PANalytical instrument, a PIXcel1D detector was used at the secondary beam side. The recorded data was evaluated using the Bruker TOPAS 5.0 software[47] applying the fundamental parameter approach and the Rietveld method.[48,49] Details of the refinements are given in Tables 1−3. All recorded powder X-ray patterns are shown in the Supporting Information (SI) in Figures S1−S19.

Single-Crystal X-ray Diffraction. From the annealed crushed samples, single crystals of nominal $Hf(V_{0.083}Al_{0.917})_2$, $Hf(V_{0.125}Al_{0.875})_2$, $Hf(V_{0.167}Al_{0.833})_2$, and $Hf(V_{0.417}Al_{0.583})_2$ were isolated and investigated

https://doi.org/10.1021/acs.inorgchem.4c00391
Inorg. Chem. 2024, 63, 8180−8193

Table 5. Atom Positions and Equivalent Isotropic Displacement Parameters (pm^2) for $Hf(V_{0.083}Al_{0.917})_2$, $Hf(V_{0.417}Al_{0.583})_2$, Hf_4VAl_7, and $Hf_4V_{1.13}Al_{6.87}$[a]

atom	Wyckoff position	x	y	z	U_{eq}	occupation
			nominal $Hf(V_{0.083}Al_{0.917})_2$			
Hf	4*f*	1/3	2/3	0.56043(3)	49(2)	1
Al/V1	2*a*	0	0	0	46(9)	0.67(1) Al/0.33(1) V
Al2	6*h*	0.1710(3)	2*x*	1/4	65(8)	1
			nominal Hf_4VAl_7			
Hf	2*d*	1/3	2/3	0.55311(5)	47(1)	1
Hf	2*d*	2/3	1/3	0.06235(5)	45(1)	1
V	1*a*	0	0	0	45(7)	1
Al1	1*b*	0	0	1/2	57(14)	1
Al2	6*i*	0.1697(2)	2*x*	0.2448(2)	56(4)	1
			nominal $Hf_4V_{1.13}Al_{6.87}$			
Hf	2*d*	1/3	2/3	0.55355(6)	109(2)	1
Hf	2*d*	2/3	1/3	0.06238(5)	107(1)	1
V	1*a*	0	0	0	110(7)	1
Al1	1*b*	0	0	1/2	101(14)	1
Al/V2	6*i*	0.1698(2)	2*x*	0.2452(2)	115(5)	0.98(1) Al/0.02(1) V
			nominal $Hf(V_{0.417}Al_{0.583})_2$			
Hf	4*f*	1/3	2/3	0.56410(3)	66(1)	1
Al/V1	2*a*	0	0	0	87(4)	0.82(1) Al/0.18(1) V
Al/V2	6*h*	0.17122(3)	2*x*	1/4	84(7)	0.50(1) Al/0.50(1) V

[a]U_{eq} is defined as one third of the trace of the orthogonalized U_{ij} tensor.

Table 6. Interatomic Distances (pm) for $Hf(V_{0.083}Al_{0.917})_2$, $Hf(V_{0.417}Al_{0.583})_2$, Hf_4VAl_7, and $Hf_4V_{1.13}Al_{6.87}$[a]

$Hf(V_{0.083}Al_{0.917})_2$				Hf_4VAl_7				$Hf_4V_{1.13}Al_{6.87}$				$Hf(V_{0.417}Al_{0.583})_2$			
Hf	3	Al/V1	307.5	Hf1	3	Al2	303.7	Hf1	3	Al/V2	303.4	Hf	9	Al/V1	307.9
	9	Al2	309.1		3	Al1	307.7		3	Al1	307.4		3	Al/V2	309.0
	3	Hf	320.4		6	Al2	315.5		6	Al/V2	314.7		1	Hf	319.7
	1	Hf	326.4		3	Hf1	317.6		3	Hf1	317.5		3	Hf	323.4
Al/V1	6	Al2	265.5		1	Hf2	329.8		1	Hf2	329.2	Al/V1	6	Al/V2	265.7
	6	Hf	307.5	Hf2	3	Al2	302.8	Hf2	3	Al/V2	302.9		6	Hf	309.0
Al2	2	Al2	255.6		6	Al2	306.5		6	Al/V2	306.3	Al/V2	2	Al/V2	256.2
	2	Al/V1	265.5		3	V	309.0		3	V	308.6		2	Al/V1	265.7
	2	Al2	269.3		3	Hf2	322.6		3	Hf2	322.2		2	Al/V2	270.5
	2	Hf	305.3		1	Hf1	329.8		1	Hf1	329.2		2	Hf	307.9
	4	Hf	309.1	V	6	Al2	261.0	V	6	Al/V2	261.0		4	Hf	308.1
					6	Hf2	309.0		6	Hf2	308.6				
				Al1	6	Al2	268.2	Al1	6	Al/V2	267.7				
					6	Hf1	307.7		6	Hf1	307.4				
				Al2	2	Al2	258.5	Al/V2	2	Al/V2	258.2				
					1	V	261.0		1	V	261.0				
					1	Al1	268.2		1	Al1	267.7				
					2	Al2	268.6		2	Al/V2	268.2				
					1	Hf2	302.8		1	Hf2	302.9				
					1	Hf1	303.7		1	Hf1	303.4				
					2	Hf2	306.5		2	Hf2	306.3				
					2	Hf1	315.5		2	Hf1	314.7				

[a]All distances of the first coordination spheres are listed. All standard uncertainties were less than 0.2 pm.

at room temperature on a Bruker X8 APEX2, Nonius κ-CCD diffractometer, operating with graphite monochromated Mo Kα (λ = 0.71073 Å) radiation. Multiscan absorption corrections using the Bruker SadABS data package[51] were applied to the data set. The data was solved and refined using Superflip[52] and Jana2006[53,54] (*vide infra*). Details on the structure refinement, atomic coordinates, and interatomic distances are compiled in Tables 4−6. Structural drawings were generated with Diamond 4[55] and edited with Adobe Illustrator CS6.

Scanning Electron Microscopy/Energy-Dispersive X-ray Spectroscopy (SEM/EDX) Data. Semiquantitative EDX analyses of the bulk samples were conducted on a JEOL 7000F (JEOL, Freising, Germany) scanning electron microscope equipped with an EDAX Genesis 2000 EDX detector (EDAX, Unterschleissheim, Germany). The samples were sprinkled on conductive carbon tape, and one area scan as well as three independent data points were measured. The results of the SEM/EDX investigations are listed in Table 7.

^{27}Al Solid-State NMR. The ^{27}Al MAS NMR spectra were recorded at 104.31 MHz on an Avance III 400 WB spectrometer (Bruker, Billerica; 9.4 T) using magic-angle spinning (MAS) conditions. The samples were ground to a fine powder and mixed with an appropriate amount of NaCl (sample/NaCl = 1:9) to reduce the density and the

https://doi.org/10.1021/acs.inorgchem.4c00391
Inorg. Chem. 2024, 63, 8180−8193

Table 7. Chemical Composition Determined by SEM/EDX[a]

composition	x_{theo}	Hf (atom %)	V (atom %) theoretical	Al (atom %)	Hf (atom %)	V (atom %) experimental	Al (atom %)
$HfAl_2$	1	33.3	0	66.7	33		67
$Hf(V_{0.05}Al_{0.95})_2$	0.95	33.3	3.3	63.4	34	3	63
$Hf(V_{0.083}Al_{0.917})_2$	0.917	33.3	5.5	61.2	33	6	61
$Hf(V_{0.125}Al_{0.875})_2$	0.875	33.3	8.3	58.4	34	7	59
$Hf(V_{0.167}Al_{0.833})_2$	0.833	33.3	11.1	55.6	36	11	53
$Hf(V_{0.25}Al_{0.75})_2$	0.75	33.3	16.7	50.0	35	15	50
$Hf(V_{0.33}Al_{0.67})_2$	0.67	33.3	22.2	44.5	35	21	44
$Hf(V_{0.417}Al_{0.583})_2$	0.583	33.3	27.8	38.9	36	26	38
$Hf(V_{0.5}Al_{0.5})_2$	0.5	33.3	33.4	33.4	36	30	34
$Hf(V_{0583}Al_{0.417})_2$	0.417	33.3	38.9	27.8	34	35	31
$Hf(V_{0.67}Al_{0.33})_2$	0.33	33.3	44.5	22.2	36	42	22
$Hf(V_{0.75}Al_{0.25})_2$	0.25	33.3	50.0	16.7	36	47	18
$Hf(V_{0.8}Al_{0.2})_2$	0.2	33.3	60.0	6.7	34	49	17
$Hf(V_{0.875}Al_{0.125})_2$	0.125	33.3	58.4	8.3	35	54	11
$Hf(V_{0.9}Al_{0.1})_2$	0.1	33.3	60.0	6.7	36	55	9
$Hf(V_{0.95}Al_{0.05})_2$	0.05	33.3	63.4	3.3	36	61	5
HfV_2	0	33.3	66.7	0	35	65	

[a]The standard deviations are ±2 atom %. ^{27}Al solid-state NMR.

electrical conductivity of the sample. The diluted samples were loaded into a cylindrical ZrO_2 rotor with a diameter of 4 mm and spun at a magic angle with a frequency between 8 and 13 kHz. All experiments conducted were single-pulse experiments with typical pulse length of 0.83 μs and relaxation delays of 1 s. Resonance shifts were referenced to aqueous 1 molar $AlCl_3$ solutions. The NMR spectra were recorded using the Bruker TOPSPIN software,[56] and the analysis was performed with the help of the DMFIT program package.[57] The extracted data is compiled in Table 8.

Table 8. Summary of the NMR Observables of $MgZn_2$ Types $HfAl_2$ and Trigonal Hf_4VAl_7 (Own Type) Extracted from the DMFit Simulation of the ^{27}Al MAS-NMR Spectra with δ Being the Resonance (in ppm), C_Q Being the Quadrupolar Parameter (in kHz), and η_Q Being the Asymmetry Parameter[a]

compound	site	δ	$C_{Q,theo}$	$C_{Q,exp}$	$\eta_{Q,theo}$	$\eta_{Q,exp}$
$HfAl_2$	Al1 (2*a*)	+46	4096	5306	0	0.42
	Al2 (6*h*)	−43	643	1188	0.97	0.98
Hf_4VAl_7	Al1 (1*b*)[b]	+76	2581		0	
	Al2 (6*i*)[b]	−76	5514		0.235	

[a]Theoretically calculated values from DFT are given with the subscript theo. [b]Site assignment is not clear due to the low resolution in the spectrum. It is nevertheless reasonable to link the larger signal in amplitude and area to the 6i Al site.

Physical Property Measurements. *Susceptibility Measurements.* The polycrystalline samples of $HfAl_2$, HfV_2, as well as selected members of the solid solution $Hf(V_{1-x}Al_x)_2$ for x = 0.05, 0.25, 0.5, and 0.75 were investigated by temperature-dependent magnetic susceptibility measurements at external fields up to 80 kOe (1 kOe = 7.96 × 10^4 A m^{-1}). The samples were ground to a fine powder, filled into polypropylene capsules, and attached to the sample holder rod of a vibrating sample magnetometer (VSM) option of a physical property measurement system (PPMS) by quantum design. The magnetization data $M(T)$ of the samples was investigated in the temperature range between 1.8 and 300 K.

Heat Capacity. For the heat capacity measurements of $Hf(V_{0.95}Al_{0.05})_2$, a piece was fixed to a precalibrated heat capacity puck using Apiezon N grease and investigated in the temperature range of 1.8−300 K with 1 K steps.

The results of the physical property investigations are summarized in Table 9.

Quantum-Chemical Calculations. The electronic structure and chemical bonding properties were obtained based on calculations within the density functional theory (DFT).[58,59] For an accurate assessment of the charge trends in the present family of valence isoelectronic ternary compounds, the Vienna ab initio simulation package (VASP) code[60,61] with the projector augmented wave (PAW) method[61,62] was used. The valence wave function (vfn) tends to have rapid oscillations near ion cores due to necessary orthogonality rules. Large computational efforts are then needed to describe it accurately, making early need for pseudopotentials as those early derived ultrasoft pseudopotentials USPP derived by Vanderbilt.[63] More adapted to heavier elements such as Hf used herein, the PAW method provides a solution through an augmentation procedure within the intraatomic zone by transforming the vfn rapid oscillations into smooth ones. This is a computationally convenient procedure allowing calculation with reasonable computational efforts of all-electron properties from the produced smooth and true vfns. Regarding the DFT exchange-correlation XC effects, they were accounted for within the generalized gradient approximation (GGA) according to Perdew, Burke, and Ernzerhof.[64] The calculations were started from the experimental structure parameters (lattice constants and atomic positions in Tables 1,

Table 9. Magnetic Properties of the Investigated Compounds of the Solid Solution $Hf(V_{1-x}Al_x)_2$ for x = 0, 0.05, 0.25, 0.75, and 1

compound	structure	T_C (K) type	susceptibility at 300 K
$HfAl_2$	$MgZn_2$		χ(300 K) = −5.28 × 10^{-5} emu mol^{-1}
$Hf(V_{0.25}Al_{0.75})_2$	$MgZn_2$		χ(300 K) = +3.36 × 10^{-5} emu mol^{-1}
$Hf(V_{0.75}Al_{0.25})_2$	$MgZn_2$		χ(300 K) = +5.82 × 10^{-5} emu mol^{-1}
$Hf(V_{0.95}Al_{0.05})_2$	$MgCu_2$	7.6(1)	χ(300 K) = +7.25 × 10^{-4} emu mol^{-1}
HfV_2	$MgCu_2$	nd[a]	χ(300 K) = +6.77 × 10^{-4} emu mol^{-1}
HfV_2[44]	$MgCu_2$	9.57	nd

[a]nd = not determined.

https://doi.org/10.1021/acs.inorgchem.4c00391
Inorg. Chem. 2024, 63, 8180−8193

Table 10. Atom-Averaged Cohesive Energies in eV and Augmented Bader Charges (for Details, See Text)

compound	$HfAl_2$	HfV_2	Hf_4VAl_7
structure type	$MgZn_2$, C14	$MgCu_2$, C15	own type, $P\bar{3}m1$
E_{coh}/at.	−1.47	−0.30	−0.72
Bader charges	2× Hf (+0.98) = +1.96	4× Hf = (+0.16) = +0.32	2× Hf1 (+0.407) = +0.814
	4× Al (−0.49) = −1.96	8× V = (−0.08) = −0.32	2× Hf2 (+0.395) = +0.79
			1× V (−0.011) = −0.011
			1× Al1 (−0.273) = −0.273
			6× Al2 (−0.220) = −1.32
balance ±	±1.96	±0.32	±1.60
remarks	ionocovalent-like due to Al (p)	covalence (intermetallic)	covalence induced by insertion of V

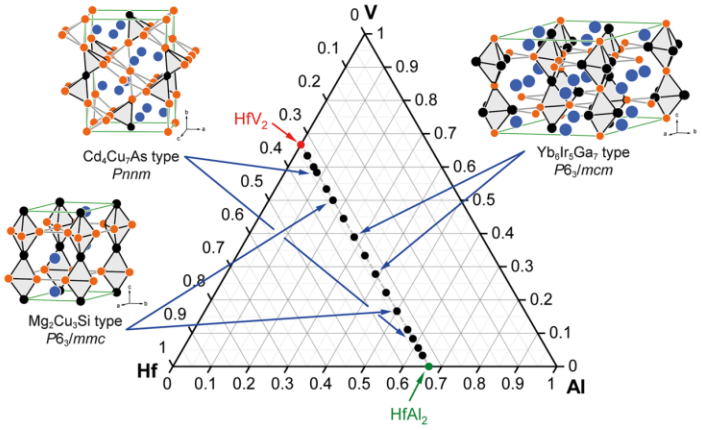

Figure 1. Potential superstructures plotted with respect to their chemical composition as members of the solid solution $Hf(V_{1-x}Al_x)_2$ and those of the superstructures. The three envisioned structure types are shown. The Mg/Cd/Yb/Hf atoms are shown in blue, the Cu/Ir/V atoms are in orange, and the Si/As/Ga/Al atoms are in black.

2, 4, and 5). The calculated corresponding parameters of the relaxed structures were found to be in good agreement with the experiment. From the calculations' outcome, the charge densities were particularly examined to obtain the so-called Bader charges based on Atom in Molecule AIM theory approach[65] developed by Bader, who devised an intuitive way of splitting molecules into atoms based purely on the electronic charge density. The charge density in a chemical compound reaches a minimum between atoms, thus, defining a region separating atoms from each other. In the case of a family of compounds having similarities, such an analysis can be useful to establish trends. In other words, the analysis does not evaluate the absolute ionizations. Core electrons are included for an accurate account of the charge density. The analysis is done using a fast algorithm operating on a charge density grid. The obtained charges are listed in Table 10.

The all-electron calculations with the GGA were carried out for a full description of the electronic structure and the properties of chemical bonding using the full potential scalar relativistic augmented spherical wave (ASW) method.[66,67] Self-consistency was achieved when charge transfers and energy changes between two successive cycles were below 10^{-8} and 10^{-6} eV, respectively. BZ integrations were performed by using the linear tetrahedron method within the irreducible wedge. Besides the electronic band structures and the site-projected density of states, pair interactions based on the overlap population analysis with the crystal orbital overlap population (COOP)[68] are qualitatively discussed. In the plots, positive, negative, and zero COOP indicate bonding, antibonding, and nonbonding interactions, respectively.

RESULTS AND DISCUSSION

Crystal Chemistry. The structures of the Laves phases will be discussed only very briefly as they pose very prominent structure types. In both prototypes, the Al or V atoms form networks of empty Al_4 or V_4 tetrahedra, which are connected over all four corners (V_4, cubic $MgCu_2$ type) or form dimeric units via condensation over a common face along with further connection over the corners (Al_4, hexagonal $MgZn_2$ type). Within the networks, cavities that host the Hf atoms are formed, which are arranged in a cubic/hexagonal diamond pattern.

Along the solid solution $Hf(V_{1-x}Al_x)_2$, different values of x were chosen, which correspond to potential superstructures of the $MgZn_2$ or $MgCu_2$ types. Due to their relationship to the two prototypic Laves phases, their structures are also closely related and can be derived by coloring and (subtle) distortions. Two review articles summarizing the structural relationships have been published recently.[22,23] Figure 1 illustrates the different structure types that were targeted. These are the Mg_2Cu_3Si type that corresponds to a coloring variant of the $MgZn_2$ type (x = 0.25 and 0.75), while both the $Yb_6Ir_5Ga_7$ (x = 0.417 and 0.583) and Cd_4Cu_7As types (x = 0.125 and 0.875) are superstructures with significant distortions alongside different coloring. In addition, values of x = 0.5 (HfVAl) as well as x = 0.05, 0.1, and 0.95 as compositions near the respective end members and finally x = 0.333 and 0.667 resembling $Hf_3V_2Al_4$ and $Hf_3V_4Al_2$ (no superstructures of the Laves phases with these compositions are known) were chosen.

Power X-ray Diffraction. All samples were investigated by powder X-ray diffraction experiments at room temperature. The diffraction patterns of $HfAl_2$, HfV_2, and $Hf(V_{0.75}Al_{0.25})_2$ are exemplarily shown in Figure 2. All samples could be obtained as X-ray pure material, and details of the respective refinements can be found in Tables 1−3 and the Supporting Information (SI). It

https://doi.org/10.1021/acs.inorgchem.4c00391
Inorg. Chem. 2024, 63, 8180−8193

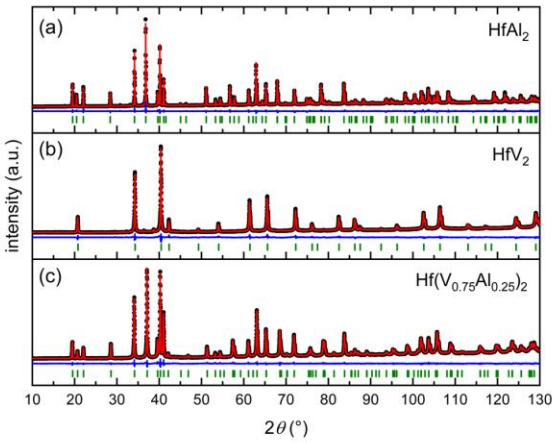

Figure 2. Powder X-ray diffraction patterns of (a) hexagonal $HfAl_2$ ($MgZn_2$ type, $P6_3/mmc$), (b) cubic HfV_2 ($MgCu_2$ type, $Fd\bar{3}m$), and (c) hexagonal $Hf(V_{0.75}Al_{0.25})_2$ ($MgZn_2$ type, $P6_3/mmc$). Experimental data are shown as black dots, refined data as red lines, the difference is shown as continuous blue lines, and the Bragg positions are shown as green ticks.

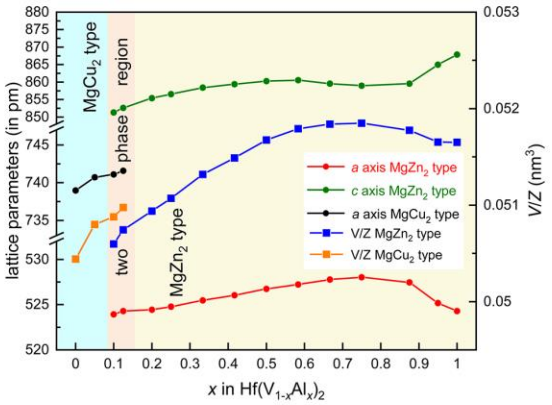

Figure 3. Plot of lattice parameters a (red/black) and c (black) as well as the normalized unit cell volumes (V/Z, blue/orange) for solid solution $Hf(V_{1-x}Al_x)_2$ as a function of x. The different structure types are color-coded. $MgCu_2$ type in cyan, $MgZn_2$ type in yellow, and two-phase region in orange.

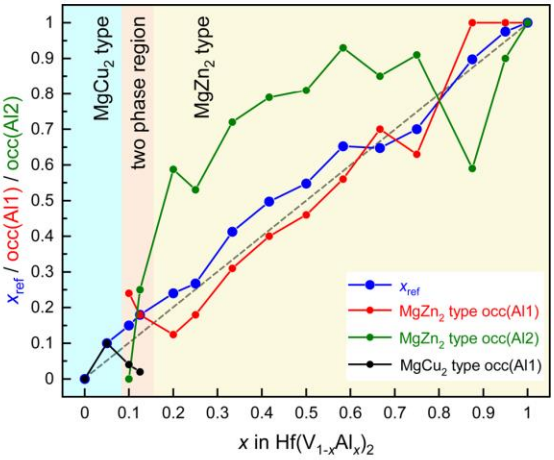

Figure 4. Plot of the refined composition (blue) as well as the site occupation factors for $MgZn_2$ (red: Al1; green: Al2) and $MgCu_2$ (black) type structures for the solid solution $Hf(V_{1-x}Al_x)_2$ as a function of x. The different structure types are color-coded. $MgCu_2$ type in cyan, $MgZn_2$ type in yellow, and two-phase region in orange.

is interesting to note that even though different compositions that can form superstructures were targeted, only the cubic $MgCu_2$ or the hexagonal $MgZn_2$ type structures could be identified and refined based on their powder X-ray diffraction data.

All compounds within the solid solution $Hf(Al_{1-x}V_x)_2$ including the end members adopt Laves phase type structures based on powder X-ray diffraction data. For x = 0.2−1, the hexagonal $MgZn_2$ type structure is observed, while for x = 0 and 0.05, the cubic $MgCu_2$ type structure is found. In between, for x = 0.1 and 0.125, a two-phase region is found, where both structure types coexist. The refinement of the site occupancies (Table 2) in the two-phase region revealed that the hexagonal phase is Al-rich, while the cubic phase is Al-poor. The trend of the lattice parameters and unit cell volumes per formula unit is shown in Figure 3 and listed in Table 1. As can be seen, upon substitution of V by Al, the cubic $MgCu_2$ type structure persists and the lattice parameters increase in line with the atomic radii (Al: 143 pm; V: 132 pm).[69] This trend continues for the $MgZn_2$ type representatives up to $x \sim 0.75$. For larger values, the unit cell volume decreases slightly, most likely caused by the increasing number of bonding interactions between the Al atoms.

When the site occupancies for the two different structure types are refined, the overall value of x follows the nominal value (Figure 4). However, the individual sites show differences in their occupation behavior. For small degrees of substitution of Al by V, at first, the Al2 site gets mixed occupied, followed by an almost linear decrease in substitution for the Al1 site, while the occupation on the Al2 site increases before finally decreasing.

^{27}Al Solid-State NMR Spectroscopic Investigations. ^{27}Al NMR spectra for the samples $HfAl_2$ as well as the members of the solid solution $Hf(V_{1-x}Al_x)_2$ for x = 0.917, 0.875, 0.833, 0.583, and 0.5 were measured at a magnetic flux density of 9.4 T. Table 8 summarizes the parameters obtained from the MAS NMR spectra as well as the calculated values for quadrupole parameters C_Q and η_Q. Based on the respective crystal chemistry (*vide infra*), one would expect one central transition for the $MgCu_2$ type structures and two for the $MgZn_2$ type compounds due to one and two crystallographic Al sites. However, for the samples that form solid solutions, the signals should be significantly broadened, leading to a Gaussian-type shape as shown, e.g., for Na_2Au_3Al,[40] the *AE*Au*X*[43] or the Sc*T*Al[70] and $Sc(T_{0.5}T'_{0.5})_2Al$[71] compounds.

Figure 5 depicts the ^{27}Al NMR spectra of $HfAl_2$. As expected, two main signals can be observed, one being rather sharp and symmetrical and the other being significantly broadened. In this case, the broadened signal is caused by an anisotropic electric field gradient around the Al nuclei. Based on the quantum-chemical calculations (*vide infra*) and the assessment of the crystal structure, it becomes clear that the rather sharp signal can be attributed to the Al1 (2*a*) site, while the signal showing quadrupolar broadening originates from the Al2 (6*h*) site.

In the ^{27}Al NMR spectra of members of the solid solution $Hf(V_{1-x}Al_x)_2$ (Figure 6), expected broad signals can be

https://doi.org/10.1021/acs.inorgchem.4c00391
Inorg. Chem. 2024, 63, 8180−8193

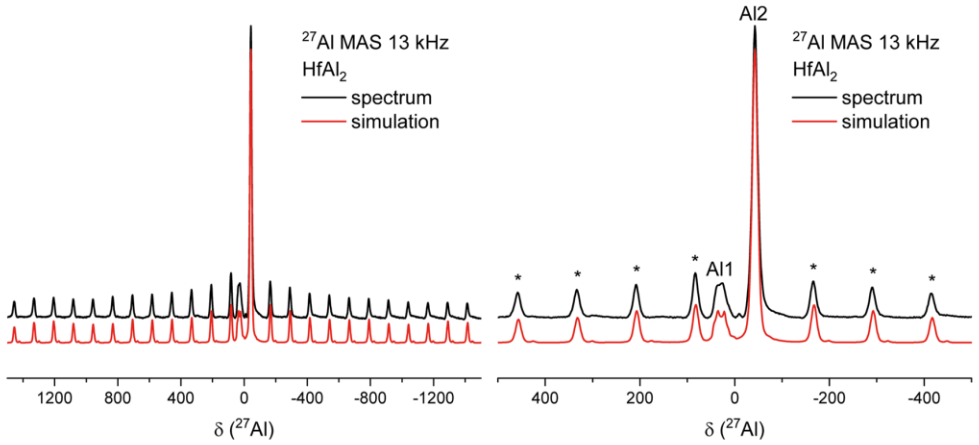

Figure 5. (left) ^{27}Al MAS NMR spectra of hexagonal $HfAl_2$ ($MgZn_2$ type). (right) Zoom of the region around the central $|+1/2\rangle \leftrightarrow |-1/2\rangle$ transitions. The small signals marked with asterisks are rotational side bands caused by the MAS conditions. The fits are depicted in red.

observed, which originate from the disorder. Even at small degrees of V substitution (x = 0.05, Figure 6a), the signal is extremely broadened; however, the general shape with two signals and similar shifts is still visible. This is also true for x = 0.083 (Figure 6b), 0.167 (Figure 6d), 0.417 (Figure 6e), and finally 0.5 (Figure 6f). The clear exception, however, is $Hf(V_{0.125}Al_{0.875})_2$ (Figure 6c). Here, two rather sharp signals can be observed, with none of them being significantly quadrupolar broadened. Furthermore, the signal intensities are switched in comparison to $HfAl_2$. This leads to the question of how this sample differs from the other ones.

Single-crystal X-ray Diffraction and Group−Subgroup Relations. Due to the anomalies observed in the ^{27}Al NMR spectra of $Hf(V_{0.125}Al_{0.875})_2$ (*vide supra*), crystals of this compound were selected and investigated by single-crystal X-ray diffraction experiments. In addition, single crystals of the neighboring phases $Hf(V_{0.083}Al_{0.917})_2$, $Hf(V_{0.167}Al_{0.833})_2$, as well as $Hf(V_{0.417}Al_{0.583})_2$ were investigated. While all investigated crystals show the expected unit cell of the $MgZn_2$ type ($P6_3/mmc$, $a \sim 530$ pm, $c \sim 860$ pm, Table 4), only the structures of $Hf(V_{0.083}Al_{0.917})_2$ and $Hf(V_{0.417}Al_{0.583})_2$ could be refined without problems in the $MgZn_2$ type structure. For the other two structures, problems with the anisotropic refinement of the V/Al mixture at the 2*a* position occurred. The single-crystal data of $Hf(V_{0.125}Al_{0.875})_2$ (refined in space group $P6_3/mmc$) furthermore leads to a refined occupancy of ∼48% V and ∼52% Al on the Wyckoff site 2*a*. According to the International Tables for Crystallography Volume A1,[72] a 1:1 splitting is possible in the subgroup $P\bar{3}m1$ via a translationengleiche transition of index 2. Subsequent refinement as a twinned structure (absent 2-fold axis as a twinning element) led to significantly improved residuals with all atomic sites being fully occupied (Tables 4−6). Due to the translationengleiche transition, no additional superstructure reflections occur in the powder X-ray diffraction patterns; therefore, the only differences are observed in the intensities due to the V/Al ordering. The small difference in the scattering contrasts, however, only modifies the intensities slightly. The Rietveld refinements are shown in Figures S4−S7. The obtained atomic arrangement corresponds to a new superstructure of the hexagonal Laves $MgZn_2$ with the sum formula Hf_4VAl_7 (≡ $Hf(V_{0.125}Al_{0.875})_2$), Wyckoff sequence id^2ba, and Pearson code $hP12$. The Pearson database[24] revealed that ∼100 entries are known with the respective Wyckoff sequence in space group $P\bar{3}m1$. Of these, however, no entry is an intermetallic compound. The majority belongs to the $KAl[MoO_4]_2$ type structure[73] and four entries are listed for the $SrMg_2FeH_8$ type structure,[74,75] along with representatives of the $K_2[SO_3]$ type structure.[76] All of these compounds exhibit the same space group symmetry and have the same Wyckoff positions occupied; however, distinctly different atomic coordinates can be found for the respective atoms, and a totally different crystal chemistry and bonding situation is present. Therefore, these compounds are only isopointal to Hf_4VAl_7 and by no means isostructural. Also, $Hf(V_{0.167}Al_{0.833})_2$ could be refined in the Hf_4VAl_7 type structure with a composition of $Hf_4V_{1.13(1)}Al_{6.87(1)}$, in line with the respective nominal composition.

At this point, we want to draw back to NMR studies. As mentioned before (*vide supra*), the ^{27}Al NMR spectrum of "$Hf(V_{0.125}Al_{0.875})_2$" clearly shows two sharp resonances, suggesting two crystallographic positions that are solely occupied by Al alongside only small amounts of disorder due to quality of the NMR spectrum, which was proven to be correct, based on the gathered single-crystal data. Figure 7 depicts the crystal structure of $Hf(V_{0.125}Al_{0.875})_2$ based on the single-crystal structure refinement, indicating the ordered V and Al positions. In the $MgZn_2$ type, crystallographically equivalent positions on the corners and the edges along [001] are now independent, leading to a coloring of this position for the V and Al atoms. Subsequently, two different coordination environments arise, both in a trigonal prismatic (distorted octahedral) coordination geometry. Figure 7 depicts the different surroundings. The interatomic distances to the central atom vary slightly, in line with the different sizes of the V and Al atoms (Al: 143 pm; V: 132 pm[69]). Finally, Figure 8 illustrates the structural relationship between $MgZn_2$ and Hf_4VAl_7 using the Bärnighausen formalism.[77−80]

Physical Properties. $HfAl_2$, HfV_2, as well as three members of the solid solution $Hf(V_{1-x}Al_x)_2$ were investigated by temperature-dependent magnetic susceptibility measurements. For all compounds, diamagnetic behavior is expected due to the absence of unpaired localized electrons. However, due to the metallic character of these compounds, the Pauli paramagnetism, caused by the conduction electrons, can overcompensate the intrinsic diamagnetism. This is observed for all investigated

https://doi.org/10.1021/acs.inorgchem.4c00391
Inorg. Chem. 2024, 63, 8180−8193

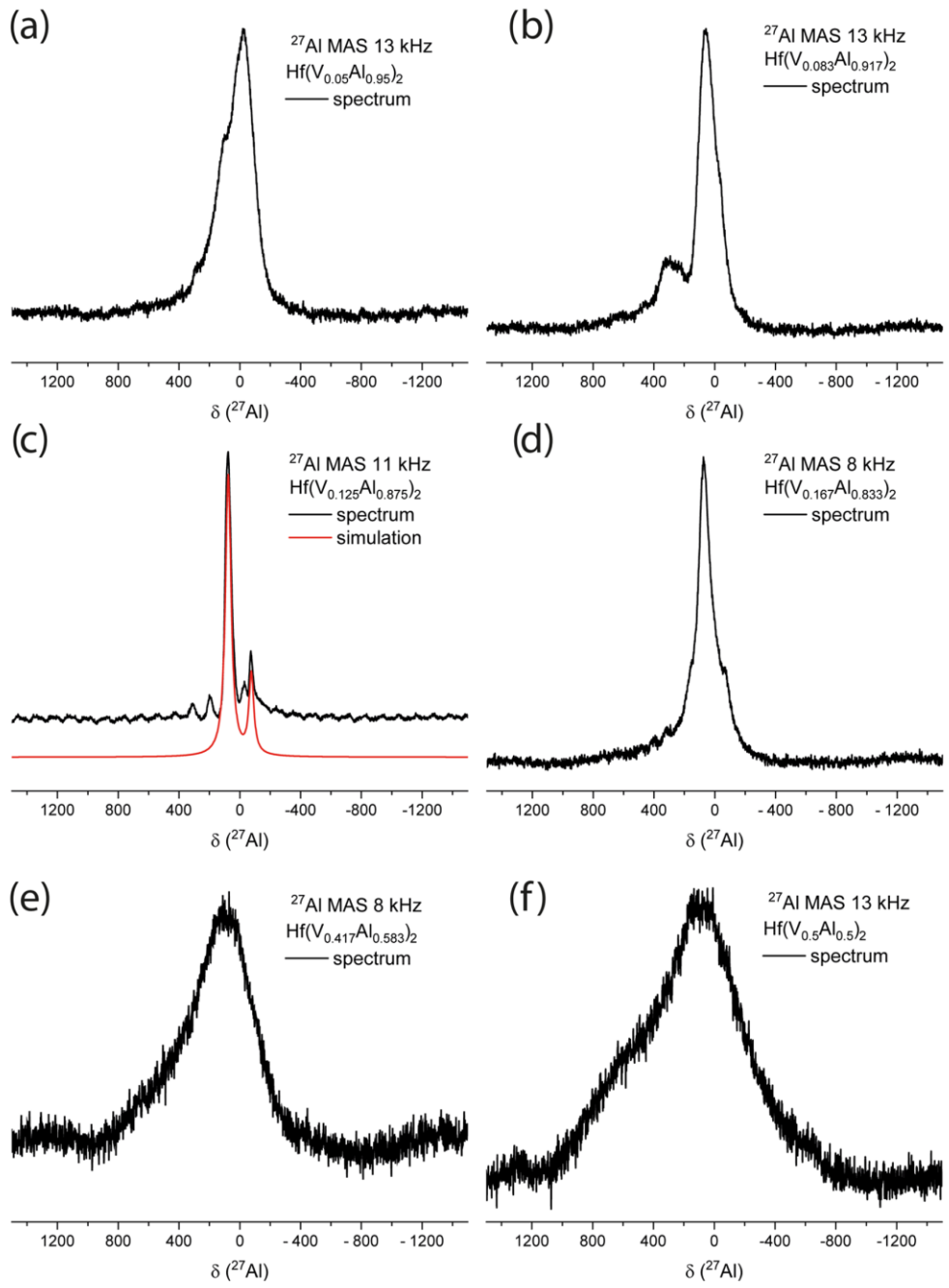

Figure 6. ^{27}Al MAS NMR spectra of (a) Hf(V$_{0.05}$Al$_{0.95}$)$_2$, (b) Hf(V$_{0.083}$Al$_{0.917}$)$_2$, (c) Hf(V$_{0.125}$Al$_{0.875}$)$_2$, (d) Hf(V$_{0.167}$Al$_{0.833}$)$_2$, (e) Hf(V$_{0.417}$Al$_{0.583}$)$_2$, and (f) Hf(V$_{0.5}$Al$_{0.5}$)$_2$.

compounds, except for $HfAl_2$. Figure 9 depicts the recorded data. For all compounds, slight upturns are visible below 20 K, which can be attributed to traces of paramagnetic impurities. For Hf(V$_{0.95}$Al$_{0.05}$)$_2$ (Figure 9, purple) and HfV_2 (Figure 9, orange), however, a drop of the susceptibility can be observed below ∼8 K. This might be caused by the superconducting transition observed in HfV_2 (T_C ∼ 8.9(1) K) and Hf(V$_{0.95}$Al$_{0.05}$)$_2$ (T_C = 7.6(1) K, *vide infra*) as these anomalies are in good agreement with the critical temperatures of both compounds. It must be mentioned that the magnetic susceptibilities of both compounds are rather smooth, and no distinct bump around 120 K is visible, which could indicate the structural phase transition that has been shown for HfV_2.

https://doi.org/10.1021/acs.inorgchem.4c00391
Inorg. Chem. 2024, 63, 8180−8193

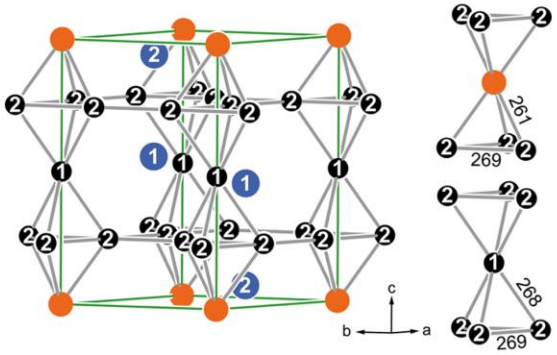

Figure 7. (left) Unit cell of Hf_4VAl_7. (right) Coordination environment of V and Al1 atoms. Interatomic distances are given in pm. Hf atoms are depicted in blue, V atoms in orange, and Al atoms in black.

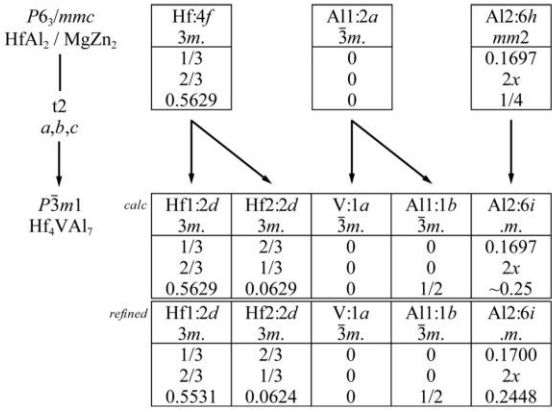

Figure 8. Group−subgroup relationship of $HfAl_2$ (hexagonal Laves phase, $MgZn_2$ type) and Hf_4VAl_7 (own type) according to the Bärnighausen formalism.[77−80]

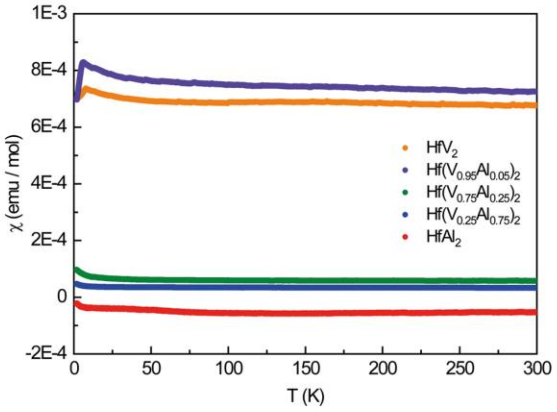

Figure 9. Magnetic susceptibility data of $HfAl_2$, HfV_2, and the members with x = 0.75, 0.25, and 0.05 of the solid solution $Hf(V_{1-x}Al_x)_2$. Measurements were conducted in zero-field-cooled (ZFC) mode.

Since $Hf(V_{0.95}Al_{0.05})_2$ adopts the cubic $MgCu_2$ type structure, it could principally also be superconducting despite the disorder introduced by the substitution of Al on the V site. Therefore, low-field susceptibility measurements (20 Oe) were conducted in zero-field/field-cooled mode (Figure 10a). Indeed, a sharp

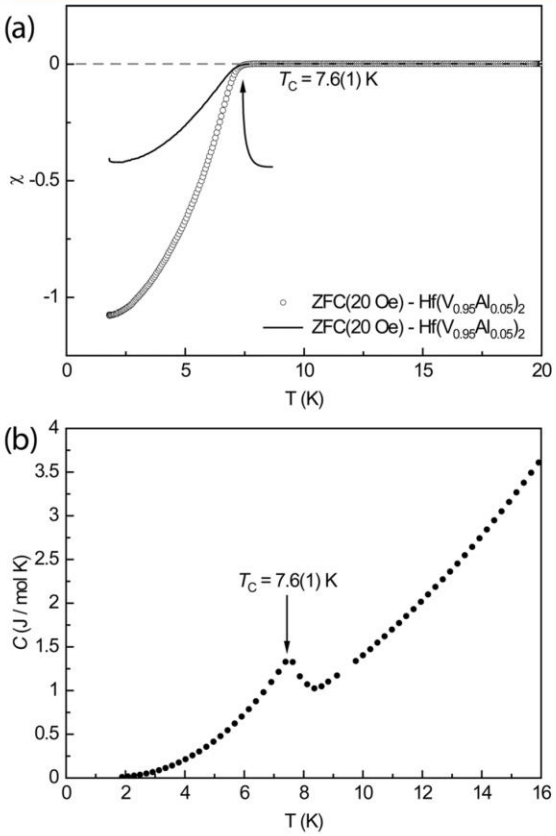

Figure 10. (a) Magnetic susceptibility data of $Hf(V_{0.95}Al_{0.05})_2$ measured in zero-field/field-cooled (ZFC/FC) mode. (b) Heat capacity measurements of $Hf(V_{0.95}Al_{0.05})_2$ in zero-field.

decrease of the susceptibility can be observed with the crossover from Pauli paramagnetic to diamagnetic behavior at T_C = 7.6(1) K. The shift to lower temperatures is expected due to the aforementioned disorder. In field-cooled mode, the susceptibility is less negative, but still, a pronounced drop is visible. Due to the susceptibility χ being <−1, the Meissner fraction is 100%. Heat capacity measurements show a λ-like anomaly, confirming the transition temperature of T_C = 7.6(1) K (Figure 10b).

Quantum-Chemical Calculations. The first criterion for assessing the relative stabilities is the atom-averaged cohesive energies provided for the different compounds under consideration. The atomic energies of the different constituents obtained from calculations of the atoms isolated in a large box (E_{Hf} = −9.77 eV, E_{Al} = −3.37 eV, and E_V = −8.95 eV) are subtracted from the total energies to obtain the cohesive energies provided in Table 10 as atom-averaged to allow comparisons. The most cohesive is the $HfAl_2$ C14 Laves phase ($MgZn_2$ type), and the least cohesive is the HfV_2 C15 Laves phase ($MgCu_2$ type); the ternary intermetallic Hf_4VAl_7 has an intermediate value. These results highlight the ionocovalent behavior explained by the chemical natures of the different compounds, i.e., a combination of a 5d transition metal Hf with the p element

https://doi.org/10.1021/acs.inorgchem.4c00391
Inorg. Chem. 2024, 63, 8180−8193

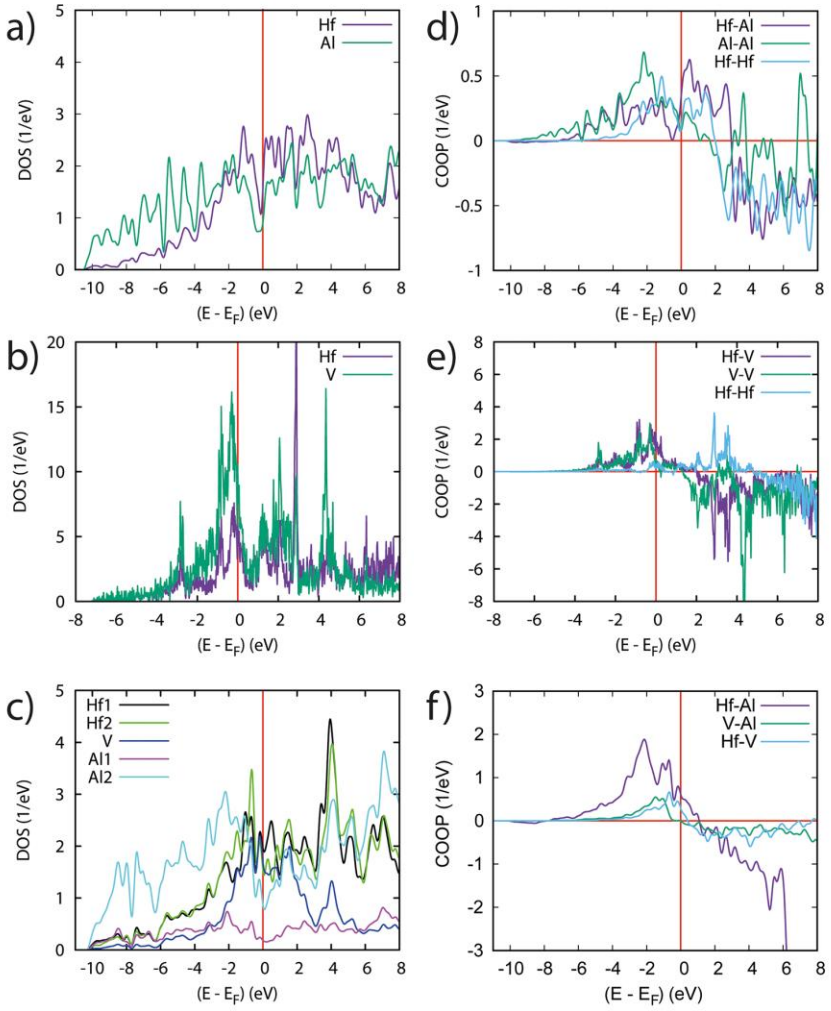

Figure 11. Electronic structures of $HfAl_2$ (a and d), HfV_2 (b and e), and Hf_4VAl_7 (c and f) with site-projected density of states DOS (left) and chemical bonding with COOP criterion (right).

Al versus a combination of two transition elements, 5d Hf and 3d V, for the two binaries while a mixture is found in the ternary system Hf_4VAl_7.

Furthering these results, the trends of charge transfers were inferred from the analyses of the charge density. Due to the light element Al, the core + semicore valence populations were included for constituent elements. Al is found negatively charged, while Hf is positively charged. Vanadium is found to be slightly negatively charged. These trends follow from the electronegativity χ according to Pauling,[69] with χ(Hf) = 1.3, χ(V) = 1.6, and χ(Al) = 1.5. The resulting balance charge ± magnitudes follow the cohesive energy magnitudes.

Using all-electrons scalar relativistic ASW method[67] and the experimental lattice parameters, the electronic properties were calculated with the outcome of the site-projected density of states DOS, and the properties of chemical bonding between two atomic constituents with the COOP (crystal orbital overlap populations) based on the overlap integral criterion following Hoffmann et al.[68] In shorthand notation, the COOPs are the overlap integral S_{ij} modulated DOS. In the COOP panels, positive, negative, and nil COOP intensities point to bonding, antibonding, and nonbonding interactions, respectively.

Figure 11 shows the DOS and COOP plots for the two binary systems and the trigonal Hf_4VAl_7. The role of each atomic constituent in the electronic structure can be observed, with the details provided by the site-projected DOS shown in Figure 11a−c. The right-hand side panels (Figure 11d−f) depict the COOP. Along the horizontal axis, the zero energy is with respect to the Fermi level E_F. The DOS (and COOP) along the vertical directions are given in 1/eV unit. As a general observation, DOS with similar skylines and energies indicates quantum mixing of the valence states, i.e., the chemical interactions as observed in the DOS panels within the valence band VB (below E_F). In the lower part of the VB of the three panels, i.e., below −6 eV, the s,p-like states prevail; note, for instance, the large intensity Al DOS in both a and c panels. On the other part of the VB, from −4 eV up to E_F, the transition metal (Hf, V) states are prevailing. E_F is crossed by DOS contributed by all constituents, thus confirming

https://doi.org/10.1021/acs.inorgchem.4c00391
Inorg. Chem. 2024, 63, 8180−8193

the metallic character of the three chemical systems. Similar DOS shapes between constituents are also observed above E_F in the empty states; however, they are expected to be of an antibonding nature.

In all panels depicting the COOP (Figure 11d–f), the occupied states within the VB present positive COOP, describing bonding interactions in agreement with the cohesive energies (Table 10). $HfAl_2$ (Figure 11a) shows besides the heteroatomic Hf–Al interaction homoatomic Al–Al and Hf–Hf. It is proposed that the "p–d"-like character of $HfAl_2$ favors such a feature. Oppositely, in "d–d" Hf–V_2 Laves phase, the VB shows that most of the bonding is from −4 eV up to E_F with a larger d–d contribution and similar skylines. Note also that the bonding character of positive COOP intensities continues up to 2 eV with the empty conduction band (CB), alike $HfAl_2$. This is because Hf and V are early transition elements and thus have their d-states little occupied, leaving the remainder of the d orbitals available for extra electrons arising from the quantum mixing leading to the bonding. In the last COOP panel relevant to the ternary, the plots consider all atoms of each chemical nature to have a qualitative representation of relative COOP magnitudes. Here, the prevailing interaction is heteroatomic between Hf and Al due to the large number of Al in the structure; the other two interactions show lower magnitudes.

CONCLUSIONS

Phase analytical investigations in the Hf–V–Al system revealed that the solid solution between HfV_2 and $HfAl_2$, $Hf(V_{1-x}Al_x)_2$, exists for many compounds. Since both compounds adopt different crystal structures, the existence ranges were probed, and the cubic $MgCu_2$ type was observed for HfV_2 and low amounts of Al (x = 0.05 and 0.1). After a small two-phase region, the hexagonal $MgZn_2$ type can be identified in line with $HfAl_2$. Powder X-ray diffraction was used to track the changes in the unit cell dimensions and the mixing of V and Al. Furthermore, ^{27}Al NMR spectroscopic investigations were conducted on $HfAl_2$, clearly validating its crystal structure. In addition, members of the solid solution of $Hf(V_{1-x}Al_x)_2$ were measured. The majority shows the expected line broadening due to the local disorder. However, $Hf(V_{0.125}Al_{0.875})_2$ showed two sharp resonances, leading to the interpretation that in this compound, almost full atomic ordering is present. Detailed single-crystal X-ray investigations revealed that $Hf(V_{0.125}Al_{0.875})_2$ is indeed an, thus far, unknown new ordering variant of the hexagonal $MgZn_2$ type structure with composition Hf_4VAl_7. The structural relationship between $MgZn_2$ and Hf_4VAl_7 has been illustrated based on a group–subgroup scheme using the Bärnighausen formalism. Finally, several compounds were investigated by magnetic susceptibility measurements, indicating a Pauli-paramagnetic behavior. $Hf(V_{0.95}Al_{0.05})_2$ additionally shows superconductivity below T_C = 7.6(1) K, in line with pure HfV_2 (T_C = 9.57 K).

ASSOCIATED CONTENT

Supporting Information

The Supporting Information is available free of charge at https://pubs.acs.org/doi/10.1021/acs.inorgchem.4c00391.

Additional powder X-ray data (PDF)

Accession Codes

CCDC 2325587–2325590 contain the supplementary crystallographic data for this paper. These data can be obtained free of charge via www.ccdc.cam.ac.uk/data_request/cif, by emailing data_request@ccdc.cam.ac.uk, or by contacting The Cambridge Crystallographic Data Centre, 12 Union Road, Cambridge CB2 1EZ, UK; fax: +44 1223 336033.

AUTHOR INFORMATION

Corresponding Author

Oliver Janka − *Inorganic Solid State Chemistry, Saarland University, 66123 Saarbrücken, Germany*; orcid.org/0000-0002-9480-3888; Email: oliver.janka@uni-saarland.de

Authors

Elias C. J. Gießelmann − *Inorganic Solid State Chemistry, Saarland University, 66123 Saarbrücken, Germany*; orcid.org/0000-0001-6137-9729

Stefan Engel − *Inorganic Solid State Chemistry, Saarland University, 66123 Saarbrücken, Germany*; orcid.org/0000-0002-6813-8490

Jasper Baldauf − *Institut für Anorganische und Analytische Chemie, Universität Münster, 48149 Münster, Germany*

Jutta Kösters − *Institut für Anorganische und Analytische Chemie, Universität Münster, 48149 Münster, Germany*

Samir F. Matar − *Lebanese German University, 1200 Jounieh, Lebanon*; orcid.org/0000-0001-5419-358X

Guido Kickelbick − *Inorganic Solid State Chemistry, Saarland University, 66123 Saarbrücken, Germany*; orcid.org/0000-0001-6813-9269

Complete contact information is available at: https://pubs.acs.org/10.1021/acs.inorgchem.4c00391

Author Contributions

All authors have accepted responsibility for the entire content of this submitted manuscript and approved the submission.

Notes

The authors declare no competing financial interest.

ACKNOWLEDGMENTS

We thank Dr. Maximilian Kai Reimann for the help with the measurements of the physical properties. Instrumentation and technical assistance for this work were provided by the Service Center X-ray Diffraction with financial support from Saarland University and German Research Foundation (project numbers INST 256/506-1 and INST 256/349-1) and by the Service Center NMR with financial support from Saarland University and German Research Foundation DFG. The magnetometer was funded by the German Science Foundation DFG through INST 211/1034-1. Funding was provided by the Deutsche Forschungsgemeinschaft DFG (JA 1891-10-1).

REFERENCES

(1) Fischer, W.; Fritz, H. Laves—an ideal for generations. *Z. Kristallogr. - Cryst. Mater.* **2006**, *221*, 305–310.

(2) Parthé, E.; Fritz, H. Laves—100 years young. *Z. Kristallogr. - Cryst. Mater.* **2006**, *221*, 301–304.

(3) Schulze, G. E. R. Zur Kristallchemie der intermetallischen AB_2-Verbindungen (Laves-Phasen). *Angew. Phys. Chem.* **1939**, *45*, 849–865.

(4) Friauf, J. B. The Crystal Structure of Magnesium Di-Zincide. *Phys. Rev.* **1927**, *29*, 34–40.

(5) Tarschisch, L.; Titow, A. T.; Garjanow, F. K. Röntgenographische Untersuchung der Verbindung $MgZn_2$. *Phys. Z. Sowjetunion* **1934**, *5*, 503–510.

(6) Laves, F.; Witte, H. Die Kristallstruktur des $MgNi_2$ und seine Beziehungen zu den Typen $MgCu_2$ und $MgZn_2$. *Metallwirtsch., Metallwiss., Metalltech.* **1935**, *14*, 645–649.

(7) Lieser, K. H.; Witte, H. Untersuchungen in den ternären Systemen Magnesium-Kupfer-Zink, Magnesium-Nickel-Zink und Magnesium-Kupfer-Nickel. *Int. J. Mater. Res.* **1952**, *43*, 396−401.
(8) Laves, F.; Witte, H. Der Einfluß von Valenzelektronen auf die Kristallstruktur ternärer Magnesiumlegierungen. *Metallwirtsch., Metallwiss., Metalltech.* **1936**, *15*, 840−842.
(9) Friauf, J. B. The crystal structures of two intermetallic compounds. *J. Am. Chem. Soc.* **1927**, *49*, 3107−3114.
(10) Paufler, P.; Gustav, E. R. Schulze's pioneering work on Laves phases. *Z. Kristallogr. - Cryst. Mater.* **2006**, *221*, 311−318.
(11) Gschneidner, K. A., Jr.; Pecharsky, V. K. Binary rare earth Laves phases—an overview. *Z. Kristallogr. - Cryst. Mater.* **2006**, *221*, 375−381.
(12) Yokosawa, T.; Söderberg, K.; Boström, M.; Grüner, D.; Kreiner, G.; Terasaki, O. Microscopic Structures of Laves Phases and Structurally Related Compounds: A Transmission Electron Microscopy Study. *Z. Kristallogr. - Cryst. Mater.* **2006**, *221*, 357−374.
(13) Grüner, D.; Stein, F.; Palm, M.; Konrad, J.; Ormeci, A.; Schnelle, W.; Grin, Y.; Kreiner, G. Preparation, phase stability and structure of the C36 Laves phase $Nb_{1-x}Co_{2+x}$. *Z. Kristallogr. - Cryst. Mater.* **2006**, *221*, 319−333.
(14) Conrad, M.; Pohling, C.; Webert, H.; Harbrecht, B. Atomic ordering in the Laves phases L1 $V(Co_{1-x}Si_x)_2$ (x = 0.43 and 0.56). *Z. Kristallogr. - Cryst. Mater.* **2006**, *221*, 349−356.
(15) Grytsiv, A.; Chen, X.-Q.; Witusiewicz, V. T.; Rogl, P.; Podloucky, R.; Pomjakushin, V.; Maccio, D.; Saccone, A.; Giester, G.; Sommer, F. Atom order and thermodynamic properties of the ternary Laves phase $Ti(Ti_yNi_xAl_{1-x-y})_2$. *Z. Kristallogr. - Cryst. Mater.* **2006**, *221*, 334−348.
(16) Gießelmann, E. C. J.; Engel, S.; Kostusiak, W.; Zhang, Y.; Herbeck-Engel, P.; Kickelbick, G.; Janka, O. Raman and NMR spectroscopic and theoretical investigations of the cubic Laves-phases $REAl_2$ (*RE* = Sc, Y, La, Yb, Lu). *Dalton Trans.* **2023**, *52*, 3391−3402.
(17) Engel, S.; Gießelmann, E. C. J.; Schank, L. E.; Heymann, G.; Brix, K.; Kautenburger, R.; Beck, H. P.; Janka, O. Theoretical and ^{27}Al NMR spectroscopic investigations of binary intermetallic alkaline-earth aluminides. *Inorg. Chem.* **2023**, *62*, 4260−4271.
(18) Gießelmann, E. C. J.; Engel, S.; El Saudi, I.; Schumacher, L.; Radieowski, M.; Gerdes, J. M.; Janka, O. On the RE_2TiAl_3 (*RE* = Y, Gd−Tm, Lu) series—the first aluminum representatives of the rhombohedral Mg_2Ni_3Si type structure. *Solids* **2023**, *4*, 160−180.
(19) Eustermann, F.; Stegemann, F.; Gausebeck, S.; Janka, O. Structural and magnetic investigations of the pseudo ternary RE_2TAl_3 series (*RE* = Sc, Y, La−Nd, Sm, Gd−Lu; *T* = Ru, Rh, Ir)—Size dependent formation of two different structure types. *Z. Naturforsch., B* **2018**, *73*, 819−830.
(20) Seidel, S.; Pöttgen, R. $Yb_6Ir_5Ga_7$—A $MgZn_2$ Superstructure. *Z. Anorg. Allg. Chem.* **2017**, *643*, 261−265.
(21) Eustermann, F.; Stegemann, F.; Radzieowski, M.; Janka, O. Intermetallic $RE_6T_5Al_7$ phases (*RE* = Sc, Y, Ce−Nd, Sm, Gd−Lu, *T* = Ru, Ir): Diversity in their magnetic, magnetocaloric and critical properties. *Inorg. Chem.* **2019**, *58*, 16211−16226.
(22) Gießelmann, E. C. J.; Pöttgen, R.; Janka, O. Laves phases: superstructures induced by coloring and distortions. *Z. Anorg. Allg. Chem.* **2023**, *649*, No. e202300109.
(23) Janka, O.; Pöttgen, R. Isopointal intermetallics: The cP24, dca phases as a representative set of examples, along with their vacancy-ordered variants β-Mn and $SrSi_2$. *Z. Naturforsch., B* **2024**, *79*, No. 2.
(24) Villars, P.; Cenzual, K. *Pearson's Crystal Data: Crystal Structure Database for Inorganic Compounds*, release 2022/23; ASM International: Materials Park, Ohio, USA, 2023.
(25) Nowotny, H.; Wormnes, E.; Mohrnheim, A. Untersuchungen in den Systemen Aluminium-Kalzium, Magnesium-Kalzium und Magnesium-Zirkon. *Int. J. Mater. Res.* **1940**, *32*, 39−42.
(26) Cordier, G.; Czech, E.; Schäfer, H. Über eine Hochdruckmodifikation des $SrAl_2$/On a High Pressure Modification of $SrAl_2$. *Z. Naturforsch., B* **1982**, *37*, 1442−1445.
(27) Cordier, G.; Czech, E.; Schäfer, H. Zur Kenntnis der Hochdruckphase $BaAl_2$/On $BaAl_2$, a High Pressure Phase. *Z. Naturforsch., B* **1984**, *39*, 421−423.
(28) Kal, S.; Stoyanov, E.; Belieres, J.-P.; Groy, T. L.; Norrestam, R.; Häussermann, U. High-pressure modifications of $CaZn_2$, $SrZn_2$, $SrAl_2$, and $BaAl_2$: Implications for Laves phase structural trends. *J. Solid State Chem.* **2008**, *181*, 3016−3023.
(29) Nowotny, H. N. Beitrag zur Kenntnis der Systeme Aluminium-Cer und Aluminium-Lanthan. *Int. J. Mater. Res.* **1942**, *34*, 22−24.
(30) Rundle, R. E.; Wilson, A. S. The structures of some metal compounds of uranium. *Acta Crystallogr.* **1949**, *2*, 148−150.
(31) Runnalls, O. J. C. Neptunium-aluminum intermetallic compounds. *JOM* **1953**, *5*, 1460−1462.
(32) Runnalls, O. J. C. The crystal structures of some intermetallic compounds of plutonium. *Can. J. Chem.* **1956**, *34*, 133−145.
(33) Geller, S.; Matthias, B. T.; Goldstein, R. Some new intermetallic compounds with the "β-wolfram" structure. *J. Am. Chem. Soc.* **1955**, *77*, 1502−1504.
(34) Compton, V. B.; Matthias, B. T. Laves phase compounds of rare earths and hafnium with noble metals. *Acta Crystallogr.* **1959**, *12*, 651−654.
(35) Wilson, C. G. The crystal structure of $ZrAl_2$. *Acta Crystallogr.* **1959**, *12*, 660−662.
(36) Edshammar, L.-E.; Andersson, S.; et al. Studies on the zirconium-aluminium and hafnium-aluminium systems. *Acta Chem. Scand.* **1960**, *14*, 223−224.
(37) Witte, H. Untersuchungen im System Magnesium-Kupfer-Silicium mit besonderer Berücksichtigung des Schnittes $MgCu_2$-$MgSi_2$. *Z. Angew. Mineral.* **1938**, *1*, 255−268.
(38) Chumak, I. V.; Pavlyuk, V. V.; Hlukhyy, V. H.; Pöttgen, R. In *Mg2MnGa3—An Orthorhombic Derivative of the Hexagonal Laves Phase MgZn2*, Abstracts of 9th International Conference on Crystal Chemistry of Intermetallic Compounds, 2005; p 83.
(39) Noréus, D.; Eriksson, L.; Göthe, L.; Werner, P. E. Structure determination of Mg_2SiNi_3. *J. Less-Common Met.* **1985**, *107*, 345−349.
(40) Stegemann, F.; Benndorf, C.; Zhang, Y.; Bartsch, M.; Zacharias, H.; Fokwa, B. P. T.; Eckert, H.; Janka, O. Network formation by condensed tetrahedral $[Au_3Al]$ units in Na_2Au_3Al: Crystal and electronic structure, spectroscopic investigations, and physical properties of an ordered ternary auride. *Inorg. Chem.* **2017**, *56*, 1919−1931.
(41) Osters, O.; Nilges, T.; Schöneich, M.; Schmidt, P.; Rothballer, J.; Pielnhofer, F.; Weihrich, R. Cd_4Cu_7As, The first representative of a fully ordered, orthorhombically distorted $MgCu_2$ Laves phase. *Inorg. Chem.* **2012**, *51*, 8119−8127.
(42) Benndorf, C.; Eckert, H.; Janka, O. Structural characterization of intermetallic compounds by ^{27}Al solid state NMR spectroscopy. *Acc. Chem. Res.* **2017**, *50*, 1459−1467.
(43) Benndorf, C.; Stegemann, F.; Seidel, S.; Schubert, L.; Bartsch, M.; Zacharias, H.; Mausolf, B.; Haarmann, F.; Eckert, H.; Pöttgen, R.; Janka, O. Equiatomic *AEAuX* (*AE* = Ca-Ba, *X* = Al-In) Intermetallics: A Systematic Study of their Electronic Structure and Spectroscopic Properties. *Chem. - Eur. J.* **2017**, *23*, 4187−4196.
(44) Sadagopan, V.; Pollard, E.; Gatos, H. C. Superconducting transition temperatures of $ZrMo_2$, HfV_2 and $PbAu_2$. *Solid State Commun.* **1965**, *3*, 97−98.
(45) Pöttgen, R.; Gulden, T.; Simon, A. *Miniaturisierte Lichtbogenapperatur für den Laborbedarf*; GIT Labor-Fachzeitschrift, 1999; Vol. *43*, pp 133−136.
(46) Pöttgen, R.; Lang, A.; Hoffmann, R.-D.; Künnen, B.; Kotzyba, G.; Müllmann, R.; Mosel, B. D.; Rosenhahn, C. The stannides YbPtSn and $Yb_2Pt_3Sn_5$. *Z. Kristallogr.* **1999**, *214*, 143−150.
(47) *Topas*, version 5; Bruker AXS Inc.: Karlsruhe (Germany), 2014.
(48) Rietveld, H. M. Line profiles of neutron powder-diffraction peaks for structure refinement. *Acta Crystallogr.* **1967**, *22*, 151−152.
(49) Rietveld, H. M. A profile refinement method for nuclear and magnetic structures. *J. Appl. Crystallogr.* **1969**, *2*, 65−71.
(50) Elliott, R. P.; Rostoker, W. The occurrence of Laves-type phases among transition elements. *Trans. ASM* **1958**, *50*, 617−633.
(51) *Saint+*, version 6.02; includes XPREP and SADABS; Bruker AXS Inc.: Madison, WI, USA, 1999.

https://doi.org/10.1021/acs.inorgchem.4c00391
Inorg. Chem. 2024, 63, 8180−8193

(52) Palatinus, L.; Chapuis, G. SUPERFLIP—a computer program for the solution of crystal structures by charge flipping in arbitrary dimensions. *J. Appl. Crystallogr.* **2007**, *40*, 786−790.
(53) Petříček, V.; Dušek, M.; Palatinus, L. *The Crystallographic Computing System*; Institute of Physics: Praha (Czech Republic), 2006.
(54) Petříček, V.; Dušek, M.; Palatinus, L. Crystallographic computing system JANA2006: General features. *Z. Kristallogr. - Cryst. Mater.* **2014**, *229*, 345−352.
(55) Brandenburg, K. *Crystal Impact Diamond*, version 4.6.8; Bonn, Germany, 2022.
(56) *Topspin*, version 2.1; Bruker Corp: Karlsruhe, 2008.
(57) Massiot, D.; Fayon, F.; Capron, M.; King, I.; Le Calvé, S.; Alonso, B.; Durand, J.-O.; Bujoli, B.; Gan, Z.; Hoatson, G. Modelling one- and two-dimensional solid-state NMR spectra. *Magn. Reson. Chem.* **2002**, *40*, 70−76.
(58) Hohenberg, P.; Kohn, W. Inhomogeneous electron gas. *Phys. Rev. B* **1964**, *136*, 864−871.
(59) Kohn, W.; Sham, L. J. Self-consistent equations including exchange and correlation effects. *Phys. Rev. A* **1965**, *140*, 1133−1138.
(60) Kresse, G.; Furthmüller, J. Efficient iterative schemes for ab initio total-energy calculations using a plane-wave basis set. *Phys. Rev. B* **1996**, *54*, 11169−11186.
(61) Kresse, G.; Joubert, D. From ultrasoft pseudopotentials to the projector augmented-wave method. *Phys. Rev. B* **1999**, *59*, 1758−1775.
(62) Blöchl, P. E. Projector augmented-wave method. *Phys. Rev. B* **1994**, *50*, 17953−17979.
(63) Vanderbilt, D. Soft self-consistent pseudopotentials in a generalized eigenvalue formalism. *Phys. Rev. B* **1990**, *41*, 7892−7895.
(64) Perdew, J. P.; Burke, K.; Ernzerhof, M. Generalized Gradient Approximation made simple. *Phys. Rev. Lett.* **1996**, *77*, 3865−3868.
(65) Bader, R. F. W. A quantum theory of molecular structure and its applications. *Chem. Rev.* **1991**, *91*, 893−928.
(66) Williams, A. R.; Kübler, J.; Gelatt, C. D. Cohesive properties of metallic compounds: Augmented-spherical-wave calculations. *Phys. Rev. B* **1979**, *19*, 6094−6118.
(67) Eyert, V. *The Augmented Spherical Wave Method—A Comprehensive Treatment*; Springer-Verlag: Berlin Heidelberg, 2013.
(68) Hoffmann, R. How chemistry and physics meet in the solid state. *Angew. Chem., Int. Ed.* **1987**, *26*, 846−878.
(69) Emsley, J. *The Elements*; Oxford University Press: Oxford, NY, 1998.
(70) Radzieowski, M.; Benndorf, C.; Haverkamp, S.; Eckert, H.; Janka, O. On new ternary equiatomic scandium transition metal aluminum compounds ScTAl with T = Cr, Ru, Ag, Re, Pt, and Au. *Z. Naturforsch., B* **2016**, *71*, 553−566.
(71) Benndorf, C.; Niehaus, O.; Eckert, H.; Janka, O. ^{27}Al and ^{45}Sc NMR Spectroscopy on ScT_2Al and $Sc(T_{0.5}T'_{0.5})_2Al$ ($T = T'$ = Ni, Pd, Pt, Cu, Ag, Au) Heusler Phases and Superconductivity in $Sc(Pd_{0.5}Au_{0.5})_2Al$. *Z. Anorg. Allg. Chem.* **2015**, *641*, 168−175.
(72) Wondratschek, H.; Müller, U. *International Tables for Crystallography, Vol. A1: Symmetry Relations between Space Groups*; John Wiley & Sons: Chichester, Großbritannien, 2011; Vol. *A1*.
(73) Klevtsova, R. F.; Klevtsov, R. V. Synthesis and crystal structure of double molybdates $KR(MoO_4)_2$ for R^{3+} = Al, Sc, and Fe and tungstate $KSc(WO_4)_2$. *Sov. Phys. Crystallogr.* **1971**, *15*, 829−834.
(74) Huang, B.; Yvon, K.; Fischer, P. Strontium dimagnesium iron octahydride, $SrMg_2FeH_8$, containing octahedral $[FeH_6]^{4-}$ complex anions. *J. Alloys Compd.* **1992**, *187*, 227−232.
(75) Huang, B.; Yvon, K.; Fischer, P. New iron(II) complex metal hydrides with $SrMg_2FeH_8$ type structure. *J. Alloys Compd.* **1995**, *227*, 121−124.
(76) Andersen, L.; Strömberg, D.; et al. The structure of potassium sulfite. *Acta Chem. Scand.* **1986**, *40a*, 479−480.
(77) Bärnighausen, H.; Müller, U. *Symmetriebeziehungen zwischen den Raumgruppen als Hilfsmittel zur straffen Darstellung von Strukturzusammenhängen in der Kristallchemie*; Universität Karlsruhe und Universität-Gh Kassel: Germany, 1996.
(78) Müller, U. *Symmetry Relationships between Crystal Structures*; Oxford University Press, 2013.
(79) Bärnighausen, H. Group-subgroup relations between space groups: A useful tool in crystal chemistry. *MATCH, Commun. Math. Comput. Chem.* **1980**, *9*, 139−175.
(80) Müller, U. Kristallographische Gruppe-Untergruppe-Beziehungen und ihre Anwendung in der Kristallchemie. *Z. Anorg. Allg. Chem.* **2004**, *630*, 1519−1537.

https://doi.org/10.1021/acs.inorgchem.4c00391
Inorg. Chem. 2024, 63, 8180−8193

5.1.4 Systematic Investigations of the Solid Solution $Zr(V_{1-x}Al_x)_2$ Adopting the Laves Phase Structures

Published as an article (under CC-BY-NC-ND):

Elias C. J. Gießelmann, Lars Schumacher, Samir F. Matar, Stefan Engel, Guido Kickelbick and Oliver Janka, *Chem. Eur. J.* **2025**, *31*, e202404248.

https://doi.org/10.1002/chem.202404248

Contributions of the authors to this manuscript

Elias C. J. Gießelmann did the synthetic work, the evaluation of the PXRD measurements, the solid state NMR spectroscopic investigations and provided an initial draft of the manuscript. PD Dr. Oliver Janka helped with the measurement and evaluation of the SCXRD data. Dr. Stefan Engel measured the SEM/EDX data. Lars Schumacher did magnetic property measurements. Prof. Dr. Samir Matar conducted the quantum chemical calculations. Prof. Dr. Guido Kickelbick and PD Dr. Oliver Janka supervised the work and finalized the manuscript.

Summary

The results from the investigation of the previously described solid solution in the ternary system Hf–V–Al led to several new questions that had to be answered.

The first one was whether the existence of the singular compound Hf_4VAl_7 adopting the newly discovered trigonal structure type could immediately be extended by simply replacing Hf with Zr. This is highly likely as these two elements show the same electron configuration with both being a group IV element and have nearly identical ionic radii (Zr: 87, Hf: 84 pm), atomic radii (Zr: 160, Hf: 156 pm) as well as covalent radii (Zr: 145, Hf: 144 pm).[41] In addition, the question arose whether one observes the same two-phase region and amount of V that can be incorporated in the $ZrAl_2$ structure type before the structure switches from the hexagonal to the cubic Laves phase, so the same approach to synthesize the solid solution now being $Zr(V_{1-x}Al_x)_2$ was used. In contrast to the system Hf–V–Al, the system Zr–V–Al was investigated before in literature. The Pearson's Crystal Data database lists three entries (*vide infra*), being solid solutions in the Laves phase structure types as well as two publications about the phase diagram at 800 and 1100 °C are present.[205, 239] In contrast to these, a synthetic approach of slow cooling to enhance crystallinity was chosen.

The results are presented in the following publication. By combining the same methods used before, namely PXRD analysis and solid state NMR, no ordered structure could be observed regardless of the composition. For two samples, this was additionally shown with the analysis of two single crystals. For nominal compositions with $x < 0.4$, higher annealing temperatures were needed to obtain crushable and therefore analyzable melting beads. In case of the Hf system, all compounds could easily be made by applying the same temperature program. For the Zr system, no two-phase region was identified and only one sample in the cubic $MgCu_2$ structure type could be made with the nominal composition of $Zr(V_{0.875}Al_{0.125})_2$. For this, superconductivity slightly below the reported temperature of ZrV_2 (T_C = 8.2 K) was identified. For the structural parameters obtained, namely being the change in lattice parameters and (preferred) site occupancy of V and Al, an identical trend in comparison to the work on Hf–V–Al before was found. All refined compositions could be additionally underlined by SEM/EDX measurements.

Attempts to find other ternary ordered compounds were made by trying nominal composition leaving the solid solution mentioned above. This came together with the identical problem mentioned above; even higher annealing times were necessary to get to crushable melting beads that could be analyzed. Despite long annealing times and slow cooling of the samples, no further ternary compounds could be identified. All powder X-ray diffractograms show only binary phases with hints of solid solutions of V and Al in multiple structure types. These results correspond to the work published in the literature on the phase diagram.

Chemistry–A European Journal

Research Article
doi.org/10.1002/chem.202404248

Chemistry Europe
European Chemical Societies Publishing

www.chemeurj.org

Systematic Investigations of the Solid Solution $Zr(V_{1-x}Al_x)_2$ Adopting the Laves Phase Structures

Elias C. J. Gießelmann,[a] Lars Schumacher,[b] Samir F. Matar,[c] Stefan Engel,[a] Guido Kickelbick,[a] and Oliver Janka*[a]

Laves phases are an interesting field of research when it comes to structural chemistry and physical properties. Investigations of the ternary system Zr–V–Al showed, in contrast to the system Hf–V–Al, that no superstructures can be observed within the solid solution $Zr(V_{1-x}Al_x)_2$. High values of x form aluminum rich phases that adopt the hexagonal $MgZn_2$ type structure while low values of x lead to vanadium rich phases that adopt the cubic $MgCu_2$ type. All samples were investigated by powder X-ray diffraction experiments. Single crystal studies indicated that no superstructure formation is present in the investigated samples. ^{27}Al MAS NMR investigations confirmed these findings. For $ZrAl_2$, quantum-chemical calculations helped with the analysis of the ^{27}Al NMR spectrum of the binary endmember of the solid solution. Some of the prepared samples were investigated with respect to their magnetic properties. The investigated compounds show Pauli-paramagnetism, in $Zr(V_{0.875}Al_{0.125})_2$ in addition superconductivity with a critical temperature of $T_C = 4.17(1)$ K was observed. Investigations of compositions that do not belong to the Laves phase regime clearly indicate that the $MgZn_2$ type structure is still the dominant phase. Regardless of the starting composition chosen, the hexagonal Laves phase was mostly present.

Introduction

The investigations of ternary ordered variants of Laves phases within our group just recently led to the finding of the first representatives of the rhombohedral Mg_2Ni_3Si (space group $R\bar{3}m$) type structure in Al based intermetallics within the RE_2TiAl_3 (RE = Y, Gd–Tm, Lu)[1] series. In addition, we discovered a new structure type with the composition Hf_4VAl_7 (space group $P\bar{3}m1$) found during the systematic investigation of the solid solution $Hf(V_{1-x}Al_x)_2$ with x between 0 and 1.[2] Both structures are superstructures of binary Laves phases of either $MgCu_2$ in the case of the RE_2TiAl_3 series or $MgZn_2$ for Hf_4VAl_7. These observations inspired more research on the combination of two early transition metals/rare earth atoms and aluminum. While for the combination of alkaline earth metals or the rare earth elements with late transitions metals (Fe, Co and Ni group) a large number of aluminum compounds is listed in the Pearson database (>2000 entries),[3] for the combination of two early transition metals only two prominent structure types were reported namely the aluminum rich $CeCr_2Al_{20}$[4,5] and $Ho_6Mo_4Al_{43}$.[6]

Laves phases all exhibit the same general composition AB_2, however, they crystallize in three distinct structure types, namely $MgCu_2$ $(Fd\bar{3}m)$,[7] $MgZn_2$[8,9] and $MgNi_2$[10,11] (both $P6_3/mmc$). They are of general interest because of their interesting physical properties and the possibilities for applications. To give some examples, Laves phases can be used as hydrogen storage materials,[12] exhibit superconductivity,[13] and are investigated as magnetocaloric materials.[14] Their structure types play a major role in intermetallic aluminum chemistry with all rare earth elements,[15,16] Ca–Ba[17] and the group IV elements Zr and Hf forming compounds with the general composition MAl_2.[18,19] Moreover, the structural variety of superstructures that can be derived from the three prototypes by coloring and distortions was presented in a recent review article and shall only be briefly discussed here.[20]

A simple coloring of the two Zn positions in the $MgZn_2$ type structure leads to the formation of the Mg_2Cu_3Si type structure adopting the same space group $P6_3/mmc$.[21] The same stoichiometry is not allowed for the cubic $MgCu_2$ type without a symmetry reduction leading to the already mentioned Mg_2Ni_3Si type crystallizing with space group $R\bar{3}m$.[22] The Mo_2Al_3C type structure (space group $P4_132$)[23] as well as a coloring variant of URe_2 (space group $Cmcm$),[24] itself being a distortion variant of $MgZn_2$, and Mg_2MnGa_3[25] are known. The list of possible superstructures can be continued with $Yb_6Ga_5Ir_7$ (space group $P6_3/mcm$),[26] Cd_4Cu_7As (space group $Pnnm$)[27] or $MnCu_4In$ (space group $P6_3mc$).[28] For more detailed information we refer to the review articles[20,29] and primary literature mentioned before.

In the above-mentioned study of the ternary system Hf–V–Al, the solid solution $Hf(V_{1-x}Al_x)_2$ was synthesized for many different values of x = 0–1. For small values of x a disorder in

[a] E. C. J. Gießelmann, S. Engel, G. Kickelbick, O. Janka
Inorganic Solid State Chemistry, Saarland University, Campus C4.1, 66123 Saarbrücken, Germany
E-mail: oliver.janka@uni-saarland.de

[b] L. Schumacher
Institut für Anorganische und Analytische Chemie, Universität Münster, Corrensstrasse 30, 48149 Münster, Germany

[c] S. F. Matar
Lebanese German University, P.O. Box 206, Sahel-Alma, Jounieh 1200, Lebanon

Supporting information for this article is available on the WWW under https://doi.org/10.1002/chem.202404248

the cubic $MgCu_2$ type was observed, followed by a two-phase region. With medium to high Al content ($x > 0.75$) a solid solution crystallizing in the $MgZn_2$ type was observed. The chemical compositions could be proven by SEM/EDX measurements alongside Rietveld refinements of the powder X-ray diffraction data. The formation of a disordered solid solution was furthermore proven by ^{27}Al solid state NMR except for the nominal composition $Hf(V_{0.125}Al_{0.875})_2$, which surprisingly showed two distinct signals. Subsequent single crystal X-ray analysis revealed a new superstructure of $MgZn_2$ with the composition Hf_4VAl_7, crystallizing in the trigonal crystal system with space group $P\bar{3}m1$.[2] Motivated by this work, we extended the characterization of Laves phases to the ternary system Zr–V–Al. With Zr and Hf both being a group 4 elements and having almost identical covalent radii (Zr: 145; Hf: 144 pm[30]) one could expect a similar behavior e.g. superstructure formation. It is moreover possible to investigate the samples with ^{27}Al NMR[31] as well as SEM/EDX.

In the related Zr–V–Al system, thus far only four entries ($Zr_{0.88}V_{0.36}Al_{2.76}$, Cu_3Au type[32]; ZrVAl, $MgZn_2$ type[33,34]; and $ZrV_{1.85}Al_{0.15}$ $MgCu_2$ type[34]) can be found in the Pearson database.[3] In addition to the literature focusing on the crystal-chemical aspects of these intermetallic compounds, also important publications addressing the phase diagram at the isothermal section at 1073 K (800 °C)[35] and 1373 K (1100 °C)[32] must be mentioned. Here, another ternary compound is mentioned. The compound exhibits a chemical composition with 10.0–16.5 at% Zr, 52.8–55.2 at% Al and 29.3–36.3 at% V and crystallizes in a tetragonal structure with lattice parameters of $a = 658.5$ and $c = 517.3$ pm.[35] A detailed crystallographic investigation of this compound, however, is yet missing. Furthermore, a detailed analysis of the *Liquidus* projection[36] has been reported. In all of these reports a wide existence range of the hexagonal Laves phase is observed.

The absence of ordered ternary compounds besides the above-mentioned structure types, however, does not apply to the adjacent elements of Al in the periodic table. Here, the gallides $Zr_3V_2Ga_4$ (own type),[37] $Zr_2V_3Ga_4$ ($Zr_2Nb_3Ge_4$ type),[38] ZrV_2Ga_4 ($YbMo_2Al_4$ type),[39] the silicide ZrVSi (PbFCl/MnAlGe type)[40] and the germanide ZrVGe (UGeTe type)[41] are known besides many disordered pseudo-ternary compounds.[3] Therefore, it should be emphasized that we searched for possible fully ordered ternary compounds instead of pseudo-ternaries from a crystal chemical point of view. In contrast to the studies of isothermal sections of the phase diagram a synthesis based strategy, involving long annealing times and rather slow cooling rates (in contrast to quenching the samples) was employed.

Motivated by the observation of the new ternary ordering variant Hf_4VAl_7, we choose to investigate the Zr–V–Al system focusing on the solid solution $Zr(V_{1-x}Al_x)_2$ with special focus on changes in the lattice parameters and structural investigations using single crystal X-ray diffraction in combination with NMR crystallography on the ^{27}Al nucleus to search for possible superstructures in this system.

Experimental

Synthesis

Starting materials for the synthesis of all compounds described herein were zirconium, vanadium and aluminum, all purchased from Onyxmet (Olsztyn, Poland) with stated purities higher than 99.9%. For the synthesis of all compounds discussed, stochiometric amounts of the elements were used, samples were prepared on the 300–400 mg scale. In all cases, the starting materials were arc-melted[42] in a custom build arc-melting apparatus in a water-cooled copper hearth under 800 mbar argon pressure. The argon gas was purified with titanium sponge (873 K), molecular sieves, active carbon and silica gel. The obtained buttons were remelted several times to ensure high homogeneity. The as-cast buttons were sealed in fused silica ampoules and annealed in muffle furnaces (Nabertherm 11/HR, Lilienthal/Bremen, Germany). Corundum crucibles were used for some samples. The exact annealing temperatures and times can be found in Table 1. The samples were heated to the given temperature within six hours and then dwelled at this temperature for the time listed, followed by cooling to 623 K or 773 K at a rate of 5 K min^{-1}. Subsequently, the furnace was switched off and allowed to cool to room temperature. Unless stated otherwise, the annealing led to X-ray pure samples; the specimens are stable in air over months and show metallic luster, ground samples are grey.

Powder X-Ray Diffraction

The pulverized samples of all discussed compounds were investigated by powder X-ray diffraction experiments at room temperature on a D8-A25-Advance diffractometer (Bruker, Karlsruhe, Germany) in Bragg-Brentano θ-θ-geometry (goniometer radius 280 mm) with non-monochromatic Cu $K_{\alpha1,2}$-radiation ($\lambda = 154.0596$ and 154.4425 pm). Diffraction patterns were recorded between 6

Table 1. Annealing temperatures and times after arc-melting of the solid solution $Zr(V_{1-x}Al_x)_2$ for $x = 0.125$–1, and other compositions in the ternary system Zr–V–Al.

Nominal composition	Annealing	PXRD
$ZrAl_2$	as-cast	S1
$Zr(V_{0.125}Al_{0.875})_2$	1273 K – 10 d	S2
$Zr(V_{0.25}Al_{0.75})_2$	1273 K – 10 d	S3
$Zr(V_{0.334}Al_{0.667})_2$	1123 K – 12 d	S4
$Zr(V_{0.417}Al_{0.583})_2$	1123 K – 12 d	S5
$Zr(V_{0.5}Al_{0.5})_2$	1123 K – 12 d	S6
$Zr(V_{0.583}Al_{0.417})_2$	1123 K – 12 d	S7
$Zr(V_{0.625}Al_{0.375})_2$	1273 K – 10 d	S8
$Zr(V_{0.667}Al_{0.334})_2$	1273 K – 10 d	S9
$Zr(V_{0.75}Al_{0.25})_2$	1273 K – 10 d	S10
$Zr(V_{0.875}Al_{0.125})_2$	1273 K – 10 d	S11
$ZrVAl_6$	1273 K – 10 d	S12
$ZrVAl_2$	1273 K – 10 d	S13
ZrV_2Al	1273 K – 10 d	S14
Zr_2Val	1423 K – 4 d	S15
Zr_2V_2Al	1273 K – 10 d	S16
Zr_2VAl_2	As-cast	S17
ZrV_2Al_2	1423 K – 4 d	S18

and 130° 2θ with a step size of 0.013° and a total scan time of 1 h. A 12 μm Ni foil working as K_β filter and a variable divergence slit were mounted at the primary beam side. On the secondary beam side, a LYNXEYE detector with 192 channels was used. The recorded data was evaluated using the Bruker TOPAS 5.0 software[43] using the fundamental parameter approach and the Rietveld method.[44,45] Details of the refinements are listed in Tables 2–4. All recorded powder X-ray patterns are shown in the electronic supporting information (ESI) in Figures S1–S18.

Single-Crystal X-Ray Diffraction

From the annealed crushed samples, single crystals of nominal compositions $Zr(V_{0.625}Al_{0.375})_2$ and $Zr(V_{0.125}Al_{0.875})_2$ were isolated and investigated at room temperature on a Bruker X8 APEX2 Nonius κ-CCD or a Bruker D8 Venture diffractometer, both operating with graphite monochromated Mo $K_{\alpha1}$ ($\lambda = 71.073$ pm) radiation. Multi-scan absorption corrections using the Bruker SadABS data package[47] were applied to the data sets. The data was solved and

Table 2. Lattice parameters, refined from powder X-ray diffraction, of the solid solution $Zr(V_{1-x}Al_x)_2$ for $x = 0.125–1$, as well as the refined composition x_{ref}. Standard deviations of the refined lattice parameters are ≤0.1 pm and ≤0.02 for x of the refined composition. The values obtained from single crystal studies are highlighted by §.

Compound	x_{theo}	x_{ref}	obs. Prototype	a/pm	c/pm	V/nm^3	Ref.
$ZrAl_2$ – PXRD	1	1	$MgZn_2$	528.4	875.0	0.2116	*
$ZrAl_2$	1	1	$MgZn_2$	528.2	874.8	0.2114	[18]
$Zr(V_{0.125}Al_{0.875})_2$	0.875	0.92	$MgZn_2$	530.6	869.4	0.2120	*
$Zr(V_{0.125}Al_{0.875})_2$	0.875	0.88	$MgZn_2$	530.3	868.6	0.2115	*,§
$Zr(V_{0.25}Al_{0.75})_2$	0.75	0.75	$MgZn_2$	531.6	867.4	0.2122	*
$Zr(V_{0.334}Al_{0.667})_2$	0.667	0.76	$MgZn_2$	531.5	867.0	0.2121	*
$Zr(V_{0.417}Al_{0.583})_2$	0.583	0.675	$MgZn_2$	531.0	866.8	0.2116	*
$Zr(V_{0.5}Al_{0.5})_2$	0.5	0.63	$MgZn_2$	530.3	867.0	0.2111	*
$Zr(V_{0.5}Al_{0.5})_2$	0.5	–	$MgZn_2$	530.9	865.5	0.2113	[33]
$Zr(V_{0.5}Al_{0.5})_2$	0.5	–	$MgZn_2$	529.8	865.8	0.2105	[34]
$Zr(V_{0.583}Al_{0.417})_2$	0.417	0.43	$MgZn_2$	529.5	866.9	0.2105	*
$Zr(V_{0.625}Al_{0.375})_2$	0.375	0.36	$MgZn_2$#	529.0	866.5	0.2100	*
$Zr(V_{0.625}Al_{0.375})_2$	0.375	0.39	$MgZn_2$	528.2	865.3	0.2091	*,§
$Zr(V_{0.667}Al_{0.334})_2$	0.334	0.39	$MgZn_2$#	528.6	866.2	0.2096	*
$Zr(V_{0.75}Al_{0.25})_2$	0.25	0.28	$MgZn_2$#	527.9	865.5	0.2089	*
$Zr(V_{0.875}Al_{0.125})_2$	0.125	0.21	$MgCu_2$#	746.0	*a*	0.4152	*
$Zr(V_{0.925}Al_{0.075})_2$	0.075	–	$MgCu_2$	744.8	*a*	0.4118	[34]
ZrV_2	0	0	$MgCu_2$	745.0	*a*	0.4135	[46]

* This work; § single crystal data (see Table 5 and 6); # In these synthesis "ZrV" (Ti_2Ni type) and V (W type) could be identified as impurities <3 mass%.

Table 3. Atomic positions and the refined site occupancies for the members of the solid solution $Zr(V_{1-x}Al_x)_2$ for $x = 0.125–1$. Standard deviations of the refined site occupancies are ≤0.01. The values obtained from single crystal studies are highlighted.

Compound	Obs. Prototype	Occ(Al)/occ(V)		Atomic positions		
		*M*1(6*h*)	*M*2(2*a*)	M_{cub} (16*c*)	*z*(Zr)	*x*(*M*1)
$ZrAl_2$	$MgZn_2$	1/0	1/0	–	0.56447(7)	0.1702(2)
$Zr(V_{0.125}Al_{0.875})_2$	$MgZn_2$	1/0	0.68/0.32	–	0.56192(8)	0.1715(2)
$Zr(V_{0.125}Al_{0.875})_2$	$MgZn_2$	0.96/0.04	0.65/0.35	–	0.56170(2)	0.16991(4)*
$Zr(V_{0.25}Al_{0.75})_2$	$MgZn_2$	0.77/0.23	0.67/0.33	–	0.56295(8)	0.1673(2)
$Zr(V_{0.334}Al_{0.667})_2$	$MgZn_2$	0.81/0.19	0.59/0.41	–	0.56327(7)	0.1690(2)
$Zr(V_{0.417}Al_{0.583})_2$	$MgZn_2$	0.65/0.55	0.75/0.25	–	0.56387(7)	0.1700(2)
$Zr(V_{0.5}Al_{0.5})_2$	$MgZn_2$	0.62/0.38	0.66/0.34	–	0.56388(7)	0.1697(2)
$Zr(V_{0.583}Al_{0.417})_2$	$MgZn_2$	0.38/0.62	0.59/0.41	–	0.56262(7)	0.1695(2)
$Zr(V_{0.625}Al_{0.375})_2$	$MgZn_2$	0.31/0.69	0.5/0.5	–	0.56193(10)	0.1693(2)
$Zr(V_{0.625}Al_{0.375})_2$	$MgZn_2$	0.33/0.67	0.58/0.42	–	0.56292(2)	0.17028(4)*
$Zr(V_{0.667}Al_{0.334})_2$	$MgZn_2$	0.32/0.68	0.59/0.41	–	0.56304(11)	0.1701(2)
$Zr(V_{0.75}Al_{0.25})_2$	$MgZn_2$	0.23/0.77	0.41/0.59	–	0.56094(10)	0.1690(2)
$Zr(V_{0.875}Al_{0.125})_2$	$MgZn_2$	–	–	0.21/0.79	3/8	0

* Single crystal data (see Table 5 and 6).

Table 4. Rietveld results for the other compositions. In the cases of mixed occupied sites, the obtained *x* values determined are given. Standard deviations of the refined lattice parameters are ≤0.1 pm, ≤1 for the mass% and ≤0.02 for the refined composition.

Nominal comp.	observed phases	mass%	structure type	space group	*a*/pm	*c*/pm	x_{ref}
$ZrVAl_6$	$ZrAl_3$	59	own type	*I*4/*mmm*	400.4	1726.8	–
	VAl_3	41	$TiAl_3$	*I*4/*mmm*	379.8	838.0	–
$ZrVAl_2$	$Zr(V_{1-x}Al_x)_2$	77	$MgZn_2$	$P6_3/mmc$	530.8	869.4	0.88
	V	23	W	$Im\bar{3}m$	305.6	*a*	–
ZrV_2Al	$Zr(V_{1-x}Al_x)_2$	72	$MgZn_2$	$P6_3/mmc$	530.3	866.8	0.59
	V	24	W	$Im\bar{3}m$	303.3	*a*	–
	ZrV	4	Ti_2Ni	$Fd\bar{3}m$	1221.7	*a*	–
Zr_2VAl	$Zr(V_{1-x}Al_x)_2$	42	$MgZn_2$	$P6_3/mmc$	530.3	867.8	0.51
	ZrV	38	Ti_2Ni	$Fd\bar{3}m$	1222.0	*a*	–
	Zr_5Al_3	20	Mn_5Si_3	$P6_3/mcm$	817.5	564.6	–
Zr_2V_2Al	$Zr(V_{1-x}Al_x)_2$	77	$MgZn_2$	$P6_3/mmc$	528.6	866.5	0.28
	ZrV	12	Ti_2Ni	$Fd\bar{3}m$	1220.9	*a*	–
	Zr_2Al	11	$Co_{1.75}Ge$ (Ni_2In)	$P6_3/mmc$	488.9	592.9	–
Zr_2VAl_2	$Zr(V_{1-x}Al_x)_2$	78	$MgZn_2$	$P6_3/mmc$	532.3	868.1	0.65
	$(Zr_{1-x}V_x)_3Al_2$	22	own type	$P4_2/mnm$	762.2	700.2	0.08
ZrV_2Al_2	$Zr(V_{1-x}Al_x)_2$	59	$MgZn_2$	$P6_3/mmc$	531.5	867.8	0.76
	V	41	W	$Im\bar{3}m$	303.3	*a*	–

refined using SUPERFLIP[48] and JANA2006[49,50] (*vide infra*). Details on the structure refinement, atomic coordinates as well as interatomic distances are compiled in Tables 5–7. Structural drawings were generated with Diamond 4[51] and edited with Adobe Illustrator CS6.

Deposition numbers 2390074 and 2395006 contain the supplementary crystallographic data for this paper. This data is provided free of charge by the joint Cambridge Crystallographic Data Centre and Fachinformationszentrum Karlsruhe Access Structures service.

SEM/EDX Data

Semiquantitative EDX analyses of the bulk samples were conducted on a JEOL 7000F (JEOL, Freising, Germany) scanning electron microscope equipped with an EDAX Genesis 2000 EDX detector (EDAX, Unterschleissheim, Germany). The powdered samples were sprinkled on conductive carbon tape and one area scans as well as three independent data points were measured. The results of the SEM/EDX investigations are listed in Table 8.

^{27}Al Solid State NMR

The ^{27}Al MAS-NMR spectra were recorded at 104.31 MHz on an Avance III 400 WB spectrometer (Bruker, Karlsruhe, Germany) using magic-angle spinning (MAS) conditions. The samples were ground to a fine powder and mixed with an appropriate amount of NaCl (sample:NaCl = 1:9), to reduce the density and the electrical conductivity of the sample. The diluted samples were loaded into a cylindrical ZrO_2 rotor with a diameter of 4 mm and spun at the magic angle with a frequency between 8 and 13 kHz. All experiments conducted were single-pulse experiments with typical pulse length of 0.83 μs and relaxation delays of 1 s. Resonance shifts were referenced to aqueous 1 molar $AlCl_3$ solutions. The NMR-spectra were recorded using the Bruker TOPSPIN software,[52] the analysis was performed with the help of the DMFIT program package.[53] The extracted data is compiled in Table 9.

Physical Property Measurements

The polycrystalline samples of $ZrAl_2$ as well as selected members of the solid solution $Zr(V_{1-x}Al_x)_2$ for $x = 0.5$ and 0.125 were investigated by temperature dependent magnetic susceptibility measurements at external fields up to 80 kOe (1 kOe = 7.96×10^4 A m^{-1}). The samples were glued to silica paddles using a low temperature varnish (General Electrics) and attached to the sample holder rod of a Vibrating Sample Magnetometer (VSM) option of a Physical Property Measurement System (PPMS) by Quantum Design (San Diego, USA). The magnetization data *M*(*T*,*H*) of the samples was investigated in the temperature range between 1.8 and 300 K with applied fields up to 25 kOe. The results of the physical property investigations are summarized in Table 10.

Quantum-chemical Calculations

The electronic structure of binary $ZrAl_2$ was calculated within the framework of density functional theory (DFT).[55,56] For an accurate assessment of the NMR parameters the Vienna ab initio simulation package (VASP) code[57,58] with the projector augmented wave (PAW) method[58,59] was used. The DFT exchange-correlation XC effects were accounted for within the generalized gradient approximation GGA according to Perdew, Burke and Ernzerhof.[60] The calculations were started from the experimental structure parameters (lattice constants and atomic positions in Tables 2 and 3). The calculated lattice parameters of the relaxed structures were found to be in good agreement with the experiment.

Results and Discussion

Figure 1 (green points) shows all gross compositions in the ternary system Zr–V–Al which were synthesized and annealed within this work. For the samples of the solid solution targeting

Table 5. Crystallographic data and structure refinement from single crystal X-ray diffraction experiments for nominal $Zr(V_{0.625}Al_{0.375})_2$ and $Zr(V_{0.125}Al_{0.875})_2$.

CSD number		2390074	2395006
Nominal composition		$Zr(V_{0.625}Al_{0.375})_2$	$Zr(V_{0.125}Al_{0.875})_2$
Refined composition		$Zr(V_{0.61(1)}Al_{0.39(1)})_2$	$Zr(V_{0.12(1)}Al_{0.86(1)})_2$
Structure type		$MgZn_2$	$MgZn_2$
Lattice parameters	*a* (pm)	528.24(1)	530.28(2)
	c (pm)	865.28(2)	868.63(3)
	V (nm^3)	0.2091	0.2115
Molar mass, g mol^{-1}		174.4	150.9
Density calc., g cm^{-3}		5.54	4.74
Crystal size, μm		50×40×30	50×20×20
Detector distance, mm		40	40
Exposure time, s		10	10
Range in *hkl*		h ± 8, *k* ± 8, *l* ± 14	h ± 8, *k* ± 8, *l* ± 14
θ_{min}, θ_{max}, deg		4.46, 36.31	4.44, 36.15
Linear absorption coeff., mm^{-1}		10.2	6.4
No. of reflections		6020	5608
R_{int}/R_{σ}		0.0288/0.0085	0.0298/0.0101
No. of independent reflections		226	225
Reflections used [$I \geq 3\sigma(I)$]		207	209
F(000), e		313	274
*R*1/*wR*2 for $I \geq 3\sigma(I)$		0.0094/0.0266	0.0087/0.0271
*R*1/*wR*2 for all data		0.0125/0.0280	0.0097/0.0278
Data/parameters		226/13	225/13
Goodness-of-fit on F^2		0.99	1.10
Extinction coefficient		150(30)	210(50)
Diff. Fourier residues /e^- $Å^{-3}$		+0.39/−0.31	+0.30/−0.23

Table 6. Atom positions and equivalent isotropic displacement parameters (pm^2) for nominal $Zr(V_{0.625}Al_{0.375})_2$. U_{eq} is defined as one third of the trace of the orthogonalized U_{ij} tensor.

Atom	Wyckoff position	*x*	*y*	*z*	U_{eq}	Occupation: Al/V
$Zr(V_{0.625}Al_{0.375})_2$						
Zr	4*f*	1/3	2/3	0.56292(2)	71(1)	1
Al1/V1	6*h*	0.17028(4)	2*x*	1/4	98(2)	0.33(1)/0.67(1)
Al2/V2	2*a*	0	0	0	118(1)	0.58(1)/0.42(1)
$Zr(V_{0.125}Al_{0.875})_2$						
Zr	4*f*	1/3	2/3	0.56170(2)	59(1)	1
Al1/V1	6*h*	0.16991(4)	2*x*	1/4	77(2)	0.96(1)/0.04(1)
Al2/V2	2*a*	0	0	0	84(1)	0.65(1)/0.35(1)

the Laves phase formula according to nominal $Zr(V_{1-x}Al_x)_2$ all samples could be characterized. Besides this, other compositions in the ternary system, being permutations of the general compositions 1–1–2 and 1–2–2 were tested. Moreover, the composition 1–1–6 was targeted as well since this represents a solid solution between $ZrAl_3$ and VAl_3 with the general composition $(Zr_{0.5}V_{0.5})Al_3$. One problem during this systematic investigation was that the initial annealing conditions (1123 K, 12 d) were not sufficient to obtain crushable samples. This can be due to low crystallinity or toughness of the formed phases within the melting bead. This was observed for samples with high Zr and V content. To overcome this issue, some samples had to be treated at different temperatures (see Table 1).

Table 7. Interatomic distances (pm) for nominal $Zr(V_{0.625}Al_{0.375})_2$ and $Zr(V_{0.125}Al_{0.875})_2$. Standard deviations for the interatomic distances are ≤0.2 pm.

$Zr(V_{0.625}Al_{0.375})_2$				$Zr(V_{0.125}Al_{0.875})_2$			
Zr	3	Al1/V1	309.1	Zr	3	Al1/V1	309.6
	6	Al1/V1	309.8		6	Al1/V1	311.5
	3	Al2/V2	309.8		3	Al2/V2	310.8
	4	Zr	323.8		3	Zr	324.4
					1	Zr	327.1
Al2/V2	6	Al1/V1	266.6	Al2/V2	6	Al1/V1	267.4
	6	Zr	309.8		6	Zr	310.8
Al1/V1	2	Al1/V1	258.4	Al1/V1	2	Al1/V1	259.7
	2	Al2/V2	266.6		2	Al2/V2	267.4
	2	Al1/V1	269.8		2	Al1/V1	270.3
	2	Zr	309.1		2	Zr	309.6
	4	Zr	309.8		4	Zr	311.5

Table 8. Chemical compositions determined by SEM/EDX for the members of the solid solution $Zr(V_{1-x}Al_x)_2$ for $x = 0.125–1$.

Compound	Theoretical composition (at%)			Experimental composition (at%)		
	Hf	V	Al	Hf	V	Al
$ZrAl_2$	33.3	0	66.7	36	0	64
$Zr(V_{0.125}Al_{0.875})_2$	33.3	8.3	58.3	35	9	56
$Zr(V_{0.25}Al_{0.75})_2$	33.3	16.7	50	35	16	49
$Zr(V_{0.334}Al_{0.667})_2$	33.3	22.2	44.4	35	22	43
$Zr(V_{0.417}Al_{0.583})_2$	33.3	27.8	38.9	35	27	38
$Zr(V_{0.5}Al_{0.5})_2$	33.3	33.3	33.3	35	33	32
$Zr(V_{0.583}Al_{0.417})_2$	33.3	38.9	27.8	34	39	27
$Zr(V_{0.625}Al_{0.375})_2$	33.3	41.7	25	34	42	24
$Zr(V_{0.667}Al_{0.334})_2$	33.3	44.4	22.2	35	43	22
$Zr(V_{0.75}Al_{0.25})_2$	33.3	50	16.7	35	48	16
$Zr(V_{0.875}Al_{0.125})_2$	33.3	58.3	8.3	34	57	8

Table 9. Summary of the NMR observables of $MgZn_2$ type $ZrAl_2$ extracted from the DMFit simulation of the ^{27}Al MAS-NMR spectrum with δ being the resonance shift (in ppm), C_Q the quadrupolar parameter (in kHz) and η_Q the asymmetry parameter. Theoretically calculated values from DFT are given with the subscript *calc.*

Compound	Site	δ	$C_{Q,calc}$	$C_{Q,exp}$	$\eta_{Q,calc}$	$\eta_{Q,exp}$
$ZrAl_2$	Al1 (6*h*)	−87	935	1847	0.3	0.8
	Al2 (2*a*)	−130	4802	4996	0	0.4

Investigations on the Solid Solution $Zr(V_{1-x}Al_x)_2$

X-Ray Diffraction

The members of the solid solution (light green dots in the Gibbs triangle, Figure 1) were analyzed by powder X-ray diffraction. The diffraction patterns for three examples namely for $x = 1$, 0.5 and 0.125 are depicted in Figure 2. A change in the formed structure type was apparent for high V content where the cubic Laves phase is formed. This was also observed for the

Table 10. Magnetic properties of the investigated compounds of the solid solution $Zr(V_{1-x}Al_x)_2$ for $x = 0$, 0.5, 0.125 and 1 with T_C being the critical temperature of the superconducting transition.

Compound	Structure type	T_C (K)	Susceptibility at 300 K	Ref.
$ZrAl_2$	–	–	$\chi(300\ K) = -1.07\times10^{-5}$ emu mol^{-1}	*
$Hf(V_{0.5}Al_{0.5})_2$	$MgZn_2$	–	$\chi(300\ K) = +4.99\times10^{-4}$ emu mol^{-1}	*
$Hf(V_{0.875}Al_{0.125})_2$	$MgCu_2$	4.17(1)	$\chi(300\ K) = +7.75\times10^{-4}$ emu mol^{-1}	*
ZrV_2	$MgCu_2$	8.2	–	[54]

* This work.

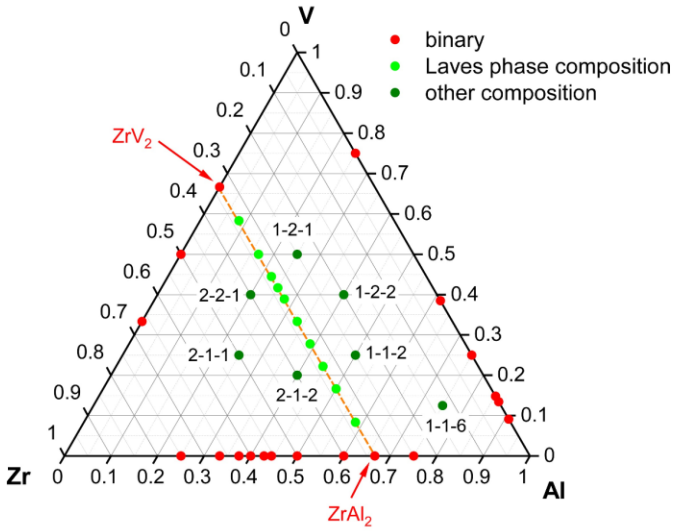

Figure 1. Gibbs triangle indicating the weighed compositions within the Zr–V–Al system. Red dots mark known binary phases. Light green dots with the orange line show the solid solution $Zr(V_{1-x}Al_x)_2$ targeting Laves phases. The dark green dots show other combinations for which the powder diffraction patterns could be analyzed.

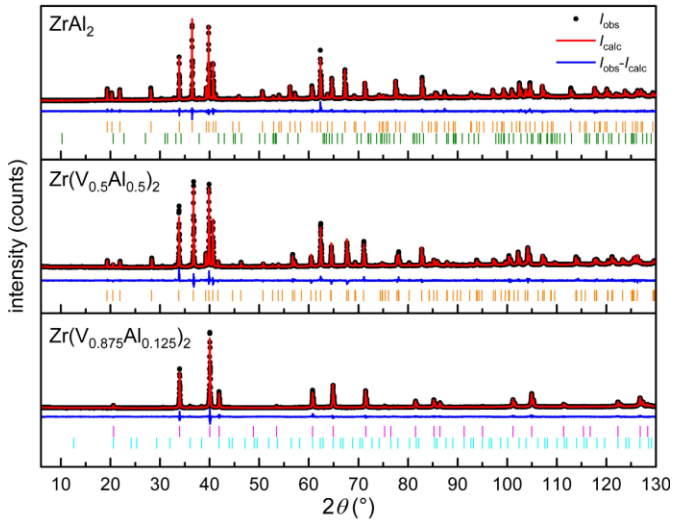

Figure 2. Powder X-ray diffraction patterns of two selected samples of the solid solution $Zr(V_{1-x}Al_x)_2$ and the end member $ZrAl_2$. Experimental data is shown as black dots, simulated diffraction patterns from refinements as red lines, the difference is shown as continuous blue lines, and the Bragg positions are shown as orange (hexagonal Laves phase, space group $P6_3/mmc$), pink (cubic Laves phase, space group $Fd\bar{3}m$), green ($ZrAl_3$, space group $I4/mmm$) and cyan ("ZrV", space group $Fd\bar{3}m$) ticks.

already discussed Hf–V–Al system.[2] Into the cubic $MgCu_2$ type structure of ZrV_2 only small amounts of Al can be incorporated, which is also reported in the literature.[34] Therefore, for all other members the $MgZn_2$ structure type was found. Figure 3 and Tables 2 and 3 depict and list the obtained lattice parameters and the resulting *V/Z* plot in dependence of *x* as well as the refined site occupancies and impurity phases.

A trend in good agreement to the Hf–V–Al system can be seen. The solid solution does not follow Vegard's rule as can be seen from the lattice parameters (Figure 3a). *V/Z* (unit cell volume per formula unit) goes through a maximum for $0.7 < x < 0.8$. This cannot be explained by a pure statistical mixing of V and Al in the structure but with some preferences regarding the site occupation. When looking at the site occupation factors (Figure 3b), a cross-over from the red and black line (occupational factor for the 2*a* and 6*h* position) is observed. This is in line with reports from the literature, e.g. $Nb(Cr_{1-x}Co_x)_2$.[61] A review by Stein and Leineweber (especially section 3.3) de-

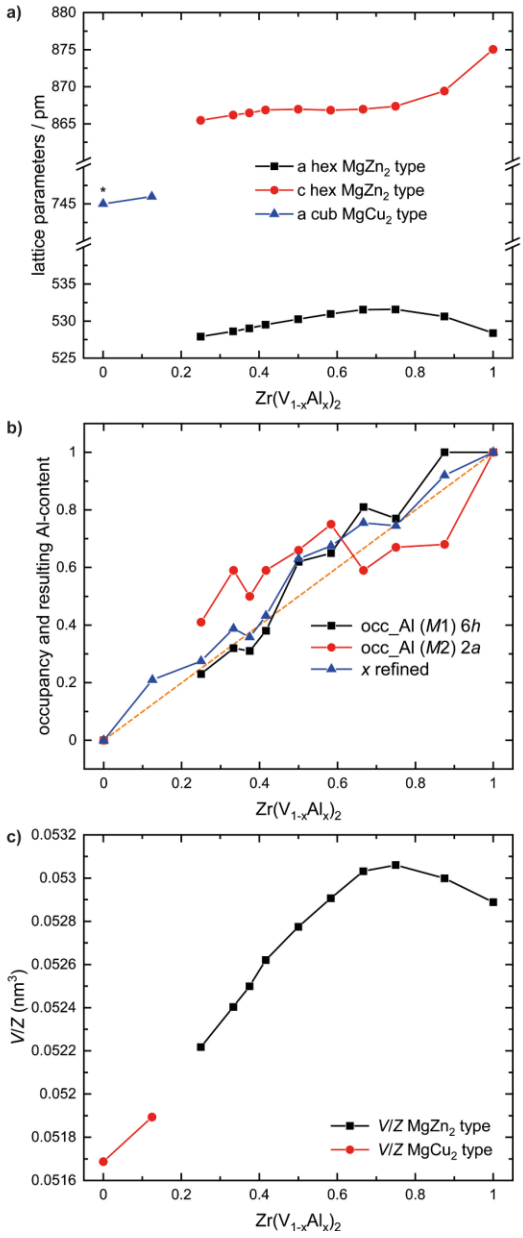

Figure 3. a) Lattice parameters, b) occupancy factors for the two Al sites in $MgZn_2$ and $MgCu_2$ structure type as well as the c) resulting volume per formula unit (*V*/*Z*), with $Z=4$ for the hexagonal $MgZn_2$ type and $Z=8$ for the cubic $MgCu_2$ type, for the solid solution $Zr(V_{1-x}Al_x)_2$.

scribes this effect in great depth.[62] The analysis of the occupancy of the two atomic positions shows that for small V contents there is a small preference for the 2*a* site (vide infra). For high vanadium contents no preference can be observed.

From two samples of the solid solution $Zr(V_{1-x}Al_x)_2$ with the nominal compositions $Zr(V_{0.625}Al_{0.375})_2$ and $Zr(V_{0.125}Al_{0.875})_2$ single crystals were isolated and investigated by X-ray diffraction measurements. The diffraction patterns showed a hexagonal lattice and space group $P6_3/mmc$ was derived to be the correct one. Isotypism with the hexagonal $MgZn_2$ type structure was already evident from the powder diffraction patterns. During the refinement, full disorder of V and Al atoms on the two respective sites (2*a* and 6*h*) was observed for nominal $Zr(V_{0.625}Al_{0.375})_2$, while for the nominal $Zr(V_{0.125}Al_{0.875})_2$, V is almost only found on the 2*a* site. But no hints for the formation of the newly discovered Hf_4VAl_7 type by symmetry reduction and full ordering were observed. The final difference Fourier syntheses were contour-less. It should be mentioned that the refined compositions $Zr(V_{0.61(1)}Al_{0.39(1)})_2$ and $Zr(V_{0.12(1)}Al_{0.86(1)})_2$ are in good agreement with the weighed ones $Zr(V_{0.625}Al_{0.375})_2$ and $Zr(V_{0.125}Al_{0.875})_2$. Details of the refinement can be found in Tables 5–7. Figure 4 depicts the unit cells of the two refined structures. At this point a detailed description of the structural details should be excluded; this can be found in detail in the literature.[2,20,63]

^{27}Al Solid State NMR

Solid state MAS-NMR experiments for all members of the solid solution resulted in very broad featureless lines. As two representatives for the whole series the NMR spectra of the above discussed samples which were investigated by single crystal X-ray diffraction (see Figure S19) underlining the fact that no distinct atomic ordering is observed in accordance with the X-ray analysis of powder and single crystals. Nevertheless, the endmember $ZrAl_2$ could nicely be analyzed, see Figure 5. Here, two resonances originating from the $|+1/2\rangle \leftrightarrow |-1/2\rangle$ central transitions can be identified which is in excellent agreement with the crystal structure. One resonance occurs as a sharp symmetric central transition with a wide spinning sideband manifold. The second one shows an asymmetric broadening due to second order quadrupolar interactions. This is also in agreement with the values for the EFG tensor obtained via DFT calculations. Details of the analysis can be found in Table 9.

Physical Properties

Hexagonal $MgZn_2$ type $ZrAl_2$ and nominal $Zr(V_{0.5}Al_{0.5})_2$ as well as cubic $MgCu_2$ type with the nominal composition $Zr(V_{0.875}Al_{0.125})_2$ were investigated by temperature dependent magnetic susceptibility measurements between 3 and 300 K at an applied field of 10 kOe. For all three compounds, diamagnetic behavior is expected due to the absence of unpaired localized electrons. The metallic character of these compounds alongside their conduction electrons, however, will induce Pauli paramagnetism. This is known to overcompensate the intrinsic diamagnetism for quite a few compounds. Figure 6a depicts the magnetic susceptibility data for all investigated compounds. It is clearly visible that all traces show a temperature independent behavior with the data of $ZrAl_2$ being negative. Here intrinsic diamagnetism dominates over the Pauli paramagnetism. For $Zr(V_{0.875}Al_{0.125})_2$, a sudden drop of susceptibility can be observed

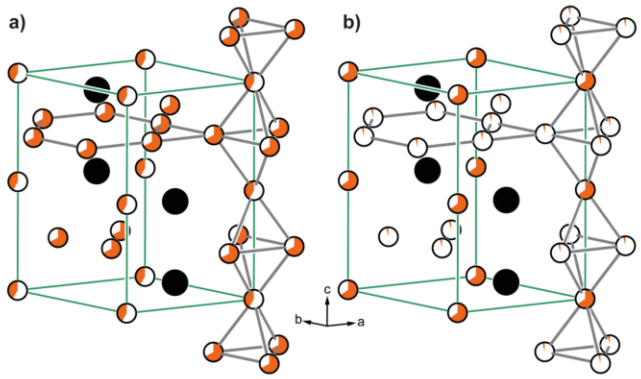

Figure 4. Single crystal structure of a) $Zr(V_{0.61(1)}Al_{0.39(1)})_2$ and b) $Zr(V_{0.12(1)}Al_{0.84(1)})_2$ both adopting the hexagonal $MgZn_2$ structure type. Zr atoms are depicted in black. The mixed site occupancy of Al (white) and V (orange) is indicated.

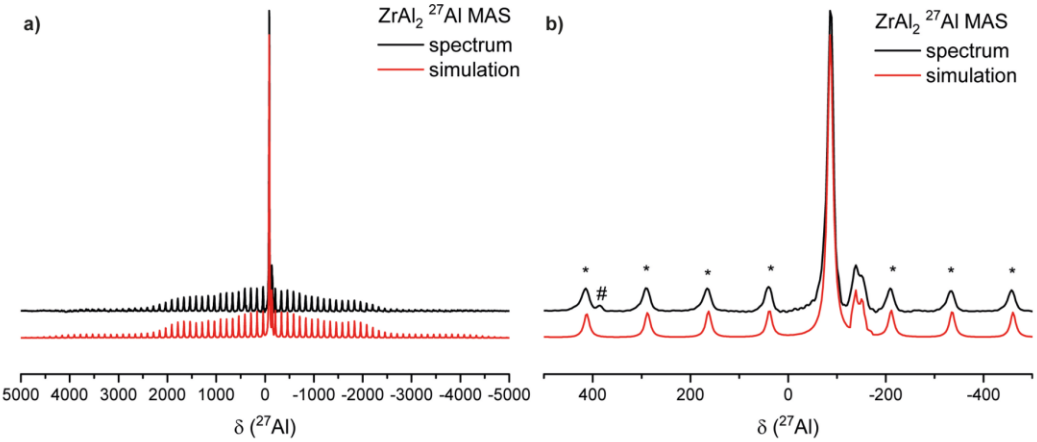

Figure 5. ^{27}Al MAS NMR spectrum of $ZrAl_2$ with a) a view of the full spectrum with all spinning sidebands while b) shows a zoom of the central transitions.

below ~6 K. This must be attributed to a superconducting transition. It is highly interesting that the superconductivity seems to be stable even at 10 kOe. The superconductivity of $Zr(V_{0.875}Al_{0.125})_2$ is not overly surprising since type-II superconductivity was already reported for ZrV_2 (cubic $MgCu_2$ type) with $T_C = 8.2$ K with a critical field of ~80 kOe.[54] Subsequently, low field measurements were conducted at an applied field of 20 Oe between 2 and 20 K. Figure 6b shows a shift of T_C to lower temperatures, which is expected due to the mixed-occupied sites in $Zr(V_{0.875}Al_{0.125})_2$. In field cooled mode, the susceptibility is less negative, but still a pronounced drop is visible. Due to the susceptibility χ being < -1, the Meissner fraction is 100%. Finally, a magnetization isotherm at 2 K was recorded (Figure 6c). In the first magnetization cycle (red) the strong diamagnetic response is visible. At ~18 kOe, the superconductivity vanishes, underlining the observed drop in susceptibility in the 10 kOe measurement (Figure 6a). The shape of the magnetization isotherm clearly indicates that $Zr(V_{0.875}Al_{0.125})_2$ is a type-II superconductor, in line with what has been observed for ZrV_2.

Investigations of other Compounds in the System Zr–V–AlPossible Zr/V Mixing in Compounds with the Formula MAl_3

As mentioned before, the investigation of the solid solution $Zr(V_{1-x}Al_x)_2$ revealed no ordered compounds, therefore, a more in-depth investigation of the ternary system was carried out, searching for other possible ternary compounds. In the first attempt it was tried to obtain mixing of V and Zr in two closely related structures with the nominal compositions $ZrAl_3$ and VAl_3. The result of the analysis of the powder X-ray diffraction data of the nominal composition $ZrVAl_6 \mathrel{\hat{=}} (Zr_{0.5}V_{0.5})Al_3$ can be seen in Figure 7. It shows the formation of the binary phases $ZrAl_3$ and VAl_3. In both structures no hints for the formation of a homogeneous solid solution according to $(Zr_{1-x}V_x)Al_3$ and $(V_{1-x}Zr_x)Al_3$ were observed. The observed two phase region of the two compounds is in accordance to findings in literature.[35] Details on the refinement and the phases identified can be found in Table 4.

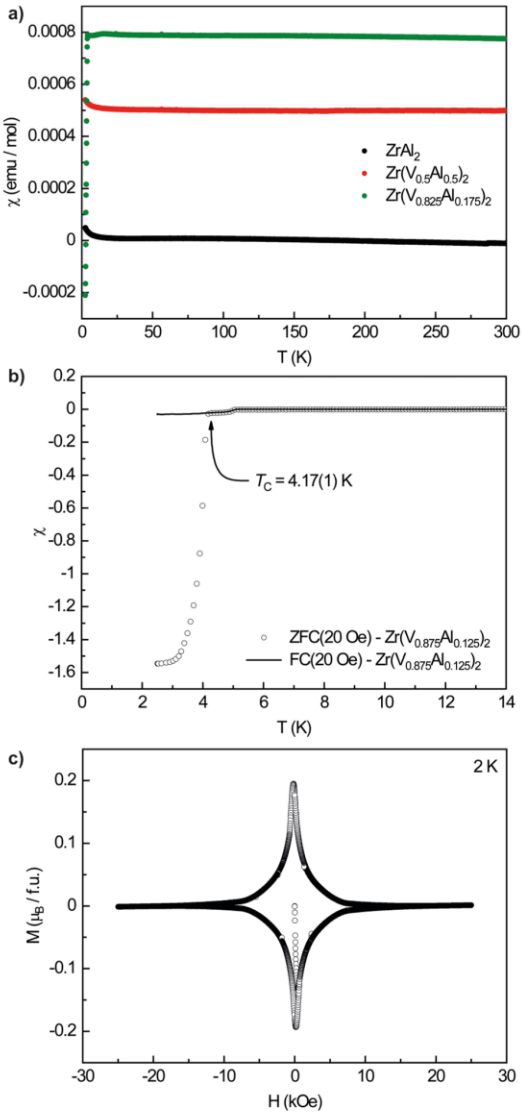

Figure 6. a) Magnetic susceptibility data of $ZrAl_2$ and the members with $x = 0.5$ and 0.125 of the solid solution $Zr(V_{1-x}Al_x)_2$. Measurements were conducted in zero-field cooled (ZFC) mode. b) Magnetic susceptibility data of $Hf(V_{0.875}Al_{0.125})_2$ measured in zero-field/field cooled (ZFC/FC) mode with 20 Oe. c) *M*(*H*) measurements of $Hf(V_{0.95}Al_{0.05})_2$ at 2 K.

Permutations of the Nominal Composition 1–1–2 & 1–2–2

As can be seen in the Gibbs diagram depicted in Figure 1 also other regions were investigated. It was tried to synthesize compounds with compositions besides the nominal AB_2 composition of the Laves phase. Known structure types for the composition 1–1-2 and its permutations are e.g. the $MgCuAl_2$ type (*Cmcm*),[64,65] the cubic Heulser phases $MnCu_2Al$ ($Fm\bar{3}m$)[66] or Cr_2AlC ($P6_3/mmc$)[67] while for 1–2–2 the important prototypes $CaBe_2Ge_2$ (*P*4/*nmm*),[68] $ThCr_2Si_2$ (*I*4/*mmm*)[69] or Mo_2FeB_2 (*P*4/*mbm*)[70] can be named. In all samples (permutations of the nominal compositions 1–1–2 and 1–2–2) the hexagonal $MgZn_2$ type structure could be identified as the main phase. Powder X-ray patterns are shown in Figure 8 for the 1–1–2 and Figure 9 for the 1–2–2 compositions. As already discussed above, the samples highly differ in crystallinity. Therefore, different annealing strategies had to be applied. Details can be found in Table 1. While the sample with the nominal composition Zr_2VAl_2 fractured after doing the reaction in the arc furnace and being a highly crystalline powder (Figure 9b), Zr_2VAl and ZrV_2Al_2 needed temperatures of 1423 K for four days to turn into a crushable melting bead enabling the analysis via powder diffraction.

Table 4 shows all the identified phases to describe the powder patterns reasonably good. All data for the refinement was taken from the Pearson crystallographic database.[3] For $ZrVAl_2$ and ZrV_2Al_2 the main side product was elemental V (and its solid solution $V_{1-x}Al_x$), adopting the W type structure. This is in line with the investigations of Zhu and coworkers.[35] This was also observed for ZrV_2Al as well as a phase crystallizing in the Ti_2Ni ($Fd\bar{3}m$) structure type, which is prone to be stabilized by impurities such as O, N or C. This is reported for the V–Zr system with different composition, either in an 1 to 1 ratio e.g. Zr_3V_3O (W_3Fe_3C type, $Fd\bar{3}m$, Zr on 48*f*, V on 32*e* and 16*d*)[71] or in a 2 to 1 ratio as observed in Zr_2V (W_4Co_2C type, $Fd\bar{3}m$, Zr on 48*f* and 16*d*, V on 32*e*)[72] with a possible stabilization by undetected impurity elements. For the Rietveld refinement of the powder diffraction data, the equiatomic composition ("ZrV") was used. Attempts to synthesize compounds with aluminum in that structure type failed.

These findings are in good agreement with the previously done experiments concerning the phase diagram at the isothermal section of 800 °C. A large range of the hexagonal $MgZn_2$ type despite the nominal composition is reported. Moreover, the reported side phases are in good to fair agreement with the findings reported here. Elemental V or the solid solution of Al and Zr in the V-structure respectively are reported to occur in the ternary system next to the $ZrAl_2$ structure. In contrast to the literature, we observe the formation of the Ti_2Ni structure as discussed above.

Although no phase pure samples were obtained it was possible to determine the lattice parameters and refine the occupancies for V and Al in the obtained $MgZn_2$ type solid solution $Zr(V_{1-x}Al_x)_2$. Figure 10a depicts the lattice parameters of the "off-stochiometric" observed $MgZn_2$ type compounds as well as the stoichiometric ones discussed above. In contrast to Figure 3, they are plotted now as a function of the refined value for *x* calculated based on the refined site occupancies, not the nominal *x*. One can easily see that they are all in good agreement with the nominal ones. A clear trend between the occupancy, or rather the solubility of V in the structure and the lattice parameters can be identified. In line with the literature discussed above all results show that the hexagonal Laves phase structure clearly dominates the ternary system Zr–V–Al. Finally Figure 10b also shows the ternary plot with the nominal compositions in dark green and the obtained composition of the $MgZn_2$ structure type.

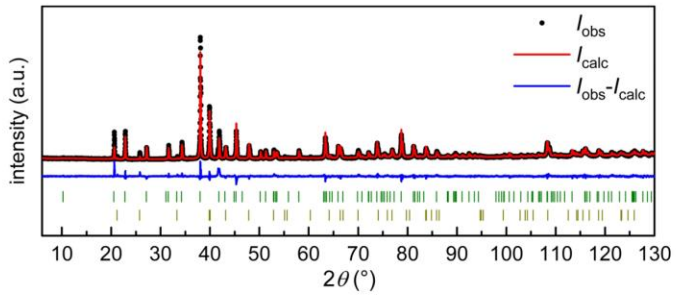

Figure 7. Powder X-ray diffraction pattern of the sample with the nominal composition $ZrVAl_6$. Experimental data is shown as black dots, simulated diffraction patterns from refinements as red lines, the difference is shown as continuous blue line, and the Bragg positions are shown as green ($ZrAl_3$, space group *I*4/*mmm*) and dark yellow (VAl_3, space group *I*4/*mmm*).

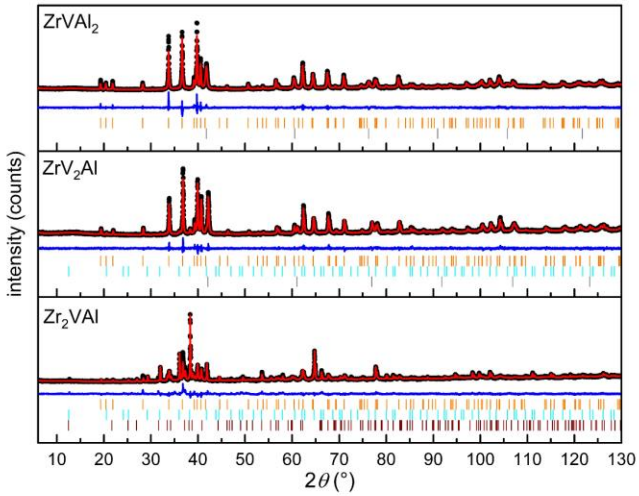

Figure 8. Powder X-ray diffraction patterns of the samples with the nominal composition $ZrVAl_2$, ZrV_2Al and Zr_2VAl. Experimental data are shown as black dots, simulated diffraction patterns from refinements as red lines, the difference is shown as continuous blue lines, and the Bragg positions are shown as orange ($MgZn_2$ type, space group $P6_3/mmc$), grey (elemental V, space group *Im*3*m*), cyan (ZrV, space group *Fd*3*m*) and brown (Zr_5Al_3, space group $P6_3/mcm$) ticks.

Conclusions

A systematic investigation of the ternary system Zr–V–Al confirmed the dominance of the $MgZn_2$ structure type described in the literature before. In all the synthesis done here, no ordered ternary compounds could be identified. Within the solid solution $Zr(V_{1-x}Al_x)_2$ adopting mainly the $MgZn_2$ type structure the analysis of lattice parameters and site occupancies shows a disordered mixing of V and Al. For two selected samples this could be additionally proven by solid state ^{27}Al NMR and single crystal X-ray measurements. For three selected samples measurements of the magnetic and physical properties were carried out. The compound $ZrAl_2$ and the solid solution $Zr(V_{0.5}Al_{0.5})_2$ both crystallizing in $MgZn_2$ structure type were found to be diamagnetic, for $Zr(V_{0.875}Al_{0.125})_2$ adopting the $MgCu_2$ structure type superconductivity below 4.17(1) K was observed. Further synthesis with different compositions all resulted in the formation of a $MgZn_2$ type structure with different side phases. In all cases different amounts of V were incorporated in the hexagonal structure of $ZrAl_2$ shown by analysis of the respective lattice parameters and site occupancies.

Author Contributions

All authors have accepted responsibility for the entire content of this submitted manuscript and approved the submission.

Acknowledgements

We thank Lukas E. Schank for the help with the preparation of some of the samples. Instrumentation and technical assistance for this work were provided by the Service Center X-ray Diffraction, with financial support from Saarland University and

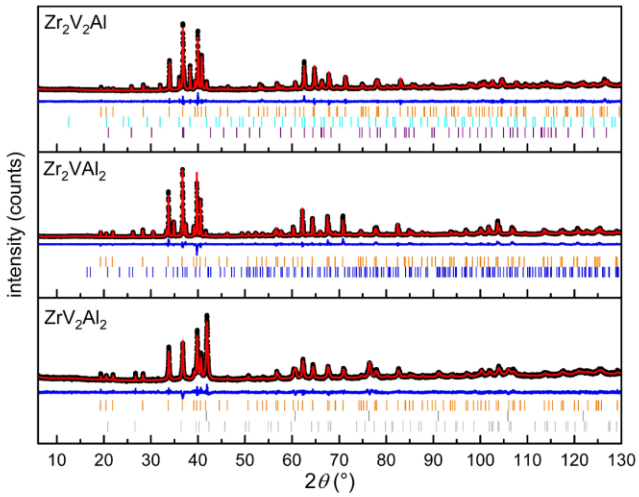

Figure 9. Powder X-ray diffraction patterns of the samples with the nominal compositions a) Zr_2V_2Al, b) Zr_2VAl_2 and c) ZrV_2Al_2. Experimental data are shown as black dots, simulated diffraction patterns from refinements as red lines, the difference is shown as continuous blue lines, and the Bragg positions are shown as orange ($MgZn_2$ type, space group $P6_3/mmc$), grey (elemental V, space group $Im3m$), cyan (ZrV, space group $Fd3m$), purple (Zr_2Al, space group $P6_3/mmc$), and blue (Zr_3Al_2, space group $P4_2/mnm$) ticks.

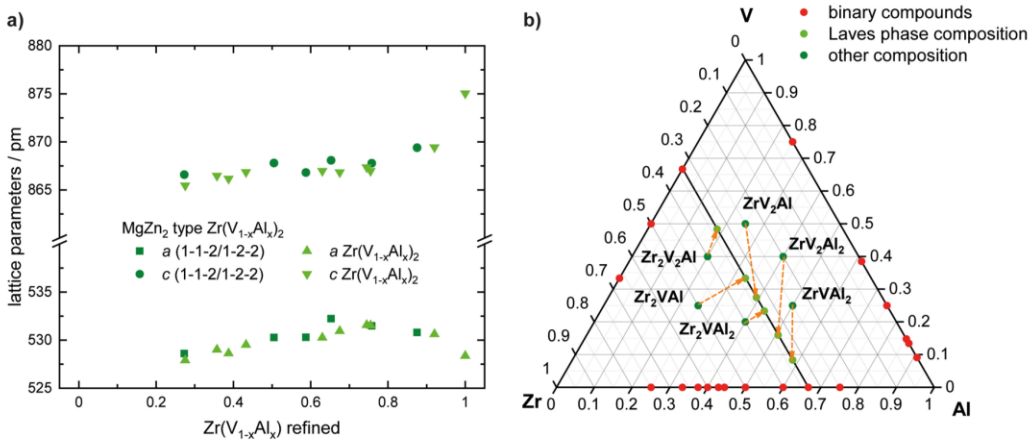

Figure 10. a) Lattice parameters shown in comparison to the refined V/Al ratio, obtained from powder X-ray diffraction. b) Ternary Zr–V–Al system with the six experimentally attempted different compositions and the Laves phase adopting $MgZn_2$ structure with the formula $Zr(V_{1-x}Al_x)_2$ obtained.

German Research Foundation (project numbers INST 256/506-1 and INST 256/349-1) and by the Service Center NMR with financial support from Saarland University and German Research Foundation DFG (project number INST 256/384-1). The magnetometer was funded by German Science Foundation DFG through INST 211/1034-1. Funding was provided by the German Science Foundation DFG (JA 1891-10-1). Open Access funding enabled and organized by Projekt DEAL.

Conflict of Interests

The authors declare no conflicts of interest regarding this article.

Data Availability Statement

The data that support the findings of this study are available from the corresponding author upon reasonable request.

Keywords: Intermetallic phases · Solid solution · Laves phases · Solid-state structures · Magnetic properties · Superconductors · Solid-state NMR

[1] E. C. J. Gießelmann, S. Engel, I. El Saudi, L. Schumacher, M. Radieowski, J. M. Gerdes, O. Janka, *Solids* **2023**, *4*, 166–180.
[2] E. C. J. Gießelmann, S. Engel, J. Baldauf, J. Kösters, S. F. Matar, G. Kickelbick, O. Janka, *Inorg. Chem.* **2024**, *63*, 8180–8193.

[3] P. Villars, K. Cenzual, *Pearson's Crystal Data: Crystal Structure Database for Inorganic Compounds*, ASM International®, Materials Park, Ohio, USA **2023**.
[4] S. Niemann, W. Jeitschko, *J. Solid State Chem.* **1995**, *114*, 337–341.
[5] R. Pöttgen, O. Janka, *Rev. Inorg. Chem.* **2023**, *43*, 357–383.
[6] S. Niemann, W. Jeitschko, *Z. Metallkd.* **1994**, *85*, 345–349.
[7] J. B. Friauf, *J. Am. Chem. Soc.* **1927**, *49*, 3107–3114.
[8] J. B. Friauf, *Phys. Rev.* **1927**, *29*, 34–40.
[9] L. Tarschisch, A. T. Titow, F. K. Garjanow, *Phys. Z. Sowjetunion* **1934**, *5*, 503–510.
[10] F. Laves, H. Witte, *Metallwirtsch* **1935**, *14*, 645–649.
[11] K. H. Lieser, H. Witte, *Z. Metallkd.* **1952**, *43*, 396–401.
[12] V. A. Yartys, M. V. Lototskyy, *J. Alloys Compd.* **2022**, *916*, 165219.
[13] V. Sadagopan, E. Pollard, H. C. Gatos, *Solid State Commun.* **1965**, *3*, 97–98.
[14] K. A. Gschneidner Jr, V. K. Pecharsky, A. O. Tsokol, *Rep. Prog. Phys.* **2005**, *68*, 1479.
[15] E. C. J. Gießelmann, S. Engel, W. Kostusiak, Y. Zhang, P. Herbeck-Engel, G. Kickelbick, O. Janka, *Dalton Trans.* **2023**, *52*, 3391–3402.
[16] K. A. Gschneidner Jr, V. K. Pecharsky, *Z. Kristallogr.* **2006**, *221*, 375–381.
[17] S. Engel, E. C. J. Gießelmann, L. E. Schank, G. Heymann, K. Brix, R. Kautenburger, H. P. Beck, O. Janka, *Inorg. Chem.* **2023**, *62*, 4260–4271.
[18] C. Wilson, *Acta Crystallogr.* **1959**, *12*, 660–662.
[19] L.-E. Edshammar, S. Andersson, *Acta Chem. Scand.* **1960**, *14*, 223–224.
[20] E. C. J. Gießelmann, R. Pöttgen, O. Janka, *Z. Anorg. Allg. Chem.* **2023**, *649*, e202300109.
[21] H. Witte, *Z. Angew. Mineral.* **1938**, *1*, 255–268.
[22] D. Noréus, L. Eriksson, L. Göthe, P. E. Werner, *J. Less-Common Met.* **1985**, *107*, 345–349.
[23] W. Jeitschko, H. Nowotny, F. Benesovsky, *Monatsh. Chem.* **1963**, *94*, 247–251.
[24] B. Hatt, *Acta Crystallogr.* **1961**, *14*, 119–123.
[25] N. Pavlyuk, I. Chumak, V. Pavlyuk, H. Ehrenberg, S. Indris, V. Hlukhyy, R. Pöttgen, *Z. Naturforsch.* **2022**, *77b*, 727–733.
[26] S. Seidel, R. Pöttgen, *Z. Anorg. Allg. Chem.* **2017**, *643*, 261–265.
[27] O. Osters, T. Nilges, M. Schöneich, P. Schmidt, J. Rothballer, F. Pielnhofer, R. Weihrich, *Inorg. Chem.* **2012**, *51*, 8119–8127.
[28] A. Provino, D. Paudyal, M. L. Fornasini, I. Dhiman, S. K. Dhar, A. Das, Y. Mudryk, P. Manfrinetti, V. K. Pecharsky, *Acta Mater.* **2013**, *61*, 2236–2243.
[29] O. Janka, R. Pöttgen, *Z. Naturforsch.* **2024**, *79b*, 63–70.
[30] J. Emsley, *The Elements*, Clarendon Press, Oxford University Press, Oxford, New York **1998**.
[31] C. Benndorf, H. Eckert, O. Janka, *Acc. Chem. Res.* **2017**, *50*, 1459–1467.
[32] A. Raman, *J. Mater. Res.* **1966**, *57*, 535–540.
[33] E. Ganglberger, H. Nowotny, F. Benesovsky, *Monatsh. Chem.* **1965**, *96*, 1658–1659.
[34] O. Kurylo, Y. V. Verbovytsky, O. R. Myakush, I. V. Koval'chuck, B. Y. Kotur, *Visn. Lviv. Derzh. Univ., Ser. Khim.* **2009**, *50*, 126–132.
[35] Y. Zhu, X. Ouyang, F. Yin, M. Zhao, J. Lou, *Metall. Mater. Trans. A* **2018**, *49*, 1859–1868.
[36] D. F. Barros, C. Nabil, J. C. P. d. Santos, D. A. Abreu, C. S. Barros, V. M. Silveira, C. A. Nunes, G. C. Coelho, *Calphad* **2024**, *84*, 102663.
[37] V. Y. Markyiv, N. M. Bjelyavyina, *Dopov. Akad. Nauk. Ukr. RSR, Ser. B* **1986**, *4*, 43–47.
[38] Y. Grin, I. S. Gavrilenko, V. Y. Markyiv, Y. P. Yarmolyuk, *Dopov. Akad. Nauk Ukr. RSR, Ser. A* **1980**, *8*, 73–76.
[39] M. C. J. Marker, H. S. Effenberger, K. W. Richter, *Solid State Sci.* **2009**, *11*, 1475–1483.
[40] Y. P. Yarmolyuk, J. Loub, E. I. Gladyshevskii, *Dopov. Akad. Nauk Ukr. RSR, Ser. A* **1973**, *10*, 943–945.
[41] A. V. Morozkin, *J. Alloys Compd.* **1999**, *289*, 10–11.
[42] R. Pöttgen, T. Gulden, A. Simon, *GIT Labor-Fachz.* **1999**, *43*, 133–136.
[43] Bruker AXS Inc., *Topas, Version 5*, Karlsruhe, Germany **2014**.
[44] H. M. Rietveld, *Acta Crystallogr.* **1967**, *22*, 151–152.
[45] H. M. Rietveld, *J. Appl. Crystallogr.* **1969**, *2*, 65–71.
[46] R. P. Elliott, W. Rostoker, *Trans. ASM* **1958**, *50*, 617–633.
[47] G. M. Sheldrick, *SADABS*, University of Göttingen, Germany **1996**.
[48] L. Palatinus, G. Chapuis, *J. Appl. Crystallogr.* **2007**, *40*, 786–790.
[49] V. Petříček, M. Dušek, L. Palatinus, *The Crystallographic Computing System*, Institute of Physics, Praha, Czech Republic **2006**.
[50] V. Petříček, M. Dušek, L. Palatinus, *Z. Kristallogr.* **2014**, *229*, 345–352.
[51] K. Brandenburg, *Crystal Impact*, Diamond, Bonn, Germany **2022**.
[52] Bruker Corp., *Topspin*, Version 2.1, Karlsruhe, Germany **2008**.
[53] D. Massiot, F. Fayon, M. Capron, I. King, S. Le Calvé, B. Alonso, J.-O. Durand, B. Bujoli, Z. Gan, G. Hoatson, *Magn. Reson. Chem.* **2002**, *40*, 70–76.
[54] S. B. Roy, *Phil. Mag. B* **1992**, *65*, 1435–1443.
[55] P. Hohenberg, W. Kohn, *Phys. Rev. B* **1964**, *136*, 864–871.
[56] W. Kohn, L. J. Sham, *Phys. Rev. A* **1965**, *140*, 1133–1138.
[57] G. Kresse, J. Furthmüller, *Phys. Rev. B* **1996**, *54*, 11169–11186.
[58] G. Kresse, D. Joubert, *Phys. Rev. B* **1999**, *59*, 1758–1775.
[59] P. E. Blöchl, *Phys. Rev. B* **1994**, *50*, 17953–17979.
[60] J. P. Perdew, K. Burke, M. Ernzerhof, *Phys. Rev. Lett.* **1996**, *77*, 3865–3868.
[61] A. Kerkau, D. Grüner, A. Ormeci, Y. Prots, H. Borrmann, W. Schnelle, E. Bischoff, Y. Grin, G. Kreiner, *Z. Anorg. Allg. Chem.* **2009**, *635*, 637–648.
[62] F. Stein, A. Leineweber, *J. Mater. Sci.* **2021**, *56*, 5321–5427.
[63] O. Janka, *Comprehensive Inorganic Chemistry III*, Elsevier, **2023**.
[64] B. Heying, R.-D. Hoffmann, R. Pöttgen, *Z. Naturforsch.* **2005**, *60b*, 491–494.
[65] H. Perlitz, A. Westgren, *Ark. Kemi Mineral. Geol.* **1943**, *16B*, 1–5.
[66] D. P. Oxley, R. S. Tebble, K. C. Williams, *J. Appl. Phys.* **1963**, *34*, 1362–1364.
[67] W. Jeitschko, H. Nowotny, F. Benesovsky, *Monatsh. Chem.* **1963**, *94*, 672–676.
[68] B. Eisenmann, N. May, W. Müller, H. Schäfer, *Z. Naturforsch.* **1972**, *27b*, 1155–1157.
[69] Z. Ban, M. Sikirica, *Acta Crystallogr.* **1965**, *18*, 594–599.
[70] W. Rieger, H. Nowotny, F. Benesovsky, *Monatsh. Chem.* **1964**, *95*, 1502–1503.
[71] F. J. Rotella, H. E. Flotow, D. M. Gruen, J. D. Jorgensen, *J. Chem. Phys.* **1983**, *79*, 4522–4531.
[72] Y. V. Voroshilov, Y. B. Kuz'ma, *Sov. Powder Metall. Met. Ceram.* **1967**, *6*, 466–469.

Manuscript received: November 18, 2024
Accepted manuscript online: December 13, 2024
Version of record online: January 16, 2025

5.1.5 Hf_6Al_7 and $Hf_{4.44(1)}Nb_{1.56(1)}Al_7$ – The First Fully Ordered Main Group Metal Containing W_6Fe_7 Type Compound and its Ternary Coloring Variant

Published as an article (under CC BY):

Elias C. J. Gießelmann, Lena Ruck, Bernd Morgenstern, Stefan Engel, Lars Schumacher, Guido Kickelbick and Oliver Janka, *Z. Anorg. Allg. Chem.* **2025**, *651*, e202500044.

https://doi.org/10.1002/zaac.202500044

Contributions of the authors to this manuscript

Elias C. J. Gießelmann together with the assistance of Lena Ruck did the synthetic work. Elias C. J. Gießelmann evaluated the PXRD measurements, solid state NMR spectra and provided an initial draft of the manuscript. PD Dr. Oliver Janka and Dr. Bernd Morgenstern helped with the measurement and evaluation of the SCXRD data. Dr. Stefan Engel measured the SEM/EDX data. Lars Schumacher conducted magnetic property measurements. PD Oliver Janka did the quantum chemical calculations. Prof. Dr. Guido Kickelbick and PD Dr. Oliver Janka supervised the work and finalized the manuscript.

Summary

Going back to the results of the investigation of the solid solution $Hf(V_{1-x}Al_x)_2$ and the newly discovered ordering variant Hf_4VAl_7, the next question was about changing the transition metal within the network. The results for the compounds Hf_4TAl_7 (T = Ti, Ta, Cr, Mo, W, Fe and Ni) will be discussed in section 5.2.1 as unpublished results. This is because the result of the nominal composition Hf_4NbAl_7 deserved the most attention.

The analysis of the obtained powder X-ray diffractograms after annealing a sample of the nominal composition Hf_4NbAl_7 revealed the formation of a $MgZn_2$ type structure. The remaining Bragg reflections in the powder pattern could not be described with a binary Hf–Al phase present in the Pearson‘s Crystal Data database. Indexing the remaining reflections revealed a rhombohedral structure whose lattice parameters gave a match in the database. This compound, namely $Hf_{3.6}Nb_{2.3}Al_{7.1}$, is described as a ternary compound adopting the W_6Fe_7 type with a mixing of the three metals on the three W sites (3 × 6*c*) and Al occupying the two Fe sites (3*b* and 18*h*). This finding in combination with the rather obscure entry in the database led to questions about whether a ternary ordered compound or even the binary compound Hf_6Al_7 could exist. Both are answered in the following publication. The results are quite similar for Ti,

Ta and W. For following detailed studies, probably resulting in clarification about annealing strategies, Nb was chosen due to the good electron difference of the three elements which makes X-ray analysis a lot easier compared to Al/Ti or Hf/Ta/W.

A ternary ordered variant of this compound could be obtained and no mixing of all elements on the three positions is observed. The compound that forms here is nominal $Hf_4Nb_2Al_7$ with Al sitting on the two iron positions as reported, but Hf on two W positions and Nb only to be found on one site, labelling this compound a ternary ordering variant of the W_6Fe_7 structure type. Nevertheless, a full site occupation could not be detected even when using a higher amount of Nb. In single-crystal and powder analysis, a maximum of 85% Nb on this one site accompanied with a mixing with Hf was detected. The refined sum formula of this compound is then $Hf_{4.44(1)}Nb_{1.56(1)}Al_7$ or for a clarification of the site occupancy $Hf_4(Hf_{0.22}Nb_{0.78})_2Al_7$. This compound could easily be made using the arc furnace. Annealing led to better homogeneity and less mixed site-occupancy. These findings negated the question of whether a compound with an even higher amount of Nb could exist in this structure type. One could possibly think of replacing another Hf atom making the compounds $Hf_2Nb_4Al_7$. The answer to the question of what happens in this stoichiometry is not part of this thesis and must be clarified in the future. The same applies for the question what happens if one thinks about replacing one Al atom with Nb making a nominal Hf_6NbAl_6. Besides thinking about this coloring variant of W_6Fe_7, one could also think about a binary compound Hf_6Al_7, which indeed could be realized in this work, labelling it the first binary main group compound adopting this structure type. The synthetic problems making this compound are described in detail in the manuscript. No annealing strategy led to phase pure samples; the phase was observed only phase pure in two single attempts within the arc furnace labelling the compound as not very stable in comparison to other binary compounds within the phase diagram Hf–Al. Both title compounds were synthesized phase pure according to X-ray powder diffraction. Single-crystal analysis could be performed. Solid state NMR showed only one signal for the binary phase although one would expect two signals based on the crystal structure. However, the one Al site has only a Wyckoff multiplicity of 3 compared to 18 and a higher quadrupolar interaction and therefore is not visible in the NMR. The ternary compound shows a shift of the central transition compared to the binary of ~ 90 ppm showing the electronic differences between Nb and Hf. Quantum chemical calculations supported the finding that Nb only occupies one site in the structure with the two alternatives being higher in energy, probably due to strong Nb–Nb interactions shown by DFT

based calculations followed by an analysis with LOBSTER. Both samples do not show any anomaly in the magnetic susceptibility measurements being Pauli-paramagnetic.

Journal of Inorganic and General Chemistry
ZAAC
Zeitschrift für anorganische und allgemeine Chemie
www.zaac.wiley-vch.de
RESEARCH ARTICLE

DOI: 10.1002/zaac.202500044

Hf_6Al_7 and $Hf_{4.44(1)}Nb_{1.56(1)}Al_7$—the First Fully Ordered Main Group Metal Containing W_6Fe_7 Type Compound and its Ternary Coloring Variant

Elias C. J. Gießelmann, Lena Ruck, Stefan Engel, Bernd Morgenstern, Lars Schumacher, Guido Kickelbick, and Oliver Janka*

Dedicated to Professor Gordon Miller on the Occasion of his 65th Birthday

Attempts to synthesize Hf_4NbAl_7 led to the discovery of nominal $Hf_4Nb_2Al_7$ instead of the envisioned product. It was identified based on powder diffraction data. The compound can be described as a substitutional/coloring variant of the rhombohedral W_6Fe_7 type structure (space group $R\bar{3}m$). The formation of the ternary compound motivates the synthesis of the binary compound Hf_6Al_7. Different synthetic strategies lead to its discovery. The crystal structures of the binary as well as its ternary coloring variant are refined from single-crystal X-ray diffraction data showing both the same obverse–reverse twinning. For the Nb-containing phase, a composition of $Hf_{4.44(1)}Nb_{1.56(1)}Al_7$ is refined, in agreement with the powder X-ray data. Solid-state ^{27}Al NMR investigations indicate the formation of a crystalline compound; however, only one distinct signal can be observed in contrast to the two crystallographic Al positions. Magnetic susceptibility measurements confirm the expected Pauli-paramagnetic character. Quantum-chemical calculations alongside analyses of the chemical bonding with the LOBSTER program package show that a strong Hf–Hf interaction is present, which transforms into an even stronger Nb–Nb interaction in nominal $Hf_4Nb_2Al_7$. For the latter, three substitutional variants are calculated, clearly indicating the experimentally observed one as the most stable.

1. Introduction

Intermetallic aluminum compounds of the general composition $M_xT_yAl_z$ containing two early transition metals (e.g., M = group 4; T = group 5) are rather scarcely investigated and structurally characterized. The Pearson database[1] lists less than 100 entries when searching for M = Ti, Zr and Hf and T = V, Nb alongside Al. The majority of these entries are solid solutions in various structure types. Besides a mixture of all three elements on one crystallographic position, e.g., in the Mg ($P6_3/mmm$)[2] or W ($Im\bar{3}m$) type structure,[3] a significant number of entries are reported to adopt the tetragonal CuAu ($P4/mmm$)[4] or $TiAl_3$ ($I4/mmm$)[5] or the rhombohedral W_6Fe_7 ($R\bar{3}m$) type structures.[6] As for the fully ordered compounds, only $Ti_4Nb_3Al_9$ ($P4/mmm$, own type)[7] and the recently reported Hf_4VAl_7 ($P\bar{3}m1$, own type)[8] are known. The latter is a new superstructure and ternary ordering variant of $HfAl_2$,[9] which adopts the hexagonal Laves phase ($P6_3/mmc$, $MgZn_2$ type structure[10]) and was found during phase analytical investigations in the ternary system Hf–V–Al.[8] When changing to the lighter homologue of Hf, Zr, no distinct superstructures of Laves phases or any ternary ordering variant could be observed.[11] Recent review articles summarize the concept of coloring and ordering variants of Laves phases.[12,13]

Upon attempts to synthesize Hf_4NbAl_7, in analogy to Hf_4VAl_7,[8] a $MgZn_2$ type Laves phase, $Hf(Nb_{1-x}Al_x)_2$ was observed alongside a compound crystallizing in the W_6Fe_7 type structure. The latter had been reported by Fedorova as $Hf_{3.6}Nb_{2.3}Al_{7.1}$ with mixing of Hf, Nb, and Al on the three crystallographic W positions of the prototype.[14] In the rhombohedral W_6Fe_7 type structure ($R\bar{3}m$),[6] three W positions ($3 \times 6c$) and two Fe ($3b$ and $18h$) are present. The compound can be classified as a so-called Frank–Kasper phase. Frank–Kasper phases can be viewed as topologically closed packed structures with high coordination numbers (CNs) of CN = 12, 14, 15, and 16. All coordination polyhedra exhibit solely triangular faces and are strongly interpenetrating.[15,16] Examples for these Frank–Kasper phases are the A15 phases (Cr_3Si type),[17,18] the Laves phases ($MgCu_2$, $MgZn_2$ and $MgNi_2$ types),[12,17–19] and the aforementioned μ phases with W_6Fe_7 being one representative. For this specific structure type, the majority of compounds known are formed with an early transition metal (Nb, Ta, Mo, or W) together with a 3*d* transition metal (Fe, Co, Ni, and Zn). The only main group element that was reported in this structure type is Si, however, with a composition of $\approx Mn_{11}Si_2$ showing severe Mn/Si disorder.[1]

E. C. J. Gießelmann, L. Ruck, S. Engel, B. Morgenstern, G. Kickelbick, O. Janka
Solid State Inorganic Chemistry, Saarland University, Campus C4 1, 66123 Saarbrücken, Germany
E-mail: oliver.janka@uni-saarland.de
L. Schumacher
Institut für Anorganische und Analytische Chemie, Universität Münster, Corrensstrasse 28/30, 48149 Münster, Germany

Supporting information for this article is available on the WWW under https://doi.org/10.1002/zaac.202500044

In this contribution, we report on our successful syntheses of the new binary phase Hf_6Al_7 alongside its ternary coloring variant with a nominal composition close to $Hf_4Nb_2Al_7$ (both W_6Fe_7 type) and their spectroscopic characterization and the analysis of the peculiar chemical bonding.

2. Experimental Section

2.1. Synthesis

Initially, Hf_4NbAl_7 was targeted in analogy to the recently reported Hf_4VAl_7. The latter exhibited a new ternary ordering variant of the hexagonal Laves phase $MgZn_2$.[8] After phase analysis and identification of the formed products (vide infra), Hf_6Al_7 and nominal $Hf_4Nb_2Al_7$ were synthesized on-stoichiometry. All samples were prepared from the elements using hafnium and niobium pieces and aluminum turnings (all Onyxmet, Olsztyn, Poland) with stated purities above 99.5%. Samples were prepared on a 150 to 300 mg scale. For the reaction, the elements were arc-melted[20] in water-cooled copper crucible in an argon atmosphere of about 800 mbar with the different molar ratios given in Table S1 (Supporting Information). The argon gas was purified over titanium sponge (873 K), molecular sieves, and silica gel prior to the use. Subsequently, some of the arc-melted ingots were sealed in silica glass ampoules and heat-treated in muffle furnaces (Nabertherm 11/HR, Lilienthal/Bremen, Germany) with different temperature schemes for different lengths. A summary of the conducted syntheses alongside their analysis is given in Table S1 (Supporting Information). All melting beads are silver metallic; ground powders are grey. The samples were stable in air over weeks.

2.2. Powder and Single-Crystal X-Ray Diffraction

The pulverized samples of all discussed compounds were investigated by powder X-ray diffraction experiments at room temperature on a D8-A25-Advance diffractometer (Bruker-AXS, Karlsruhe, Germany) in Bragg-Brentano θ-θ-geometry (goniometer radius 280 mm) with non-monochromatic Cu $K_{\alpha1,2}$-radiation ($\lambda = 154.0596$ and 154.4425 pm). Diffraction patterns were recorded between 6 and 130° 2θ with a step size of 0.013° and a total scan time of 1 h. A 12 µm Ni foil working as K_β filter and a variable divergence slit were mounted at the primary beam side. On the secondary beam side, a LYNXEYE detector with 192 channels was used. The recorded data was evaluated using the Bruker TOPAS 5.0 software[21] employing the fundamental parameter approach and the Rietveld method.[22,23] Details regarding the refined sample compositions are listed in **Table 1**, the lattice parameters and refined compound compositions of the single-phase samples according to powder X-ray diffraction data are listed in **Table 2**. Additional powder X-ray patterns are shown in the electronic Supporting Information in Figure S1–S3.

From the annealed crushed samples, single crystals of Hf_6Al_7 and nominal $Hf_4Nb_2Al_7$ were isolated and investigated at room temperature on a Synergy-S diffractometer (Rigaku, Neu-Isenburg, Germany), operating with monochromatic Mo $K_{\alpha1}$ ($\lambda = 0.71073$ Å) radiation. Multiscan absorption corrections and scaling using the Crysalis program package[24] were applied to the data sets. The crystal structures were solved by direct methods using SHELXT[25] and refined by full matrix least squares calculations on F^2 (SHELXL2018[26]), part of the SHELX program package,[27] in the graphical user interface ShelXle.[28] Details on the structure refinement and atomic coordinates as well as interatomic distances are compiled in **Table** 2 and **3** and S2 (Supporting Information). Structural drawing were generated with Diamond 4[29] and edited with Adobe Illustrator CS6.

CSDs 2420799 and 2420800 contain the supplementary crystallographic data for this paper. The data can be obtained free of charge from The Cambridge Crystallographic Data Centre via www.ccdc.cam.ac.uk/structures.

2.3. Energy-Dispersive X-Ray Spectroscopy (EDX)

The powdered samples of Hf_6Al_7 and nominal $Hf_4Nb_2Al_7$ were semiquantitatively analyzed on a JEOL 7000F (JEOL, Freising, Germany) scanning electron microscope equipped with an EDAX Genesis 2000 EDX detector (EDAX, Unterschleissheim, Germany). The powdered samples were sprinkled on conductive carbon tape and one area scans as well as three independent data points were measured. The results of the SEM/EDX investigations are listed in **Table 4**.

Table 1. Lattice parameters and atomic positions, refined from powder X-ray diffraction, of Hf_6Al_7, $Hf_{4.30(1)}Nb_{1.70(1)}Al_7$, and literature data. Standard deviations, the *z* coordinates for Hf1, Hf2, Hf/Nb3, and Al2 as well as the occupational factor of the Hf/Nb3 position are given.

Compound	*a*/pm	*c*/pm	*V*/nm³	occ(Hf/Nb3)		References
Hf_6Al_7	530.10(1)	2912.18(6)	0.7087	1		*
$Hf_{3.6}Nb_{2.3}Al_{7.1}$	520	2850	0.6674	–		[14]
$Hf_{4.30(1)}Nb_{1.70(1)}Al_7$	525.27(1)	2864.63(5)	0.6845	0.15(1)/0.85(1)		*
	z(Hf1)	*z*(Hf2)	*z*(Hf/Nb3)	*x*(Al2)	*z*(Al2)	References
Hf_6Al_7	0.33430(6)	0.14938(7)	0.04534(5)	0.5112(2)	0.0900(2)	*
$Hf_{3.6}Nb_{2.3}Al_{7.1}$	no positional parameters determined					[14]
$Hf_{4.30(1)}Nb_{1.70(1)}Al_7$	0.33447(5)	0.14909(6)	0.04416(7)	0.5017(9)	0.0905(2)	*

*This work.

Table 2. Crystallographic data and structure refinement from single-crystal X-ray diffraction experiments for Hf_6Al_7 and $Hf_{4.44(1)}Nb_{1.56(1)}Al_7$ ($R\bar{3}m$, W_6Fe_7 type, $Z = 3$).

CSD number	2420800	2420799
Nominal composition	Hf_6Al_7	$Hf_4Nb_2Al_7$
Refined composition	Hf_6Al_7	$Hf_{4.44(1)}Nb_{1.56(1)}Al_7$
Lattice parameters a (pm)	530.49(1)	525.53(1)
c (pm)	2916.38(8)	2866.12(9)
V (nm^3)	0.71077	0.68552
Molar mass [g mol^{-1}]	1529.80	1125.95
Density calc. [g cm^{-3}]	8.83	8.18
Crystal size [µm]	40 × 10 × 10	50 × 10 × 10
Detector distance [mm]	31	31
Range in hkl	$h \pm 7, k \pm 7, l \pm 40$	$h \pm 8, k \pm 8, l \pm 47$
θ_{min}, θ_{max}, deg	4.193, 29.571	4.266, 36.262
Linear absorption coeff. [mm^{-1}]	66.0	52.7
No. of reflections	4948	6292
R_{int}/R_σ	0.0561/0.0154	0.0368/0.0140
No. of independent reflections	294	471
Reflections used [$I \geq 3\sigma(I)$]	289	464
$F(000)$, e	1569	1424
$R1/wR2$ for $I \geq 3\sigma(I)$	0.0156/0.0402	0.0181/0.0411
$R1/wR2$ for all data	0.0161/0.0405	0.0186/0.0413
Data/parameters	294/20	471/21
Goodness-of-fit on F^2	1.152	1.284
Extinction coefficient	0.00014(3)	0.00030(4)
BASF	0.256	0.068
Diff. Fourier residues/e$^-$ Å^{-3}	−2.04/+1.54	−2.25/+3.00

Table 3. Atom positions and equivalent isotropic displacement parameters (pm^2) from single-crystal X-ray diffraction studies for Hf_6Al_7 and $Hf_{4.44(1)}Nb_{1.56(1)}Al_7$ ($R\bar{3}m$, W_6Fe_7 type, $Z = 3$). U_{eq} is defined as one third of the trace of the orthogonalized U_{ij} tensor. Refined site occupancies are listed.

Atom	Wyckoff position	x	y	z	U_{eq}	occ.
Hf_6Al_7						
Hf1	6*c*	0	0	0.33437(2)	52(2)	1
Hf2	6*c*	0	0	0.14936(2)	53(2)	1
Hf3	6*c*	0	0	0.04577(2)	63(2)	1
Al1	3*b*	0	0	1/2	72(10)	1
Al2	18*h*	0.5025(3)	−*x*	0.09060(6)	69(4)	1
$Hf_{4.44(1)}Nb_{1.56(1)}Al_7$						
Hf1	6*c*	0	0	0.33453(2)	44(1)	1
Hf2	6*c*	0	0	0.14878(2)	47(1)	1
Hf/Nb3	6*c*	0	0	0.04413(2)	47(2)	0.22(1)/0.78(1)
Al1	3*b*	0	0	1/2	32(5)	1
Al2	18*h*	0.50220(14)	−*x*	0.08949(4)	40(2)	1

Table 4. Chemical compositions determined by SEM/EDX for Hf_6Al_7 and nominal $Hf_4Nb_2Al_7$.

	Theoretical composition [at%]			Experimental composition [at%]		
Compound	Hf	Nb	Al	Hf	Nb	Al
Hf_6Al_7	46.2	–	53.8	45(2)	–	55(2)
$Hf_4Nb_2Al_7$	30.8	15.4	53.8	28(2)	16(2)	56(2)

2.4. ^{27}Al Solid-State NMR

The ^{27}Al MAS-NMR spectra were recorded at 104.31 MHz on an Avance III 400 WB spectrometer (Bruker, Billerica, USA) using magic-angle spinning (MAS) conditions. The samples were ground to a fine powder and mixed with an appropriate amount of NaCl (sample:NaCl = 1:9), to reduce the density and the electrical conductivity of the sample. The diluted samples were loaded into cylindrical ZrO_2 rotors with a diameter of 4 mm and spun at the magic angle with frequencies between 8 and 13 kHz. All experiments conducted were single-pulse experiments with typical pulse length of 0.83 µs and relaxation delays of 1 s. Resonance shifts were referenced to a 1 molar aqueous $AlCl_3$ solution. The NMR spectra were recorded using the Bruker TOPSPIN software,[30] the analysis was performed with the help of the DMFIT program package.[31] The extracted data is compiled in **Table 5**.

Table 5. Summary of the NMR observables of W_6Fe_7 type Hf_6Al_7 and its ternary coloring variant $Hf_4Nb_2Al_7$. The data was extracted from the DMFit simulation of the ^{27}Al MAS-NMR spectra with δ being the resonance shift (in ppm), C_Q the quadrupolar parameter (in kHz), η_Q the asymmetry parameter, *d*Cs chemical shift anisotropy parameter (in ppm). Theoretically calculated values from Density Functional Theory (DFT) are given with the subscript *calc*.

Compound	Site	δ	$C_{Q,calc}$	$\eta_{Q,calc}$	$C_{Q,exp}$	$\eta_{Q,exp}$	*d*Cs
Hf_6Al_7	Al1 (3*b*)	n.d.	2698	0.000	–	–	–
	Al2 (18*h*)	273	1816	0.220	3054	–	102
$Hf_4Nb_2Al_7$	Al1 (3*b*)	n.d.	1915	0.000	–	–	–
	Al2 (18*h*)	184	1483	0.738	–	–	–

2.5. Physical Property Measurements

The polycrystalline samples of Hf_6Al_7 and nominal $Hf_4Nb_2Al_7$ were investigated by temperature dependent magnetic susceptibility measurements at external fields up to 80 kOe (1 kOe = 7.96×10^4 A m^{-1}). The samples were glued to silica paddles using a low temperature varnish (General Electrics) and attached to the sample holder rod of a Vibrating Sample Magnetometer option of a Physical Property Measurement System (PPMS) by Quantum Design (San Diego, USA). The magnetization data *M*(*T*) of the samples was investigated in the temperature range between 2.5 and 300 K with an applied field of 10 kOe.

Table 6. Calculated total energies of Hf_6Al_7 and the three potential coloring variants for $Hf_4Nb_2Al_7$.

Compound	Nb occupied site	Total energy [eV]
Hf_6Al_7	–	−342.530
$Hf_4Nb_2Al_7$	Hf1 (6*c*)	−325.188
$Hf_4Nb_2Al_7$	Hf2 (6*c*)	−325.196
$Hf_4Nb_2Al_7$	Hf3 (6*c*)	−328.438

2.6. Quantum-Chemical Calculations

Electronic structure calculations were performed on Hf_6Al_7 and $Hf_4Nb_2Al_7$, the latter in a fully ordered variant using the projector augmented wave method of Blöchl[32,33] coded in the Vienna ab initio simulation package (VASP).[34,35] VASP calculations employed the potentials Hf_sv, Nb_sv, and Al. The cutoff energy for the plane wave calculations was set to 800 eV, and the Brillouin zone integration was carried out using a *k*-point mesh with a spacing of ≈0.02 ($11 \times 11 \times 3$) using the Monkhorst Pack algorithm.[36] The exchange–correlation effects were accounted for within the generalized gradient approximation GGA according to Perdew, Burke, and Ernzerhof.[37] The calculations were conducted starting from the experimental crystal data

Table 7. Löwdin charges and bonding interactions alongside their ICOBI values for Hf_6Al_7 and $Hf_4Nb_2Al_7$.

atom1	Löwdin Charge	atom2	#	*d* (pm)	ICOBI	atom1	Löwdin Charge	atom2	#	*d* (pm)	ICOBI
Hf_6Al_7						**$Hf_4Nb_2Al_7$**					
Hf1 (6*c*)	+0.51	Al2	3	299.1	0.24	Hf1 (6*c*)	+0.44	Al2	3	294.3	0.23
		Al2	3	303.6	0.22			Al2	3	298.7	0.21
		Hf1	3	304.9	0.34			Hf1	3	301.5	0.31
		Hf3	3	330.8	0.25			Nb	3	326.8	0.25
		Hf3	3	332.9	0.25			Nb	3	328.8	0.24
Hf2 (6*c*)	+0.65	Hf3	1	300.6	0.40	Hf2 (6*c*)	+0.51	Nb	1	295.2	0.40
		Al1	3	309.0	0.22			Al1	3	305.5	0.21
		Al2	3	312.1	0.19			Al2	3	307.0	0.19
		Al2	6	314.9	0.19			Al2	6	310.8	0.18
		Hf2	3	321.1	0.26			Hf2	3	317.3	0.29
Hf3 (6*c*)	+0.35	Hf3	1	262.1	0.70	Nb (6*c*)	+1.16	Nb	1	257.4	0.90
		Al2	6	293.8	0.23			Al2	6	290.2	0.22
		Hf2	1	300.6	0.40			Hf2	1	295.2	0.40
		Hf1	3	330.8	0.25			Hf1	3	326.8	0.25
		Hf1	3	332.9	0.25			Hf1	3	328.8	0.24
Al1 (3*b*)	−0.35	Al2	6	269.2	0.33	Al1 (3*b*)	−0.48	Al2	6	265.1	0.30
		Hf2	6	309.0	0.22			Hf2	6	305.5	0.21
Al2 (18*h*)	−0.44	Al2	2	264.0	0.35	Al2 (18*h*)	−0.62	Al2	2	261.1	0.30
		Al2	2	264.0	0.40			Al2	2	261.1	0.33
		Al1	1	269.2	0.33			Al1	1	265.1	0.30
		Hf3	2	293.8	0.23			Nb	2	290.2	0.22
		Hf1	1	299.1	0.24			Hf1	1	294.3	0.23
		Hf1	1	303.6	0.22			Hf1	1	298.7	0.21
		Hf2	1	312.1	0.19			Hf2	1	307.0	0.19
		Hf2	2	314.9	0.19			Hf2	2	310.8	0.18

and the whole cell underwent constrained geometry relaxation where the positional parameters had to be fixed. For $Hf_4Nb_2Al_7$, three models were employed with Nb fully replacing either Hf1, Hf2, or Hf3. The results are shown in **Table 6**.

For the optimized structures, the electronic structures of Hf_6Al_7 and $Hf_4Nb_2Al_7$ were projected from the plane-wave base onto a local orbital basis set using the LOBSTER (Local Orbital Basis Suite Towards Electronic-Structure Reconstruction) program package.[38–42] Based on these projections, the local density-of-states-matrices can be accessed enabling the calculation of Löwdin-related gross populations as well as atomic charges.[43] In addition, the recently introduced crystal orbital bond index (COBI) can be derived.[44] The COBI can be rationalized as the solid state pendant to the molecular bond index as introduced by Wiberg and Mayer.[45,46] When integrating the COBI values (then called ICOBI), they correspond to the covalent bond orders within the context of solid-state materials. The results of the chemical bonding analysis are given in **Table 7**.

3. Results

3.1. Synthesis and Powder X-Ray Diffraction

A sample with the element ratios Hf:Nb:Al of 4:1:7 was prepared, in analogy to Hf_4VAl_7, which is a new ternary ordering variant of the hexagonal Laves phase $MgZn_2$,[12] as reported recently.[8] The powder X-ray diffraction pattern (**Figure 1**a) indicates the formation of a multiphase mixture. Besides the hexagonal $MgZn_2$ type $Hf(Nb_{1-x}Al_x)_2$ also a rhombohedral phase could be identified. According to Pearson's Crystal Data,[1] only one compound has been reported in the ternary system Hf–Nb–Al, which is $Hf_{3.6}Nb_{2.3}Al_{7.1}$.[14] $Hf_{3.6}Nb_{2.3}Al_{7.1}$ crystallizes in the rhombohedral crystal system with space group $R\bar{3}m$ in the W_6Fe_7 type structure.[6] The sole report on this phase states that Hf, Nb, and Al show mixing on all three crystallographically independent Hf positions with the relative ratios of 0.6 Hf, 0.383 Nb, and 0.017 Al. A mixing of Hf and Nb indeed seems likely, since both elements tend to occupy cavities in a polyanionic framework, examples are $Nb(Cu_{0.5}Al_{0.5})_2$ or $Nb_6Ni_{3.1}Al_{3.9}$.[1] However, aluminum usually plays its role as a network-forming element, therefore mixing of Al onto the three Hf positions seems odd, especially with respect to the coordination environments of the Hf positions (Frank–Kasper polyhedra with CN = 14–16).

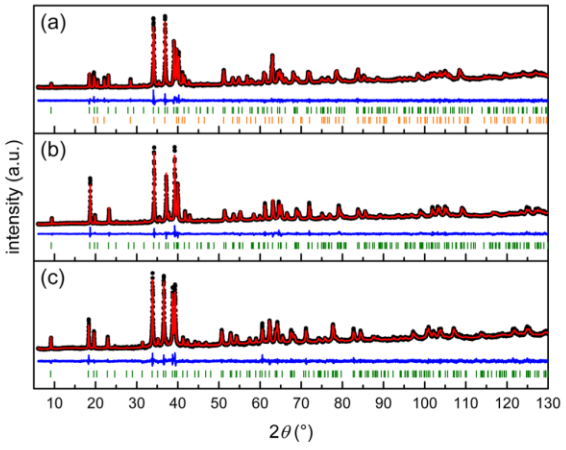

Figure 1. Rietveld refinements of different powder X-ray diffraction patterns. a) nominal Hf_4NbAl_7, b) on stoichiometry $Hf_4Nb_2Al_7$, and c) binary Hf_6Al_7. Collected data are shown as black dots, the refinement as red, and the difference as blue line. Green ticks indicate the Bragg positions of the rhombohedral W_6Fe_7 type compounds and orange ticks the $MgZn_2$ type structure.

A refinement of the site occupation factors in our sample clearly suggested that only the Hf3 position is substituted by Nb. Therefore, we decided to target the composition $Hf_4Nb_2Al_7$, where one of the three 6*c* sites (all Hf) could be solely occupied by Nb if a fully ordered structure forms. Regarding the respective coordination environments, the Hf3 position, as already observed, was expected to be the most suited one for hosting the Nb atoms due to the smallest CN (CN = 14). Syntheses with this on-stoichiometry composition led to X-ray pure compounds already in the first try (Table S1 (Supporting Information), #1). To enhance ordering of Nb and Hf atoms, the sample was annealed at 1123 K for 192 h. Based on the obtained powder X-ray diffraction data from the annealed sample (Figure 1b), the question whether the reported mixing of Hf, Nb, and Al on the three (3 × 6*c*) crystallographic sites is real was addressed. While the positions Hf1, Hf2, Al1, and Al2 were fully occupied with the respective elements, the third 6*c* position was found to be mixed-occupied by ≈86% Nb alongside ≈14% Hf (Table 2 and 3). Due to this off-stoichiometry observed both in the powder and in the single crystal (vide infra), several syntheses with varying compositions according to $Hf_{4-x}Nb_{2+x}Al_7$ with $x = 0.22$ to 1 and different annealing strategies were conducted (Table S1 (Supporting Information), #2–8). Interestingly, all of them resulted in a similar Nb/Hf mixing on the Hf3 position leading to the assumption that the Hf3 site can only be occupied with ≈85–87% Nb despite the fact that no side phases were observed until a composition of $Hf_3Nb_3Al_7$. However, during analysis of the powder X-ray diffraction patterns, it became apparent that the respective main phase showed different lattice parameters. This observation was not further investigated.

Since the ternary compound with the nominal composition $Hf_4Nb_2Al_7$ readily formed, the binary phase Hf_6Al_7 was targeted. Here, it was observed that the compound could only be obtained by arc-melting the elements (Figure 1c, Table S1 (Supporting Information), #9&10). During subsequent syntheses, it was investigated if the sample mass plays a role, since the sample mass used in during arc-melting influences the cooling rate of the sample sometimes leading to the formation of *meta*-stable high-temperature phases. However, no dominant effect was observed. Thermal treatment of samples containing side phases after arc-melting did not yield pure samples based on X-ray diffraction (Table S1 (Supporting Information) #11). Different annealing strategies of the arc-melted beads right after synthesis (without analysis) in parts led to the formation of the targeted Hf_6Al_7; however, again, no single-phase samples according to

powder X-ray diffraction were obtained (Table S1 (Supporting Information) #12–16).

3.2. Single-Crystal X-Ray Diffraction and Structure Refinement

From the single-phase samples of Hf_6Al_7 and nominal $Hf_4Nb_2Al_7$, single crystals were isolated and prepared for the diffraction experiments as stated before. The automated indexing routine identified the correct unit cell right away; however, all investigated crystals had additional domains stuck to them (**Figure 2**, red circles). The reflections of these non-merohedral twin domains do not overlap with those of the main domain and can be separated. Structure solutions and refinements were based on the data obtained from the powder X-ray diffraction experiments with Nb partially occupying one of the 6*c* positions (Hf3 site). The refinement of both data sets led to relatively high *R*-values (e.g., ≈14% wR_2 and ≈6% R_1 for $Hf_4Nb_2Al_7$) alongside high residual electron densities (13 e^- for Hf_6Al_7; 24–57 e^- for $Hf_4Nb_2Al_7$). The reconstructed reciprocal layers (Figure 2a,c) clearly indicate the presence of obverse/reverse twinning, with a twofold rotational axis along [001] being the twinning element. After introducing the twin law (–1 0 0, 0 –1 0, 0 0 1), the residual electron densities and the *R*-values dropped to the values given in Table 2. Details on the potential twin laws are given in Figure S4 of the electronic Supporting Information.

For Hf_6Al_7, no mixing between Hf and Al was observed; however, for nominal $Hf_4Nb_2Al_7$, mixing of Hf and Nb was observed on the Hf3 site. In agreement with the powder X-ray data, the former Hf3 position is occupied by 78(1)% Nb and 22(1)% Hf leading to a refined overall composition of $Hf_{4.44(1)}Nb_{1.56(1)}Al_7$. No further mixed occupied sites were observed. After the introductions of the twin law and the mixed occupied atomic position, the difference Fourier analysis showed no significant electron density minima or maxima.

Details of the structure determination, atomic parameters and interatomic distances can be found in Table 3–5. CSDs 2420799 and 2420800 contain the supplementary crystallographic data for this paper. These data can be obtained free of charge from The Cambridge Crystallographic Data Centre via www.ccdc.cam.ac.uk/data_request/cif.

3.3. Crystal Chemistry

The crystal structure of Hf_6Al_7 can be described in two ways. One can focus on the Al substructure in view of a polyanion as it is often done for ternary intermetallic compounds. In Hf_6Al_7, the Al1 atoms are surrounded by the Al2 atoms in a distorted trigonal anti-prismatic coordination environment forming three layers, which are stacked along [001] in an ⋯*ABC*⋯ sequence. The Hf2 atoms reside in cavities formed by the Al substructure. The Hf1 and Hf3 atoms connect two of these layers (**Figure 3**a). As a side note, the Hf2-Al layers are a cutout of the hexagonal $MgZn_2$ type structure.[12,19]

An alternative is the description via the respective coordination polyhedra (Figure 3b) since the compound represents a Frank–Kasper phase. All five crystallographic positions exhibit spherical coordination environments with CNs between 12 and 16. The coordination polyhedra are shown in **Figure 4**. The polyhedra of Hf1, Hf2, and Al2 are connected along the *c*-axis via common Al_3 triangles. The Hf3 atoms finally are a corner of the Hf2 coordination environment, therefore, the Hf2 and Hf3 polyhedra interpenetrate. When looking at the interatomic distances, one realizes that the Hf–Hf interactions are between 302 and 335 pm, except for one shorter Hf3–Hf3 distance with 267 pm (single crystal data). While the long distances are above the sum of the covalent radii (r_{cov}(Hf) = 144 pm),[47] this short interaction points towards somehow strong covalent bonding interactions (vide infra). Such short Hf–Hf interactions are rather rare; structurally fully ordered examples are HfIr (262 pm)[48] or $HfTe_2$ (266 pm).[49] In comparison with elemental Hf (d(Hf–Hf) = 332 and 334 pm),[50] the distances are shorter indicating somehow covalent bonding interactions. The Hf–Al interactions range between 296 and 316 pm, which is significantly longer than the sum of the covalent radii (144 + 125 = 269 pm)[47] but in line with other binaries such as $HfAl_2$ ($MgZn_2$ type, 311–312 pm)[9] or HfAl (TlI type, 279–308 pm).[51] The Al–Al interactions, finally, range between 261 and 271 pm, which is also in the typical range

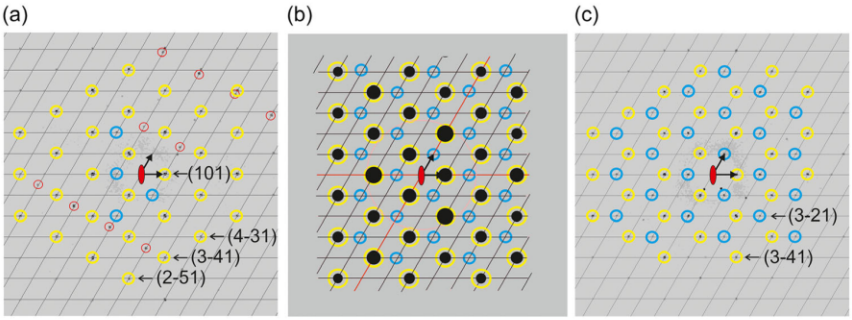

Figure 2. Reconstructed reciprocal *hk*1 layers of a) Hf_6Al_7, b) theoretical diffraction pattern created with XPrep,[68] and c) $Hf_4Nb_2Al_7$. Yellow circles indicate the reflections of the main domain (*obverse*), blue circles indicate the reflections of the twin domain (*reverse*), and red circles indicate the nonmerohedral twin domain. Selected reflections are indexed. The reflection condition for space group $R\bar{3}m$ is: $-h + k + l = 3n$ with $l = 1$.

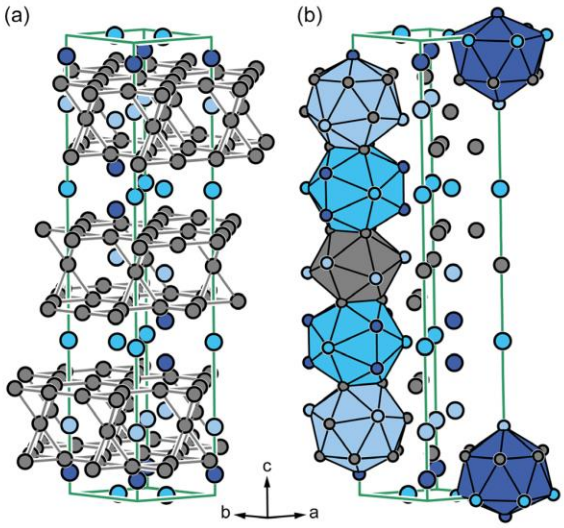

Figure 3. Crystal structure of Hf_6Al_7. a) Representation highlighting the polyanion formed by the Al atoms. b) Polyhedra representation. Al atoms are shown as grey spheres, Hf1 as light blue, Hf2 as cyan, and Hf3 as dark blue spheres.

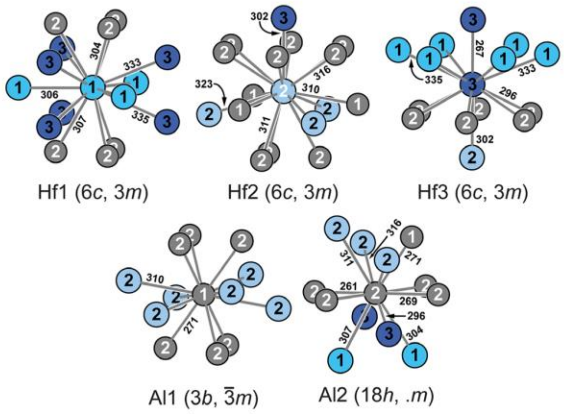

Figure 4. Coordination environments of the different crystallographically independent atomic positions in binary Hf_6Al_7. Al atoms are shown as grey spheres, Hf1 as light blue, Hf2 as cyan, and Hf3 as dark blue spheres. Interatomic distances are given in pm.

of intermetallic Al compounds (269 pm in HfAl[51] and 260–269 pm in $HfAl_2$[9]).

Upon substitution of Hf by Nb in nominal $Hf_4Nb_2Al_7$, the crystal chemistry remains the same rendering $Hf_4Nb_2Al_7$ a coloring variant of Hf_6Al_7.[52] In the following paragraph, the fully ordered denomination will be used for a better readability, knowing that the Hf/Nb3 position contains the above-mentioned occupational mixing. The Hf–Hf and Hf–Nb distances now are 300–330 pm long while the Nb–Nb interactions is now shorter with 253 pm. Similar distances can be found in the W_5Si_3 type structures (*I*4/*mcm*) given in the Pearson database.[1] From a molecular point of view, different complexes with a wide range of Nb–Nb interactions were reported. These range from nonbonding via intermediate distances between 260 and 280 pm for example in binuclear alkoxide complexes (d(Nb–Nb) = 261 pm),[53] down to extremely short Nb—Nb bonds reported by Cotton and coworkers as well as Gambarotta et al. with only 220 pm[54] and 226 pm, respectively.[55] The Hf/Nb–Al interactions now range between 293 and 313 pm. The Al–Al distances now are between 259 and 270 pm. Overall, all distance are shorter than before, in line with the smaller covalent radius of Nb (134 pm) versus Hf (144 pm).[47]

The question that arises is why is only the Hf3 position substituted by Nb and none of the other two. One reason might be the difference of the CNs of Hf1-Hf3, which can also be caused by the smaller covalent radius. Another possibility could be the shortening of the Nb–Nb distance leading to the formation of a more bonding interaction (vide infra).

3.4. ^{27}Al NMR Investigations

Since solid-state NMR spectroscopy is a local probe,[56] in principle, one would expect one resonance per crystallographically independent Al site. Therefore, this technique can be used to verify crystal structures. This has shown before in the cases of $Ba_3Al_4Pt_4$ (own type),[57] $ZrAl_2$[11] and $HfAl_2$,[8] or the $AEAl_4$ series (AE = Ca–Ba)[58] where all of these compounds have two different Al positions. In $Sr_2Al_8Pt_3$, the three Al sites could be resolved[59] and in YAl_5Pt_3; finally, all five resonances could be observed.[60]

Hf_6Al_7 and nominal $Hf_4Nb_2Al_7$ contain two different crystallographic Al sites; therefore, in their ^{27}Al MAS-NMR spectra also, two resonances are expected. Full spectra as well as the zoomed region of the central transitions are depicted in **Figure 5**a,b. The spectrum of Hf_6Al_7 shows one relatively sharp central transition originating from the $|+1/2\rangle \leftrightarrow |-1/2\rangle$ transition. The presence of quadrupolar interactions due to ^{27}Al being a $I = 5/2$ nucleus causes the observed spinning side band manifold based on the satellite transitions $|\pm1/2\rangle \leftrightarrow |\pm3/2\rangle$ and $|\pm3/2\rangle \leftrightarrow |\pm5/2\rangle$. However, the expected second signal is not clearly visible. This can have three reasons: 1) the site multiplicities are 18*h* and 3*b*, resulting in an expected signal ratio of 6:1, 2) a significant overlap of both signals, and 3) different quadrupolar coupling constants (C_Q) for the two Al sites, leading to a different degree of broadening of the resonances. The latter has been observed in the $MgZn_2$ type compounds $ZrAl_2$ and $HfAl_2$.[8,11] The quadrupolar coupling constants extracted from the DFT calculations (Table 5), however, are not that significantly different, excluding the reason number three. At a closer look (Figure 5b), a slight asymmetry of the signal of Hf_6Al_7 (black line) marked with the black arrow can be observed, leading to the assumption that an overlap of the signals seems the likeliest explanation. Taking the DFT-based asymmetry (η_Q) and quadrupolar coupling constants (C_Q) as starting values for the simulation, a significantly larger quadrupolar coupling constant can be deduced from the fit of the intensity profile of the spinning side bands (Table 5, Figure S5, Supporting Information).

When switching to the spectrum of nominal $Hf_4Nb_2Al_7$, two aspects are visible right away. Firstly, the signal is broadened

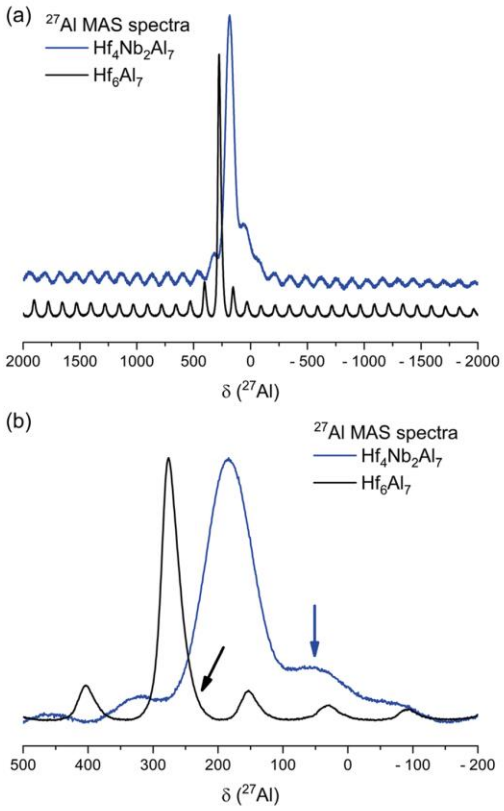

Figure 5. ^{27}Al MAS-NMR spectra of Hf_6Al_7 (black line) and nominal $Hf_4Nb_2Al_7$ (blue line). a) Full spectra of both compounds, the spectrum of nominal $Hf_4Nb_2Al_7$ is shifted along *y* for a better visibility. b) Zoomed spectra of Hf_6Al_7 (black line) and nominal $Hf_4Nb_2Al_7$. The arrows indicate the possible positions of the second signal.

compared to the one of Hf_6Al_7 and secondly, a bump at a higher resonance frequency (lower resonance shift) is visible. Both is directly linked to the incorporation of Nb into the structure. As described above, a random mixing of Nb and Hf is observed, leading to the refined formula of $Hf_{4.44(1)}Nb_{1.56(1)}Al_7$ (single crystal data), being responsible for the line broadening. However, this effect is not as pronounced as for other examples of solid solutions (e.g., $Zr(V_{1-x}Al_x)_2$,[11] $Na_2Au_{3-x}Al_{1+x}$[61] or ScTAl,[62] and $Sc(T_{0.5}T'_{0.5})_2Al$[63]). Due to the different electronic situation of Nb in comparison with Hf, a shift of about 100 ppm of the main resonance is observed; in addition, a more pronounced second resonance, marked by the blue arrow in Figure 5b, is visible most likely originating from the second Al position.

3.5. Physical Properties

Rhombohedral Hf_6Al_7 as well as its nominal substitutional coloring variant $Hf_4Nb_2Al_7$ was investigated via temperature-depending susceptibility measurements between 2.5 and 300 K at an applied external field of 10 kOe. Due to the absence of localized unpaired electrons but metallic character of the compounds, both samples show Pauli-paramagnetism over the whole investigated temperature range. **Figure 6** depicts the magnetic susceptibility data for the two investigated compounds. It is clearly visible that both traces show an overall temperature independent behavior with an upturn at low temperatures originating from traces of Curie-paramagnetic impurities.

3.6. Quantum–Chemical Calculations

Quantum–chemical calculations were performed on the DFT level using the experimental lattice parameters and atomic positions as starting points. The idealized structures, with respect to mixed occupancies, were used. In all cases, the atomic positions had to be fixed in order to get converged results. To understand the selective mixing of Hf and Nb on the Hf3 position in $Hf_4Nb_2Al_7$, three ordered models were calculated with Nb occupying either the Hf1, Hf2, or Hf3 position of the binary variant in a fully ordered fashion. Total energy calculations clearly showed (Table 6) that the observed ordering variant with Nb on the Hf3 position is energetically more stable (−328.438 eV) compared to the other two (Nb on Hf1: −325.188 eV; Nb on Hf2: −325.196 eV) underlining the experimental results.

Subsequently, the chemical bonding of Hf_6Al_7 and $Hf_4Nb_2Al_7$ was addressed using Löwdin charges and ICOBI (integrated crystal orbital bond indices) values recently introduced into LOBSTER.[39,40,43,44,64] For strong covalent bonds, ICOBI values up to one can be observed; while contrasting, values near zero will indicate no (for large distances) or rather ionic interactions (for appropriate distances).[44,65] For metallic materials exhibiting delocalization of their bonding,[66] multicenter bonding is observed. This is rationalized by ICOBI values somewhere between 0 and 1. Recent reports have shown the application towards intermetallic compounds.[64,67] Table 7 lists the Löwdin charges alongside the ICOBI values for selected interactions. For both binary Hf_6Al_7 and ternary $Hf_4Nb_2Al_7$, the Al atoms carry negative Löwdin charges, rendering these compounds aluminides, as expected from the electronegativities, while the Hf

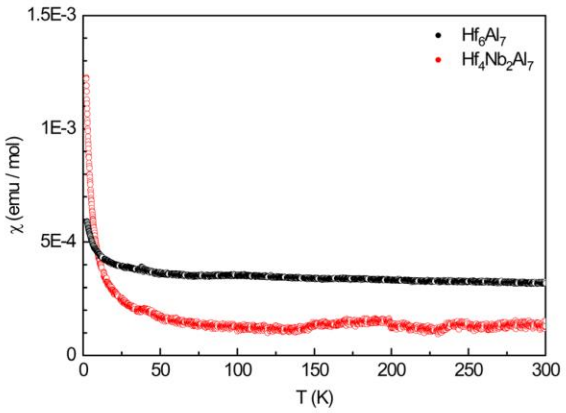

Figure 6. Magnetic susceptibility data of Hf_6Al_7 and nominal $Hf_4Nb_2Al_7$. Measurements were conducted in zero-field cooled mode at an applied field of 10 kOe.

and Nb atoms are cationic. One interesting aspect concerns the charges of the Hf3/Nb atoms. While Hf3 carries the lowest positive charge of +0.35, Nb has a charge of +1.16. In turn, the Löwdin charges of the Al atoms in $Hf_4Nb_2Al_7$ increase, but at the same time, the charges of Hf1 and Hf2 decrease for compensation.

When looking at the ICOBI values, the Al–Al interactions are in the typical range of other intermetallic compounds.[64,67] The Hf–Al interactions, however, are significantly stronger (ICOBI 0.19–0.23) when compared to, e.g., the Sr–Al interactions in $SrAl_8Rh_2$ (ICOBI 0.02–0.04). One striking feature of both Hf_6Al_7 and $Hf_4Nb_2Al_7$ are the short Hf3–Hf3 (DFT: 262.1 pm)/Nb–Nb (DFT: 257.4 pm) interaction. For the binary compound, the ICOBI value is 0.70, indicating a strong covalent contribution (70% of a single bond); for the ternary phase, this value increases even further to 0.90, in line with a covalent single Nb—Nb bond.

4. Conclusion

Motivated by our recent discovery of Hf_4VAl_7, we tried to extend the knowledge on this singular compound by replacing vanadium with other early transition metals. With Hf_6Al_7, a new binary compound crystallizing in the W_6Fe_7 type structure (μ phase, Frank–Kasper phase) as well as its ternary coloring variant, nominal $Hf_4Nb_2Al_7$, was discovered starting from the results of a synthesis targeting nominal "Hf_4NbAl_7." The compounds were synthesized from the elements and structurally characterized. While the Nb-containing phase forms quite readily, getting phase pure samples of binary Hf_6Al_7 was challenging. The Nb substitution was found to occur only on one of the three crystallographic Hf positions of the prototype with the smallest coordination polyhedron. Quantum-chemical calculations indicate that the substitution on the Hf3 site is, compared to the other possibilities, energetically favored in line with the smaller covalent radius of Nb versus Hf alongside the formation a Nb—Nb single bond. Both compounds are Pauli-paramagnets as expected based on their metallic nature and the absence of localized unpaired electrons. ^{27}Al solid-state NMR investigations revealed only one signal, contradicting the expected two signals based on the crystal structure. However, the relative ratio of the two signals is expected to be 6:1 leading to one strong signal alongside a second one being potentially overlapped with the main signal or rotational sidebands.

It is interesting to note that Hf_6Al_7, besides $HfAl_2$ and Hf_4Al_3, is already the third Frank–Kasper phase in the binary system Hf–Al. In contrast to Hf_4VAl_7 (ordering variant of $MgZn_2$), however, $Hf_4Nb_2Al_7$ exhibits a mixing on the Hf positions rather than the Al positions. This raises several questions: 1) can a trend of the substitutional behavior of the third element in binary Hf–Al Frank–Kasper phases be established? 2) Are there other ternary representatives in analogy to $Hf_4Nb_2Al_7$? 3) Are there further substitutional variants of the $MgZn_2$ type $HfAl_2$ or the W_6Fe_7 type Hf_6Al_7? 4) Are ternary (ordered) substitutions possible in Hf_4Al_3? And finally 5) can other *M*—*M* single bonds be established in the W_6Fe_7 type structure?

Acknowledgements

Instrumentation and technical assistance for the X-ray diffraction part this work were provided by the Service Center X-ray Diffraction, with financial support from Saarland University and German Research Foundation (project numbers INST 256/349-1 and INST 256/582-1). Instrumentation and technical assistance for the NMR part were provided by the Core Facility NMR with financial support from Saarland University and German Research Foundation DFG (INST 256/384-1). This research was funded by Universität Münster and German Research foundation (INST 211/1034-1).

Open Access funding enabled and organized by Projekt DEAL.

Conflict of Interest

The authors declare no conflict of interest.

Author Contributions

All authors have accepted responsibility for the entire content of this submitted manuscript and approved the submission.

Data Availability Statement

The data that support the findings of this study are available from the corresponding author upon reasonable request.

Keywords: density functional theory calculations · intermetallics · single-crystal · solid-state NMR

[1] P. Villars, K. Cenzual, *Pearson's Crystal Data: Crystal Structure Database for Inorganic Compounds*, ASM International, Materials Park, Ohio, USA **2023**.
[2] A. W. Hull, *Phys. Rev.* **1917**, *10*, 661.
[3] P. Debye, *Phys. Z.* **1917**, *18*, 483.
[4] C. H. Johansson, J. O. Linde, *Ann. Phys.* **1925**, *78*, 439.
[5] G. Brauer, *Naturwissenschaften* **1938**, *26*, 710.
[6] H. Arnfelt, A. Westgren, *Jernkontorets Ann.* **1935**, *119*, 185.
[7] G. L. Chen, J. G. Wang, X. D. Ni, J. P. Lin, Y. L. Wang, *Intermetallics* **2005**, *13*, 329.
[8] E. C. J. Gießelmann, S. Engel, J. Baldauf, J. Kösters, S. F. Matar, G. Kickelbick, O. Janka, *Inorg. Chem.* **2024**, *63*, 8180.
[9] L.-E. Edshammar, S. Andersson, *Acta Chem. Scand.* **1960**, *14*, 223.
[10] L. Tarschisch, A. T. Titow, F. K. Garjanow, *Phys. Z. Sowjetunion* **1934**, *5*, 503.
[11] E. C. J. Gießelmann, L. Schumacher, S. F. Matar, S. Engel, G. Kickelbick, O. Janka, *Chem. Eur. J.* **2025**, *31*, e202404248.
[12] E. C. J. Gießelmann, R. Pöttgen, O. Janka, *Z. Anorg. Allg. Chem.* **2023**, *649*, e202300109.
[13] O. Janka, R. Pöttgen, *Z. Naturforsch.* **2024**, *79b*, 63.
[14] M. A. Fedorova, V. V. Byrnashova, E. M. Sokolovskaya, P. I. Krypyakevych, *Tezizy Dokl. Vses. Konf. Kristallokhim. Intermet. Soeden.* **1974**, *2*, 18.
[15] F. C. Frank, J. S. Kasper, *Acta Crystallogr.* **1958**, *11*, 184.
[16] F. C. Frank, J. S. Kasper, *Acta Crystallogr.* **1959**, *12*, 483.

[17] R. Pöttgen, D. Johrendt, *Intermetallics - Synthesis, Structure, Function*, De Gruyter, Berlin, Boston **2014**.
[18] R. Pöttgen, D. Johrendt, *Intermetallics - Synthesis, Structure, Function*, De Gruyter, Berlin, Boston **2019**.
[19] O. Janka, *Comprehensive Inorganic Chemistry III*, Elsevier, Amsterdam **2023**.
[20] R. Pöttgen, T. Gulden, A. Simon, *GIT Labor-Fachz.* **1999**, *43*, 133.
[21] Bruker AXS Inc., Topas, Karlsruhe (Germany) **2014**.
[22] H. M. Rietveld, *Acta Crystallogr.* **1967**, *22*, 151.
[23] H. M. Rietveld, *J. Appl. Crystallogr.* **1969**, *2*, 65.
[24] Agilent, CrysAlis PRO, Agilent Technologies Ltd., Yarnton, Oxfordshire, England **2014**.
[25] G. Sheldrick, *Acta Crystallogr.* **2015**, *A71*, 3.
[26] G. Sheldrick, *Acta Crystallogr.* **2015**, *C71*, 3.
[27] G. M. Sheldrick, *Acta Crystallogr.* **2008**, *A64*, 112.
[28] C. B. Hübschle, G. M. Sheldrick, B. Dittrich, *J. Appl. Crystallogr.* **2011**, *44*, 1281.
[29] K. Brandenburg, Crystal Impact, Diamond, Bonn (Germany) **2022**.
[30] Bruker Corp., Topspin, Karlsruhe **2008**.
[31] D. Massiot, F. Fayon, M. Capron, I. King, S. Le Calvé, B. Alonso, J.-O. Durand, B. Bujoli, Z. Gan, G. Hoatson, *Magn. Reson. Chem.* **2002**, *40*, 70.
[32] P. E. Blöchl, *Phys. Rev. B* **1994**, *50*, 17953.
[33] G. Kresse, D. Joubert, *Phys. Rev. B* **1999**, *59*, 1758.
[34] G. Kresse, J. Furthmüller, *Phys. Rev. B* **1996**, *54*, 11169.
[35] G. Kresse, J. Furthmüller, *Comput. Mater. Sci.* **1996**, *6*, 15.
[36] H. J. Monkhorst, J. D. Pack, *Phys. Rev. B* **1976**, *13*, 5188.
[37] J. P. Perdew, K. Burke, M. Ernzerhof, *Phys. Rev. Lett.* **1996**, *77*, 3865.
[38] R. Dronskowski, P. E. Blöchl, *J. Phys. Chem.* **1993**, *97*, 8617.
[39] R. Nelson, C. Ertural, J. George, V. L. Deringer, G. Hautier, R. Dronskowski, *J. Comput. Chem.* **2020**, *41*, 1931.
[40] S. Maintz, V. L. Deringer, A. L. Tchougréeff, R. Dronskowski, *J. Comput. Chem.* **2016**, *37*, 1030.
[41] S. Maintz, V. L. Deringer, A. L. Tchougréeff, R. Dronskowski, *J. Comput. Chem.* **2013**, *34*, 2557.
[42] V. L. Deringer, A. L. Tchougréeff, R. Dronskowski, *J. Phys. Chem. A* **2011**, *115*, 5461.
[43] C. Ertural, S. Steinberg, R. Dronskowski, *RSC Adv.* **2019**, *9*, 29821.
[44] P. C. Müller, C. Ertural, J. Hempelmann, R. Dronskowski, *J. Phys. Chem. C* **2021**, *125*, 7959.
[45] I. Mayer, *Chem. Phys. Lett.* **1983**, *97*, 270.
[46] K. B. Wiberg, *Tetrahedron* **1968**, *24*, 1083.
[47] J. Emsley, *The Elements*, Clarendon Press, Oxford University Press, Oxford, New York **1998**.
[48] K. Schubert, A. Raman, W. Rossteutscher, *Naturwissenschaften* **1964**, *51*, 506.
[49] S. Mangelsen, P. G. Naumov, O. I. Barkalov, S. A. Medvedev, W. Schnelle, M. Bobnar, S. Mankovsky, S. Polesya, C. Näther, H. Ebert, W. Bensch, *Phys. Rev. B* **2017**, *96*, 205148.
[50] W. Noethling, S. Tolksdorf, *Z. Kristallogr. – Cryst. Mater.* **1925**, *62*, 255.
[51] L.-E. Edshammar, *Acta Chem. Scand.* **1961**, *15*, 403.
[52] R. Pöttgen, *Z. Anorg. Allg. Chem.* **2014**, *640*, 869.
[53] F. A. Cotton, M. P. Diebold, W. J. Roth, *Inorg. Chem.* **1985**, *24*, 3509.
[54] F. A. Cotton, J. H. Matonic, C. A. Murillo, *J. Am. Chem. Soc.* **1997**, *119*, 7889.
[55] M. Tayebani, K. Feghali, S. Gambarotta, G. P. A. Yap, *Inorg. Chem.* **2001**, *40*, 1399.
[56] C. Benndorf, H. Eckert, O. Janka, *Acc. Chem. Res.* **2017**, *50*, 1459.
[57] F. Stegemann, C. Benndorf, T. Bartsch, R. S. Touzani, M. Bartsch, H. Zacharias, B. P. T. Fokwa, H. Eckert, O. Janka, *Inorg. Chem.* **2015**, *54*, 10785.
[58] S. Engel, E. C. J. Gießelmann, L. E. Schank, G. Heymann, K. Brix, R. Kautenburger, H. P. Beck, O. Janka, *Inorg. Chem.* **2023**, *62*, 4260.
[59] F. Stegemann, T. Block, S. Klenner, Y. Zhang, B. P. T. Fokwa, C. Doerenkamp, H. Eckert, O. Janka, *Eur. J. Inorg. Chem.* **2021**, 3832.
[60] S. Engel, E. C. J. Gießelmann, L. Schumacher, Y. Zhang, F. Müller, O. Janka, *Dalton Trans.* **2024**, *53*, 12176.
[61] F. Stegemann, C. Benndorf, Y. Zhang, M. Bartsch, H. Zacharias, B. P. T. Fokwa, H. Eckert, O. Janka, *Inorg. Chem.* **2017**, *56*, 1919.
[62] M. Radzieowski, C. Benndorf, S. Haverkamp, H. Eckert, O. Janka, *Z. Naturforsch.* **2016**, *71b*, 553.
[63] C. Benndorf, O. Niehaus, H. Eckert, O. Janka, *Z. Anorg. Allg. Chem.* **2015**, *641*, 168.
[64] L. S. Reitz, J. Hempelmann, P. C. Müller, R. Dronskowski, S. Steinberg, *Chem. Mater.* **2024**, *36*, 6791.
[65] J. Simons, J. Hempelmann, K. S. Fries, P. C. Müller, R. Dronskowski, S. Steinberg, *RSC Adv.* **2021**, *11*, 20679.
[66] S. Steinberg, R. Dronskowski, *Crystals* **2018**, *8*, 225.
[67] S. Engel, M. K. Reimann, E. Svanidze, M. Krnel, N. Zaremba, M. König, O. Janka, *Z. Kristallogr.* **2025**, *240*, 1.
[68] G. M. Sheldrick, B. AXS, XPREP, Madison, WI (USA) **2008**.

Manuscript received: February 28, 2025
Revised manuscript received: April 25, 2025
Version of record online:

5.2 Synthesis and spectroscopic investigations of intermetallic compounds (unpublished)

This chapter presents the remaining results dealing with the investigation of intermetallic compounds in the way of a small monography that were not published yet.

5.2.1 Further attempts to synthesize compounds in the newly discovered Hf_4VAl_7 structure type

As already explained before, the discovery of the new ternary ordering variant of $MgZn_2$ namely Hf_4VAl_7 (own type $P\bar{3}m1$) inspired additional work on these types of compounds. Two follow-up studies have been discussed before; the substitution of Hf by Zr and the results from attempts to replace vanadium by niobium leading to discovery of a different Frank-Kasper phase within these systems. This chapter presents the results of further investigations all based on the existence of Hf_4VAl_7. It was attempted to replace the minor component vanadium by other early transition metals. Table 2 sums up the relevant obtained lattice parameters and structure types.

Table 2. Refined lattice parameters for structures of the Hf_4VAl_7 type as well as $HfAl_2$.

Compound / Nominal Comp.	structure type	method	*a* / pm	*c*/ pm	Ref.
$HfAl_2$	$MgZn_2$	powder	524.1	867.4	[240]
Hf_4VAl_7	Hf_4VAl_7	powder	527.5	859.6	[240]
Hf_4VAl_7	Hf_4VAl_7	single crystal	527.1	857.7	[240]
Hf_4MoAl_7	Hf_4VAl_7	powder	528.2	863.6	*, Figure 25
Hf_4MoAl_7	Hf_4VAl_7	single crystal	527.9	862.9	*
$Hf(Cr_{0.125}Al_{0.875})_2$	$MgZn_2$	powder	525.3	856.3	*, Figure 28
$Hf(Fe_{0.125}Al_{0.875})_2$	$MgZn_2$	powder	521.9	854.4	*, Figure 29
$Hf(Fe_{0.125}Al_{0.875})_2$	$MgZn_2$	single crystal	521.4	853.8	*

* This work. The standard deviations for the lattice parameters are ±0.1 pm or smaller.

5.2.1.1 The compound Hf_4MoAl_7

As could be shown in section 5.1.5 the substitution of V by Nb does not lead to the formation of the desired compound Hf_4NbAl_7 but replacing vanadium by the neighboring element molybdenum, gave the diffractogram shown in Figure 25. The elements were arc-melted and afterwards the sample was annealed at 1123 K for 6 d. As can already be seen in the powder diffraction data the additional reflections that are created by the symmetry reduction from $MgZn_2$ ($P6_3/mmc$) to Hf_4VAl_7 ($P\bar{3}m1$) are visible in the powder pattern. This is due to the electron difference of Mo compared to V. This combination also forms the ternary ordered variant.

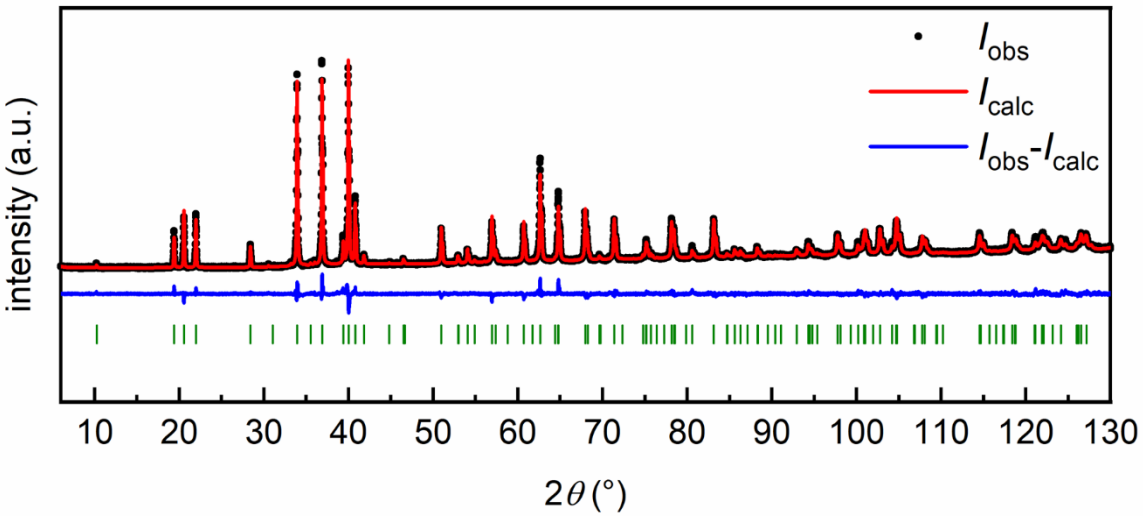

Figure 25. Powder X-ray diffraction pattern of the sample with the nominal composition Hf_4MoAl_7. Experimental data is shown as black dots, simulated diffraction patterns from refinements as red lines, the difference is shown as continuous blue lines. Bragg positions are shown as green (Hf_4MoAl_7, space group $P\bar{3}m1$) ticks.

The formation was further proven by single-crystal investigations. During the refinement of a single crystal obtained from the batch given above, various problems concerning residual electron density occurred, although overall good agreement factors could be obtained. Table 3 gives the results for two different structure types that could match the real structure of Hf_4MoAl_7. The first is identical to the Hf_4VAl_7 type (space group $P\bar{3}m1$), however slightly better values could be obtained by lowering the symmetry to space group $P\bar{3}$.

Table 4 shows the atomic positions and Table 5 the obtained bond distances for the refinement in this space group. Figure 26 depicts the structural relationship using the Bärnighausen formalism. It becomes evident that the symmetry reduction gives an additional degree of freedom for the Al2 atoms within the Kagomé network, which could be the reason.

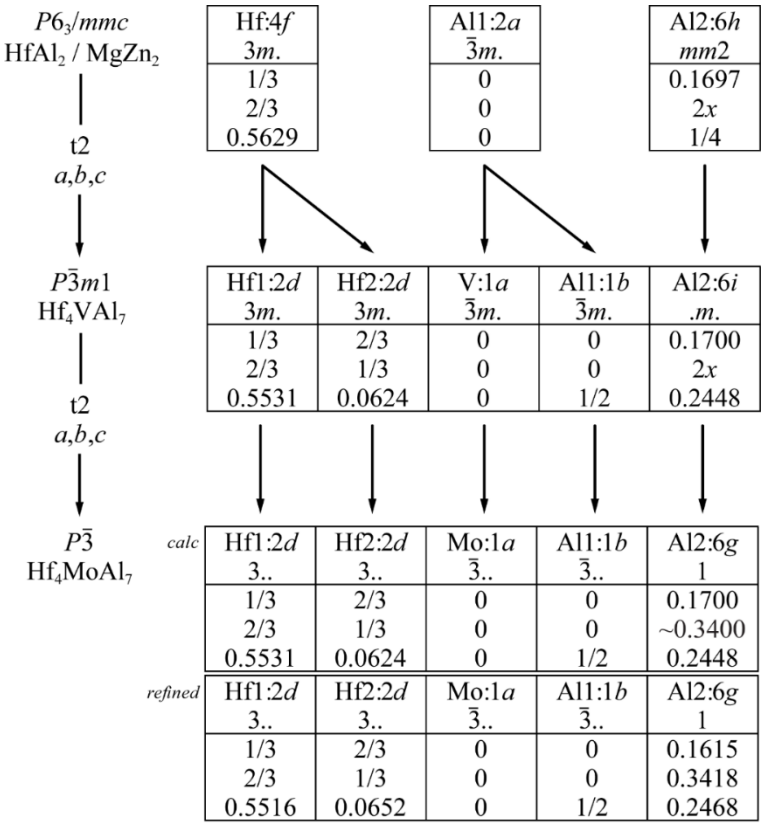

Figure 26. Bärnighausen formalism[45-48] expressing the structural relationship of $HfAl_2$, Hf_4VAl_7 and possible structure solution for the compound Hf_4MoAl_7 adopting a new structure type with space group $P\bar{3}m$.

To conclude, this data is not suitable for publishing, yet, since the overall electron density is too high and the isotropic displacement parameters obtained are too high as well. For additional structural validation new batches using higher annealing times and/or new single crystals are required. Nevertheless, the compound Hf_4MoAl_7 either shows another new structure type or is a representative of the Hf_4VAl_7 type. Lastly Figure 27 shows the ^{27}Al NMR spectrum recorded for the compound. In analogy to the ordered vanadium compound distinct sharp signals are visible, proving the local order of this compound in comparison to a solid solution.

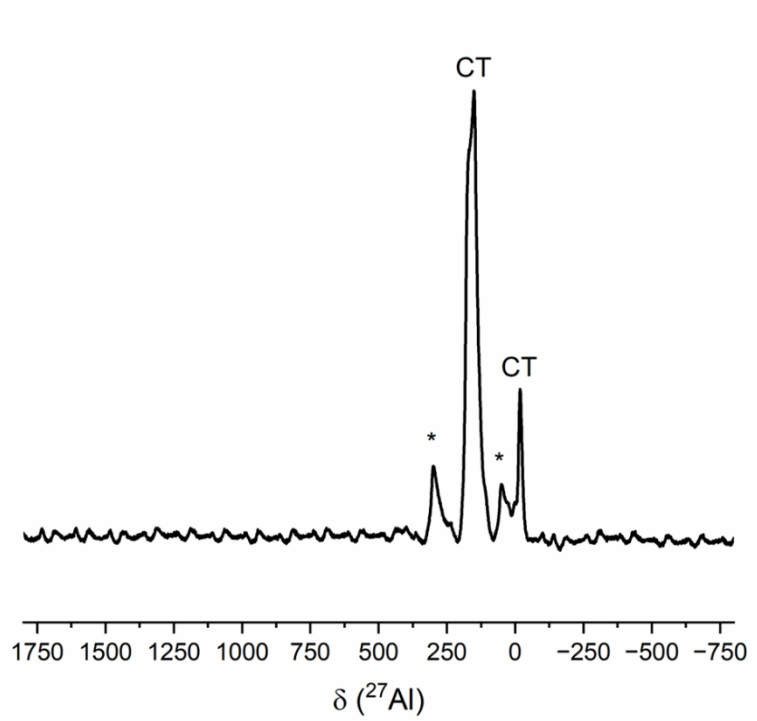

Figure 27. ^{27}Al solid state NMR spectrum of Hf_4MoAl_7 record at a MAS frequency of 13 kHz. Spinning sidebands close to the central transitions are marked with an asterix.

Table 3. Crystallographic data and structure refinement from single-crystal X-ray diffraction experiments for nominal Hf_4MoAl_7.

Nominal composition		Hf_4MoAl_7	Hf_4MoAl_7
Refined composition		$Hf_4Mo_{1.25}Al_{6.75}$	$Hf_4Mo_{1.14}Al_{6.86}$
Structure type		Hf_4VAl_7 ($P\bar{3}m1$)	own type ($P\bar{3}$)
Lattice parameters	a (pm)	527.90(1)	527.90(1)
	c (pm)	862.89(2)	862.89(2)
	V (nm^3)	0.20825	0.20825
Molar mass, g mol^{-1}		1015.8	1008.1
Density calc., g cm^{-3}		8.0997	8.0382
Crystal size, µm		50×40×30	40×30×20
Detector distance, mm		38	38
Exposure time, s		10	10
Range in hkl		h ± 7, k ± 7, l ± 12	h ± 7, k ± 7, l ± 12
θ_{min}, θ_{max}, deg		2.36, 30.15	2.36, 30.15
Linear absorption coeff., mm^{-1}		51.766	51.766
No. of reflections		4748	4748
R_{int} / R_σ		0.029 / 0.0144	0.0281 / 0.0151
No. of independent reflections		274	424
Reflections used [$I \geq 3\sigma(I)$]		274	424
F(000), e		431	425
$R1$ / $wR2$ for $I \geq 3\sigma(I)$		0.0221 / 0.0404	0.0182 / 0.0618
$R1$ / $wR2$ for all data		0.0221 / 0.0404	0.0182 / 0.0618
Data / parameters		274 / 21	424 / 26
Goodness-of-fit on F^2		3.39	2.45
Extinction coefficient		200(40)	180(30)
Diff. Fourier residues /e$^-$ Å^{-3}		+3.03 / –5.51	+5.01 / –3.98

Table 4. Atom positions and equivalent isotropic displacement parameters (pm^2) for nominal Hf_4MoAl_7, refined with the space group $P\bar{3}$. U_{eq} is defined as one third of the trace of the orthogonalized U_{ij} tensor. Grey lines are shown for better visibility.

Atom	Wyckoff position	x	y	z	Occ	U_{eq}
Hf1	2d	1/3	2/3	0.55164(6)	1	63(1)
Hf2	2d	2/3	1/3	0.06522(6)	1	49(1)
Mo	1a	0	0	0	1	48(3)
Al1	1b	0	0	1/2	0.967	230(20)
Mo1’	1b	0	0	1/2	0.033	230(20)
Al2	6g	0.1615(5)	0.3418(4)	0.2468(2)	0.983	60(16)
Mo2’	6g	0.1615(5)	0.3418(4)	0.2468(2)	0.017	60(16)

Table 5. Interatomic distances (in pm) for nominal Hf_4MoAl_7. Standard deviations for the interatomic distances are ≤0.2 pm.

Hf1 (2*d*)	3	Al2/Mo2'	302.1	Mo (1*a*)	6	Al2/Mo2	264.2
	3	Al1/Mo1'	308.0		6	Hf2	309.9
	3	Al2/Mo2'	312.0	Al1/Mo1' (1*b*)	6	Al2/Mo2	268.7
	3	Hf1	317.5		6	Hf1	308.0
	3	Al2/Mo2'	320.3	Al2/Mo2' (6*g*)	2	Al2/Mo2	257.4
	1	Hf2	330.6		1	Mo	264.2
Hf2 (2*d*)	6	Al2/Mo2'	302.7		1	Al1/Mo1	268.7
	3	Mo	307.5		2	Al2/Mo2	270.8
	3	Al2/Mo2'	309.9		1	Hf1	302.1
	3	Hf2	311.3		1	Hf2	302.7
	1	Hf1	324.9		1	Hf2	307.5
					1	Hf2	311.3
					1	Hf1	312.0
					1	Hf1	320.3

5.2.1.2 The incorporation of Cr and Fe

The nominal compositions Hf_4CrAl_7 and Hf_4FeAl_7 were synthesized and the powder X-ray diffractograms, shown in Figure 28 (nominal Hf_4CrAl_7) and Figure 29 (nominal Hf_4FeAl_7), were collected. No observations of any ordering could be made here. It seems that only a solid solution of $MgZn_2$ has formed. This was verified for the Cr compound collecting a solid state ^{27}Al NMR spectrum. Only a broad reflection in analogy to the solid solution $Zr(V_{1-x}Al_x)_2$ was recorded (data not shown). Table 2 sums up the obtained lattice parameters.

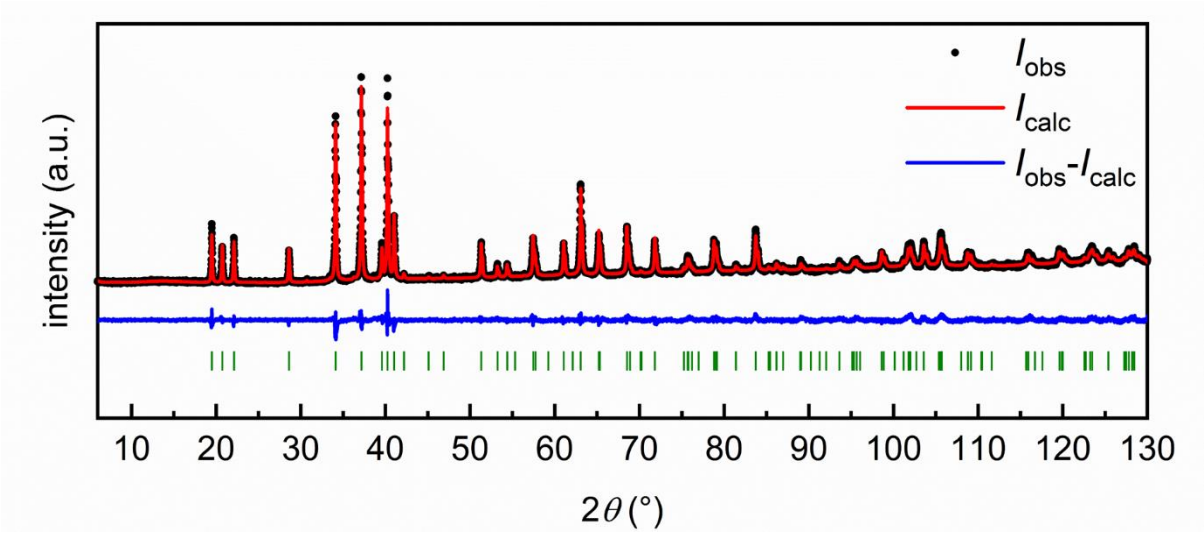

Figure 28. Powder X-ray diffraction pattern of the sample with the nominal composition Hf_4CrAl_7. Experimental data is shown as black dots, simulated diffraction patterns from refinements as red lines, the difference is shown as continuous blue lines. Bragg positions are shown as green ($MgZn_2$ type $Hf(Cr_{1-x}Al_x)_2$, space group $P6_3/mmc$) ticks.

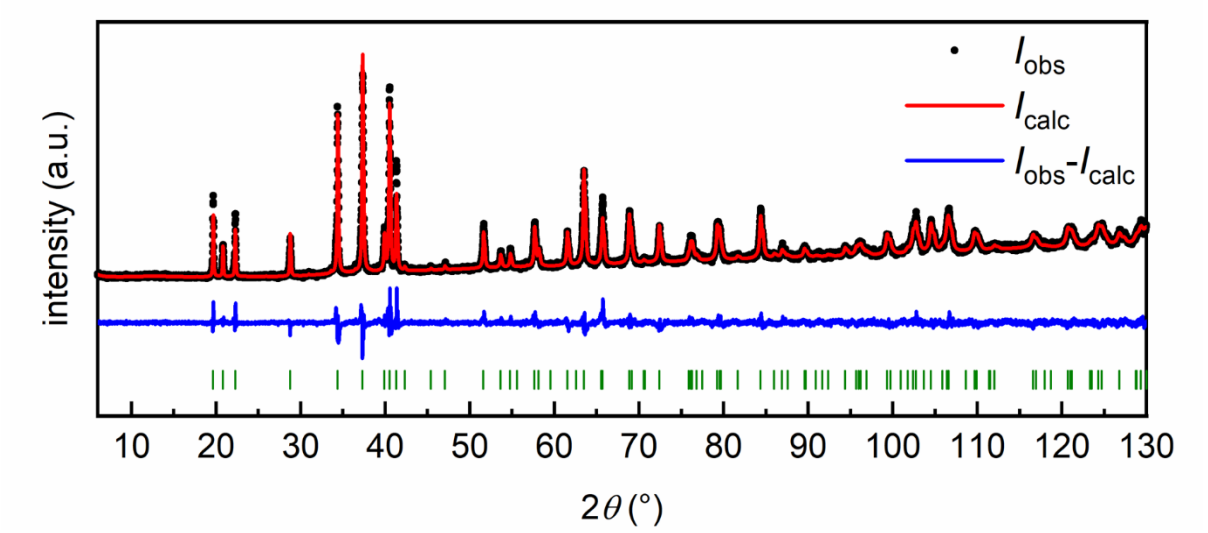

Figure 29. Powder X-ray diffraction pattern of the sample with the nominal composition Hf_4FeAl_7. Experimental data is shown as black dots, simulated diffraction patterns from refinements as red lines, the difference is shown as continuous blue lines. Bragg positions are shown as green ($MgZn_2$ type $Hf(Fe_{1-x}Al_x)_2$, space group $P6_3/mmc$) ticks.

For the iron compound a single-crystal analysis was performed. Results are summed up in Tables 6-8. As can be seen, refinement can be done by assuming hexagonal symmetry adopting the $MgZn_2$ structure type. For both Al sites a mixing with iron is detected that does not show a large preference. The overall sum formula obtained is close to the nominal composition.

Table 6. Crystallographic data and structure refinement from single-crystal X-ray diffraction experiments for nominal Hf_4FeAl_7 respectively $Hf(Fe_{0.125}Al_{0.875})_2$.

Nominal composition		Hf_4FeAl_7
Refined composition		$Hf(Fe_{0.15}Al_{0.0.85})_2$
Structure type		$MgZn_2$ ($P6_3/mmc$)
Lattice parameters	a (pm)	521.42(1)
	c (pm)	853.79(3)
	V (nm^3)	0.20103
Molar mass, g mol^{-1}		241.1
Density calc., g cm^{-3}		7.9666
Crystal size, μm		30×25×15
Detector distance, mm		38
Exposure time, s		20
Range in hkl		$-7 \le h,k \le 7$, $-12 \le l \le 12$
θ_{min}, θ_{max}, deg		4.51, 30.53
Linear absorption coeff., mm^{-1}		54.194
No. of reflections		4688
R_{int} / R_σ		0.0259 / 0.007
No. of independent reflections		146
Reflections used [$I \ge 3\sigma(I)$]		135
F(000), e		408
$R1$ / $wR2$ for $I \ge 3\sigma(I)$		0.0125 / 0.0188
$R1$ / $wR2$ for all data		0.0139 / 0.0197
Data / parameters		146 / 12
Goodness-of-fit on F^2		1.69
Extinction coefficient		–
Diff. Fourier residues /e$^-$ Å^{-3}		+2.56 / –0.77

Table 7. Atom positions and equivalent isotropic displacement parameters (pm^2) for nominal Hf_4FeAl_7 respectively $Hf(Fe_{0.125}Al_{0.875})_2$. U_{eq} is defined as one third of the trace of the orthogonalized U_{ij} tensor. Grey lines are shown for better visibility.

Atom	Wyckoff position	x	y	z	Occ	U_{eq}
Hf	4f	1/3	2/3	0.56550(3)	1	47(1)
Al1	2a	0	0	0	0.83(1)	122(10)
Fe1	2a	0	0	0	0.17(1)	122(10)
Al2	6h	0.17071(17)	2x	1/4	0.86(1)	82(6)
Fe2	6h	0.17071(17)	2x	1/4	0.14(1)	82(6)

Table 8. Interatomic distances (pm) for refined $Hf(Fe_{0.15}Al_{0.0.85})_2$. Standard deviations for the interatomic distances are ≤0.2 pm.

Hf (4*f*)	6	Al2/Fe2	304.6
	3	Al1/Fe1	306.2
	3	Al2/Fe2	306.8
	1	Hf	315.0
	3	Hf	321.1
Al1/Fe1 (2*a*)	6	Al2/Fe2	263.3
	6	Hf	306.2
Al2/Fe2 (6*h*)	2	Al2/Fe2	254.4
	2	Al1/Fe1	263.3
	2	Al2/Fe2	267.0
	4	Hf	304.6
	2	Hf	306.8

For all compositions discussed, Figure 30 shows the magnetic susceptibility data recorded in ZFC mode at a magnetic field strength of 10 kOe. For comparison the magnetic data for the published compound Hf_4VAl_7 is also included. All compounds show Pauli-paramagnetic behavior as expected since no elements with a permanent magnetic moment are present. The small increase in susceptibility at low temperatures can be attributed to paramagnetic impurities within the samples.

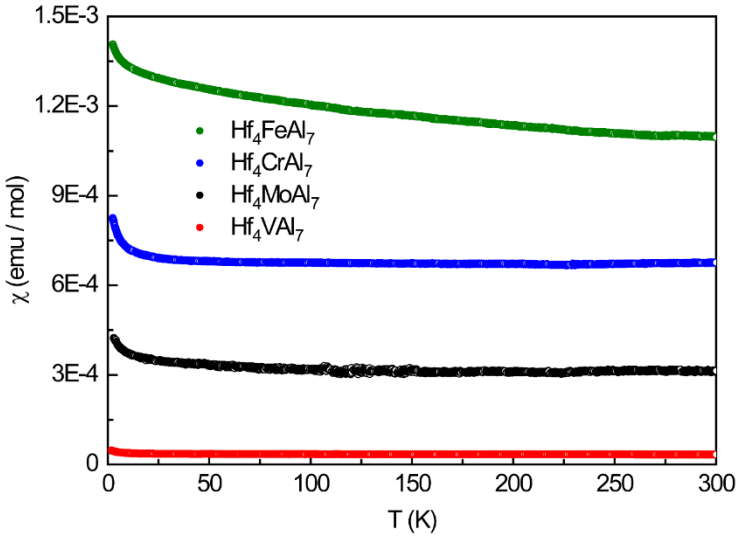

Figure 30. Magnetic susceptibility data for the nominal compositions $Hf(Cr_{0.125}Al_{0.875})_2$ and $Hf(Fe_{0.125}Al_{0.875})_2$ as well as for Hf_4MoAl_7. Data for Hf_4VAl_7 are included for comparison.[240] Measurements were conducted in zero-field-cooled (ZFC) mode at a magnetic field strength of 10 kOe.

5.2.1.3 More early transition metals – Ti and Ta

The powder diffractogram for the synthesis of Hf_4TiAl_7 is depicted in Figure 31. Taking $HfAl_2$ ($MgZn_2$ type, space group $P6_3/mmc$) and Hf_6Al_7 (W_6Fe_7 type, space group $R\bar{3}m$) as starting points for the refinement, both phases could be identified. The same applies for the attempt using tantalum so the nominal composition Hf_4TaAl_7. In the powder pattern (Figure 32) it is likewise possible to identify the hexagonal $MgZn_2$ phase and the trigonal W_6Fe_7 phase. Table 9 lists the refined lattice parameters. A refinement of the occupancy factors was performed; however, only mixed site occupancies of the elements were identified. The formation of the two Frank-Kasper phases seems to compete. A clarification of the compositions as it was done for the ternary system Hf-Nb-Al is necessary by attempting different compositions and annealing strategies.

Table 9. Identified phases, as well as obtained lattice parameters for the nominal compositions Hf_4TiAl_7 and Hf_4TaAl_7.

Compound/ Nominal Comp.	Identified structure type(s)	*a* / pm	*c* / pm	Ref.
$HfAl_2$	$MgZn_2$	524.1	867.4	[240]
Hf_4VAl_7	own type	527.1	857.7	[240]
Hf_6Al_7	W_6Fe_7	530.5	2916.4	[241]
$Hf_4Nb_2Al_7$	W_6Fe_7	525.3	2866.1	[241]
Hf_4TiAl_7	$MgZn_2$ (71(1) mass%)	528.5	867.6	*, Figure 31
	W_6Fe_7 (29(1) mass%)	528.1	2885.5	
Hf_4TaAl_7	$MgZn_2$ (36(1) mass%)	525.1	868.9	*, Figure 32
	W_6Fe_7 (64(1) mass%)	525.1	2888.7	
$Hf_{4.42}Ta_{2.21}Al_{6.37}$	W_6Fe_7	528	2875	[242]

* This work. The standard deviations for the lattice parameters are ±0.1 pm or smaller.

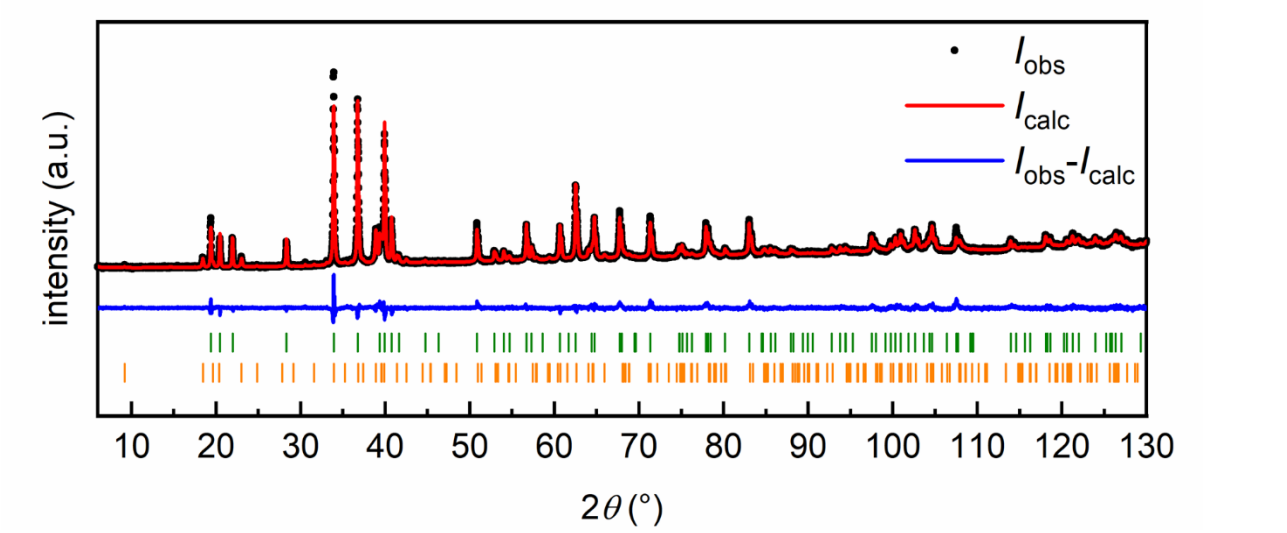

Figure 31. Powder X-ray diffraction pattern of the sample with the nominal composition Hf_4TiAl_7. Experimental data is shown as black dots, simulated diffraction patterns from refinements as red lines, the difference is shown as continuous blue lines. Bragg positions are shown as green ($MgZn_2$ type, space group $P6_3/mmc$) and orange (W_6Fe_7 type, space group $R\bar{3}m$) ticks. The refined mass% are given in Table 9.

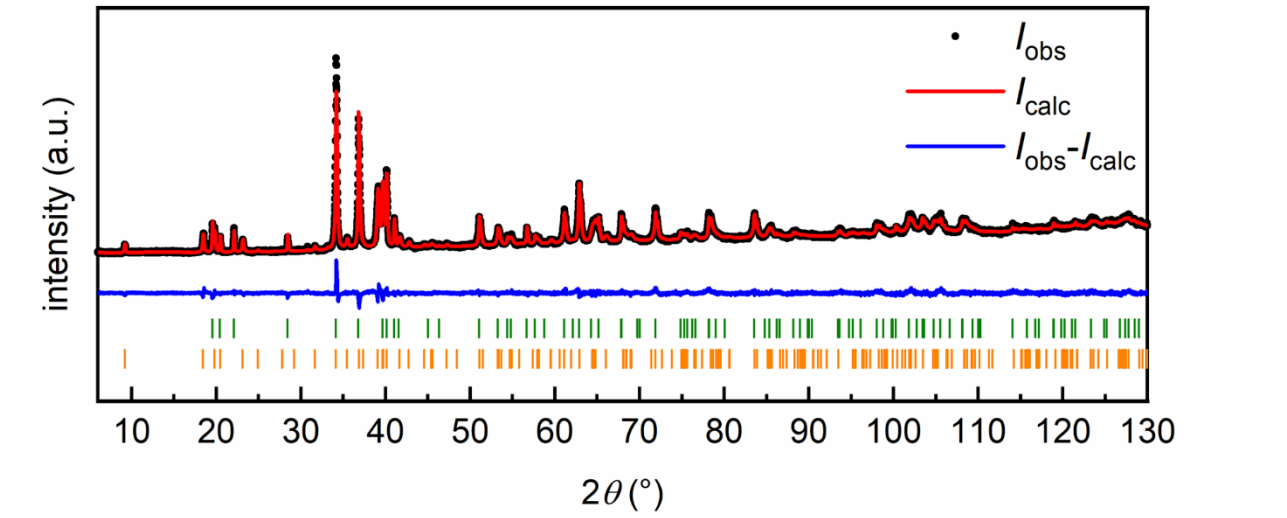

Figure 32. Powder X-ray diffraction pattern of the sample with the nominal composition Hf_4TaAl_7. Experimental data is shown as black dots, simulated diffraction patterns from refinements as red lines, the difference is shown as continuous blue lines. Bragg positions are shown as green ($MgZn_2$ type, space group $P6_3/mmc$) and orange (W_6Fe_7 type, space group $R\bar{3}m$) ticks. The refined mass% are given in Table 9.

5.2.1.4 *Hard to differentiate but interesting observations – W*

After observing the formation of a phase pure solid solution of $MgZn_2$, respectively an ordering variant of the same, or the formation of two different Frank-Kasper phases, the results for the nominal composition Hf_4WAl_7 differ from these. Figure 33 shows the powder X-ray diffractogram of nominal Hf_4WAl_7.

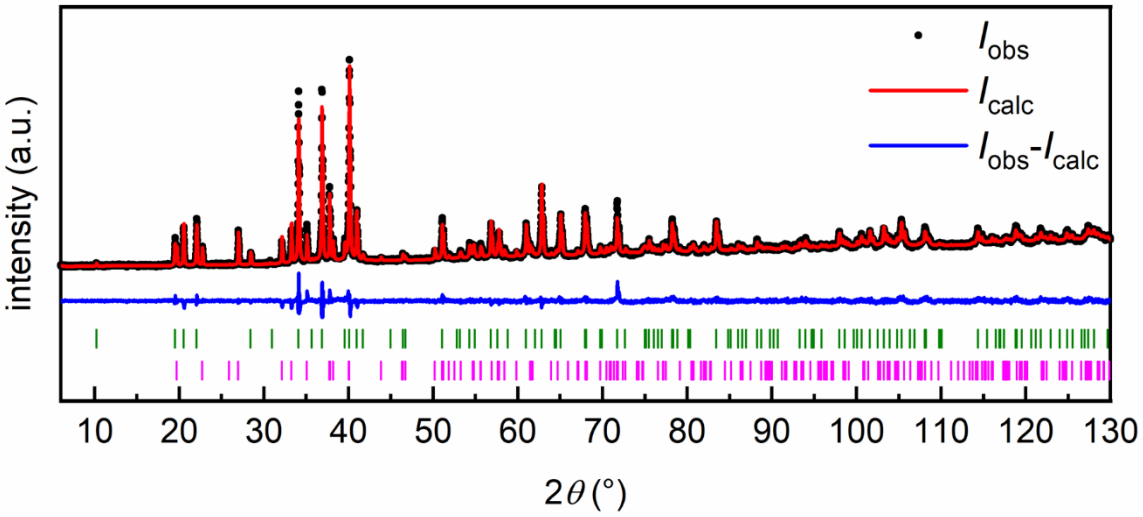

Figure 33. Powder X-ray diffraction pattern of the sample with the nominal composition Hf_4WAl_7. Experimental data is shown as black dots, simulated diffraction patterns from refinements as red lines, the difference is shown as continuous blue lines. Bragg positions are shown as green (Hf_4VAl_7 type, space group $P\bar{3}m1$, 74(1) mass%) and pink (Zr_2Al_3 type, space group *Fdd*2, 26(1) mass%) ticks.

Within the powder X-ray diffractogram the formation of the ternary ordered variant could be resolved due to the presence of the superstructure reflection at low 2θ angles around 10.2° which corresponds to the (001) reflection. As an additional phase, nominal Hf_2Al_3 (Zr_2Al_3 type, *Fddd*)[243] could be identified. Lattice parameters were refined as a = 951.4(1), b = 1375.7(1) and c = 551.2(1) pm, which are in good agreement with the literature data, however small deviations give a hint on mixed site occupancies. Within this structure a mixing of Hf and W could be possible but cannot be resolved by diffraction data.

Repeating the experiment with shorter annealing times (6 d at 1223 K compared to 12 d) gave nearly the same PXRD pattern (data not shown) but without the visible superstructure reflections. Now only the formation of a solid solution in the $MgZn_2$ type structure is visible. For further clarification additional synthetic attempts with different annealing strategies and/or differing starting compositions are necessary to clearly identify the phases formed within this specific ternary system.

5.2.2 The first ternary ordered compound in the system Zr–V–Al adopting the $YbMo_2Al_4$ type structure

In an investigation of the ternary system Zr–V–Al at the isothermal section of 1073 K, Zhu and coworkers describe the observation of a new ternary compound with variable compositions.[205] The authors state that the new compound could be identified in various alloys with different nominal compositions after annealing arc-melted samples at 1073 K for 60 d. The authors give a compositional range of $Zr_{10.5\text{-}16.5}V_{29.3\text{-}26.3}Al_{52.8\text{-}55.2}$ based on SEM/EDX investigations. For the structure description, the authors give a tetragonal unit cell with a = 658.5 and c = 517.3 pm, however, no further information or structure determination using single-crystal analysis is conducted.

This investigation got our attention since it was not possible to identify any ordered compound and structurally characterize them in the ternary system, despite using different approaches for the synthesis, as described in section 5.1.4. The lattice parameters and symmetry mentioned in the study, however, matched a series of gallium compounds adopting the $YbMo_2Al_4$ structure type crystallizing in the tetragonal crystal system with space group $I4/mmm$.[121] Besides the series $M Ti_2Ga_4$ (M = Sc, Y, Tb-Tm, Lu and Zr)[117] also the V compounds MV_2Ga_4 (M = Sc, Zr, Hf and Tb-Tm)[117, 244] are listed in the Pearson‘s Crystal Data database. The corresponding compound ZrV_2Ga_4 has unit cell constants of a = 646.2 and c = 520.7 pm. In aluminum chemistry only the series $RE Mo_2Al_4$ (RE = Y, Gd-Lu) has been reported so far.[122]

Three questions arose: (1) Can the findings of Zhu et al. be reproduced? (2) Does the $YbMo_2Al_4$ structure match the compound described in literature although the composition determined by SEM/EDX by Zhu et al. does not match a potential ZrV_2Al_4 and (3) can the literature results be reproduced by slow cooling a sample instead of quenching?

Figure 34 depicts the PXRD pattern after arc-melting the nominal composition ZrV_2Al_4. The powder pattern does not show a single hint for the $YbMo_2Al_4$ structure. The diffractogram can be perfectly described using a $MgZn_2$ phase (space group $P6_3/mmc$), $ZrAl_3$ (space group $I4/mmm$)[107] and elemental V (space group $Im\bar{3}m$), respectively a solid solution of Al in the V structure, indicated by a larger lattice parameter found after Rietveld refinement. The reason for this was not further investigated.

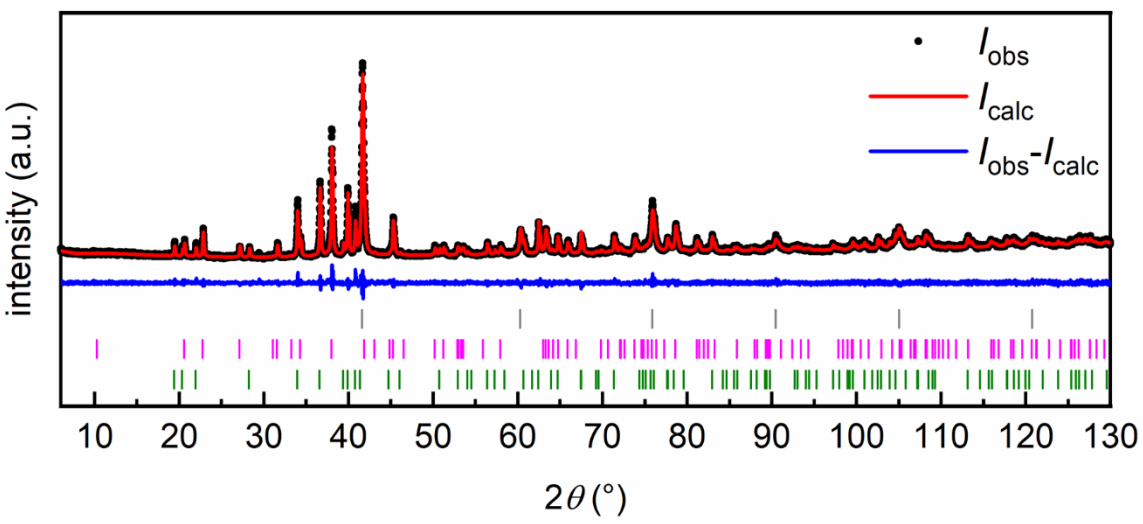

Figure 34. Powder X-ray diffraction pattern of the sample with the nominal composition ZrV_2Al_4 after arc-melting. Experimental data is shown as black dots, simulated diffraction patterns from refinements as red lines, the difference is shown as continuous blue lines. Bragg positions are shown as dark grey (elemental V, space group $Im\bar{3}m$, 40(1) mass%), pink ($ZrAl_3$, space group $I4/mmm$, 33(1) mass%) and green ($MgZn_2$ type $Zr(V_{1-x}Al_x)_2$, space group $P6_3/mmc$, 27(1) mass%), and ticks.

Different attempts to anneal samples according to a program described in the work by Zhu et al. using shorter annealing times (< 4 d) and higher temperatures (up to 1373 K) with various compositions did not lead to significant changes, therefore the data are not discussed here. To conclude, it was not possible to obtain the desired compounds using short annealing times. Figure 35 depicts the powder X-ray diffraction pattern obtained after arc-melting the nominal composition $Zr_{12}V_{33}Al_{55}$ (composition given in literature[205]) and subsequent annealing at1073 K for 27 d. The sample was quenched in liquid nitrogen.

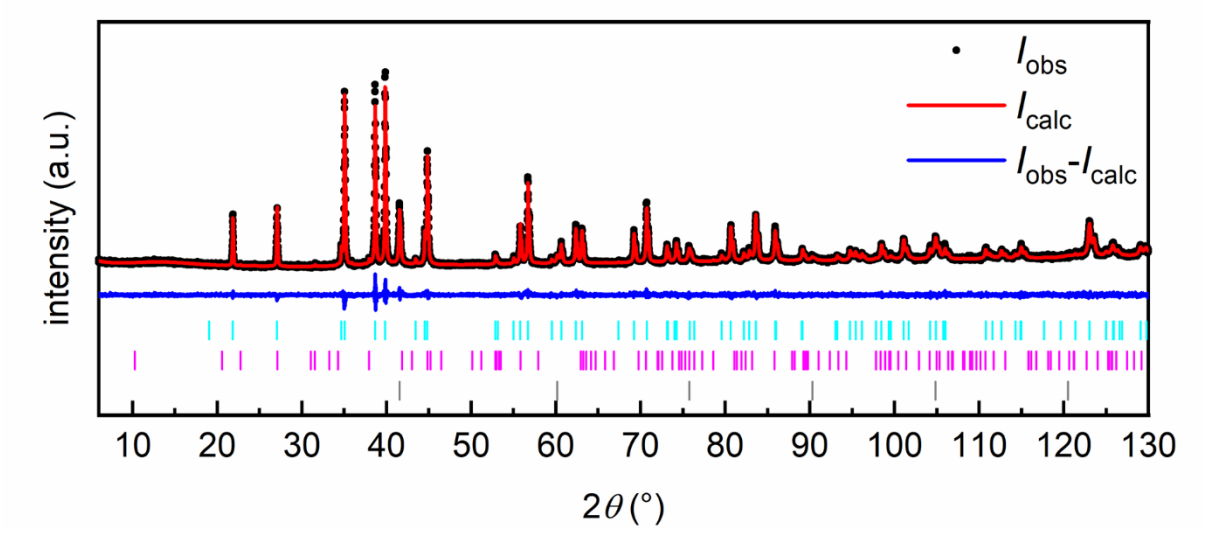

Figure 35. Powder X-ray diffraction pattern of the sample with the nominal composition $Zr_{12}V_{33}Al_{55}$ after arc-melting and subsequent annealing at 1073 K for 27 days followed by quenching. Experimental data is shown as black dots, simulated diffraction patterns from refinements as red lines, the difference is shown as continuous blue lines. Bragg positions are shown as cyan (ZrV_2Al_4, space group *I4/mmm*, 88(1) mass%), pink ($ZrAl_3$, space group *I4/mmm*, 1(1) mass%) and dark grey (elemental V, space group $Im\bar{3}m$, 11(1) mass%) ticks.

Most of the reflections could nicely be described by using the $YbMo_2Al_4$ structure. The remaining reflections could be described with the structure of elemental V, which is reasonable since it should be left over. ZrV_2Al_4 was identified with 88.5 mass%. The lattice parameters were identified as a = 658.7 and c = 517.3 pm, which is in good agreement with literature data.[205] The matching intensity profile in the powder diffractogram also shows that the assumption of a ZrV_2Al_4 adopting the $YbMo_2Al_4$ type with Zr occupying the Yb and V the Mo position is reasonable. This matching to the structure type has been missing in the literature yet. Sadly, it has not been possible as of now to obtain single crystals that could be measured, which could be a result of quenching the sample. With the new ternary compound very likely to be ZrV_2Al_4, further investigations with this compound were carried out. One question to answer was, which annealing time is necessary to obtain the compound at all, another goal was to obtain phase pure samples for further analysis such as single-crystal X-ray diffraction, solid state NMR and magnetic property measurements.

To target the first question, multiple samples of now stoichiometric ZrV_2Al_4 were arc-melted and annealed at 1073 K for different times. The samples were quenched in liquid nitrogen since it was not clear at this point whether the compound is only stable at high temperatures and decomposes under slow cooling. Figure 36 shows the diffractograms after 7 and 29 days. Two more times in between are shown in the appendix (Figure S1). Annealing the sample for longer time does not change the result anymore and interestingly a higher annealing temperature of 1273 K did not lead to any product formation. By applying this annealing

program after arc-melting, it was not possible to obtain a single-phase sample. The formation of the compound, however, takes up to 22 days.

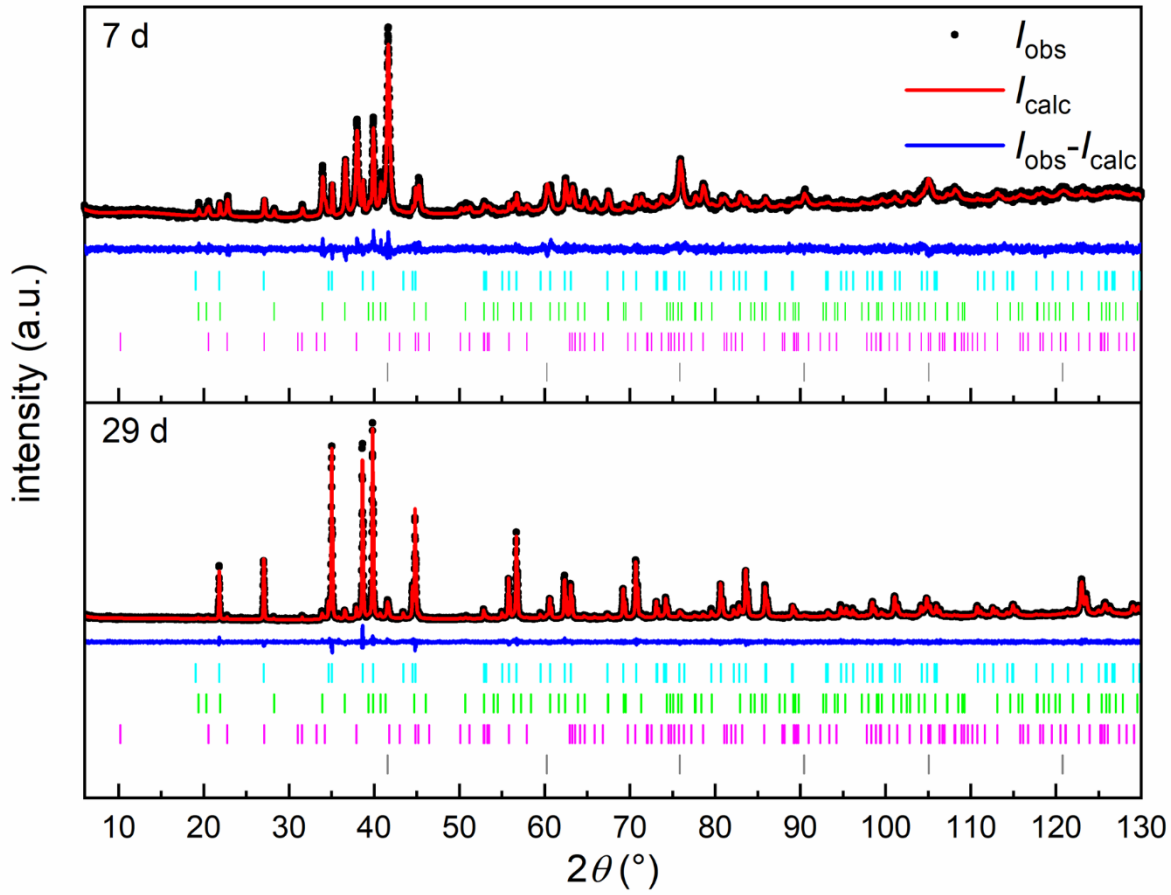

Figure 36. Powder X-ray diffraction pattern of the sample with the nominal composition ZrV_2Al_4 after arc-melting and subsequent annealing at 1073 K for (*top*) 9 and (*bottom*) 29 days followed by quenching. Experimental data is shown as black dots, simulated diffraction patterns from refinements as red lines, the difference is shown as continuous blue lines. Bragg positions are shown as cyan (ZrV_2Al_4, space group *I4/mmm*, (*top*) 11(1) mass%, (*bottom*) 88(1) mass%), green ($MgZn_2$ type $Zr(V_{1-x}Al_x)_2$, space group $P6_3/mmc$, (*top*) 24(1) mass%, (*bottom*) 5(1) mass%), pink ($ZrAl_3$, space group *I4/mmm*, (*top*) 29(1) mass%, (*bottom*) 3(1) mass%) and dark grey (elemental V, space group $Im\bar{3}m$, (*top*) 36(1) mass%, (*bottom*) 4(1) mass%) ticks.

Additionally, experiments that involve slow cooling (5 K h^{-1}) instead of quenching and higher annealing temperatures (1123 K and 1173 K) were carried out. Annealing the sample at 1123 K for 39 days results in the same results as shown in Figure 37 corresponding to an amount of the desired phase of ~88 mass%. The corresponding powder X-ray diffractograms are shown in the appendix (Figure S2 & Figure S3). As can be seen there is no difference between the quenched and the slowly cooled sample. The same applies for the annealing at 1173 K for the same time. However, at the slightly increased temperature the compound could be obtained with a purity of ~96 mass%. The corresponding powder pattern for the sample quenched at a temperature of 1173 K is shown in Figure 37. Slowly cooling the sample did not result in a

change of the sample (Figure S4). Therefore, the compound cannot be labelled as a high-temperature phase.

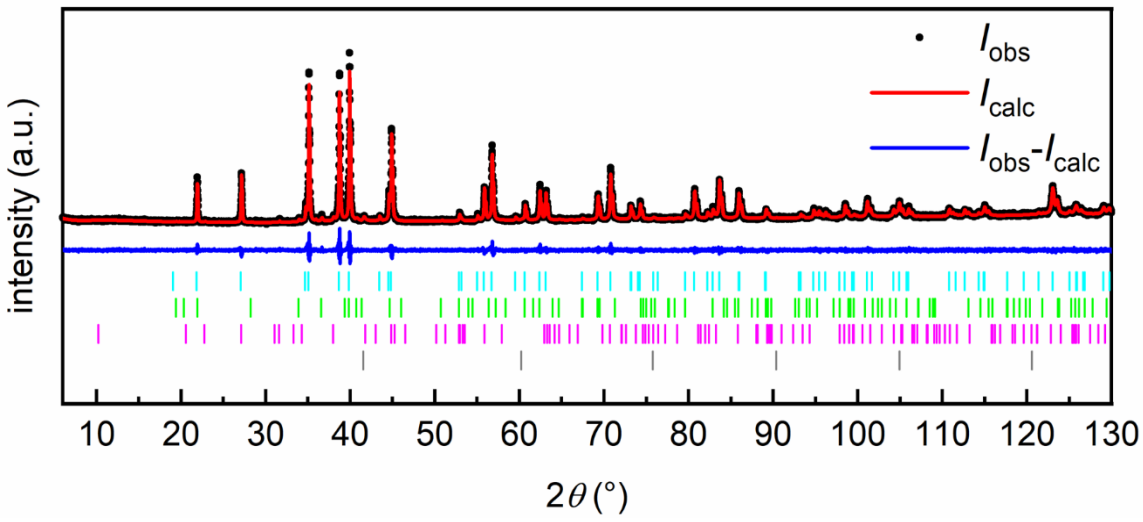

Figure 37. Powder X-ray diffraction pattern with nominal composition ZrV_2Al_4 after arc-melting and subsequent annealing at 1173 K for 39 d followed by quenching in liquid nitrogen. Experimental data is shown as black dots, simulated diffraction patterns from refinements as red lines, the difference is shown as continuous blue lines. Bragg positions are shown as cyan (ZrV_2Al_4, space group *I4/mmm*, 96(1) mass%), green ($MgZn_2$ type $Zr(V_{1-x}Al_x)_2$, space group $P6_3/mmc$, 2(1) mass%), pink ($ZrAl_3$, space group *I*4/*mmm*, 1(1) mass%) and dark grey (elemental V, space group $Im\bar{3}m$, 1(1) mass%) ticks.

As described before, it was not yet possible to isolate single crystals of measurable quality. The same applies for these samples. However, based on the assumption that ZrV_2Al_4 adopts the $YbMo_2Al_4$ structure type a Rietveld refinement was performed. The data shown in Figure 37 were used for the analysis. The results for the analysis are given in Table 10. Refined atomic positions are given in Table 11. The calculated bond lengths are summed up in Table 12. Figure 38 shows the crystal structure based on this refinement. It shall briefly be discussed. ZrV_2Al_4 adopts the tetragonal body centered $YbMo_2Al_4$ structure type (space group *I*4/*mmm*), with Zr occupying the corners and center of the unit cell. The lattice parameters were refined as a = 658.7 and c = 517.3 pm. This is in the range of the corresponding gallium compound ZrV_2Ga_4. Here a = 646.2 and c = 520.7 pm were reported.[117] The Zr atom is coordinated by 12 Al atoms, in a shape of a double truncated octahedron. Additionally, eight V atoms surround the Zr atoms as squared prism resulting in a total coordination number of 20 according to $Zr@V_8Al_{12}$. The V atoms form chains along the crystallographic *c*-axis, resulting in a linear coordination environment taking only the V atoms into account. Eight Al atoms coordinate the V as distorted squared antiprism and finally, four additional Zr atoms form a tetrahedron. The Al coordination consists of three Zr atoms occupying two corners and the center of the unit cell. Four Al atoms form a distorted tetrahedron with two short and two long edges. The four V atoms coordinate

equally separated as a rectangular but not perpendicular to the Al–Zr connection. Looking at the distances found within this compound the respectively short Zr–Al and V–V distances stand out. The Zr–Al distance found in binary intermetallic such as $ZrAl_2$ (310 pm)[38] $ZrAl_3$ (284.7 pm)[245] or Zr_4Al_3 (269.5 pm)[88] differ in length, however the observed Zr–Al distances within this compound is rather sort with the 282 pm. The Al–Al distances with 260 pm being the shortest found in this compound, however, are all in the range of the above discussed compounds $ZrAl_2$ (258-268 pm), $ZrAl_3$ (277-283 pm) and Zr_4Al_3 (272 pm). They are significantly shorter than the distances within the elemental structure (286 pm)[246] With the V–V distances in the binary ZrV_2, HfV_2 and TaV_2 all being in the range of 253-263 pm[42, 247] is interesting to note that within this ternary compounds the observed distances are 259 pm indicating somehow covalent interaction of the V atoms. This distance is subject to quantum-chemical analysis. A comparable result was obtained for the Nb–Nb interactions discussed in section 5.1.5.

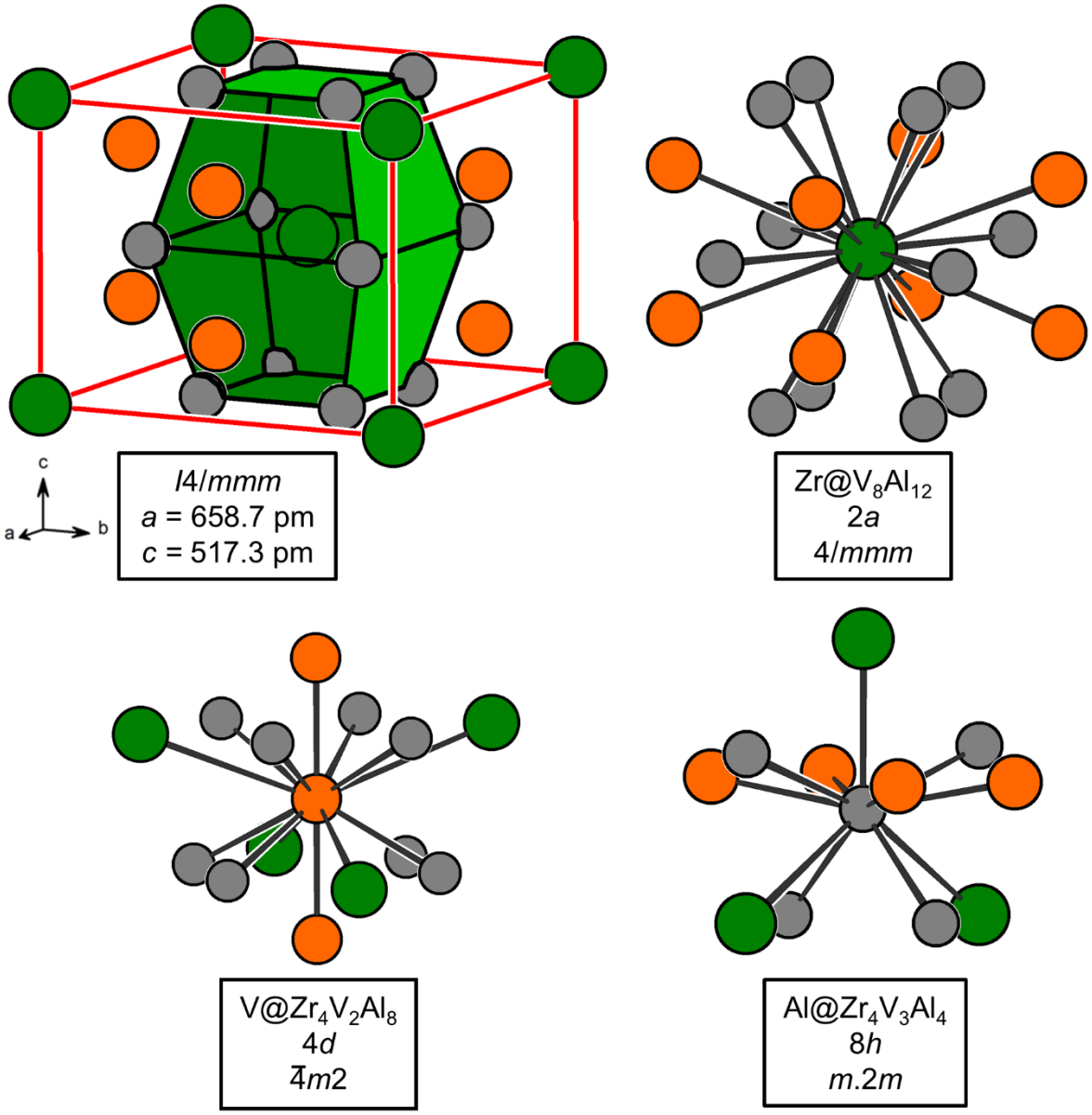

Figure 38. Structure drawing of ZrV_2Al_4 ($YbMo_2Al_4$ structure type, space group *I*4/*mmm*) refined from powder X-ray analysis presented in Figure 37 and Table 10-12. Zr, V and Al atoms are represented as green, orange and grey spheres.

Table 10. Crystallographic powder data for the tetragonal ZrV_2Al_4.

Empirical formula	ZrV_2Al_4	
Crystal system	tetragonal	
Space group	*I*4/*mmm* (no. 139)	
Structure type	$YbMo_2Al_4$	
a / pm	658.73(1)	
c / pm	517.30(1)	
V / nm^3	0.224476	
Formula units per unit cell	2	
Temperature	293 K	
Number of reflections	73	
Radiation	Cu $K_{\alpha 1,2}$	
Wavelength / pm	154.0552 / 154.4425	
R_{exp}	5.34	
R_{wp}	6.53	
R_P	5.07	
GOF	1.22	
Startin angle	6	
Final angle	130	
Step width	0.013	
Amount determined by Rietveld	96 mass%	
Side phases	$ZrAl_2$ ($MgZn_2$ type, space group $P6_3/mmc$)	2 mass%
	$ZrAl_3$ (own type, space group *I*4/*mmm*)	1 mass%
	$V_{1-x}Al_x$ (W type, space group $Im\bar{3}m$)	1 mass%

Table 11. Atom positions and isotropic displacement parameters B_{eq} (Å^2) for nominal ZrV_2Al_4 refined from powder X-ray diffraction data.

Atom	Wyckoff position	*x*	*y*	*z*	B_{eq}
Zr	2*a*	0	0	0	0.41(3)
V	4*d*	0	1/2	1/4	0.24(3)
Al	8*h*	0.30262(15)	*x*	0	0.47(3)

Table 12. Interatomic distances (pm) obtained from powder data for the tetragonal ZrV_2Al_4. Standard deviations for the interatomic distances are ≤0.2 pm.

Zr(2*a*)	4	Al	281.9
	8	Al	317.4
	8	V	353.9
V(4*d*)	2	V	258.6
	8	Al	270.9
	4	Zr	353.9
Al(8*h*)	2	Al	260.0
	4	V	270.9
	2	Al	276.6
	1	Zr	281.9
	2	Zr	317.4

The first experiment with the goal of synthesizing the isostructural Hf compound failed. Annealing an arc melted sample of HfV_2Al_4 at 1073 K for 34 d did not give the desired compound as can be seen in Figure 39. This is another example of differences between Hf and Zr in intermetallic chemistry. However, it is possible, that a theoretical "HfV_2Al_4" has a different thermal stability and can be obtained using an alternative annealing strategy.

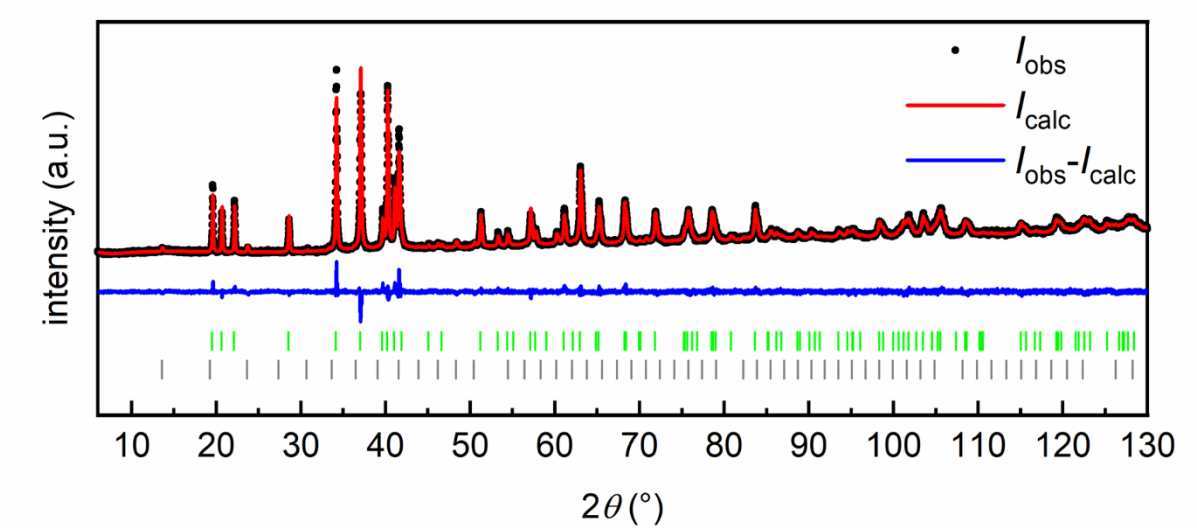

Figure 39. Powder X-ray diffraction pattern of the sample with the nominal composition HfV_2Al_4 after arc-melting and subsequent annealing at 1073 K for 34 d followed by quenching. Experimental data is shown as black dots, simulated diffraction patterns from refinements as red lines, the difference is shown as continuous blue lines. Bragg positions are shown as green ($MgZn_2$ type $Hf(V_{1-x}Al_x)_2$, space group $P6_3/mmc$, 56(1) mass%) and grey (V_5Al_8, space group $I\bar{4}3m$, 44(1) mass%) ticks.

5.2.3 Synthesis and magnetic characterization of the solid solution $Gd(Fe_{1-x}Al_x)_2$

Based on the findings of solid solutions of Laves phases, another idea for an investigation was to use a late transition metal in combination with a magnetic rare earth element. The use of solid state NMR to identify possible structural ordering, however, is not possible in this case due to the high magnetic moments, but the solid solutions within these systems can be investigated using magnetic measurements. As the first system, the solid solution $Gd(Fe_{1-x}Al_x)_2$ was chosen and synthesized for selected values of x. All samples were produced by arc-melting the elements and annealing the melting bead within a closed silica ampoule for 8 d at 1123 K. Three samples for x = 0.5, 0.25 and 0.125 were resynthesized and annealed at 1273 K for 10 d. Table 13 sums up all nominal compositions together with the respective annealing procedure. Table 14 sums up the lattice parameters obtained after Rietveld refinement of the obtained powder X-ray diffractograms. The system Gd–Fe–Al was already investigated towards the formation of different structure types stated as pseudo binary compounds adopting either the $MgZn_2$ or $MgCu_2$ type structure.[248, 249] Motivation for the presented study is the possible formation of superstructures applying long annealing times, which was not achieved. Selected examples for different compositions are also given in Table 14.

Figure 40 depicts three powder X-ray diffractograms exemplarily for the series, namely for x = 0.125, 0.5 and 0.875. The first and latter show only the presence of the solid solution adopting the $MgCu_2$ type, while for x = 0.5 a mixture of the two discussed Laves phase structure types was observed, with $MgZn_2$ being the dominant one. Interestingly for the composition range of $0.33 \leq x \leq 0.67$ both Laves phase structure types could be clearly identified. For the composition GdFeAl a literature report states that a phase pure sample adopting $MgZn_2$ type could be identified.[249] The findings concerning the structural data presented here are in good agreement with literature data.[248] A difference, however, is the finding, that for all compositions both structure types could be identified in contrast to literature studies. No hints for the formation of superstructures were observed.

These results are clearly in contrast to the systems investigated within this thesis so far. However, the findings are in line with literature data reported on solid solutions. The synthesis of the binary endmembers of the solid solution was not easily doable, therefore the lattice parameters were taken from literature.

Table 13. Syntheses in the system $Gd(Fe_{1-x}Al_x)_2$. Grey lines are shown for better visibility of the three samples annealed at a different temperature.

Composition Nominal	Composition as Laves phase	x_{theo}	Annealing	Figure
Gd_4FeAl_7	$Gd(Fe_{0.125}Al_{0.875})_2$	0.875	1123 K – 8 d	Figure 40, Figure S5
Gd_2FeAl_3	$Gd(Fe_{0.25}Al_{0.75})_2$	0.75	1123 K – 8 d	Figure S6
$Gd_3Fe_2Al_4$	$Gd(Fe_{0.33}Al_{0.67})_2$	0.67	1123 K – 8 d	Figure S7
$Gd_5Fe_4Al_6$	$Gd(Fe_{0.4}Al_{0.6})_2$	0.6	1123 K – 8 d	Figure S8
GdFeAl	$Gd(Fe_{0.5}Al_{0.5})_2$	0.5	1123 K – 8 d	Figure 40, Figure S9
GdFeAl	$Gd(Fe_{0.5}Al_{0.5})_2$	0.5	1273 K – 10 d	Figure S10
$Gd_3Fe_4Al_2$	$Gd(Fe_{0.67}Al_{0.33})_2$	0.33	1123 K – 8 d	Figure S11
Gd_2Fe_3Al	$Gd(Fe_{0.75}Al_{0.25})_2$	0.25	1123 K – 8 d	Figure S12
Gd_2Fe_3Al	$Gd(Fe_{0.75}Al_{0.25})_2$	0.25	1273 K – 10 d	Figure S13
Gd_4Fe_7Al	$Gd(Fe_{0.875}Al_{0.125})_2$	0.125	1123 K – 8 d	Figure 40, Figure S14
Gd_4Fe_7Al	$Gd(Fe_{0.875}Al_{0.125})_2$	0.125	1273 K – 10 d	Figure S15

Table 14. Observed lattice parameters and refined mass fractions for multi-phase samples for the different species obtained in the system $Gd(Fe_{1-x}Al_x)_2$. Grey lines are shown for better visibility of the three samples annealed at a different temperature. Deviations for the given mass fractions obtained after Rietveld refinement are ±1 mass%.

Nominal Composition	x_{theo}	$MgCu_2$ type structure		$MgZn_2$ type structure			Literature
		a / pm	mass%	*a* / pm	*c* / pm	mass%	
$GdAl_2$	1	790.0		–	–		[250]
Gd_4FeAl_7	0.875	785.3		–	–		*
Gd_2FeAl_3	0.75	778.8		–	–		*
$Gd(Fe_{0.3}Al_{0.7})_2$	0.7	776.8		–	–		[248],$
$Gd_3Fe_2Al_4$	0.67	774.8		–	–		*
$Gd_5Fe_4Al_6$	0.6	772.1	92	548.0	880.3	8	*
GdFeAl	0.5	–		541.4	881.2		[249]
GdFeAl	0.5	–		541.4	881.2		[248] ,$
GdFeAl	0.5	766.4	25	542.8	879.3	75	*
GdFeAl	0.5	770.0	23	543.2	879.2	77	*
$Gd_3Fe_4Al_2$	0.33	756.8	16	535.2	874.8	84	*
Gd_2Fe_3Al	0.25	752.1		–	–		[248] ,$
Gd_2Fe_3Al	0.25	752.1		–	–		*
Gd_2Fe_3Al	0.25	751.9		–	–		*
Gd_4Fe_7Al	0.125	745.7		–	–		*
Gd_4Fe_7Al	0.125	745.6		–	–		*
$GdFe_2$	0	739.6		–	–		[251]

* This work, $ Within reference [248] more compositions were analyzed, however, only selected data are presented here.

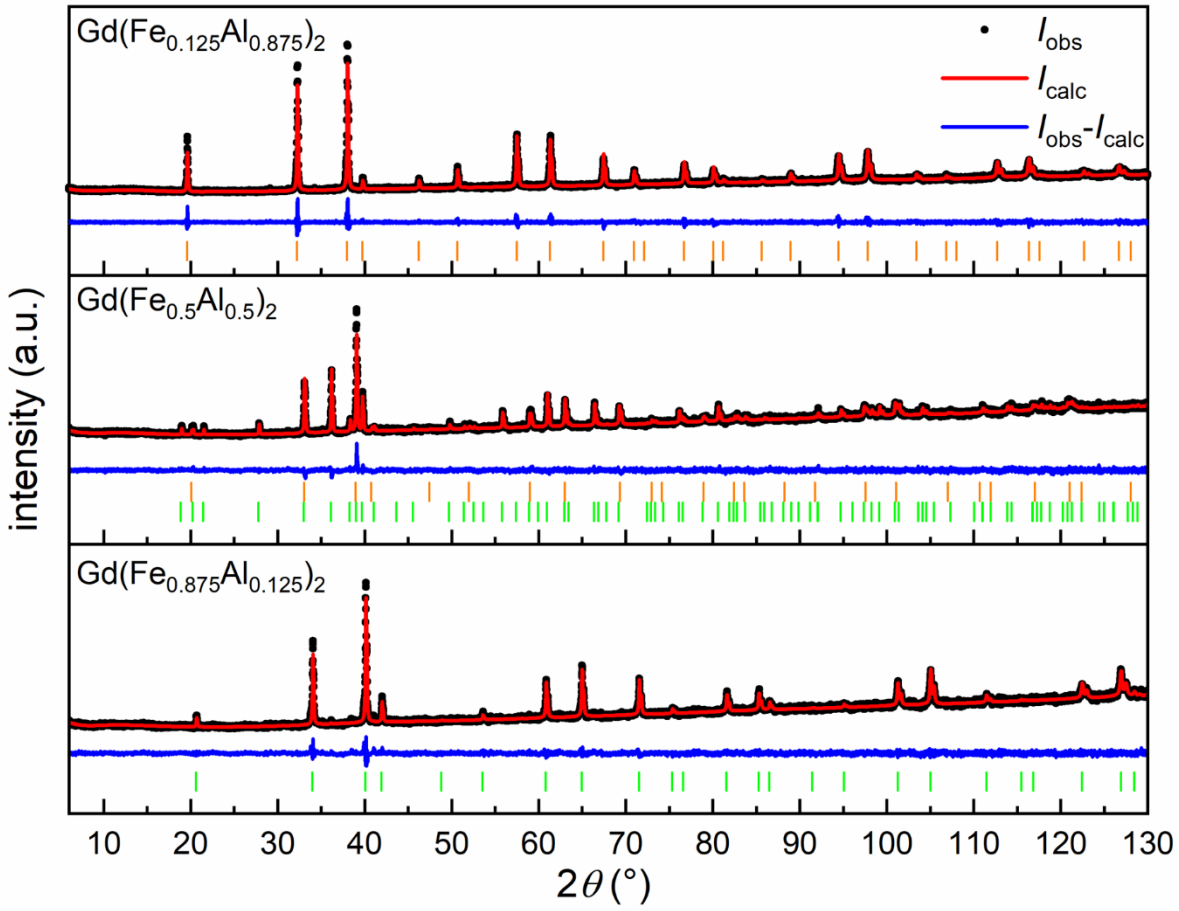

Figure 40. Powder X-ray diffraction patterns of three samples of the solid solution $Gd(Fe_{1-x}Al_x)_2$ for (from *top* to *bottom*) x = 0.875, 0.5 and 0.125. Experimental data is shown as black dots, simulated diffraction patterns from refinements as red lines, the difference is shown as continuous blue lines. Bragg positions are shown as orange ($MgCu_2$ type, space group $Fd\bar{3}m$) and green ($MgZn_2$ type, space group $P6_3/mmc$) ticks. The refined mass% are given in Table 14.

Figure 41 graphically depicts the observed lattice parameters. Data for the binary endmembers were taken from literature as stated in Table 14. Also, in contrast to the systems of mainly early transition metals discussed before, bigger changes in the lattice parameters are observed (~ 40 pm). Moreover, the trend shows almost linear behavior corresponding to Vegard's rule, which has not been observed in the previously discussed systems. A refinement of the site occupancy factors of Al and Fe, which mix on the respective Zn or Cu positions of the prototypes was performed, if possible. However, no trends or hints for possible superstructure formations were observed. For detailed analysis single-crystal analysis could be useful.

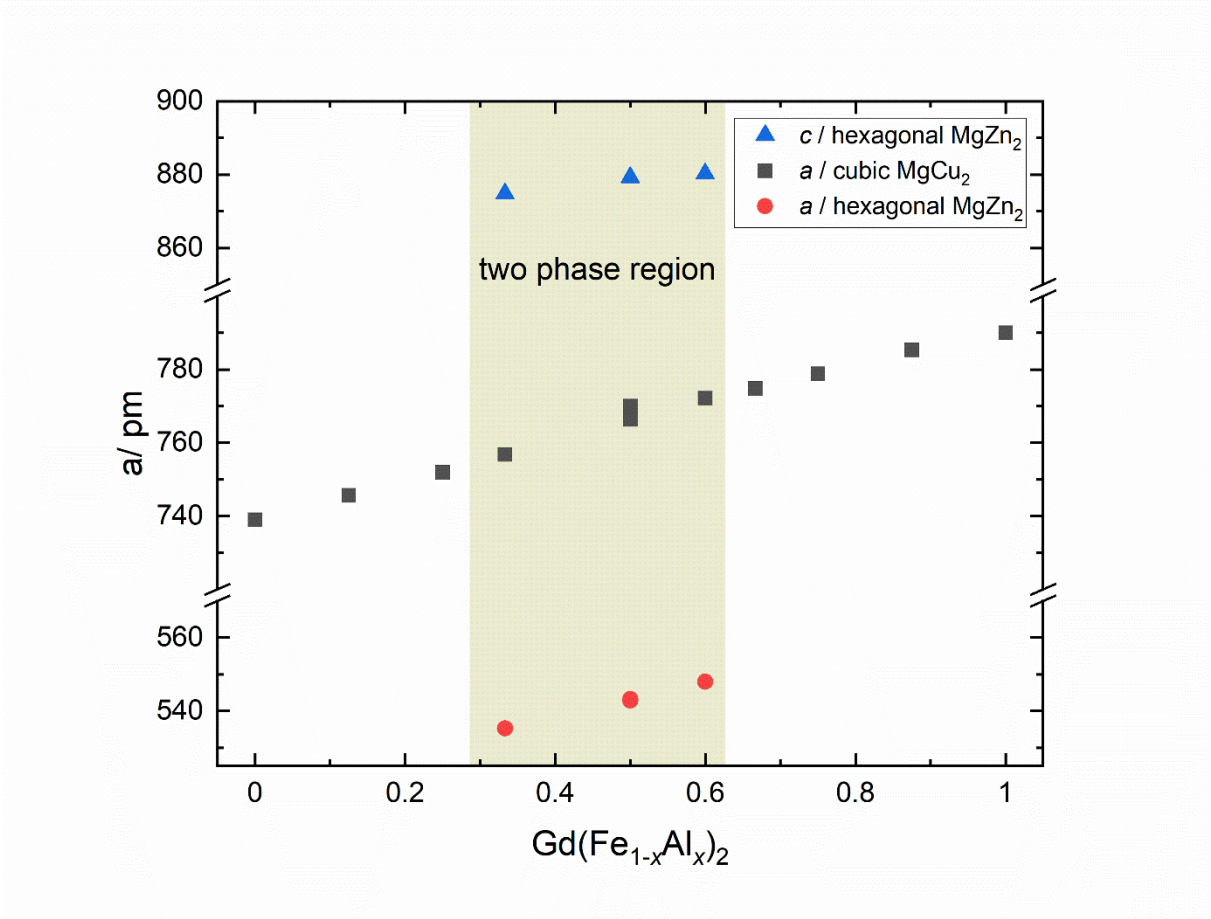

Figure 41. Lattice parameter obtained after the analysis of the powder X-ray diffractograms of the solid solution $Gd(Fe_{1-x}Al_x)_2$. For some compositions a mixture of hexagonal $MgZn_2$ and cubic $MgCu_2$ type was identified.

For some members of the synthesized solid solutions magnetic measurements were performed. The results are summarized in Table 15. All three samples investigated show a ferromagnetic transition at temperatures above 100 K. The data for each sample is shown in the appendix. To compare the magnetic ordering temperatures, they are depicted in Figure 42. One can see a dramatic change compared to the endmember $GdFe_2$. The temperatures are comparable to the aluminide $GdAl_2$. All magnetic characterization is in good agreement with literature data, which were obtained for slightly different composition.[248]

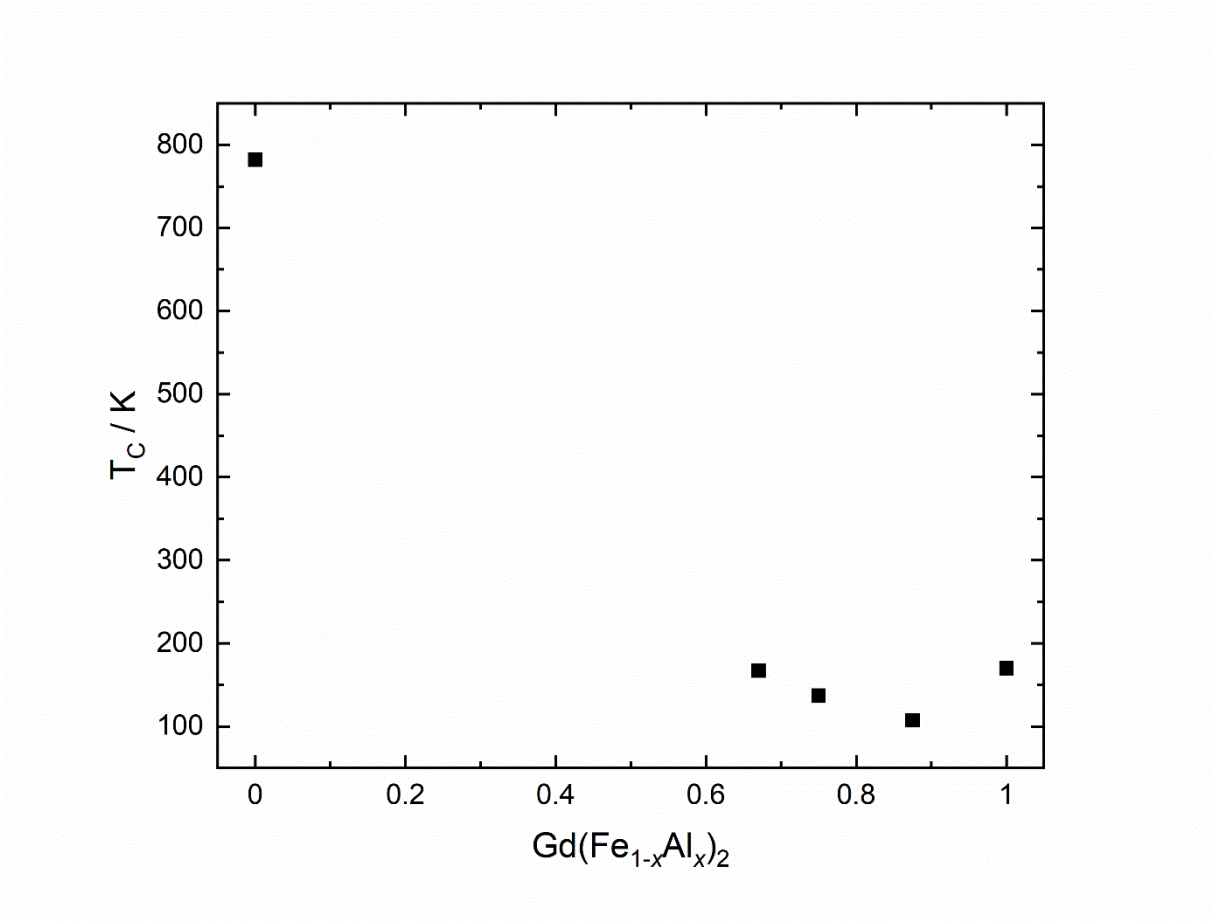

Figure 42. Ferromagnetic ordering temperatures for the three investigated samples of the solid solution $Gd(Fe_{1-x}Al_x)_2$. Data for the binary endmembers were taken from literature.

Table 15. Magnetic measurement data of selected samples of the solid solution $Gd(Fe_{1-x}Al_x)_2$.

Compound	T_C / K	μ_{eff} (μ_B)	θ_P / K	μ_{sat} (μ_B)	Literature
$GdFe_2$	782	–		3.35	[252]
$Gd(Fe_{0.33}Al_{0.66})_2$	167(1)	7.39(2)	118(1)	6.23(2)	*
$Gd(Fe_{0.25}Al_{0.75})_2$	137(1)	8.94(2)	150(1)	6.63(2)	*
$Gd(Fe_{0.125}Al_{0.875})_2$	107(1)	9.39(2)	210(1)	6.98(2)	*
$GdAl_2$	170	8.2	169	7.2	[253]

* This work.

5.2.4 Comparing order and disorder in rare earth aluminum silicides using ^{27}Al, ^{29}Si and ^{45}Sc NMR

Compounds with the general formula RE_2AlSi_2 are known for several rare earth elements. The compounds containing the closed shell rare earth metals being either diamagnetic or Pauli-paramagnetic offer the opportunity to investigate these compounds by solid state NMR, since ^{27}Al and ^{29}Si are both NMR active nuclei. For the scandium containing compound an additional local probe is available with the ^{45}Sc nucleus. Since these compounds are mainly characterized by X-ray crystallography, the question about the local order of the Al and Si atoms can be asked. It is possible that the two atoms, which can hardly be differentiated by X-ray diffraction methods, do order as strictly as the description of the ternary compounds suggest.

A focus was put on the rare earth elements Sc, Y and Lu. The Sc compound Sc_2AlSi_2 adopts the tetragonal Mo_2FeB_2 structure type (*P*4/*mbm*),[254] which is a coloring variant of the U_3Si_2 type structure, which is formed in compounds with the general formula M_3Si_2 (*M* = La, Zr, Hf, Ce, Pr, Th, U-Pu).[255] The compounds Y_2AlSi_2 and Lu_2AlSi_2 are reported to crystallize in the orthorhombic W_2CoB_2 structure type (*Immm*).[256] Both structure types exhibit only one crystallographic independent site per atom making these compounds a suitable candidate for solid state NMR investigations.

Synthesis of the compounds was done by arc-melting the elements followed by annealing of the samples in fused silica ampoules for different dwelling times and temperatures. Table 16 summaries all synthetic attempts together with the respective nominal composition, the annealing strategy and the results of the Rietveld refinement targeting the obtained impurities or product ratios. Table 17 summarizes the refined lattice parameters for the compounds of interest. The powder X-ray diffractograms for the three samples, which were synthesized by arc-melting and annealing the sample at 973 K for 14 d are shown in Figure 43.

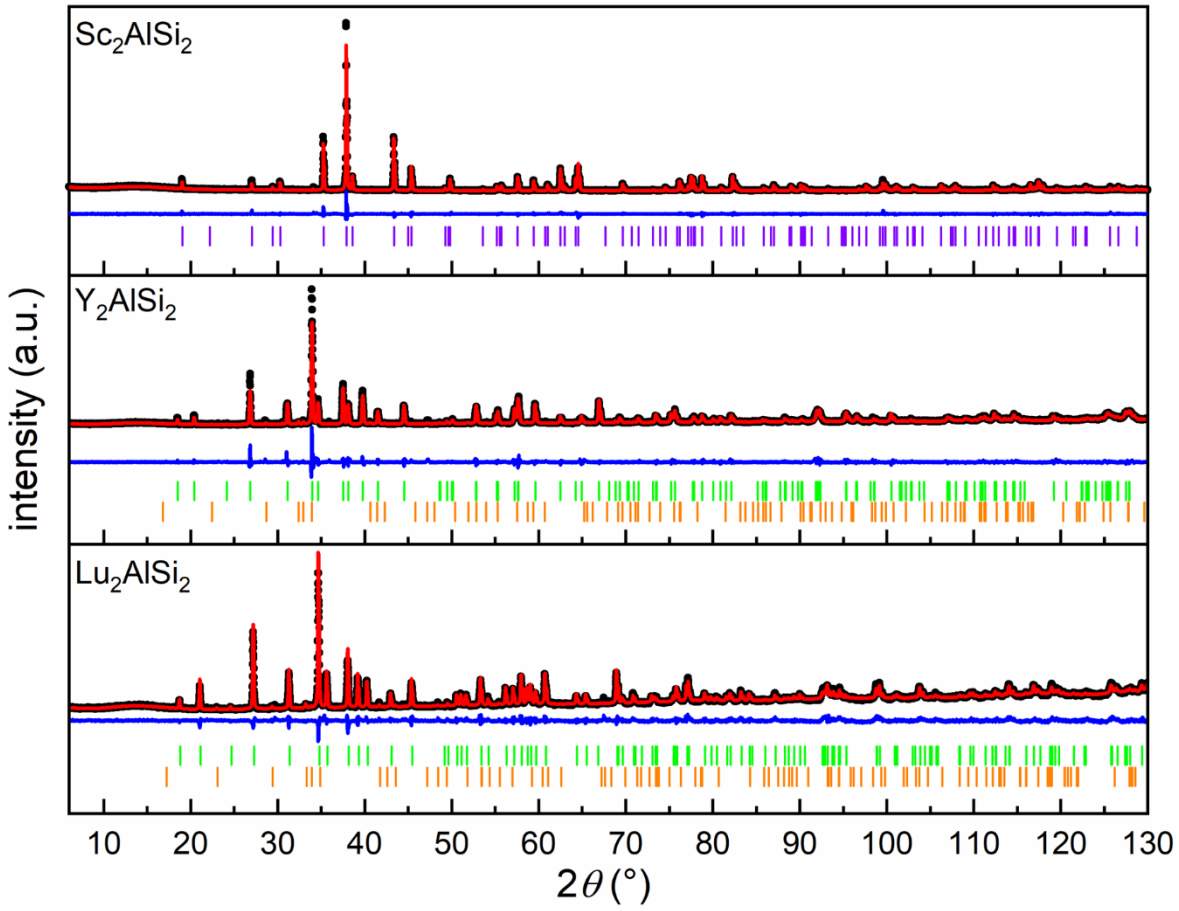

Figure 43. Powder X-ray diffraction patterns of the three compounds RE_2AlSi_2 (*RE* = Sc, Y, Lu) Experimental data is shown as black dots, simulated diffraction patterns from refinements as red lines, the difference is shown as continuous blue lines. Bragg positions are shown as purple (Mo_2FeB_2 structure type, space group *P*4/*mbm*), green (W_2CoB_2 structure type, space group *Immm*) and orange (*RE*Si, space group *Cmcm*) ticks. The refined mass% are given in Table 16.

As can be seen, the three compounds could be obtained, the structure could be confirmed based on the PXRD data. However, within the Y and Lu compound a small impurity of *RE*Si with <4 mass% could be identified. At first, the NMR data of the Sc compound shall be discussed. All recorded spectra are shown in Figure 44. As can be seen the three spectra exhibit one sharp central transition for each nucleus. This perfectly corresponds to the structure description. The sharp transitions as well as the pronounced set of spinning sidebands for the quadrupolar nuclei are a good hint for a clearly ordered structure, especially the ordering between Si and Al. Details of the simulation of the spectra as well as the positions of the resonances such as calculated parameters can be found in Table 18.

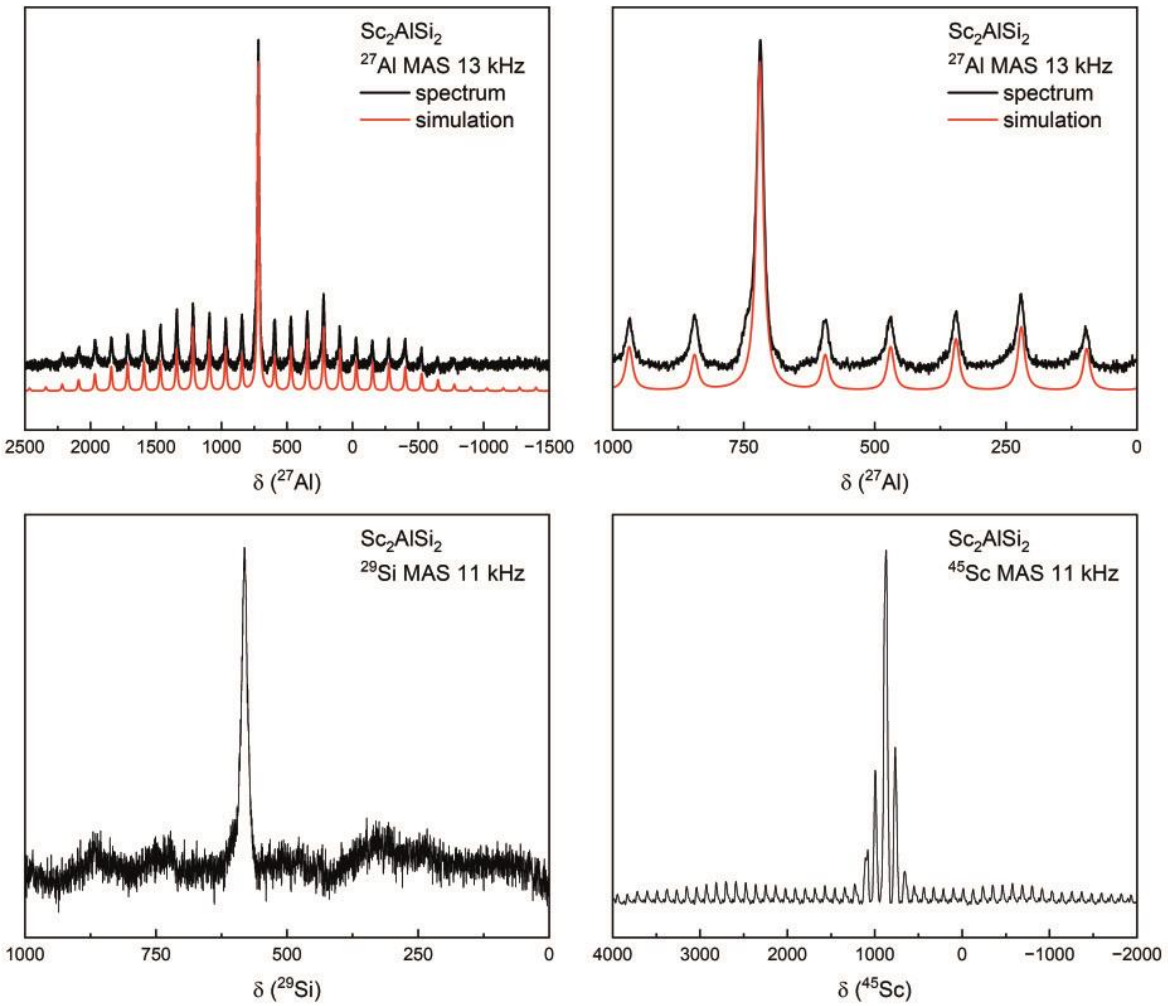

Figure 44. ^{27}Al full spectrum (*top left*) and zoomed region on the central transition (*top right*), ^{29}Si (*bottom left*), and ^{45}Sc (*bottom right*) solid state NMR spectra of Sc_2AlSi_2.

The situation is different for the other two compounds. For the Lu compound it was not possible to record a useful spectrum. The line broadening is severe (data not shown). The ^{27}Al NMR spectrum for the yttrium compound is shown in Figure 45. The spectrum shows a broadened central transition around 1150 ppm, the absence of a well-resolved spinning sideband pattern as well as a strong signal likely to originate from an impurity (~ 700 ppm). This gives rise to the assumtion that rather a solid solution of Al and Si is present in the strucures than a fully ordered compound, especially when compared to the scandium compound Furthermore it was not possile to measure a ^{29}Si spectrum; no signal was observed at all.

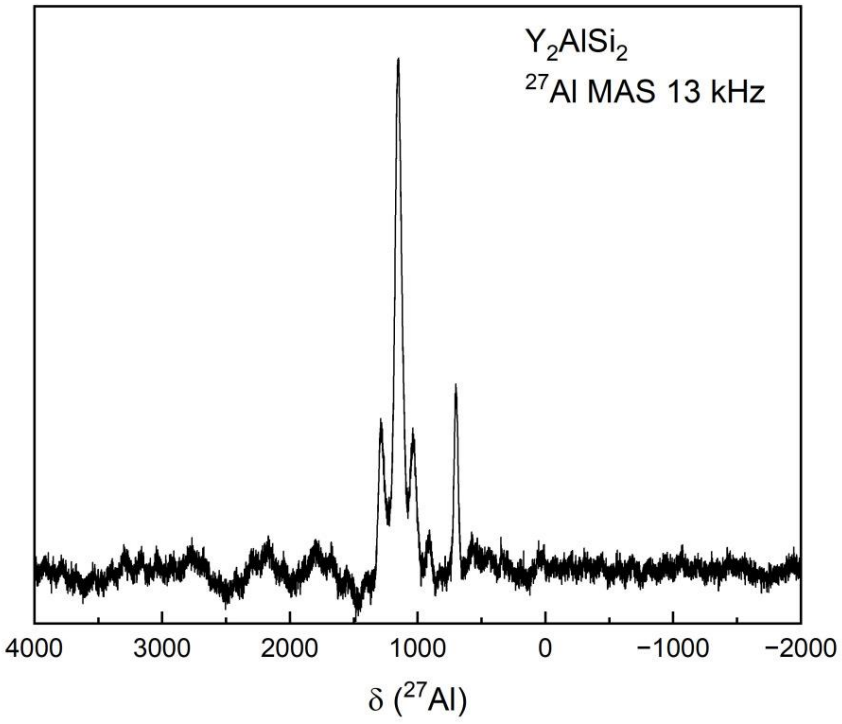

Figure 45. ^{27}Al solid state NMR spectrum of Y_2AlSi_2 recorded at a MAS frequency of 13 kHz.

These observations, however, rose the question whether it is possible to increase the ordering by changing the composition a little. Therefore, more samples with slight changes in the Si/Al ratio were prepared. They are summarized in Table 16, however, not all powder diffractograms are shown and discussed here. The annealing startegy was changed with the goal to get a higher degree of ordering when the sample is annealed at higher temperature and slowly cooled. However, again, no phase pure samples could be obtained but the synthesis of Y_2AlSi_2 was reproduced.

This observation is again a hint, that although it is not visible in the NMR spectra an ordering takes place and the system can not form any kind of solid solution by arbitratily changing the Al/Si ratio. For the lutetium compound an interesting observation was made. By changing the Al/Si ratio all of a sudden the tetragonal structure type (Mo_2FeB_2, *P*4/*mbm*) was observed within the diffractograms. This polymorphism of Lu_2SiAl_2 is not known to literature. The highest amounts of this structure type could be obtained by annealing the arc-melted sample at significantly higher temperatures (1373 K) for four days. One can therefore expect the phase to be the high temperature phase. A phase-pure synthesis was not possible yet. Figure 46 depicts the result of the explained synthesis. The refined lattice parameters for this potential new compound within the system Lu–Al–Si are given in Table 17.

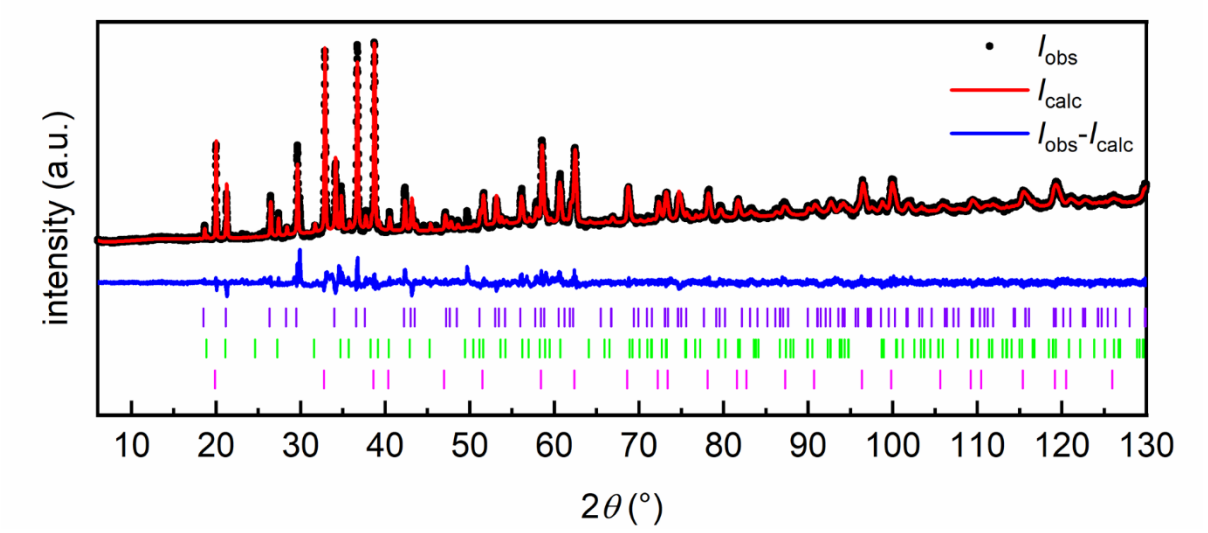

Figure 46. Powder X-ray patterns of nominal Lu_2Al_2Si annealed at 1373 K for 96 hours. Experimental data is shown as black dots, simulated diffraction patterns from refinements as red lines, the difference is shown as continuous blue lines. Bragg positions are shown as violet (Mo_2FeB_2 structure type, space group *P*4/*mbm*), green (W_2CoB_2 structure type, space group *Immm*) and magenta ($LuAl_2$, space group $Fd\bar{3}m$) ticks. The refined mass% are given in Table 16.

For the case of yttrium, a nominal $Y_2Al_{1.5}Si_{1.5}$ adopting the tetragonal Mo_2FeB_2 structure type is known. Any attempts to re-isolate the phase have not been successful yet. It was further not possible to isolate single crystals that could give more information about the correct structure. It is not clear whether the polymorphism depends on the temperature or composition or both. For dysprosium a change in composition is reported to flip the structure types. The compound Dy_2Al_2Si is reported to adopt the tetragonal,[257] while Dy_2AlSi_2 adopts the orthorhombic structure.[258]

To conclude, for the Sc compound adopting the tetragonal Mo_2FeB_2 structure type (*P*4/*mbm*) ordering of the Al and Si atoms could be proven by the local probe solid state NMR. The investigations of the systems Lu/Y–Al–Si however raised interesting questions about the ordering, which give many ideas for future investigations. For the Lu system a polymorphism could be shown, which is not fully understood yet and must be resolved in the future.

Table 16. Weighed and refined compositions alongside the weight fractions based on powder X-ray diffraction experiments and Rietveld refinements. Refined compositions are calculated based on the mass fractions obtained during Rietveld refinement.

Compositions weighed	refined	annealing temperatures	mass fractions / mass%	Figure
Sc_2AlSi_2	Sc_2AlSi_2	700 °C, 14 d	100, Sc_2AlSi_2 (*P*4/*mbm*)	Figure 43
Y_2AlSi_2	$Y_2Al_{0.97}Si_2$	700 °C, 14 d	97(1), Y_2AlSi_2 (*Immm*) 3(1), YSi (*Cmcm*)	Figure 43
$Y_2Al_{0.75}Si_{2.25}$	–	850 °C, 16 d	Y_2AlSi_2 (*Immm*) unidentified side phase	$
$Y_2Al_{1.25}Si_{1.75}$	$Y_2Al_{1.14}Si_{1.86}$	850 °C, 16 d	79(1), Y_2AlSi_2 (*Immm*) 11(1), YSi (*Cmcm*) 10(1), YAl_2 ($Fd\bar{3}m$)	$
$Y_2Al_{1.5}Si_{1.5}$	$Y_2Al_{1.15}Si_{1.72}$	850 °C, 16 d	60(1), Y_2AlSi_2 (*Immm*) 24(1), YSi (*Cmcm*) 16(1), YAl_2 ($Fd\bar{3}m$)	$
Y_2Al_2Si	$Y_2Al_{1.93}Si_{1.07}$	850 °C, 16 d	7(1), Y_2AlSi_2 (*Immm*) 42(1), YSi (*Cmcm*) 51(1), YAl_2 ($Fd\bar{3}m$)	$
Lu_2AlSi_2	$Lu_2Al_{0.96}Si_2$	700 °C, 14 d	96(1), Lu_2AlSi_2 (*Immm*) 4(1), LuSi (*Cmcm*)	Figure 43
$Lu_2Al_{1.5}Si_{1.5}$	$Lu_2Al_{1.40}Si_{1.69}$	850 °C, 16 d	33(1), Lu_2AlSi_2 (*P*4/*mbm*) 45(1), Lu_2AlSi_2 (*Immm*) 6(1), LuSi (*Cmcm*) 16(1), $LuAl_2$ ($Fd\bar{3}m$)	$
Lu_2Al_2Si	$Lu_2Al_{1.68}Si_{1.36}$	850 °C, 16 d	40(1), Lu_2AlSi_2 (*P*4/*mbm*) 26(1), LuSi (*Cmcm*) 33(1), $LuAl_2$ ($Fd\bar{3}m$)	$
Lu_2Al_2Si	$Lu_2Al_{2.18}Si_{1.22}$	1100 °C, 4 d	51(1), Lu_2AlSi_2 (*P*4/*mbm*) 7(1), Lu_2AlSi_2 (*Immm*) 42(1), $LuAl_2$ ($Fd\bar{3}m$)	Figure 46

$ PXRD data not shown.

Table 17. Lattice parameters and unit cell volumes (powder, DFT and literature data) of the members of the RE_2AlE_2 series. The respective structure types are given.

compound	structure type	*a* (pm)	*b* (pm)	*c* (pm)	*V* (nm^3)	Ref.
Sc_2AlSi_2	Mo_2FeB_2	659.38(1)	*a*	399.61(1)	0.1737	*, PXRD
Sc_2AlSi_2	Mo_2FeB_2	655.65	*a*	395.93	0.1702	*, DFT
Sc_2AlSi_2	Mo_2FeB_2	659.7(2)	*a*	399.4(2)	0.1738	[254]
Y_2AlSi_2	W_2CoB_2	406.68(1)	573.96(1)	869.38(1)	0.2029	*, PXRD
Y_2AlSi_2	W_2CoB_2	405.92	563.82	866.18	0.1982	*, DFT
Y_2AlSi_2	W_2CoB_2	405.0	574.8	866.3	0.2017	[256]
Lu_2AlSi_2	W_2CoB_2	398.65(1)	569.63(1)	839.39(1)	0.1906	*, PXRD
Lu_2AlSi_2	W_2CoB_2	399.77	555.87	834.58	0.1855	*, DFT
Lu_2AlSi_2	W_2CoB_2	400.1(1)	566.2(2)	841.6(6)	0.1907	[256]
Lu_2AlSi_2	Mo_2FeB_2	676.76(1)	*a*	420.32(1)	0.1925	*, PXRD
Lu_2AlSi_2	Mo_2FeB_2	668.08	*a*	413.02	0.1843	*, DFT

* This work.

Table 18. Summary of the NMR observables of the members of the RE_2AlSi_2, extracted from the DMFit simulation of the ^{27}Al, ^{29}Si and ^{45}Sc MAS-NMR spectra with δ being the resonance (in ppm), C_Q the quadrupolar parameter (in kHz) and η_Q the asymmetry parameter. Calculated values from DFT are given with the subscript *calc*.

compound	nucleus	δ	C_Q	η_Q	$C_{Q,calc}$	$\eta_{Q,calc}$
Sc_2AlSi_2	^{45}Sc	~870	–	–	–10527	0.745
	^{27}Al	719	898	0.14	–742	0.745
	^{29}Si	581	–	–	0	0.165
Y_2AlSi_2	^{27}Al	~1150 (impurity detected)			–5350	0.426
	^{29}Si	not detected			0	0.850
Lu_2AlSi_2	^{27}Al	extremely broadened signal			–4783	0.723
	^{29}Si	not detected			0	0.816

5.2.5 $YbTi_2Al_{19.4}Sn_{0.6}$; a quaternary aluminum compound in the $CeCr_2Al_{20}$ type structure

Attempts to incorporate a heavier also NMR active nuclei in the $CeCr_2Al_{20}$ type structure were tried with the compound $YbTi_2Al_{20}$. A major drawback of the literature-known synthesis is that the studies focus on the growth of large single crystals, usually based on flux growth. A phase-pure synthesis with the correct stoichiometric amount of the elements was targeted in the studies here. Figure 47 shows the diffractogram of X-ray pure $YbTi_2Al_{20}$. The compound could be synthesized by placing the elements in the correct stoichiometric amount into an alumina crucible, sealing it in an evacuated quartz ampoule and annealing it for 30 days at 1273 K. Lattice parameters are summed up in Table 19.

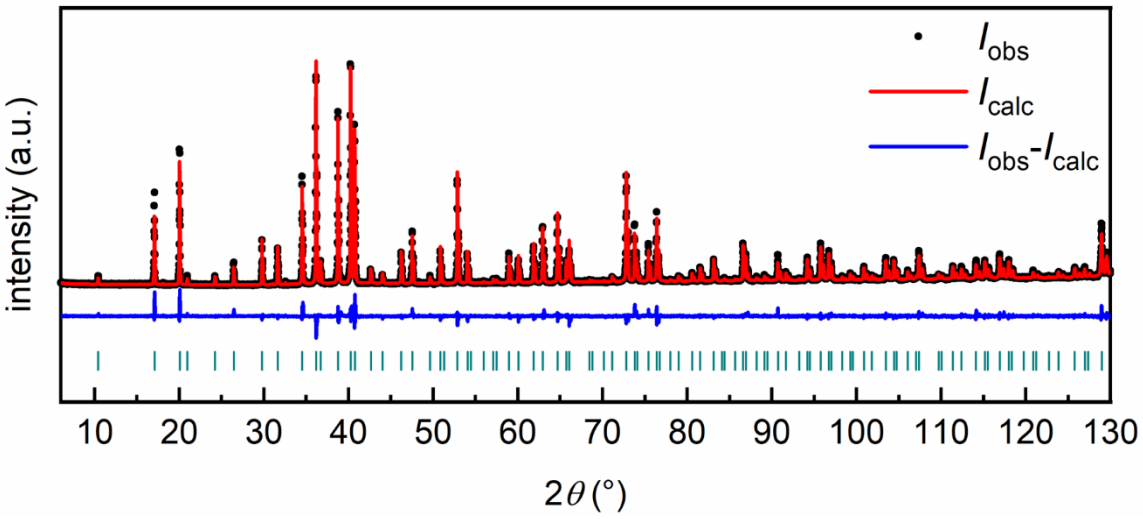

Figure 47. Powder X-ray diffraction patterns of $YbTi_2Al_{20}$. Experimental data is shown as black dots, simulated diffraction patterns from refinement as red lines, the difference is shown as continuous blue lines. Bragg positions are shown as green ($YbTi_2Al_{20}$, space group $Fd\bar{3}m$) ticks.

The identical procedure described was tested for nominal 1-2-18-2, substituting two Al atoms with Sn. The powder X-ray diffractogram for nominal $YbTi_2Al_{18}Sn_2$ is shown in Figure 48. It becomes immediately clear that the full incorporation of Sn into the structure did not work, nevertheless the $CeCr_2Al_{20}$ structure could be identified. The Rietveld refinement revealed a change of the lattice parameter increasing from a = 1468.6 to 1474.5 pm giving a hint of at least some solubility of Sn. To clarify this a single-crystal analysis has been carried out. The results are given in Table 20-22. The structure has been described in detail in the introduction. As expected, the larger tin atoms can only be found in the largest coordination environment, being the bi-capped hexagonal prism, $Al/Sn@Yb_2Al_{12}$. The bicapped pentagonal prisms are only occupied with aluminum. However, a complete filling of this position was not

possible with the applied synthetic strategy. Longer annealing times or different methods need to be applied to succeed here.

Table 19. Obtained lattice parameters for the investigations in the system $YbTi_2Al_{20-x}Sn_x$.

Nominal composition	method	*a* / pm	Ref.
$YbTi_2Al_{20}$	powder	1468.6(1)	*, Figure 47
$YbTi_2Al_{20}$	powder	1468.1(1)	[135]
$YbTi_2Al_{20}$	single crystal	14.6890(18)	[259]
$YbTi_2Al_{18}Sn_2$	powder	1474.5(1)	*, Figure 48
$YbTi_2Al_{18}Sn_2$	single crystal	1471.9	*

* This work.

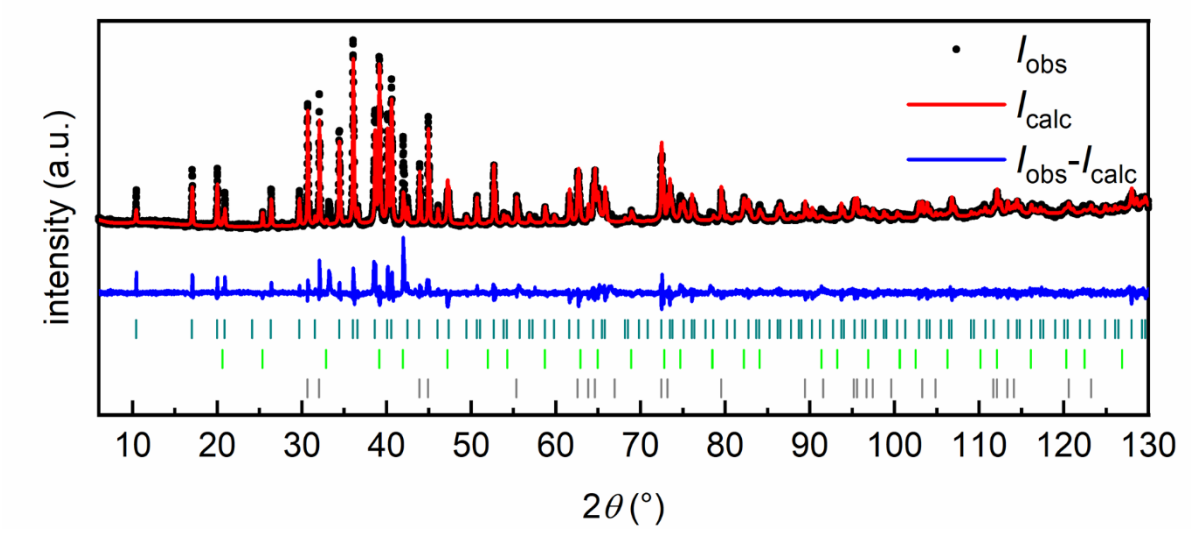

Figure 48. Powder X-ray diffraction pattern of nominal $YbTi_2Al_{18}Sn_2$. Experimental data is shown as black dots, simulated diffraction patterns from refinements as red lines, the difference is shown as continuous blue lines. Bragg positions are shown as blue-green ($YbTi_2Al_{20}$, space group $Fd\bar{3}m$, 56(1) mass%), green ($TiAl_3$, space group $I4/mmm$, 34(1) mass%) and grey (elemental Sn, space group $I4_1/amd$, 10(1) mass%) ticks.

Table 20. Crystallographic data and structure refinement from single-crystal X-ray diffraction experiments for nominal $YbTi_2Al_{18}Sn_2$.

Nominal composition	$YbTi_2Al_{18}Sn_2$
Refined composition	$YbTi_2Al_{19.38(1)}Sn_{0.62(1)}$
Structure type	$CeCr_2Al_{20}$ ($Fd\bar{3}m$)
Lattice parameters a (pm)	1471.9
V (nm^3)	3.18873
Molar mass, g mol^{-1}	865.8
Density calc., g cm^{-3}	3.61
Crystal size, µm	60×50×35
Detector distance, mm	40
Exposure time, s	40
Range in hkl	$-24 \le h \le 22$, $-22 \le k \le 17$, $-23 \le l \le 24$
θ_{min}, θ_{max}, deg	2.4, 36.36
Linear absorption coeff., mm^{-1}	8.8
No. of reflections	6975
R_{int} / R_σ	0.0829 / 0.0445
No. of independent reflections	417
Reflections used [$I \ge 3\sigma(I)$]	305
F(000), e	3177
$R1$ / $wR2$ for $I \ge 3\sigma(I)$	0.0255 / 0.0431
$R1$ / $wR2$ for all data	0.0516 / 0.0505
Data / parameters	417 / 18
Goodness-of-fit on F^2	1.02
Extinction coefficient	880(150)
Diff. Fourier residues /e$^-$ Å^{-3}	+2.14 / –0.31

Table 21. Atom positions and equivalent isotropic displacement parameters (pm^2) for nominal $YbTi_2Al_{18}Sn_2$. U_{eq} is defined as one third of the trace of the orthogonalized U_{ij} tensor. Grey lines are shown for better visibility.

Atom	Wyckoff position	x	y	z	Occ	U_{eq}
Yb	8*b*	1/8	1/8	1/8	1	117(1)
Ti	16*c*	1/2	1/2	1/2	1	57(1)
Al1	16*d*	0	0	0	0.31(1)	152(2)
Sn1	16d	0	0	0	0.69(1)	152(2)
Al2	48*f*	0.48622(9)	1/8	1/8	1	94(3)
Al3	96*g*	0.05931(5)	*x*	0.32473(7)	1	122(2)

Table 22. Interatomic distances (pm) for nominal $YbTi_2Al_{18}Sn_2$. Standard deviations for the interatomic distances are ≤0.2 pm.

Yb (8*a*)	Al1/Sn1	4	318.7
	Al3	12	324.2
Ti (16*d*)	Al2	6	261.0
	Al3	6	286.0
Al1/Sn1 (16*c*)	Al3	12	313.8
	Yb	2	318.7
Al2 (48*f*)	Ti	2	261.0
	Al3	2	274.2
	Al2	4	288.9
	Al3	4	289.1
Al3 (96*g*)	Al3	1	273.5
	Al2	1	274.2
	Al3	2	279.0
	Ti	1	286.0
	Al2	2	289.1
	Al3	2	297.9
	Al1/Sn1	2	313.8
	Yb	1	324.2

5.3 Moving between the worlds – the appearance of an unexpected intermetallic sub-oxide

Published as an article:

Formation of the Sub-oxide $Sc_4Au_2O_{1-x}$ and the Drastically Negative ^{27}Al NMR Shift in Sc_2Al

Elias C. J. Gießelmann, Mathis Radzieowski, Samir F. Matar and Oliver Janka, *Inorg. Chem.* **2023**, *62*, 9602.

https://doi.org/10.1021/acs.inorgchem.3c01097

Contributions of the authors to this manuscript

Elias C. J. Gießelmann and Dr. Mathis Radzieowski did the synthetic work, as well as data evaluation. Solid state NMR spectra were measured and evaluated by Elias C. J. Gießelmann who also provided an initial draft of the manuscript. Prof. Dr. Samir Matar did the quantum chemical calculations. PD Dr. Oliver Janka supervised the work and finalized the manuscript.

Summary

During explorative syntheses in the scandium rich corner of the ternary system Sc–Au–Al, Mathis Radzieowski found the solid solution of Sc_2Au ($PbCl_2$ type, *Pnma*) and Sc_2Al (Ni_2In / $Co_{1.75}Ge$ type, $P6_3/mmc$). This showed a solubility of Au and Al in the respective opposing structure types as well as a two-phase region. The endmembers of the solid solution could nicely be characterized with ^{27}Al and ^{45}Sc NMR. A site assignment of Sc in both compounds was possible due to the large difference in the quadrupolar coupling constants, which were calculated by DFT calculations. The ^{27}Al spectrum of Sc_2Al shows a significant negative resonance shift of –673 ppm, which is to the best of our knowledge the lowest observed ^{27}Al shift in metallic systems with them ranging usually from around 0 to 1200 ppm.

Interestingly, in one attempt to synthesize Sc_2Au a powder pattern was observed, which could not be described using one of the two structure types. This could later be indexed with the cubic W_4Co_2C type structure, which formed due to unwanted contamination during the reaction with oxygen leading to the sub-oxide $Sc_4Au_2O_{1-x}$. Attempts to synthesize the product

under strict exclusion of oxygen did not lead to the same result eliminating the possibility of the cubic structure to be a high temperature phase of Sc_2Au.

The binary phase Sc_2Au proved to be unstable under ambient conditions decomposing into Sc_2O_3 and elemental Au, which was shown by simply letting a powdered sample sitting in the laboratory and recording a powder X-ray pattern after several days. This is in so far highly interesting as elemental Sc is stable in air and only forms a small passivating oxide layer. The electronic situation in the intermetallic compound seems to have an influence on the oxidation behavior. A thermal analysis confirmed this behavior. As a result of heating the sample under oxygen a mass increase was observed. The product is crystalline Sc_2O_3 and elemental Au. With this knowledge, one can propose that the newly found sub-oxide seems to stabilize the the cubic W_4Co_2C type structure. A targeted synthesis of the mentioned sub-oxide could be achieved by different routes, either melting Sc, Au and Sc_2O_3 in the correct stoichiometry (10:6:1) or starting with arc-melted intermetallic "$Sc_{10}Au_6$" which was then ground to a powdered sample, mixed with the correct amount of Sc_2O_3 followed by arc-melting. Attempts to isolate the sub-oxide using in situ high-temperature PXRD under air resulted in the same result. Not included in the publication is a third approach that was tested to obtain the described sub-oxide. Sc_2Au was placed in a corundum crucible on top of a second crucible containing BaO_2, which upon heating releases one oxygen atom per formula unit (see section 5.5.1.6). Both crucibles were sealed in an evacuated silica ampoule and heated to 1223 K, kept there for 48 hours and cooled to room temperature (10 K h^{-1}). Regardless of the synthesis, the same results were obtained. The sub-oxide could be obtained by ~66 mass% accompanied by Sc_2Au, ScAu, Sc_2O_3 and elemental Au. The corresponding powder X-ray diffractogram is shown in Figure 49.

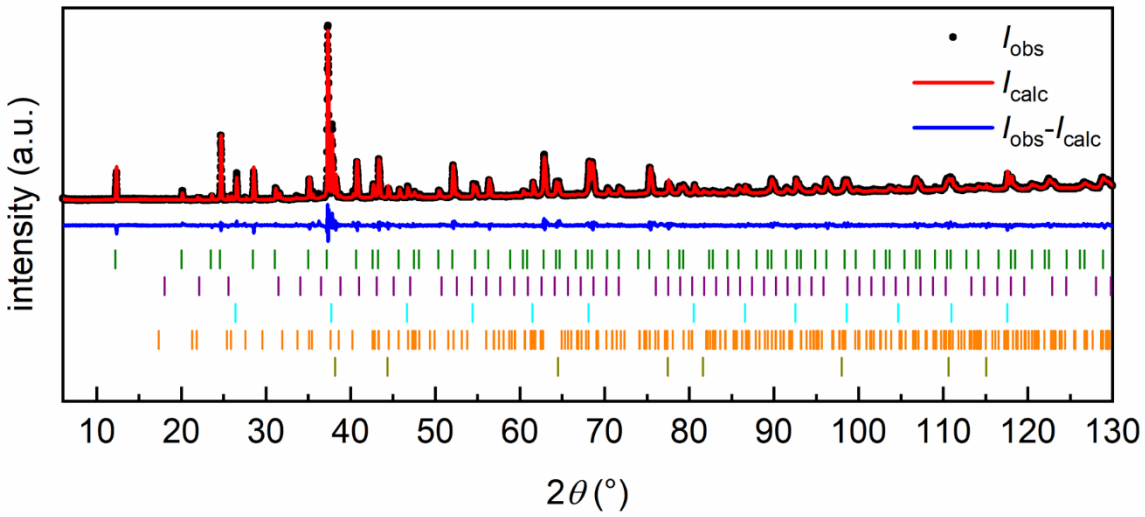

Figure 49. Powder X-ray pattern of Sc_2Au annealed with one equivalent of BaO_2. Experimental data is shown as black dots, simulated diffraction patterns from refinements as red lines, the difference is shown as continuous blue lines. Bragg positions are shown as green ($Sc_4Au_2O_{1-x}$, space group $Fd\bar{3}m$, 66(1) mass%), purple (Sc_2O_3, space group $Ia\bar{3}$, 14(1) mass%), cyan (ScAu, space group $Pm\bar{3}m$, 11(1) mass%), orange (Sc_2Au, space group *Pnma*, 5(1) mass%) and dark yellow (elemental Au, space group $Fm\bar{3}m$, 4(1) mass%) ticks.

Inorganic Chemistry

pubs.acs.org/IC Article

Formation of the Sub-oxide $Sc_4Au_2O_{1-x}$ and the Drastically Negative ^{27}Al NMR Shift in Sc_2Al

Elias C. J. Gießelmann, Mathis Radzieowski, Samir F. Matar, and Oliver Janka*

Cite This: *Inorg. Chem.* 2023, 62, 9602−9617 Read Online

ACCESS | Metrics & More | Article Recommendations | Supporting Information

ABSTRACT: During attempts to synthesize Sc_4AuAl in the cubic Gd_4RhIn-type structure, the solid solution $Sc_2Au_{0.5}Al_{0.5}$ in the $PbCl_2$-type structure formed instead. Subsequently, the solid solution $Sc_2Au_{1-x}Al_x$ was investigated with respect to its existence range along with the structure types formed for different compositions with x = 0, 0.25, 0.5, 0.75, and 1. According to X-ray powder diffraction studies, Sc_2Al and nominal $Sc_2Au_{0.25}Al_{0.75}$ crystallized in the hexagonal Ni_2In-type structure ($P6_3/mmc$), while $Sc_2Au_{0.5}Al_{0.5}$, $Sc_2Au_{0.75}Al_{0.25}$, and Sc_2Au were found to crystallize in the orthorhombic $PbCl_2$-type structure ($Pnma$). The crystal structures of Sc_2Au and $Sc_2Au_{0.59(1)}Al_{0.41(1)}$ were refined from single-crystal data (Sc_2Au: a = 648.0(1), b = 467.2(1), c = 835.2(2) pm, $wR2$ = 0.0382, 535 F^2 values, 25 variables; $Sc_2Au_{0.59(1)}Al_{0.41(1)}$: a = 632.48(5), b = 472.16(3), c = 848.67(6) pm, $wR2$ = 0.0484, 540 F^2 values, 21 variables). Contamination with air during the synthesis of Sc_2Au led to the discovery of a compound adopting the cubic W_4Co_2C-type structure (stuffed cubic Ti_2Ni type). Using Sc_2O_3 as a defined oxygen source led to samples with high amounts of $Sc_4Au_2O_{1-x}$. All intermetallic compounds exhibited *Pauli* paramagnetic behavior in the investigated temperature range of 2.1 to 300 K, and no superconductivity was observed at low temperatures and low fields. Sc_2Au and Sc_2Al were investigated by ^{27}Al and ^{45}Sc solid-state NMR investigations. For Sc_2Al, one signal was found in the ^{27}Al NMR spectra in line with the crystal structure; however, an extremely negative resonance shift of δ = −673 ppm was observed. In both compounds, two Sc resonances were observed, in line with the proposed crystal structure. Finally, it was observed that the stability of Sc_2Au in air is limited. This was investigated *via* thermal analysis and (temperature-dependent) powder X-ray diffraction. DFT calculations helped in assessing charge analysis, electronic properties, and chemical bonding.

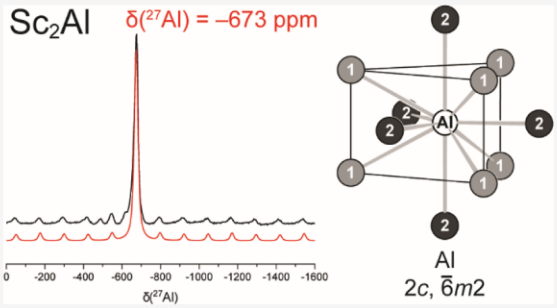

1. INTRODUCTION

In the rare-earth-rich sections ($RE \geq 60$ at. %) of the ternary systems RE−T−X (RE = rare-earth element, T = transition metal, X = group 13 element), the orthorhombic Ho_6Co_2Ga ($Immm$),[1−10] the hexagonal Pr_8CoGa_3 ($P6_3mc$)[11−13] and $Y_{10}RuCd_3$ ($P6_3/mmc$),[9,14−17] the tetragonal $Ce_{12}Pt_7In$ ($I4/mcm$),[18,19] $Er_{12}Fe_3In_3$ ($I4/mmm$),[20] and $Gd_{14}Co_3In_{2.7}$ ($P4_2/nmc$),[21−26] and finally the cubic $Sm_{12}Ni_6In$[27] and Gd_4RhIn-type structures ($F\bar{4}3m$) are prominent representatives. Of the latter, over 200 compounds were reported for different combinations of rare-earth and transition metals. Besides the respective aluminum compounds,[9,28−30] the isostructural indium,[24,31,32] cadmium[17,28,33−35] and magnesium[28,36−49] representatives have also been reported. Of these, *e.g.*, Eu_4PdMg exhibits exceptional good magnetocaloric properties in a large temperature window.[50] Attempts to extend the existence range of the Gd_4RhIn-type structure with aluminum as the X element toward the smaller rare-earth elements and the more electronegative transition metal Au resulted in the formation of the solid solution $Sc_2Au_{0.5}Al_{0.5}$ (≡Sc_4AuAl), crystallizing in the orthorhombic $PbCl_2$-type structure. Subsequently, we investigated the solid solution $Sc_2Au_{1-x}Al_x$ with respect to its existence range as well as the physical and ^{27}Al and ^{45}Sc NMR spectroscopic properties of the non-substituted compounds Sc_2Au and Sc_2Al. Additionally, the sub-oxide $Sc_4Au_2O_{1-x}$ (a = 1253.6(1) pm, $Fd\bar{3}m$, cubic W_4Co_2C type) could be synthesized and characterized by powder X-ray diffraction.

2. EXPERIMENTAL SECTION

2.1. Synthesis. Starting materials for the synthesis of the end members Sc_2Au and Sc_2Al as well as the solid solution $Sc_2Au_{1-x}Al_x$ and $Sc_4Au_2O_{1-x}$ were pieces of sublimed scandium ingots (Smart Elements, Onyxmet), gold foil (Agosi) and aluminum turnings (Koch Chemicals, Onyxmet), and Sc_2O_3 (Sigma-Aldrich), all with stated

Received: April 5, 2023
Published: June 2, 2023

https://doi.org/10.1021/acs.inorgchem.3c01097
Inorg. Chem. 2023, 62, 9602−9617

Table 1. Lattice Parameters Refined from Powder X-ray Diffraction of the $Sc_2Au_{1-x}Al_x$ (x = 0, 0.25, 0.5, 0.75, and 1) Solid Solution and Literature Values

composition	prototype	a (pm)	b (pm)	c (pm)	V (nm^3)
Sc_2Al [P a]	Ni_2In ($P6_3/mmc$)	488.84(1)	a	617.25(1)	0.1277
Sc_2Al [P 55]	Ni_2In ($P6_3/mmc$)	488.8	a	616.6	0.1276
$Sc_2Au_{0.25}Al_{0.75}$ [P a]	Ni_2In ($P6_3/mmc$)	486.7(4)	a	619.0(4)	0.1270
$Sc_2Au_{0.5}Al_{0.5}$ [P a]	$PbCl_2$ ($Pnma$)	631.4(2)	471.9(1)	849.1(2)	0.2523
$Sc_2Au_{0.59(1)}Al_{0.41(1)}$ [SC a]	$PbCl_2$ ($Pnma$)	632.48(5)	472.16(3)	848.67(6)	0.2534
$Sc_2Au_{0.75}Al_{0.25}$ [P a]	$PbCl_2$ ($Pnma$)	640.5(2)	468.2(1)	842.0(2)	0.2525
Sc_2Au [P a]	$PbCl_2$ ($Pnma$)	647.52(2)	466.56(1)	834.30(2)	0.2520
Sc_2Au [SC a]	$PbCl_2$ ($Pnma$)	648.0(1)	467.2(1)	835.2(2)	0.2528
Sc_2Au [P 56]	$PbCl_2$ ($Pnma$)	647.0	466.7	835.8	0.2524

[a]This work; [P] indicates powder X-ray data; [SC] indicates single-crystal X-ray data.

purities higher than 99.9%. For the synthesis of Sc_2Au, Sc_2Al, and the solid solution $Sc_2Au_{1-x}Al_x$ with x = 0, 0.25, 0.5, and 0.75, stochiometric amounts of the elements were used. For the synthesis of $Sc_4Au_2O_{1-x}$, elemental Sc, Au, and Sc_2O_3 were mixed in a 10:6:1 ratio. In all cases, the starting materials were arc-melted[51] in a custom-built arc-melting apparatus in a water-cooled copper hearth under 800 mbar argon pressure. The argon gas was purified with a titanium sponge (873 K), molecular sieves, and silica gel. As an alternative synthetic approach, elemental Sc and Au were weighed in a 10:6 ratio and pre-reacted by arc-melting.[51] The obtained material was used without any further characterization and ground to a fine powder. Appropriate amounts of Sc_2O_3 were added (3% excess); the mixture was homogenized and cold-pressed to a pellet (Ø 6 mm, 100 bar). The pellet was transferred into the arc-furnace and arc-melted as described before. In all cases, the obtained buttons were remelted several times to ensure phase pure samples with high homogeneity. The as-cast buttons were crushed, and fragments were placed in the water-cooled sample chamber of a high-frequency furnace (Typ TIG 5/300, Hüttinger Elektronik, Freiburg, Germany)[52] and heated to approximately 1073 K and kept at this temperature for 2 h before cooling to room temperature. Alternatively, the samples were annealed in muffle furnaces. They were heated to 1123 K within 2 h and then kept at this temperature for 12 days. These different annealing procedures led to pure X-ray samples. Besides Sc_2Au, the specimens are stable in air over months and show metallic luster; ground samples are gray. Sc_2Au starts to surface oxidize already after a few hours (*vide infra*).

2.2. X-ray Diffraction. The polycrystalline samples of the solid solution $Sc_2Au_{1-x}Al_x$ were characterized by powder X-ray diffraction on a Guinier camera (equipped with an image plate system Fujifilm, BAS-1800) using Cu Kα_1 radiation and α-quartz (a = 491.30, c = 540.46 pm, Riedel-de-Haën) as an internal standard. The lattice parameters (Table 1) were obtained from a least-squares fit. Proper indexing of the diffraction lines was ensured by an intensity calculation.[53]

Additionally, the pulverized samples of Sc_2Au and Sc_2Al used for the oxidation studies and NMR experiments were investigated at room temperature on a D8-A25-Advance diffractometer (Bruker, Karlsruhe, Germany) in Bragg−Brentano θ-θ-geometry (goniometer radius 280 mm) with Cu K$_\alpha$-radiation (λ = 154.0596 pm). PXRD patterns at elevated temperatures were recorded on the same instrument using a XRK 900 (Anton Paar GmbH, Graz, Austria) reactor chamber. The samples were investigated in air in the temperature range of 303−873 K with increments of 50 K and heating rates of 10 K min^{-1}, respectively. Diffraction patterns were recorded between 6 and 130° 2θ with a step size of 0.013° and a total scan time of 1 h for each temperature. The thermal expansion of the reaction chamber and sample holder was determined using elemental Si (NIST standard reference material 640f, a = 5.4311(1) nm). A 12 μm Ni foil working as a K$_\beta$ filter and a variable divergence slit were mounted at the primary beam side. A LYNXEYE detector with 192 channels was used at the secondary beam side. The recorded data was evaluated using the Bruker TOPAS 5.0 software,[54] with the observed reflections being treated *via* single-line fits.

Irregularly shaped crystal fragments of the Sc_2Au and $Sc_2Au_{0.59(1)}Al_{0.41(1)}$ were obtained from the annealed crushed buttons. The crystals were glued to quartz fibers using beeswax, and their quality for intensity data collection was checked by Laue photographs on a Buerger camera (white molybdenum radiation, image plate technique, Fujifilm, BAS-1800). Intensity data of a suitable crystal was collected at room temperature using a IPDS-II diffractometer (Stoe, Karlsruhe, Germany). A numerical absorption correction was applied to the data set. All relevant crystallographic data, deposition, and details of the data collection and evaluation are listed in Tables 2−4.

Table 2. Crystallographic Data and Structure Refinement for Sc_2Au and $Sc_2Au_{0.59(1)}Al_{0.41(1)}$ (Both *Pnma*, Z = 4, $PbCl_2$-Type)

compound	Sc_2Au	$Sc_2Au_{0.59(1)}Al_{0.41(1)}$
CCDC number	1858159	1858160
lattice parameters	see Table 1	see Table 1
molar mass, g mol^{-1}	286.9	218.9
density calc., g cm^{-3}	7.58	5.74
crystal size, μm	20 × 20 × 10	65 × 55 × 30
detector distance, mm	70	70
exposure time, s	360	360
integr. param. A, B, EMS	12.0, 3.0, 0.020	12.0, 3.0, 0.020
range in hkl	±9; ±7; −12, +11	±9; ±7; ±13
θ_{min}, θ_{max}, deg	3.99, 33.29	4.03, 33.52
linear absorption coeff., mm^{-1}	63.0	39.8
no. of reflections	6325	7207
R_{int}/R_σ	0.0947/0.0132	0.0517/0.0193
no. of independent reflections	535	540
reflections used [$I \geq 3\sigma(I)$]	456	420
F(000), e	484	377
$R1/wR2$ for $I \geq 3\sigma(I)$	0.0179/0.0369	0.0247/0.0428
$R1/wR2$ for all data	0.0250/0.0382	0.0369/0.0434
data/parameters	535/20	540/21
goodness-of-fit on F^2	1.21	2.04
extinction coefficient	1740(110)	−
diff. Fourier residues/e$^-$ Å^{-3}	−2.07/+2.07	−1.76/+1.91

CCDC 1858159 and 1858160 contain the supplementary crystallographic data for this paper. The data can be obtained free of charge from The Cambridge Crystallographic Data Centre *via* www.ccdc.cam.ac.uk/structures.

2.3. Scanning Electron Microscopy/Energy-Dispersive X-ray Data. The crystals Sc_2Au (Figure 1) and $Sc_2Au_{0.59(1)}Al_{0.41(1)}$ measured on the diffractometer were analyzed semi-quantitatively using an EVO MA10 scanning electron microscope (Zeiss, Jena, Germany) with ScF_3, Au, and Al_2O_3 as standards. No impurity elements heavier than

https://doi.org/10.1021/acs.inorgchem.3c01097
Inorg. Chem. 2023, 62, 9602−9617

Table 3. Atom Positions and Equivalent Isotropic Displacement Parameters (pm^2) for Sc_2Au (*Pnma*, *Z* = 4, $PbCl_2$-Type), $Sc_2Au_{0.59(1)}Al_{0.41(1)}$ (*Pnma*, *Z* = 4, $PbCl_2$-Type), and $Sc_4Au_2O_{1-x}$ ($Fd\bar{3}m$, *Z* = 16, W_4Co_2C-Type)

atom	Wyckoff position	*x*	*y*	*z*	U_{eq}/B_{eq} [c]
		Sc_2Au			
Sc1	4*c*	0.01927(17)	1/4	0.68816(17)	84(3)
Sc2	4*c*	0.15666(17)	1/4	0.07575(15)	76(3)
Au	4*c*	0.24038(3)	1/4	0.39929(3)	80(1)
		$Sc_2Au_{0.59(1)}Al_{0.41(1)}$			
Sc1	4*c*	0.0189(3)	1/4	0.7044(3)	178(5)
Sc2	4*c*	0.1769(4)	1/4	0.0739(2)	187(6)
Au/Al[a]	4*c*	0.23818(11)	1/4	0.40079(7)	148(2)
		$Sc_4Au_2O_{1-x}$			
Sc1	48*f*	0.4436(3)	1/8	1/8	102(6)
Sc2	16*d*	0	0	0	102(6)
Au	32*e*	0.21566(5)	*x*	*x*	127(2)
O[b]	16*c*	1/2	1/2	1/2	203(6)

[a]Au/Al mixed occupation of 0.59(1)/0.41(1). [b]Occupancy refined to 0.45(3). [c]U_{eq} is defined as one-third of the trace of the orthogonalized U_{ij} tensor. B_{eq}(Sc1) = B_{eq}(Sc2); B_{eq}(O) = 2× B_{eq}(Sc1).

sodium (detection limit of the instrument) were observed. The experimentally determined averaged element ratios (Sc_2Au: 65.9 at. % Sc and 34.1 at. % Au; $Sc_2Au_{0.59(1)}Al_{0.41(1)}$: 66.0 at. % Sc, 20.4 at. % Au, and 13.6 at. % Al) were obtained from five measurements and are in good agreement with the refined compositions from single-crystal X-ray diffraction (Sc_2Au: 66.7 at. % Sc and 33.3 at. % Au; $Sc_2Au_{0.59(1)}Al_{0.41(1)}$: 66.7 at. % Sc, 20.0 at. % Au, and 13.3 at. % Al). Differences originate from the conchoidal fractures of the crystallites.

2.4. Thermal Analysis. Thermogravimetric (TG) measurements of Sc_2Au and samples containing $Sc_4Au_2O_{1-x}$ were carried out on a

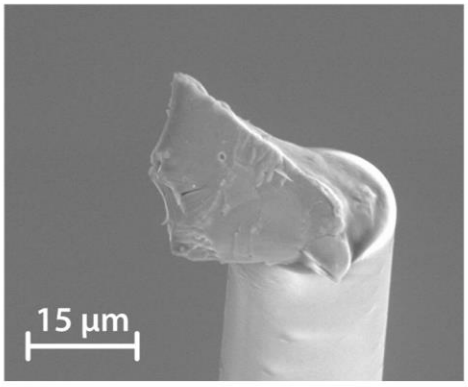

Figure 1. Scanning electron microscopy (SEM) image of the single crystal of Sc_2Au used for the single-crystal diffraction experiments.

TGA/DSC STARe System 1 (Mettler-Toledo, Schwerzenbach, Switzerland) with a heating rate of 20 K min^{-1} between 298 and 1273 K under a gas flow (O_2/Ar = 1:1) of 40 mL min^{-1}. Every 200 K, an isothermal section with a duration of 1 h was inserted before the heating was continued. The sample was kept at the maximum temperature for 1 h. Afterward, the system was brought to room temperature with a passive cooling rate of 20 K min^{-1}.

2.5. Physical Property Measurements. Fragments of the annealed buttons of all synthesized members of the solid solution $Sc_2Au_{1-x}Al_x$ were attached to the sample holder rod of a vibrating sample magnetometer unit (VSM) using Kapton foil for measuring the magnetization $M(T)$ in a physical property measurement system (PPMS, Quantum Design, San Diego, USA). The samples were investigated in the temperature range of 2.1−6 K with an external magnetic field of 20 Oe to check for superconductivity and from 3 to

Table 4. Interatomic Distances (pm) for Sc_2Au (*Pnma*, *Z* = 4, $PbCl_2$-Type), $Sc_2Au_{0.59(1)}Al_{0.41(1)}$ (*Pnma*, *Z* = 4, $PbCl_2$-Type), and $Sc_4Au_2O_{1-x}$ ($Fd\bar{3}m$, *Z* = 16, W_4Co_2C-Type)[a]

						Sc_2Au					
Sc1	1	Au	280.1	Sc2	1	Au	270.2	Au	1	Sc2	270.2
	2	Au	294.6		1	Au	275.1		1	Sc2	275.1
	1	Sc2	321.7		2	Au	283.6		1	Sc1	280.1
	2	Sc2	325.6		1	Sc1	321.7		2	Sc2	283.6
	2	Sc2	327.2		2	Sc1	325.6		2	Sc1	296.4
	2	Au	330.9		2	Sc1	327.2		2	Sc1	330.9
	1	Sc2	335.2		2	Sc2	333.7				
	2	Sc1	339.6		1	Sc1	335.2				
						$Sc_2Au_{0.59(1)}Al_{0.41(1)}$					
Sc1	1	Au/Al	292.2	Sc2	1	Au/Al	278.1	Au/Al	1	Sc2	278.1
	2	Au/Al	300.1		1	Au/Al	279.9		1	Sc2	279.9
	1	Sc2	320.2		2	Au/Al	283.4		2	Sc2	283.4
	2	Sc2	323.9		1	Sc1	320.2		1	Sc1	292.2
	2	Sc2	325.8		2	Sc1	323.9		2	Sc1	300.1
	1	Sc2	326.4		2	Sc1	326.4		2	Sc1	327.5
	2	Au/Al	327.5		1	Sc1	329.7				
	2	Sc1	329.7		2	Sc2	348.4				
						$Sc_4Au_2O_{1-x}$					
Sc1	2	O	232.4	Sc2	6	Au	277.0	Au	3	Sc2	277.0
	2	Au	284.0		6	Sc1	329.3		2	Sc1	284.0
	4	Sc1	320.5						6	Au	321.1
	2	Au	328.6						3	Sc1	328.6
	2	Sc2	329.3								
	4	Sc1	366.6					O	6	Sc1	232.4

[a]All distances of the first coordination spheres are listed. All standard uncertainties were less than 0.2 pm.

https://doi.org/10.1021/acs.inorgchem.3c01097
Inorg. Chem. 2023, 62, 9602−9617

300 K with an external magnetic field of 10 kOe. The results of the magnetic measurements are summarized in Table 5.

Table 5. Magnetic Properties of the $Sc_2Au_{1-x}Al_x$ (x = 0, 0.25, 0.5, 0.75, and 1) Solid Solution

Sc_2Al	*Pauli* paramagnetic χ(300 K) = 22.8(1) × 10^{-6} emu mol^{-1}
$Sc_2Au_{0.25}Al_{0.75}$	*Pauli* paramagnetic χ(300 K) = 137.2(2) × 10^{-6} emu mol^{-1}
$Sc_2Au_{0.5}Al_{0.5}$	*Pauli* paramagnetic χ(300 K) = 114.8(2) × 10^{-6} emu mol^{-1}
$Sc_2Au_{0.75}Al_{0.25}$	*Pauli* paramagnetic χ(300 K) = 103.9(2) × 10^{-6} emu mol^{-1}
LT-Sc_2Au	*Pauli* paramagnetic χ(300 K) = 64.8(1) × 10^{-6} emu mol^{-1}

2.6. ^{27}Al and ^{45}Sc Solid-State NMR. The ^{27}Al- and ^{45}Sc-MAS-NMR spectra were recorded at 104.31 MHz and 97.24 MHz on an Avance III 400 WB spectrometer (Bruker, Billerica, US; 9.4 T) using magic-angle spinning (MAS) conditions. The samples were ground to a fine powder and mixed with an appropriate amount of NaCl (sample/NaCl = 1:9) to reduce the density and electrical conductivity of the sample. The diluted samples were loaded into a cylindrical ZrO_2 rotor with a diameter of 4 mm and spun at the magic angle with a frequency of 13 kHz. All experiments conducted were single-pulse with a typical pulse length of 0.83 μs and relaxation delays of 1 s. Resonance shifts were referenced to aqueous 1 mol $AlCl_3$ and $ScCl_3 \cdot n H_2O$ solutions. The NMR-spectra were recorded using the Bruker TOPSPIN software;[57] the analysis was performed with the help of the DMFIT program package.[58] The extracted data is compiled in Table 6.

2.7. Quantum-Chemical Calculations. The electronic structure and chemical bonding properties were obtained based on calculations within the density functional theory (DFT).[59,60] For an accurate assessment of the charge trends in the present family of valence isoelectronic ternary compounds, the Vienna *ab initio* simulation package code[61,62] with the projector augmented wave (PAW) method[62,63] was used. The valence wave function (vfn) tends to have rapid oscillations near ion cores due to necessary orthogonality rules. Large computational efforts are then needed to describe it accurately, making the early need for pseudo potentials as those early-derived ultra-soft pseudo-potentials USPP derived by Vanderbilt.[64] More adapted to heavier elements such as those used herein, the PAW method provides through an augmentation procedure within an intra-atomic zone—a solution through a transformation of the vfn rapid oscillations into a smooth one. This is a computationally convenient procedure that lets us calculate with reasonable computational efforts all-electron properties from the produced smooth and true vfns. For the sake of obtaining accurate trends of charge transfers, semi-cores as np^6 states were included in the calculations.

Regarding the account for exchange correlation (XC) effects within DFT, local density approximation (LDA) based on the homogeneous electron gas was initially derived. However, LDA is known to be overly binding, leading to underestimated lattice constants and interatomic distances and energy gaps. Better results were obtained through introducing gradients into the electron gas distribution, leading to the generalized gradient approximation (GGA) used herein.[65] The calculations are done starting from the experimental crystal data, and the whole cell undergoes unconstrained geometry relaxation of the structure parameters and coordinates. At a high precision integration of the Brillouin-zone (BZ) (12 × 12 × 12) , the charge density issued from the accurate calculations was analyzed using the AIM (atoms in molecules theory) approach[66] developed by Bader, who devised an intuitive way of splitting molecules into atoms as based purely on the electronic charge density. The charge density in a chemical compound reaches a minimum between atoms, thus defining a region separating atoms from each other. In the case of a family of compounds having similarities, such an analysis can be useful to establish trends. In other words, the analysis does not evaluate absolute ionizations. Core electrons are included for an accurate account of the charge density. The analysis is done using a fast algorithm operating on a charge density grid. The obtained charges are listed in Table 7.

The all-electron calculations with the GGA were carried out for a full description of the electronic structure and the properties of chemical bonding using the full potential scalar-relativistic augmented spherical wave (ASW) method.[67,68] In the minimal ASW basis set, the outermost shells were chosen to represent the valence states, and the matrix elements were constructed using partial waves up to l_{max}+1 = 3 for Sc and Au and l_{max}+1 = 2 for Al and O. Self-consistency was achieved when charge transfers and energy changes between two successive cycles were below 10^{-8} and 10^{-6} eV, respectively. BZ integrations were performed using the linear tetrahedron method within the irreducible wedge. Besides the electronic band structures and the site projected density of states, the pair interactions based on the overlap population analysis with the crystal orbital overlap population (COOP)[69] are qualitatively discussed. In the plots, positive, negative, and zero COOP indicate bonding, anti-bonding, and non-bonding interactions, respectively.

3. RESULTS AND DISCUSSION

3.1. Synthesis and Powder X-ray Diffraction. During attempts to synthesize new aluminum intermetallics of the Gd_4RhIn-type structure[31] nominal Sc_4AuAl was synthesized. The obtained sample was found to be phase pure according to SEM investigations; however, instead of the cubic Gd_4RhIn-type ($F\bar{4}3m$), an orthorhombic diffraction pattern was observed in powder X-ray diffraction experiments. Single-crystal X-ray diffraction experiments revealed that the compound crystallized in the orthorhombic $PbCl_2$-type structure (*Pnma*) and that a solid solution according to $Sc_2Au_{0.5}Al_{0.5}$ (≡Sc_4AuAl) was formed. Subsequently, the other members of the solid solution $Sc_2Au_{1-x}Al_x$ with x = 0, 0.25, 0.5, 0.75, and 1 were prepared and investigated with respect to their crystal structures. During these investigations, phase pure samples of the solid solution as well as the endmembers Sc_2Al (hexagonal Ni_2In type, $P6_3/mmc$)[55] and Sc_2Au (orthorhombic $PbCl_2$ type, *Pnma*)[56] were obtained (Figure 2). Furthermore, single crystals of Sc_2Au could be isolated and structurally

Table 6. Summary of the NMR Observables of Hexagonal Sc_2Al (Ni_2In-Type) and Orthorhombic Sc_2Au ($PbCl_2$-Type), Extracted from the DMFit Simulation of the ^{27}Al and ^{45}Sc MAS-NMR Spectra, with δ Being the Resonance Shifts (in ppm), C_Q the Quadrupolar Parameter (in kHz), η_Q the Asymmetry Parameter, G/L the Gaussian to Lorentz Ratio, and dCs the Chemical Shift Anisotropy Parameter (in ppm)[a]

compound	site	δ	$C_{Q,calc}$	$C_{Q,exp}$	$\eta_{Q,theo}$	$\eta_{Q,exp}$	G/L	dCS
Sc_2Al	Sc1 (2*a*)	+1866	9364		0.01			
	Sc2 (2*d*)	+2914	4246		0.03		0	
	Al (2*c*)	−673	3289	3170	0.01	0	0.27	−4
Sc_2Au	Sc1 (4*c*)	+1266	7359		0.06		0	
	Sc2 (4*c*)	+1201	10,871		0.41			

[a]Theoretically calculated values from DFT are given with the subscript calc.

https://doi.org/10.1021/acs.inorgchem.3c01097
Inorg. Chem. 2023, 62, 9602−9617

Table 7. Bader Charges Considering Valence and Core/Semi-core States

E_{coh}/at. (eV)	Bader charges (valence)			augmented Bader charges (all)		
	Sc1/Sc2	Al/Au	O	Sc1/Sc2	Al/Au	O
hex. Sc_2Al	+1.08/+1.05	−2.13 (Al)		−0.025/+0.237	−0.424	
hex. Sc_2AlAu	+1.17/+1.25	−2.24 (Al)/		+0.55/+0.48	−0.46(Al)	
(hypothetic)	−2.61 (Au)	−1.60(Au)				
orth. Sc_2Au	+1.32/+1.31	−2.63 (Au)		+0.51/+0.52	−1.03 (Au)	
cub. $Sc_4Au_2O_{1-x}$	+1.1/+1.4	−2.04 (Au)	−1.48	+0.62/+0.43	−0.90 (Au)	−0.80

investigated since this compound structure had been described only by powder diffraction data before.[56]

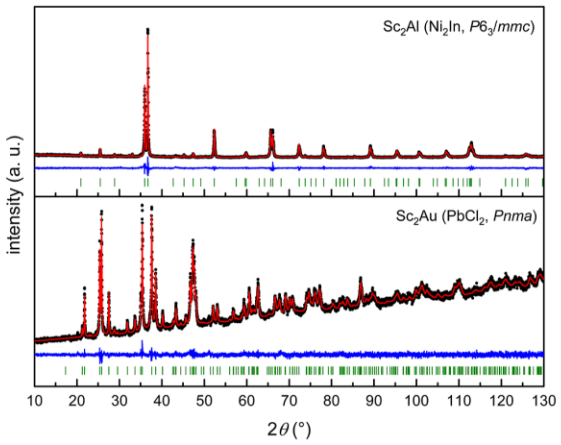

Figure 2. X-ray powder patterns of (top) hexagonal Sc_2Al (Ni_2In-type, $P6_3/mmc$) and (bottom) Sc_2Au ($PbCl_2$-type, $Pnma$). Experimental data is shown as black dots, refined data as a red line, the difference is shown as a continuous blue line, and the Bragg positions are shown as green ticks.

During one attempt to synthesize Sc_2Au, a diffraction pattern was observed, which could be indexed with a cubic unit cell with $a \sim 1254$ pm. A check with the Pearson database[70] revealed the Ti_2Ni-type structure ($Fd\bar{3}m$) as a possible match. Therefore, the formation of a high-temperature phase was initially suspected; however, all attempts to resynthesize "HT-Sc_2Au", *e.g.*, by quenching small sample masses of arc-melted samples, failed. A more thorough search in the Pearson database revealed that the W_4Co_2C type ($Fd\bar{3}m$) can be considered as the filled Ti_2Ni type, with the additional carbon atoms located in octahedral voids on the 16*d* (1/2, 1/2, 1/2) position. Numerous transition metal carbides, *e.g.*, Zr_4T_2C (T = Fe, Os),[71,72] M_4T_2C (M = V, Nb, Ta; T = Co, Ni),[71,72] and M_4T_2C (M = Mo, W; T = Fe, Co, Ni)[71−73] have been reported to adopt this structure type. Besides a carbon atom as a filling entity of the Ti_2Ni type, also the hydrides Mg_4Pd_2H[74] and $Zr_4T_2O_{0.6}H_x$ (T = Fe, Ni; x = 1.84, 2.5),[75] the borides $Nb_4Ni_2B_{0.32}$ and $Sc_{4.3}Cr_{1.68}B_{0.4}$,[76,77] numerous nitrides M_4T_2N (M = V, Zr, Nb, Hf-W; T = V, Fe-Ni, Zn, Ru-Pd, Re-Pt),[71,78−81] and the oxides M_4T_2O (M = Ti, Zr, Nb, Hf; T = Cr, Fe-Cu, Rh, Pd, Re, Ir, Pt)[81−91] have been reported. Subsequently, attempts were made to prepare what was expected to be "$Sc_4Au_2O_{1-x}$" from Sc, Au, and Sc_2O_3, as described in the experimental section. Figure 3 depicts the powder X-ray diffraction pattern of an obtained sample. Besides cubic $Sc_4Au_2O_{1-x}$ (57(1) wt %, W_4Co_2C-type) as the main phase, also unreacted Sc_2Au (17(1) wt %, $PbCl_2$ type), ScAu (17(1) wt %, CsCl-type), and Sc_2O_3 (9(1) wt %, bixbyite-type) could be observed to be present in the diffraction pattern. It is interesting to note that, regardless of the synthetic approach described in the experimental section, the amount of $Sc_4Au_2O_{1-x}$ in all cases is nearly the same (∼55−60 wt %).

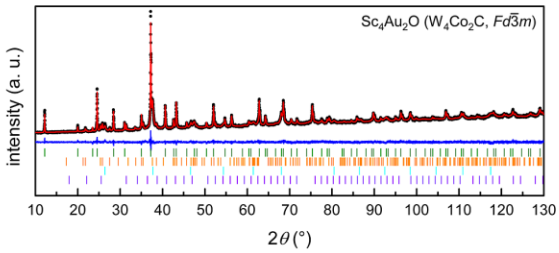

Figure 3. X-ray powder patterns of the attempt to synthesize $Sc_4Au_2O_{1-x}$. Experimental data is shown as black dots, refined data as a red line, the difference is shown as a continuous blue line, and the Bragg positions are shown as colored ticks: $Sc_4Au_2O_{1-x}$ (W_4Co_2C type) in green, Sc_2Au ($PbCl_2$ type) in orange, ScAu (CsCl type) in cyan, and Sc_2O_3 (bixbyite type) in purple.

3.2. Structure Refinements. Careful analysis of the obtained single-crystal intensity data sets of Sc_2Au and nominal $Sc_2Au_{0.5}Al_{0.5}$ revealed orthorhombic *P*-centered lattices; the centrosymmetric group *Pnma* was found to be correct during structure refinement. Isotypism with a $PbCl_2$-type structure was evident from the powder diffraction patterns and the entry of Sc_2Au in the Pearson database.[70] The starting atomic parameters were obtained using SuperFlip[92] implemented in Jana2006.[93,94] The structure was refined on F^2 with anisotropic displacement parameters for all atoms. As a check for the correct composition and site assignment, the occupancy parameters were refined in a separate series of least-squares cycles. For Sc_2Au, all sites were fully occupied within three standard deviations; for nominal $Sc_2Au_{0.5}Al_{0.5}$, mixing of Au and Al on one crystallographic site was observed that led to the refined composition of $Sc_2Au_{0.59(1)}Al_{0.41(1)}$. No significant residual peaks were evident in the final difference Fourier syntheses. The relevant crystallographic data, deposition, and details of the data collection, and evaluation are listed in Tables 2−4.

The refinement of the structure of $Sc_4Au_2O_{1-x}$ was conducted from powder X-ray diffraction data using the Topas software package.[54] Indexing of the prominent reflections resulted in a cubic unit cell with $a \sim 1254$ pm, which was inserted in the structural data of W_4Co_2C[95] taken from the Pearson database.[70] The two crystallographic W positions were occupied by Sc, the Co position by Au, and the C site by O. Refinement of the site occupancies led to fully occupied Sc and Au positions (within three standard

https://doi.org/10.1021/acs.inorgchem.3c01097
Inorg. Chem. 2023, 62, 9602−9617

deviations) for the oxygen site, and an occupancy factor of 0.45(3) was obtained. The result of the refinement is shown in Figure 3, and refined positional parameters are listed in Table 2.

3.3. Solid Solution and Crystal Chemistry. For the solid solution $Sc_2Au_{1-x}Al_x$ two different structure types occur: for x = 0, 0.25, and 0.5, the orthorhombic $PbCl_2$-type structure (*Pnma*) is found. For x = 0.75 and 1, the hexagonal Ni_2In-type structure ($P6_3/mmc$) is observed. Figure 4 depicts the trend of

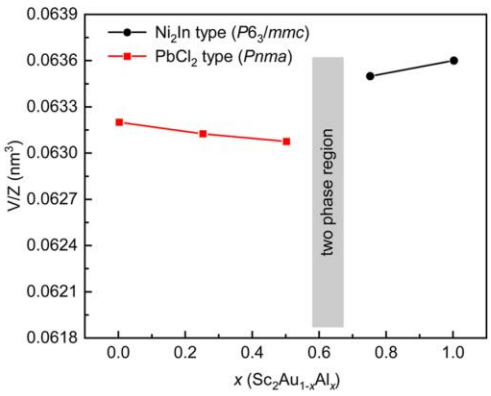

Figure 4. Plot of the normalized unit cell volumes (V/Z) for the solid solution $Sc_2Au_{1-x}Al_x$ as a function of x.

the normalized unit cell volumes (V/Z). Upon substitution of Au by Al in Sc_2Au, the unit cell contracts in line with the smaller covalent radius of Al in comparison to Au (125 *vs* 134 pm[96]). For nominal $Sc_2Au_{0.375}Al_{0.625}$, a two-phase region is found in which both structure types can be identified by powder X-ray diffraction experiments. SEM-EDX investigations revealed phase segregation into an Au- and an Al-rich phase. They crystallize in the structure types of their respective endmembers.

In both structure types, two crystallographically distinct Sc positions can be found along with one Au or Al position. In the members of the solid solutions, the latter positions get mixed and are occupied by Au and Al. In the following paragraph, the structure types will be explained briefly.

In the crystal structure of hexagonal Sc_2Al (Ni_2In-type, $P6_3/mmc$, filled NiAs-type) (Figure 5, top left) , the Sc1 atoms are surrounded by 12 atoms in the shape of a hexagonal prism, with alternations of Sc2 and Al atoms in the two six-membered rings. The Sc2 and the Al atoms are coordinated by six Sc1 atoms in the shape of a trigonal prism along with five additional atoms forming the caps (Figure 6, left). These prisms are condensed over common triangular faces to form strands along [001], which are connected over the rectangular faces to form a network. The Sc2 and Al prisms alternate along the c axis; hence, neighboring atoms form additional contacts (Figure 5, top left). The interatomic distance ranges from 282 to 322 pm for the Sc−Al contacts and from 308 to 322 pm for the Sc−Sc contacts, both slightly above the sum of the covalent radii of 288 pm for Sc + Sc and 269 pm for Sc + Al.[96]

In the crystal structure of Sc_2Au ($PbCl_2$-type; Figure 5, top right), the two Sc positions are spherically surrounded in the shape of a fivefold capped pentagonal prism and a fourfold capped cuboid (Figure 6, right) by both Sc and Au atoms. The Au atoms are solely surrounded by nine Sc atoms in the shape

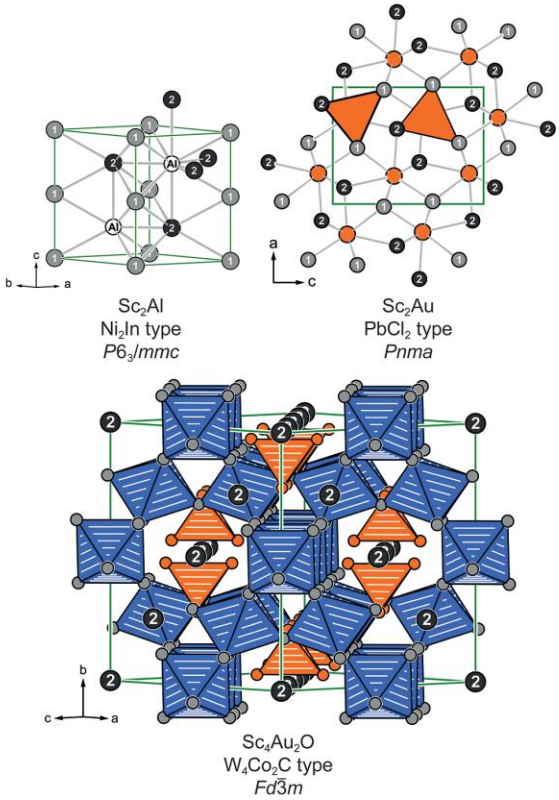

Figure 5. Crystal structures of hexagonal Sc_2Al (Ni_2In type, top left), orthorhombic Sc_2Au ($PbCl_2$ type, top right), and $Sc_4Au_2O_{1-x}$ (W_4Co_2C type, bottom). Scandium, aluminum, gold, and oxygen atoms are drawn as gray, open, orange, and blue circles, respectively.

of a tricapped trigonal prism. The prisms connect to strands over the triangular faces; the caps of the prism are utilized to connect the strands to neighboring ones. Hence, the strands are shifted by y = 1/2 with respect to each other (Figure 5, top right). The two different prisms surrounding the Au atoms are highlighted by different line thicknesses. The interatomic Sc−Au distances range from 257 to 345 pm; the shortest ones are below the sum of the covalent radii (144 + 134 = 278 pm[96]), indicating substantial bonding. The Sc−Sc distances range between 316 and 359 pm; here, no distinct bonding can be found. The distances in both structure types are in line with the ones found in the elements (Sc: 325 and 331 pm;[97] Au: 287 pm;[98] Al: 286 pm[99]) and other binary (Sc−Sc: 329 pm, Sc−Al: 315 pm in $ScAl_2$;[100] Sc−Sc: 351 pm, Sc−Au: 287−293 pm in $ScAu_2$[101]) or ternary scandium intermetallics (Sc−Au: 283 pm, Sc−Al: 327 pm in $ScAu_2Al$;[102,103] Sc−Au: 283−291 pm, Sc−Al: 303−318 pm, Sc−Sc: 363−367 pm in ScAuAl[104]).

$Sc_4Au_2O_{1-x}$ crystallizes in the cubic crystal system with space group $Fd\bar{3}m$ (Figure 5, bottom). For the structure description, the oxygen site will be considered fully occupied. In the crystal structure, two crystallographically independent Sc positions are found as well as a single Au and O site. The O atoms are surrounded by six Sc1 atoms in the shape of a perfect octahedron (Figure 7), while the Sc2 and Au atoms are surrounded in the shape of a distorted cuboctahedron (Sc2@$Sc1_6Au_6$ and Au@$Sc1_6Sc2_3Au_3$). The Sc1 atoms are finally

https://doi.org/10.1021/acs.inorgchem.3c01097
Inorg. Chem. 2023, 62, 9602−9617

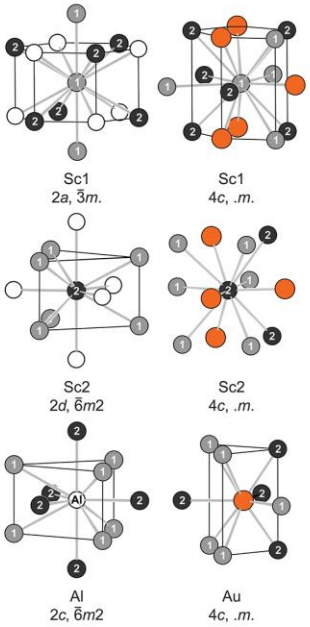

Figure 6. Coordination polyhedra surrounding the (left) scandium and aluminum atoms in Sc_2Al and (right) scandium and aluminum atoms in Sc_2Au. Scandium, aluminum, and gold atoms are drawn as blue, open, and orange circles, respectively. The local site symmetries are given.

surrounded by eight Sc1, two Sc2, four Au, and two O atoms. In the unit cell, the $[OSc1_6]$ octahedra form chains running along [110] by condensation *via* trans-corners. The remaining four corners are connected to two different octahedra of other chains of the same type, running perpendicular. Due to the restricted size of coordination polyhedra, no linear chains are possible, but a slight undulation is observed. Within this Sc1/O framework, the Au atoms form isolated, empty tetrahedral entities. The remaining Sc2 atoms are located in between these polyhedra. Taking a closer look at the Au_4 fragments, it becomes evident that the Sc2 atoms cap the four tetrahedral faces (Figure 7, bottom). Therefore, this fragment can be also considered a $[Sc2_4Au_4]$ heterocubane-like unit. Similar fragments have been observed in $Ba_3Pt_4Al_4$,[105] $Na_3Pt_4Ge_4$,[106] and $A_2Zn_5As_4$ (A = K, Rb);[107] however, here, these entities are formed by Pt/Al, Pt/Ge, or Zn/As atoms. When adding the Sc1 atoms to the surrounding of the Au_4 unit, they reside over the six edges of the tetrahedron (Figure 7, bottom). The Sc−Sc (321−337 pm) distances are in line with the ones found in the element (Sc: 325 and 331 pm[97]), while the Au−Au (321 pm) distances (Au: 287 pm[98]) are significantly longer. The Sc−Au (277−329 pm) distances are in line with the sum of the covalent radii (144 + 134 = 278 pm[96]). The homo- as well as the heteroatomic distances are also in line with binary (Sc−Sc: 329 pm in $ScAl_2$;[100] Sc−Sc: 351 pm, Sc−Au: 287−293 pm in $ScAu_2$[101]) scandium intermetallics. Finally, the Sc−O distances in the $[OSc1_6]$ octahedron are 232 pm long, which is significantly longer compared to Sc_2O_3 (bixbyite type; Sc−O = 208−212 pm[108]); however, in this structure, the O atoms are tetrahedrally coordinated by Sc atoms. Scandium monoxide, ScO, in contrast, adapts the NaCl-type structure, where the Sc−O distances are enlarged (CN(O) = 6; 223 pm[109]). This

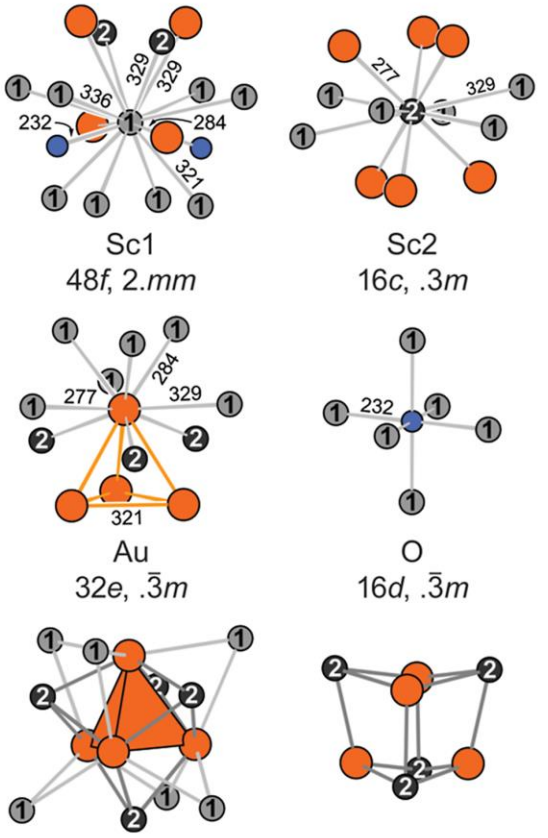

Figure 7. Coordination polyhedra surrounding the (top) scandium, gold (middle, left), and oxygen (middle, right) atoms in $Sc_4Au_2O_{1-x}$. The local coordination environments surrounding the empty Au_4 tetrahedra are shown at the bottom. Sc, Au, and O atoms are shown in gray, orange, and blue, respectively.

leads to the assumption that the Sc−O interactions in $Sc_4Au_2O_{1-x}$ are significantly weaker compared to the pure oxidic materials, which has been addressed by quantum-chemical calculations (*vide infra*).

3.4. Oxidation Behavior and Thermoanalytical Investigations. Due to the air sensitivity of Sc_2Au, its oxidation behavior was investigated. When freshly ground powders of Sc_2Au are kept in air, they change color within a few hours from a light gray to a dark gray. Over the course of several days, the powder finally turns black. Powder X-ray investigations indicated no significant changes in the diffraction patterns within the first few days; however, after 10 days, a clear change is observed. The changes get more pronounced over time, and after 35*d*, a nano-crystalline material is obtained. The reflections arising from Sc_2Au have vanished; instead, the significantly broadened reflections of elemental Au and Sc_2O_3 can be identified (Figure 8, top right).

In order to understand this process better, Sc_2Au was heated to 1273 K in an STA under a flow of O_2/Ar with a 1:1 ratio (Figure 8, left). Here, a more crystalline product of Au and Sc_2O_3 is obtained (Figure 8, middle right), underlining the observations of the oxidation in air. As seen in the TG data, the sample starts to gain mass slightly above 310 K until an equilibrium state is reached after a total mass increase of 17.8

https://doi.org/10.1021/acs.inorgchem.3c01097
Inorg. Chem. 2023, 62, 9602−9617

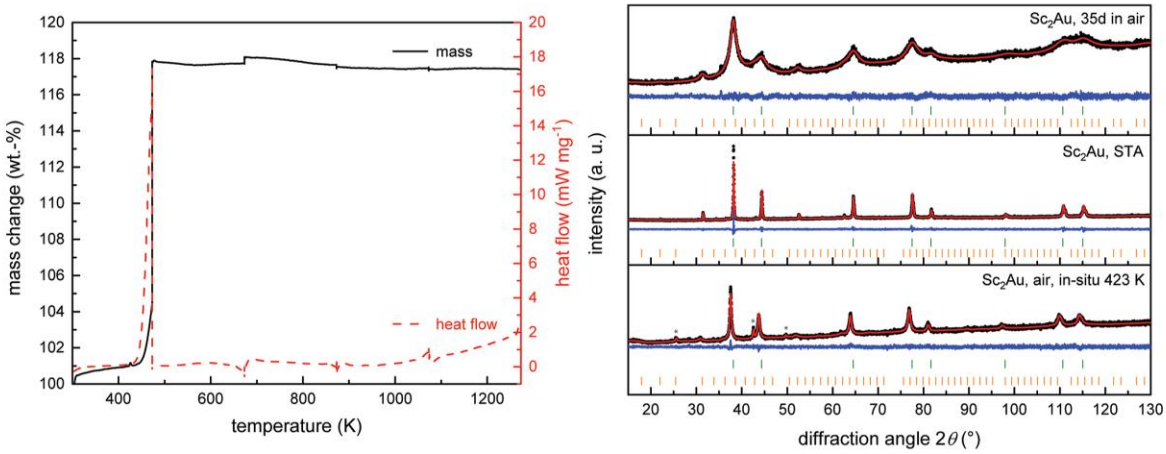

Figure 8. (left) Temperature dependence of mass change (black) and heat flow (red) of Sc_2Au heated in an STA under a mixture of O_2/Ar of 1:1. (right) Powder X-ray diffraction patterns of (top) Sc_2Au stored for 35*d* in air, (middle) after heating to 1273 K in an STA and (bottom) measured at 423 K *in situ* in air. Experimental data is shown as black dots, the refinement as a red line, and the difference in blue. Green ticks indicate the Bragg positions of elemental gold, and orange ticks the ones of Sc_2O_3 (bixbyite-type).

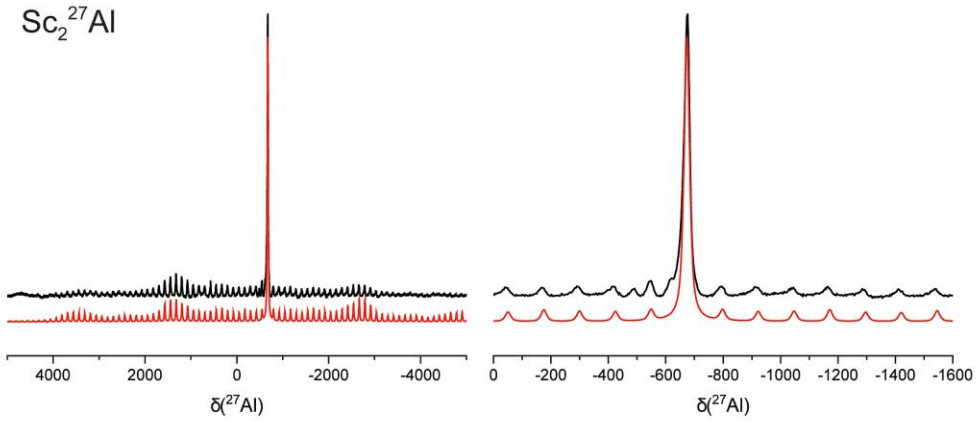

Figure 9. ^{27}Al MAS-NMR spectra (left) of hexagonal Sc_2Al (Ni_2In-type). Zoom of the region around the central $|+1/2\rangle \leftrightarrow |-1/2\rangle$ transition is shown on the right. The small signals are rotational side bands caused by the MAS conditions. The fits are depicted in red.

wt %, in good agreement with the total oxidation of Sc_2Au to Sc_2O_3 and elemental gold (14.3 wt % increase). In the heat flow, a sharp exothermic signal with an on-set temperature of ~446 K (T_{peak} = 473 K) is observed. *In situ* heating of a sample of Sc_2Au in air indicated a full oxidation into Sc_2O_3 and Au already at 423 K (Figure 8, bottom right). Heating to higher temperatures does not change the diffraction patterns.

3.5. Magnetic Properties. Magnetic susceptibility data has been obtained for the members of the solid solution $Sc_2Au_{1-x}Au_x$ for x = 0, 0.25, 0.5, 0.75, and 1. No superconductivity was observed for any of the samples down to 2.1 K at applied external fields of 20 Oe. The temperature dependence of the magnetic susceptibility of all investigated compounds is depicted in Figure S7 (ESI). All members are *Pauli* paramagnetic materials, with positive room temperature susceptibilities (Table 5) underlining the visually observed metallic character. The weak upturns at low temperatures arise from small amounts of paramagnetic impurities. The present data clearly proves the absence of local moments on all constituent atoms, enabling NMR spectroscopic investigations on these compounds.

3.6. ^{27}Al and ^{45}Sc Solid-State NMR Spectroscopic Investigations. Samples of Sc_2Au and Sc_2Al were measured at a magnetic flux density of 9.4 T. Table 6 summarizes the parameters obtained from the MAS-NMR spectra as well as the calculated values for the quadrupole parameters C_Q and η_Q.

The ^{27}Al spectrum of Sc_2Al (Figure 9) shows only one sharp central transition, which is in line with one crystallographic Al position. This transition originates from the $|+1/2\rangle \leftrightarrow |-1/2\rangle$ Zeeman transition. The main resonance is observed at δ = −673 ppm, which is significantly different compared to the majority of investigated intermetallic aluminum compounds. For example, the binary alkaline-earth and rare-earth dialuminides exhibit positive resonance shifts of δ = +1091 and +1152 ppm for $AEAl_2$ (AE = Ca and Sr)[110] and δ = +213 to +924 ppm for $REAl_2$ (RE = Sc, Y, La, Yb, Lu).[111] Ternary aluminum intermetallics also exhibit positive shifts, *e.g.*, δ = 440−851 (ScT_2Al and $Sc(T,T')_2Al$; T = T' = Ni, Pd, Pt, Cu, Ag, Au),[103] 762 and 1031 ($Ba_3Pt_4Al_4$),[105] 273−636 ppm

https://doi.org/10.1021/acs.inorgchem.3c01097
Inorg. Chem. 2023, 62, 9602−9617

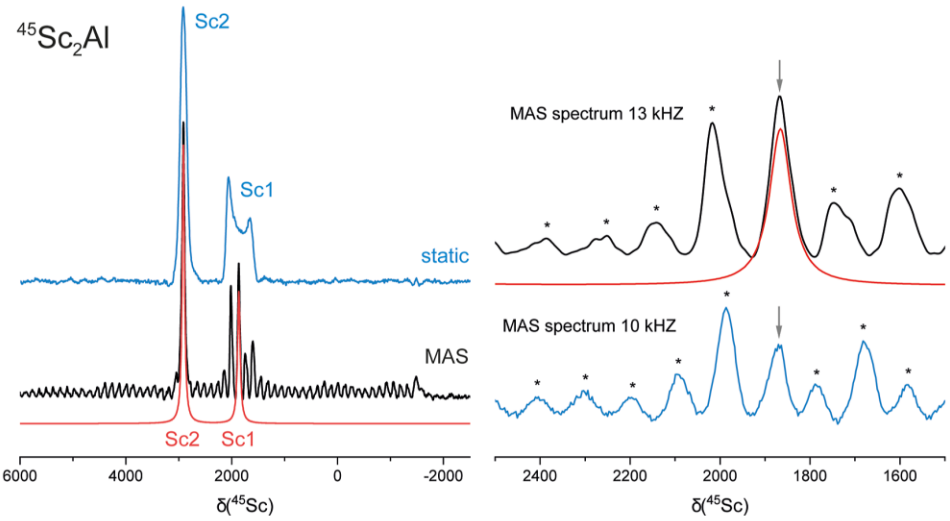

Figure 10. ^{45}Sc MAS-NMR spectrum (left, black) and static spectrum (left, blue) of hexagonal Sc_2Al (Ni_2In-type). (right) Measurement of the central transition around 1900 pm at two different rotational speeds. Fits are depicted as red lines. The site assignment is given.

(RET_5Al_2; *RE* = Y, Lu; *T* = Pd, Pt),[112] or 419−767 ($MTAl_2$; *M* = Ca-Ba, Sc, Y, La, Lu; *T* = Ni, Pd, Pt).[113,114] Negative ^{27}Al NMR shifts, in contrast, are scarce and have, to the best of our knowledge, only been observed for the binary compounds VAl_3 (δ = −170 and −100[115]/−97 and −130[116] ppm), Fe_4Al_{13} (δ = −175 ppm[117]) and TiAl (δ = −170 ppm[116]). The origin of this drastically different NMR behavior must originate from a significantly different electronic situation at the Al nucleus. Two competing magnetic screening mechanisms were described by Ferreira: the so-called *Knight* shift that originates from the hyperfine interaction between the nucleus with the spins of itinerant (conduction) electrons and the hyperfine interaction with local magnetic moments at the transition metal site. While the *Knight* contribution leads to a de-shielding at the Al atoms (and therefore a strong positive shift), the latter contribution can counter compensate this effect. DFT calculations on binary intermetallic aluminum compounds showed that, for example, in VAl_3 and TiAl, the orbital contribution gets surpassed by the spin contribution, leading to an overall negative NMR shift. In $CuAl_2$, for example, both contributions point in the same direction.[118] It is interesting to note that metal−organic Al(I) compounds like Cp*Al (δ = −150 ppm), $(C_5H_2(SiMe_3)_3)Al$ (δ = −165 ppm), or $(C_5H_3(SiMe_3)_2)Al$ (δ = −168 ppm) reported by Schnöckel and co-workers also show negative chemical shifts.[119] This extreme shielding was explained by significant π-bonding interactions between the Al and the ligand and therefore an energetic separation between the HOMO and LUMO. This paramagnetic (orbital) contribution was later proven by DFT calculations.[120] A similar behavior has, *e.g.*, been observed for the ^{195}Pt resonances in the *MPtX* series (*M* = Ti, Zr, Hf; *X* = Si, Ge, Sn), where TiPtGe is dimorphic and crystallizes either as an HT-phase in the orthorhombic TiNiSi-type (*Pnma*) structure or as an LT-phase in the cubic MgAgAs-type ($F\bar{4}3m$).[121] In these two compounds, the isotropic *Knight* shift of the ^{195}Pt resonance spans over 6000 ppm with δ = 320 ppm for LT-TiPtGe and δ = −6156 ppm for HT-TiPtGe. The authors attributed this observation to the differences in the Ti−Pt interactions as well as the different charge densities at the Pt sites.[121]

In addition to the dominant central Zeeman transitions, the MAS-NMR spectra of ^{27}Al show a wide spinning sideband manifold, arising from the outer $|\pm1/2\rangle \leftrightarrow |\pm3/2\rangle$ and $|\pm3/2\rangle \leftrightarrow |\pm5/2\rangle$ Zeeman transitions. These satellite transitions are anisotropically broadened by first-order nuclear electric quadrupolar perturbations. Since the coordination environments of the Al and Sc atoms are not spherical (Figure 6), the quadrupole moments of both nuclei interact with the local electrical field gradient, resulting in the specific form of the NMR signal and the observed spinning sideband pattern.[122] For the ^{27}Al spectrum of Sc_2Al, a refinement of the C_Q parameter could be done based on the intensity profile of the spinning sideband manifold. Here, the values from DFT calculations were used as a starting point and are in good agreement with the refined parameter (Table 6).

The recorded ^{45}Sc spectrum of Sc_2Al exhibits two main signals, as expected from a structure with two Sc sites. Again, the two most intense signals originate from the $|+1/2\rangle \leftrightarrow |-1/2\rangle$ Zeeman transitions. However, due to ^{45}Sc being a nucleus with I = 7/2, satellite transitions are caused by the $|\pm1/2\rangle \leftrightarrow |\pm3/2\rangle$, $|\pm3/2\rangle \leftrightarrow |\pm5/2\rangle$, and $|\pm5/2\rangle \leftrightarrow |\pm7/2\rangle$ Zeeman transitions.[123] As shown in Figure 10 (left), the ^{45}Sc MAS spectrum (13 kHz) of Sc_2Al is rather complicated due to the large number of rotational side bands. To be able to distinguish between main signals and rotational side bands, an additional ^{45}Sc spectrum was recorded at a MAS frequency of 10 kHz. Here, the main signals remain at their characteristic resonance shifts, while the side bands move, enabling an identification of the main lines (Figure 10, right). Figure 10 also depicts the static ^{45}Sc spectrum for this compound. Based on the C_Q parameters received from DFT calculations, a site assignment is possible since the obtained parameters differ by the factor of two. The signal around δ = 1870 ppm shows a significantly higher quadrupole line broadening compared to the signal at δ = 2910 ppm, which can be described well with a Gaussian−Lorentz function. Based on this spectrum, no refinement of the quadrupole parameters was performed.

https://doi.org/10.1021/acs.inorgchem.3c01097
Inorg. Chem. 2023, 62, 9602−9617

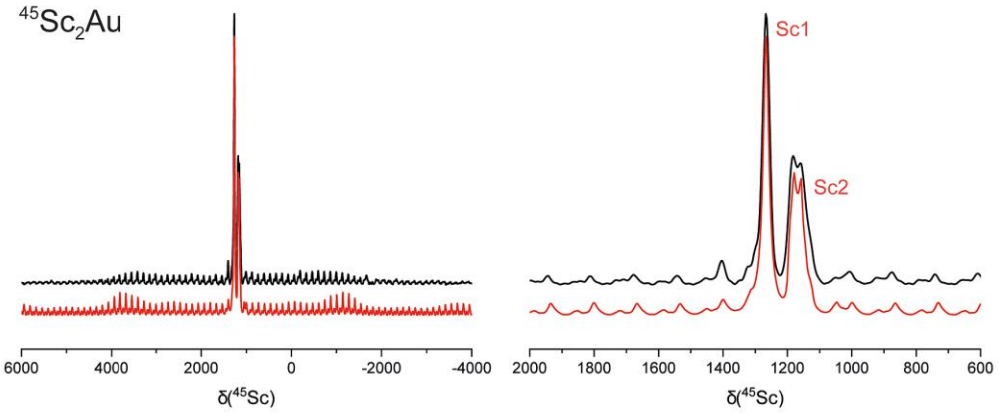

Figure 11. ^{45}Sc MAS-NMR spectra (left) of orthorhombic Sc_2Au ($PbCl_2$ type). Zoom of the region around the central $|+1/2\rangle \leftrightarrow |-1/2\rangle$ transition is shown on the right. The small signals are rotational side bands caused by MAS conditions. The site assignment is given. The fits are depicted in red.

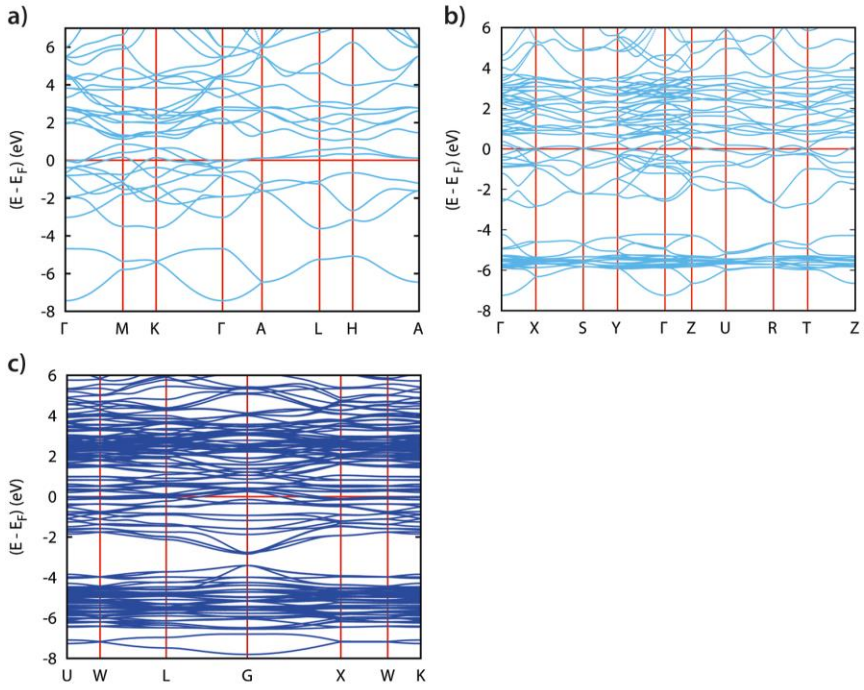

Figure 12. Electronic band structures of (a) Sc_4Al_2, (b) Sc_8Au_4, and (c) $Sc_{16}Au_8O_4$.

Due to the problem of site assignment and the broad signals in the spectrum, a sample of Sc_2Al was annealed in a closed quartz ampule for 12 days at 1123 K. The temperature treatment did not lead to a sharper spectrum. Therefore, the quadrupolar interaction is not caused by defects of comparable interactions in the material.

Finally, the ^{45}Sc spectrum of Sc_2Au (Figure 11) also shows two main transitions and the discussed spinning sideband patterns for the two signals. One of the signals is significantly affected by second-order quadrupole effects, which is visible in the characteristic (anisotropic) line shape. The other signal can be described by a Gaussian−Lorentz fit. Here, second-order quadrupole effects seem to be less dominant. Based on the values for C_Q and η_Q obtained by DFT calculations, an assignment of the signals to the respective Sc sites could be achieved.

3.7. Quantum-Chemical Calculations. The quantum mechanical calculations were started from the experimental lattice parameters submitted to unconstrained geometry relaxations. The converged structures were found to be very close to the experimental inputs.

The first criteria for assessing the relative stabilities are the atom-averaged cohesive energies provided for the different compounds under consideration. The atomic energies of the different constituents obtained from calculations of the atoms isolated in a large box (E(Sc_sv) = −4.19 eV, E(Al) = −3.37

https://doi.org/10.1021/acs.inorgchem.3c01097
Inorg. Chem. 2023, 62, 9602−9617

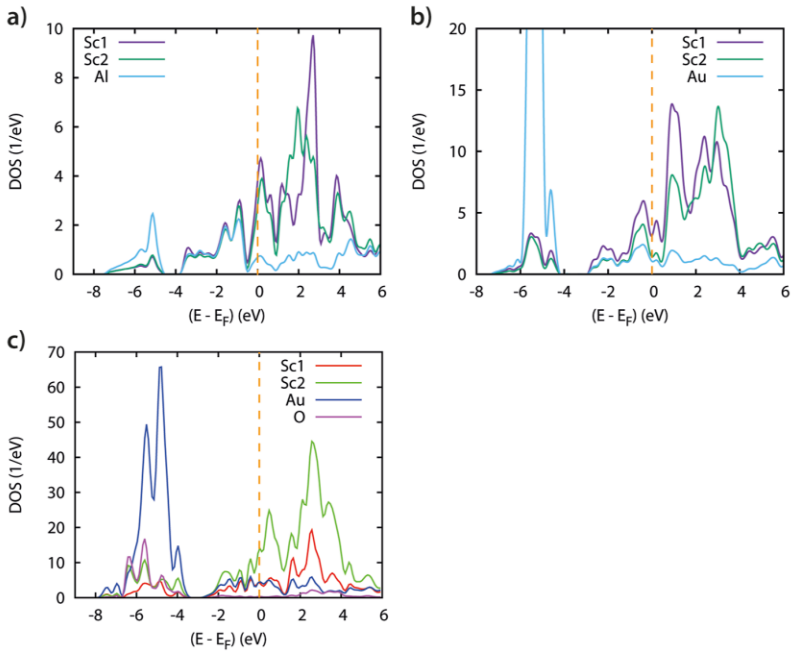

Figure 13. Site-projected electronic density of states (DOS) of (a) Sc_4Al_2, (b) Sc_8Au_4, and (c) $Sc_{16}Au_8O_4$.

eV, and E(Au) = −3.21 eV, E(O) = −5.5 eV) are subtracted from the total energies to obtain the cohesive energies that are subsequently atom-averaged to allow comparisons:

hexagonal Sc_2Al (Z = 2): $E_{tot.}$ = −34.89 eV; E_{coh}/atom = −1.89 eV,

simulated hexagonal Sc_2AlAu (Z = 2): $E_{tot.}$ = −34.89 eV; E_{coh}/atom = −1.94 eV,

orthorhombic Sc_2Au (Z = 8): $E_{tot.}$ = −71.43 eV; E_{coh}/atom = −2.09 eV,

cubic $Sc_4Au_2O_{1-x}$ (Z = 8): $E_{tot.}$ = −118.6 eV; E_{coh}/atom = −0.135 eV.

It can be observed that the cohesive energy increases upon introducing Au, leading to Sc_2AuAl (simulated) and then to the pure Sc_2Au found to be most cohesive. The observed behavior can be related to the larger electronegative character of Au (χ = 2.54) versus Al (χ = 1.50).[96] However, the introduction of oxygen is likely to destabilize the intermetallic system. This feature will be further discussed below in Section 3.7.3.

In a second step, the trends of charge transfers were obtained from the analyses of the charge density along with two schemes: (i) an exclusive valence population, and (ii) an inclusion of core + semi-core valence populations with "augmented Bader charges". The results were analyzed according to the Bader approach introduced above.

The results, according to the two approaches, are displayed in Table 7. By accounting only for valence states, the charge transfer is large, ionic, and not illustrative of an alloy/metallic system. Oppositely, when augmented charges are considered (right hand side of Table 7), the charges are more indicative of a metallic system, and they follow the trends of electronegativities according to Pauling:

χ(Sc) = 1.36, χ(Al) = 1.50, χ(Au) = 2.54, χ(O) = 3.44.

Furthering on these observations, the electronic properties were then illustrated with the electronic band structures, the site-projected density of states DOS, and the properties of chemical bonding. The calculations were carried out with all electrons using the scalar relativistic ASW method introduced in the section Quantum-chemical calculations.

3.7.1. Electronic Band Structures. Figure 12 displays the electronic band structures. The bands develop along the main directions of the respective hexagonal and orthorhombic Brillouin zones. The zero energy along the vertical direction is with respect to the Fermi level E_F: all three systems are metallic, with bands crossing the Fermi level. Below −4 eV, the bands correspond to s states, followed by p states. In the Sc_2Au and $Sc_4Au_2O_{1-x}$ panels, the low energy lying filled Au $5d^{10}$ bands are found in a 1 eV narrow energy window.

3.7.2. Site-Projected DOS. The role of each atomic constituent is better observed from the site-projected DOS shown in Figure 13. The energy axis is now horizontal, and the zero energy is with respect to E_F. The DOS along the vertical directions are given in 1/eV unit. As a general characteristic, DOS with similar skylines and energies point to quantum mixing of the valence states, *i.e.*, chemical interactions. This is clearly observed in Figure 13a of Sc_2Al within the valence band (below E_F), especially from −4 eV up to E_F, where p-states ensure the bonding; around −6 eV, the s-like binding is observed with less intensity, and relatively intense Al(s) are less involved with the chemical interactions. Generally, the p-states with more directional character versus smeared s-states are more involved with the bonding. Similar DOS shapes between constituents are also observed above E_F in the empty states. In Figure 13b reporting on Sc_2Au, the aforementioned Au($5d^{10}$) bands correspond to narrow DOS in the energy window −6 to −5 eV and are found not mixing with Sc states. The low intensity below them corresponds to s-like Sc and Au states. This feature is also found in Figure 13c ($Sc_4Au_2O_{1-x}$), where

https://doi.org/10.1021/acs.inorgchem.3c01097
Inorg. Chem. 2023, 62, 9602−9617

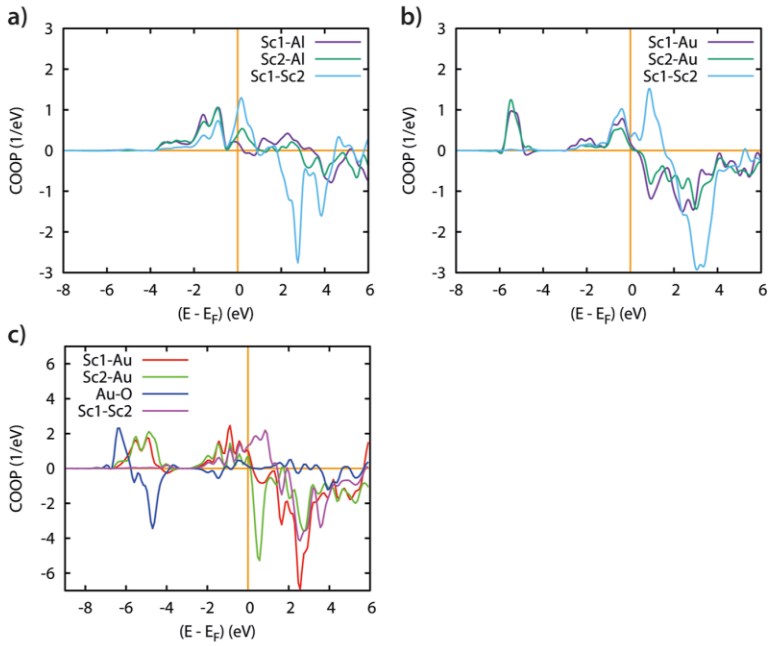

Figure 14. Chemical interactions with the COOP qualitative criterion (*cf.* text) of (a) Sc_4Al_2, (b) Sc_8Au_4, and (c) $Sc_{16}Au_8O_4$.

the Au-filled 5*d* states at −5 eV are less involved with the bonding. The similar DOS shapes of Au and O around −4 eV highlight bonding between them.

3.7.3. Chemical Bonding Analysis via COOP. The chemical bonding is qualitatively obtained from the overlap population S_{ij} within the COOP criterion and displayed in Figure 14. Along the *y*-axis, positive, negative, and zero magnitudes correspond to bonding, antibonding, and non-bonding pair interactions. All occupied states below E_F are positive, describing bonding interactions, with favoring Sc−Al bonds over less intense Sc−Sc (Figure 14a). Similarly, in Figure 14b, the bonding is mainly between Sc and Au. Note the involvement of Au *d* states at −6 eV with the bonding. In Figure 14c ($Sc_4Au_2O_{1-x}$), the Au−O interaction (blue) is half bonding/half antibonding destabilizing versus the intermetallic part with nearly equal positive/negative COOP magnitudes. Concomitantly, COOP(Sc−Au) are all positive. This goes along with the smallest amount of cohesive energy accounted for numerically above.

4. CONCLUSIONS

Samples of Sc_2Al, Sc_2Au, and the solid solution $Sc_2Au_{1-x}Al_x$ were synthesized from the elements and investigated by single-crystal and powder X-ray diffraction. Phase pure samples were obtained with respect to powder diffraction experiments, and the structures of Sc_2Au and $Sc_2Au_{0.59(1)}Al_{0.41(1)}$ were refined from single-crystal data. The solid solution exhibits a Vegard-like behavior within one structure type; however, a two-phase region was observed for $x \sim 0.6$, indicating that for $x = 0$−0.5, the hexagonal Ni_2In-type is formed, while for $x = 0.75$ and 1, the orthorhombic $PbCl_2$ type is observed. Sc_2Au is an air-sensitive compound that decomposes within a month to form Sc_2O_3 and elemental Au. The decomposition was additionally studied by thermal analysis and temperature-dependent powder X-ray diffraction. However, oxygen contaminations during synthesis led to the formation of the sub-oxide $Sc_4Au_2O_{1-x}$ that was subsequently synthesized from Sc, Au, and Sc_2O_3 and characterized by powder X-ray diffraction. Magnetic susceptibility measurements indicate Pauli's paramagnetic behavior in line with a metallic character and the absence of localized magnetic moments. The ^{45}Sc NMR investigations of both Sc_2Al and Sc_2Au showed two resonances, in line with the crystal structures. Due to the differences in the coordination environment and the subsequent differences in the quadrupolar interactions, a site assignment was possible. The ^{27}Al NMR of Sc_2Al showed one resonance, however, with the, to the best of our knowledge, most negative resonance shift of $\delta = -673$ ppm known thus far. This shift arises from a very special electronic situation in the spin and orbital contributions. Finally, quantum chemical calculations showed that the investigated compounds are metallic in nature and stabilized by hetero-atomic bonding interactions.

■ ASSOCIATED CONTENT

Supporting Information

The Supporting Information is available free of charge at https://pubs.acs.org/doi/10.1021/acs.inorgchem.3c01097.

Additional powder X-ray data (PDF)

Accession Codes

CCDC 1858159−1858160 contain the supplementary crystallographic data for this paper. These data can be obtained free of charge via www.ccdc.cam.ac.uk/data_request/cif, or by emailing data_request@ccdc.cam.ac.uk, or by contacting The Cambridge Crystallographic Data Centre, 12 Union Road, Cambridge CB2 1EZ, UK; fax: +44 1223 336033.

https://doi.org/10.1021/acs.inorgchem.3c01097
Inorg. Chem. 2023, 62, 9602−9617

AUTHOR INFORMATION

Corresponding Author

Oliver Janka − *Anorganische Festkörperchemie, Universität des Saarlandes, Saarbrücken 66123, Germany;* orcid.org/0000-0002-9480-3888; Email: oliver.janka@uni-saarland.de

Authors

Elias C. J. Gießelmann − *Anorganische Festkörperchemie, Universität des Saarlandes, Saarbrücken 66123, Germany;* orcid.org/0000-0001-6137-9729

Mathis Radzieowski − *Institut für Anorganische und Analytische Chemie, Westfälische Wilhelms-Universität Münster, Münster 48149, Germany*

Samir F. Matar − *Lebanese German University, Jounieh 206, Lebanon;* orcid.org/0000-0001-5419-358X

Complete contact information is available at: https://pubs.acs.org/10.1021/acs.inorgchem.3c01097

Author Contributions

All authors have accepted responsibility for the entire content of this submitted manuscript and approved the submission.

Notes

The authors declare no competing financial interest.

ACKNOWLEDGMENTS

We thank Dipl.-Ing. Jutta Kösters and Dipl.-Ing. Ute Ch. Rodewald for the collection of the single-crystal diffraction data and Dr. Frank Stegemann for the help with the magnetic measurements. Instrumentation and technical assistance for this work were provided by the Service Center X-ray Diffraction, with financial support from the Saarland University and German Research Foundation (project number INST 256/349-1) and by the Service Center NMR with financial support from the Saarland University and German Research Foundation DFG.

REFERENCES

(1) Gladyshevskii, R. E.; Grin, Yu.; Yarmolyuk, Y. P. The crystal structure of R_6GaCo_2 compounds (R = Y, Tb, Dy, Ho, Er, Tm, Lu). *Dopov. Akad. Nauk Ukr. RSR* **1983**, *2A*, 67−70.

(2) Sichevich, O. M.; Komarovskaya, L. P.; Gun, Y. N.; Yarmolyuk, Y. P.; Skolozdra, R. V. Crystal structure and magnetic properties of $R_6Ga(Co,Ni)_2$ and R_6SnNi_2 (R = rare-earth metal). *Ukr. Fiz. Zh. Russ. Ed.* **1984**, *29*, 1342−1345.

(3) Vasilechko, L. O.; Ermolyuk, Y. P.; Grin, Y. Phase equilibria in the Lu-Ni-Ga system at 870 °C. *Russ. Metall.* **1985**, *5*, 201−205.

(4) Kalychak, J. M.; Zaremba, V. I.; Zavalij, P. Y. Crystal structure of holmium cobalt indium (6/2/1), $Ho_6Co_{2+x}In_{1-x}$, x = 0.135. *Z. Kristallogr.* **1993**, *208*, 380−382.

(5) Kalychak, Y. M. Composition and crystal structure of rare-earths−Co−In compounds. *J. Alloys Compd.* **1999**, *291*, 80−88.

(6) Zaremba, R. I.; Kalychak, Y. M.; Rodewald, U. C.; Poettgen, R.; Zaremba, V. I. New indides $Sc_6Co_{2.18}In_{0.82}$, $Sc_{10}Ni_9In_{19.44}$ and $ScCu_4In$ - synthesis, structure, and crystal chemistry. *Z. Naturforsch.* **2006**, *37*, 924−948.

(7) Zaremba, V. I.; Kalychak, Y. M.; Dzevenko, M. V.; Rodewald, U. C.; Hoffmann, R.-D.; Pöttgen, R. Syntheses and structure of $Er_6Co_{2.19(1)}In_{0.81(1)}$. *Monatsh. Chem.* **2007**, *138*, 101−105.

(8) Tyvanchuk, Y. B.; Lukachuk, M.; Pöttgen, R.; Szytuła, A.; Kalychak, Y. M. The ternary system Tm−Ni−In at 870 K. *Z. Naturforsch.* **2015**, *70*, 665−670.

(9) Verbovytskyy, Y.; Łątka, K.; Przewoźnik, J.; Kinzhybalo, V. Crystal structure and magnetic properties of the selected phases from the R-{Co, Ni}-Al (R = Y, Gd-Tm) systems. *J. Alloys Compd.* **2018**, *758*, 122−130.

(10) Stegemann, F.; Janka, O. Two series of rare earth metal-rich ternary aluminium transition metallides − RE_6Co_2Al (RE = Sc, Y, Nd, Sm, Gd−Tm, Lu) and $RE_6Ni_{2.25}Al_{0.75}$ (RE = Y, Gd−Tm, Lu). *Z. Naturforsch.* **2018**, *73*, 927−942.

(11) Grin, Y.; Sichevich, O. M.; Gladyshevskii, E. I.; Yarmolyuk, Y. P. The crystal structure of the compounds R_8Ga_3Co (R = Ce, Pr, Nd, Sm, Tb, Dy, Ho, Er, Tm). *Sov. Phys. Crystallogr.* **1984**, *29*, 419−421.

(12) Pustovoychenko, M. M.; Dzevenko, M. D.; Bigun, I.; Havela, L.; Kalychak, Y. M. The crystal structure of new ternary rare-earth rich indides RE_8CoIn_3. *Abstr. 12th Int. Conf. Crystal Chem. Intermet. Compd.*, 2013; p 114.

(13) Dzevenko, M.; Bigun, I.; Pustovoychenko, M.; Havela, L.; Kalychak, Y. Rare-earth rich indides RE_8CoIn_3 (RE = Y, Dy−Tm, Lu). *Intermetallics* **2013**, *38*, 14−18.

(14) Johnscher, M.; Block, T.; Pöttgen, R. $RE_{10}TCd_3$ (RE = Y, Tb − Tm, Lu; T = Fe, Co, Ni, Ru, Rh, Pd) − rare earth-rich phases with ordered anti-Co_2Al_5 structure. *Z. Anorg. Allg. Chem.* **2015**, *641*, 369−374.

(15) Benndorf, C.; Eckert, H.; Janka, O. Ternary rare-earth aluminium intermetallics $RE_{10}TAl_3$ (RE = Y, Ho, Tm, Lu; T = Fe, Co, Ni, Ru, Rh, Pd, Os, Ir, Pt) with an ordered anti-Co_2Al_5 structure. *Dalton Trans.* **2017**, *46*, 1083−1092.

(16) Block, T.; Klenner, S.; Heletta, L.; Pöttgen, R. Rare earth-rich cadmium compounds $RE_{10}TCd_3$ (RE = Y, Tb, Dy, Ho, Er, Tm, Lu; T = Rh, Pd, Ir, Pt) with an ordered Co_2Al_5-type structure. *Z. Naturforsch.* **2018**, *73*, 35−42.

(17) Block, T.; Pöttgen, R. Cd_3 and Cd_4 clusters in the rare earth (RE) metal-rich phases $RE_{10}OsCd_3$ and RE_4OsCd. *Monatsh. Chem.* **2019**, *150*, 975−982.

(18) Zaremba, V. I.; Galadzhun, Y. V.; Kalychak, Y. M.; Davydov, V. M.; Stepien Damm, J.; Pietraszko, A. $R_{12}Pt_7In$ (R = Ce, Pr, Nd) − The new representatives of superstructure to Gd_3Ga_2-type. *Abstr. 7th Int. Conf. Crystal Chem. Intermet. Compd.*, 1999; p PB24.

(19) Galadzhun, Y. V.; Zaremba, V. I.; Kalychak, Y. M.; Davydov, V. M.; Pikul, A. P.; Stępień-Damm, A.; Kaczorowski, D. $R_{12}Pt_7In$ (R = Ce, Pr, Nd, Gd, Ho) − new derivatives of the Gd_3Ga_2-type. *J. Solid-state Chem.* **2004**, *177*, 17−25.

(20) Dzevenko, M. V.; Zaremba, R. I.; Hlukhyy, V. H.; Rodewald, U. C.; Pöttgen, R.; Kalychak, Y. M. Fe_2 Pairs as Structural Units in the Indides $RE_{12}Fe_2In_3$ (RE = Ho, Er, Tm, Lu). *Z. Anorg. Allg. Chem.* **2007**, *633*, 724−728.

(21) Canepa, F.; Napoletano, M.; Fornasini, M. L.; Merlo, F. Structure and magnetism of Gd_2Co_2Ga, Gd_2Co_2Al and $Gd_{14}Co_3In_{2.7}$. *J. Alloys Compd.* **2002**, *345*, 42−49.

(22) Lukachuk, M. y.; Galadzhun, Y. V.; Zaremba, R. I.; Dzevenko, M. V.; Kalychak, Y. M.; Zaremba, V. I.; Rodewald, U. Ch.; Pöttgen, R. New rare earth metal-rich indides $RE_{14}Ni_3In_3$ (RE = Sc, Y, Gd−Tm, Lu) - synthesis and crystal chemistry. *J. Solid-state Chem.* **2005**, *178*, 2724−2733.

(23) Zaremba, V. I.; Kalychak, Y. M.; Dzevenko, M. V.; Rodewald, U. C.; Heying, B.; Pöttgen, R. A single-crystal study of $RE_{14}Co_3In_3$ (RE = Y, Tb, Dy, Ho, Er). *Z. Naturforsch.* **2006**, *61*, 23−28.

(24) Zaremba, R.; Rodewald, U. C.; Pöttgen, R. Synthese und Struktur der metallreichen Verbindungen $Y_{14}T_3In_3$ (T = Rh, Ir) und RE_4IrIn (RE = Gd−Er). *Z. Anorg. Allg. Chem.* **2006**, *632*, 2106.

(25) Zaremba, R.; Rodewald, U. C.; Pöttgen, R. Transition metal-centered trigonal prisms as building units in $RE_{14}T_3In_3$ (RE = Y, Ho, Er, Tm, Lu; T = Pd, Ir, Pt) and Y_4IrIn. *Z. Naturforsch.* **2007**, *62*, 1574−1580.

(26) Zaremba, R.; Pöttgen, R. Rare earth metal-rich indides $RE_{14}Rh_{3-x}In_3$ (RE = Y, Dy, Ho, Er, Tm, Lu). *J. Solid-state Chem.* **2007**, *180*, 2452−2458.

(27) Kalychak, Y. M.; Zaremba, V. I.; Stepien Damm, J.; Galadzhun, Y. V.; Akselrud, L. G. Crystal structure of $Sm_{12}Ni_6In$ and related compounds. *Kristallografiya* **1998**, *43*, 17−20.

(28) Tappe, F.; Schwickert, C.; Linsinger, S.; Pöttgen, R. New rare earth-rich aluminides and indides with cubic Gd_4RhIn-type structure. *Monatsh. Chem.* **2011**, *142*, 1087−1095.
(29) Engelbert, S.; Janka, O. RE_4TAl (RE = Y, Sm, Gd−Tm, Lu; T = Pd, Pt) − Synthesis and magnetism of new aluminum representatives with the Gd_4RhIn type structure. *Intermetallics* **2018**, *96*, 84−89.
(30) Riani, P.; Freccero, R.; Sufryd, K.; Arrighi, L.; Cacciamani, G. The 500 °C isothermal section of the Al-Co-Nd ternary system. *J. Phase Equilibria Diffus.* **2020**, *41*, 347−364.
(31) Zaremba, R.; Rodewald, U. C.; Hoffmann, R.-D.; Pöttgen, R. The rare earth metal-rich indides RE_4RhIn (RE = Gd−Tm, Lu). *Monatsh. Chem.* **2007**, *138*, 523−528.
(32) Zaremba, R.; Rodewald, U. C.; Hoffmann, R.-D.; Pöttgen, R. Rare earth metal-rich indides RE_4IrIn (RE = Gd−Er), $RE_4IrInO_{0.25}$ (RE = Gd, Er), and $RE_4TIn_{1-x}Mg_x$ (RE = Y, Gd; T = Rh, Ir). *Monatsh. Chem.* **2008**, *139*, 481−487.
(33) Schappacher, F. M.; Pöttgen, R. Rare earth-rich cadmium compounds RE_4TCd (T = Co, Ru, and Rh) with Gd_4RhIn type structure. *Monatsh. Chem.* **2008**, *139*, 1137−1142.
(34) Doğan, A.; Rayaprol, S.; Pöttgen, R. Structure and magnetic properties of RE_4CoCd and RE_4RhCd (RE = Tb, Dy, Ho). *J. Phys.: Condens. Matter* **2007**, *19*, 076213.
(35) Schappacher, F. M.; Rodewald, U. C.; Pöttgen, R. Rare Earth-rich Cadmium Compounds RE_4TCd (T= Ni, Pd, Ir, Pt). *Z. Naturforsch.* **2008**, *63*, 1127−1130.
(36) Tuncel, S.; Rodewald, U. C.; Chevalier, B.; Pöttgen, R. Rare earth-rich magnesium compounds RE_4RhMg (RE = Y, La−Nd, Sm, Gd−Tm, Lu). *Z. Naturforsch.* **2007**, *62*, 642−646.
(37) Tuncel, S.; Chevalier, B.; Matar, S. F.; Pöttgen, R. Synthesis, structure and chemical bonding of RE_4RuMg (RE = La−Nd, Sm, Gd−Ho). *Z. Anorg. Allg. Chem.* **2007**, *633*, 2019−2024.
(38) Tuncel, S.; Roquefère, J. G.; Stan, C.; Bobet, J.-L.; Chevalier, B.; Gaudin, E.; Hoffmann, R.-D.; Rodewald, U. C.; Pöttgen, R. Rare earth metal rich magnesium compounds RE_4NiMg (RE = Y, Pr−Nd, Sm, Gd−Tm, Lu) − Synthesis, structure, and hydrogenation behavior. *J. Solid-state Chem.* **2009**, *182*, 229−235.
(39) Tuncel, S.; Chevalier, B.; Pöttgena, R. Rare earth-rich magnesium compounds RE_4PdMg (RE = Y, Sm, Gd) and RE_4PtMg (RE = Y, Nd, Sm, Gd). *Z. Naturforsch.* **2008**, *63*, 600−602.
(40) De Negri, S.; Saccone, A.; Rogl, P.; Giester, G. The ternary system Yb−Cu−Mg: Isothermal section at 400°C in the range from 0 to 67 at.% Cu. *Intermetallics* **2008**, *16*, 1285−1291.
(41) Rodewald, U. Ch.; Tuncel, S.; Chevalier, B.; Pöttgen, R. Rare earth metal-rich magnesium compounds RE_4IrMg (RE = Y, La, Pr, Nd, Sm, Gd, Tb, Dy) and $RE_{23}Ir_7Mg_4$ (RE = La, Ce, Pr, Nd). *Z. Anorg. Allg. Chem.* **2008**, *634*, 1011−1016.
(42) Solokha, P.; De Negri, S.; Pavlyuk, V.; Saccone, A. Crystal chemical peculiarities of rare earth (R) rich magnesium intermetallic compounds in R−T−Mg (T = transition element) systems. *Chem. Met. Alloys* **2009**, *2*, 39−48.
(43) Linsinger, S.; Hermes, W.; Chevalier, B.; Couillaud, S.; Bobet, J.-L.; Eul, M.; Pöttgen, R. Transition from antiferromagnetic ordering to cluster-glass behaviour in the solid solution $Gd_4NiMg_{1-x}Al_x$ ($0 \le x \le 0.9$). *Intermetallics* **2009**, *17*, 1028−1034.
(44) Couillaud, S.; Linsinger, S.; Duée, C.; Rougier, A.; Chevalier, B.; Pöttgen, R.; Bobet, J.-L. Hydrogenation behavior of the solid solutions $RE_4NiMg_{1-x}Al_x$ and $RE_{4-y}NiMg_{1+y}$ with RE = Gd and Y. *Intermetallics* **2010**, *18*, 1115−1121.
(45) Kersting, M.; Matar, S. F.; Schwickert, C.; Pöttgen, R. Segregation of calcium and magnesium into different substructures. $Ca_4Ag_{0.948}Mg$ and other compounds with Gd_4RhIn-type structure. *Z. Naturforsch.* **2012**, *67*, 61−69.
(46) de Negri, S.; Solokha, P.; Saccone, A. The 400 °C isothermal section of the La-Co-Mg ternary system. *J. Phase Equilibria Diffus.* **2014**, 35, 377−383.
(47) Shtender, V. V.; Zelinska, O. Y.; Pavlyuk, V. V.; Denys, R. V.; Paul-Boncour, V.; Zavaliy, I. Y.; Marciniak, B.; Różycka-Sokołowska, E. Phase equilibria in the Nd−Mg−Co system at 300 and 500 °C, crystal structure and hydrogenation behavior of selected compounds. *Intermetallics* **2017**, *87*, 61−69.
(48) Block, T.; Stein, S.; Heletta, L.; Pöttgen, R. Osmium and magnesium: structural segregation in the rare earth-rich intermetallics RE_4OsMg (RE = La−Nd, Sm) and RE_9TMg_4 (RE = Gd, Tb). *Z. Naturforsch.* **2019**, *74*, 519−525.
(49) Shtender, V. V.; Pavlyuk, V. V.; Zelinska, O. Y.; Nitek, W.; Paul-Boncour, V.; Dmytriv, G. S.; Łasocha, W.; Zavaliy, I. Y. The Y−Mg−Co ternary system: alloys synthesis, phase diagram at 500 °C and crystal structure of the new compounds. *J. Alloys Compd.* **2020**, *812*, 152072.
(50) Li, L.; Niehaus, O.; Kersting, M.; Pöttgen, R. Reversible table-like magnetocaloric effect in Eu_4PdMg over a very large temperature span. *Appl. Phys. Lett.* **2014**, *104*, 092416.
(51) Pöttgen, R.; Gulden, T.; Simon, A. Miniaturisierte Lichtbogenapparatur für den Laborbedarf. *GIT Labor-Fachz.* **1999**, *43*, 133−136.
(52) Pöttgen, R.; Lang, A.; Hoffmann, R.-D.; Künnen, B.; Kotzyba, G.; Müllmann, R.; Mosel, B. D.; Rosenhahn, C. The stannides YbPtSn and $Yb_2Pt_3Sn_5$. *Z. Kristallogr.* **1999**, *214*, 143−150.
(53) Yvon, K.; Jeitschko, W.; Parthé, E. LAZY PULVERIX, a computer program, for calculating X-ray and neutron diffraction powder patterns. *J. Appl. Crystallogr.* **1977**, *10*, 73−74.
(54) Bruker AXS Inc. *Topas*, version 5: Karlsruhe (Germany), 2014.
(55) Eymond, S.; Parthé, E. Sc_2Al with Ni_2In structure type. *J. Less Common Met.* **1969**, *19*, 441−443.
(56) Palenzona, A.; Manfrinetti, P. The phase diagram of the Sc-Au system. *J. Alloys Compd.* **1997**, *257*, 224−226.
(57) Bruker Corp. *Topspin*, version 2.1: Karlsruhe, 2008.
(58) Massiot, D.; Fayon, F.; Capron, M.; King, I.; Le Calvé, S.; Alonso, B.; Durand, J.-O.; Bujoli, B.; Gan, Z.; Hoatson, G. Modelling one- and two-dimensional solid-state NMR spectra. *Magn. Reson. Chem.* **2002**, *40*, 70−76.
(59) Hohenberg, P.; Kohn, W. Inhomogeneous electron gas. *Phys. Rev. B* **1964**, *136*, 864−871.
(60) Kohn, W.; Sham, L. J. Self-consistent equations including exchange and correlation effects. *Phys. Rev. A* **1965**, *140*, 1133−1138.
(61) Kresse, G.; Furthmüller, J. Efficient iterative schemes for ab initio total-energy calculations using a plane-wave basis set. *Phys. Rev. B: Condens. Matter Mater. Phys.* **1996**, *54*, 11169−11186.
(62) Kresse, G.; Joubert, D. From ultrasoft pseudopotentials to the projector augmented-wave method. *Phys. Rev. B: Condens. Matter Mater. Phys.* **1999**, *59*, 1758−1775.
(63) Blöchl, P. E. Projector augmented-wave method. *Phys. Rev. B: Condens. Matter Mater. Phys.* **1994**, *50*, 17953−17979.
(64) Vanderbilt, D. Soft self-consistent pseudopotentials in a generalized eigenvalue formalism. *Phys. Rev. B: Condens. Matter Mater. Phys.* **1990**, *41*, 7892−7895.
(65) Perdew, J. P.; Burke, K.; Ernzerhof, M. Generalized Gradient Approximation made simple. *Phys. Rev. Lett.* **1996**, *77*, 3865−3868.
(66) Bader, R. F. W. A quantum theory of molecular structure and its applications. *Chem. Rev.* **1991**, *91*, 893−928.
(67) Williams, A. R.; Kübler, J.; Gelatt, C. D. Cohesive properties of metallic compounds: Augmented-spherical-wave calculations. *Phys. Rev. B: Condens. Matter Mater. Phys.* **1979**, *19*, 6094−6118.
(68) Eyert, V. *The Augmented Spherical Wave Method—a Comprehensive Treatment*; Springer-Verlag: Berlin Heidelberg, 2013.
(69) Hoffmann, R. How chemistry and physics meet in the solid state. *Angew. Chem., Int. Ed.* **1987**, *26*, 846−878.
(70) Villars, P.; Cenzual, K. *Pearson's Crystal Data: Crystal Structure Database for Inorganic Compounds, Release 2022/23*; ASM International: Materials Park, Ohio, USA, 2023.
(71) Holleck, H.; Thümmler, F. Ternäre Komplex-carbide, -nitride und -oxide mit teilweise aufgefüllter Ti_2Ni-Struktur. *Monatsh. Chem.* **1967**, *98*, 133−134.
(72) Holleck, H. Binäre und ternäre Carbide und Nitride der Übergangsmetalle und ihre Phasenbeziehungen. Habilitationsschrift; Universität Karlsruhe, 1981.

https://doi.org/10.1021/acs.inorgchem.3c01097
Inorg. Chem. 2023, 62, 9602−9617

(73) Kuo, K. The formation of η carbides. *Acta Metall.* **1953**, *1*, 301−304.
(74) Goto, Y.; Kakuta, H.; Kamegawa, A.; Takamura, H.; Okada, M. High-pressure synthesis of novel hydride in Mg−M systems (M = Li, Pd). *J. Alloys Compd.* **2005**, *404*−*406*, 448−452.
(75) Zavalii, I. Y.; Riabov, A. B. The hydrogenation of $Zr_3M_3O_x$ (M = V, Cr, Mn) and $Zr_4M_2O_x$ (M = Fe, Co, In) compounds. *Abstr. 6th Int. Conf. Crystal Chem. Intermet. Compd.*, 1995; p 21.
(76) Vandenberg, J. M.; Matthias, B. T.; Corenzwit, E.; Barz, H. Superconductivity of a new metastable phase of scandium-chromium. *J. Solid-state Chem.* **1976**, *18*, 395−396.
(77) Sobolev, A. S.; Kuz'ma, Y. B.; Fedorov, T. F. System niobium-nickel-boron. *Inorg. Mater.* **1967**, *3*, 561−565.
(78) Weil, K. S.; Kumta, P. N. Synthesis of a New Ternary Nitride, Fe_4W_2N, with a Uniqueη-Carbide Structure. *J. Solid-state Chem.* **1997**, *134*, 302−311.
(79) El-Shahat, M. F.; Holleck, H. Zum Aufbau der Systeme V-(Fe, Co, Ni)-N. *Monatsh. Chem.* **1978**, *109*, 193−201.
(80) Jeitschko, W.; Holleck, H.; Nowotny, H.; Benesovsky, F. Phasen mit aufgefülltem Ti_2Ni-Typ. *Monatsh. Chem.* **1964**, *95*, 1004−1006.
(81) Holleck, H.; Thümmler, F. Untersuchungen über die Bildung von nichtmetallstabilisierten zirkonreichen Übergangsmetallphasen. *J. Nucl. Mater.* **1967**, *23*, 88−94.
(82) Mueller, M. H.; Knott, H. W. The crystal structures of Ti_2Cu, Ti_2Ni, Ti_4Ni_2O, and Ti_4Cu_2O. *Trans. Metall. Soc. AIME* **1963**, *227*, 674−678.
(83) Stioui, C.; Fruchart, D.; Rouault, A.; Fruchart, R.; Roudaut, E.; Rebiére, J. Absorption d'hydrogene par Ti_4Fe_2O et diverses phases M_6O. *Mater. Res. Bull.* **1981**, *16*, 869−876.
(84) Rupp, B.; Fischer, P. Reinvestigation of the oxygen stabilized Ti_2Ni-type phase $Ti_4Fe_2O_{0.4}$ by neutron diffraction. *J. Less Common Met.* **1988**, *144*, 275−281.
(85) Leonard, S. R.; Snyder, B. S.; Brewer, L.; Stacy, A. M. Structure determinations of two new ternary oxides: Ti_3PdO and Ti_4Pd_2O. *J. Solid-state Chem.* **1991**, *92*, 39−50.
(86) Mackay, R.; Miller, G. J.; Franzen, H. F. New oxides of the filled-Ti_2Ni type structure. *J. Alloys Compd.* **1994**, *204*, 109−118.
(87) Zavaliy, I. Y.; Riabov, A. B.; Yartys, V. A.; Wiesinger, G.; Michor, H.; Hilscher, G. $(Hf\ Zr)_2Fe$ and $Zr_4Fe_2O_{0.6}$ compounds and their hydrides: phase equilibria, crystal structure and magnetic properties. *J. Alloys Compd.* **1998**, *265*, 6−14.
(88) Zavaliy, I. Y. Effect of oxygen content on hydrogen storage capacity of Zr-based η-phases. *J. Alloys Compd.* **1999**, *291*, 102−109.
(89) Yartys, V. A.; Fjellvåg, H.; Harris, I. R.; Hauback, B. C.; Riabov, A. B.; Sørby, M. H.; Zavaliy, I. Y. Hydrogen ordering and H-induced phase transformations in Zr-based intermetallic hydrides. *J. Alloys Compd.* **1999**, *293*−*295*, 74−87.
(90) Cantrell, J. S.; Bowman, R. C.; Maeland, A. J. X-ray diffraction, neutron scattering and NMR studies of hydrides formed by Ti_4Pd_2O and Zr_4Pd_2O. *J. Alloys Compd.* **2002**, *330*−*332*, 191−196.
(91) Brinks, H. W.; Maeland, A. J.; Hauback, B. C.; Bowman, R. C.; Cantrell, J. S. Determination of deuterium site occupation in $Zr_4Pd_2OD_{4.5}$. *J. Alloys Compd.* **2003**, *361*, 108−112.
(92) Palatinus, L.; Chapuis, G. SUPERFLIP - a computer program for the solution of crystal structures by charge flipping in arbitrary dimensions. *J. Appl. Crystallogr.* **2007**, *40*, 786−790.
(93) Petříček, V.; Dušek, M.; Palatinus, L. *Jana2006. The Crystallographic Computing System*; Institute of Physics: Praha (Czech Republic), 2006.
(94) Petříček, V.; Dušek, M.; Palatinus, L. Crystallographic Computing System JANA2006: General features. *Z. Kristallogr.* **2014**, *229*, 345−352.
(95) Kiessling, R. Investigations on the double carbides in the cobalt-tungsten-carbon system; *Proc. Int. Conf. React. Solids*: Gothenburg, Sweden, 1954; pp 1065−1068.
(96) Emsley, J. *The Elements*; Clarendon Press, Oxford University Press: Oxford, New York, 1998.
(97) Spedding, F. H.; Daane, A. H.; Herrmann, K. W. The crystal structures and lattice parameters of high-purity scandium, yttrium and the rare earth metals. *Acta Crystallogr.* **1956**, *9*, 559−563.
(98) Vegard, L. VI. Results of crystal analysis. *Philos. Mag.* **1916**, *32*, 65−96.
(99) Hull, A. W. A new method of X-ray crystal analysis. *Phys. Rev.* **1917**, *10*, 661−696.
(100) Rechkin, V. N.; Lamikhov, L. K.; Samsonova, T. I. Crystal structures of some scandium aluminides. *Sov. Phys. Crystallogr.* **1964**, *9*, 325−327.
(101) Dwight, A. E.; Downey, J. W.; Conner, R. A. Some C11b-type compounds of Sc, Y and the lanthanides with Cu, Ag and Au. *Acta Crystallogr.* **1967**, *22*, 745−747.
(102) Dwight, A. E.; Kimball, C. W. ScT_2X and LnT_2X compounds with the $MnCu_2Al$-type structure. *J. Less Common Met.* **1987**, *127*, 179−182.
(103) Benndorf, C.; Niehaus, O.; Eckert, H.; Janka, O. ^{27}Al and ^{45}Sc NMR Spectroscopy on ScT_2Al and $Sc(T_{0.5}T'_{0.5})_2Al$ (T = T′ = Ni, Pd, Pt, Cu, Ag, Au) Heusler Phases and Superconductivity in $Sc(Pd_{0.5}Au_{0.5})_2Al$. *Z. Anorg. Allg. Chem.* **2015**, *641*, 168−175.
(104) Radzieowski, M.; Benndorf, C.; Haverkamp, S.; Eckert, H.; Janka, O. On new ternary equiatomic scandium transition metal aluminum compounds ScTAl with T = Cr, Ru, Ag, Re, Pt, and Au. *Z. Naturforsch.* **2016**, *71*, 553−566.
(105) Stegemann, F.; Benndorf, C.; Bartsch, T.; Touzani, R. S.; Bartsch, M.; Zacharias, H.; Fokwa, B. P. T.; Eckert, H.; Janka, O. $Ba_3Pt_4Al_4$ − structure, properties, and theoretical and NMR spectroscopic investigations of a complex platinide featuring heterocubane $[Pt_4Al_4]$ units. *Inorg. Chem.* **2015**, *54*, 10785−10793.
(106) Thronberens, W.; Schuster, H.-U. $Na_6Pt_8Ge_8$, eine ternäre intermetallische Phase mit tetraedrischen Platinclustern. *Z. Naturforsch.* **1979**, *34*, 781−783.
(107) Stoyko, S. S.; Khatun, M.; Mar, A. Ternary arsenides $A_2Zn_5As_4$ (A = K, Rb): Zintl phases built from Stellae Quadrangulae. *Inorg. Chem.* **2012**, *51*, 9517−9521.
(108) Milligan, W. O.; Vernon, L. W.; Levy, H. A.; Peterson, S. W. Neutron diffraction studies on scandium orthovanadate and scandium oxide. *J. Phys. Chem.* **1953**, *57*, 535−537.
(109) Dufek, V.; Petrů, F.; Brožek, V. Über Sauerstoff-haltige Verbindungen vom Strukturtyp B1 der ersten vier Übergangsmetalle. *Monatsh. Chem.* **1967**, *98*, 2424−2430.
(110) Engel, S.; Gießelmann, E. C. J.; Schank, L. E.; Heymann, G.; Brix, K.; Kautenburger, R.; Beck, H. P.; Janka, O. Theoretical and ^{27}Al NMR spectroscopic investigations of binary intermetallic alkaline-earth aluminides. *Inorg. Chem.* **2023**, *62*, 4260−4271.
(111) Gießelmann, E. C. J.; Engel, S.; Kostusiak, W.; Zhang, Y.; Herbeck-Engel, P.; Kickelbick, G.; Janka, O. Raman and NMR spectroscopic and theoretical investigations of the cubic Laves-phases $REAl_2$ (RE = Sc, Y, La, Yb, Lu). *Dalton Trans.* **2023**, *52*, 3391−3402.
(112) Benndorf, C.; Stegemann, F.; Eckert, H.; Janka, O. New transition metal-rich rare-earth palladium/platinum aluminides with RET_5Al_2 composition: structure, magnetism and ^{27}Al NMR spectroscopy. *Z. Naturforsch.* **2015**, *70*, 101−110.
(113) Stegemann, F.; Block, T.; Klenner, S.; Zhang, Y.; Fokwa, B. P. T.; Timmer, A.; Mönig, H.; Doerenkamp, C.; Eckert, H.; Janka, O. From 3D to 2D: structural, spectroscopical and theoretical investigations of the dimensionality reduction in the $[PtAl_2]^{\delta-}$ polyanions of the isotypic $MPtAl_2$ series (M = Ca−Ba, Eu). *Chem.—Eur. J.* **2019**, *25*, 10735−10747.
(114) Radzieowski, M.; Stegemann, F.; Doerenkamp, C.; Matar, S. F.; Eckert, H.; Dosche, C.; Wittstock, G.; Janka, O. Correlations of crystal and electronic structure via NMR and XPS spectroscopy in the $RETMAl_2$ (RE = Sc, Y, La−Nd, Sm, Gd−Tm, Lu; TM = Ni, Pd, Pt) series. *Inorg. Chem.* **2019**, *58*, 7010−7025.
(115) Lue, C.-S.; Chepin, S.; Chepin, J.; Ross, J. H. NMR study of trialuminide intermetallics. *Phys. Rev. B: Condens. Matter Mater. Phys.* **1998**, *57*, 7010−7014.
(116) Bastow, T. J.; Forwood, C. T.; Gibson, M. A.; Smith, M. E. Local site symmetry and electronic structure of trialuminide and

https://doi.org/10.1021/acs.inorgchem.3c01097
Inorg. Chem. 2023, 62, 9602−9617

related intermetallic alloys probed by solid-state NMR. *Phys. Rev. B: Condens. Matter Mater. Phys.* **1998**, *58*, 2988−2997.
(117) Jeglič, P.; Vrtnik, S.; Bobnar, M.; Klanjšek, M.; Bauer, B.; Gille, P.; Grin, Y.; Haarmann, F.; Dolinšek, J. M-Al-M groups trapped in cages of $Al_{13}M_4$ (M = Co,Fe,Ni,Ru) complex intermetallic phases as seen via NMR. *Phys. Rev. B: Condens. Matter Mater. Phys.* **2010**, *82*, 104201.
(118) Ferreira, A. R. DFT-GIPAW ^{27}Al NMR Simulations for Intermetallics: Accuracy Issues and Magnetic Screening Mechanisms. *J. Phys. Chem. C* **2019**, *123*, 9371−9381.
(119) Sitzmann, H.; Lappert, M. F.; Dohmeier, C.; Üffing, C.; Schnöckel, H. Cyclopentadienylderivate von Aluminium(I). *J. Organomet. Chem.* **1998**, *561*, 203−208.
(120) Gauss, J.; Schneider, U.; Ahlrichs, R.; Dohmeier, C.; Schnoeckel, H. ^{27}Al NMR spectroscopic investigation of aluminum(I) compounds: ab initio calculations and experiment. *J. Am. Chem. Soc.* **1993**, *115*, 2402−2408.
(121) Benndorf, C.; Eckert, H.; Pöttgen, R. Si, 47Ti ^{49}Ti and ^{195}Pt solid-state MAS NMR spectroscopic investigations of ternary silicides TPtSi, germanides TPtGe (T = Ti, Zr, Hf) and stannide TiPtSn. *Dalton Trans.* **2016**, *45*, 8215−8223.
(122) Benndorf, C.; Eckert, H.; Janka, O. Structural characterization of intermetallic compounds by ^{27}Al solid-state NMR spectroscopy. *Acc. Chem. Res.* **2017**, *50*, 1459−1467.
(123) Eckert, H.; Pöttgen, R. ^{45}Sc Solid-state NMR Spectroscopy − a complementary tool to X-ray crystallography for structure determination of intermetallic compounds. *Z. Anorg. Allg. Chem.* **2010**, *636*, 2232−2243.

https://doi.org/10.1021/acs.inorgchem.3c01097
Inorg. Chem. 2023, 62, 9602−9617

5.4 Oxidation behavior of intermetallic compounds (published)

Coming from solely intermetallic compounds in which oxygen (or nitrogen) is the worst enemy concerning impurities completely changing e.g. the magnetic properties over one oxygen atom that changes and stabilizes a structure in an unexpected sub-oxide, the main idea behind the following two chapters is the use of intermetallic compounds as precursors to synthesize valence-precise compounds, leaving the metallic state behind.

As explained in section 2.2, a main focus of the oxidation chemistry of Al compounds was about the corrosion resistance due to forming a passivating layer of the highly oxophilic Al (or the formation of other stable oxides on the surface) in comparison to the other metallic elements, e.g. Ni. Our approach was to use evenly oxophilic metals that can be combined with Al with the idea of forming ternary oxides, while not just passivating the surface. Promising compounds to test this hypothesis were the binary aluminides of the alkaline earth and rare earth metals in the compositions $M\mathrm{Al_2}$ (M = Ca, Sr, Ba, Sc, Y, La, Eu, Yb) and $AE\mathrm{Al_4}$ (AE = Ca, Sr, Ba) of which many were already discussed in detail in section 5.1.1. As a first starting point, a simple reaction of these compounds in an STA system under oxygen atmosphere at 1273 K for different dwelling times was performed. As one would expect, all these compounds oxidize below 1273 K indicated by a mass increase and a sometimes sharp, sometimes broadened signal in the DSC-curve. The now mainly white or grey powders were analyzed after the reactions using PXRD. All these results will be discussed in the following chapters sorted by the composition and the element combined with aluminum.

Going down in the chalcogenide group, studies using sulfur and selenium were conducted. Here, phase pure samples could easily be obtained, as explained in section 2.2.1. The first focus was set on already known literature examples, including repeated synthesis as well as spectroscopic characterization. For some examples, single crystals could nicely be analyzed providing the structural characterization or correcting structures in the literature.

5.4.1 Systematic mechanistic studies on the thermal oxidation behavior of the cubic laves phase $CaAl_2$

Published as two articles (under CC BY-NC 3.0):

Mechanistic studies on the formation of ternary oxides by thermal oxidation of the cubic laves phase $CaAl_2$

Elias C. J. Gießelmann, Stefan Engel, Johnnes G. Volpini, Hubert Huppertz, Guido Kickelbick and Oliver Janka, *Inorg. Chem. Front*. **2024**, *11*, 286.

https://doi.org/10.1039/d3qi01604h

Contribution of the authors to the manuscript (as published in the manuscript)

Conceptualization by GK and OJ, synthetic work by ECJG, SE and JGV, initial draft of the manuscript by ECJG. ECJG performed the STA and ^{27}Al NMR investigations, SE performed the SEM/EDX investigations, OJ performed the DFT calculations. The entire work was supervised, guided, and revised by GK and OJ. The manuscript was corrected by all authors and finalized by HH, GK, and OJ.

Changing the reaction pathway of the $CaAl_2$ oxidation using ball milling

Elias C. J. Gießelmann, Guido Kickelbick and Oliver Janka, *Dalton Trans.* **2025**, *54*, 1173.

https://doi.org/10.1039/d4dt02459a

Contribution of the authors to the manuscript (as published in the manuscript)

Conceptualization by GK and OJ; synthetic work by ECJG; initial draft of the manuscript by ECJG. ECJG performed the XRD, STA and ^{27}Al NMR investigations; the entire work was supervised, guided, and revised by GK and OJ. The manuscript was corrected by all authors and finalized by GK and OJ.

Summary

In the first part, all results dealing with the oxidation of the cubic Laves phase $CaAl_2$ will be presented. This process has been examined in greater detail for several reasons. $CaAl_2$ is easy to make in high quantities (500 mg per batch with only minor impurity of $CaAl_4$); Ca is rather inexpensive in comparison to the rare earth elements; in the ternary system Ca–Al–O many ternary oxides of different compositions are well known and finally, the findings of the

initial oxidation reaction of $CaAl_2$ were quite unexpected in the first place. Before discussing these actual results, one should think about all possible outcomes of this reaction.

One possibility, and by far the most boring, would be that both metals oxidize individually and/or phase segregate after the reaction, forming a 1:2 mixture of CaO and Al_2O_3. A nice proof-of-principle would be the direct one-step synthesis of the known ternary oxide $CaAl_2O_4$ as it was e.g. reported for $LiGaO_2$ and $LiGaS_2$ so to say overcoming the passivating effect of aluminum. Another possibility could be the passivation of the compound by either forming Al_2O_3 and leaving elemental Ca or the other way around, giving information about the oxide stability under these conditions. The final thought could be the formation of a compound with a different composition than $CaAl_2O_4$, as it was observed for $LiGa_5O_3$ or a combination as it was shown for Li_3GaN_2 and GaN (see section 2.2.1).

In the case of $CaAl_2$, after initial oxidation, the main product that could be identified in the powder patterns matched the phase $Ca_{12}Al_{14}O_{33}$ ($Ca_6Al_7O_{16.5}$), which gained interest as a cage compound and electride. Together with this so-called mayenite (mineral name), the mixture showed another ternary oxide, $Ca_3Al_2O_6$, that could be identified depending on the conditions alongside the two binary oxides CaO and Al_2O_3 and finally elemental Al. Interestingly, the expected product $CaAl_2O_4$ was not observed at all in the first place. To sum up, a combination of the above-mentioned expectations came together. Indeed, a passivation of the material leaving elemental Al took place. The passivation occurred by the formation of a so to say kinetically favored ternary oxide, $Ca_{12}Al_{14}O_{33}$, showing the higher oxophilicity of Ca compared to Al with all oxides observed being enriched in Ca compared to the intermetallic precursor. Within the two following articles our findings and efforts to synthesize the desired oxide $CaAl_2O_4$ are reported.

Different combinations of annealing times and regrinding of the powder were used and the effect on the oxidation product was checked. Synthesis conditions were further changed by using a home-built tube furnace setup allowing the use of a pure oxygen atmosphere instead of air-oxidation in classic muffle furnaces. The findings were additionally strengthened by solid state NMR investigations, SEM/EDX measurements and DFT calculations. An exciting experiment, oxidizing $CaAl_2$ in an induction furnace, additionally revealed the intermediate formed phase $CaAl_4$ strengthening the hypothesis of Ca being oxidized first leaving behind an Al enriched intermetallic and finally elemental Al. The attempts to conduct an oxidation

reaction with the hypothetical intermetallic precursor $Ca_{12}Al_{14}$ (Ca_6Al_7) failed since it was a mixture of at least 3 intermetallic compounds.

In the second study, the effect of high-energy ball milling of the intermetallic $CaAl_2$ prior to the oxidation reaction was shown. After several hours of grinding, the compound, which is normally air stable over months, turns pyrophoric, in combination with a change in the outcome of the oxidation reaction. The formation of the expected oxidation product $CaAl_2O_4$ is highly favored upon using the by ball milling activated material. A switch of the oxidation reactant from oxygen (or air) to water in the form of “wet argon” showed no effect on the outcome of the reaction at all.

INORGANIC CHEMISTRY
FRONTIERS

RESEARCH ARTICLE

View Article Online
View Journal | View Issue

Cite this: *Inorg. Chem. Front.*, 2024, **11**, 286

Mechanistic studies on the formation of ternary oxides by thermal oxidation of the cubic laves phase $CaAl_2$†

Elias C. J. Gießelmann, [a] Stefan Engel, [a] Johannes G. Volpini, [b] Hubert Huppertz, [b] Guido Kickelbick *[c] and Oliver Janka *[d]

Oxide materials are of key importance in many aspects of everyday life. However, their solid-state syntheses require high temperatures and often multiple steps when conducted from the binary oxides. Herein, we report a proof-of-concept investigation addressing the possibility to synthesize oxides from a phase-pure, well-defined, and highly crystalline intermetallic starting material *via* oxidation with elemental oxygen. The thermal oxidation behavior of the cubic Laves phase $CaAl_2$ was investigated under various atmospheric environments by thermal analysis or by different bulk synthesis techniques. Besides different furnace types, also varying O_2 concentrations and different heating rates, and annealing times were explored. Interestingly, the reaction progresses *via* the intermediate $Ca_{12}Al_{14}O_{33}$ (12 CaO·7 Al_2O_3) before the expected stoichiometric oxidation product, monoclinic $CaAl_2O_4$ (CaO·Al_2O_3), is finally observed. This is highly surprising, since the intermediate has a different Ca to Al ratio compared to the starting material. Different strategies were employed to optimize the synthetic conditions and to decipher the reaction mechanism. The formation of the various products was followed by a detailed analysis of the powder X-ray diffraction data *via* Rietveld refinements and additionally by ^{27}Al MAS NMR experiments, while quantum-chemical calculations supported the proposed reaction mechanism.

Received 16th August 2023,
Accepted 11th November 2023

DOI: 10.1039/d3qi01604h

rsc.li/frontiers-inorganic

1 Introduction

Lightweight alloys, based on Mg, Al, Ti, or Be are an important class of materials for a plethora of modern technical applications ranging from automotive and transportation applications[1–4] to architecture,[5,6] to corrosion resistant parts for air- and spacecrafts,[7–11] non-sparking tools,[12,13] all the way to materials for medical applications like stents or implants.[9–11,14] Intermetallic compounds play an important role in some of these alloys. For example, the most commonly used aluminum-based alloys (Al–Cu or Al–Mg–Cu) get their significantly improved mechanical properties, with respect to elemental Al, from the formation of intermetallic precipitations like $CuAl_2$ ($I4/mcm$ [15]) or $MgCuAl_2$ (S-phase, $Cmcm$ [16]).[1,17–19]

The chemical and thermal resistance as well as the mechanical properties of some of these materials are astonishing.[20] Alloys from the Ti–Al system for example are described as some of the best materials for aircraft and gas turbines due to their low density and high mechanical strength.[21,22] However, their corrosion resistance, especially at high temperatures, is insufficient, thus, alloying with different elements or defined structuring was employed.[23–25] Therefore, oxidation studies of these compounds are an important field of research.[25–29] Ni–Al alloys, in contrast, are of great importance when it comes to corrosion stability under extreme conditions. It has been shown in NiAl, that aluminum atoms, due to their high oxophilicity, form a protective layer of aluminum oxide Al_2O_3 (corundum, space group $R\bar{3}m$) when exposed to air at elevated temperatures, protecting the unreacted substance underneath.[30–32] The addition of small amounts of $CaAl_2$ to an aluminum alloy was shown to increase the protection of the surface from damage through oxidation.[33]

From a synthetic and preparative point of view, the oxidation of intermetallics or alloys could be used to synthesize ternary oxides from binary starting materials, quaternary oxides from ternary phases and so on. Hoppe and co-workers prepared different AMO_2 phases (A = Li–K, M = In, Tl) from the Zintl phases NaTl, KTl, and LiIn.[34–36] Also, CsAuO could be obtained by the reaction of CsAu with dry O_2.[37] The high-temp-

[a]*Inorganic Solid-State Chemistry, Saarland University, Campus C4.1, 66123 Saarbrücken, Germany*
[b]*Institute for General, Inorganic and Theoretical Chemistry, University of Innsbruck, Innrain 80-82, 6020 Innsbruck, Austria*
[c]*Inorganic Solid-State Chemistry, Saarland University, Campus C4.1, 66123 Saarbrücken, Germany. E-mail: guido.kickelbick@uni-saarland.de*
[d]*Inorganic Solid-State Chemistry, Saarland University, Campus C4.1, 66123 Saarbrücken, Germany. E-mail: oliver.janka@uni-saarland.de*
†Electronic supplementary information (ESI) available. See DOI: https://doi.org/10.1039/d3qi01604h

erature superconductor $YBa_2Cu_3O_{7-\delta}$ [38] could also be prepared by the oxidation of BaCu and YCu as well as related compounds.[39–41] Jung and coworkers finally used a wide variety of homo- and heterogeneous alloys for the synthesis of a plethora of different oxides.[42–50] For example, Tl/Ni/P alloys were used for the synthesis of different phosphates, *e.g.* $TlNi_4(PO_4)_3$, $Tl_4Ni_7(PO_4)_6$, and $Tl_2Ni_4(P_2O_7)(PO_4)_2$ [42] while the oxide-oxovanadate $TlCu_5O(VO_4)_3$ [50] was obtained from Tl/Cu/V alloys.

However, studies that closely examine the specific oxidation behavior of a phase-pure and well-defined intermetallic compound as a starting material are rare. One example is from Grin and coworkers reporting on the behavior of $CaAg_2$ in catalytic ethylene epoxidation reactions.[51] They observe the formation of elemental Ag besides Ca_2Ag_7 and CaO, $Ca(OH)_2$ as well as $CaCO_3$ based on the different reaction pathways during catalysis. Furthermore, due to the large variety with respect to composition and elemental combinations, one could think about using binary intermetallics as starting materials for the synthesis of *e.g.*, new ternary oxides/chalcogenides/halides that might not be targetable *via* classic reactions of the respective binary oxides/chalcogenides/halides. Moreover, one can learn a lot not only about the stability of the intermetallic compounds, but also about the formation of the reaction products and the underlying reaction mechanisms. One of the rare studies applying this approach was successfully presented by Hoch and coworkers synthesizing ternary compounds in the system $Li_xGa_yX_z$ (starting with the equiatomic LiGa intermetallic and X = N, S, O).[52]

The present paper focuses on the oxidation of the cubic Laves phase $CaAl_2$ ($Fd\bar{3}m$). One might immediately think of $CaAl_2O_4$ ($CaO{\cdot}Al_2O_3$; CA; $P2_1/c$)[53] as the most likely oxidation product since it has the same Ca to Al ratio as the intermetallic compound. In addition to the RT phase, two high-pressure polymorphs (own type, $P2_1/m$; $CaGa_2O_4$ type, $P2_1/c$, CaV_2O_4 type, *Pnma*) have been reported.[54,55] Other oxides in the ternary system Ca–Al–O, that might be possible oxidation products, are *e.g.* orthorhombic $Ca_5Al_6O_{14}$ ($5\,CaO{\cdot}3\,Al_2O_3$; C5A3; $Cmc2_1$),[56] cubic $Ca_3Al_2O_6$ ($3CaO{\cdot}Al_2O_3$; C3A; $Pa\bar{3}$)[57] or cubic $Ca_{12}Al_{14}O_{33}$ ($12\,CaO{\cdot}7\,Al_2O_3$; mineral mayenite, C12A7; $I\bar{4}3d$).[58] The latter one has gained a lot of attention within the last two decades due to its ability to form an electride.[59–61] In the course of this paper, different approaches to oxidize $CaAl_2$ are described along with thermoanalytical investigations, compositional studies *via* Rietveld refinements of the powder X-ray diffraction data, ^{27}Al NMR studies, and DFT calculations to investigate the respective stabilities leading to a concise picture of the oxidation mechanism of $CaAl_2$.

2 Experimental

2.1 Synthesis

Precursor $CaAl_2$. Calcium pieces (ChemPur, Karlsruhe, Germany, 99.5%) and aluminum pellets (Onyxmet, Olsztyn, Poland, 99.99%) were used as received as starting materials for the synthesis of the intermetallic precursors $CaAl_2$ and nominal "Ca_6Al_7". The binary starting materials were prepared on a 350 mg (nominal Ca_6Al_7) and 400 mg ($CaAl_2$) scale. The Ca pieces were stored under an argon atmosphere, surface contaminations were removed mechanically prior to use. The synthesis of the binary compounds was carried out in a custom-build arc furnace. Elements were transferred under argon into a water-cooled copper hearth and arc melted under dried argon at 800 mbar.[62] The argon was purified prior to use with titanium sponge (873 K), silica gel, and molecular sieves. To avoid evaporation of Ca, the Al pieces were piled on top and enclosed in Al foil. Careful melting created an encapsulation of the Ca pieces. The resulting bead was turned over and remelted three times to increase the homogeneity. The weight loss in all cases was <1 mass%. As-cast samples are silver metallic, ground powders are grey and stable in air over months.

Solid-state synthesis. The conventional solid-state synthesis was carried out in a chamber furnace (HTC 03/16/P330, Nabertherm, Lilienthal Bremen, Germany) under ambient conditions starting from of $Ca(NO_3)_2{\cdot}4\,H_2O$ (Merck, Darmstadt, Germany, ≥99.0%) and $Al(NO_3)_3{\cdot}9\,H_2O$ (Merck, Darmstadt, Germany, ≥99.99%) with molar ratios of 1 : 1 and 1 : 2. The starting materials were mixed in an agate mortar, transferred to a corundum boat, and heated to 1473 K with a heating rate of 1.6 K min^{-1}. After calcinating for 4 h, the chamber furnace was turned off and the sample was cooled to room temperature.

Oxidation of $CaAl_2$. Oxidation reactions were performed in an STA system (TGA/DSC 1 Star HT/1600 system, Mettler Toledo, Columbus, OH, USA), a muffle oven, a custom-built oxidation tube furnace or in an induction furnace. A muffle oven model N 11/Hr (Nabertherm, Lilienthal Bremen, Germany) with a C30 temperature control unit was used at ambient pressure and atmosphere. The intermetallic powders were directly used and placed in porcelain (likely to be a mixture of Al_2O_3, SiO_2 and MgO) boats. All oxidation experiments using a muffle oven were performed under air at 1273 K reached within ≈5.5 h (≈3 K min^{-1}). The samples were dwelled at 1273 K for different durations (*vide infra*). Afterwards, the oven was allowed to cool to room temperature with the door closed (≈20 h; ≈1 K min^{-1}).

Oxidation reactions using higher O_2 concentrations were carried out in a custom-built oxidation furnace (Carbolite Gero GmbH & Co. KG, Neuhausen, Germany). The samples were placed in porcelain boats and centered in the tube furnace. The argon was purified prior to use with titanium sponge (873 K). The flow rates of Ar/O_2 or pure O_2 were regulated using variable area flow meters (Kobold Messring GmbH, Hofheim am Taunus, Germany). For the reactions using 50% O_2, the flow rates were 20 mL min^{-1} O_2 and 20 mL min^{-1} Ar, for the reactions using pure O_2 a flow rate of 20 mL min^{-1} was used.

Finally, oxidation reactions were tested in a high-frequency furnace (Typ TIG 5/300, Hüttinger Elektronik, Freiburg,

Germany). For these experiments, the samples were pressed to pellets, placed in corundum crucibles which in turn were placed in the water-cooled reaction chamber and heated to approximately 1073 K under vacuum. After a constant temperature was reached, the sample chamber was opened to air, which exposed the red glowing sample to the atmosphere.

2.2 Thermal analysis

Simultaneous thermogravimetric analysis (TGA) and differential scanning calorimetry (DSC) were carried out with a TGA/DSC 1 Star HT/1600 system (Mettler Toledo, Columbus, OH, USA) under an Ar/O_2 atmosphere with flow rates of 40 mL min^{-1} each. Temperature programs are given with the experiments, the heating rates were typically 20 K min^{-1} if not specified otherwise. Samples were placed into alumina crucibles (ø 6 mm, h = 4.5 mm) for the STA measurements.

2.3 X-ray diffraction

Powder X-ray diffraction (PXRD) patterns of the pulverized samples were recorded at room temperature on a D8-A25-Advance diffractometer (Bruker, Karlsruhe, Germany) in Bragg Brentano θ–θ-geometry (goniometer radius 280 mm) with CuKα-radiation (λ = 154.0596 pm). A 12 μm Ni foil working as Kβ filter and a variable divergence slit were mounted at the primary beam side. A LYNXEYE detector with 192 channels was used at the secondary beam side. Experiments were carried out in a 2θ range of 6–130° with a step size of 0.013° and a total scan time of 1 h. The recorded data was evaluated using the Bruker TOPAS 5.0 software[63] and the fundamental instrument parameters were used to fit the data.

To investigate the phase composition of the powder samples synthesized by the solid-state approach, diffraction experiments were performed on a Stoe Stadi P diffractometer (STOE & Cie. GmbH, Darmstadt, Germany) using Ge(111)-monochromatized primary X-ray radiation ($MoK\alpha_1$, λ = 0.7093 Å) and a Mythen 1K detector (Dectris AG, Baden-Daettwil, Switzerland). Data acquisition and processing were carried out in Winxpow.[64] The X-ray diffraction patterns were taken in the 2θ range from 2.0 to 46.0 with a step size of 0.015° and 29.0 s per step. Rietveld refinements based on the powder data was performed in Topas 4.2.[65]

2.4 Scanning electron microscopy/energy dispersive X-ray spectroscopy (SEM/EDX)

Semiquantitative EDX analyses of the bulk samples were conducted on a JEOL 7000F (Jeol, Freising, Germany) equipped with an EDAX Genesis 2000 EDX detector (EDAX, Unterschleissheim, Germany).

2.5 ^{27}Al solid-state MAS NMR

^{27}Al solid-state MAS NMR spectra were recorded using a Avance III 400 WB (Bruker, Karlsruhe, Germany) at 104.35 MHz using magic-angle spinning (MAS) and static conditions. The samples were used as fine powders. To reduce density and electrical conductivity, samples were mixed with dried sodium chloride in a ratio of 1 : 9 or higher contents of NaCl if the amount of sample was not enough. The diluted samples were loaded into a cylindrical ZrO_2 rotor with a diameter of 4 mm and spun at the magic angle at a frequency of 13 kHz. All experiments conducted were single-pulse experiments with a typical pulse length of 0.83 μs (≈30° pulse) and a relaxation delay of 1 s. Resonance shifts were referenced to an aqueous 1 molar $AlCl_3$ solution. The NMR spectra were recorded using the Bruker Topspin[66] software; the analysis was performed with the help of the Dmfit software.[67]

2.6 Quantum-chemical calculations

Electronic structure calculations of the compounds in the binary and ternary systems Ca–O/Al–O/Ca–Al–O were performed using the projector augmented wave method (PAW) of Blöchl[68,69] coded in the Vienna *ab initio* simulation package (VASP).[70,71] VASP calculations employed the potentials PAW_PBE Ca_sv 06Sep2000, PAW_PBE Al 04Jan2001, and PAW_PBE O_h 06Feb2004. The cutoff energy for the plane wave calculations was set to 800 eV and the Brillouin zone integration was carried out using a k-point mesh with a spacing of ≈0.02 for all compounds.

3 Results and discussion

3.1 Crystal structures and precursor characterization

The cubic Laves phase $CaAl_2$ ($MgCu_2$ type, $Fd\bar{3}m$) was prepared from the elements and characterized by powder X-ray diffraction. Phase pure samples with respect to the measurement technique were obtained and subsequently used in the oxidation experiments. In the cubic crystal structure (a = 804.02(1) pm), the Al atoms (Al on 16c with 0,0,0) form empty Al_4 tetrahedra which are connected over all corners forming a network. The Ca atoms (Ca on 8b with 3/8,3/8,3/8) are found within the cavities of said framework adapting the topology of cubic diamond (Fig. S1†). More information about the structural chemistry of Laves phases can be found in a recent review article.[72] ^{27}Al solid-state NMR investigations showed an intense central line originating from the $|+1/2\rangle \leftrightarrow |-1/2\rangle$ transition which can be modelled with a Gauss-Lorentz fit. The resonance signal can be found at δ = 1091 ppm (Fig. S2†), in line with the literature.[73,74]

$Ca_{12}Al_{14}O_{33}$ (C12A7) sometimes also referred to as $Ca_6Al_7O_{16.5}$, crystallizes in the cubic crystal system with space group $I\bar{4}3d$ (Fig. 1a). The compound can be obtained by solid-state synthesis from the reaction of 12 equivalents of CaO with 7 equivalents of Al_2O_3. However, during single crystal[75] and neutron powder investigations[76] it became clear, that the structure exhibits defects of oxygen atoms (position O3) and the formation of an electride can be observed upon removal of this oxide anion. This is possible by *e.g.* the reaction of the mayenite with Ti or V under an inert gas atmosphere.[60,61] In the crystal structure, the Ca atoms are coordinated by seven oxygen anions (d(Ca–O) = 239–252 pm) in the shape of a dis-

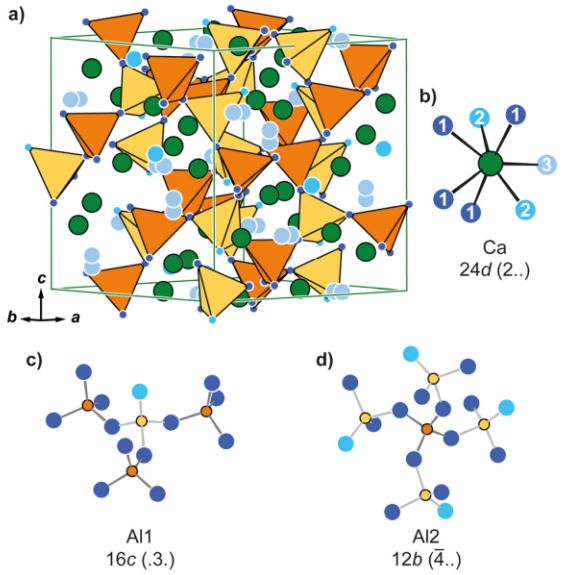

Fig. 1 (a) Unit cell and coordination polyhedron of the (b) Ca atoms in cubic $Ca_{12}Al_{14}O_{33}$ ($I\bar{4}3d$, own type, mayenite). (c) and (d) coordination of the Al1 and Al2 atoms. Ca atoms are depicted in green, Al atoms as light and dark orange, and O atoms as light blue, blue, and cyan circles. The Al1 atoms and their polyhedra are shown in light, the Al2 atoms and their polyhedra in dark orange. The connecting O1 atoms in the $[AlO_4]$ tetrahedra are depicted in blue, the terminal O2 atoms in cyan, and the only partially occupied O3 sites in light blue. Wyckoff positions and site symmetries are given.

torted mono-capped trigonal prism (Fig. 1b), while the two crystallographically distinct Al atoms are tetrahedrally surrounded by four O^{2-} anions and form a network. While all four corners of the $[Al2O_4]$ unit (Fig. 1d; d(Al–O) = 172 pm) are connected to $[Al1O_4]$ tetrahedra, one corner of the latter is terminal (Fig. 1c; d(Al–O) = 174 + 178 pm). Finally, O3 is not part of the tetrahedral network, but is only found in the coordination environment of the Ca atoms.

$CaAl_2O_4$ crystallizes, despite what one might expect, not in the cubic $MgAl_2O_4$ type (spinel) but in the monoclinic crystal system and adopts its own structure type with space group $P2_1/c$. The $[AlO_4]$ tetrahedra (d(Al–O) = 172–178 pm) arrange as layers in the *ac*-plane formed by six-membered rings with two different topologies (Fig. 2a). In one ring, the $[AlO_4]$ tetrahedra are oriented according to UDUDUD (U = up, D = down) while the neighboring rings orient UUDDUD (Fig. 2b). These layers are stacked along [010] whereas the connected layer has the inverse arrangement of the tetrahedra. Of the three crystallographically independent Ca atoms, Ca1 and Ca2 exhibit significantly deformed octahedral coordination environments (Fig. 2c and d) while Ca3 has nine oxidic neighbors in the shape of a distorted tri-capped trigonal prism (Fig. 2e). The distances in the octahedra (d(Ca–O) = 229–272 pm) are slightly shorter than the ones in the Ca3 polyhedra (d(Ca–O) = 234–317 pm).

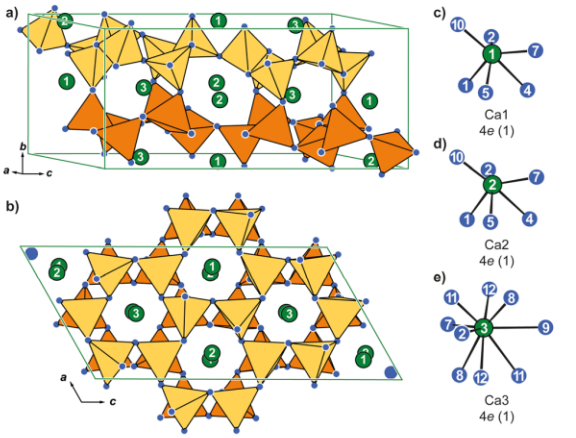

Fig. 2 Unit cell of the of monoclinic $CaAl_2O_4$ ($P2_1/c$, own type) in (a) side view and (b) along [010]. (c–e) Coordination environments of the Ca atoms. Wyckoff positions and site symmetries are given. Ca atoms are depicted in green, Al atoms as orange and O atoms as blue circles. The two layer-like arrangements of the $[AlO_4]$ tetrahedra are depicted in light and dark orange.

3.2 Oxidation of $CaAl_2$ under STA conditions

First reactions targeting the oxidation behavior of the cubic Laves phase $CaAl_2$ were performed in an STA (Simultaneous Thermal Analysis) system. The powdered samples were heated in an Al_2O_3 crucible with two different gas flows of O_2 (reaction gas) : Ar (inert gas) in a 1 : 4 ratio mimicking air as well as in a 1 : 1 ratio for more oxidizing conditions. Fig. 3 and Table 1 summarize the resulting data of the thermal analysis. For all measurements a maximum temperature of 1273 K was chosen, heating rates are given in Table 1. At first, for both gas mixtures, immediate cooling after reaching the maximal temperature was chosen. The mass change remains almost constant until an onset temperature of ≈800 K is reached. An increase of ≈40 mass% can be observed over at least two steps, however, a steady state is reached when reaching the maximum temperature. The heat flow confirms that the oxidation takes place in two close steps due to two signals at $T_{peak,1}$ = 1165 and $T_{peak,2}$ = 1183 K. Using the same experimental conditions in the STA experiments (T_{max} = 1273 K, 20 K min^{-1}) but adding an isothermal section of 5 h at 1273 K leads to a very similar result. The total mass gain is slightly higher (≈50 mass%), however, the onset and peak temperatures in the heat flow are almost identical. Once reaching the maximum temperature, an additional mass gain of ≈8 mass% occurs during the 5 h annealing step. It must be noted that the mass gain is significantly lower compared to the expected mass gain (69 mass%) for the total oxidation of $CaAl_2$ to $CaAl_2O_4$. In both cases, white-grey powders were obtained which are stable in air. The diffraction patterns indicate the formation of mayenite $Ca_{12}Al_{14}O_{33}$ (12 CaO·7 Al_2O_3, C12A7) as the main phase. In addition, the targeted oxidation product $CaAl_2O_4$, as well as elemental aluminum ($Fm\bar{3}m$), and calcium

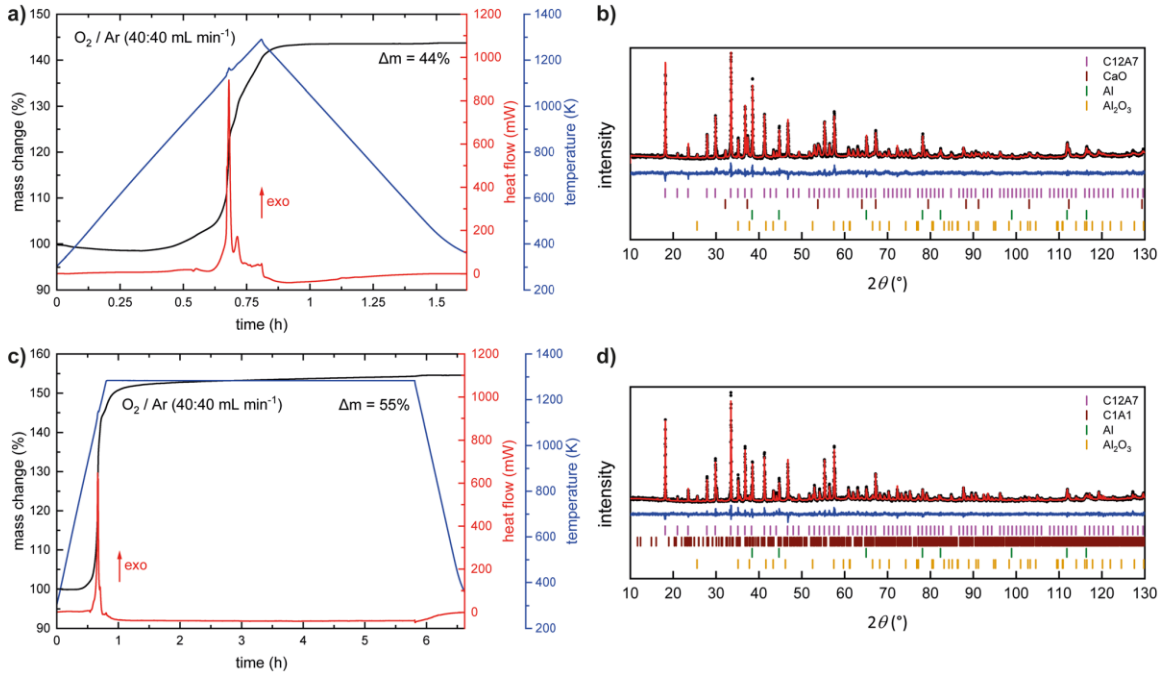

Fig. 3 STA experiments (a and c) and the corresponding Rietveld refinements (b and d) of the collected powder X-ray diffraction data.

Table 1 Results of the Rietveld refinements from powder X-ray diffraction data of the STA treated samples. All specimen were heated to 1273 K with different O_2 : Ar ratios and different dwelling times. The standard deviations for the determined mass% are ±1 mass%

			Phase contributions obtained by PXRD (mass%)						
Ar : O_2 ratio (%)	Dwelling time (h)	Heating rate (K min^{-1})	$Ca_{12}Al_{14}O_{33}$	$CaAl_2O_4$	$Ca_3Al_2O_6$	CaO	Al_2O_3	Al	Figure
80 : 20	0	20	72	7	5	3	3	10	Fig. S3†
	5	20	62	11	10	1	9	7	Fig. S4†
50 : 50	0	5	75	9	1	0	9	6	Fig. S5†
	0	10	73	11	1	0	7	8	Fig. S6†
	0	20	66	8	3	6	6	11	Fig. S7†
	0	40	69	9	5	2	5	10	Fig. S8†
	5	5	71	13	2	0	9	5	Fig. S9†
	5	10	68	14	4	0	9	5	Fig. S10†
	5	20	65	14	2	0	11	8	Fig. S11†
	5	40	56	11	14	2	12	5	Fig. S12†

oxide ($Fm\bar{3}m$) could be identified. Besides a heating rate of 20 K min^{-1}, also heating rates of 5, 10, and 40 K min^{-1} were used, however, the obtained phase compositions are in line with the ones shown before. Table 1 lists the results from the powder X-ray diffraction for the different heating rates and annealing times. The powder X-ray diffraction patterns can be found in the ESI† under the numbers given in the table.

It is interesting to note, that $CaAl_2$ reacts with O_2 and initially forms $Ca_{12}Al_{14}O_{33}$ (mayenite) instead of directly reacting to $CaAl_2O_4$ being the reaction product of a stoichiometric reaction. This is especially surprising since $Ca_{12}Al_{14}O_{33}$ has a different Ca : Al ratio with respect to the starting material $CaAl_2$. However, using prolonged reaction times, $CaAl_2O_4$ is successively formed (Scheme 1). At the same time, the amounts of Al and CaO decrease while more Al_2O_3 is formed. The fact, that $CaAl_2$ vanishes completely but at the same time elemental Al is found gives rise to the hypothesis that the oxidation of the intermetallic phase, which is happening on the surface of the crystalline powder, is accompanied by a decomposition of the Laves phase into CaO and elemental Al, which is subsequently oxidized to Al_2O_3.

What is even more striking is the fact that a 'classical' solid-state reaction starting from $Ca(NO_3)_2{\cdot}4\ H_2O$ and $Al(NO_3)_3{\cdot}9\ H_2O$ shows comparable results. An equimolar reaction of the two salts leads to almost phase pure $Ca_{12}Al_{14}O_{33}$ (Fig. S37†), while a reaction in a ratio of $Ca(NO_3)_2{\cdot}4\ H_2O$ with 2 $Al(NO_3)_3{\cdot}$

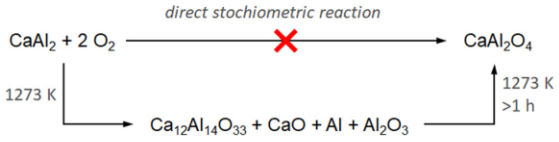

Scheme 1 Reaction pathway for the oxidation of $CaAl_2$ with elemental O_2.

9 H_2O leads to $Ca_{12}Al_{14}O_{33}$, monoclinic $CaAl_4O_7$ (*C*2/*c*), and $CaAl_2O_4$ (Fig. S38†). This is somehow expected, since the reaction occurs from a stoichiometric mixture leading to a Ca-rich besides a Ca-poor phase and the desired reaction product. This clearly shows, that the mayenite type structure is the initial product formed in all these reactions.

To prove that elemental Al is formed during this reaction, ^{27}Al NMR spectra of the oxidation products were recorded. They reveal that the signal of $CaAl_2$ (δ = 1092 ppm) disappears, however, four resonances at δ = 1640, 85, 79, and 11 ppm appear (Fig. 4). The resonance at δ = 1640 ppm corresponds to elemental Al[77–79] while the one at δ = 11 ppm corresponds to Al_2O_3.[80] The rather broad signals at ≈80 ppm can be attributed to $Ca_{12}Al_{14}O_{33}$ according to the literature.[81] Due to the two different coordination environments of the Al atoms (*vide supra*), two signals arise, showing significant overlap. As reported, the sharp signal at $\delta_{iso}(^{27}Al)$ = 79 ppm is caused by the [Al2O_4] entities (Q^4) forming the framework while the broad signal at $\delta_{iso}(^{27}Al)$ = 85 ppm originates from the branching [Al1O_4] units (Q^3) containing one terminal oxygen atom.

To summarize the STA and solid-state experiments, it can be concluded that all reactions are exothermic, however, instead of $CaAl_2O_4$, the expected oxidation product, first $Ca_{12}Al_{14}O_{33}$ is formed, especially when using short annealing times. In addition, it is quite intriguing, that elemental Al is formed, leading to the assumption, that $CaAl_2$ decomposes into a ternary oxide and elemental Al. Finally, it can be concluded, that the reaction is a surface reaction as the oxidation process stops at a certain point. Therefore, the oxidation in air was performed in different approaches (*vide infra*).

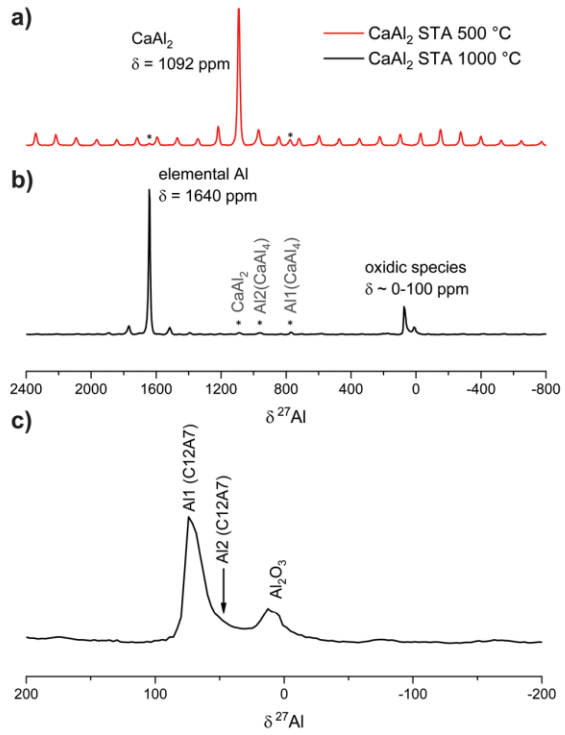

Fig. 4 ^{27}Al NMR investigations of the oxidation product (b) of $CaAl_2$ (a). The full spectrum is shown in the top panels, a zoom of the region of the oxidic species at the bottom (c).

3.3 Oxidation of $CaAl_2$ in air in a muffle furnace

After the observations made during the oxidation reactions carried out in the STA system with different heating rates and O_2/Ar mixtures, bulk oxidations were carried out using air. For these reactions, the powdered $CaAl_2$ sample was treated using different heating schemes (Scheme 2). For all reactions the samples were heated to 1273 K followed by different isothermal steps: (1) annealing of different samples for 1, 5, 48 and 96 h, (2) annealing of the same sample for 1, 1, 5, 10 and 20 h with intermediate grinding of the sample between the heating cycles and (3) 10 cycles of heating a sample to 1273 K followed by direct cooling to RT and subsequent grinding. In addition, five samples were simultaneously heated to 1273 K kept for one hour and analyzed subsequently to get an idea about the standard deviation regarding the chemical composition of the samples. The results of the X-ray diffraction experiments indicate that the product composition is very consistent among this batch of five samples (Table S1†). Fig. 5a–c summarizes

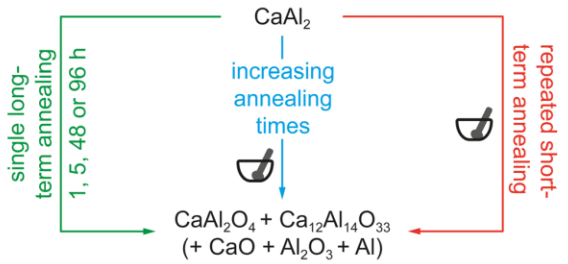

Scheme 2 Illustration of the three different synthetic approaches for the oxidation reaction of $CaAl_2$. For details see manuscript text.

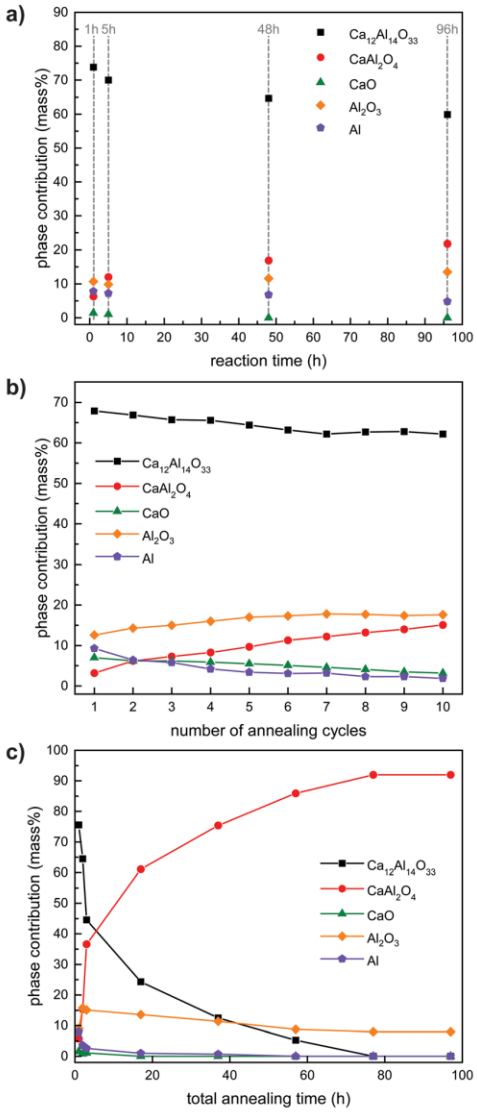

Fig. 5 Results of the Rietveld refinements of the different oxidation approaches of $CaAl_2$. (a) single long-term annealing, (b) repeated heating to 1273 K followed by grinding, and (c) increasing annealing times with intermediate grinding. The values are documented in Table 2.

the results of Rietveld analysis of the products after the muffle oven syntheses (1–3), the numbers are given in Table 2. It is clearly visible, that for all synthesis strategies, $Ca_{12}Al_{14}O_{33}$ is primarily formed. The obtained amount of $CaAl_2O_4$ increases with increasing reaction time in syntheses when only a single oxidation step is conducted (Scheme 2, green; Fig. 5a). However, increasing the reaction time from 1 to 5 to 12 to 24 to 48 to even 96 h only slightly increases the weight-fraction of the targeted oxidation product $CaAl_2O_4$. In the case of multiple short oxidation steps (dwelling only for 1 min at 1273 K) and if the product is ground in blank between (Scheme 2, red; Fig. 5b), the obtained amount of the target phase $CaAl_2O_4$ also increases rather slowly. These observations indicate that long reaction times or multiple steps alone do not lead to the formation of the desired compounds, let alone phase-pure materials. Finally, using a combination of both, prolonged reaction times and multiple annealing steps with in between grinding of the sample, gives the largest amounts of $CaAl_2O_4$ (Scheme 2, blue; Fig. 5c). After five annealing steps with increasing reaction times a maximum of 90 mass% $CaAl_2O_4$ was obtained. In the same fashion, repetitive annealing for 5 h each was conducted over 100 h leading to the same result (Fig. S13 and Table S2†).

The final product described above was also investigated by ^{27}Al NMR spectroscopy. Here, one main signal at δ = 78 ppm is observed (Fig. 6) alongside two minor resonances at δ = 1640 ppm (elemental Al [77–79]) and δ = 14 ppm (Al_2O_3 [80]) and a vast spinning side band manifold originating from the satellite transitions of ^{27}Al (I = 5/2). The chemical shift of the main resonance as well as the quadrupolar interaction (C_Q = 6.5 MHz) and the asymmetry parameter (η = 0.89) is in very good agreement with the literature.[81]

3.4 Oxidation of $CaAl_2$ in different O_2/Ar mixtures

To verify that nitrogen and other atmospheric components do not play a critical role in the described oxidation processes, the reactions were repeated in a tube furnace using a mixture of 50% O_2/50% Ar and 100% O_2 at temperatures of 1273 K and different reaction times. The results from the reactions in the muffle furnaces clearly indicate, that intermediate grinding is key to getting high amounts of $CaAl_2O_4$ in the oxidation product, therefore, the samples oxidized in high O_2 concentrations should give comparable results. Indeed, as documented in Table 3, $Ca_{12}Al_{14}O_{33}$ is formed as the main phase underlining that surface nature of the oxidation, regardless of the O_2 to Ar ratio and the reaction time.

As an intermediate conclusion the following aspects can be summarized:

(1) the oxidation of $CaAl_2$ in O_2/Ar mixtures or in air is a diffusion or even self-limited surface reaction, therefore,

(2) intermediate grinding is essential to remove the oxidic layer and allow for a continuation of the reaction.

(3) Only oxygen seems to play a role in the conducted reactions, N_2 and other constituents of the air are not necessary.

(4) $Ca_{12}Al_{14}O_{33}$ is the initial product in all reactions which subsequently disappears, rendering the mayenite phase the kinetic product while $CaAl_2O_4$ is the thermodynamic product.

Subsequently, two final questions must be addressed: (1) why is $Ca_{12}Al_{14}O_{33}$ formed at first and (2) what is the mechanism of the oxidation?

3.5 Oxidation of $CaAl_2$ in an induction furnace

As already shown, $Ca_{12}Al_{14}O_{33}$ forms as initial (intermediate) product. This compound is significantly richer in Ca compared

Table 2 Summary of the Rietveld fit results of the powder X-ray diffraction data collected from the samples oxidized in a muffle furnace in air. The samples were all heated to 1273 K (≈15 K min^{-1}) with different dwelling times and processing. The standard deviations for the determined mass% are ±1 mass%

		Phase contributions obtained by PXRD (mass%)					
Dwelling time (h)	Total time (h)	$Ca_{12}Al_{14}O_{33}$	$CaAl_2O_4$	CaO	Al_2O_3	Al	Figure
Single long-term annealing							
1	1	73	8	2	10	7	Fig. S14†
5	5	70	12	1	10	7	Fig. S15†
48	48	65	18	0	11	6	Fig. S16†
96	96	60	24	0	11	5	Fig. S17†
Increasing annealing times with intermediate grinding							
1	1	74	7	2	9	8	Fig. S18†
1	2	64	18	1	14	3	Fig. S19†
5	7	44	39	1	14	2	Fig. S20†
10	17	24	62	1	12	1	Fig. S21†
20	37	13	75	0	11	1	Fig. S22†
20	57	6	85	0	9	0	Fig. S23†
20	77	0	92	0	8	0	Fig. S24†
20	97	0	92	0	8	0	Fig. S25†

	Phase contributions obtained by PXRD (mass%)					
Number of cycles	$Ca_{12}Al_{14}O_{33}$	$CaAl_2O_4$	CaO	Al_2O_3	Al	Figure
Repeated heating to 1273 K followed by grinding						
1	72	0	8	11	9	Fig. S26†
2	67	9	6	12	6	Fig. S27†
9	64	16	3	15	2	Fig. S28†
10	63	17	3	15	2	Fig. S29†

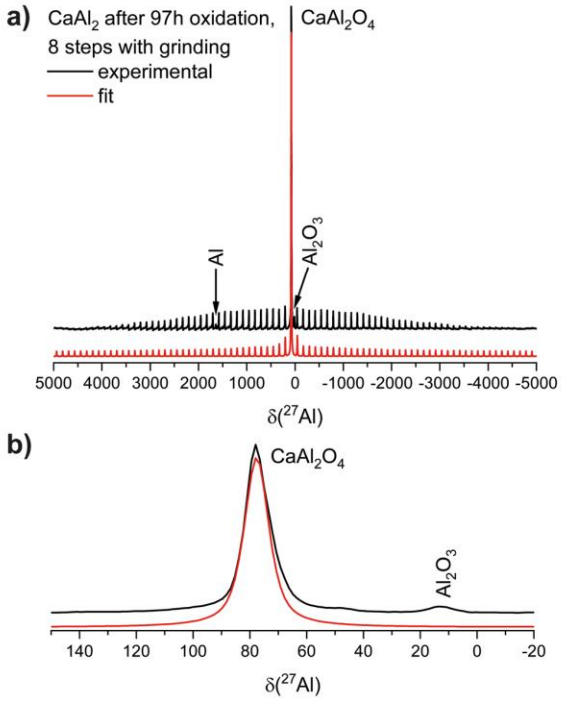

Fig. 6 ^{27}Al NMR investigations of the oxidation product of $CaAl_2$ (black line) plotted *versus* the fitted data (red line). The full spectrum (a) is shown in the top panel, a zoom of the region (b) of the oxidic species at the bottom.

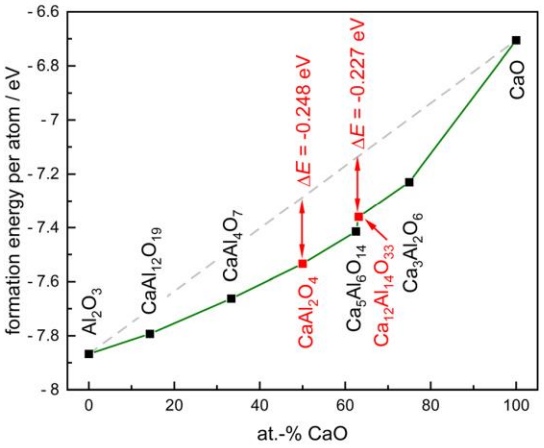

Fig. 7 Convex-hull diagram (formation energy per atom *versus* chemical composition) for the ternary system Ca–Al–O with respect to the binary oxides CaO and Al_2O_3. The formation energy per atom is obtained from DFT calculations.

to the starting material $CaAl_2$. In addition, elemental Al can be observed, leading to two possible scenarios: Ca atoms diffuse to the surface enabling the formation of a more Ca-rich compound or Al atoms diffuse away from the surface leaving a Ca-rich phase. This question has been addressed by the following experiment. A sample of $CaAl_2$ was pressed to a pellet and placed in a corundum crucible inside an induction furnace.

Table 3 Summary of the Rietveld fit results of the powder X-ray diffraction data collected from the samples oxidized in a tube furnace using different Ar to O_2 ratios. The samples were all heated to 1273 K (≈4 K min^{-1}) with different dwelling times

		Phase contributions obtained by PXRD (mass%)						
Ar : O_2 ratio (%)	Dwelling time (h)	$Ca_{12}Al_{14}O_{33}$	$CaAl_2O_4$	$Ca_3Al_2O_6$	CaO	Al_2O_3	Al	Figure
50 : 50	0	73	9	0	0	9	9	Fig. S30†
0 : 100	0	78	3	0	1	9	9	Fig. S31†
0 : 100	5	72	9	2	0	10	7	Fig. S32†

The sample chamber was evacuated and subsequently, the sample was heated to ≈1273 K. At this temperature, the sample chamber was opened to air. Due to the oxidation of the sample, the induction heating is quenched since the formed oxides to not interact with the induction field anymore. The powder X-ray diffraction pattern of the resulting product is shown in Fig. S33†. Besides the expected oxidation product $Ca_{12}Al_{14}O_{33}$ (6 mass%), $CaAl_2$ remains as unreacted educt with 49 mass%. Additionally, CaO (6 mass%) and $CaAl_4$ (39 mass%) can be observed. This unambiguously leads to the conclusion that Ca atoms diffuse to the surface of the particles, leaving the Al-rich intermetallic phase $CaAl_4$. If the Al atoms would be the determining species, elemental Al should have been visible in this experiment.

3.6 Oxidation reactions of the composition 'Ca_6Al_7'

Finally, due to the observation that $CaAl_2$ does not fully oxidize to $CaAl_2O_4$ but forms $Ca_{12}Al_{14}O_{33}$ at first, attempts were made to obtain the latter compound as main product. For this, nominal 'Ca_6Al_7' was prepared by arc-melting of the elements having the Ca : Al ratio equal to that of $Ca_{12}Al_{14}O_{33}$. Characterization by powder X-ray diffraction revealed that a mixture of $CaAl_2$ and Ca_8Al_3 has formed (Fig. S34†). The sample was again investigated *via* STA measurements (heating 20 K min^{-1}, T_{max} = 1273 K, cooling 20 K min^{-1}) with and without an isothermal section of 5 h (Fig. S35 and S36†). In contrast to the previous STA investigations, the TG curves show a two-step mass increase in agreement with the simultaneously measured DSC indicating two exothermic reactions. One signal is observed around $T \approx 823$ K, the second at 1000 K. The latter temperature can be correlated with the oxidation process of $CaAl_2$ described above although the temperature is lowered by almost ≈150 K. The step at lower temperatures therefore must be attributed to the oxidation reaction of the second intermetallic compound present, Ca_8Al_3. Rietveld analysis of the powder diffraction pattern from the oxidation product obtained without the isothermal section revealed the formation of the mayenite phase alongside traces of CaO, Al_2O_3, and elemental Al, similar to the investigations using pure $CaAl_2$ as a precursor. The samples that were dwelled for 5 h at 1273 K showed a decrease of the amount of the mayenite phase in favor of the formation of the Ca-rich cubic oxide $Ca_3Al_2O_6$ ($Pa\bar{3}$)[57] with a significant amount of 21 mass%. This, however, is not that surprising, since Ca_8Al_3 is a Ca-rich compound and therefore most likely the source for cubic $Ca_3Al_2O_6$.

3.7 SEM/EDX

Two samples were additionally investigated *via* EDX. The sample with the highest content of $CaAl_2O_4$, obtained after 97 h of annealing with intermediate grinding (last data point in Fig. 5c and Fig. S25†) as well as the sample obtained by oxidation in pure O_2 after 5 h (Fig. S32†). While the latter contains significant amounts of $Ca_{12}Al_{14}O_{33}$, the first one contains only $CaAl_2O_4$ (≈90 mass%) besides Al_2O_3. Area scans on the sample annealed for 97 h show the expected Ca to Al radio of 1 : 2 (34(1) to 66(1) at%) while the mayenite containing sample exhibits a Ca to Al ratio of 1 : 1.4 (42(1) to 58(1) at%) in good agreement with the 12 : 14 ratio of mayenite.

3.8 Quantum-chemical calculations

To address the final question why $Ca_{12}Al_{14}O_{33}$ is formed as the first oxide, the stability of the different phases in the ternary system Ca–Al–O was investigated *via* quantum-chemical calculations. The formation energy per atom was calculated, resulting in the convex-hull diagram given in Fig. 7. In these plots the stability of the respective oxidic compounds relative to the energy of their constituent binary oxides is shown (Table S3†). At 0 K, every calculated ternary compound can be obtained by the reaction of appropriate amounts of CaO and Al_2O_3 since their formation energy per atom is larger (more negative) than the average energy per atom between the two binaries (dashed line in Fig. 7).

When calculating the energy difference between the formation energy per atom and the average energy per atom, it becomes clear that of the two observed compounds, $CaAl_2O_4$ is the most stable compound (ΔE = −0.248 eV) in this system. However, $Ca_{12}Al_{14}O_{33}$ has only a slightly smaller energy difference (ΔE = −0.227 eV) rendering this compound kinetically stabilized, nicely underlining why this phase is initially formed. In addition, the fact that the $Ca_{12}Al_{14}O_{33}$ can exhibit oxygen vacancies can also play a role here. It could be possible, that the O-deficiencies lead to an entropic stabilization at higher temperatures, however, this cannot be addressed by our calculations.

4 Conclusion

The oxidation of the well-defined, phase-pure, and highly crystalline intermetallic phase $CaAl_2$ ($MgCu_2$ type, cubic Laves phase) was studied by thermal analysis and different bulk oxi-

dation reactions in air and various O_2/Ar mixtures. STA investigations indicate that the oxidation reaction starts above ≈1100 K and is highly exothermic. The observed mass gain (≈40 mass%) is significantly lower compared to an expected full oxidation (69 mass%). Adding a 5 h isothermal section at the maximum temperature of 1273 K leads to a mass gain of about 50 mass%. Powder X-ray diffraction experiments on the oxidation products indicate a multi-phase mixture with cubic mayenite type $Ca_{12}Al_{14}O_{33}$ being the main product. Additionally, Al_2O_3 and elemental Al were observed in significant amounts. The formation of the Al containing compounds, as well as the disappearance of the starting material, was confirmed by ^{27}Al MAS NMR spectroscopy. Bulk studies could show that the oxidation of this intermetallic compound is a surface reaction. However, short reaction times are not sufficient to obtain the expected oxidation product $CaAl_2O_4$. Samples with high amounts of the targeted compound could be obtained by multiple prolonged reactions with intermediate grinding. The formation of the intermediate product $Ca_{12}Al_{14}O_{33}$ was underlined by DFT calculations, which yielded the energy of formation per atom for most known compounds in the ternary Ca–Al–O system. Finally, rapid quenching of the oxidation reaction could prove that the Ca atoms diffuse towards the surface of the particle, explaining the formation of elemental Al as an intermediate. This type of synthesis opens a totally new synthetic approach for ternary and even multinary oxides due to the manifold among the intermetallic starting materials and enables studies on the mechanism of the oxidation of different intermetallics.

Author contributions

Conceptualization by GK and OJ, synthetic work by ECJG, SE and JGV, initial draft of the manuscript by ECJG. ECJG performed the STA and ^{27}Al NMR investigations, SE performed the SEM/EDX investigations, OJ performed the DFT calculations. The entire work was supervised, guided, and revised by GK and OJ. The manuscript was corrected by all authors and finalized by HH, GK, and OJ.

Data availability

Representation of the crystal structure of $CaAl_2$, ^{27}Al NMR spectroscopic data of $CaAl_2$, information on the theoretical calculations, figures and details on the Rietveld refinements can be found in the ESI.†

Conflicts of interest

The authors declare no competing interests.

Acknowledgements

Special thanks goes to Sylvia Beetz from the MWWT/Inorganic Chemistry workshop of Saarland University and to Britta Schreiber from the central glassblowing workshop for installing the furnace for oxidation experiments. Instrumentation and technical assistance for this work were provided by the Service Center X-ray Diffraction, with financial support from Saarland University and German Science Foundation (project number INST 256/349-1) and by the Service Center NMR with financial support from Saarland University and German Research Foundation DFG.

References

1 F. Ostermann, *Anwendungstechnologie Aluminium*, Springer Vieweg, Berlin, Heidelberg, Germany, 2014.
2 C. Kammer, *Aluminium-Taschenbuch 1: Grundlagen und Werkstoffe*, Aluminium-Zentrale, Düsseldorf, Germany, 1995.
3 C. Jaschik, H. Haferkamp and M. Niemeyer, in *Magnesium Alloys and their Applications*, Wiley-VCH Verlag GmbH, Weinheim, Germany, 2000, pp. 41–46, DOI: **10.1002/3527607552.ch7**.
4 M. K. Kulekci, Magnesium and its alloys applications in automotive industry, *Int. J. Adv. Des. Manuf. Technol.*, 2008, **39**, 851–865.
5 Empire State Realty Trust, *Empire State Building Fact Sheet*, **https://www.esbnyc.com/sites/default/files/esb_fact_sheet_4_9_14_14.pdf**.
6 FMGB Guggenheim Bilbao Museoa, **https://www.guggenheim-bilbao.eus/de/**, (accessed 28.06.2023).
7 C. Veiga, J. P. Davim and A. J. R. Loureiro, Properties and applications of titanium alloys: A brief review, *Rev. Adv. Mater. Sci.*, 2012, **32**, 14–34.
8 M. V. Ribeiro, M. R. V. Moreira and J. R. Ferreira, Optimization of titanium alloy (6Al–4 V) machining, *J. Mater. Process. Technol.*, 2003, **143–144**, 458–463.
9 M. Peters, J. Hemptenmacher, J. Kumpfert and C. Leyens, in *Titanium and Titanium Alloys*, Wiley-VCH Verlag GmbH, Weinheim, Germany, 2003, pp. 1–36, DOI: **10.1002/3527602119.ch1**.
10 J. Barksdale, in *The encyclopedia of the chemical elements*, ed. C. A. Hampel, Reinhold Book Corp., New York, USA, 1968, pp. 732–738.
11 P. Enghag, in *Encyclopedia of the Elements: Technical Data – History – Processing – Applications*, ed. P. Enghag, Wiley VCH Verlag GmbH, Weinheim, Germany, 2004, pp. 493–509, DOI: **10.1002/9783527612338.ch18**.
12 E. Gillam, H. P. Rooksby and L. D. Brownlee, Structural relationships in beryllium-titanium alloys, *Acta Crystallogr.*, 1964, **17**, 762–763.
13 O. Janka and R. Pöttgen, The role of beryllium in alloys, Zintl phases and intermetallic compounds, *Z. Naturforsch.*, 2020, **75b**, 421–439.

14 M. Peters and C. Leyens, *Titan und Titanlegierungen*, Wiley-VCH, Weinheim, Germany, 2002.
15 J. B. Friauf, The crystal structures of two intermetallic compounds, *J. Am. Chem. Soc.*, 1927, **49**, 3107–3114.
16 H. Perlitz and A. Westgren, The crystal structure of Al_2CuMg, *Ark. Kemi, Mineral. Geol.*, 1943, **16B**, 1–5.
17 J. R. Davis, *ASM Specialty Handbook: Aluminum and Aluminum Alloys*, ASM International, Materials Park, OH, USA, 1993.
18 O. Janka, in *Applied Inorganic Chemistry*, ed. R. Pöttgen, T. Jüstel and C. Strassert, De Gruyter, Berlin, Germany, 2022, pp. 158–173, DOI: 10.1515/9783110733143-010.
19 D. Altenpohl, *Aluminium und Aluminiumlegierungen*, Springer, Berlin, Heidelberg, Germany, 1965.
20 P. K. Datta, H. L. Du, J. S. Burnell-Gray and R. E. Ricker, in *Corrosion: Materials*, ASM International, Materials Park, OH, USA, 2005, vol. 13B.
21 R. K. Gupta and B. Pant, in *Intermetallic Matrix Composites*, ed. R. Mitra, Woodhead Publishing, Sawston, Cambridge, England, 2018, pp. 71–93, DOI: 10.1016/B978-0-85709-346-2.00004-2.
22 F. Appel, U. Brossmann, U. Christoph, S. Eggert, P. Janschek, U. Lorenz, J. Müllauer, M. Oehring and J. D. H. Paul, Recent progress in the development of gamma titanium aluminide alloys, *Adv. Eng. Mater.*, 2000, **2**, 699–720.
23 C. Kenel, A. Lis, K. Dawson, M. Stiefel, C. Pecnik, J. Barras, A. Colella, C. Hauser, G. J. Tatlock, C. Leinenbach and K. Wegener, Mechanical performance and oxidation resistance of an ODS γ-TiAl alloy processed by spark plasma sintering and laser additive manufacturing, *Intermetallics*, 2017, **91**, 169–180.
24 K. Meng, K. Guo, Q. Yu, D. Miao, C. Yao, Q. Wang and T. Wang, Effect of annealing temperature on the microstructure and corrosion behavior of Ti-6Al-3Nb-2Zr-1Mo alloy in hydrochloric acid solution, *Corros. Sci.*, 2021, **183**, 109320.
25 P. A. Loginov, G. M. Markov, N. V. Shvyndina, G. V. Smirnov and E. A. Levashov, Oxidation resistance of γ-TiAl based alloys modified by C, Si and Y_2O_3 microdopants, *Ceramics*, 2022, **5**, 389–403.
26 S. A. Kekare and P. B. Aswath, Oxidation of TiAl based intermetallics, *J. Mater. Sci.*, 1997, **32**, 2485–2499.
27 Z. Li, W. Gao, Y. He and S. Li, Oxidation of Ti_3Al and TiAl intermetallic compounds under controlled oxygen partial pressures, *High Temp. Mater. Processes*, 2002, **21**, 35–46.
28 R. Pflumm, S. Friedle and M. Schütze, Oxidation protection of γ-TiAl-based alloys – A review, *Intermetallics*, 2015, **56**, 1–14.
29 A. Rahmel, M. Schütze and W. J. Quadakkers, Fundamentals of TiAl oxidation – A critical review, *Mater. Corros.*, 1995, **46**, 271–285.
30 G. Geramifard, C. Gombola, P. Franke and H. J. Seifert, Oxidation behaviour of NiAl intermetallics with embedded Cr and Mo, *Corros. Sci.*, 2020, **177**, 108956.
31 H. J. Grabke, M. W. Brumm and B. Wagemann, The oxidation of NiAl, *Mater. Corros.*, 1996, **47**, 675–677.
32 H. Qin, X. Chen, L. Li, P. W. Sutter and G. Zhou, Oxidation-driven surface dynamics on NiAl(100), *Proc. Natl. Acad. Sci. U. S. A.*, 2015, **112**, E103–E109.
33 Y.-O. Yoon, S.-H. Ha, G.-Y. Yeom, H. K. Lim and S. K. Kim, in *Light Metals 2013*, Springer, Cham, Germany, 2013, pp. 323–326, DOI: 10.1002/9781118663189.ch56.
34 R. Hoppe and H.-J. Röhrborn, Oxidationsprodukte binärer intermetallischer Phasen der Alkalimetalle: $NaTlO_2$ (kubisch) aus NaTl, *Naturwissenschaften*, 1961, **48**, 453–454.
35 R. Hoppe and H.-J. Röhrborn, Oxydationsprodukte intermetallischer Phasen. I. Untersuchungen am $NaTlO_2$, *Z. Anorg. Allg. Chem.*, 1964, **327**, 199–206.
36 R. Hoppe, New routes in the synthesis of metal oxides, II, *J. Solid State Chem.*, 1986, **65**, 127–144.
37 H. D. Wasel-Nielen and R. Hoppe, Oxoaurate(I) der Alkalimetalle: CsAuO, *Z. Anorg. Allg. Chem.*, 1968, **359**, 36–40.
38 P. J. Yvon, R. B. Schwarz, C. B. Pierce, L. Bernardez, A. Conners and R. Meisenheimer, Oxygen isotope effect in $YBa_2Cu_3O_7$ prepared by burning YBa_2Cu_3 in ^{16}O and ^{18}O, *Phys. Rev. B: Condens. Matter Mater. Phys.*, 1989, **39**, 6690–6693.
39 W. Schauerte, H. U. Schuster, N. Knauf and R. Müller, Ein alternativer Weg zur Darstellung von $Bi_2Sr_2CaCu_2O_x$, $YBa_2Cu_3O_{7-\delta}$, und $YBa_2Cu_{3-x}M_xO_{7-\delta}$ (M = Ni, Ag und $x \leq$ 33 Mol%), *Z. Anorg. Allg. Chem.*, 1992, **616**, 186–190.
40 B. Cogel and H. U. Schuster, Oxidationsreaktionen an Legierungen zur Synthese des Hochtemperatur-Supraleiters $Tl_2Ba_2CaCu_2O_8$, *Z. Anorg. Allg. Chem.*, 1993, **619**, 1765–1770.
41 H. Schuster and J. Wittrock, Zur Thermischen Analyse der Oxidation von Abgeschreckten Legierungen als Vorstufen von Hochtemperatursupraleitern, *J. Therm. Anal. Calorim.*, 1993, **39**, 1397–1401.
42 A. Panahandeh and W. Jung, The Oxidation of heterogeneous Tl/Ni/P-alloys - Preparation and crystal structures of the thallium nickel phosphates $TlNi_4(PO_4)_3$, $Tl_4Ni_7(PO_4)_6$, and $Tl_2Ni_4(P_2O_7)(PO_4)_2$, *Z. Anorg. Allg. Chem.*, 2003, **629**, 1651–1660.
43 P. Moser, W. Jung and H. U. Schuster, Die Kristallstruktur von $(Al_{0,5}Ga_{0,5})CuOAsO_4$ – Kupfer zwischen planarer und geschlossener Koordination, *Z. Anorg. Allg. Chem.*, 1997, **623**, 1781–1785.
44 P. Moser and W. Jung, Tl_2CuAsO_4 – ein Zwischenprodukt bei der Oxidation von Tl/Cu/As-Legierungen im Sauerstoffstrom, *Z. Anorg. Allg. Chem.*, 1998, **624**, 1251–1255.
45 P. Moser, H. M. Schwunck and W. Jung, Die Schichtstruktur von $Tl[CuAsO_4]$ und $Tl[CuPO_4]$ mit Zwischenschichten aus Thallium(I) mit stereoaktivem Elektronenpaar, *Z. Anorg. Allg. Chem.*, 1998, **624**, 1256–1261.
46 H. M. Schwunck, P. Moser and W. Jung, Das Kupfer(II)-oxidphosphat $Cu_4O(PO_4)_2$ in einer neuen, orthorhombischen Modifikation durch Oxidation einer Tl/Cu/P-Legierung, *Z. Anorg. Allg. Chem.*, 1998, **624**, 1262–1266.
47 H. M. Schwunck, P. Moser and W. Jung, Das Kupfer(II)-indium-oxidphosphat $CuInOPO_4$ mit α-Fe_2OPO_4-Struktur,

dargestellt durch die Oxidation einer Cu/In/P-Legierung im Sauerstoffstrom, *Z. Anorg. Allg. Chem.*, 1999, **625**, 407–410.
48 H. M. Schwunck, P. Moser and W. Jung, $TlCu^{I}Cu^{II}P_2O_7$ mit Kupfer in gemischter Valenz – ein Zwischenprodukt bei der Oxidation einer Tl/Cu/P-Legierung mit Sauerstoff, *Z. Anorg. Allg. Chem.*, 1999, **625**, 463–466.
49 P. Moser, V. Cirpus and W. Jung, $CuInOVO_4$ – Einkristalle eines Kupfer(II)-indiumoxidvanadats durch Oxidation von Cu/In/V-Legierungen, *Z. Anorg. Allg. Chem.*, 1999, **625**, 714–718.
50 P. Moser and W. Jung, $TlCu_5O(VO_4)_3$ mit $KCu_5O(VO_4)_3$-Struktur - ein Thallium-kupfer(II)-oxidvanadat als Oxidationsprodukt einer Tl/Cu/V-Legierung, *Z. Anorg. Allg. Chem.*, 2000, **626**, 1421–1425.
51 I. Antonyshyn, O. Sichevych, K. Rasim, A. Ormeci, U. Burkhardt, S. Titlbach, S. A. Schunk, M. Armbrüster and Y. Grin, Chemical behaviour of $CaAg_2$ under ethylene epoxidation conditions, *Eur. J. Inorg. Chem.*, 2018, **2018**, 3933–3941.
52 J. Sappl, F. Jung and C. Hoch, Facile one-step syntheses of several complex ionic lithium gallates from LiGa as intermetallic precursors, *Chem. Mater.*, 2020, **32**, 866–873.
53 W. Hörkner and H. Müller-Buschbaum, Zur Kristallstruktur von $CaAl_2O_4$, *J. Inorg. Nucl. Chem.*, 1976, **38**, 983–984.
54 S. Ito, K. Suzuki, M. Inagaki and S. Naka, High-pressure modifications of $CaAl_2O_4$ and $CaGa_2O_4$, *Mater. Res. Bull.*, 1980, **15**, 925–932.
55 B. Lazić, V. Kahlenberg, J. Konzett and R. Kaindl, On the polymorphism of $CaAl_2O_4$ - structural investigations of two high pressure modifications, *Solid State Sci.*, 2006, **8**, 589–597.
56 E. Aruja, The unit cell of orthorhombic pentacalcium trialuminate, $5CaO{\cdot}3Al_2O_3$, *Acta Crystallogr.*, 1957, **10**, 337–339.
57 H. E. Swanson, N. T. Gilfrich and G. M. Ugrinic, Standard X-ray diffraction patterns. Tri-calcium aluminate, $3CaO{\cdot}Al_2O_3$ (cubic), *Natl. Bur. Stand. Circ. (U. S.)*, 1955, **5**, 10–13.
58 W. Büssem, Die Struktur des Pentacalciumtrialuminats, *Z. Kristallogr.*, 1936, **95**, 175–188.
59 S. Matsuishi, Y. Toda, M. Miyakawa, K. Hayashi, T. Kamiya, M. Hirano, I. Tanaka and H. Hosono, High-density electron anions in a nanoporous single crystal: $[Ca_{24}Al_{28}O_{64}]^{4+}(4e^-)$, *Science*, 2003, **301**, 626–629.
60 L. Palacios, Á. G. De La Torre, S. Bruque, J. L. García-Muñoz, S. García-Granda, D. Sheptyakov and M. A. G. Aranda, Crystal xtructures and *in situ* formation study of mayenite electrides, *Inorg. Chem.*, 2007, **46**, 4167–4176.
61 L. Palacios, A. Cabeza, S. Bruque, S. García-Granda and M. A. G. Aranda, Structure and electrons in mayenite electrides, *Inorg. Chem.*, 2008, **47**, 2661–2667.
62 R. Pöttgen, T. Gulden and A. Simon, Miniaturisierte Lichtbogenapperatur für den Laborbedarf, *GIT Labor-Fachz.*, 1999, **43**, 133–136.
63 *Topas, Version 5*, Bruker AXS Inc., 2014.
64 *Winxpow*, STOE & Cie. GmbH, 2015.
65 *Topas, Version 4.2*, Bruker AXS Inc., 2009.
66 *Topspin*, Bruker Corp., 2008.
67 D. Massiot, F. Fayon, M. Capron, I. King, S. Le Calvé, B. Alonso, J.-O. Durand, B. Bujoli, Z. Gan and G. Hoatson, Modelling one- and two-dimensional solid-state NMR spectra, *Magn. Reson. Chem.*, 2002, **40**, 70–76.
68 P. E. Blöchl, Projector augmented-wave method, *Phys. Rev. B: Condens. Matter Mater. Phys.*, 1994, **50**, 17953–17979.
69 G. Kresse and D. Joubert, From ultrasoft pseudopotentials to the projector augmented-wave method, *Phys. Rev. B: Condens. Matter Mater. Phys.*, 1999, **59**, 1758–1775.
70 G. Kresse and J. Furthmüller, Efficient iterative schemes for ab initio total-energy calculations using a plane-wave basis set, *Phys. Rev. B: Condens. Matter Mater. Phys.*, 1996, **54**, 11169–11186.
71 G. Kresse and J. Furthmüller, Efficiency of *ab initio* total energy calculations for metals and semiconductors using a plane-wave basis set, *Comput. Mater. Sci.*, 1996, **6**, 15–50.
72 E. C. J. Gießelmann, R. Pöttgen and O. Janka, Laves phases: superstructures induced by coloring and distortions, *Z. Anorg. Allg. Chem.*, 2023, **649**, e202300109.
73 R. G. Barnes, W. H. Jones and T. P. Graham, Large anisotropic Knight shifts in intermetallic compounds, *Phys. Rev. Lett.*, 1961, **6**, 221–223.
74 S. Engel, E. C. J. Gießelmann, L. E. Schank, G. Heymann, K. Brix, R. Kautenburger, H. P. Beck and O. Janka, Theoretical and ^{27}Al NMR spectroscopic investigations of binary intermetallic alkaline-earth aluminides, *Inorg. Chem.*, 2023, **62**, 4260–4271.
75 H. Bartl and T. Scheller, Zur Struktur des $12CaO{\cdot}7Al_2O_3$, *Neues Jahrb. Mineral., Monatsh.*, 1970, 547–552.
76 A. N. Christensen, Neutron powder diffraction profile refinement studies on $Ca_{11.3}Al_{14}O_{32.3}$ and CaClO $(D_{0.88}H_{0.12})$, *Acta Chem. Scand.*, 1987, **41a**, 110–112.
77 E. R. Andrew, W. S. Hinshaw and R. S. Tiffen, More precise determination of the Knight shift of aluminium, *Phys. Lett. A*, 1973, **46**, 57–58.
78 W.-M. Shyu, T. P. Das and G. D. Gaspari, Direct and core-polarization contributions to the Knight shift in metallic aluminum, *Phys. Rev.*, 1966, **152**, 270–278.
79 C. Benndorf, H. Eckert and O. Janka, Structural characterization of intermetallic compounds by ^{27}Al solid state NMR spectroscopy, *Acc. Chem. Res.*, 2017, **50**, 1459–1467.
80 S. Xu, N. R. Jaegers, W. Hu, J. H. Kwak, X. Bao, J. Sun, Y. Wang and J. Z. Hu, High-field one-dimensional and two-dimensional ^{27}Al magic-angle spinning nuclear magnetic resonance study of θ-, δ-, and γ-Al_2O_3 dominated aluminum oxides: Toward understanding the Al sites in γ-Al_2O_3, *ACS Omega*, 2021, **6**, 4090–4099.
81 D. Müller, W. Gessner, A. Samoson, E. Lippmaa and G. Scheler, Solid-state ^{27}Al NMR studies on polycrystalline aluminates of the system $CaO{\cdot}Al_2O_3$, *Polyhedron*, 1986, **5**, 779–785.

Dalton Transactions

ROYAL SOCIETY OF CHEMISTRY

PAPER

View Article Online
View Journal | View Issue

Check for updates

Cite this: *Dalton Trans.*, 2025, **54**, 1173

Changing the reaction pathway of the $CaAl_2$ oxidation using ball milling†

Elias C. J. Gießelmann, Guido Kickelbick and Oliver Janka *

Received 29th August 2024,
Accepted 3rd November 2024

DOI: 10.1039/d4dt02459a

rsc.li/dalton

As previously shown, $CaAl_2$ can be oxidized using elemental O_2 to form $CaAl_2O_4$. This reaction, however, proceeds *via* $Ca_{12}Al_{14}O_{33}$ and elemental Al as intermediates which are subsequently transformed into the stoichiometric reaction product. High-energy ball milling is known to decrease the crystallite size of a material and to significantly produce defects enabling different reaction pathways compared to a highly crystalline bulk material. In this subsequent study, a different oxidizing agent (H_2O) as well as the ball milling behavior of $CaAl_2$ and the consecutive oxidation *via* elemental O_2 were studied. While the use of H_2O as the oxidizing agent showed only minor differences in the reaction products, ball milling of $CaAl_2$ decreases, as expected, the crystallite size of the material and introduces defects. This is visible both in the powder X-ray diffraction patterns and in the ^{27}Al solid-state MAS NMR spectra. In the subsequent steps, the ball milled material was oxidized in an STA system. Already 5 min of ball milling significantly changes the energy pattern of the reaction. Powder X-ray diffraction studies on the oxidized material clearly indicate that a different reaction pathway occurs. Samples ball milled for 180 min even get pyrophoric.

1. Introduction

Light weight alloys are of key importance for modern technical applications such as automotive and transportation applications,[1–5] architecture,[5–7] but also as corrosion resistant parts for air- and spacecrafts,[8–12] for medical applications like implants or stents,[10–15] or as non-sparking tools for gas stations, oil rigs or fire fighters.[16–18] In some of these alloys, intermetallic compounds play an important role.[1,5,19,20] The thermal and chemical resistance alongside astonishing mechanical properties of materials from the Ti–Al system[21] led to their use in aircraft and gas turbines.[22,23] However, the corrosion resistance of many materials is insufficient at elevated temperatures, which can be improved by alloying or special structuring.[24–26] Therefore, oxidation studies are an important field of research.[26–30] Alloys based on Ni and Al show supreme corrosion stability under extreme conditions. In AlNi for example, a protective layer of aluminum oxide Al_2O_3 (corundum, space group $R\bar{3}m$) is formed when the material is exposed to air at elevated temperatures.[31–33] Finally, aluminum alloys can be protected from oxidation by addition of small amounts of $CaAl_2$.[34]

Since intermetallic compounds are, in contrast to ionic compounds, not restricted to charge neutrality with respect to their compositions, they exhibit a plethora of different compositions and crystal structures[35] in their respective binary phase diagrams.[36] This manifold could, in theory, be utilized to synthesize valence precise *e.g.* ternary chalcogenides. Hoppe and co-workers prepared different AMO_2 phases (A = Li–K, M = In, Tl) starting from the Zintl phases NaTl, KTl, and LiIn[37–39] and also CsAuO could be obtained by the reaction of CsAu with dry O_2.[40] The oxidation of BaCu and YCu as well as related compounds led to the high-temperature superconductor $YBa_2Cu_3O_{7-\delta}$.[41–44] Jung and coworkers used different homo- and heterogeneous alloys for the synthesis of various different oxides,[45–53] but also $CaAl_2S_4$ and $SrAl_2S_4$[54] as well as Eu_2GeS_4,[55] $EuAl_2S_4$[56] and $LiGaX_2$ (X = O, S)[57] were synthesized by this route.

Recently, we have shown that the cubic Laves phase $CaAl_2$ (space group $Fd\bar{3}m$) can also be oxidized to the expected product $CaAl_2O_4$ (space group $P2_1/c$);[58] however, the reaction is far away from being straightforward. When heat-treating $CaAl_2$ under air, Ar/O_2 mixtures or elemental oxygen, initially $Ca_{12}Al_{14}O_{33}$ (mineral mayenite; space group $I\bar{4}3d$) is formed. This compound is significantly richer in calcium as the starting material, leaving unoxidized elemental aluminum behind. This was proven by X-ray diffraction and ^{27}Al NMR experiments. Repetitive grinding and oxidation finally led to almost phase pure $CaAl_2O_4$ samples. In this paper, we report a follow-up study in which a different oxidizing agent, H_2O, was used

Inorganic Solid State Chemistry, Saarland University, Campus C4.1, 66123 Saarbrücken, Germany. E-mail: oliver.janka@uni-saarland.de

†Electronic supplementary information (ESI) available. See DOI: https://doi.org/10.1039/d4dt02459a

to investigate the differences between water and O_2. Furthermore, it is known that ball milling can not only be used to reduce the particle and crystallite size of a material, but also to introduce defects, activating the material. This can lead to phase transitions,[59] partial reduction[59] or can be used to *e.g.* surface modify transition metal oxides[60,61] or to intercalate Li into activated transition metal oxides.[62,63] Therefore, the precursor $CaAl_2$ was activated *via* high-energy ball milling. The different reaction pathways as well as their intermediates were investigated with the help of powder X-ray diffraction experiments, ^{27}Al solid-state NMR studies, and thermal analyses.

2. Experimental

Synthesis

Precursor $CaAl_2$. Calcium pieces (ChemPur, Karlsruhe, Germany, 99.5%) and aluminum pellets (Onyxmet, Olsztyn, Poland, 99.99%) were used as received for the synthesis of the intermetallic starting material $CaAl_2$. The binary precursor was prepared on a 400–500 mg scale. The Ca pieces were stored under an argon atmosphere; surface contaminations were removed mechanically prior to use. The synthesis of the binary compounds was carried out in a custom-build arc furnace. Elements were transferred under argon into a water-cooled copper hearth and arc-melted under dried argon at 800 mbar.[64] The argon was purified prior to use with titanium sponge (873 K), silica gel, and molecular sieves. To avoid evaporation of Ca, the Al pieces were piled on top and additionally enclosed in Al foil. Careful melting created an encapsulation of the Ca pieces. The resulting bead was turned over and remelted three times to increase the homogeneity. The weight loss in all cases was <1 mass%. The as-cast samples are silver metallic; ground powders are grey and stable in air for months. Phase purity was checked by powder X-ray diffraction (*vide infra*).

High-energy ball milling. For ball milling small amounts of $CaAl_2$ (~1 g of material), a home built stainless steel jar (stainless steel 1.4125) with a volume of approximately 5 mL was used in a Mixer Mill, MM400 (Retsch, Haan, Germany) using one stainless steel ball (∅ = 10 mm; mass of ~4 g) and a frequency of 30 Hz for different times (5–180 min). Before each milling step 300 μL of DME (1,2-dimethoxyethane) were added to the milling jar to avoid cementation. The milling jar was loaded in an argon filled glove box (MBraun UNIlab pro eco) with H_2O and O_2 values below 0.1 and 0.5 ppm, respectively. After every milling step, the jar was transferred back to the glovebox to empty out the milling jar. The powder stuck to the walls was mechanically removed and a small portion was taken for X-ray powder diffraction and thermal analysis/oxidation in an STA system (*vide infra*).

Caution: Ball-milled metals and intermetallic compounds can get pyrophoric after milling. The handling of the samples under an inert atmosphere (*e.g.* inside an Ar filled glove box) is advised.

Oxidation of $CaAl_2$. Oxidation reactions were performed in a STA system (*vide infra*) and a custom-built oxidation setup using a tube furnace (Carbolite Gero GmbH & Co. KG, Neuhausen, Germany) as the heating device. Pure oxygen, as well as wet argon were used as oxidation media. The flow rate for all gases was 20 mL min^{-1}. For the wet argon, argon was bubbled through demineralized, degassed H_2O before entering the furnace. The samples were placed in porcelain boats and centered in the tube furnace.

Thermal analysis/oxidation

Simultaneous thermogravimetric analysis (TGA) and differential scanning calorimetry (DSC) were carried out with a TGA/DSC 1 Star HT/1600 system (Mettler Toledo, Columbus, OH, USA) under an Ar/O_2 atmosphere with flow rates of 40 mL min^{-1} each. For all oxidation experiments heating and cooling rates of 20 K min^{-1} and dwelling periods of 60 min were applied. Samples were placed into alumina crucibles (∅ = 6 mm, h = 4.5 mm) for the STA measurements.

Powder X-ray diffraction

Powder X-ray diffraction (PXRD) patterns of the pulverized samples were recorded at room temperature on a D8-A25-Advance diffractometer (Bruker, Karlsruhe, Germany) in Bragg Brentano θ–θ-geometry (goniometer radius 280 mm) with CuK_α-radiation (λ = 154.0596 pm). A 12 μm Ni foil working as the K_β filter and a variable divergence slit were mounted at the primary beam side. A LYNXEYE detector with 192 channels was used at the secondary beam side. Experiments were carried out in the 2θ range of 6–130° with a step size of 0.013° and a total scan time of 1 h. The recorded data was evaluated using Rietveld refinements[65,66] with the Bruker TOPAS 5.0 software,[67] the fundamental instrument parameters were determined beforehand. The crystallite sizes were determined from TOPAS using the LVol-IB values. For the ball-milled samples, the strain L parameter was refined additionally. To determine the amorphous part of a sample, ~15 mass% of elemental Si were added to the sample and homogenized. During the Rietveld analysis, the contribution of the internal standard was fixed to the weighed value, enabling the determination of an amorphous fraction where present.

SEM/EDX data

Semi-quantitative EDX analyses of one ball-milled sample of $CaAl_2$ were conducted on a JEOL 7000F (JEOL, Freising, Germany) scanning electron microscope equipped with an EDAX Genesis 2000 EDX detector (EDAX, Unterschleissheim, Germany). The sample was sprinkled on conductive carbon tape and one area scans as well as three independent data points were measured.

^{27}Al solid-state MAS NMR

^{27}Al solid-state MAS NMR spectra were recorded on an Avance III 400 WB (Bruker Biospin, Ettlingen, Germany) at 104.35 MHz using magic-angle spinning (MAS). The samples were used as fine powders. To reduce density and electrical

conductivity, samples were mixed with dried sodium chloride in a ratio of 1 : 9 (sample : NaCl) or higher. The diluted samples were loaded into a cylindrical ZrO_2 rotor with a diameter of 4 mm and spun at the magic angle at a frequency of 13 kHz. All experiments conducted were single-pulse experiments with a typical pulse length of 0.83 μs (≈30° pulse) and a relaxation delay of 1 s. Resonance shifts were referenced to an aqueous 1 molar $AlCl_3$ solution. The NMR spectra were recorded using the Bruker Topspin[68] software; the analysis was performed with the help of the Dmfit software.[69]

3. Results and discussion

Precursor characterization

As the starting material, the cubic Laves phase $CaAl_2$ ($MgCu_2$ type, space group $Fd\bar{3}m$, a = 804.02(1) pm)[58,70] was used. It could be shown by XRD and NMR investigations that ~5 mass% of the Al richer phase $CaAl_4$ is present ($CaGa_4$ type, space group $C2/m$, a = 616.91(1), b = 618.50(1) c = 634.34(1) pm, β = 118.03(1)°).[70] When oxidizing this compound with air or pure O_2 the structures of the main products are the ternary oxides $Ca_{12}Al_{14}O_{33}$ (mineral mayenite, own type, space group $I\bar{4}3d$, a = 1198.2 pm)[71] and the expected product $CaAl_2O_4$ (own type, space group $P2_1/c$, a = 870, b = 809.2, c = 1746.9 pm, β = 119.589).[72] Besides these two ternaries, the binary oxides CaO (NaCl type, space group $Fm\bar{3}m$, a = 474 pm)[73] and Al_2O_3 (own type, space group $R\bar{3}c$, a = 486, c = 1324 pm)[73] as well as two other ternary oxides $Ca_3Al_2O_6$ (own type, space group $Pa\bar{3}$, a = 1526.2 pm)[74] and $CaAl_4O_7$ (own type, space group $C2/c$, a = 1289, b = 888, c = 545 pm, β = 107.05°)[75] have to be mentioned as important compounds that are observed during oxidation. A detailed discussion of the chemical structures of these can be found in the original literature cited above or in the previously published work.[58] Fig. 1 depicts a comparative schematic of the previously published results[58] in comparison to the outcome of this work based on the crystal structures involved.

Oxidation of $CaAl_2$ using wet argon

In a first approach of changing the outcome of the oxidation reaction of $CaAl_2$ the idea of using different oxygen sources came up. One possibility is to use water instead of oxygen in the home-built tube furnace setup. However, instead of using pure water, an argon stream was bubbled through degassed, demineralized water and fed into the furnace. The result does not show any noticeable difference to the outcome of the O_2 oxidation, with mayenite ($Ca_{12}Al_{14}O_{33}$) still being the main product. One exception might be that in contrast to small amounts of cubic $Ca_3Al_2O_6$, approximately 5 mass% of the monoclinic oxide $CaAl_4O_7$ could be identified in the powder diffraction pattern (Fig. 2; Table 1).

Ball milling experiments

In the second approach, instead of changing the oxidizing agent, milling of the powders was employed. This can be used to reduce the average crystallite size, increase the surface area of the starting material and introduce defects and amorphous regions or even induce phase transitions.[76–78] At first,

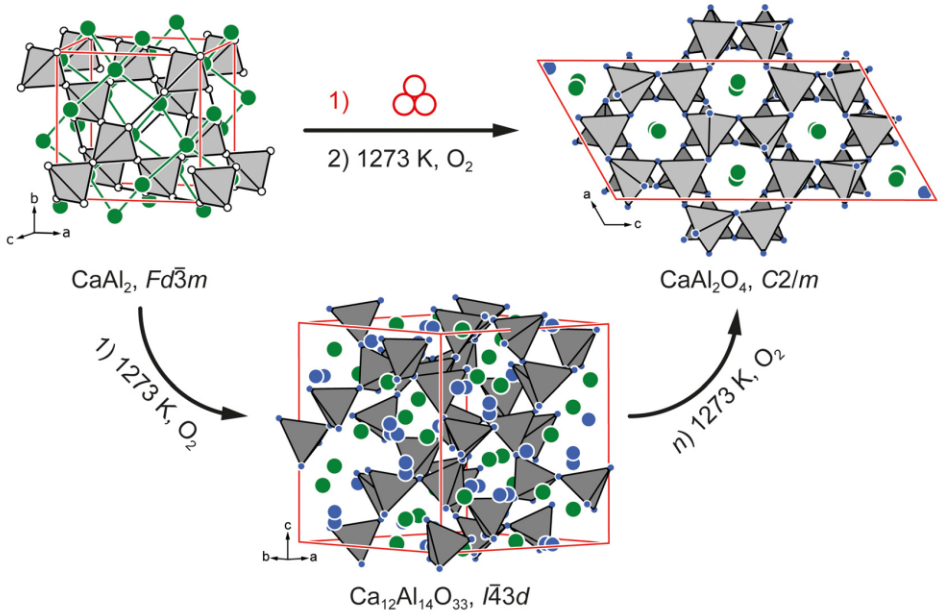

Fig. 1 Two reaction pathways for the oxidation of cubic $CaAl_2$ at 1273 K with elemental O_2. A direct formation of monoclinic $CaAl_2O_4$ is observed when activating the material by ball milling. Without ball milling, cubic $Ca_{12}Al_{14}O_{33}$ is formed initially as previously reported.[58]

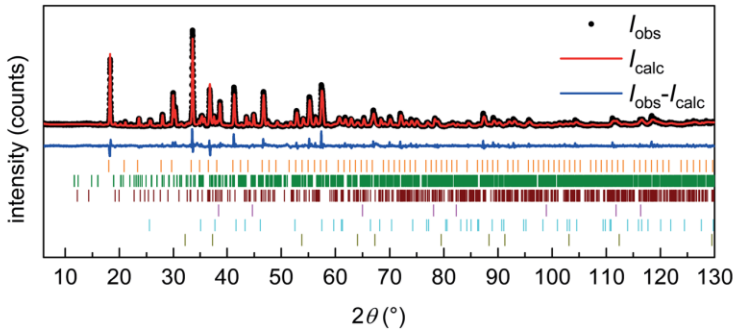

Fig. 2 Powder X-ray diffraction pattern of the oxidation product of $CaAl_2$ in a tube furnace at 1273 K for 1 h using wet argon. Experimental data are shown as black dots, the simulated diffraction pattern from refinement as the red line, the difference is shown as a continuous blue line, and the Bragg positions for $Ca_{12}Al_{14}O_{33}$, $CaAl_2O_4$, $CaAl_4O_7$, Al, Al_2O_3 and CaO are shown as orange, green, brown, pink, cyan and olive ticks.

Table 1 Phase contributions obtained by PXRD (mass%) *via* Rietveld refinement for the oxidation of $CaAl_2$ using wet argon. The standard deviations are ±1 mass%

$Ca_{12}Al_{14}O_{33}$	$CaAl_2O_4$	$CaAl_4O_7$	CaO	Al_2O_3	Al	Fig.
63	13	10	1	8	5	S1

intermetallic $CaAl_2$ was treated in a vibrating ball mill for up to three hours. A significant decrease of the crystallite size during milling could be observed using powder X-ray diffraction. The broadening of the reflections is already visible in the comparison of the powder diffractograms shown in Fig. 3. From the diffraction data it can also be seen that no change in the crystal structures or the phase composition is observed. Fig. 4a illustrates the decrease of the crystallite size over time; for a second batch the crystallite sizes of the starting material and the 30 min milled material are shown. The crystallite size decreases with an almost exponential decay over the milling intervals starting from >350 nm down to roughly 50 nm after three hours (Table 2). A second batch that was milled for 30 min straight shows comparable results. The decrease in crystallite size could also be proven by ^{27}Al solid state NMR experiments. The spectra for the species milled for 90 and 180 minutes show almost identical shifts and signal shapes; only a broadening of the central transition and spinning sidebands is visible as can be seen in Fig. 4b. However, a significant effect is visible when compared to pristine $CaAl_2$.[70,79] This clearly shows that the crystallite size is reduced alongside the formation of defects leading to broadened NMR resonances. Detailed simulations of the spectra can be found in the ESI.† To verify this even further, powder X-ray diffraction experiments with known amounts of Si as the internal standard were conducted on the 30 and 180 min ball milled samples. In this way, the amorphous phase contribution can be determined. For the 30 min milled sample the amorphous phase amounts to 5(1) mass% while at 180 min 20(1) mass% are observed. Fig. S37 and S38† show the respective diffraction data along with the Rietveld fits. The sample milled for 30 min was additionally examined by SEM/EDX investigations. No abrasion of the milling jar can be observed as no Fe can be found in the EDX results.

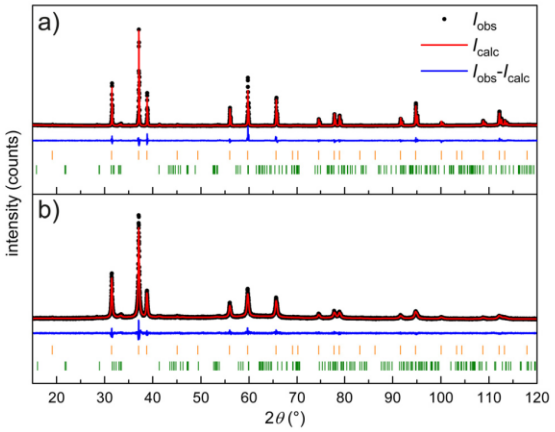

Fig. 3 Powder X-ray diffraction patterns of $CaAl_2$ as the pristine material obtained (a) after arc melting and (b) after 180 min ball milling. Experimental data are shown as black dots, the simulated diffraction pattern from refinement as the red line, the difference is shown as a continuous blue line, and the Bragg positions for $CaAl_2$ and $CaAl_4$ are shown in orange and green ticks.

Oxidation experiments after ball milling

To study the impact of the milling on the oxidation behavior the milled samples were transferred to an STA system. Since the transfer of the samples into the system was not possible fully under argon, the measurement was started as fast as possible. For all samples except for the one milled for 180 min, no obvious oxidation during the transfer was observed. However, for the latter, a pyrophoric behavior was observed. Powder X-ray diffraction did not show a decomposition of the starting material after 180 min of ball milling (Fig. S11†). However, since a significant amorphous contri-

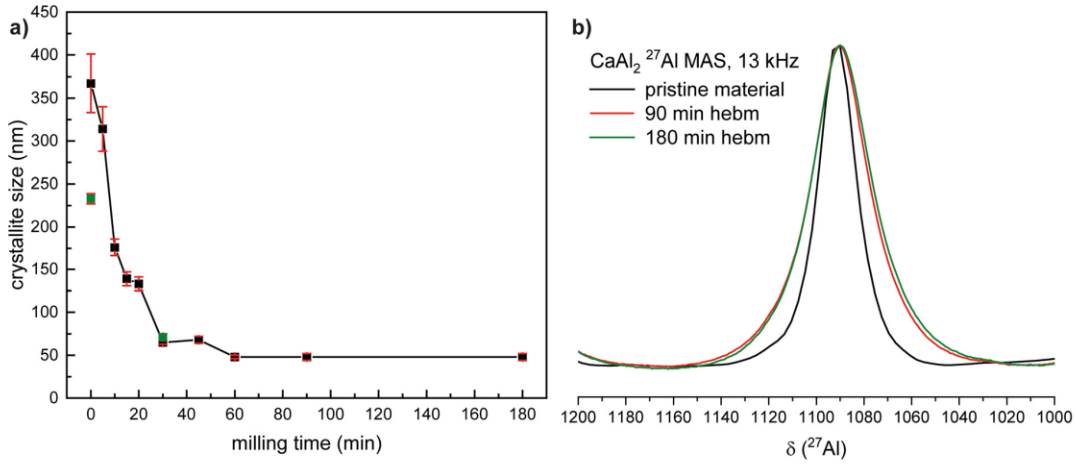

Fig. 4 (a) Decrease of the crystallite size (determined as LVol-IB) as a function of milling time, extracted from the powder diffractograms using the TOPAS software. The estimated standard deviations are indicated by error bars. The data of a second batch are shown in green. (b) ^{27}Al MAS NMR spectra for $CaAl_2$ as the pristine material (black) and after 90 and 180 minutes (red and green) of ball milling.

Table 2 Crystallite size (determined as LVol-IB) of the milled $CaAl_2$ samples at different milling times. The determined amorphous phase contributions are given

Milling time/min	Crystallite size/nm	Amorphous phase/mass%	Fig.
0	367(34)	0	S2
5	314(26)		S3
10	176(10)		S4
15	139(8)		S5
20	133(8)		S6
30	65(2)	5(1)	S7/S37
45	68(4)		S8
60	48(2)		S9
90	48(4)		S10
180	48(4)	20(1)	S11/S38

bution was deduced (*vide supra*), it is likely that the mechanochemical treatment produced a material with an increased surface area and introduced defects near/at the surface. As known for nanoparticles of ignoble metals, these are highly pyrophoric.[76–78,80–83] A similar situation could be assumed here.

Fig. 5 shows a comparison of the obtained STA data for the starting material and the milled materials after 90 and 180 minutes. For pristine $CaAl_2$, a highly exothermic reaction (Fig. 5a, red trace) at 1130 K can be observed, raising the temperature inside the STA system significantly (Fig. 5a, green trace). Furthermore, a multi-step reaction seems to take place as multiple effects are visible in the heat flux curve. In addition, a significant mass increase can be observed (Fig. 5a, black trace). The powder X-ray diffraction pattern also significantly changes. After oxidation, (Fig. 5b), several oxides can be observed, in line with what was reported previously.[58] When oxidizing the material that was ball milled for 5 min in the STA system (Fig. S14†), an increase of $CaAl_2O_4$ can be observed right away based on powder X-ray diffraction. Fig. 5c depicts the STA results of $CaAl_2$ ball milled for 90 min. In the heat flux (red trace) it becomes evident that the heat signature becomes smeared and less intense (note that the scale bar for the heat flux is the same in all STA graphs). The overall area remains almost the same, indicating an earlier onset and an overall less pronounced reaction onset. The mass increase is a little steeper than before; however, the overall mass gain (+53 mass%) is the same for pristine and 90 min ball milled $CaAl_2$. The corresponding powder diffraction pattern is shown in Fig. 5d, indicating a different phase composition compared to the oxidized pristine material (Fig. 5b). Fig. 5e finally shows the STA results from the pyrophoric $CaAl_2$ that was ball milled for 180 min and Fig. 5f shows the corresponding powder X-ray diffraction pattern. When the sample was transferred to the STA crucible, an initial reaction was observed that stopped by itself after some seconds. It is assumed that this initial oxidation only happens on the surface and does not proceed throughout the sample, similar to what was shown for *e.g.* AlNi.[84] This assumption is strengthened by the STA results. There is still a mass increase of +42 mass%, which is, however, smaller than the one for the pristine and 90 min milled material. Finally, the amorphous phase contributions of the 30 and 180 min milled oxidized materials were determined. In both cases, the amorphous phase contribution amounts to <1 mass% (Fig. S39 and S40†).

Overall, it can be seen that with prolonged milling times, the amount of $Ca_{12}Al_{14}O_{33}$ steadily decreases while at the same time the amount of $CaAl_2O_4$ increases (Table 3). Fig. 6 depicts the evolution of the ratio between the two interesting main oxides; a plot of all phases present is shown in Fig. S36† and is given in Table 3. This observation underlines our previous assumption: Ca diffuses to the surface of the particle,

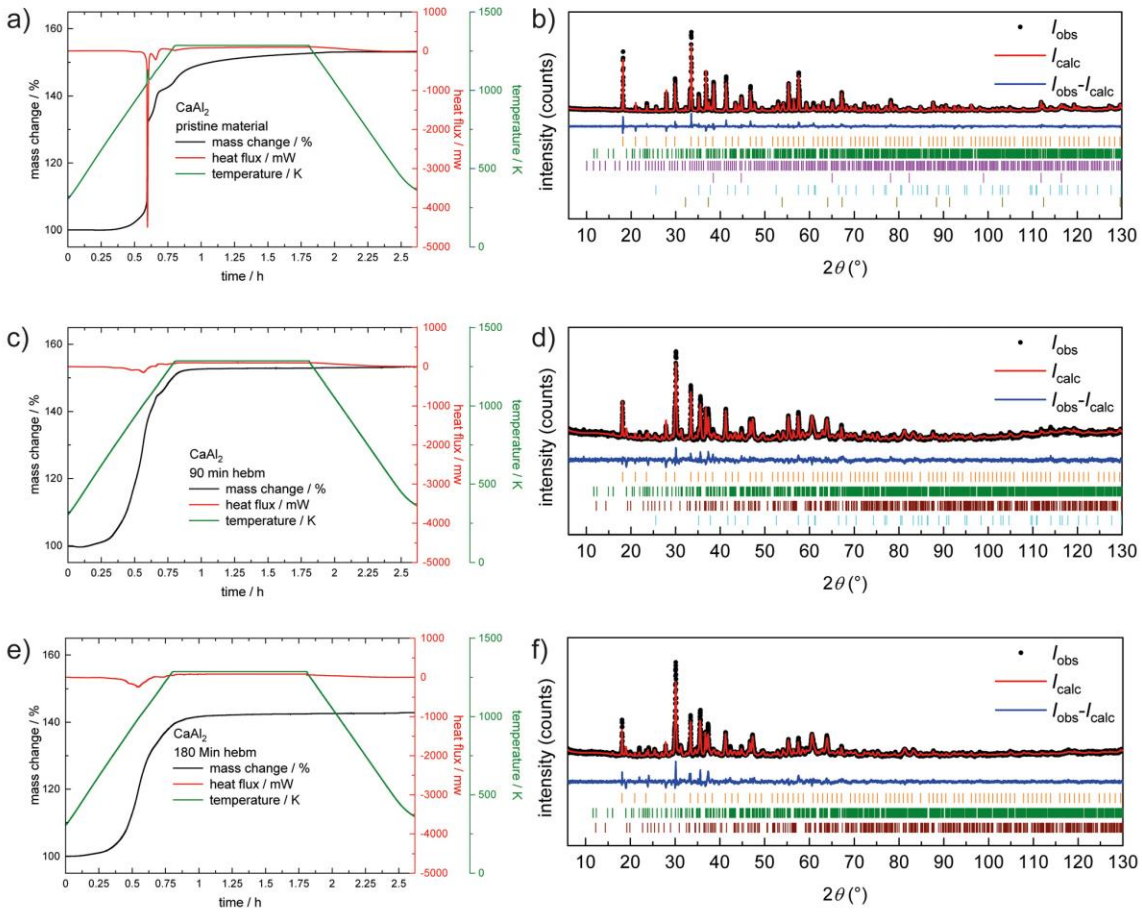

Fig. 5 STA experiments (mass change in black, heat flux in red and temperature program in green) and the corresponding Rietveld refinements of the collected powder X-ray diffraction data for the respective oxidation products of pristine (a, b) $CaAl_2$ and after 90 (c, d) and 180 (e, f) minutes ball milling. Experimental data are shown as black dots, the simulated diffraction pattern from refinement as the red line, the difference is shown as a continuous blue line, and the Bragg positions for $Ca_{12}Al_{14}O_{33}$, $CaAl_2O_4$, $Ca_3Al_2O_6$, $CaAl_4O_7$, Al, Al_2O_3 and CaO are shown as orange, green, purple, brown, pink, cyan and olive ticks.

Table 3 Results of the Rietveld refinements from powder X-ray diffraction data of the STA treated samples after different milling times. The standard deviations for the determined mass% are ±1 mass%

	Phase contributions obtained by PXRD (mass%)							
Milling time (min)	$Ca_{12}Al_{14}O_{33}$	$CaAl_2O_4$	$Ca_3Al_2O_6$	$CaAl_4O_7$	CaO	Al_2O_3	Al	Fig.
0	56	8	10	0	3	13	10	S13
5	57	20	4	0	0	11	8	S14
10	50	32	0	7	0	8	3	S15
15	46	37	0	7	0	7	3	S16
20	40	44	0	8	0	6	2	S17
30	34	50	0	7	0	7	2	S18
45	28	61	0	6	0	4	1	S19
60	26	63	0	8	0	3	0	S20
90	26	65	0	7	0	2	0	S21
180	19	69	0	12	0	0	0	S22

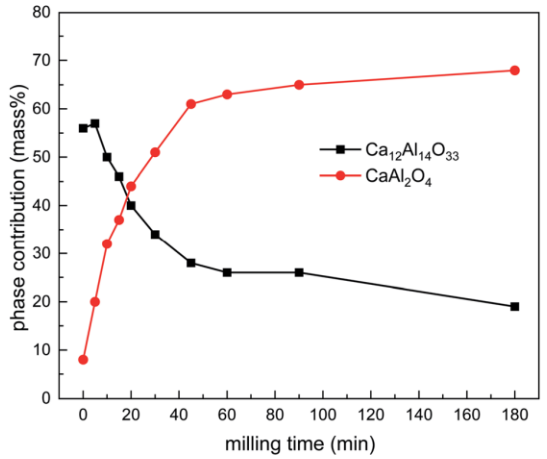

Fig. 6 Results of the Rietveld refinements of the oxidation reactions after different milling times (selected phases only). For all observed phases see Fig. S36.†

enabling the formation of $Ca_{12}Al_{14}O_{33}$ and leaving elemental Al behind.[58] When ball milling $CaAl_2$, the crystallite size gets significantly reduced, shortening the Ca diffusion path length, hampering the formation of the mayenite type structure and enabling the direct formation of $CaAl_2O_4$. This is furthermore in line with our previous quantum-chemical calculations,[58] rendering both competing oxides similar in formation energy with $CaAl_2O_4$ being the thermodynamically slightly more stable compound.

Finally, we want to address the crystallite sizes determined for the oxidized material. As shown in Fig. 4a, the crystallite size of the ball milled $CaAl_2$ steadily decreases with increasing milling time. When analyzing the crystallite sizes of the oxidized material from the STA investigations, the sample after 5 min of ball milling shows 36(3) nm for $CaAl_2O_4$ and 84(2) nm for $Ca_{12}Al_{14}O_{33}$. The crystallite sizes of $CaAl_2O_4$ roughly stay the same regardless of the applied milling time; for $Ca_{12}Al_{14}O_{33}$ an increase to ~120 nm for 10–30 min is visible followed by a decrease to ~50 nm for the 60 and 90 min milled samples. However, there is no clear trend visible in these data (Table S1†).

4. Conclusion

The intermetallic Laves phase $CaAl_2$ was oxidized in two ways: using water (in Ar) and pure O_2 after ball milling. While in the first case no difference between elemental oxygen and the unball milled material can be observed, the ball milled $CaAl_2$ is oxidized in a significantly different way. This can be attributed to a reduced crystallite size of $CaAl_2$ which is ~50 nm after 180 min of ball milling. Interestingly, ^{27}Al solid-state MAS NMR investigations on the milled material clearly showed that alongside the drastically reduced crystallite size also strain is observed in the material as the NMR signals broaden. STA investigations finally confirmed that ball milling has an influence on the oxidation behavior. While the pristine un-milled sample shows an intense sharp exothermic reaction, the milled samples show a significantly broadened effect while the area of the signal is approximately the same as for pristine $CaAl_2$. Up to 90 minutes of milling all samples exhibit a similar mass gain of ~150 mass%. When $CaAl_2$ is milled for 180 min, the sample becomes pyrophoric; however, the reaction is not self-sustaining. This leads to the assumption that only the surface is oxidized as an additional mass gain is still observed in the STA experiments. The main product of the oxidation reaction of pristine $CaAl_2$ is $Ca_{12}Al_{14}O_{33}$ which crystallizes in the so called mayenite type structure. For the milled samples, the respective amount of $Ca_{12}Al_{14}O_{33}$ drops in almost an exponential fashion while instead the stochiometric oxidation product $CaAl_2O_4$ is formed in higher amounts. The presented results clearly show that already short ball milling times can significantly influence the reaction pathway and therefore drastically shift the product scope.

Author contributions

Conceptualization by GK and OJ; synthetic work by ECJG; initial draft of the manuscript by ECJG. ECJG performed the XRD, STA and ^{27}Al NMR investigations; the entire work was supervised, guided, and revised by GK and OJ. The manuscript was corrected by all authors and finalized by GK and OJ.

Data availability

Details on the Rietveld refinements, crystallite sizes, STA curves, and ^{27}Al NMR spectroscopic data can be found in the ESI.†

The data supporting this article have been included as part of the ESI.†

Conflicts of interest

The authors declare no competing interests.

Acknowledgements

We thank Stefan Engel for the SEM/EDX investigations. Special thanks to Sylvia Beetz from the MWWT/Inorganic Chemistry workshop of Saarland University and to Britta Schreiber from the central glassblowing workshop for supplying parts and installing the furnace for the oxidation experiments. Instrumentation and technical assistance for this work were provided by the Service Center X-ray Diffraction, with financial support from Saarland University and German Science Foundation (project number INST 256/349-1) and by the Service Center NMR with financial support from Saarland University and German Research Foundation DFG (INST 256/384-1).

References

1 F. Ostermann, *Anwendungstechnologie Aluminium*, Springer Vieweg, Berlin, Heidelberg, Germany, 2014.
2 C. Kammer, *Aluminium-Taschenbuch 1: Grundlagen und Werkstoffe*, Aluminium-Zentrale, Düsseldorf, Germany, 1995.
3 C. Jaschik, H. Haferkamp and M. Niemeyer, *in Magnesium Alloys and their Applications*, Wiley-VCH Verlag GmbH, Weinheim, Germany, 2000, pp. 41–46.
4 M. K. Kulekci, *Int. J. Adv. Des. Manuf. Technol.*, 2008, **39**, 851–865.
5 O. Janka, in *Applied Inorganic Chemistry*, ed. R. Pöttgen, T. Jüstel and C. A. Strassert, De Gruyter, Berlin, Germany, 2023, pp. 158–173.
6 Empire State Realty Trust, Empire State Building Fact Sheet, **https://www.esbnyc.com/sites/default/files/esb_fact_sheet_4_9_14_14.pdf**.
7 FMGB Guggenheim Bilbao Museoa, **https://www.guggenheim-bilbao.eus/de/**, (accessed 28.06.2023).
8 C. Veiga, J. P. Davim and A. J. R. Loureiro, *Rev. Adv. Mater. Sci.*, 2012, **32**, 14–34.
9 M. V. Ribeiro, M. R. V. Moreira and J. R. Ferreira, *J. Mater. Process. Technol.*, 2003, **143–144**, 458–463.
10 M. Peters, J. Hemptenmacher, J. Kumpfert and C. Leyens, in *Titanium and Titanium Alloys*, Wiley-VCH Verlag GmbH, Weinheim, Germany, 2003, pp. 1–36.
11 J. Barksdale, in *The encyclopedia of the chemical elements*, ed. C. A. Hampel, Reinhold Book Corp., New York, USA, 1968, pp. 732–738.
12 P. Enghag, in *Encyclopedia of the Elements: Technical Data – History – Processing – Applications*, ed. P. Enghag, Wiley VCH Verlag GmbH, Weinheim, Germany, 2004, pp. 493–509.
13 M. Peters and C. Leyens, *Titan und Titanlegierungen*, Wiley-VCH, Weinheim, Germany, 2002.
14 S. Engel and O. Janka, in *Applied Inorganic Chemistry*, ed. R. Pöttgen, T. Jüstel and C. A. Strassert, De Gruyter, 2023, pp. 255–264.
15 S. Engel and O. Janka, in *Applied Inorganic Chemistry*, ed. R. Pöttgen, T. Jüstel and C. A. Strassert, De Gruyter, 2023, pp. 265–270.
16 E. Gillam, H. P. Rooksby and L. D. Brownlee, *Acta Crystallogr.*, 1964, **17**, 762–763.
17 O. Janka and R. Pöttgen, *Z. Naturforsch., B: Chem. Sci.*, 2020, **75**, 421–439.
18 M. Buchner and O. Janka, in *Applied Inorganic Chemistry*, ed. R. Pöttgen, T. Jüstel and C. A. Strassert, De Gruyter, 2023, pp. 221–228.
19 J. R. Davis, *ASM Specialty Handbook: Aluminum and Aluminum Alloys*, ASM International, Materials Park, OH, USA, 1993.
20 D. Altenpohl, *Aluminium und Aluminiumlegierungen*, Springer, Berlin, Heidelberg, Germany, 1965.
21 P. K. Datta, H. L. Du, J. S. Burnell-Gray and R. E. Ricker, in *Corrosion: Materials*, ASM International, Materials Park, OH, USA, 2005, vol. 13B.
22 R. K. Gupta and B. Pant, in *Intermetallic Matrix Composites*, ed. R. Mitra, Woodhead Publishing, Sawston, Cambridge, England, 2018, pp. 71–93.
23 F. Appel, U. Brossmann, U. Christoph, S. Eggert, P. Janschek, U. Lorenz, J. Müllauer, M. Oehring and J. D. H. Paul, *Adv. Eng. Mater.*, 2000, **2**, 699–720.
24 C. Kenel, A. Lis, K. Dawson, M. Stiefel, C. Pecnik, J. Barras, A. Colella, C. Hauser, G. J. Tatlock, C. Leinenbach and K. Wegener, *Intermetallics*, 2017, **91**, 169–180.
25 K. Meng, K. Guo, Q. Yu, D. Miao, C. Yao, Q. Wang and T. Wang, *Corros. Sci.*, 2021, **183**, 109320.
26 P. A. Loginov, G. M. Markov, N. V. Shvyndina, G. V. Smirnov and E. A. Levashov, *Ceramics*, 2022, **5**, 389–403.
27 S. A. Kekare and P. B. Aswath, *J. Mater. Sci.*, 1997, **32**, 2485–2499.
28 Z. Li, W. Gao, Y. He and S. Li, *High Temp. Mater. Processes*, 2002, **21**, 35–46.
29 R. Pflumm, S. Friedle and M. Schütze, *Intermetallics*, 2015, **56**, 1–14.
30 A. Rahmel, M. Schütze and W. J. Quadakkers, *Mater. Corros.*, 1995, **46**, 271–285.
31 G. Geramifard, C. Gombola, P. Franke and H. J. Seifert, *Corros. Sci.*, 2020, **177**, 108956.
32 H. J. Grabke, M. W. Brumm and B. Wagemann, *Mater. Corros.*, 1996, **47**, 675–677.
33 H. Qin, X. Chen, L. Li, P. W. Sutter and G. Zhou, *Proc. Natl. Acad. Sci. U. S. A.*, 2015, **112**, E103–E109.
34 Y.-O. Yoon, S.-H. Ha, G.-Y. Yeom, H. K. Lim and S. K. Kim, in *Light Metals 2013*, Springer, Cham, Germany, 2013, pp. 323–326.
35 P. Villars and K. Cenzual, *Pearson's Crystal Data: Crystal Structure Database for Inorganic Compounds*, ASM International®, Materials Park, Ohio, USA, 2023.
36 T. B. Massalski, H. Okamoto, P. R. Subramanian and L. Kacprzak, *Binary alloy phase diagrams*, ASM International, Ohio, U.S.A., 2nd edn, 1990.
37 R. Hoppe and H.-J. Röhrborn, *Naturwissenschaften*, 1961, **48**, 453–454.
38 R. Hoppe and H.-J. Röhrborn, *Z. Anorg. Allg. Chem.*, 1964, **327**, 199–206.
39 R. Hoppe, *J. Solid State Chem.*, 1986, **65**, 127–144.
40 H. D. Wasel-Nielen and R. Hoppe, *Z. Anorg. Allg. Chem.*, 1968, **359**, 36–40.
41 P. J. Yvon, R. B. Schwarz, C. B. Pierce, L. Bernardez, A. Conners and R. Meisenheimer, *Phys. Rev. B: Condens. Matter Mater. Phys.*, 1989, **39**, 6690–6693.
42 W. Schauerte, H. U. Schuster, N. Knauf and R. Müller, *Z. Anorg. Allg. Chem.*, 1992, **616**, 186–190.
43 B. Cogel and H. U. Schuster, *Z. Anorg. Allg. Chem.*, 1993, **619**, 1765–1770.
44 H. Schuster and J. Wittrock, *J. Therm. Anal. Calorim.*, 1993, **39**, 1397–1401.
45 A. Panahandeh and W. Jung, *Z. Anorg. Allg. Chem.*, 2003, **629**, 1651–1660.

46 P. Moser, W. Jung and H. U. Schuster, *Z. Anorg. Allg. Chem.*, 1997, **623**, 1781–1785.
47 P. Moser and W. Jung, *Z. Anorg. Allg. Chem.*, 1998, **624**, 1251–1255.
48 P. Moser, H. M. Schwunck and W. Jung, *Z. Anorg. Allg. Chem.*, 1998, **624**, 1256–1261.
49 H. M. Schwunck, P. Moser and W. Jung, *Z. Anorg. Allg. Chem.*, 1998, **624**, 1262–1266.
50 H. M. Schwunck, P. Moser and W. Jung, *Z. Anorg. Allg. Chem.*, 1999, **625**, 407–410.
51 H. M. Schwunck, P. Moser and W. Jung, *Z. Anorg. Allg. Chem.*, 1999, **625**, 463–466.
52 P. Moser, V. Cirpus and W. Jung, *Z. Anorg. Allg. Chem.*, 1999, **625**, 714–718.
53 P. Moser and W. Jung, *Z. Anorg. Allg. Chem.*, 2000, **626**, 1421–1425.
54 B. Eisenmann, M. Jakowski, W. Klee and H. Schäfer, *Rev. Chim. Miner.*, 1983, **20**, 255–263.
55 M. Tampier, D. Johrendt, R. Pöttgen, G. Kotzyba, H. Trill and B. D. Mosel, *Z. Anorg. Allg. Chem.*, 2002, **628**, 1243–1245.
56 E. C. J. Gießelmann, S. Engel, S. Pohl, M. Briesenick, L. P. Rüthing, C. Kloos, A. Koldemir, L. Schumacher, J. Schmedt auf der Günne, G. Kickelbick and O. Janka, *Chem. Mater.*, 2024, DOI: 10.1021/acs.chemmater.4c02093.
57 J. Sappl, F. Jung and C. Hoch, *Chem. Mater.*, 2020, **32**, 866–873.
58 E. C. J. Gießelmann, S. Engel, J. G. Volpini, H. Huppertz, G. Kickelbick and O. Janka, *Inorg. Chem. Front.*, 2024, **11**, 286–297.
59 A. Betke and G. Kickelbick, *New J. Chem.*, 2014, **38**, 1264–1270.
60 A. Fischer, C. Ney and G. Kickelbick, *Eur. J. Inorg. Chem.*, 2013, **2013**, 5701–5707.
61 A. Betke and G. Kickelbick, *Inorganics*, 2014, **2**, 410–423.
62 D. Becker, M. Klos and G. Kickelbick, *Inorg. Chem.*, 2019, **58**, 15021–15024.
63 D. Becker, R. Haberkorn and G. Kickelbick, *Eur. J. Inorg. Chem.*, 2019, **2019**, 4835–4845.
64 R. Pöttgen, T. Gulden and A. Simon, *GIT Labor-Fachz.*, 1999, **43**, 133–136.
65 H. M. Rietveld, *Acta Crystallogr.*, 1967, **22**, 151–152.
66 H. M. Rietveld, *J. Appl. Crystallogr.*, 1969, **2**, 65–71.
67 Bruker AXS Inc., *Topas, Version 5*, Karlsruhe, Germany, 2014.
68 Bruker Corp., *Topspin*, Karlsruhe, 2008.
69 D. Massiot, F. Fayon, M. Capron, I. King, S. Le Calvé, B. Alonso, J.-O. Durand, B. Bujoli, Z. Gan and G. Hoatson, *Magn. Reson. Chem.*, 2002, **40**, 70–76.
70 S. Engel, E. C. J. Gießelmann, L. E. Schank, G. Heymann, K. Brix, R. Kautenburger, H. P. Beck and O. Janka, *Inorg. Chem.*, 2023, **62**, 4260–4271.
71 W. Büssem and A. Eitel, *Z. Kristallogr.*, 1936, **95**, 175–188.
72 W. Hörkner and H. Müller-Buschbaum, *J. Inorg. Nucl. Chem.*, 1976, **38**, 983–984.
73 W. P. Davey and E. O. Hoffman, *Phys. Rev.*, 1920, **15**, 333.
74 H. E. Swanson, N. T. Gilfrich and G. M. Ugrinic, *Natl. Bur. Stand. Circ.*, 1955, **5**, 10–13.
75 E. Boyko and L. G. Wisnyl, *Acta Crystallogr.*, 1958, **11**, 444–445.
76 H. Yang and H. Bakker, *Mater. Sci. Eng., A*, 1994, **181–182**, 1207–1211.
77 P. Baláž, M. Achimovičová, M. Baláž, P. Billik, Z. Cherkezova-Zheleva, J. M. Criado, F. Delogu, E. Dutková, E. Gaffet, F. J. Gotor, R. Kumar, I. Mitov, T. Rojac, M. Senna, A. Streletskii and K. Wieczorek-Ciurowa, *Chem. Soc. Rev.*, 2013, **42**, 7571–7637.
78 D. Tan and F. García, *Chem. Soc. Rev.*, 2019, **48**, 2274–2292.
79 C. Benndorf, H. Eckert and O. Janka, *Acc. Chem. Res.*, 2017, **50**, 1459–1467.
80 A. Egeberg, T. Block, O. Janka, O. Wenzel, D. Gerthsen, R. Pöttgen and C. Feldmann, *Small*, 2019, **15**, 1970200.
81 T. Klein, C. Pauly, F. Mücklich and G. Kickelbick, *Intermetallics*, 2020, **124**, 106851.
82 T. Klein and G. Kickelbick, *Nanotechnology*, 2020, **31**, 265605.
83 S. Riegsinger, R. Popescu, D. Gerthsen and C. Feldmann, *Chem. Commun.*, 2022, **58**, 7499–7502.
84 G. Kresse, M. Schmid, E. Napetschnig, M. Shishkin, L. Köhler and P. Varga, *Science*, 2005, **308**, 1440–1442.

5.4.2 Rapid Synthesis of a Green Emitting Phosphor by Sulfidation of Intermetallic $EuAl_2$ and its Use in a Hybrid Material

Published as an article:

Elias C. J. Gießelmann, Stefan Engel, Svenja Pohl, Max Briesenick, Lukas P. Rüthing, Cedric Kloos, Aylin Koldemir, Lars Schumacher, Joshua Wiethölter, Jörn Schmedt auf der Günne, Guido Kickelbick and Oliver Janka, *Chem. Mater.* **2025**, *37,* 97.

https://doi.org/10.1021/acs.chemmater.4c02093

Elias Gießelmann, Dr. Stefan Engel and Cedric Kloos conducted the synthetic work of the intermetallic compounds and sulfidation products. Svenja Pohl and Max Briesenick did the incorporation of the $EuAl_2S_4$ into a melting gel and measured the UV-Vis and Fluorescence spectra. Aylin Koldemir and Joshua Wiethölter performed the Mößbauer spectroscopic investigations, Lars Schumacher the magnetic characterization experiments. Lukas Rüthing and Prof. Dr. Jörn Schmedt auf der Günne measured the solid state NMR MQ/MAS spectra. Prof. Dr. Guido Kickelbick and PD Dr. Oliver Janka supervised the work and finalized the manuscript.

Summary

As explained in section 2.2.1, the use of an intermetallic precursor for the synthesis of ternary aluminum compounds was already known to literature for the synthesis of the isostructural aluminum sulfides $CaAl_2S_4$ and $SrAl_2S_4$. Since the *AE* to Al ratios correspond to the compositions of the before investigated Laves phases $CaAl_2$, respectively $SrAl_2$ (KHg_2 type, *Imma*), this seemed to be a good starting point for the research on the synthesis of the heavier chalcogenides. In addition to these two aluminum sulfides, a third known isostructural compound, $EuAl_2S_4$, was reported. This compound was previously obtained by the reaction of EuS, elemental Al and gaseous H_2S.

In the following study all three sulfides were synthesized from the intermetallic precursor. All compounds could be obtained as X-ray pure samples. A detailed spectroscopic characterization was conducted. For the diamagnetic Sr and Ca compounds simple single pulse excitation ^{27}Al solid state NMR spectra showed an unresolvable overlap of two signals. A 2D

experiment, namely MQ-MAS, was applied to resolve the line shape and confirm the crystal structure with two slightly different Al sites.

For the air-stable Eu compound, ^{151}Eu Mössbauer spectra, the temperature dependent magnetic properties and luminescence spectra were measured, all confirming the divalent oxidation state of europium. It should be mentioned that an excess of sulfur within the reaction mixture did not lead to further oxidation of Eu. In cooperation with Svenja Pohl and Max Briesenick from the Kickelbick group, the highly luminescent powder of $EuAl_2S_4$ was embedded in multiple polysiloxane-polysilsequioxane matrices that function as an optical filter on one hand and a barrier towards moisture and oxygen on the other.

CHEMISTRY OF MATERIALS

pubs.acs.org/cm

Article

Rapid Synthesis of a Green Emitting Phosphor by Sulfidation of Intermetallic $EuAl_2$ and its Use in a Hybrid Material

Published as part of Chemistry of Materials special issue "In Memory of Prof. Francis DiSalvo".

Elias C. J. Gießelmann,[#] Stefan Engel,[#] Svenja Pohl, Max Briesenick, Lukas P. Rüthing, Cedric Kloos, Aylin Koldemir, Lars Schumacher, Joshua Wiethölter, Jörn Schmedt auf der Günne, Guido Kickelbick, and Oliver Janka*

Cite This: *Chem. Mater.* 2025, 37, 97−108

Read Online

ACCESS | Metrics & More | Article Recommendations | Supporting Information

ABSTRACT: Ternary sulfides are usually synthesized from the binary sulfidic precursors at elevated temperatures using prolonged reaction times and sometimes H_2S atmosphere to remove residual oxygen. The direct synthesis from the elements is usually hampered by the highly exothermic reaction vaporizing the sulfur. One way to suppress this exothermic reaction is to use a prereacted metallic precursor. In this work, the well-defined and crystalline intermetallic compounds $CaAl_2$, $SrAl_2$, and $EuAl_2$ have been reacted with elemental sulfur in less than 24 h at 1173 K achieving phase pure samples of $CaAl_2S_4$, $SrAl_2S_4$, and $EuAl_2S_4$, according to powder X-ray diffraction. While the first two are extremely sensitive to moisture, the latter is air and moisture stable and could therefore be characterized with respect to its magnetic and luminescent properties as well as by ^{151}Eu Mössbauer spectroscopy. All methods clearly confirm the divalent oxidation state of the Eu atoms. Since $CaAl_2S_4$ and $SrAl_2S_4$ are diamagnetic materials, we have investigated these by ^{27}Al solid state MAS NMR to verify the crystal structure and gain further information about the local Al environment. Subsequently, three polysiloxane-polysilsesquioxane-based materials with phenyl, naphthyl, and phenanthrenyl groups were used as a water impermeable material to embed powdered $EuAl_2S_4$ and investigate the luminescent properties of the resulting hybrid material.

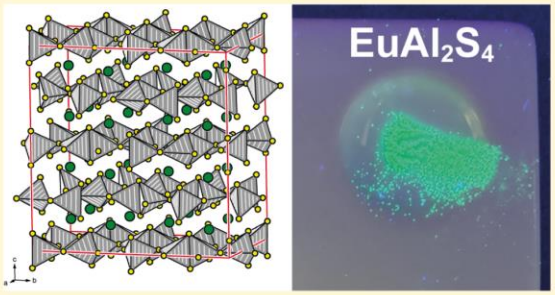

INTRODUCTION

Alloys and intermetallic compounds are an important class of materials for numerous modern everyday applications. Light weight alloys, usually of Be, Mg, Al, and Ti, are used in transportation, construction and consumer goods,[1−7] while *RE*−Co (*RE* = rare earth) and Nd−Fe−B magnets belong to the most commonly used permanent magnets nowadays.[8,9] Several intermetallic materials, Ni_3Al, NiAl, Ti_3Al, TiAl and $TiAl_3$, just to name a few, can be further used due to their high thermal stability and corrosion resistance,[10−13] while others are capable materials for heterogeneous catalysis.[14−19] Among the most common and probably also most investigated intermetallic compounds are the so-called Laves phases, named after the German mineralogist *Fritz H. Laves*.[20−22] The Pearson database[23] lists over 3000 entries and they are still an active field of research.[24−34] The binary Laves phases, all have the same AB_2 general composition and three prototypes are known: the two hexagonal variants $MgZn_2$ (C14)[35,36] and $MgNi_2$ (C36)[37,38] (both space group type $P6_3/mmc$)[39] and the cubic $MgCu_2$ (C15, $Fd\bar{3}m$) type.[40] The importance of the Laves-phases was honored in a special issue of *Zeitschrift für Kristallographie* in 2006 on the occasion of Laves' 100th birthday.[20,21,41−46]

As indicated above, several intermetallic compounds are used as highly corrosion resistant materials, especially if (late) transition metals are involved. However, intermetallic compounds of oxophilic elements such as aluminum and e.g., the alkaline-earth elements could potentially be used as starting materials for the synthesis of known and thus far unknown oxides. Recently, we have shown that the oxidation of $CaAl_2$ is less straightforward as one would expect. Instead of the expected oxidation product $CaAl_2O_4$, mayenite type $Ca_{12}Al_{14}O_{33}$ is initially formed which can be processed multiple times to finally yield the expected product.[47] In a recently published paper, an intermetallic precursor could be used to form the oxide as well as

Received: July 26, 2024
Revised: November 12, 2024
Accepted: November 12, 2024
Published: December 23, 2024

Table 1. Lattice Parameters, Refined From Powder X-ray Diffraction, and Structure Types of $CaAl_2$, $SrAl_2$, $EuAl_2$, $CaAl_2S_4$, $SrAl_2S_4$ and $EuAl_2S_4$ As Well As Literature Values[a]

Nominal composition	Structure type	a (pm)	b (pm)	c (pm)	V (nm^3)	ref.
$CaAl_2$	$MgCu_2$ ($Fd\bar{3}m$)	804.0	a	a	0.5198	[b]
		802.2	a	a	0.5162	65
		804.0	a	a	0.5197	66
		804.0	a	a	0.5198	30
$SrAl_2$	KHg_2 ($Imma$)	479.6	789.7	795.8	0.3013	[b]
		484	792	799	0.3063	67
		479.3	792.2	793.7	0.3013	68
		479.6	789.3	795.5	0.3011	30
$EuAl_2$	$MgCu_2$ ($Fd\bar{3}m$)	812.8	a	a	0.5370	[b]
		812.5	a	a	0.5364	69
$CaAl_2S_4$	$EuGa_2S_4$ ($Fddd$)	1205.1	2003.2	2016.3	4.8672	[b]
		1202.6	2005.2	2016.3	4.8622	53
$SrAl_2S_4$	$EuGa_2S_4$ ($Fddd$)	1213.0	2045.8	2089.7	5.1859	[b]
		1212.3	2036.0	2081.7	5.1381	53
$EuAl_2S_4$	$EuGa_2S_4$ ($Fddd$)	1211.4	2038.9	2077.7	5.1313	[b]
		1210.2	2038	2074	5.1153	54

[a]The standard deviations for the lattice parameters are ±0.1 pm or smaller. [b]This work.

the sulfide $LiGaX_2$ (X = O, S) using the intermetallic lithium gallide LiGa as starting material[48] and also Eu_2GeS_2 (both the α- and β-modification) could be obtained by the reaction of Eu_2Ge with elemental S.[49] Furthermore, Cu_2ZnSnS_4 films used for solar cells are often prepared by the initial preparation of Cu−Zn−Sn films followed by sulfurization.[50−52] The question that arose from our previous study was: what happens, if $CaAl_2$ is reacted with sulfur? The reaction product $CaAl_2S_4$ is already known to literature[53] and according to the authors, they prepared it exactly as intended by us. Ca and Al were prereacted to an uncharacterized precursor with the nominal composition of $CaAl_2$. Subsequently, the precursor was reacted with elemental S and single crystals of $CaAl_2S_4$ were obtained. Single-crystal X-ray diffraction indicated an orthorhombic unit cell and isotypism to $EuGa_2S_4$ with space group $Fddd$ was observed. In the same publication, also $SrAl_2S_4$ was described, obtained in a similar fashion.[53] Besides $CaAl_2S_4$ and $SrAl_2S_4$, also $EuAl_2S_4$ was reported to be isostructural to the alkaline earth representatives, however, here the synthesis was conducted from EuS, Al and H_2S.[54] The latter was investigated with respect to its magnetic properties,[55] however, the authors stated, that the Curie constant C deviates by 10% between the different samples. In addition the luminescent properties of $EuAl_2S_4$ were reported indicating that it exhibits a bright green emission.[56] Therefore, we decided to synthesize all three sulfides, starting from the respective binary MAl_2 (M = Ca, Sr, Eu) precursors. All compounds were characterized by powder X-ray diffraction, the alkaline-earth representatives were additionally spectroscopically investigated by ^{27}Al solid state MAS NMR. Quantum-chemical calculations on $CaAl_2S_4$ and $SrAl_2S_4$ helped to evaluate the NMR data. For $EuAl_2S_4$, the magnetic and optical properties were determined, and the valence state of the Eu atoms was furthermore confirmed by ^{151}Eu Mössbauer spectroscopic measurements. Since $EuAl_2S_4$ exhibits interesting optical properties, it was subsequently embedded in three different polysiloxanes and the resulting hybrid materials were characterized by luminescence measurements as well as UV−vis. Such encapsulation techniques could be feasible for the production of LEDs where the phosphor does not get coated onto the chip.

EXPERIMENTAL SECTION

Synthesis. Starting materials for the synthesis of $CaAl_2$, $SrAl_2$ and $EuAl_2$ were calcium, strontium, europium and aluminum pieces, all purchased from Onyxmet (Olsztyn, Poland) with stated purities higher than 99.9%. In addition to the Al pieces, Al foil (Alujet, 99.5%) was used to wrap the metal pieces, preventing the Ca, Sr or Eu from evaporating. In all cases, the starting materials were arc-melted[57] in a custom build arc-melting apparatus in a water-cooled copper hearth under 800 mbar argon pressure. The argon gas was purified with titanium sponge (873 K), molecular sieves and silica gel. The in Al foil wrapped reactants were carefully arc-melted to react the elements in a first step. After initial arc-melting, the obtained buttons were remelted several times to ensure phase pure samples with high homogeneity. For $SrAl_2$ a better homogeneity could be achieved by annealing the powder in a closed Ta-ampoule using induction heating. $EuAl_2$ was also synthesized by arc-welding the elements in a Ta-ampoule which was placed in a water-cooled sample chamber of a induction furnace (TruHeat HF5010, Hüttinger Elektronik, Freiburg, Germany)[58] and heated to approximately 1173 K and kept at this temperature for 10 min before cooling to room temperature. The annealing led to samples with high purity as determined by powder X-ray diffraction (see Supporting Information). The specimens are stable in air over months and show metallic luster, ground samples are gray.

For the sulfidation, ground samples of MAl_2 (M = Ca, Sr, Eu) were mixed with stoichiometric amounts of elemental sulfur and loaded into graphitized fused silica ampules. The reaction mixtures for $SrAl_2S_4$ and $EuAl_2S_4$ were heated in a muffle furnace (Carbolite CWF1200) to 723 K, dwelt for 10 h followed by subsequent heating to 1173 K and further annealing for 10 h. Afterward, the muffle furnace was cooled to RT. $CaAl_2S_4$ was synthesized using different dwelling temperatures and durations. The sample was heated to 673 K for 10 h and subsequently heated to 973 K and kept there for 48 h. For all heating and cooling steps rates of 50 K h^{-1}, respectively 25 K h^{-1} for the Ca sample were applied. An optimization of the synthetic conditions for $EuAl_2S_4$ was done by lowering the annealing temperature to 1073 and 973 K. $CaAl_2S_4$ is light yellow, $SrAl_2S_4$ is light red while $EuAl_2S_4$ has a greenish hue. While the latter one is stable in air over months, the other two are sensitive to moisture and decompose within minutes.

The synthesis of the softenable siloxane matrices containing aryl groups was carried out according to a modified procedure from Klein et al.[59] and described by Kickelbick et al. (see ESI).[60,61] The starting materials phenyltrimethoxysilane and dimethyldimethoxysilane were purchased from abcr with a purity of 97% each. Methanol, extra dry, (99.8%) was obtained from ACROS Organics and THF (99.8% HPLC grade) was purchased from Fischer Chemical. HCl, provided by Bernd

https://doi.org/10.1021/acs.chemmater.4c02093
Chem. Mater. 2025, 37, 97−108

Kraft GmbH, was diluted with demineralized water to pH = 2.5 and pH = 1. 1-Naphthyltrimethoxysilane and 9-phenanthrenylphenyldimethoxysilane were synthesized via a Grignard reaction according to the literature.[60,61]

To prepare the phenyl group containing siloxane **1**, a certain amount *n* of phenyltrimethoxysilane ($PhSi(OCH_3)_3$) was stirred with aqueous HCl, pH = 2.5 (1.5× $n(PhSi(OCH_3)_3)$) in a sealed headspace vial at 318 K for 6 h. After homogenization of the previously two-phase mixture, dimethyldimethoxysilane (0.25× $n(PhSi(OCH_3)_3)$) was slowly added via a syringe together with abs. MeOH (4× $n((CH_3)_2Si(OCH_3)_2)$) and stirred at 318 K for further 2 h. Afterward, the lid of the vessel was opened and a significant increase in viscosity was observed over a stirring period of 18 h at room temperature. The byproducts water and methanol of the polycondensation reaction were subsequently removed by oven treatment at 343 and 383 K for 24 h each, resulting in a transparent, glassy material at RT, which can be reversibly softened at 383 K.

The synthesis of the matrices containing naphthyl- and phenanthrenyl groups was performed in a similar way. For the polynaphthylsilsesquioxane **2**, instead of $PhSi(OCH_3)_3$, 1-naphthyltrimethoxysilane ($1\text{-}NpSi(OCH_3)_3$) was stirred for 8 h at 318 K with aqueous HCl, pH = 2.5 (1.5× $n(1\text{-}NpSi(OCH_3)_3)$). No dialkoxysilane and methanol was added. For the phenanthrenyl group containing siloxane **3**, a certain amount *n* of phenyltrimethoxysilane, dimethyldimethoxysilane (2× $n(PhSi(OCH_3)_3)$), 9-phenanthrenyl-phenyldimethoxysilane (1× $n(PhSi(OCH_3)_3)$) and 1.5 vol.-eq of THF per gram monomer were stirred in a sealed headspace vial together with aqueous HCl, pH = 1 (one equivalent per methoxy group) at 318 K for 72 h. The thermal treatment at 343 and 383 K for 24 h each took place in a vacuum oven at 10 mbar. The final materials were transparent, glass-like and resoftenable around 383 K. For the preparation of the hybrid composite materials, 1 wt% of manually ground $EuAl_2S_4$ was mixed into the viscous materials **1**−**3** at 383 K.

Powder X-ray Diffraction. The pulverized samples of $CaAl_2$, $SrAl_2$ and $EuAl_2$ as well as their corresponding sulfides $CaAl_2S_4$, $SrAl_2S_4$ and $EuAl_2S_4$ were investigated by powder X-ray diffraction experiments at room temperature on a D8-A25-Advance diffractometer (Bruker, Karlsruhe, Germany) in Bragg−Brentano θ−θ-geometry (goniometer radius 280 mm) with Cu K_α-radiation (λ = 154.0596 pm). The diffraction patterns of $CaAl_2$, $SrAl_2$, $EuAl_2$ and $EuAl_2S_4$ were recorded under ambient conditions between 6 and 130° 2θ with a step size of 0.013° and a total scan time of 1 h. $CaAl_2S_4$ and $SrAl_2S_4$ were prepared in dome sample holders inside an argon filled glovebox. A 12 μm Ni foil working as K_β filter and a variable divergence slit were mounted at the primary beam side. A LYNXEYE detector with 192 channels was used at the secondary beam side. The recorded data was evaluated using the Bruker TOPAS 5.0 software[62] using the fundamental parameter approach, the diffraction pattern was analyzed using the Rietveld method.[63,64] Details of the refinements are listed in Tables 1−3. It should be mentioned that the lattice parameters of $CaAl_2$ and $SrAl_2$ differ to the once in the literature reporting their first appearance. This could be due the fact that the lattice parameters reported were obtained from single crystal data and X-ray films. All recorded powder X-ray patterns are shown in Figures S1−S6.

Table 2. Atom Positions for $CaAl_2$ and $EuAl_2$ ($MgCu_2$ Type, $Fd\bar{3}m$) and $SrAl_2$ (KHg_2 Type, *Imma*)

Atom	Wyckoff Position	*x*	*y*	*z*	B_{eq} (Å²)
$CaAl_2$					
Ca	8*a*	3/8	3/8	3/8	0.49(1)
Al	16*d*	0	0	0	0.49(1)
$SrAl_2$					
Sr	4*e*	0	1/4	0.5510(1)	0.57(2)
Al	8*h*	0	0.0671(3)	0.1603(2)	0.94(5)
$EuAl_2$					
Eu	8*a*	3/8	3/8	3/8	0.18(2)
Al	16*d*	0	0	0	0.29(2)

Table 3. Atom Positions and for $CaAl_2S_4$, $SrAl_2S_4$ and $EuAl_2S_4$ ($EuGa_2S_4$ Type, Z = 32)[a]

Atom	Wyckoff Position	*x*	*y*	*z*	B_{eq} (Å²)
$CaAl_2S_4$					
Ca1	16*g*	1/8	1/8	0.3711(7)	0.98(6)
Ca2	8*b*	1/8	1/8	5/8	0.98(6)
Ca3	8*a*	1/8	1/8	1/8	0.98(6)
Al1	32*h*	0.1613(6)	0.2977(5)	0.9973(9)	2.5(2)
Al2	32*h*	0.3802(7)	0.0121(4)	0.9920(7)	2.5(2)
S1	32*h*	0.9962(9)	0.5014(11)	0.0833(4)	1.87(9)
S2	32*h*	0.2582(9)	0.9992(11)	0.1667(4)	1.87(9)
S3	32*h*	0.2479(6)	0.0882(4)	0.9983(12)	1.87(9)
S4	32*h*	0.2600(6)	0.3351(4)	0.2503(12)	1.87(9)
$SrAl_2S_4$					
Sr1	16*g*	1/8	1/8	0.3745(5)	0.77(4)
Sr2	8*b*	1/8	1/8	5/8	0.77(4)
Sr3	8*a*	1/8	1/8	1/8	0.77(4)
Al1	32*h*	0.1655(7)	0.2993(5)	0.9995(14)	1.7(2)
Al2	32*h*	0.3796(8)	0.0148(5)	0.0032(17)	1.7(2)
S1	32*h*	0.0000(7)	0.5007(13)	0.0813(8)	1.38(7)
S2	32*h*	0.2500(7)	0.0007(12)	0.1685(8)	1.38(7)
S3	32*h*	0.2525(9)	0.0911(5)	0.0044(8)	1.38(7)
S4	32*h*	0.2583(8)	0.3316(4)	0.2539(9)	1.38(7)
$EuAl_2S_4$					
Eu1	16*g*	1/8	1/8	0.3732(4)	0.58(3)
Eu2	8*b*	1/8	1/8	5/8	0.58(3)
Eu3	8*a*	1/8	1/8	1/8	0.58(3)
Al1	32*h*	0.1624(8)	0.3023(5)	0.0024(14)	2.6(2)
Al2	32*h*	0.3789(11)	0.0169(5)	0.000(2)	2.6(2)
S1	32*h*	0.0010(8)	0.5011(12)	0.0835(8)	1.57(8)
S2	32*h*	0.2500(9)	0.0004(13)	0.1703(8)	1.57(8)
S3	32*h*	0.2528(10)	0.0915(5)	0.9958(10)	1.57(8)
S4	32*h*	0.2564(10)	0.3290(5)	0.2426(8)	1.57(8)

[a]Isotropic displacement parameters for same atom types have been constrained to be equal.

SEM/EDX Data. Semiquantitative EDX analyses of the bulk samples ($CaAl_2$, $SrAl_2$ and $EuAl_2$) were conducted on a JEOL 7000F (JEOL, Freising, Germany) scanning electron microscope equipped with an EDAX Genesis 2000 EDX detector (EDAX, Unterschleissheim, Germany). The samples were sprinkled on conductive carbon tape and one area scans as well as three independent data points were measured. The results of the SEM/EDX investigations are listed in Table 4.

^{27}Al Solid State NMR. The ^{27}Al−MAS NMR spectra of $CaAl_2$ and $SrAl_2$ were recorded at 104.31 MHz on a Avance III 400 WB spectrometer (Bruker, Billerica, USA) using magic-angle spinning (MAS) conditions. The metallic samples were ground to a fine powder and mixed with an appropriate amount of NaCl (sample:NaCl = 1:9), to reduce the density and the electrical conductivity of the sample, the sulfides $CaAl_2S_4$ and $SrAl_2S_4$ were used without dilution. $EuAl_2$ and $EuAl_2S_4$ could not be measured due to the highly paramagnetic Eu atoms. The NMR data of $CaAl_2S_4$ and $SrAl_2S_4$ was obtained using an Avance Neo 600WB spectrometer (Bruker) using MAS conditions and a resonance frequency of 156.38 MHz. Single pulse MAS NMR experiments were done at 20 kHz rotation frequency in a 3.2 mm ZrO_2 rotor and 90° flip angle for the central transition. Triple-quantum MQMAS experiments were done using a 3-pulse z-filtered sequence[70,71] and rotor-synchronization in the direct dimension. The first and second pulse were experimentally optimized for maximum triple-quantum excitation and conversion, while the third pulse was a soft 90°-pulse optimized for the central transition. The NMR spectra were recorded using the Bruker TOPSPIN software,[72] the analysis was performed with the help of the DMFIT program package[73] and self-

https://doi.org/10.1021/acs.chemmater.4c02093
Chem. Mater. 2025, 37, 97−108

Table 4. Chemical Composition Determined by SEM/EDX[a]

Composition	M (at%) theoretical	Al (at%)	M (at%) experimental	Al (at%)
$CaAl_2$	33.3	66.7	35	65
$SrAl_2$	33.3	66.7	35	65
$EuAl_2$	33.3	66.7	36	64

[a]The standard deviations are ±2 at% with M = Ca, Sr or Eu.

Table 5. Summary of the NMR Observables of $CaAl_2$, $SrAl_2$, $CaAl_2S_4$, and $SrAl_2S_4$ Extracted From Least-Square Fitting via DMFit and Simpson Simulations of the ^{27}Al MAS NMR Spectra with δ being the Isotropic Chemical Shift, C_Q the Quadrupolar Coupling and η_Q the Asymmetry Parameter[a]

	site	δ_{exp} (ppm)	$C_{Q,theo}$ (MHz)	$\lvert C_{Q,exp}\rvert$ (MHz)	$\eta_{Q,theo}$	$\eta_{Q,exp}$	
$CaAl_2$	Al (16*c*)	1091	0.228	2.09	0	0	30
$SrAl_2$	Al (8*h*)	664	−1.757	2.18	0.92	0.86	30
$CaAl_2S_4$	Al1 (32*h*)	120.9(3)	−5.330	5.8(2)	0.31	0.23(2)	*b*
	Al2 (32*h*)	121.7(3)	−5.252	5.5(2)	0.22	0.18(2)	*b*
$SrAl_2S_4$	Al1 (32*h*)	120.1(3)	−5.190	5.6(2)	0.22	0.1(1)	*b*
	Al2 (32*h*)	121.2(3)	−4.917	5.2(2)	0.13	0.1(1)	*b*

[a]Theoretically calculated values from DFT are given with the subscript theo, experimentally fitted values are denoted with the subscript exp. [b]This work.

Table 6. Summary of the Magnetic Properties of $EuAl_2$ and $EuAl_2S_4$[a]

Compound	T_N (K)	μ_{eff} (μ_B)	μ_{calc} (μ_B)	θ_P (K)	μ_{sat} (μ_B/Eu^{2+})	$\mu_{sat,theo}$ (μ_B/Eu^{2+})	ref.
$EuAl_2$	31.3(1)	7.87(1)	7.94	−1.9(1)	2.93(1) (2 K, 90 kOe)	7	*b*
$EuAl_2$	30	8.25	7.94	13	7.3 (4.2 K, 18 kOe)	7	81
$EuAl_2S_4$	–	7.89(1)	7.94	−0.3(1)	6.70(1) (2 K, 90 kOe)	7	*b*

[a]Néel temperature, T_N; effective magnetic moment, μ_{eff}; calculated magnetic moment μ_{calc}; paramagnetic Curie temperature, θ_P; experimental saturation magnetization μ_{sat}; theoretical saturation magnetization $\mu_{sat,theo}$ according to $g_J \times J$. [b]this work.

Table 7. Fitting Parameters of the ^{151}Eu Mößbauer Spectra of $EuAl_2$ (Space Group $Fd\bar{3}m$, Z = 8) and $EuAl_2S_4$ (Space Group *Fddd*, Z = 32) Measured at 6 and 78 K[a]

Compound	T (K)	δ (mm s^{-1})	Γ (mm s^{-1})	ΔE_Q (mm s^{-1})	B_{hf} (T)	ref.
$EuAl_2$	78 K	−8.38(2)	2.96(7)	–	–	*b*
$EuAl_2$	6 K	−8.44(3)	2.55(3)	–	25.9(1)	*b*
$EuAl_2$	4.2 K	−9.7	–	–	27.8(8)	84,85
$EuAl_2S_4$	78 K	−12.72(1)	3.96(5)	4.3(1)	–	*b*

[a]δ: isomer shift; Γ: experimental line width; ΔE_Q: quadrupole splitting. [b]This work.

written fitting routines implementing local minimization by the simplex algorithm and a global search using the particle swarm algorithm in combination with Simpson-4.2.1.[74] The extracted data is compiled in Table 5. Errors were estimated from the differences between a 2-spin and a 3-spin simulation including a quadrupolar line shape for the impurity marked with an asterisk.

Quantum-Chemical Calculations. Electronic structure calculations of the compounds in the ternary systems Ca−Al−S and Sr−Al−S were performed using the projector augmented wave method (PAW) of Blöchl[75,76] coded in the Vienna *ab initio* simulation package (VASP).[77,78] VASP calculations employed the potentials PAW_PBE Ca_sv 06Sep2000, PAW_PBE Sr_sv 07Sep2000, PAW_PBE Al 04Jan2001, and PAW_PBE S 06Sep2000. The cutoff energy for the plane wave calculations was set to 800 eV and the Brillouin zone integration was carried out using a k-point mesh with a spacing of ≈0.02 for all compounds. The quadrupole parameters C_Q and asymmetry parameters η were extracted from the calculations using the quadrupole moments given by Pyykkö[79,80] and are compiled in Table 5.

Magnetic Properties. The polycrystalline samples of $EuAl_2$ and $EuAl_2S_4$ were investigated by temperature dependent magnetic susceptibility measurements at external fields up to 90 kOe (1 kOe = 7.96×10^4 A m^{-1}). The samples were ground to a fine powder, filled into polypropylene capsules and attached to the sample holder rod of a Vibrating Sample Magnetometer (VSM) option of a Physical Property Measurement System (PPMS) by Quantum Design. The magnetization data $M(T)$ of the samples was investigated in the temperature range between 2 and 300 K. Obtained parameters are given in Table 6.

^{151}Eu Mössbauer Spectroscopic Investigations. The 21.53 keV transition of ^{151}Eu with an activity of 65 MBq (1% of the total activity of a ^{151}Sm:EuF_3 source) was used for the ^{151}Eu Mössbauer spectroscopic experiments, which were conducted in the usual transmission geometry. All measurements were performed with a continuous flow He (Janis Research Co LLC) or a liquid N_2 bath cryostat system. The temperature of the absorber was set to 78 K, while the source was kept at room temperature. The temperature was controlled by a resistance thermometer (~0.5 K accuracy). The sample was enclosed in a small PMMA container, the required sample mass was calculated based on the work by Long et al.[82] $EuAl_2S_4$ was used pure, $EuAl_2$ was diluted with SiO_2. Fitting of the spectrum was performed with the WinNormos for Igor6 program package.[83] The obtained fitting parameters are listed in Table 7.

UV−Vis and Fluorescence Spectroscopic Properties. UV−vis transmission measurements were performed in aluminum frames with a hole (d = 8 mm, h = 2 mm) on a Lambda 750 instrument (PerkinElmer Inc., Shelton, USA) equipped with a 100 mm integration sphere from 200 to 800 nm with a 2 nm increment and 0.2 s integration time. Fluorescence spectroscopy was performed applying a FluoroMax 4 Spectrofluorometer (Horiba Scientific, Kyoto, Japan) with an excitation wavelength of 468 nm. Excitation spectra were recorded with an emission wavelength of 506 nm. The pure $EuAl_2S_4$ and the

https://doi.org/10.1021/acs.chemmater.4c02093
Chem. Mater. 2025, 37, 97−108

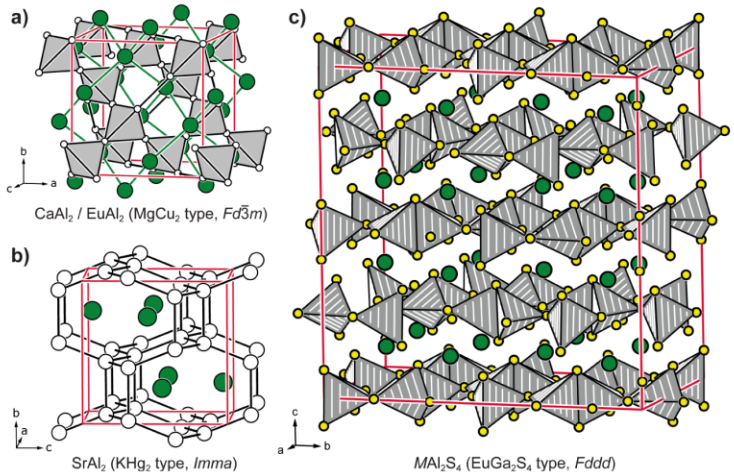

Figure 1. Crystal structures of a) $CaAl_2$ and $EuAl_2$ in the cubic Laves phase ($MgCu_2$ type), b) $SrAl_2$ in the orthorhombic KHg_2 type and c) orthorhombic MAl_2S_4 (M = Ca, Sr, Eu) adopting the $EuGa_2S_4$ type. Ca, Sr and Eu atoms are shown in green, Al atoms in white and S atoms in yellow.

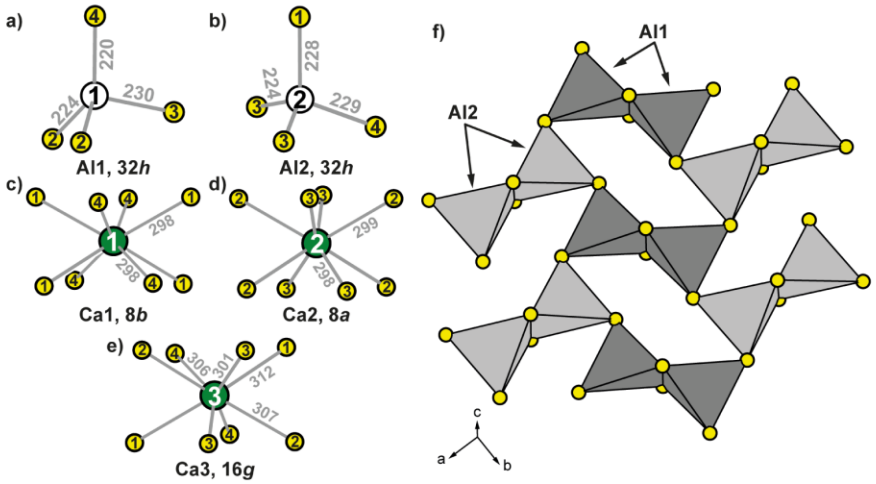

Figure 2. Coordination environments of the a) Al1, b) Al2, c) Ca1, d) Ca2 and e) Ca3 atoms in the crystal structure of $CaAl_2S_4$. Wyckoff positions and interatomic distances (in pm) are given. Ca atoms are shown in green, Al atoms in white and S atoms in yellow. f) Cut-out of the $[Al_2S_4]^{2-}$ substructure formed by the $[AlS_4]$ tetrahedra.

$EuAl_2S_4$ embedded in the polymer matrix were measured as solids in a fiber form with an approximate diameter of 1−2 mm.

RESULTS AND DISCUSSION

Crystal Chemistry. The structures of the binary phases $CaAl_2$ ($MgCu_2$ type), $SrAl_2$ (KHg_2 type) and $EuAl_2$ ($MgCu_2$ type) will be only discussed very briefly as they present common structure types. In both prototypes, the Al atoms form formally negatively charged networks with the M cations residing in cavities. In the cubic $MgCu_2$ type (Figure 1a), empty Al_4 tetrahedra are observed that are connected via all four corners, in the KHg_2 type (Figure 1b), the Al atoms are surrounded by four Al atoms in the shape of a highly distorted tetrahedron. In both cases, the Ca/Eu or Sr atoms reside in cavities of the polyanionic framework.

The three sulfides $CaAl_2S_4$, $SrAl_2S_4$ and $EuAl_2S_4$ crystallize isostructural in the orthorhombic crystal system with space group *Fddd* and show isotypism to $EuGa_2S_4$ (Figure 1c).[86] In their crystal structures, three crystallographically independent M, two Al and four S positions are found. The Al atoms are surrounded tetrahedrally by S atoms (Figure 2a,b) while the S atoms are coordinated by two Al atoms in a nonlinear fashion. All M atoms are surrounded by eight S atoms in the shape of square antiprisms (Figure 2c−e). Both $[AlS_4]$ tetrahedra form dimers by condensation via a common edge, further condensation via the two remaining corners leads to layers in the *ab* plane (Figure 2f). The dimers arrange in a herringbone pattern and stack along the crystallographic *c* axis. Between the layers, the three crystallographic independent M positions are located. The interatomic distances d(Al−S) = 220−230 pm are in the typical ranges of the known binary (Al_2S_3: 216−230 pm);[87,88] while the Ca−S distances (d(Ca−S) = 298−312 pm) are significantly longer compared to the ones in CaS (280 pm).[89] This difference might originate from the fact that the S atoms in

https://doi.org/10.1021/acs.chemmater.4c02093
Chem. Mater. 2025, 37, 97−108

$CaAl_2S_4$ are strongly bound to the Al atoms in turn weakening the Ca−S interactions and elongating the respective distances.

Powder X-ray Diffraction. In order to study the outcome of the oxidation reactions and check the quality of the obtained materials, all samples were investigated by powder X-ray diffraction experiments at room temperature. Representative diffraction patterns for the binary and ternary materials, $EuAl_2$ and $EuAl_2S_4$, are exemplarily shown in Figure 3. All samples

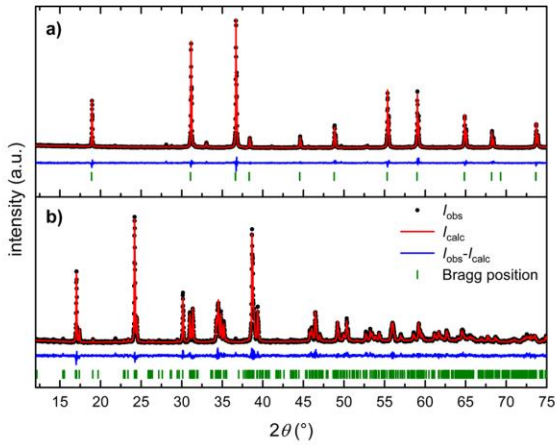

Figure 3. Powder X-ray diffraction patterns of a) cubic $EuAl_2$ ($MgCu_2$ type, $Fd\bar{3}m$) and b) orthorhombic $EuAl_2S_4$ ($EuGa_2S_4$ type, $Fddd$). Experimental data is shown as black dots, refined data as red line, the difference is shown as continuous blue line, the Bragg positions are shown as green ticks. The full 2θ range is shown in Figures S3 and S6.

could be obtained as nearly X-ray pure material, details to the respective refinements can be found in Tables 1−3 and in Figures S1−S6 in the Supporting Information. As expected, the lattice parameters of $CaAl_2S_4$ are significantly smaller than the ones of $SrAl_2S_4$ and $EuAl_2S_4$, in line with the smaller ionic radius of Ca^{2+} compared to Sr^{2+} and Eu^{2+} (all CN = 8: $r(Ca^{2+})$ = 112 pm, $r(Sr^{2+})$ = 126 pm, $r(Eu^{2+})$ = 125 pm).[90] The lattice parameters of $SrAl_2S_4$ and $EuAl_2S_4$ in contrast are nearly identical as expected by the only slight differences in their ionic radii.

^{27}Al Solid State NMR Spectroscopic Investigations. In order to study the local Al environments and to obtain a broader basis of shielding data for ^{27}Al in sulfides solid state MAS NMR investigations were conducted. The data for the starting materials $CaAl_2$ and $SrAl_2$ are in line with our previous investigations[30] and are shown in the Supporting Information, Figure S9. For both compounds, the central resonance can be observed at 1091 ($CaAl_2$) and 664 ($SrAl_2$) ppm. The large resonance shift is caused by the metallic character of the material, that is the Knight shift contribution.[91] The four-fold coordinated Al typically has isotropic chemical shifts higher than 90 ppm as seen for both $SrAl_2S_4$ and $CaAl_2S_4$. According to quantum-chemical calculations for both sites in the two compounds a quadrupolar coupling of around 5 MHz is expected, which leads to second order broadening of the central transition and considerable overlap of the corresponding peaks. Nevertheless, by a combination of 2D MQMAS experiments and least-squares fitting of the 1D line shape estimates for the isotropic shift and the quadrupolar parameters (quadrupolar coupling and asymmetry parameter) could be estimated. The results (Figure 4 and Table 5) show the presence of some minor side phases and are in agreement with an ordered structure model. The observed number of sites and electric field gradient values of the Al sites agree with the diffraction model.

Magnetic Properties. From the sum formula, it is expected that $EuAl_2S_4$ contains divalent Eu atoms which exhibit a half-filled 4f valence shell and a quite high magnetic moment of μ_{eff} = 7.94 μ_B.[92,93] Therefore, magnetic susceptibility measurements on $EuAl_2S_4$ (Figure 5) and the starting material $EuAl_2$ (Figure S8) were conducted at 10 kOe (Figures 5a and S8a) in zero-field-cooled (ZFC) and both in zero-field-cooled and field-cooled (ZFC/FC) mode at 100 Oe (Figures 5b and S8b). In the case of $EuAl_2S_4$, no magnetic ordering down to 2 K was observed while $EuAl_2$ exhibits antiferromagnetic ordering at T_N = 31.3(1) K in line with the reports in literature.[81] From the high temperature data, the effective magnetic moment of $EuAl_2S_4$ was determined to be μ_{eff} = 7.89(1) μ_B using a Curie−Weiss fit, for $EuAl_2$ μ_{eff} = 7.87(1) μ_B was derived from a modified Curie−Weiss fit. This clearly indicates, that the Eu atoms are in a divalent oxidation state, since the experimentally determined moment almost perfectly matches the theoretical moment of μ_{calc} = 7.94 μ_B.[92,93] No deviation, as reported before,[55] was observed. The Weiss constants are θ_P = −0.3(1) K for $EuAl_2S_4$ and θ_P = −1.9(1) K for $EuAl_2$, indicating no dominant magnetic

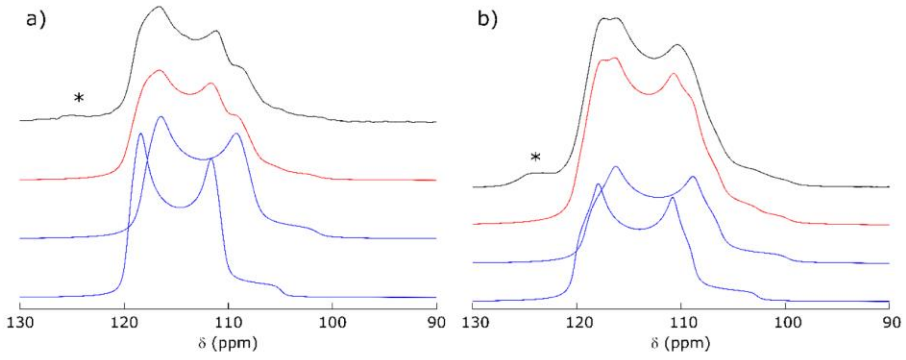

Figure 4. ^{27}Al MAS NMR spectrum (14.1 T) of a) $SrAl_2S_4$ and b) $CaAl_2S_4$ recorded at a spinning frequency of 20 kHz (black line on top). The results of the least-squares fit by SIMPSON (red line) were confirmed by comparing to traces of the MQMAS spectrum (Figure S7). The blue lines below show subspectra of the individual Al sites. Impurities are marked with an asterisk (*) and the resulting values are shown in Table 5.

https://doi.org/10.1021/acs.chemmater.4c02093
Chem. Mater. 2025, 37, 97−108

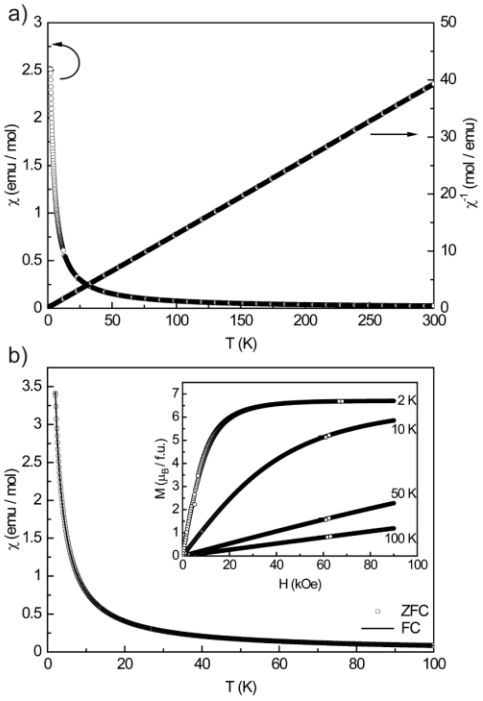

Figure 5. Magnetic properties of $EuAl_2S_4$. a) Temperature dependence of the magnetic susceptibility χ and its inverse χ^{-1} recorded at 10 kOe. b) Temperature dependence of the magnetic susceptibility χ recorded in ZFC/FC mode at 100 Oe. (inset) magnetization isotherms recorded at 2, 10, 50, and 100 K.

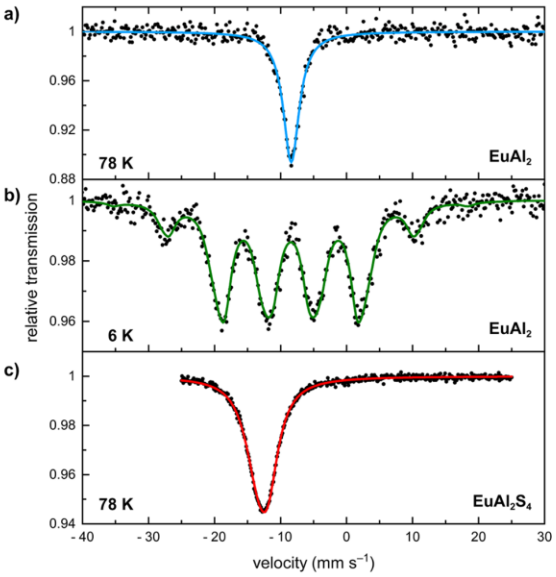

Figure 6. ^{151}Eu Mössbauer spectroscopic investigations on a) $EuAl_2$ at 78 K, b) $EuAl_2$ at 6 K, and c) $EuAl_2S_4$ at 78 K. The blue, green and red lines indicate the fit. For details see text.

interactions in the paramagnetic regime. The fact that the Weiss temperature of $EuAl_2$ is more positive as expected can be explained by an A-type antiferromagnetic ordering.[94] Here "layers" of Eu atoms couple ferromagnetically while the layers are antiparallel with respect to each other resulting in an overall antiferromagnetic ordering. The temperature independent contribution from $EuAl_2$ amounts to $\chi_0 = 412(1) \times 10^{-5}$ emu mol^{-1} which indicates the Pauli contribution from the conduction electrons. Finally, magnetization isotherms were recorded at 2, 10, 50, and 100 K (Figure 5b inset/Figure S8c). At 50 and 100 K, a linear field dependence is observed for both compounds, in line with a paramagnetic material. The 10 and 2 K isotherms of $EuAl_2S_4$, however, are curved, indicating potential saturation effects at low temperatures while the ones of $EuAl_2$ are nearly linear. At 2 K and 90 kOe, the saturation magnetization of $EuAl_2S_4$ reaches $\mu_{sat} = 6.70(1)\ \mu_B$, also in line with the expected saturation of 7 μ_B according to $g_J \times J$[92,93] while the one of $EuAl_2$ reaches only $\mu_{sat} = 2.92(1)\ \mu_B$ suggesting saturation effects.

^{151}Eu Mössbauer Spectroscopic Investigations. To prove the divalent oxidation state of the Eu atoms in $EuAl_2$ and $EuAl_2S_4$, ^{151}Eu Mössbauer spectroscopic investigations were conducted (Figure 6). The results are listed in Table 7. Since $EuAl_2S_4$ exhibits no magnetic phase transition down to 2 K, only spectra at 78 K were recorded. For $EuAl_2$, spectra were recorded at 78 and 6 K, to be compared to the low temperature spectra at 4.2 K that have been reported.[84,85] Since $EuAl_2$ exhibits only a single crystallographic Eu position (*vide supra*), only one signal is expected. The isomer shift at 78 K is $\delta = -8.38(2)$ mm s^{-1}, in line with a divalent oxidation state in a metallic system. Other intermetallic compounds show comparable isomer shifts,[95] e.g., $Eu_2Al_{15}Pt_6$ with $\delta = -7.93$ mm s^{-1},[96] $EuAl_2Pt$ with $\delta = -9.94$ mm s^{-1},[97] or the EuT_2Al_{20} representatives (T = Ti, V, Cr, Nb, Mo, W, Ta; $\delta = -8.54$ to -8.97 mm s^{-1}).[98] The line width is with $\Gamma = 2.96(7)$ mm s^{-1} also in the expected range.[95−97,99−107] At 6 K and therefore well below the Néel temperature of $T_N = 31.3(1)$ K, the signal shows a significant hyperfine field splitting of $B_{hf} = 25.9(1)$ T clearly proving that the compound is in a magnetically ordered state. The hyperfine field is in the typical range of magnetically ordered Eu^{2+} compounds.[97,99,100,102−105,107−109]

For $EuAl_2S_4$, an isomer shift of $\delta = -12.72(1)$ mm s^{-1} was observed, again clearly indicating a divalent oxidation state, however, a significantly larger isomer shift was observed in line with e.g., the europium thiogermanate Eu_2GeS_4 ($\delta = -12.44(8)$ mm s^{-1}).[49] The isomer shifts of the same oxidation state comprise quite a large range, depending on the "ionicity" of the respective compound. For EuO for example an isomer shift of $\delta = -11.9(1)$ mm s^{-1} was reported,[110] EuF_2 even has $\delta = -14.2(1)$ mm s^{-1}.[110] A recent review explains this aspect in some more detail.[95] In contrast to $EuAl_2$, $EuAl_2S_4$ exhibits three crystallographically independent Eu sites (*vide supra*) causing three signals. Since, however, the three positions are almost identical with respect to their crystallographic environment no differentiation via ^{151}Eu Mössbauer spectroscopic investigations is possible. This leads to an overlap of the three signals, which results in an increased line width of $\Gamma = 3.96(5)$ mm s^{-1}. Furthermore, no cubic site symmetry is present leading to a quadrupolar interaction of $\Delta E_Q = 4.3(1)$ mm s^{-1}.

UV−Vis and Fluorescence Spectroscopic Properties. Since Eu^{2+} containing materials are important not only with respect to their magnetic but also their optical properties, we characterized $EuAl_2S_4$ with respect to its luminescent properties and subsequently embedded powdered $EuAl_2S_4$ into three different polysiloxanes **1**−**3** to produce luminescent organic−

https://doi.org/10.1021/acs.chemmater.4c02093
Chem. Mater. 2025, 37, 97−108

inorganic hybrid materials. For this, polyphenylsilsesquioxane **1**, polynaphthylsilsesquioxane **2** and polyphenantrenyl-silsesquioxane **3** (Figure 7) were chosen as these had previously been synthesized and characterized by us.

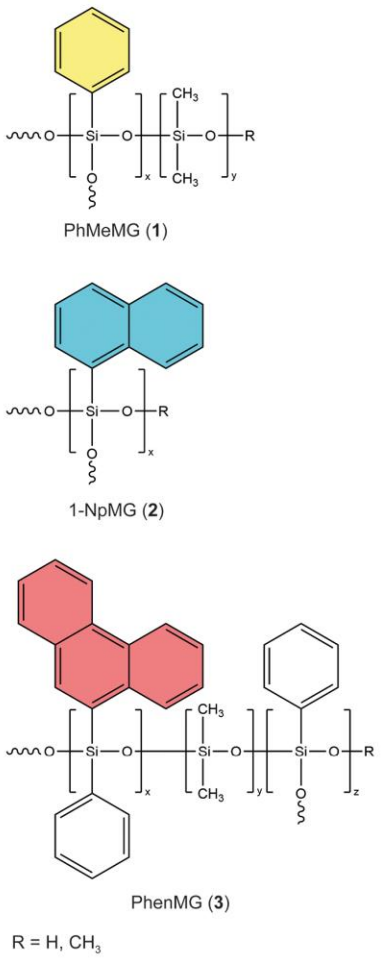

Figure 7. Overview of the polysiloxanes, containing phenyl **1**, naphthyl **2** and phenanthrenyl **3** groups.

At first, the polysiloxanes **1**−**3** were characterized by UV−vis spectroscopy (Figure 8b−d, red curve). It is clearly visible, that the normalized absorbance is small (<0.1) for all samples between 500 and 800 nm, however, below 370 nm the absorption significantly increases at 300, 325, and 350 nm for the compounds **1**, **2** and **3**, in line with the previous reports in the literature.[60,61] The shift of the absorbance to higher wavelengths can be explained by the increasing size of the π-systems of the aromatic substituents. UV−vis measurements of $EuAl_2S_4$ recorded on the solid material were obtained by measuring its diffuse reflectance. The optical bandgap was determined to be E_g = 2.3 eV using the tangent method. The observed bandgap is in line with the observed greenish color of the material.

Figure 8 depicts the excitation (486 nm) and emission (506 nm) spectra of pure $EuAl_2S_4$ and the respective hybrid composite materials (**1**−**3** with 1 wt% $EuAl_2S_4$ = $EuAl_2S_4$@**1**, $EuAl_2S_4$@**2**, $EuAl_2S_4$@**3**). Upon direct excitation (Figure 8a) into the f-d transitions (λ_{ex} = 486 nm), an intense emission band at ∼500 nm can be observed, originating from the Eu^{2+} cations. The spectra recorded at room temperature are in good agreement with the ones obtained at 77 K reported in the literature.[56] Subsequently, 1 wt% of $EuAl_2S_4$ was mixed into the polysiloxanes **1**−**3**. The excitation and emission spectra were recorded using the same conditions as the pure material and are shown in Figure 8b−d. While the green emission band stays the same in all three hybrid materials, the excitation spectra change. While pure $EuAl_2S_4$ can be excited down to 290 nm, the excitation spectra of $EuAl_2S_4$@**1**, $EuAl_2S_4$@**2** and $EuAl_2S_4$@**3** change quite drastically. Now the influence of the siloxane comes into play. As can be seen in Figure 8b−d, the absorbance of the polysiloxane acts as sort of an excitation filter for $EuAl_2S_4$ due to the intrinsic absorbance of the polysiloxanes. This can be also shown visually by UV light. Figure 8e−h, depict the differences of the samples when using different excitation wavelengths. Figure 8e shows $EuAl_2$ (left) and $EuAl_2S_4$ (right) under 254 nm UV light. It is clearly visible, that $EuAl_2$ does not show any fluorescence while $EuAl_2S_4$ exhibits a green fluorescence (506 nm). Figure 8f−h show (from left to right) the pure polysiloxanes under 254 nm UV light, $EuAl_2S_4$@**1**, $EuAl_2S_4$@**2** and $EuAl_2S_4$@**3** under 254 nm UV light and finally $EuAl_2S_4$@**1**, $EuAl_2S_4$@**2** and $EuAl_2S_4$@**3** using 365 nm UV light. It is visible, that the polysiloxanes **2** and **3** show a pale blue fluorescence without the embedded solid, while 365 nm UV light leads to a strong green fluorescence of all three compounds. Under 254 nm UV light, however, a green/cyan like fluorescence is observed for $EuAl_2S_4$@**1**, $EuAl_2S_4$@**2** and $EuAl_2S_4$@**3**, potentially originating from the polysiloxane and trace emission of $EuAl_2S_4$ underlining the filtering effect of the polysiloxane described earlier.

■ CONCLUSION

Orthorhombic $CaAl_2S_4$, $SrAl_2S_4$ and $EuAl_2S_4$ (all isostructural, $EuGa_2S_4$ type, *Fddd*) were prepared by sulfidation of the respective MAl_2 intermetallic precursors. While the alkaline-earth compounds $CaAl_2S_4$ and $SrAl_2S_4$ are highly sensitive to moisture, $EuAl_2S_4$ is stable for weeks. All precursors and products were characterized by powder X-ray diffraction and X-ray pure products were obtained for $SrAl_2S_4$ and $EuAl_2S_4$, the sample of $CaAl_2S_4$ contains traces of CaS. $CaAl_2S_4$ and $SrAl_2S_4$ were characterized by ^{27}Al solid state MAS NMR verifying the two crystallographically independent Al sites using MQ−MAS pulse sequences. The magnetic properties of $EuAl_2S_4$ were investigated by magnetization and susceptibility measurements. No magnetic ordering down to 2 K, however, saturation effects were observed. The magnetic moment is close to 7.94 μ_B, clearly indicating a divalent oxidation state for Eu. This was confirmed by ^{151}Eu Mössbauer spectroscopic investigations. The optical bandgap was determined to be E_g = 2.3 eV being in line with the observed greenish color of the material. The luminescent properties show a broad green emission upon UV excitation (254 nm) caused by the allowed f-d transition of the Eu^{2+} cations centered around 500 nm. In a final step, powdered $EuAl_2S_4$ was embedded in three different polysiloxanes creating a hybrid material which can be reversibly softened and are hard with glass-like properties at room temperature. $EuAl_2S_4$ retains its luminescent properties, however, due to the absorption of the polysiloxanes below 350 nm, the excitation with 254 nm UV light is not possible anymore. Therefore, the hybrid material has an intrinsic filter for the UV excitation of the Eu^{2+} cations.

https://doi.org/10.1021/acs.chemmater.4c02093
Chem. Mater. 2025, 37, 97−108

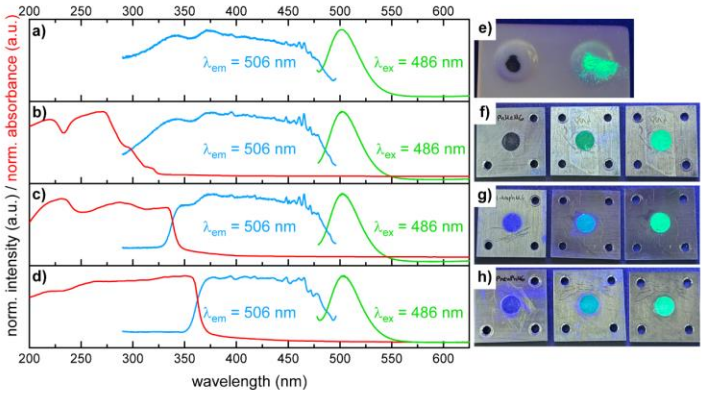

Figure 8. a) excitation and emission spectrum of pure $EuAl_2S_4$. b) 1 wt% $EuAl_2S_4$ embedded in **1**; the red line corresponds to the absorbance spectrum of **1**, the blue line to the excitation spectrum of **1** and the green line to the emission spectrum of **1**. c) 1 wt% $EuAl_2S_4$ embedded in **2**; the red line corresponds to the absorbance spectrum of **2**, the blue line to the excitation spectrum of **2** and the green line to the emission spectrum of **2**. d) 1 wt% $EuAl_2S_4$ embedded in **3**; the red line corresponds to the absorbance spectrum of **3**, the blue line to the excitation spectrum of **3** and the green line to the emission spectrum of **3**. e) $EuAl_2$ and $EuAl_2S_4$ under 254 nm excitation. f-h) from left to right: **1**−**3** under 254 nm, $EuAl_2S_4$@**1**, $EuAl_2S_4$@**2** and $EuAl_2S_4$@**3** under 254 nm and $EuAl_2S_4$@**1**, $EuAl_2S_4$@**2** and $EuAl_2S_4$@**3** under 365 nm UV light. For more details see text.

■ ASSOCIATED CONTENT

Supporting Information

The Supporting Information is available free of charge at https://pubs.acs.org/doi/10.1021/acs.chemmater.4c02093.

Additional powder X-ray data, synthetic conditions for the siloxanes, additional magnetic data, and additional NMR data (PDF)

■ AUTHOR INFORMATION

Corresponding Author

Oliver Janka − *Inorganic Solid State Chemistry, Saarland University, Saarbrücken 66123, Germany;* orcid.org/0000-0002-9480-3888; Email: oliver.janka@uni-saarland.de

Authors

Elias C. J. Gießelmann − *Inorganic Solid State Chemistry, Saarland University, Saarbrücken 66123, Germany;* orcid.org/0000-0001-6137-9729

Stefan Engel − *Inorganic Solid State Chemistry, Saarland University, Saarbrücken 66123, Germany;* orcid.org/0000-0002-6813-8490

Svenja Pohl − *Inorganic Solid State Chemistry, Saarland University, Saarbrücken 66123, Germany*

Max Briesenick − *Inorganic Solid State Chemistry, Saarland University, Saarbrücken 66123, Germany*

Lukas P. Rüthing − *Department of Chemistry and Biology, Faculty IV: School of Science and Technology, Inorganic Materials Chemistry and Center of Micro- and Nanochemistry and Engineering (Cm), University of Siegen, Siegen 57068, Germany*

Cedric Kloos − *Inorganic Solid State Chemistry, Saarland University, Saarbrücken 66123, Germany*

Aylin Koldemir − *Institut für Anorganische und Analytische Chemie, Universität Münster, Münster 48149, Germany*

Lars Schumacher − *Institut für Anorganische und Analytische Chemie, Universität Münster, Münster 48149, Germany;* orcid.org/0009-0009-9444-8773

Joshua Wiethölter − *Institut für Anorganische und Analytische Chemie, Universität Münster, Münster 48149, Germany;* orcid.org/0009-0006-8470-2764

Jörn Schmedt auf der Günne − *Department of Chemistry and Biology, Faculty IV: School of Science and Technology, Inorganic Materials Chemistry and Center of Micro- and Nanochemistry and Engineering (Cm), University of Siegen, Siegen 57068, Germany;* orcid.org/0000-0003-2294-796X

Guido Kickelbick − *Inorganic Solid State Chemistry, Saarland University, Saarbrücken 66123, Germany;* orcid.org/0000-0001-6813-9269

Complete contact information is available at: https://pubs.acs.org/10.1021/acs.chemmater.4c02093

Author Contributions

#E.C.J.G. and S.E. contributed equally. All authors have accepted responsibility for the entire content of this submitted manuscript and approved the submission.

Notes

The authors declare no competing financial interest.

■ ACKNOWLEDGMENTS

Instrumentation and technical assistance for this work were provided by the Service Center X-ray Diffraction, with financial support from Saarland University and the Deutsche Forschungsgemeinschaft (project numbers INST 256/506-1 and INST 256/349-1) and by the Service Center NMR with financial support from Saarland University and the Deutsche Forschungsgemeinschaft DFG (project number INST 256/384-1). The magnetometer at University of Münster was funded the Deutsche Forschungsgemeinschaft DFG through INST 211/1034-1. Funding was provided by the Deutsche Forschungsgemeinschaft DFG (JA 1891-10-1). We thank Dr. Theresa Block for her help with the Mössbauer spectroscopic measurements.

■ REFERENCES

(1) Altenpohl, D. *Aluminium und Aluminiumlegierungen*; Springer: Berlin, Heidelberg, Germany, 1965.

(2) Kammer, C. *Aluminium-Taschenbuch 1: Grundlagen und Werkstoffe*; Aluminium-Zentrale: Düsseldorf, 1995.
(3) Ostermann, F. *Anwendungstechnologie Aluminium*; Springer Vieweg: Berlin, Heidelberg, Germany, 2014.
(4) Janka, O. Metallic light-weight alloys: Al, Ti, Mg. In *Applied Inorganic Chemistry*, Pöttgen, R.; Jüstel, T.; Strassert, C., Eds.; De Gruyter: Berlin, Germany, 2022, pp. 158−173.
(5) Buchner, M.; Janka, O. From Construction Materials to Technical Gases. In *Applied Inorganic Chemistry*. Pöttgen, R.; Jüstel, T.; Strassert, C. A. pp. 221−228.De Gruyter, 2023
(6) Engel, S.; Janka, O. From Construction Materials to Technical Gases. In *Applied Inorganic Chemistry*. Pöttgen, R.; Jüstel, T.; Strassert, C. A. pp. 255−264.De Gruyter, 2023
(7) Engel, S.; Janka, O. From Construction Materials to Technical Gases. In *Applied Inorganic Chemistry*. Pöttgen, R.; Jüstel, T.; Strassert, C. A. pp. 265−270.De Gruyter, 2023
(8) Strnat, K.; Hoffer, G.; Olson, J.; Ostertag, W.; Becker, J. J. A Family of New Cobalt-Base Permanent Magnet Materials. *J. Appl. Phys.* **1967**, *38*, 1001−1002.
(9) Croat, J. J.; Herbst, J. F.; Lee, R. W.; Pinkerton, F. E. High-energy product Nd-Fe-B permanent magnets. *Appl. Phys. Lett.* **1984**, *44*, 148−149.
(10) Kresse, G.; Schmid, M.; Napetschnig, E.; Shishkin, M.; Köhler, L.; Varga, P. Structure of the Ultrathin Aluminum Oxide Film on NiAl(110). *Science* **2005**, *308*, 1440−1442.
(11) Datta, P. K.; Du, H. L.; Burnell-Gray, J. S.; Ricker, R. E.Corrosion of Intermetallics In *Corrosion: Materials* ASM International, Materials Park: OH, USA, 2005, Vol. *13*.
(12) Jozwik, P.; Polkowski, W.; Bojar, Z. Applications of Ni_3Al Based Intermetallic Alloys − Current Stage and Potential Perceptivities. *Materials* **2015**, *8*, 2537−2568.
(13) Rahmel, A.; Schütze, M.; Quadakkers, W. J. Fundamentals of TiAl oxidation − A critical review. *Mater. Corros.* **1995**, *46*, 271−285.
(14) Armbrüster, M.; Kovnir, K.; Behrens, M.; Teschner, D.; Grin, Y.; Schlögl, R. Pd−Ga Intermetallic Compounds as Highly Selective Semihydrogenation Catalysts. *J. Am. Chem. Soc.* **2010**, *132*, 14745−14747.
(15) Armbrüster, M.; Kovnir, K.; Friedrich, M.; Teschner, D.; Wowsnick, G.; Hahne, M.; Gille, P.; Szentmiklósi, L.; Feuerbacher, M.; Heggen, M.; Girgsdies, F.; Rosenthal, D.; Schlögl, R.; Grin, Y. $Al_{13}Fe_4$ as a low-cost alternative for palladium in heterogeneous hydrogenation. *Nat. Mater.* **2012**, *11*, 690−693.
(16) Antonyshyn, I.; Sichevych, O.; Rasim, K.; Ormeci, A.; Burkhardt, U.; Titlbach, S.; Schunk, S. A.; Armbrüster, M.; Grin, Y. Chemical behaviour of $CaAg_2$ under ethylene epoxidation conditions. *Eur. J. Inorg. Chem.* **2018**, *2018*, 3933−3941.
(17) Hodge, K. L.; Goldberger, J. E. Transition Metal-Free Alkyne Hydrogenation Catalysis with $BaGa_2$, a Hydrogen Absorbing Layered Zintl Phase. *J. Am. Chem. Soc.* **2019**, *141*, 19969−19972.
(18) Li, J.; Sun, S. Intermetallic Nanoparticles: Synthetic Control and Their Enhanced Electrocatalysis. *Acc. Chem. Res.* **2019**, *52*, 2015−2025.
(19) Armbrüster, M. Intermetallic compounds in catalysis − a versatile class of materials meets interesting challenges. *Sci. Technol. Adv. Mater.* **2020**, *21*, 303−322.
(20) Fischer, W.; Fritz, H. Laves − an ideal for generations. *Z. Kristallogr.* **2006**, *221*, 305−310.
(21) Parthé, E.; Fritz, H. Laves − 100 years young. *Z. Kristallogr.* **2006**, *221*, 301−304.
(22) Schulze, G. E. R. Zur Kristallchemie der intermetallischen AB_2-Verbindungen (Laves-Phasen). *Z. Elektrochem. Angew. Phys. Chem.* **1939**, *45*, 849−865.
(23) Villars, P.; Cenzual, K. *Pearson's Crystal Data: Crystal Structure Database for Inorganic Compounds*; ASM International, Materials Park: Ohio, USA, 2023.
(24) Stein, F.; Palm, M.; Sauthoff, G. Structure and stability of Laves phases. part I - critical assessment of factors controlling Laves phase stability. *Intermetallics* **2004**, *12*, 713−720.
(25) Stein, F.; Palm, M.; Sauthoff, G. Structure and stability of Laves phases part II - structure type variations in binary and ternary systems. *Intermetallics* **2005**, *13*, 1056−1074.
(26) Stein, F.; Leineweber, A. Laves phases: A review of their functional and structural applications and an improved fundamental understanding of stability and properties. *J. Mater. Sci.* **2021**, *56*, 5321−5427.
(27) Yartys, V. A.; Lototskyy, M. V. Laves type intermetallic compounds as hydrogen storage materials: A review. *J. Alloys Compd.* **2022**, *916*, 165219.
(28) Gießelmann, E. C. J.; Pöttgen, R.; Janka, O. Laves phases: Superstructures induced by coloring and distortions. *Z. Anorg. Allg. Chem* **2023**, *649*, No. e202300109.
(29) Gießelmann, E. C. J.; Engel, S.; Kostusiak, W.; Zhang, Y.; Herbeck-Engel, P.; Kickelbick, G.; Janka, O. Raman and NMR spectroscopic and theoretical investigations of the cubic Laves-phases $REAl_2$ (*RE* = Sc, Y, La, Yb, Lu). *Dalton Trans.* **2023**, *52*, 3391−3402.
(30) Engel, S.; Gießelmann, E. C. J.; Schank, L. E.; Heymann, G.; Brix, K.; Kautenburger, R.; Beck, H. P.; Janka, O. Theoretical and ^{27}Al NMR spectroscopic investigations of binary intermetallic alkaline-earth aluminides. *Inorg. Chem.* **2023**, *62*, 4260−4271.
(31) Gießelmann, E. C. J.; Engel, S.; Baldauf, J.; Kösters, J.; Matar, S. F.; Kickelbick, G.; Janka, O. Searching for Laves Phase Superstructures: Structural and ^{27}Al NMR Spectroscopic Investigations in the Hf−V−Al System. *Inorg. Chem.* **2024**, *63*, 8180−8193.
(32) Reimann, M. K.; Johnscher, M.; Block, T.; Bönnighausen, J.; Pöttgen, R. Ternary Laves phases with the $MgCu_4Sn$-type structure: $RECo_4Mg$ (*RE* = Gd, Dy−Tm, Lu), $EuNi_4Mg$ and RET_4Cd (*RE* = Y, La−Nd, Sm, Gd−Dy; *T* = Cu, Pt). *Z. Naturforsch.* **2023**, *78b*, 497−504.
(33) Sikdar, R.; Roy, N.; Selvaratnam, B.; Mishra, V.; Mumbaraddi, D.; Mondal, A.; Buxi, K.; Jana, P. P.; Mar, A. Ahead by a Century: Discovery of Laves Phases Assisted by Machine Learning. *Inorg. Chem.* **2024**, *63*, 5972−5981.
(34) Reimann, M. K.; Pöttgen, R. The crystal structures and magnetic properties of $YbMg_{0.75}In_{1.25}$ and $Yb_6Mg_{6.41}In_{5.59}$. *Z. Naturforsch.* **2024**, *79*, 113−120.
(35) Friauf, J. B. The Crystal Structure of Magnesium Di-Zincide. *Phys. Rev.* **1927**, *29*, 34−40.
(36) Tarschisch, L.; Titow, A. T.; Garjanow, F. K. Röntgenographische Untersuchung der Verbindung $MgZn_2$. *Phys. Z. Sowjetunion.* **1934**, *5*, 503−510.
(37) Laves, F.; Witte, H. Die Kristallstruktur des $MgNi_2$ und seine Beziehungen zu den Typen $MgCu_2$ und $MgZn_2$. *Metallwirtsch* **1935**, *14*, 645−649.
(38) Lieser, K. H.; Witte, H. Untersuchungen in den ternären Systemen Magnesium-Kupfer-Zink Magnesium-Nickel-Zink und Magnesium-Kupfer-Nickel. *Int. J. Mater. Res.* **1952**, *43*, 396−401.
(39) Laves, F.; Witte, H. Der Einfluß von Valenzelektronen auf die Kristallstruktur ternärer Magnesiumlegierungen. *Metallwirtsch* **1936**, *15*, 840−842.
(40) Friauf, J. B. The crystal structures of two intermetallic compounds. *J. Am. Chem. Soc.* **1927**, *49*, 3107−3114.
(41) Paufler, P.; Gustav, E. R. Schulze's pioneering work on Laves phases. *Z. Kristallogr.* **2006**, *221*, 311−318.
(42) Gschneidner, K. A., Jr.; Pecharsky, V. K. Binary rare earth Laves phases − an overview. *Z. Kristallogr.* **2006**, *221*, 375−381.
(43) Yokosawa, T.; Söderberg, K.; Boström, M.; Grüner, D.; Kreiner, G.; Terasaki, O. Microscopic structures of Laves phases and structurally related compounds: A transmission electron microscopy study. *Z. Kristallogr.* **2006**, *221*, 357−374.
(44) Grüner, D.; Stein, F.; Palm, M.; Konrad, J.; Ormeci, A.; Schnelle, W.; Grin, Y.; Kreiner, G. Preparation, phase stability and structure of the C36 Laves phase $Nb_{1-x}Co_{2+x}$. *Z. Kristallogr.* **2006**, *221*, 319−333.
(45) Conrad, M.; Pohling, C.; Webert, H.; Harbrecht, B. Atomic ordering in the Laves phases L1 $V(Co_{1-x}Si_x)_2$ (x = 0.43 and 0.56). *Z. Kristallogr.* **2006**, *221*, 349−356.
(46) Grytsiv, A.; Chen, X.-Q.; Witusiewicz, V. T.; Rogl, P.; Podloucky, R.; Pomjakushin, V.; Maccio, D.; Saccone, A.; Giester, G.; Sommer, F.

Atom order and thermodynamic properties of the ternary Laves phase $Ti(Ti_yNi_xAl_{1-x-y})_2$. *Z. Kristallogr.* **2006**, *221*, 334−348.
(47) Gießelmann, E. C. J.; Engel, S.; Volpini, J. G.; Huppertz, H.; Kickelbick, G.; Janka, O. Mechanistic studies on the formation of ternary oxides by thermal oxidation of the cubic laves phase $CaAl_2$. *Inorg. Chem. Front.* **2023**, *11*, 286−297.
(48) Sappl, J.; Jung, F.; Hoch, C. Facile one-step syntheses of several complex ionic lithium gallates from LiGa as intermetallic precursors. *Chem. Mater.* **2020**, *32*, 866−873.
(49) Tampier, M.; Johrendt, D.; Pöttgen, R.; Kotzyba, G.; Trill, H.; Mosel, B. D. Magnetism and ^{151}Eu Mössbauer Spectra of α- and β-Eu_2GeS_4. *Z. Anorg. Allg. Chem.* **2002**, *628*, 1243−1245.
(50) Stroyuk, O.; Raevskaya, A.; Gaponik, N. Solar light harvesting with multinary metal chalcogenide nanocrystals. *Chem. Soc. Rev.* **2018**, *47*, 5354−5422.
(51) Johnson, M.; Baryshev, S. V.; Thimsen, E.; Manno, M.; Zhang, X.; Veryovkin, I. V.; Leighton, C.; Aydil, E. S. Alkali-metal-enhanced grain growth in Cu_2ZnSnS_4 thin films. *Energy Environ. Sci.* **2014**, *7*, 1931−1938.
(52) Yoo, H.; Kim, J. Comparative study of Cu_2ZnSnS_4 film growth. *Sol. Energy Mater. Sol. Cells* **2011**, *95*, 239−244.
(53) Eisenmann, B.; Jakowski, M.; Klee, W.; Schäfer, H. Die Strukturen von $CaAl_2S_4$, $CaGa_2S_4$, $SrAl_2S_4$, $SrGa_2S_4$ und $BaIn_2S_4$. *Rev. Chim. Miner.* **1983**, *20*, 255−263.
(54) Gorochov, O.; Tien, V. V.; Dung, N. H.; Barthelemey, E.; Flahaut, J. Proprietes electriques et magnetiques de quelques composes ternaires contenant de l'europium II. *Colloq. Int. Centre Natl. Rech. Sci.* **1970**, *2*, 157−168.
(55) Rimet, R.; Buder, R.; Schlenker, C.; Zanchetta, J. V. Magnetic susceptibility and EPR of europium compounds: $EuGa_2S_4$, $EuGa_2Se_4$ and $EuAl_2S_4$. *J. Magn. Magn. Mater.* **1980**, *15−18*, 1283−1284.
(56) Yu, R.; Yang, H. K.; Moon, B. K.; Choi, B. C.; Jeong, J. H. Luminescence properties of stoichiometric EuM_2S_4 (M=Ga, Al) conversion phosphors for white LED applications. *Phys. Status Solidi A* **2012**, *209*, 2620−2625.
(57) Pöttgen, R.; Gulden, T.; Simon, A. Miniaturisierte Lichtbogenapperatur für den Laborbedarf. *GIT Labor-Fachz.* **1999**, *43*, 133−136.
(58) Pöttgen, R.; Lang, A.; Hoffmann, R.-D.; Künnen, B.; Kotzyba, G.; Müllmann, R.; Mosel, B. D.; Rosenhahn, C. The stannides YbPtSn and $Yb_2Pt_3Sn_5$. *Z. Kristallogr.* **1999**, *214*, 143−150.
(59) Jitianu, A.; Amatucci, G.; Klein, L. C. Phenyl-substituted siloxane hybrid gels that soften below 140 °C. *J. Am. Ceram. Soc.* **2009**, *92*, 36−40.
(60) Pohl, S.; Janka, O.; Füglein, E.; Kickelbick, G. Thermoplastic Silsesquioxane Hybrid Polymers with a Local Ladder-Type Structure. *Macromolecules* **2021**, *54*, 3873−3885.
(61) Briesenick, M.; Gallei, M.; Kickelbick, G. High-Refractive-Index Polysiloxanes Containing Naphthyl and Phenanthrenyl Groups and Their Thermally Cross-Linked Resins. *Macromolecules* **2022**, *55*, 4675−4691.
(62) Bruker AXS Inc. *Topas, Version 5*; Bruker AXS Inc. Karlsruhe, Germany, 2014.
(63) Rietveld, H. M. Line profiles of neutron powder-diffraction peaks for structure refinement. *Acta Crystallogr.* **1967**, *22*, 151−152.
(64) Rietveld, H. M. A profile refinement method for nuclear and magnetic structures. *J. Appl. Crystallogr.* **1969**, *2*, 65−71.
(65) Nowotny, H.; Wormnes, E.; Mohrnheim, A. Untersuchungen in den Systemen Aluminium-Kalzium, Magnesium-Kalzium und Magnesium-Zirkon. *Z. Metallkd.* **1940**, *32*, 39−42.
(66) Iandelli, A.; Palenzona, A. Magnetic susceptibility and expansion coefficient of the intermetallic compounds $YbAl_2$ and $YbAl_3$. *J. Less-Common Met.* **1972**, *29*, 293−297.
(67) Cordier, G.; Czech, E.; Schäfer, H. Die Kristallstruktur von $SrAl_2$. *Z. Naturforsch* **1982**, *24*, 1191.
(68) Bruzzone, G.; Merlo, F. The strontium-aluminium and barium-aluminium systems. *J. Less-Common Met.* **1975**, *39*, 1−6.
(69) Haszko, S. E. Intermediate Phases with the $MgCu_2$ Structure. *Trans. Am. Inst. Min. Metall. Eng.* **1960**, *218*, 958.
(70) Fernandez, C.; Amoureux, J. P. Triple-quantum MAS-NMR of quadrupolar nuclei. *Solid State Nucl. Magn. Reson.* **1996**, *5*, 315−321.
(71) Frydman, L.; Harwood, J. S. Isotropic Spectra of Half-Integer Quadrupolar Spins from Bidimensional Magic-Angle Spinning NMR. *J. Am. Chem. Soc.* **1995**, *117*, 5367−5368.
(72) Bruker Corp. *Topspin, Version 2.1*; Bruker Corp, 2008.
(73) Massiot, D.; Fayon, F.; Capron, M.; King, I.; Le Calvé, S.; Alonso, B.; Durand, J.-O.; Bujoli, B.; Gan, Z.; Hoatson, G. Modelling one- and two-dimensional solid-state NMR spectra. *Magn. Reson. Chem.* **2002**, *40*, 70−76.
(74) Bak, M.; Rasmussen, J. T.; Nielsen, N. C. SIMPSON: A General Simulation Program for Solid-State NMR Spectroscopy. *J. Magn. Reson.* **2000**, *147*, 296−330.
(75) Blöchl, P. E. Projector augmented-wave method. *Phys. Rev. B* **1994**, *50*, 17953−17979.
(76) Kresse, G.; Joubert, D. From ultrasoft pseudopotentials to the projector augmented-wave method. *Phys. Rev. B* **1999**, *59*, 1758−1775.
(77) Kresse, G.; Furthmüller, J. Efficient iterative schemes for ab initio total-energy calculations using a plane-wave basis set. *Phys. Rev. B* **1996**, *54*, 11169−11186.
(78) Kresse, G.; Furthmüller, J. Efficiency of ab-initio total energy calculations for metals and semiconductors using a plane-wave basis set. *Comput. Mater. Sci.* **1996**, *6*, 15−50.
(79) Pyykkö, P. Year-2008 nuclear quadrupole moments. *Mol. Phys.* **2008**, *106*, 1965−1974.
(80) Pyykkö, P. Year-2017 nuclear quadrupole moments. *Mol. Phys.* **2018**, *116*, 1328−1338.
(81) Wada, H.; Shiga, M. Antiferromagnetic properties of $EuAl_2$. *Phys. B* **1994**, *193*, 25−30.
(82) Long, G. J.; Cranshaw, T. E.; Longworth, G. The Ideal Mössbauer Effect Absorber Thickness. *Mössbauer Eff. Ref. Data J.* **1983**, *6*, 42−49.
(83) Brand, R. A. *WinNormos for Igor6, Version for Igor 6.2 or above: 22.02.2017*; Universität Duisburg, 2017.
(84) Atzmony, U.; Bauminger, E. R.; Nowik, I.; Ofer, S.; Wernick, J. H. Isomer shifts and Mössbauer-effect efficiencies in intermetallic compounds of europium. *Phys. Rev.* **1967**, *156*, 262−266.
(85) Wickman, H. H.; Nowik, I.; Wernick, J. H.; Shirley, D. A.; Frankel, R. B. Hyperfine Fields and Isomer Shifts in Magnetically Ordered Europium Compounds. *J. Appl. Phys.* **1966**, *37*, 1246−1247.
(86) Roques, R.; Rimet, R.; Declercq, J. P.; Germain, G. Determination de la structure cristalline de $EuGa_2S_4$. *Acta Crystallogr.* **1979**, *B35*, 555−557.
(87) Flahaut, J. Contribution à l'étude du sulfure d'aluminium et des thioaluminates. *Ann. Chimie* **1952**, *12*, 632−696.
(88) Eisenmann, B. Crystal structure of α-dialuminium trisulfide, Al_2S_3. *Z. Kristallogr.* **1992**, *198*, 307−308.
(89) Holgersson, S. Die Struktur der Sulfide von Mg, Ca, Sr und Ba. *Z. Anorg. Allg. Chem.* **1923**, *126*, 179−182.
(90) Shannon, R. D. Revised effective ionic radii and systematic studies of interatomic distances in halides and chalcogenides. *Acta Crystallogr.* **1976**, *A32*, 751−767.
(91) Benndorf, C.; Eckert, H.; Janka, O. Structural characterization of intermetallic compounds by ^{27}Al solid state NMR spectroscopy. *Acc. Chem. Res.* **2017**, *50*, 1459−1467.
(92) Jensen, J.; Mackintosh, A. R. *Rare earth magnetism: Structures and excitations*; Clarendon Press: Oxford, 1991.
(93) Lueken, H. *Magnetochemie*; B. G. Teubner: Stuttgart, Leipzig, 1999.
(94) Wollan, E. O.; Koehler, W. C. Neutron Diffraction Study of the Magnetic Properties of the Series of Perovskite-Type Compounds $[_{(1-x)}La_xCa]MnO_3$. *Phys. Rev.* **1955**, *100*, 545−563.
(95) Engel, S.; Gießelmann, E. C. J.; Pöttgen, R.; Janka, O. Trivalent europium − a scarce case in intermetallics. *Rev. Inorg. Chem.* **2023**, *43*, 571−582.
(96) Radzieowski, M.; Stegemann, F.; Block, T.; Stahl, J.; Johrendt, D.; Janka, O. Abrupt europium valence change in $Eu_2Pt_6Al_{15}$ around 45 K. *J. Am. Chem. Soc.* **2018**, *140*, 8950−8957.

(97) Stegemann, F.; Block, T.; Klenner, S.; Zhang, Y.; Fokwa, B. P. T.; Timmer, A.; Mönig, H.; Doerenkamp, C.; Eckert, H.; Janka, O. From 3D to 2D: Structural, spectroscopical and theoretical investigations of the dimensionality reduction in the $[PtAl_2]^{\delta-}$ polyanions of the isotypic $MPtAl_2$ series (M = Ca−Ba, Eu). *Chem. - Eur. J.* **2019**, *25*, 10735−10747.
(98) Koldemir, A.; Klenner, S.; Pöttgen, R. Crystal structure of europium dichromium icosaaluminum, $EuCr_2Al_{20}$. *Z. Kristallogr. - New Cryst. Struct.* **2023**, *238*, 507−509.
(99) Schmiegel, J.-P.; Block, T.; Gerke, B.; Fickenscher, T.; Touzani, R. S.; Fokwa, B. P. T.; Janka, O. $EuAu_3Al_2$: Crystal and Electronic Structures and Spectroscopic, Magnetic, and Magnetocaloric Properties. *Inorg. Chem.* **2016**, *55*, 9057−9064.
(100) Mörsen, E.; Mosel, B. D.; Müller-Warmuth, W.; Reehuis, M.; Jeitschko, W. Mössbauer and magnetic susceptibility investigations of strontium, lanthanum and europium transition metal phosphides with $ThCr_2Si_2$ type structure. *J. Phys. Chem. Solids* **1988**, *49*, 785−795.
(101) Mörsen, E.; Mosel, B. D.; Müller-Warmuth, W.; Reehuis, M.; Jeitschko, W. A ^{151}Eu Mössbauer study of the magnetic hyperfine interactions in the metallic compound $Eu_2Co_{12}P_7$ containing trivalent europium. *J. Phys. C: Solid State Phys.* **1988**, *21*, 3133−3140.
(102) Klenner, S.; Heletta, L.; Pöttgen, R. Diluting europium spins − a magnetic and ^{151}Eu Mössbauer spectroscopic investigation of the solid solution $Eu_{1-x}Sr_xPtIn_2$. *Dalton Trans.* **2019**, *48*, 3648−3657.
(103) Gerke, B.; Korthaus, A.; Niehaus, O.; Haarmann, F.; Pöttgen, R. Triangular Zn_3 and Ga_3 units in $Sr_2Au_6Zn_3$, $Eu_2Au_6Zn_3$, $Sr_2Au_6Ga_3$, and $Eu_2Au_6Ga_3$ − structure, magnetism, ^{151}Eu Mössbauer and $^{69;71}$Ga solid state NMR spectroscopy. *Z. Naturforsch.* **2016**, *71b*, 567−577.
(104) Schellenberg, I.; Pfannenschmidt, U.; Eul, M.; Schwickert, C.; Pöttgen, R. A ^{121}Sb and ^{151}Eu Mössbauer Spectroscopic Investigation of $EuCd_2X_2$ (X = P, As, Sb) and $YbCd_2Sb_2$. *Z. Anorg. Allg. Chem.* **2011**, *637*, 1863−1870.
(105) Schellenberg, I.; Eul, M.; Hermes, W.; Pöttgen, R. A ^{121}Sb and ^{151}Eu Mössbauer Spectroscopic Investigation of $EuMn_2Sb_2$, $EuZn_2Sb_2$, $YbMn_2Sb_2$, and $YbZn_2Sb_2$. *Z. Anorg. Allg. Chem.* **2010**, *636*, 85−93.
(106) Gérard, A.; Grandjean, F.; Hodges, J. A.; Braun, D. J.; Jeitschko, W. Giant hyperfine field on ^{151}Eu in $EuFe_4P_{12}$. *J. Phys. C: Solid State Phys.* **1983**, *16*, 2797−2801.
(107) Raffius, H.; Mörsen, E.; Mosel, B. D.; Müller-Warmuth, W.; Jeitschko, W.; Terbüchte, L.; Vomhof, T. Magnetic properties of ternary lanthanoid transition metal arsenides studied by Mössbauer and susceptibility measurements. *J. Phys. Chem. Solids* **1993**, *54*, 135−144.
(108) Radzieowski, M.; Block, T.; Klenner, S.; Zhang, Y.; Fokwa, B. P. T.; Janka, O. Synthesis, crystal and electronic structure, physical properties and ^{121}Sb and ^{151}Eu Mössbauer spectroscopy of the $Eu_{14}AlPn_{11}$ series (Pn = As, Sb). *Inorg. Chem. Front.* **2019**, *6*, 137−147.
(109) Radzieowski, M.; Block, T.; Fickenscher, T.; Zhang, Y.; Fokwa, B. P. T.; Janka, O. Synthesis, crystal and electronic structures, physical properties and ^{121}Sb and ^{151}Eu Mössbauer spectroscopy of the alumoantimonide Zintl-phase $Eu_5Al_2Sb_6$. *Mater. Chem. Front.* **2017**, *1*, 1563−1572.
(110) Gerth, G.; Kienle, P.; Luchner, K. Chemical effects on the isomer shift in ^{151}Eu. *Phys. Lett. A* **1968**, *27*, 557−558.

https://doi.org/10.1021/acs.chemmater.4c02093
Chem. Mater. 2025, 37, 97−108

5.5 Oxidation behavior of intermetallic compounds (unpublished)

The following chapter presents all results dealing with the investigation of the oxidation behavior of intermetallic compounds that were not suitable for publication yet in the style of a small monography.

5.5.1 Differences in the oxidation behavior of the cubic rare earth Laves phases REAl$_2$ (RE = Sc, Y, La, Eu, Yb)

After carefully investigating the oxidation behavior of the cubic Laves phase $CaAl_2$, as well as the sulfidation of $EuAl_2$ ($CaAl_2$ and $SrAl_2$), in a further step, a systematic study about the oxidation behavior of other cubic Laves phases was carried out. Thereby a focus was set on the diamagnetic examples of Sc, Y and La as well as the most promising candidates for two different oxidation states namely being Eu and Yb. First, the findings after one initial oxidation reaction of the title compounds will be discussed, followed by an in-detail description of the most interesting results.

5.5.1.1 Precursor synthesis and characterization

The synthesis of the precursors was done by arc-melting of the elements in the correct stoichiometry for Sc, Y and La. The Yb and Eu compounds were synthesized by induction heating of the elements in a sealed Ta ampoule for 10-30 minutes. The lattice parameters obtained are given in Table 23. The corresponding powder diffractograms can be found in the appendix.

Table 23. Lattice parameters of the synthesized precursors for oxidation reactions with the general formula $RE\mathrm{Al_2}$ (RE = Sc, Y, La, Eu and Yb) adopting the $\mathrm{MgCu_2}$ type structure ($Fd\bar{3}m$) as well as $\mathrm{ScAl_3}$ ($\mathrm{Cu_3Au}$ structure, $Pm\bar{3}m$).

Compound	a / pm	Ref.	Figure
$\mathrm{ScAl_2}$	757.98(1)	*	Figure S19
$\mathrm{ScAl_2}$	757.98(1)	[260]	
$\mathrm{ScAl_2}$			
$\mathrm{ScAl_3}$	410.56(1)	*	Figure S20
$\mathrm{ScAl_3}$			
$\mathrm{YAl_2}$	786.34(1)	*	Figure S21
$\mathrm{YAl_2}$	786.29(1)	[260]	
$\mathrm{YAl_2}$			
$\mathrm{LaAl_2}$	814.94(1)	*	Figure S22
$\mathrm{LaAl_2}$	814.85(1)	[260]	
$\mathrm{LaAl_2}$			
$\mathrm{EuAl_2}$	812.86(1)	*	Figure S23
$\mathrm{EuAl_2}$	812.8(1)	[261]	
$\mathrm{EuAl_2}$			
$\mathrm{YbAl_2}$	788.37(1)	*	Figure S24
$\mathrm{YbAl_2}$	788.36(1)	[260]	
$\mathrm{YbAl_2}$			

* This work.

5.5.1.2 Initial bulk oxidation reactions – thermal analysis and Rietveld refinement

Initial oxidation reactions of the REAl$_2$ compounds (RE = Sc, Y, La, Eu and Yb) were conducted in an STA setup by heating the samples to 1273 K with a heating rate of 20 K min^{-1}, holding the temperature for one hour with followed cooling. In addition, a tube furnace setup with a constant flow of 100 % oxygen at the same temperature for 5 h (heating rate of 250 K h^{-1}) was utilized. The corresponding STA diagrams (temperature, mass change and heat flow) are presented in Figure S25-S29. Despite slight differences in the crystallinity the obtained powder patterns of the STA and bulk oxidation reaction are identical, therefore only the results of the tube furnace reactions are discussed. Table 24 summarizes the results of the Rietveld refinement after oxidation reaction.

Before presenting a deeper analysis sorted by the metals, some general trends and similarities shall be highlighted. All metals in all products that could be identified are in their highest oxidation state, being the trivalent state for the five rare earth elements and aluminum as well. In only one case, namely for EuAl$_2$ a phase pure sample could be identified. However, this finding is strongly surprising because the identified phase EuAlO$_3$ (GdFeO$_3$ type, *Pnma*)[262, 263] highly differs in composition (rare earth/aluminum ratio) from the precursor EuAl$_2$. A comparable observation was made for LaAl$_2$; however, no single-phase sample was obtained. The powder X-ray diffractogram of the lanthanum compound could only be described by using two domains of the same compound, namely LaAlO$_3$.[263, 264] For the Sc, Y and Yb case a product mixture of different compounds was found. For RE = Y and Yb, two main ternary oxides that have the same structure type for both metals could be identified, namely, REAlO$_3$[265, 266] (GdFeO$_3$ type, *Pnma*)[267] as well as RE_3Al$_5$O$_{12}$[268, 269] (Y$_3$Al$_5$O$_{12}$ type, $Ia\bar{3}d$).[270]. Sc differs from the other two, since no evidence for the formation of a ternary oxide was found. Here, a phase segregation of the two oxides seems to happen. A detailed analysis of the observed elemental Al and ScAl$_3$ is presented in the following chapter.

Table 24. Results from powder X-ray diffraction data of the oxidized samples analyzed via Rietveld refinements. Starting values were taken from literature data.[24]

Compound	product	mass%	*a* (pm)	*b* (pm)	*c* (pm)	*V* (nm^3)	Figure
$ScAl_2$	Sc_2O_3	48(1)	983.73(3)	*a*	*a*	0.9520	Figure 50
	Al_2O_3	38(1)	476.12(1)	*a*	1299.7(1)	0.2552	
	$ScAl_3$	2(1)	410.5(1)	*a*	*a*	0.0692	
	Al	12(1)	405.46(1)	*a*	*a*	0.0666	
YAl_2	$YAlO_3$	57(1)	532.21(1)	737.78(2)	518.42(1)	0.2036	Figure S30
	Al_2O_3	9(1)	475.98(3)	*a*	1299.4(1)	0.2549	
	Y_2O_3	7(1)	1059.3(1)	*a*	*a*	1.1896	
	$Y_3Al_5O_{12}$	23(1)	1205.62(7)	*a*	*a*	1.7524	
	Al	4(1)	405.40(1)	*a*	*a*	0.06663	
$LaAl_2$	$LaAlO_3$ I	59(1)	537.8(1)	*a*	1317(6)	0.330	Figure 53
	$LaAlO_3$ II	41(1)	535.9(3)	*a*	1312.5(16)	0.3265	
$EuAl_2$	$EuAlO_3$	100	529.73(3)	745.64(3)	527.81(2)	0.2085	Figure 54
$YbAl_2$	$Yb_3Al_5O_{12}$	68(1)	1194.64(2)	*a*	*a*	6.7682	Figure 55
	$YbAlO_3$	26(1)	532.87(3)	732.02(3)	512.98(2)	0.2001	
	Yb_2O_3	4(1)	1042.0(1)	*a*	*a*	1.1326	
	Al	2(1)	405.61(6)	*a*	*a*	0.0667	

5.5.1.3 *Deeper investigation of the oxidation of $ScAl_2$*

As briefly mentioned in the previous section, the oxidation of $ScAl_2$ did not result in the formation of a ternary oxide. The identified products were the binary oxides Sc_2O_3 ($(Mn_{0.5}Fe_{0.5})_2O_3$ structure type, $Ia\bar{3}$)[271] and Al_2O_3.[272] However, within the Rietveld analysis, elemental Al and some small reflections matching the intermetallic phase $ScAl_3$ (Cu_3Au structure, $Pm\bar{3}m$)[273] could be identified.

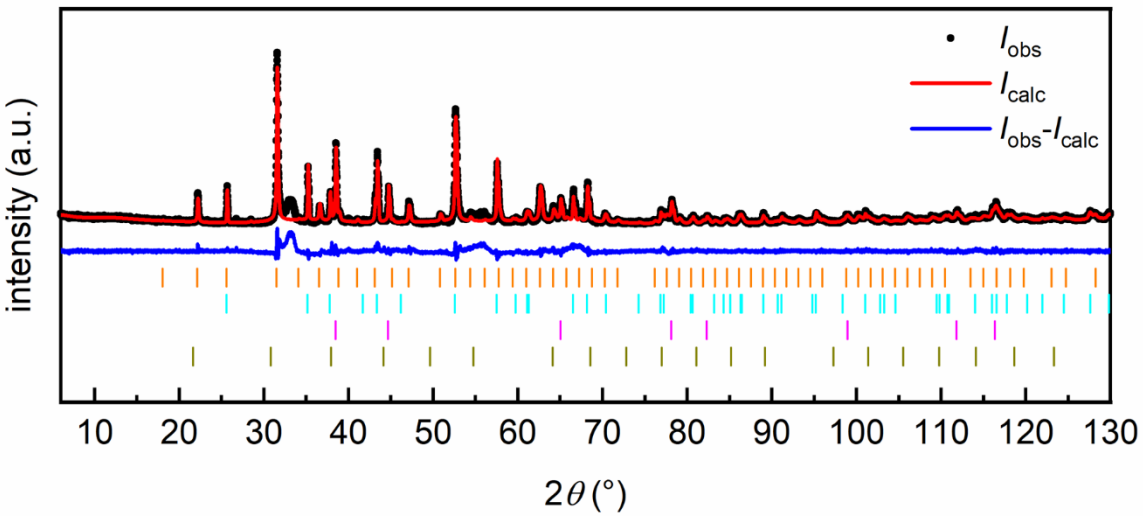

Figure 50. Powder X-ray diffraction pattern of oxidzized $ScAl_2$ in a tube furnace with pure oxygen (1273 K, 5 h). Experimental data is shown as black dots, simulated diffraction patterns from refinements as red lines, the difference is shown as continuous blue lines. Bragg positions are shown as orange (Sc_2O_3, space group $Ia\bar{3}$), cyan (Al_2O_3, space group $R\bar{3}c$), pink (elemental Al, space group $Fm\bar{3}m$) and dark yellow ($ScAl_3$, space group $Pm\bar{3}m$) ticks. The refined mass% are given in Table 24.

This was further proven by solid state NMR investigations of the oxidized product. The spectra are shown in Figure 51. Here, no clear evidence for an intermetallic compound is observed. The spectrum shows signals around 0 ppm as one would expect for oxidic species and a strong signal at 1640 ppm, matching the resonance for elemental aluminum. However, the ^{45}Sc spectrum shows a shifted signal besides a strongly broadened signal at 0 ppm, which is in the range of an intermetallic compound but not at the resonance frequency of $^{45}ScAl_2$. Independently synthesized $ScAl_3$ shows a resonance in the ^{45}Sc NMR spectra at the exact same position proving the presence of $ScAl_3$.

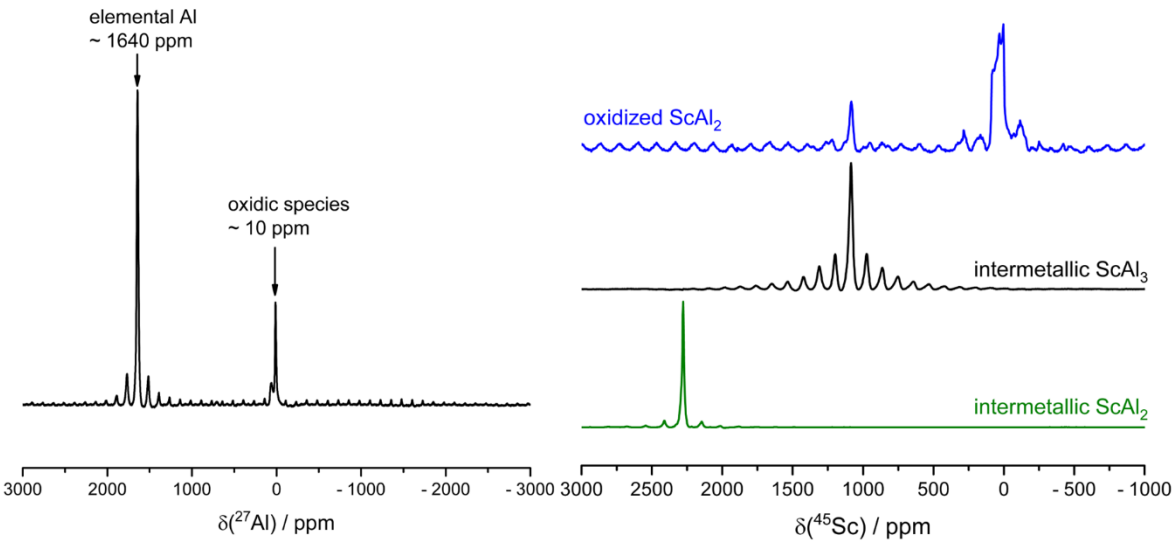

Figure 51. (*left*) ^{27}Al solid state NMR spectrum of the oxidation product of $ScAl_2$ and (*right*) the corresponding ^{45}Sc spectrum as well as the spectra of $^{45}ScAl_3$ and $^{45}ScAl_2$.

By tuning the reaction conditions, it was tested whether the formation of $ScAl_3$ as an intermediate product during the oxidation reaction could be proven. Furthermore, the oxidation behavior of phase pure $ScAl_3$ was tested. Table 25 summarizes the results of the oxidation reactions performed at differing temperatures and dwelling times. Both were reduced in comparison to the initial reaction to maybe stop the oxidation at the intermediate phase.

As can be seen from the results, the phase $ScAl_3$ is indeed formed during the oxidation process of $ScAl_2$. This is in line with the observation at the examples of $CaAl_2$, that one element shows a preferential oxidation behavior leaving either elemental aluminum or an aluminum-enriched intermetallic phase behind. In contrast to the oxidation of $CaAl_2$, here, the formation of a ternary oxide is not observed thus resulting in the two binary oxides. Oxidation reaction of $ScAl_3$ at 1273 K without dwelling showed that $ScAl_3$ has a higher oxidation resistance than $ScAl_2$, which would be in line with the fact that Sc seems to be oxidized before aluminum. Figure 52 depicts the powder X-ray diffractogram for the highest amount of $ScAl_3$ found after oxidation of $ScAl_2$. The remaining diffractograms can be found in the appendix.

These investigations clearly lead to the question of whether it is possible to identify yet unknown intermetallic compounds that can be isolated by oxidation reactions and if a tuning of the reaction conditions by e.g. high-energy ball milling can lead to the direct formation of a ternary oxide like $ScAlO_3$ ($GdFeO_3$ type Pnma)[274], which is only known as high-pressure compound. This will be part of future investigations.

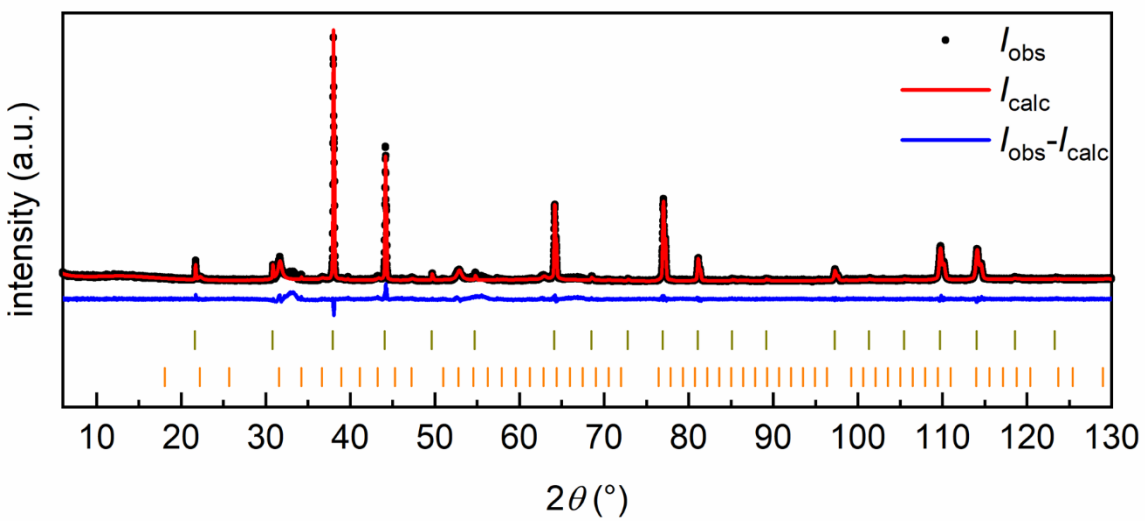

Figure 52. Powder X-ray diffraction pattern of $ScAl_2$ oxidized at 1073 K without dwelling time. Experimental data is shown as black dots, simulated diffraction patterns from refinements as red line, the difference is shown as continuous blue line. Bragg positions are shown as dark yellow ($ScAl_3$, space group $Pm\bar{3}m$), and orange (Sc_2O_3, space group $Ia\bar{3}$) ticks. The refined mass% are given in Table 25.

Table 25. Rietveld refinement of the oxidation reaction of $ScAl_2$ and $ScAl_3$ at different temperatures and dwelling times.

Temperature / K	Dwelling time / h	Phase contribution / mass%				Figure
		Sc_2O_3	Al_2O_3	$ScAl_3$	Al	
$ScAl_2$						
1273	5	47(1)	40(1)	1(1)	12(1)	Figure 50
1273	0	51(1)	24(1)	10(1)	15(1)	Figure S31
1073	0	41(1)	–	59(1)	–	Figure 52
$ScAl_3$						
1273	0	15(1)	9(1)	68(1)	8(1)	Figure S32

5.5.1.4 The oxidation product of $LaAl_2$ and $EuAl_2$

As stated in the previous section the oxidation of $LaAl_2$ resulted in the formation of $LaAlO_3$ (own type, $R\bar{3}c$).[275] However, the powder X-ray diffractogram could not be described by using only a single phase. A strong anisotropic broadening of the reflections could be observed. This could be described by using a second fraction of $LaAlO_3$ with slightly different lattice parameters (as can be seen in Table 24) and different crystallite sizes refined from the broadening of the reflections. This result clearly shows the stability of the corresponding structure type and its capability of high disorder. The corresponding powder pattern is shown in Figure 53. Additional annealing of the product at 1273 K for 1 h in the STA setup did not change the product (data not shown). To observe phase segregation or phase transformations probably higher temperatures are required. Concerning the stability of the described oxidic structure type, attempts with the existing precursor LaAl (CeAl structure type, space group *Cmcm*) could result in a single fraction product.

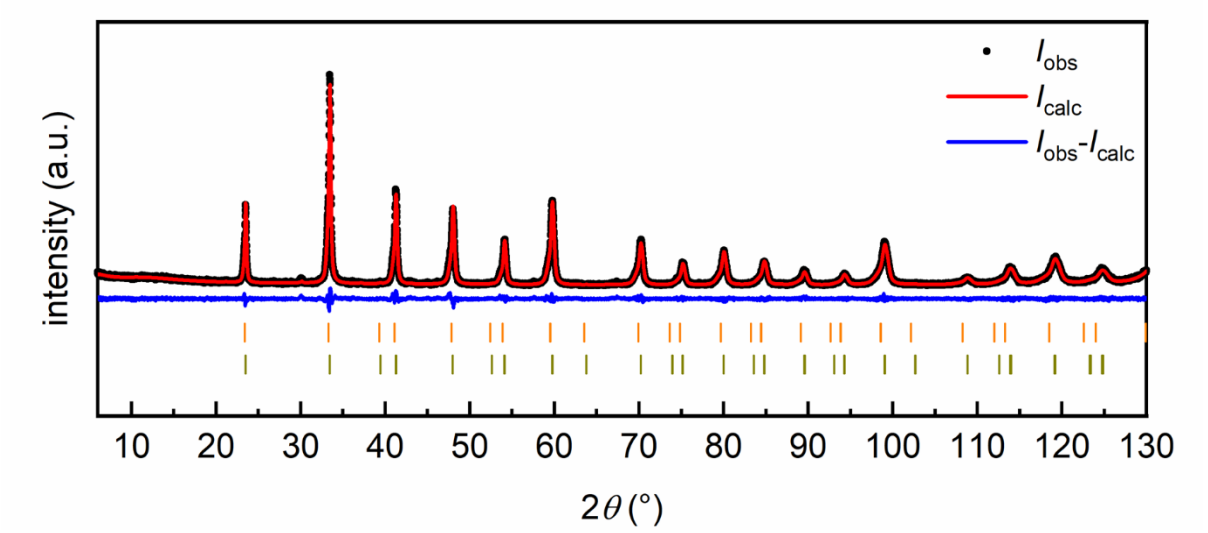

Figure 53. Powder X-ray diffraction pattern of oxidzized $LaAl_2$ in a tube furnace with 100 % oxygen (1273 K, 5 h). Experimental data is shown as black dots, simulated diffraction patterns from refinements as red lines, the difference is shown as continuous blue lines. Bragg positions are shown as orange and dark yellow (both $LaAlO_3$, space group $R\bar{3}c$) ticks. The refined mass% are given in Table 24.

The situation is comparable to the findings of the oxidation reaction of $EuAl_2$. Here, a single product was found, namely $EuAlO_3$, as discussed before. The powder X-ray diffractogram (Figure 54) could be described nicely by only applying this single phase without hints of any disorder or mixing of Eu and Al. This, however, arises the question where the "second" aluminum went. To further investigate this observation a change in the container material for the oxidation reactions is necessary since a diffusion of Al (or any other ion) into the crucible material can never be excluded. For this, the use of stainless steel or other ceramic materials such as MgO or BN would be of interest. It shall be noted that the obtained white powder shows a red fluorescence under UV light confirming the trivalent oxidation state of the Eu atoms. In analogy to the lanthanum case, an equiatomic precursor exists and would be highly promising for a direct synthesis of the obtained product.

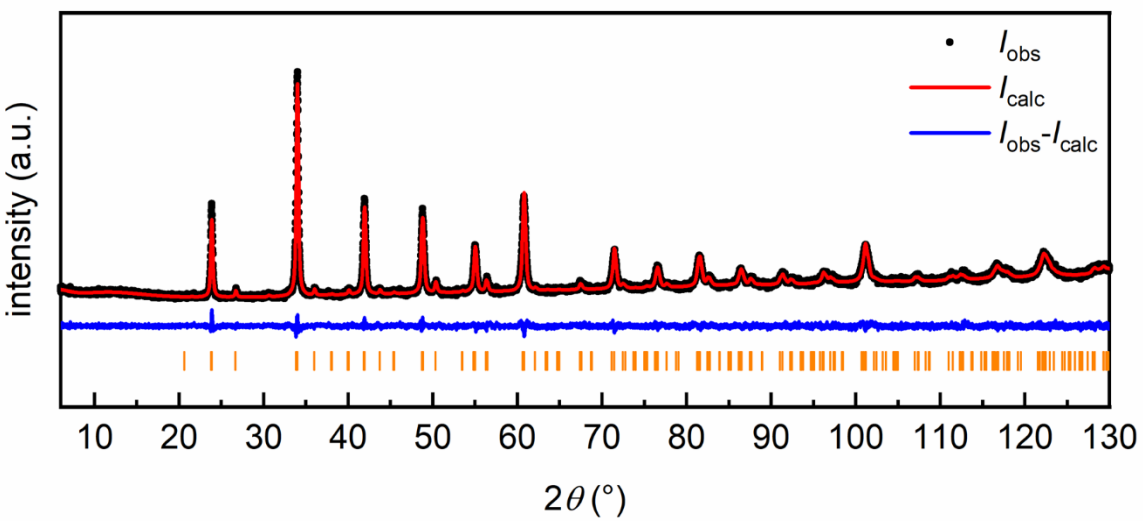

Figure 54. Powder X-ray diffraction pattern of oxidzized $EuAl_2$ in a tube furnace with 100 % oxygen (1273 K, 5 h). Experimental data is shown as black dots, simulated diffraction patterns from refinements as red lines, the difference is shown as continuous blue lines. Bragg positions are shown as orange ($EuAlO_3$, space group *Pnma*) ticks.

5.5.1.5 The oxidation of YAl_2 and $YbAl_2$

Oxidation reactions of YAl_2 and $YbAl_2$ (Figure 55) are comparable in a way that for both a mixture of the two ternary oxides $YAlO_3$ / $YbAlO_3$ and $Y_3Al_5O_{12}$ / $Yb_3Al_5O_{12}$ were found. The latter is the main product for the Yb case, while $YAlO_3$ is the main product (57 mass% determined by Rietveld analysis) for Y. Besides these, the binary rare earth oxides, both adapting the bixbyite type structure ($Ia\bar{3}$),[276, 277] could be identified. These systems were not further investigated by other bulk synthesis reactions. As a conclusion, as has been observed for the oxidation of $CaAl_2$, the formation of one or two distinct ternary oxides is highly favored. However, there is no clear tendency about the rare earth element to aluminum ratio, with the $RE_3Al_5O_{12}$ having a slightly higher rare earth element / aluminum ratio in comparison to the precursor and vice versa for the $REAlO_3$ oxide.

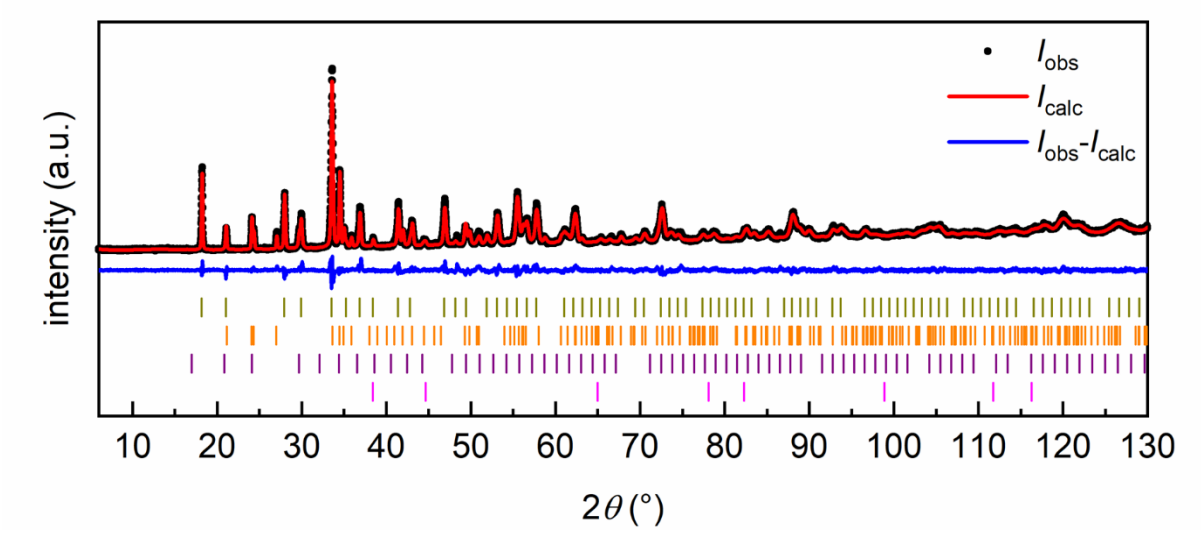

Figure 55. Powder X-ray diffraction pattern of oxidzized $YbAl_2$ in a tube furnace with 100 % oxygen (1273 K, 5 h). Experimental data is shown as black dots, simulated diffraction patterns from refinements as red lines, the difference is shown as continuous blue lines. Bragg positions are shown as dark yellow ($Yb_3Al_5O_{12}$, space group $Ia\bar{3}d$), orange ($YbAlO_3$, space group *Pnma*), purple (Yb_2O_3, space group $Ia\bar{3}$) and pink (elemental Al, space group $Fm\bar{3}m$) ticks. The refined mass% are given in Table 24.

5.5.1.6 Oxidation reactions with defined amounts of oxygen

The results discussed for the Yb and Eu compounds showed that after the reaction the rare earth atom is always found to be in its highest possible oxidation state being the trivalent one. For the sulfidation of $EuAl_2$ it was shown that the divalent state of Eu can be obtained using sulfur as reagent. The fact that divalent europium aluminates, such as $EuAl_2O_4$ ($SrAl_2O_4$ type, space group $P2_1$),[278] exist, leads to the question whether it is possible to perform a controlled oxidation of $EuAl_2$ leading to $Eu^{II}Al_2O_4$. This was approached using BaO_2, which is known to decompose to BaO and 1/2 O_2[279] as already described in section 5.3. Reactions were performed in a sealed silica ampoule with BaO_2 placed in an alumina crucible and a second crucible containing the intermetallic phase placed on top. If not stated otherwise the ampoule was heated to 1123 K, kept there for 48 h followed by heating to 1273 K for an additional 12 hours.

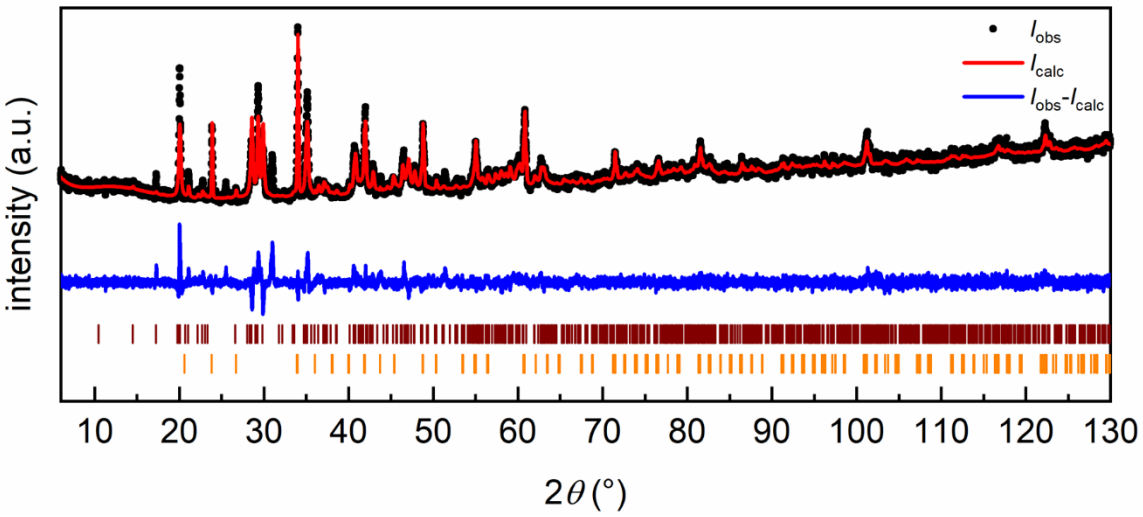

Figure 56. Powder X-ray diffraction pattern of $EuAl_2$ oxidized with four equivalents of BaO_2. Experimental data is shown as black dots, simulated diffraction patterns from refinements as red lines, the difference is shown as continuous blue lines. Bragg positions are shown as brown ($EuAl_2O_4$, space group $P2_1$, 79(1) mass%), and orange ($EuAlO_3$, space group *Pnma*, 21(1) mass%) ticks.

After an initial reaction the powder X-ray diffractogram shown in Figure 56 was obtained. Even though the crystallinity of the product and therefore the quality of the data is quite bad, the conclusion that the atmosphere of the oxidation reactions plays a crucial role can be made. Besides $Eu^{II}Al_2O_4$, 21 mass% of the known $Eu^{III}AlO_3$ could be identified. The observed oxidation of Eu to its trivalent state could be due to adsorbed water at the glass wall or oxygen from the crucible. Therefore, the amount of BaO_2 was reduced to three instead of four equivalents. The result of this reaction are shown in Figure 57. The product shows the same bad crystallinity, but the PXRD reveals $EuAl_2O_4$ with ~92 mass% as the main phase, besides $EuAlO_3$ and $Eu_4Al_2O_9$ (own type $P2_1/c$)[280] which could also be identified.

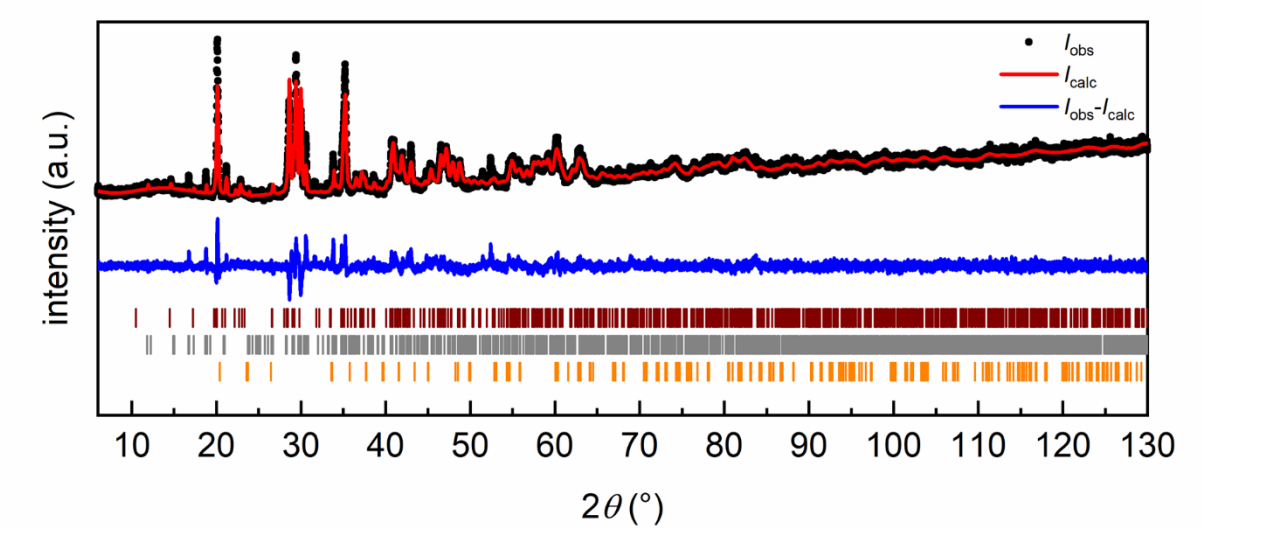

Figure 57. Powder X-ray diffraction pattern of $EuAl_2$ oxidized with three equivalents of BaO_2. Experimental data is shown as black dots, simulated diffraction patterns from refinements as red lines, the difference is shown as continuous blue lines. Bragg positions are shown as brown ($EuAl_2O_4$, space group $P2_1$, 92(1) mass%), dark grey ($Eu_4Al_2O_9$, space group $P2_1/c$, 6(1) mass%) and orange ($EuAlO_3$, space group *Pnma*, 2(1) mass%) ticks.

Changing the annealing sequence to 48 h at 1373 K (Figure 58) resulted in an improvement; the side phases shown in Figure 57 could not be identified. However, unidentified side products are visible. The product still shows the problem of bad crystallinity. However, these results clearly show that the oxidation state of Eu can be tuned by the atmosphere during oxidation reaction, but an improvement of the conditions is needed.

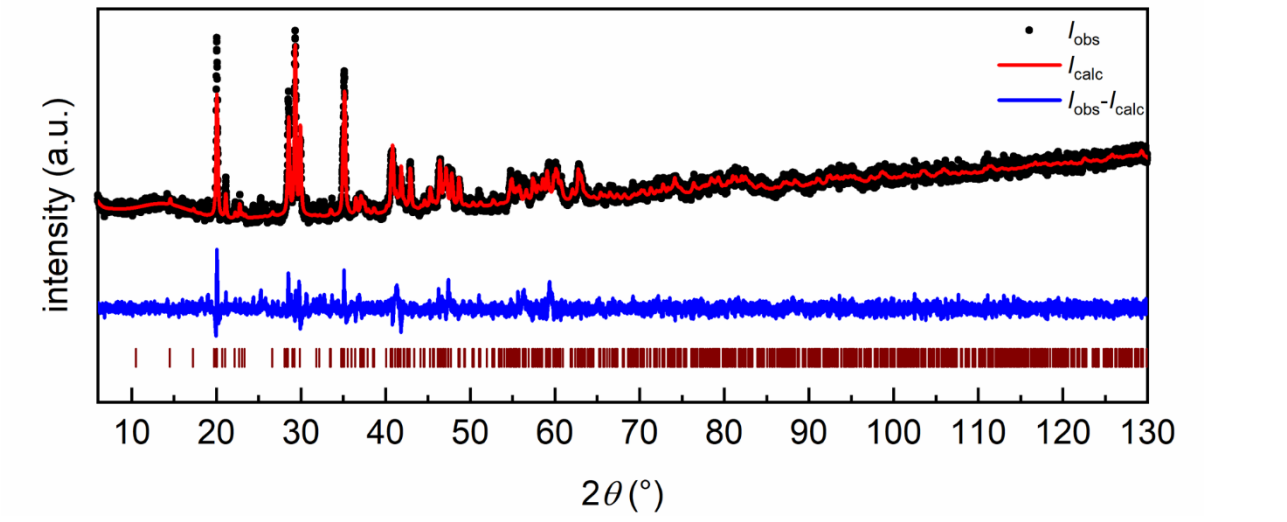

Figure 58. Powder X-ray diffraction pattern of $EuAl_2$ oxidized with three equivalents of BaO_2. Experimental data is shown as black dots, simulated diffraction patterns from refinements as red lines, the difference is shown as continuous blue lines. Bragg positions are shown as brown ($EuAl_2O_4$, space group $P2_1$) ticks.

The same approach was tested for $YbAl_2$. Here, when using stoichiometric or slightly off stoichiometric amounts of BaO_2 the reaction directly oxidizes all Yb atoms into their trivalent state and the reaction could not be stopped at the divalent state. This is in agreement with the

fact, that no divalent ytterbium aluminates are listed within the Pearson‘s Crystal Data database.[24] The main products discussed before were also identified but in slightly different ratios. Results are summed up in Table 26. The results are shown in Figure 59 (four equivalents of BaO_2) as well as in the Figure 60 (3 equivalents of BaO_2).

Table 26. Rietveld analysis for the different oxidation reactions performed with $YbAl_2$.

Method	mass% obtained by Rietveld				
	$Yb_3Al_5O_{12}$	$YbAlO_3$	Yb_2O_3	$YbAl_3$	Al
Bulk oxidation	68(1)	26(1)	4(1)	–	2(1)
4 eq. BaO_2	59(1)	33(1)	3(1)	–	5(1)
3 eq. BaO_2	93(1)	1(1)	2(1)	–	4(1)
1 eq. BaO_2	5(1)	41(1)	–	44(1)	10(1)

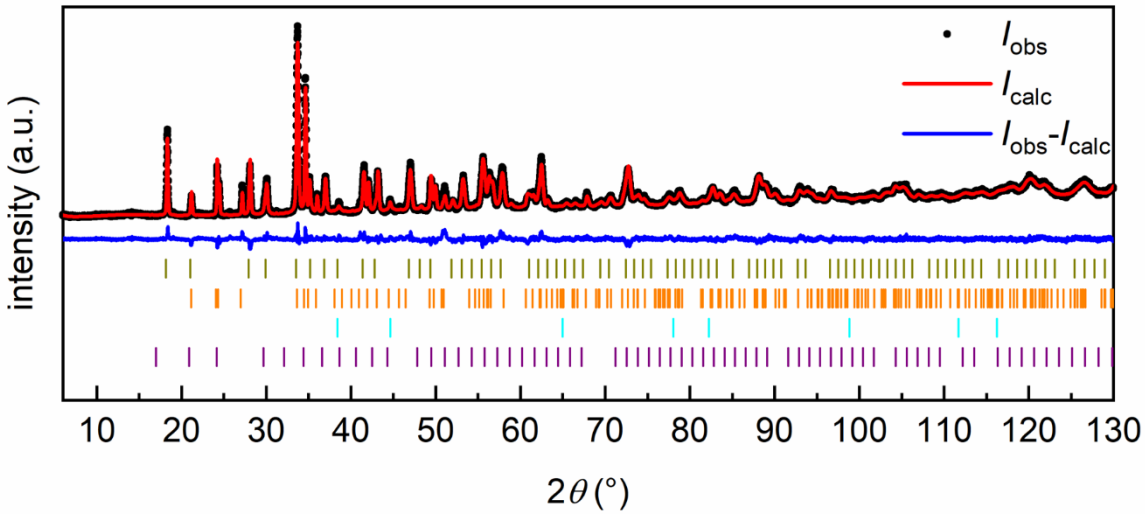

Figure 59. Powder X-ray diffraction pattern of $YbAl_2$ oxidized with four equivalents of BaO_2. Experimental data is shown as black dots, simulated diffraction patterns from refinements as red lines, the difference is shown as continuous blue lines. Bragg positions are shown as dark yellow ($Yb_3Al_5O_{12}$, space group $Ia\bar{3}d$), orange ($YbAlO_3$, space group *Pnma*), purple (Yb_2O_3, space group $Ia\bar{3}$) and pink (elemental Al, space group $Fm\bar{3}m$) ticks. The refined mass% are given in Table 26.

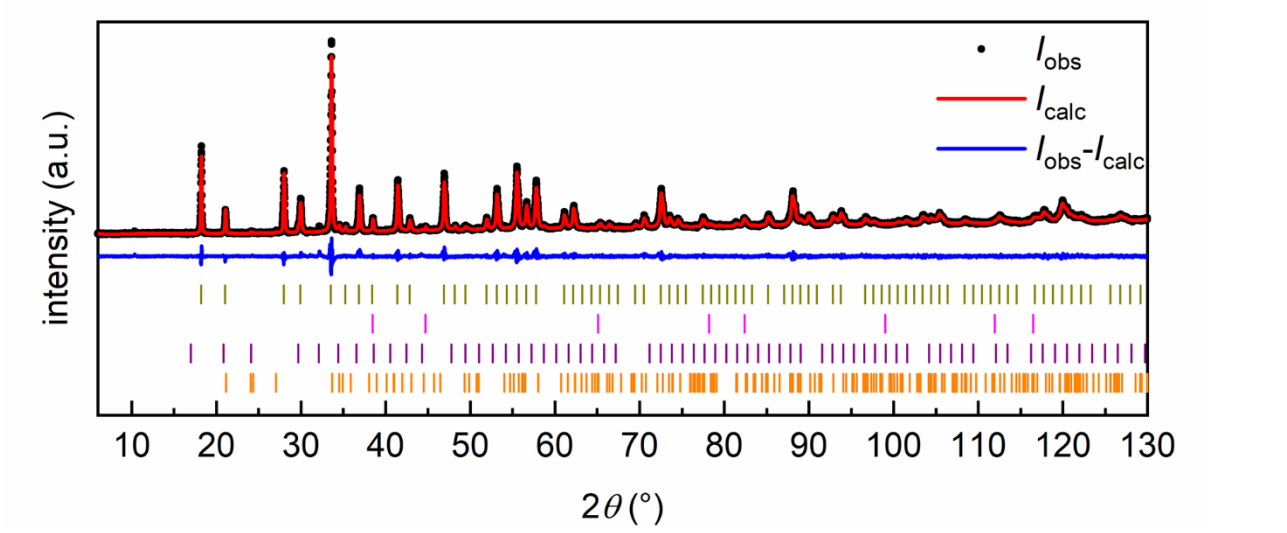

Figure 60. Powder X-ray diffraction pattern of $YbAl_2$ oxidized with three equivalents of BaO_2. Experimental data is shown as black dots, simulated diffraction patterns from refinements as red lines, the difference is shown as continuous blue lines. Bragg positions are shown as dark yellow ($Yb_3Al_5O_{12}$, space group $Ia\bar{3}d$), pink (elemental Al, space group $Fm\bar{3}m$), purple (Yb_2O_3, space group $Ia\bar{3}$) and orange ($YbAlO_3$, space group *Pnma*) ticks. The refined mass% are given in Table 26.

An interesting observation was made if a larger deficiency of oxygen is used. When only one equivalent of BaO_2 at lower temperatures (48 h at 1123 K) is used, still the ternary oxides are visible in the powder X-ray pattern, but also the intermediate intermetallic phase $YbAl_3$ (Cu_3Au structure, $Pm\bar{3}m$) can be identified in high amounts in agreement to the $ScAl_2$ oxidation, as can be seen in Figure 61.

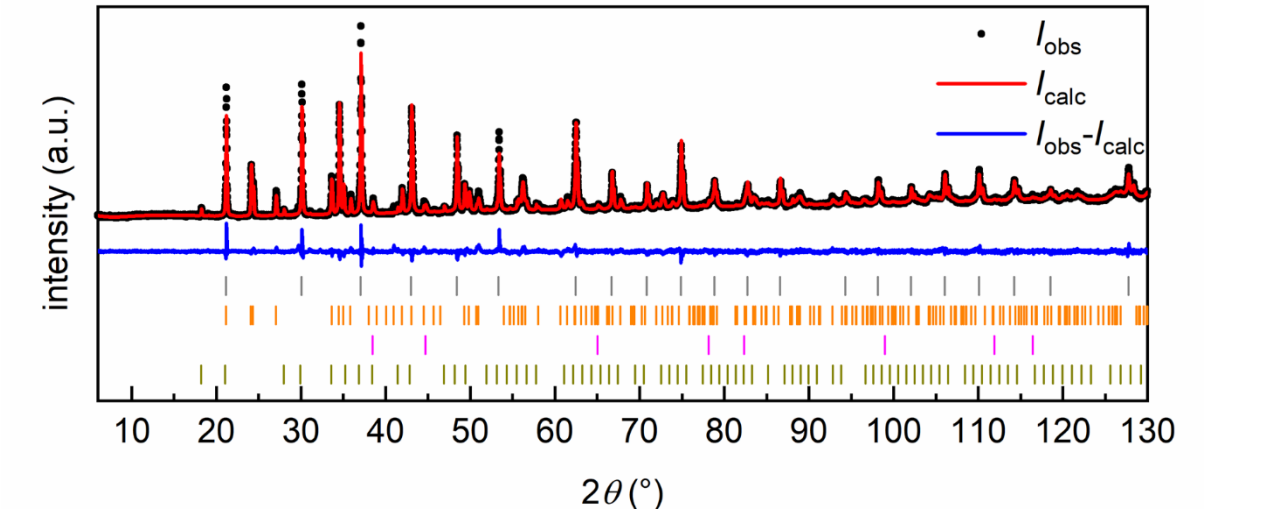

Figure 61. Powder X-ray diffraction pattern of $YbAl_2$ oxidized with one equivalent of BaO_2. Experimental data is shown as black dots, simulated diffraction patterns from refinements as red lines, the difference is shown as continuous blue lines. Bragg positions are shown as dark grey ($YbAl_3$, space group $Pm\bar{3}m$), orange ($YbAlO_3$, space group *Pnma*), pink (elemental Al, space group $Fm\bar{3}m$) and dark yellow ($Yb_3Al_5O_{12}$, space group $Ia\bar{3}d$) ticks. The refined mass% are given in Table 26.

Summing up these results, the oxidation behavior of the *RE*Al_2 series highly depends on the rare earth element with different ternary and binary oxides being the main products of the reactions. By tuning the reaction conditions for the Sc sample, an intermediate intermetallic phase could be observed that forms during the full oxidation of $ScAl_2$. The product formation in case of $EuAl_2$ highly depends on the oxygen concentration, whereas this is not the case for ytterbium, where in contrast to europium only the trivalent oxidation state was found. Nevertheless, by using only small amounts of oxygen, an intermediate intermetallic phase being aluminum richer in comparison to the intermetallic precursor $YbAl_2$ could be identified. The systematic analysis of the oxidation behavior of these compounds is promising for further investigation, especially when looking at $EuAl_2O_4$ for which an optimization of the reaction conditions is very promising. Moreover, the observation of other intermetallic compounds during the oxidation reaction raises the question whether it is possible to isolate intermetallic phases not known yet.

5.5.2 A systematic study on the oxidation behavior of the alkaline earth aluminides $AEAl_4$ (AE = Ca, Sr, Ba), $SrAl_2$ and Ba_7Al_{13}

The interesting findings on the oxidation behavior of the binary intermetallic aluminum compound $CaAl_2$ ($MgCu_2$ type $Fd\bar{3}m$) led on the one hand to the investigations of the isostructural series of $RE Al_2$ described in section 5.1.1. When looking at other group II elements it is possible to look at intermetallic compounds with the same composition as $CaAl_2$ but changing the structure type. As already discussed, $SrAl_2$ crystallizes at room temperature and ambient pressure in the orthorhombic KHg_2 structure type (*Imma*). The $MgCu_2$ type phase can only be obtained under high pressure. A nominal "$BaAl_2$" does not exist at room temperature and ambient pressure, but it is reported as a high-pressure phase. Here the phase Ba_7Al_{13} (own type, $P\bar{3}m1$), respectively $Ba_{21}Al_{40}$ (own type, $P31m$), can be used as a precursor. The phase is given as "$BaAl_2$" for simpleness in the following text. For the structural refinement of the precursor the structure model of Ba_7Al_{13} provided by either Bruzzone[281] or Häussermann[97] was used. The product formation after oxidation for these two compounds will be discussed in this section as well as another isostructural series of group II aluminides that has been mentioned already: the tetragonal MAl_4 (M = Sr, Ba) compounds as well as monoclinic $CaAl_4$.

The $AEAl_2$ compounds were synthesized by placing the elements in a closed Ta ampoule followed by heating for 10-30 minutes using induction heating. The "$BaAl_2$" precursor was stored under argon since a slow oxidation at ambient conditions was observed. The $AEAl_4$ compounds were obtained by arc-melting the elements. To avoid evaporation of the alkaline earth metal it was wrapped in the appropriate amount of aluminum foil. Lattice parameters are given in Table 27. The corresponding powder X-ray diffractograms can be found in the appendix.

If not stated otherwise, oxidation reactions were either performed in a STA setup using a mixture of oxygen and argon or in a tube furnace operating with pure oxygen in analogy to the investigations of the $RE Al_2$ series. Temperatures and dwelling times are always given with the respective reactions. Typical heating rates in the STA system are 20 K min^{-1} and 250 K h^{-1} for the reactions in the tube furnace. For some investigations, the powders were ground after initial oxidation and further annealed.

Table 27. Lattice parameters of the synthesized precursors for oxidation reactions with the general formula $AEAl_4$ (AE = Ca, Sr and Ba) as well as $AEAl_2$ (AE = Sr and "Ba").

Compound	structure type	*a* / pm	*b* / pm	*c* / pm	*β* / °	ref	Figure
$CaAl_4$	$CaGa_4$	616.92(1)	618.42(1)	634.38(1)	118.06	*	Figure S33
$CaAl_4$	$CaGa_4$	616.91	618.50	634.34	118.03	[282]	
$CaAl_4$	$CaGa_4$	615.3	617.3	632.9	118.03	[102]	
$SrAl_4$	$BaAl_4$	446.38(1)	*a*	1121.02(1)	90	*	Figure S34
$SrAl_4$	$BaAl_4$	446.4	*a*	1121.8	90	[282]	
$SrAl_4$	$BaAl_4$	446.3	*a*	1120.3	90	[283]	
$BaAl_4$	$BaAl_4$	456.73(1)	*a*	1128.43(1)	90	*	Figure S35
$BaAl_4$	$BaAl_4$	456.72	*a*	1128.63	90	[282]	
$BaAl_4$	$BaAl_4$	456.6	*a*	1125	90	[284]	
$SrAl_2$	KHg_2	479.59(1)	789.52(1)	795.92(1)	90	*	Figure S36
$SrAl_2$	KHg_2	479.62	789.30	795.51	90	[282]	
$SrAl_2$	KHg_2	484	792	799	90	[96]	
Ba_7Al_{13}	own type	610.15(1)	*a*	1727.24(2)	90	*	Figure S37
Ba_7Al_{13}	own type	609.97	*a*	1726.9	90	[97]	

*This work.

5.5.2.1 Oxidation reactions of nominal $AEAl_2$

Figure 62 shows an example of the powder X-ray diffractograms obtained for the reaction of $SrAl_2$, which was heated for 5 h in an STA system at 1273 K. Table 28 summarizes the products that could be identified for different reaction conditions. The corresponding STA data are shown in the appendix (Figure S39 & Figure S40). Table 29 shows the results of the Rietveld refinement for a sample oxidized for 12 hours at 1273 K, which was ground afterwards and annealed further for additional 12 h giving total reaction times of 24 and 36 hours. In an analogy to the $CaAl_2$ system multiple ternary oxides could be identified. However, the finding of the corresponding mayenite structure was not likely since only Sr containing solid solutions are reported.[285, 286] The main phases identified are $Sr_3Al_2O_6$ ($Ca_3Al_2O_6$ structure type $Pa\bar{3}$),[287-289] the expected $SrAl_2O_4$ (own type $P2_1$)[290] as well as the aluminum rich $SrAl_{12}O_{19}$ ($BaFe_{12}O_{19}$ type $P6_3/mmc$).[291] Besides the intermetallic compound $SrAl_4$ and elemental Al, also $SrCO_3$ ($CaCO_3$ type *Pnma*),[292] were identified. The latter is likely to result from the formation of small quantities of SrO, which forms the carbonate in contact with air after the reaction. In the case of the Ca example the binary oxide is stable enough. The observation of $SrAl_4$ can be explained in an analogous way to the formation of $YbAl_3$ in the previous section. However, it cannot be excluded that the small amounts present in the precursor do not react and are therefore identified after short reaction times.

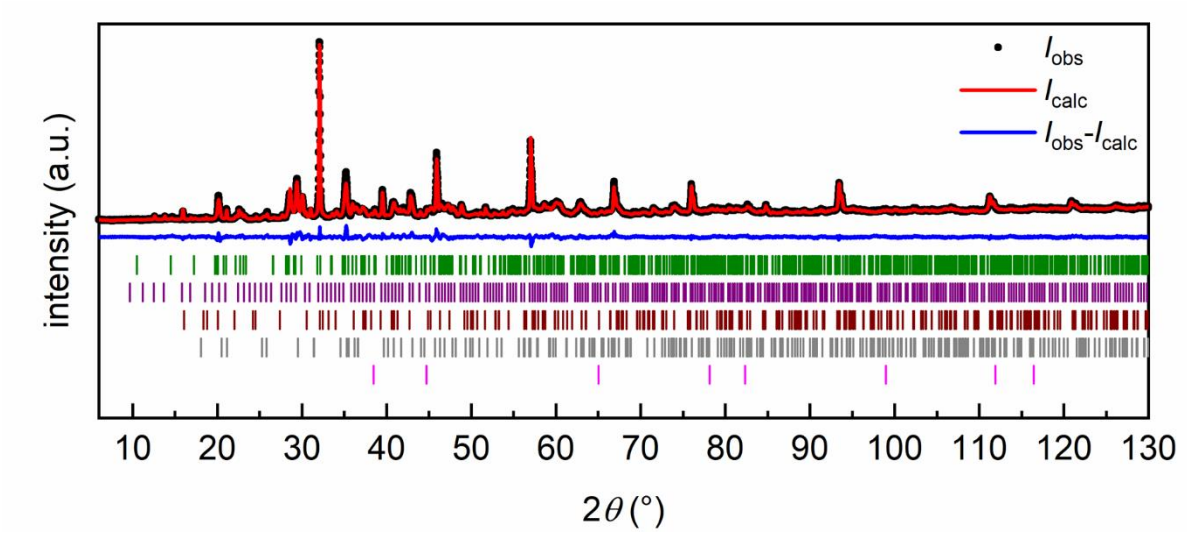

Figure 62. Powder X-ray diffraction pattern of $SrAl_2$ oxidized at 1273 K in an STA setup for 5 h. Experimental data is shown as black dots, simulated diffraction patterns from refinements as red line, the difference is shown as continuous blue line. Bragg positions are shown as green ($SrAl_2O_4$, space group $P2_1$), purple ($Sr_3Al_2O_6$, space group $Pa\bar{3}$), brown ($SrAl_{12}O_{19}$, space group $P6_3/mmc$), dark grey ($SrCO_3$, space group *Pnma*) and pink (elemental Al, space group $Fm\bar{3}m$) ticks. The refined mass% are given in Table 28.

Table 28. Results of the Rietveld refinement of the oxidation of $SrAl_2$ in an STA device for two different dwelling times at 1273 K.

Dwelling time / h	refined fractions / mass%						Figure
	$Sr_3Al_2O_6$	$SrAl_2O_4$	$SrAl_{12}O_{19}$	$SrAl_4$	$SrCO_3$	Al	
0	35(1)	31(1)	–	8(1)	14(1)	12(1)	Figure S38
5	31(1)	54(1)	9(1)	–	3(1)	2(1)	Figure 62

Table 29. Results of the Rietveld refinement of the oxidation of $SrAl_2$ in a tube furnace for subsequent annealing the sample for 12 hours at 1273 K.

Total time / h	refined fractions / mass%					Figure
	$Sr_3Al_2O_6$	$SrAl_2O_4$	$SrAl_{12}O_{19}$	$SrCO_3$	Al	
12	23(1)	56(1)	12(1)	6(1)	3(1)	
24	14(1)	79(1)	7(1)	–	–	Figure S41
36	9(1)	87(1)	4(1)	–	–	

The oxidation of $SrAl_2$ leads to a mixture of different ternary oxides. The main product found, which is formed in high amounts after multiple annealing steps, is indeed the desired product $SrAl_2O_4$. However, a full conversion was not possible, comparable to the $CaAl_2$ system. In analogy to the investigations involving $CaAl_2$ the Sr-rich (when compared to the precursor) product $Sr_3Al_2O_6$ could be identified initially. The Ca analogue $Ca_3Al_2O_6$ was also observed in the respective studies, however, the formation there was probably suppressed by the more stable mayenite phase. After multiple reaction steps this product was found in less amounts.

The resulting powder pattern of the oxidation reaction of $BaAl_2$ in an STA setup at 1273 K with a dwelling time of 5 h is shown in Figure 63. The corresponding STA data are shown in the appendix (Figure S42).

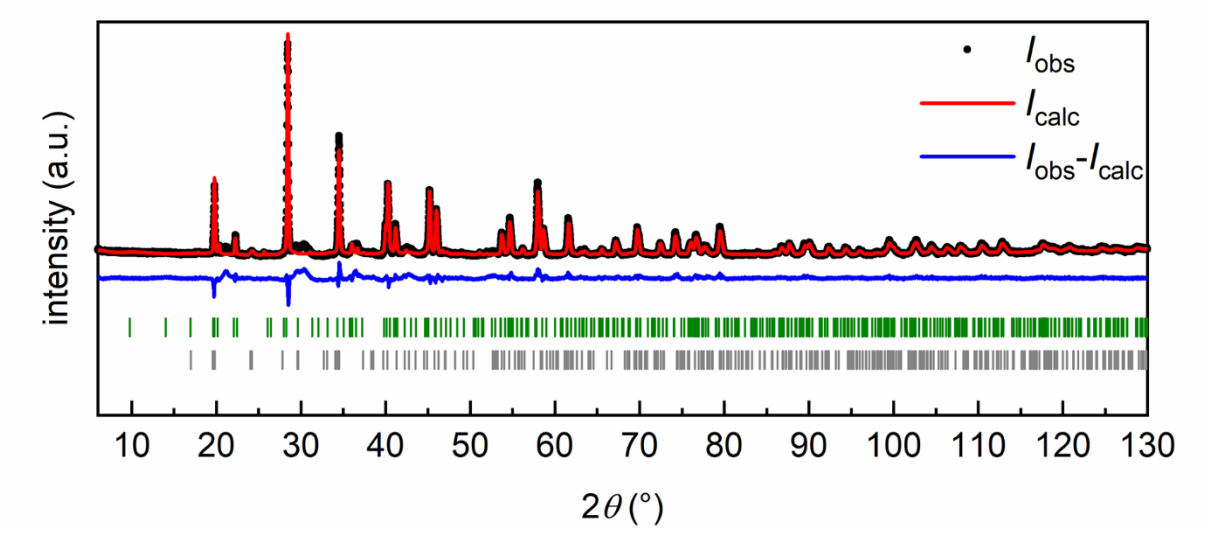

Figure 63. Powder X-ray diffraction pattern of $BaAl_2$ oxidized at 1273 K in an STA setup for 5 h. Experimental data is shown as black dots, simulated diffraction patterns from refinements as red line, the difference is shown as continuous blue line. Bragg positions are shown as green ($BaAl_2O_4$, space group $P6_3$, 97(1) mass%) and dark grey ($BaCO_3$, space group *Pnma*, 3(1) mass%) ticks.

While here the intended product $BaAl_2O_4$ (own type, $P6_3$)[293, 294] could clearly be identified as the main product; a nanocrystalline side phase, as can be seen from the significantly broadened Bragg reflections visible in Figure 63, occurred. It was therefore tried to anneal the oxidized sample to get to a phase pure sample. This was indeed possible by applying multiple reaction steps with dwelling times between 6-24 hours. Figure 64 shows the powder X-ray diffractogram for three consecutive 24-hours reactions making it 72 h reaction / annealing time in total. A second example with twelve-hour steps is shown in the appendix (Figure S43). In both cases the purity of the obtained $BaAl_2O_4$ can highly be increased.

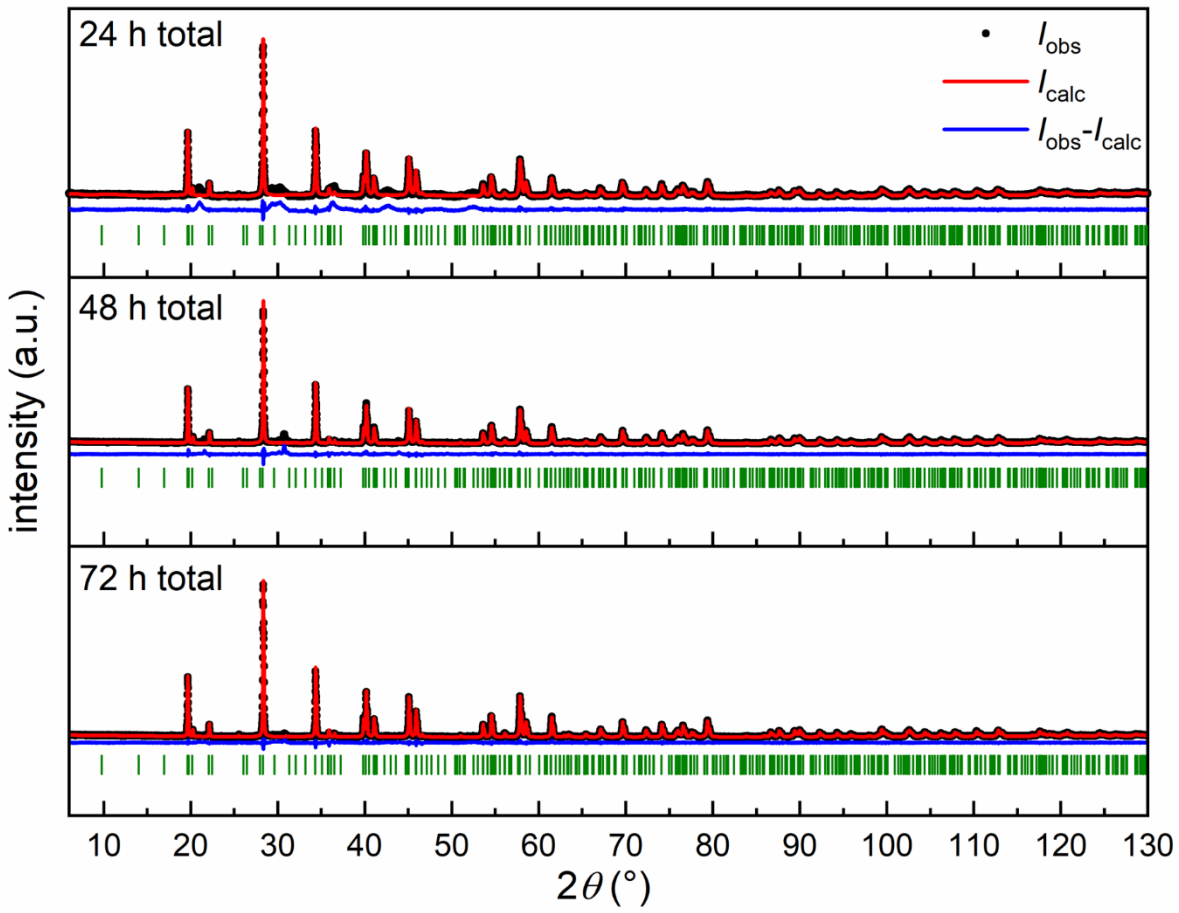

Figure 64. Powder X-ray diffraction patterns of $BaAl_2$ oxidized at 1273 K in a tube furnace operating with pure oxygen flow for (*top*) initial 24 hours, followed by grinding and additional annealing for 24 hours, resulting in total times of (*middle*) 48 and (*bottom*) 72 hours. Experimental data is shown as black dots, simulated diffraction patterns from refinements as red line, the difference is shown as continuous blue line. Bragg positions are shown as green ($BaAl_2O_4$, space group $P6_3$) ticks.

Since the compounds $BaAl_2O_4$ is reported to crystallize in a non-centrosymmetric space group, it would be interesting to test its SHG (Second Harmonic Generation)[295] properties. However, samples of $BaAl_2O_4$ obtained by oxidation reactions as well as the ones synthesized by mixing the nitrates (powder X-ray analysis shown in Figure 65) did not give any signal during SHG measurements. A detailed investigation of the obtained material in a high-resolution TEM with the goal of confirming the non-centrosymmetric structure could not be performed during this work, but is highly promising, since the complete absence of SHG properties is yet unclear.

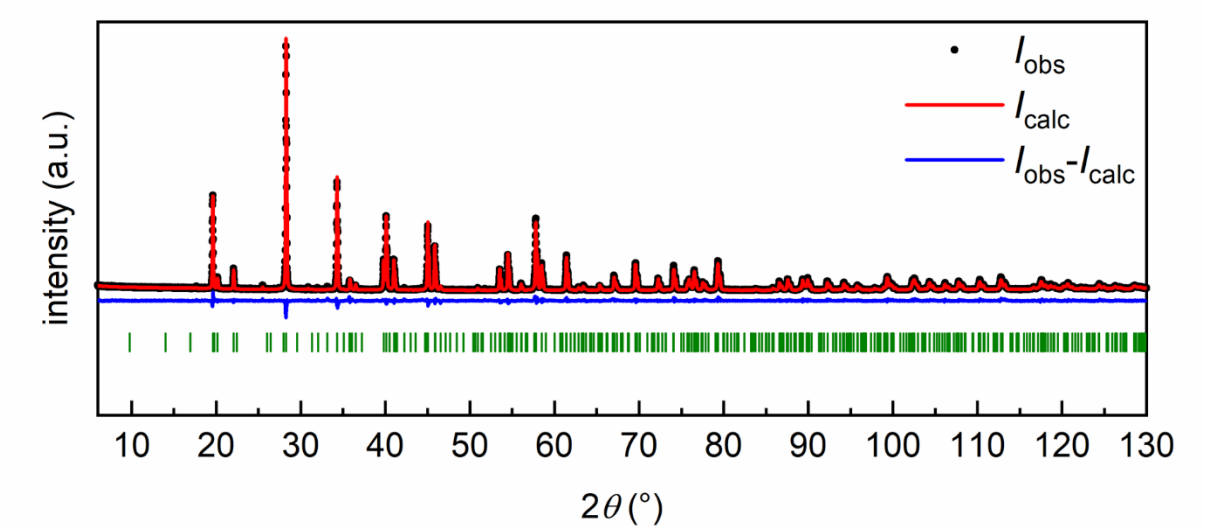

Figure 65. Powder X-ray diffraction patterns of $BaAl_2O_4$ obtained by the reaction of $Ba(NO_3)_2$ and $Al(NO_3)_3$. Experimental data is shown as black dots, simulated diffraction patterns from refinements as red line, the difference is shown as continuous blue line. Bragg positions are shown as green ($BaAl_2O_4$, space group $P6_3$) ticks.

5.5.2.2 Oxidation reactions of $AEAl_4$

Leaving the composition of 1:2, another series of compounds that is suitable for investigations is the above-mentioned series of $AEAl_4$ (*AE* = Ca, Sr, Ba). They crystallize almost isostructural with the Sr and Ba compound adopting $BaAl_4$ type (*I*4/*mmm*) and $CaAl_4$ adopting a monoclinic distortion variant at room temperature. These are also of interest for a proof-of-principle investigation, as the corresponding $AEAl_4O_7$ oxides exist for all three alkaline earth metals.[296-298]

For all three compounds the same experiments were conducted in the first place. All compounds were oxidized using the described STA setup with a mixture of argon and oxygen, applying heating rates of 20 K min^{-1} up to 1273 K for different annealing times (0 and 5 hours). Furthermore, oxidation reactions were performed in a tube furnace in a pure oxygen flow. Here different annealing times were used. The samples were initially heated for 5 hours and 24 hours. The annealing time given here as 48 hours corresponds to a second annealing of 24 hours after initial reaction for 24 hours.

Figure 66 depicts the powder X-ray diffractogram after the oxidation of $CaAl_4$ in an STA setup with a dwelling time of 5 hours. For this and all other oxidation reactions performed, Table 30 lists the phases that could be identified and the results of the Rietveld refinement. Corresponding STA data are given in the appendix (Figure S45 & Figure S46). Interestingly, the results obtained are quite comparable to the oxidation of $CaAl_2$. The mayenite phase $Ca_{12}Al_{14}O_{33}$ ($Ca_6Al_7O_{16.5}$, own type $I\bar{4}3d$),[299-301] is also found after the initial oxidation of $CaAl_4$, however, in lower amounts (mass% determined by Rietveld analysis). Besides this product, other ternary oxides, which were also identified for the $CaAl_2$ case, could be observed. The monoclinic $CaAl_2O_4$ (own type, $P2_1/c$)[302] as well as the expected product, when starting with this specific precursor, $CaAl_4O_7$ (own type).[296] A fourth ternary oxide, which was only found in small amounts is $Ca_5Al_6O_{14}$ (own type $Cmc2_1$).[303] A trend that can be observed is the vanishing of the mayenite phase with longer annealing times, respectively additional heating cycles. However, also with this precursor, it was not possible to obtain a phase-pure oxidation product.

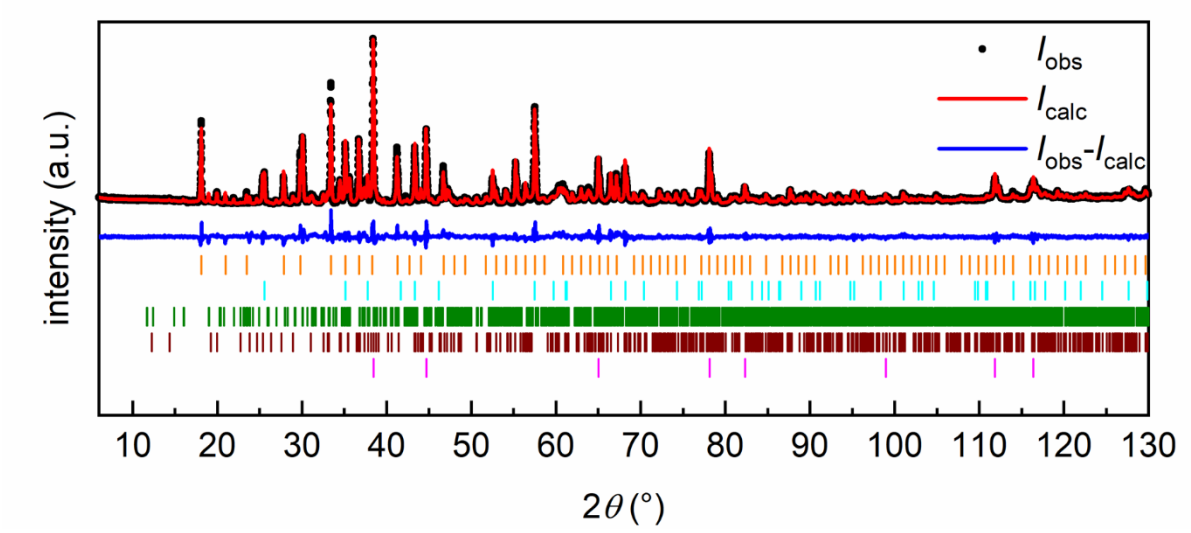

Figure 66. Powder X-ray diffraction pattern of $CaAl_4$ oxidized in an STA setup at 1273 K for 5 hours. Experimental data is shown as black dots, simulated diffraction patterns from refinements as red line, the difference is shown as continuous blue line. Bragg positions are shown as orange ($Ca_{12}Al_{14}O_{33}$, space group $I\bar{4}3d$), cyan (Al_2O_3, space group $R\bar{3}m$), green ($CaAl_2O_4$, space group $P2_1/c$), brown ($CaAl_4O_7$, space group $C2_1/c$) and pink (elemental Al, $Fm\bar{3}m$) ticks. The refined mass% are given in Table 30.

Table 30. Results of the Rietveld refinements from powder X-ray diffraction data of the STA treated $CaAl_4$ samples as well as the samples oxidized in a tube furnace for multiple times using pure elemental oxygen. Corresponding STA diagrams are shown in the appendix.

STA	phase contribution by PXRD / mass%						Figure
Dwelling time / h	$Ca_{12}Al_{14}O_{33}$	$CaAl_2O_4$	$CaAl_4O_7$	Al_2O_3	Al		
0	41(1)	17(1)	5(1)	10(1)	27(1)		Figure S44
5	27(1)	21(1)	14(1)	24(1)	14(1)		Figure 66
Tube furnace	phase contribution by PXRD / mass%						Figure
Dwelling time/ h	$Ca_{12}Al_{14}O_{33}$	$CaAl_2O_4$	$CaAl_4O_7$	$Ca_5Al_6O_{14}$	Al_2O_3	Al	
5	15(1)	30(1)	22(1)	–	22(1)	11(1)	Figure S47
24	2(1)	30(1)	32(1)	8(1)	21(1)	6(1)	Figure S48
48	1(1)	32(1)	33(1)	6(1)	25(1)	4(1)	Figure S48

The same applies for $SrAl_4$. Figure 67 depicts the diffractogram after the oxidation of $SrAl_4$ in an STA setup with a dwelling time of 5 hours. The corresponding STA data are given in the appendix (Figure S50 & Figure S51). For this and all other oxidation reactions performed, Table 31 lists the phases that could be identified and the results of the Rietveld refinement. The identified oxides have already been discussed in the discussion of the oxidation of $SrAl_2$. In comparison to $CaAl_4$ the main product found after initial oxidation is Sr rich, being $Sr_3Al_2O_6$ alongside $SrAl_2O_4$, following all trends already discussed. Interestingly, no hint for a potential $SrAl_4O_7$, which would be the expected product could be identified. Longer annealing as well as multiple reaction steps could not give phase pure products or dramatically change the outcome of the reaction.

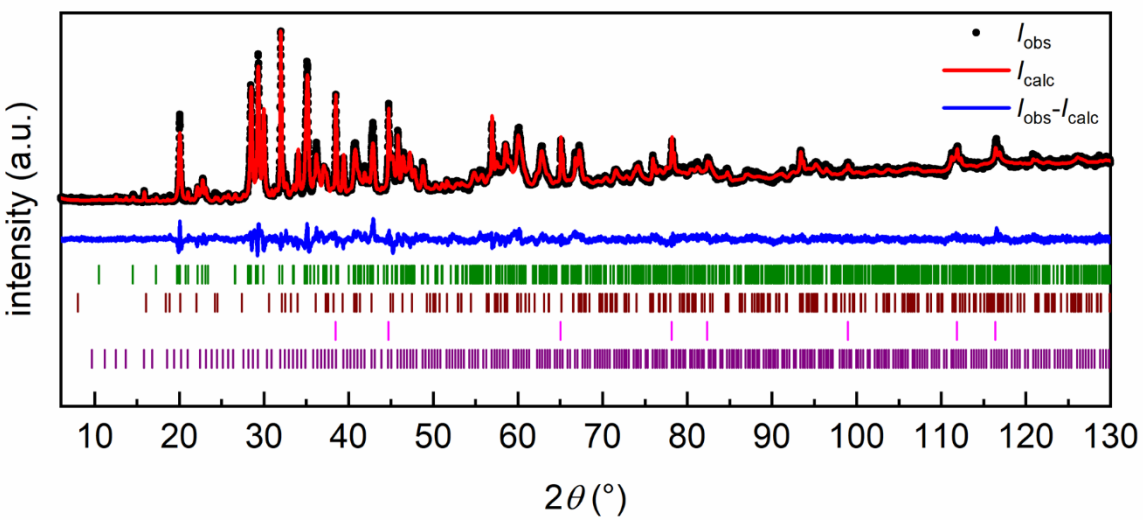

Figure 67. Powder X-ray diffraction pattern of $SrAl_4$ oxidized at 1273 K in an STA setup for 5 h. Experimental data is shown as black dots, simulated diffraction patterns from refinements as red line, the difference is shown as continuous blue line. Bragg positions are shown as green ($SrAl_2O_4$, space group $P2_1$), brown ($SrAl_{12}O_{19}$, space group $P6_3/mmc$), pink (elemental Al, space group $Fm\bar{3}m$) and purple ($Sr_3Al_2O_6$, space group $Pa\bar{3}$) ticks. The refined mass% are given in Table 31.

Table 31. Results of the Rietveld refinements from powder X-ray diffraction data of the STA treated $SrAl_4$ samples as well as the samples oxidized in a tube furnace for multiple times using pure elemental oxygen.

STA	phase contribution by PXRD / mass%					
Dwelling time / h	$Sr_3Al_2O_6$	$SrAl_2O_4$	$SrAl_{12}O_{19}$	$SrAl_4$	Al	Figure
0	6(1)	51(1)	–	26(1)	17(1)	Figure S49
5	11(1)	57(1)	23(1)	–	11(1)	Figure 67
Tube furnace	phase contribution by PXRD / mass%					
Dwelling time / h	$Sr_3Al_2O_6$	$SrAl_2O_4$	$SrAl_{12}O_{19}$	$SrAl_4$	Al	
5	9(1)	59(1)	13(1)	4(1)	14(1)	Figure S52
24	6(1)	56(1)	28(1)	–	10(1)	Figure S53
48	2(1)	62(1)	34(1)	–	2(1)	Figure S53

For the oxidation of $BaAl_4$ an analogous observation to the oxidation of "$BaAl_2$" was made. As can be seen in Figure 68 the diffractogram clearly shows $BaAl_2O_4$ as main phase after initial oxidation of $BaAl_4$ in an STA setup at 1273 K with a dwelling time of 5 hours. Besides the main product, broad reflections that cannot be refined in a meaningful way were observed. The corresponding STA data is shown in the appendix (Figure S54).

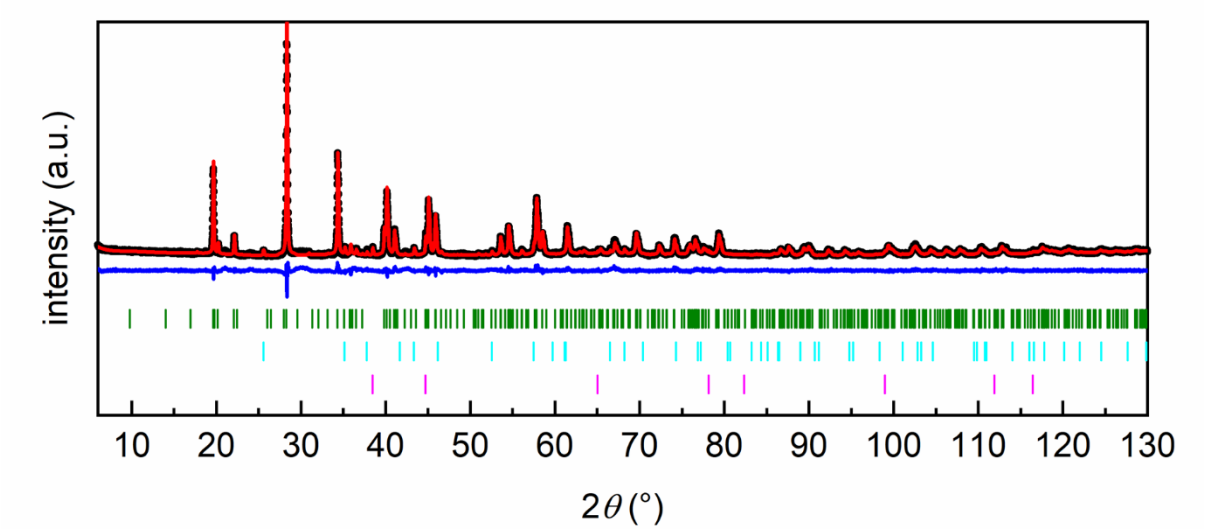

Figure 68. Powder X-ray diffraction pattern of $BaAl_4$ oxidized at 1273 K in an STA setup for 5 h. Experimental data is shown as black dots, simulated diffraction patterns from refinements as red line, the difference is shown as continuous blue line. Bragg positions are shown as green ($BaAl_2O_4$, space group $P6_3$, 82(1) mass%), cyan (Al_2O_3, space group $R\bar{3}m$, 14(1) mass%) and pink (elemental Al, space group $Fm\bar{3}m$, 4(1) mass%) ticks.

Longer reaction and annealing times yield $BaAl_2O_4$ as highly crystalline material, alongside with small reflections of a minor component, that could not be identified yet. Corresponding powder X-ray diffractograms of an initial reaction in a tube furnace setup together with the results after additional annealing for 24 h are shown in Figure 69.

To give a short conclusion, for all investigations conducted by bulk oxidation of powdered samples of $SrAl_2$, "$BaAl_2$", $CaAl_4$, $SrAl_4$ and $BaAl_4$: Only for nominal $BaAl_2$ the anticipated product could be obtained even after short reaction and dwelling times. For all other examples discussed, it was possible to identify multiple binary and ternary oxides after the reaction. A dependence on the gas atmosphere, being either pure O_2 within the tube furnace or a mixture close to air (80% argon, 20% oxygen) in the STA setup was not observed.

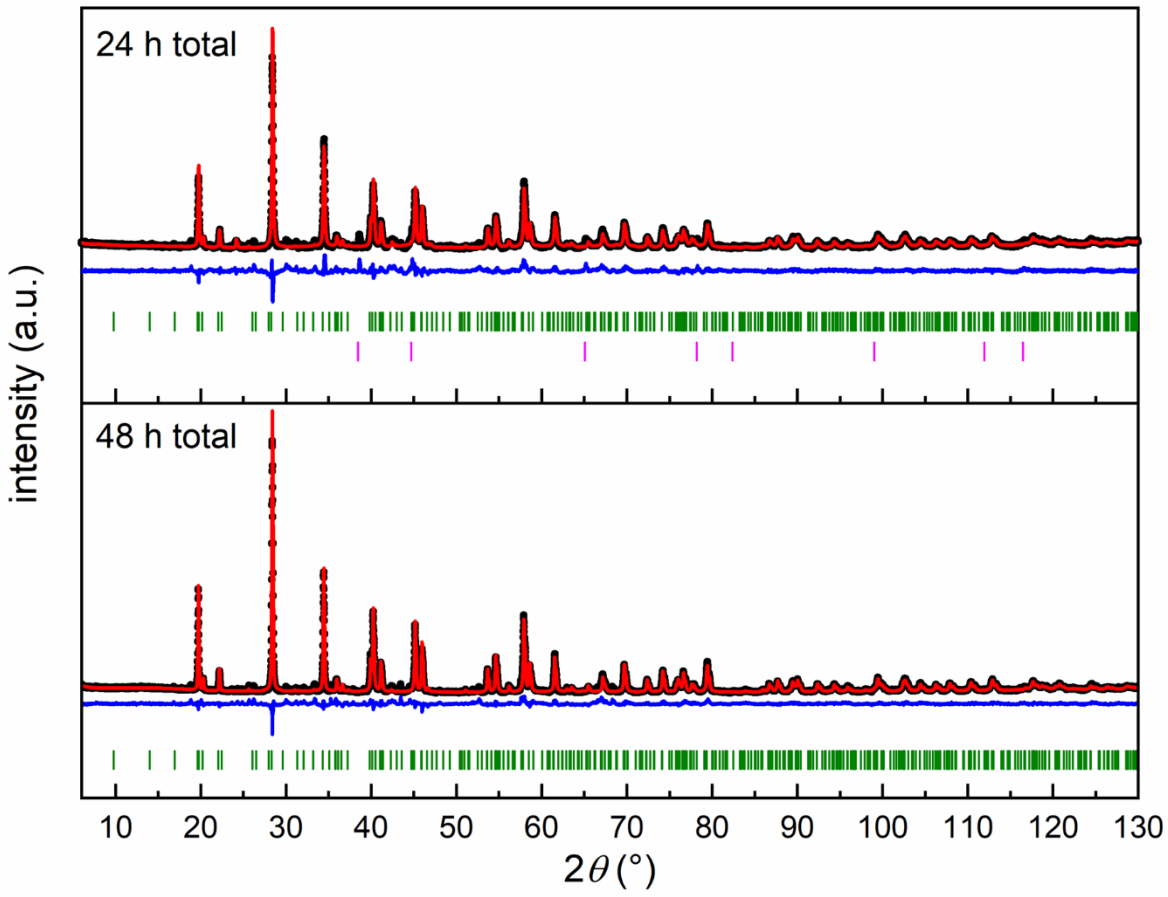

Figure 69. Powder X-ray diffraction patterns of $BaAl_4$ oxidized at 1273 K in a tube furnace operating with pure oxygen flow for (*top*) initial 24 hours, followed by grinding and additional annealing for 24 hours, resulting in a total time of (*bottom*) 48 h. Experimental data is shown as black dots, simulated diffraction patterns from refinements as red line, the difference is shown as continuous blue line. Bragg positions are shown as green ($BaAl_2O_4$, space group $P6_3$) and pink (elemental Al, space group $Fm\bar{3}m$) ticks. Besides $BaAl_2O_4$ identified as the main phase at least one unidentified impurity is present.

5.5.2.3 Reactions performed under reduced oxygen flow

To test the title compounds for possible decomposition (or phase transition) prior to the oxidation reaction, an STA measurement was carried out under inert conditions. It was found that even if the oxygen towards the device is turned off it is not completely closed. So, working under an inert atmosphere is not possible. However, the results of the ongoing reactions for these three compounds are quite interesting. It contains information about the influence of an oxygen reduced atmosphere.

For the reactions performed here, the three compounds were heated to 1273 K without additional dwelling time. The sample was immediately cooled to room temperature. Figure 70 to Figure 72 display the three diffractograms for the product of $CaAl_4$, $SrAl_4$ and $BaAl_4$. Corresponding STA data are presented in the appendix (Figure S55 - Figure S57). It can already be seen that the mass gain of the samples is below 15 %, which is less than for the oxidation reactions with higher amounts of oxygen. For all three compounds it can clearly be seen that the precursor is still visible and has not fully reacted. However, oxidic phases have formed in all cases.

In the case of the Ca compound, only the mayenite phase ($Ca_{12}Al_{14}O_{33}$) is visible as an oxidic phase (32 mass%) alongside unreacted precursor $CaAl_4$ (36 mass%) and elemental aluminum (32 mass%). This labels the mayenite phase as the phase formed at the beginning of the oxidation process underlining the claim that it is the kinetically favored product.

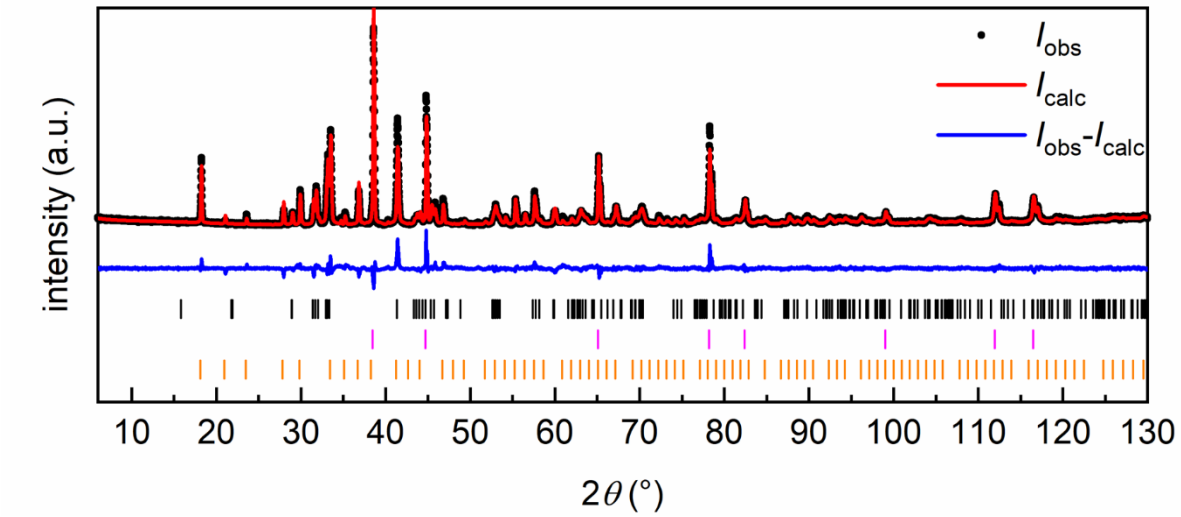

Figure 70. Powder X-ray diffraction pattern of $CaAl_4$ oxidized in an STA setup at 1273 K without dwelling time under "inert atmosphere". Experimental data is shown as black dots, simulated diffraction patterns from refinements as red line, the difference is shown as continuous blue line. Bragg positions are shown as black ($CaAl_4$, space group $C2/m$, 36(1) mass%), pink (elemental Al, space group $Fm\bar{3}m$, 32(1) mass%) and orange ($Ca_{12}Al_{14}O_{33}$, space group $I\bar{4}3d$, 32(1) mass%) ticks.

In the Sr case only minor reflections that give hints on an oxidic product can be identified. $SrAl_4$ is still the main phase (58 mass%). They can be matched to $SrAl_2O_4$ (16 mass%). Interestingly, broad reflections of $SrCO_3$ (10 mass%) can be identified, that could appear due to SrO being formed during the reaction but then reacts under ambient conditions. The binary oxide CaO was detected for the oxidation of $CaAl_2$ to form initially. Elemental Al is also present (16 mass%). For the Ba compound an analogous trend was observed. The precursor is still present in high amounts (70 mass%), however the oxidation products $BaAl_2O_4$ (19 mass%) and $BaCO_3$ (2 mass%) alongside with elemental Al (9 mass%) was identified.

The reactions performed at low oxygen content give a hint on the products formed at the beginning of the oxidation process, since the materials cannot fully oxidize. The products obtained are comparable to the bulk oxidations discussed above. These findings give a strong hint that the adjustment of the atmosphere can significantly influence the outcome of the reaction. It cannot be excluded that also the absence of dwelling time is responsible for these findings. However, for future investigations a combination of adjusting these parameters needs to be included, to further investigate the reaction mechanism and isolate the products that are formed at the beginning of oxidation.

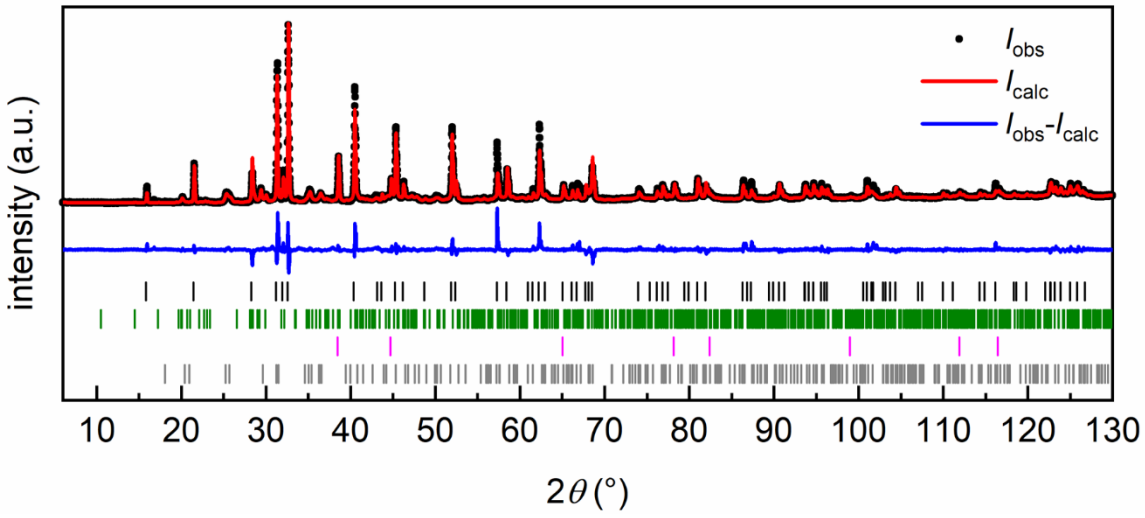

Figure 71. Powder X-ray diffraction pattern of $SrAl_4$ oxidized in an STA setup at 1273 K without dwelling time under "inert atmosphere". Experimental data is shown as black dots, simulated diffraction patterns from refinements as red line, the difference is shown as continuous blue line. Bragg positions are shown as black ($SrAl_4$, space group *I*4/*mmm*, 58(1) mass%), green ($SrAl_2O_4$, space group $P2_1$, 16(1) mass%), pink (elemental Al, space group $Fm\bar{3}m$, 16(1) mass%) and dark grey ($SrCO_3$, space group *Pnma*, 10(1) mass%) ticks.

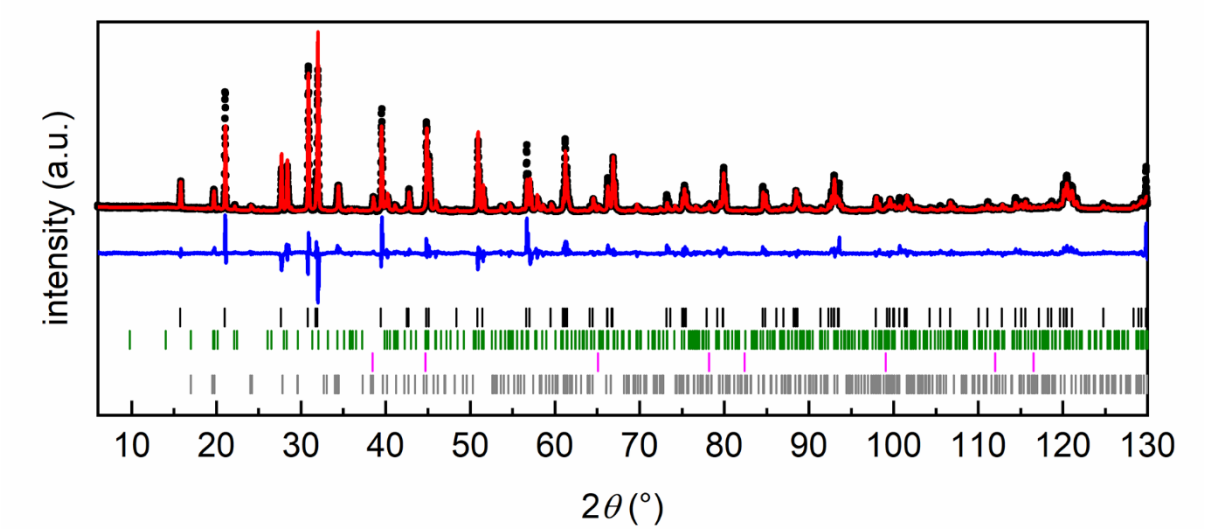

Figure 72. Powder X-ray diffraction pattern of $BaAl_4$ oxidized in an STA setup at 1273 K without dwelling time under "inert atmosphere". Experimental data is shown as black dots, simulated diffraction patterns from refinements as red line, the difference is shown as continuous blue line. Bragg positions are shown as black ($BaAl_4$, space group *I*4/*mmm*, 70(1) mass%), green ($BaAl_2O_4$, space group $P6_3$, 19(1) mass%), pink (elemental Al, space group $Fm\bar{3}m$, 9(1) mass%) and dark grey ($BaCO_3$, space group *Pnma*, 2(1) mass%) ticks.

5.5.2.4 High-energy ball milling of the precursors

For the three compounds $AEAl_4$ (*AE* = Ca, Sr, Ba), a ball milling study was carried out. Approx. 1 g of the powdered precursor was filled into a home-built stainless-steel jar (stainless-steel 1.4125) with a volume of 5 mL. This was used in a Mixer Mill, MM400 (Retsch, Haan, Germany), using one stainless steel ball (Ø = 10 mm; mass of ~4 g) and a frequency of 30 Hz for different times (5–270 min). For $SrAl_4$ and $BaAl_4$ before each milling step 300 µL of DME (1,2-dimethoxyethane) were added to the milling jar to avoid cementation. The milling of $CaAl_4$ was performed under dry conditions leading to severe problems concerning cementation. The milling jar was loaded in an argon filled glove box, also the addition of the DME was performed under inert conditions.

Powder X-ray diffractograms were obtained for samples of $CaAl_4$ (Figure 73) and $SrAl_4$ (Figure 75) ball milled for 180, respectively 270 minutes. The data for $BaAl_4$ are shown in the Appendix (Figure S58). In the case of $CaAl_4$ the side phases Al and $CaAl_2$ were present from the beginning as discussed before. In all cases, it can clearly be seen that the crystallite size decreases by the mechanical impact visible by the broadening of all reflections.

As explained for the $CaAl_4$ severe cementation of the sample occurred, also changing the mass% ratios of $CaAl_4$, $CaAl_2$ and Al. However, Figure 74 shows the diffractogram of an STA reaction after 180 minutes of milling. In contrast to all reactions discussed before, the mayenite phase could be suppressed and mainly the ternary oxide $CaAl_2O_4$ (43 mass%) and targeted $CaAl_4O_7$ (35 mass%) are present, besides Al_2O_3 and elemental Al which still could be identified. Figure S59 in the appendix depicts the corresponding STA data showing a strong exothermal signal after oxidation, which is clearly in contrast to the oxidation reactions done with the pristine material. This emphasizes the fact that the oxidation of intermetallic compounds can be tuned by ball milling the precursor.

The compounds $SrAl_4$ and $BaAl_4$ could not be further oxidized due to the pyrophoric character of the samples. The experiments for these compounds must be repeated. However, the ball milled samples show severe broadening of the reflections, promising an activated precursor.

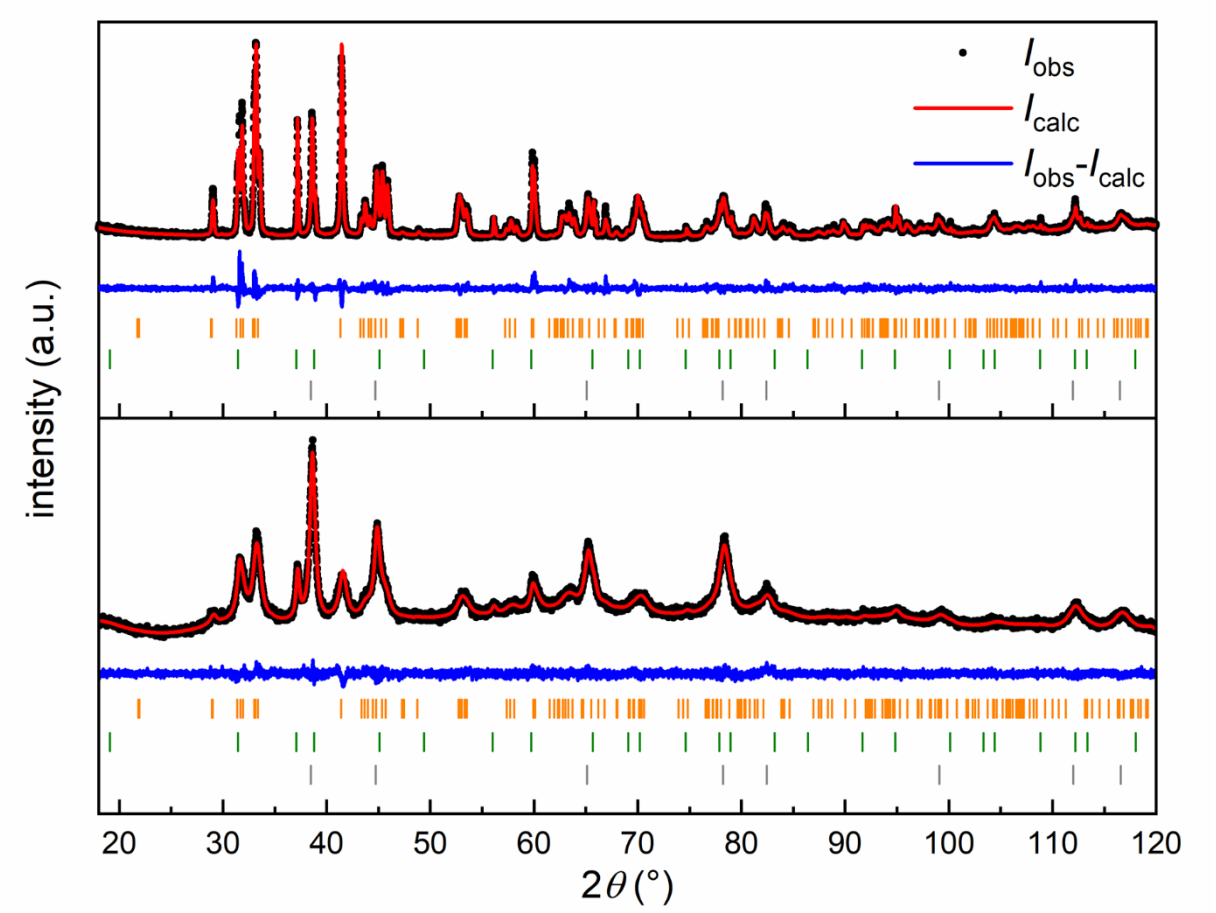

Figure 73. Powder X-ray diffraction pattern of (*top*) pristine (nominal) $CaAl_4$ and (*bottom*) ball milled for 180 minutes. Experimental data is shown as black dots, simulated diffraction patterns from refinements as red lines, the difference is shown as continuous blue lines. Bragg positions are shown as orange ($CaAl_4$, space group *C*2/*m*, (*top*) 72(1) mass%, (*bottom*) 47(1) mass%), green ($CaAl_2$, space group $Fd\bar{3}m$, (*top*) 8(1) mass%, (*bottom*) 7(1) mass%) and grey (elemental Al, space group $Fm\bar{3}m$, (*top*) 20(1) mass%, (*bottom*) 45(1) mass%) ticks.

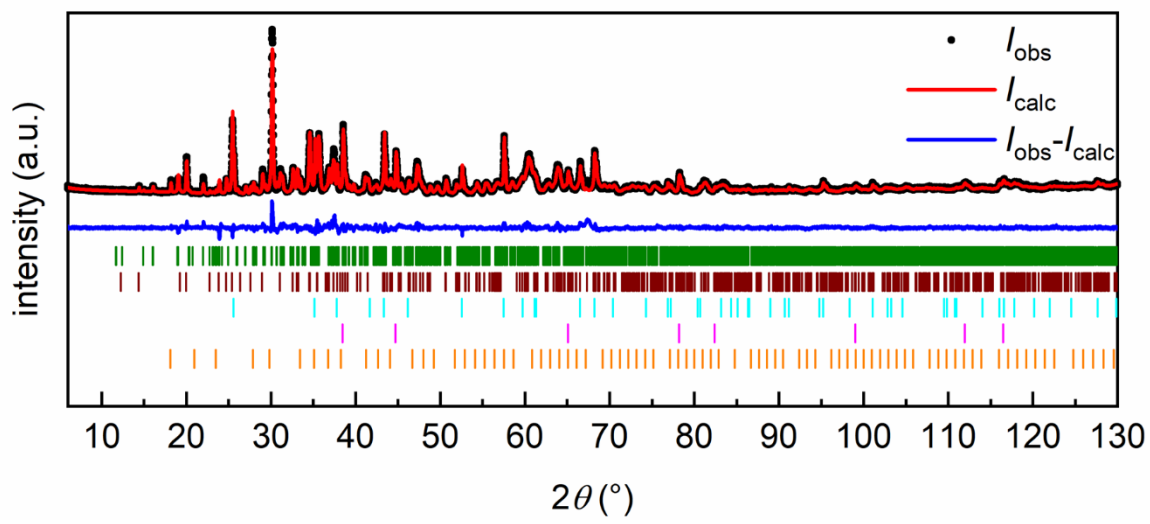

Figure 74. Powder X-ray diffraction pattern of $CaAl_4$ oxidized in an STA setup at 1273 K for 5 hours after 180 minutes of ball milling the precursor. Experimental data is shown as black dots, simulated diffraction patterns from refinements as red line, the difference is shown as continuous blue line. Bragg positions are shown as green ($CaAl_2O_4$, space group $P2_1/c$, 43(1) mass%), brown ($CaAl_4O_7$, space group $C2_1/m$, 35(1) mass%), cyan (Al_2O_3, space group $R\bar{3}m$, 16(1) mass%), pink (elemental Al, space group $Fm\bar{3}m$, 4(1) mass%) and orange ($Ca_{12}Al_{14}O_{33}$, space group $I\bar{4}3d$, 2(1) mass%) ticks.

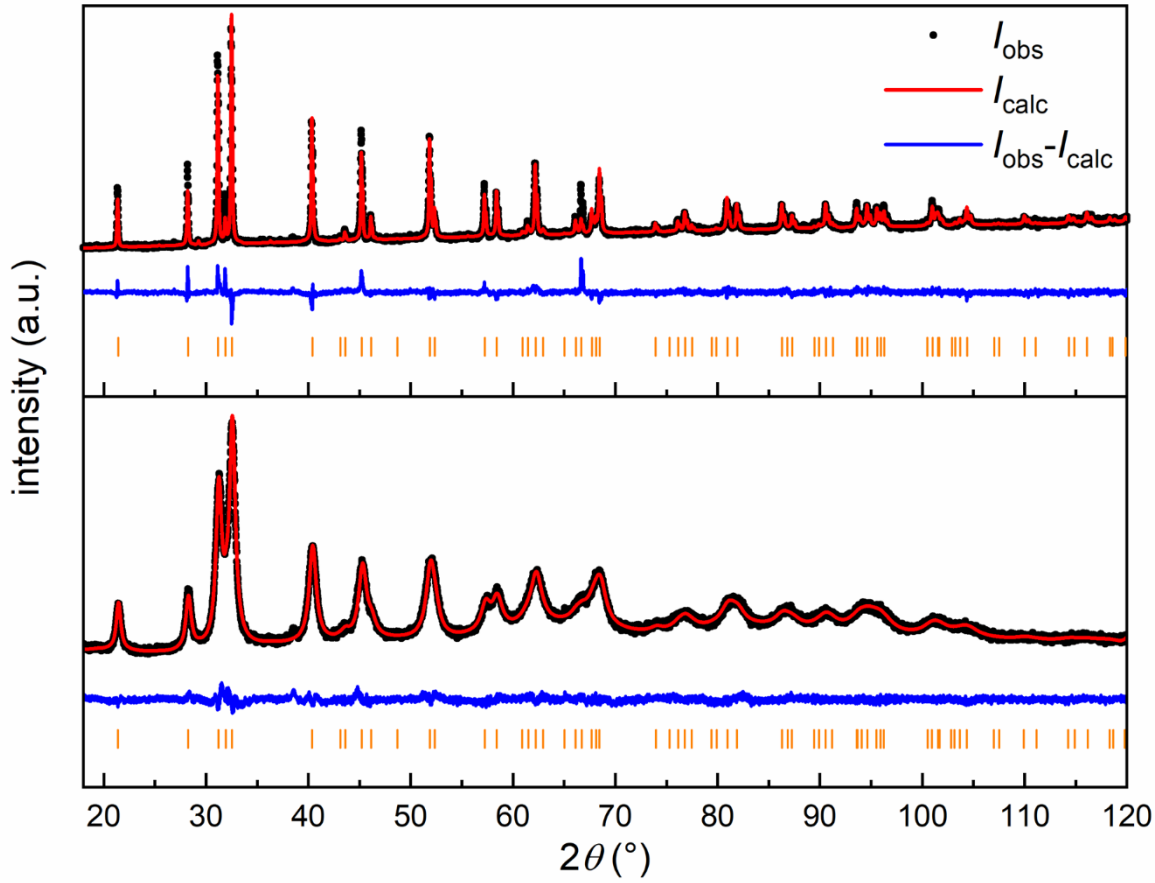

Figure 75. Powder X-ray diffraction pattern of (*top*) pristine $SrAl_4$ and (*bottom*) a ball milled sample after 270 minutes. Experimental data is shown as black dots, simulated diffraction patterns from refinements as red lines, the difference is shown as continuous blue lines. Bragg positions are shown as orange ($SrAl_4$, space group $I4/mmm$) ticks.

5.5.3 Chalcogenides of the general composition MAl_xX_y (M = Ca, Sr, Ba, Yb, Eu; X = S, Se; x = 2 and 4; y = 4 and 7) synthesized starting with intermetallic precursors

5.5.3.1 Synthesis of $BaAl_4S_7$ and attempts to expand the series to the lighter homologues

As already explained in section 2.2.1, the group of Schäfer synthesized the compound $BaAl_4S_7$ by using a precursor of $BaAl_4$. The material recently received new attention due to its large band gap of 3.95 eV making it suitable as potential mid-IR nonlinear optical material.[304] Within the latest work it was synthesized using the respective metal sulfides.

Within this work, a synthetic route as potential general procedure to this compound was tested, by grinding $BaAl_4$ and sulfur in the correct stoichiometric ratio, pressing it to a pellet and heating the sample in a corundum crucible that was sealed in an evacuated silica ampoule. The temperature program that was used included two annealing steps and 673 and 973 K with annealing times of 12 and 120 h respectively. The heating rate was 50 K h^{-1}. The sample was cooled at a rate of approximately 10 K h^{-1}. The same synthetic protocol was applied to $CaAl_4$ and $SrAl_4$. The resulting powder X-ray analysis for the Ba compound is shown in Figure 76.

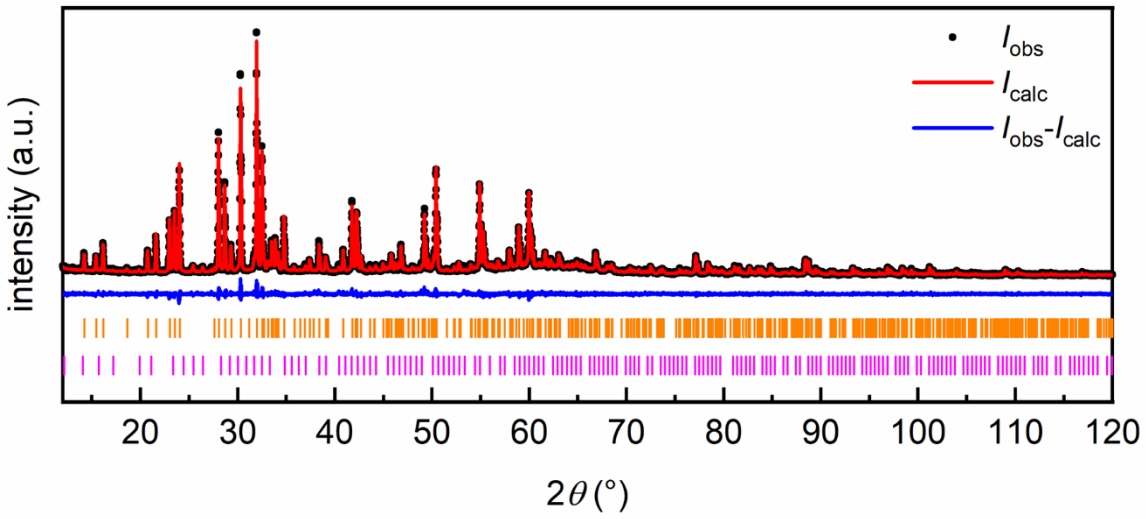

Figure 76. Powder X-ray diffraction pattern of the compound $BaAl_4S_7$ synthesized by the reaction of $BaAl_4$ with seven equivalents sulfur. Experimental data is shown as black dots, simulated diffraction patterns from refinements as red lines, the difference is shown as continuous blue lines. Bragg positions are shown as orange ($BaAl_4S_7$, space group $Pmn2_1$, 94(1) mass%) and pink ($BaAl_2S_4$, space group $Pa\bar{3}$, 6(1) mass%) ticks.

The compound was obtained almost phase-pure with an impurity of cubic $BaAl_2S_4$ (CaB_2O_4 type space group $Pa\bar{3}$) of 6 mass%. The structural model of $BaAl_4S_7$ obtained from single-crystal investigations[166] is in good agreement with the powder-pattern. The refined lattice parameters for $BaAl_4S_7$ are given in Table 32.

Table 32. Lattice parameters for the compound $BaAl_4S_7$ synthesized in this work.

Compound	method	a / pm	b / pm	c / pm	Figure
$BaAl_4S_7$	powder*	1478.84(1)	621.80(1)	588.96(1)	Figure 76
$BaAl_4S_7$	single-crystal	1481.4(4)	621.8(2)	589.1(2)	[166]

With the knowledge that the synthetic procedure chosen here works fine for the Ba compounds, the lighter homologues, which are not known to literature, were tried via the same route. The X-ray powder patterns are shown in Figure 77. In the powder pattern of the reaction of $CaAl_4$ with S_8 only the reflections of the already discussed orthorhombic $CaAl_2S_4$ could be identified. The additional reflections could not be identified up until now. For the sulfidation of $SrAl_4$, the powder pattern can be analyzed quite nicely using the structural model of orthorhombic $SrAl_2S_4$, which is found with ~65 mass% and cubic aluminum sulfide, Al_2S_3, which adopts a spinel related structure. Besides the cubic modification of Al_2S_3, also a tetragonal polymorph is reported. Both form under high pressure conditions[305, 306] or upon the incorporation of small amounts of other elements.[307, 308] The reason for the formation of the cubic polymorph must be investigated further since it could be a hint for the formation of a potential $SrAl_2S_4$ adopting the spinel type structure.

However, in both cases no evidence of a newly formed $AEAl_4S_7$ (AE = Ca, Sr) could be found, assuming that these compounds cannot be synthesized in an identical way as $BaAl_4S_7$. One idea might be to test the reaction under high-pressure conditions or use high-energy ball milling to change the reaction pathway as shown before. Despite the different compositions of the precursor, $CaAl_2S_4$ and the respective Sr compound seem to be more stable than a potential $AEAl_4S_7$ (AE = Ca, Sr).

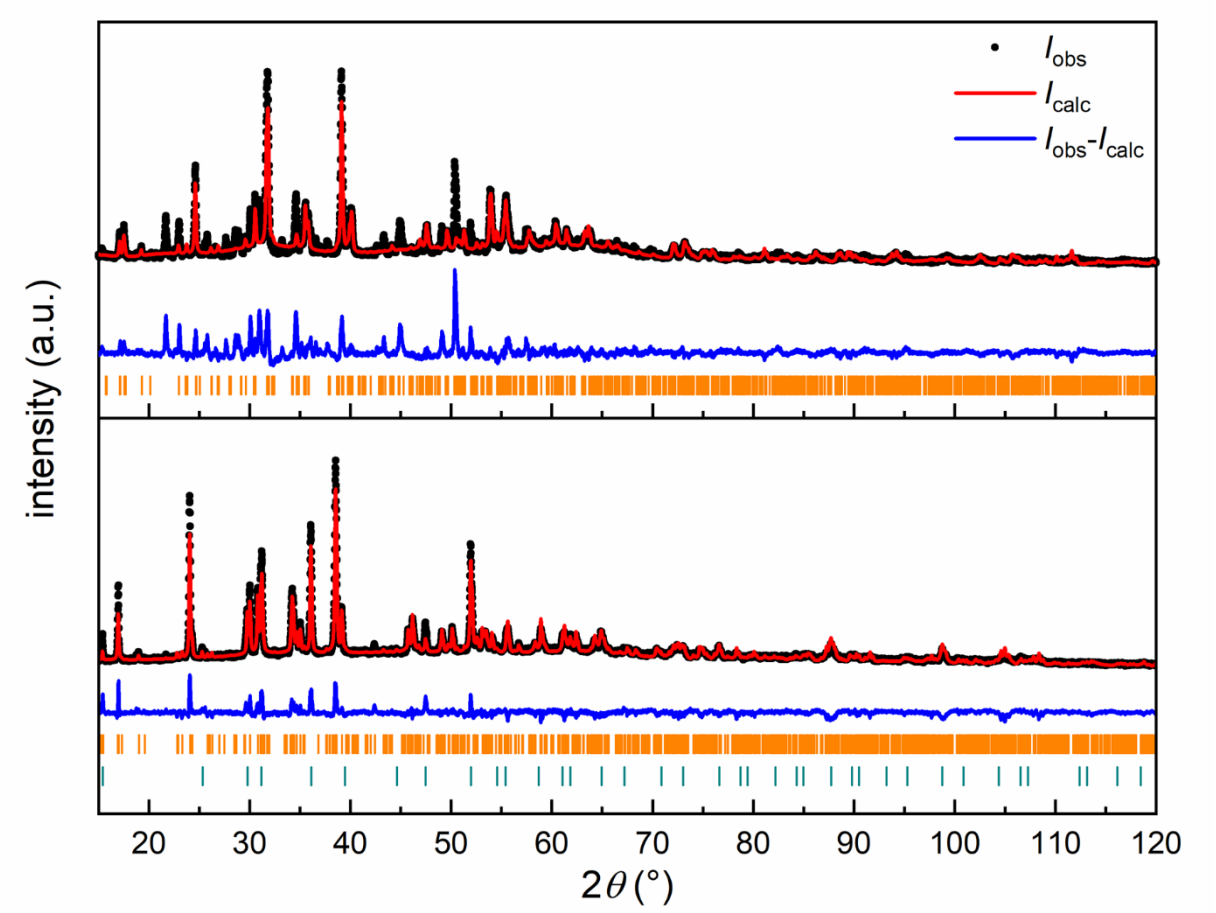

Figure 77. Powder X-ray diffraction pattern obtained after the reaction of (*top*) $CaAl_4$ and (*bottom*) $SrAl_4$ with seven equivalents of sulfur. Experimental data is shown as black dots, simulated diffraction patterns from refinements as red lines, the difference is shown as continuous blue lines. (*top*) Bragg positions are shown as orange ($CaAl_2S_4$, space group *Fddd*) ticks. (*bottom*) Bragg positions are shown as orange ($SrAl_2S_4$, space group *Fddd*, 64(1) mass%) and green ($Al_{2.67}S_4$, space group $Fd\bar{3}m$, 36(1) mass%) ticks.

5.5.3.2 Synthesis and Single-Crystal analysis of $YbAl_2S_4$

In section 2.2.1, the three isostructural compounds MAl_2S_4 (M = Ca, Sr and Eu) were discussed. The missing member of this series is the ytterbium compound, whose structure is not fully reported in literature. It was only described as a potential material for luminescent applications. Applying the same temperature program (as for $EuAl_2S_4$) for the reaction of $YbAl_2$ with four equivalents of sulfur, resulted in the X-ray powder pattern given in Figure 78. The compound $YbAl_2S_4$ adopting the $EuGa_2S_4$ structure type could be nicely identified alongside with at least one impurity that could not be identified yet.

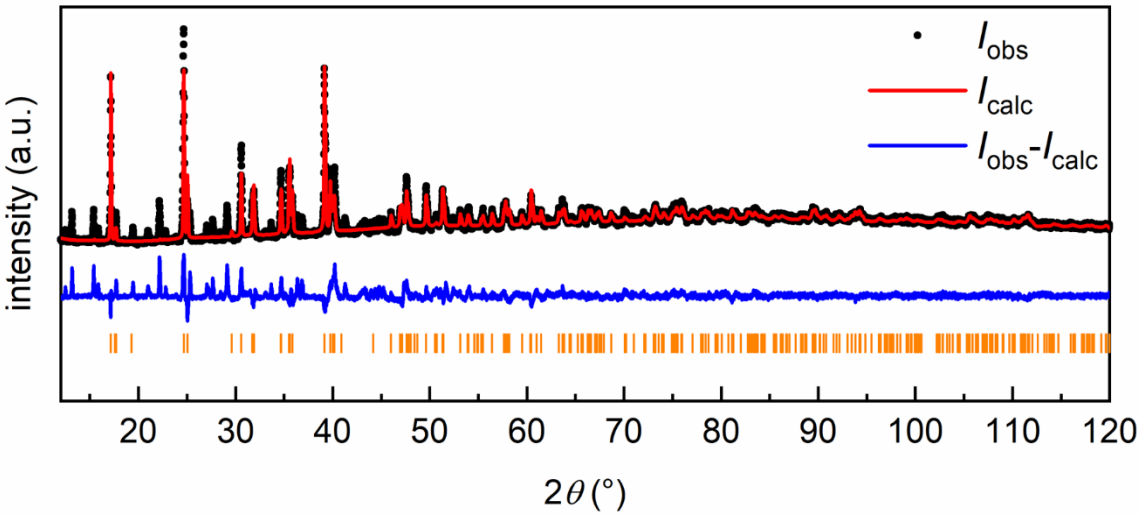

Figure 78. Powder X-ray diffraction pattern obtained after the reaction of $YbAl_2$ with four equivalents of sulfur annealed at 1173 K. Experimental data is shown as black dots, simulated diffraction patterns from refinements as red lines, the difference is shown as continuous blue lines. Bragg positions are shown as orange ($YbAl_2S_4$, space group *Fddd*) ticks.

Lowering the second annealing temperature from 1173 K to 973 improved the quality of the PXRD pattern (Figure 79). Lattice parameters are given in Table 33. Nevertheless, the compound could not be obtained phase pure yet. Cubic YbS was found as a side product (~12 mass%). Increasing the annealing temperature to 1273 K showed the desired $YbAl_2S_4$ only as a minor component (Figure 80). The remaining reflections could not yet be matched to any phase known yet. The decomposition of $YbAl_2S_4$, which is likely observed here, deserves further attention for future investigations. The batch, shown in Figure 80 however, could be used for the analysis of single crystals. A picture of the obtained orange single crystals is shown in Figure 81. All crystals that were analyzed corresponded to $YbAl_2S_4$ whose structure could be refined. A detailed structure description is not given here, since its crystal structure is isostructural to the already discussed Ca, Sr and Eu compounds. Details of the refinement are found in Table 34 - Table 36. To conclude, it seems that $YbAl_2S_4$ is formed during the reaction

of $YbAl_2$ and sulfur. However, it needs to be proven in future investigations whether the compound decomposes at higher temperatures or if there is a problem during the actual synthesis. The byproducts found in the Rietveld refinement of the X-ray diffractograms in Figure 78 and Figure 80 raise other interesting questions, since it is not clear what they are. Here the experiments need to be repeated to confirm the thus far observed behavior and to e.g. exclude contaminations by oxygen.

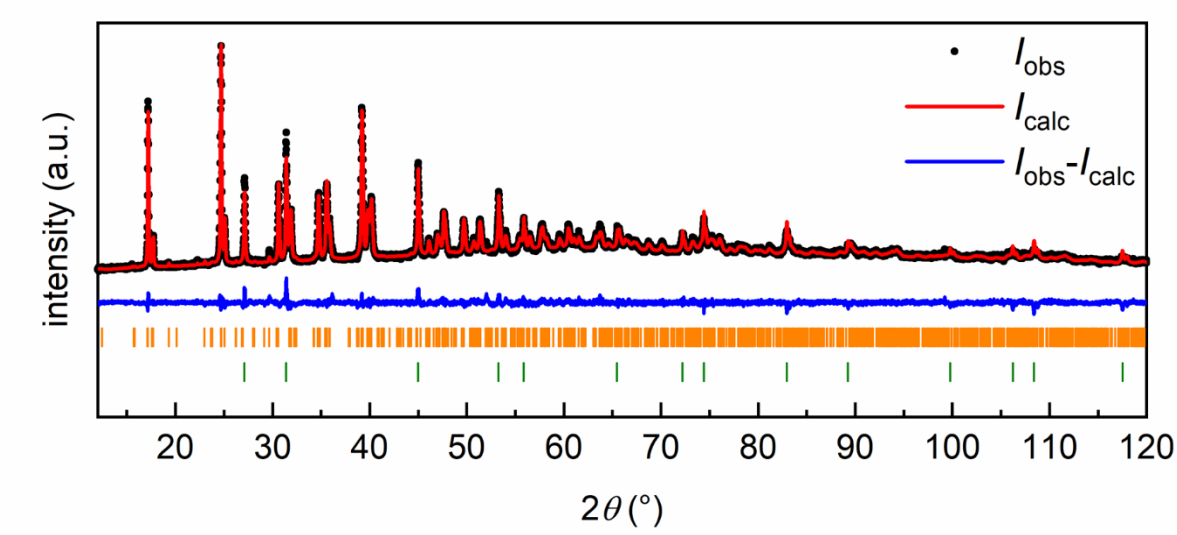

Figure 79. Powder X-ray diffraction pattern obtained after the reaction of $YbAl_2$ with four equivalents of sulfur annealed at 973 K. Experimental data is shown as black dots, simulated diffraction patterns from refinements as red lines, the difference is shown as continuous blue lines. Bragg positions are shown as orange ($YbAl_2S_4$, space group *Fddd*, 88(1) mass%) and green (YbS, space group $Fm\bar{3}m$, 12(1) mass%) ticks.

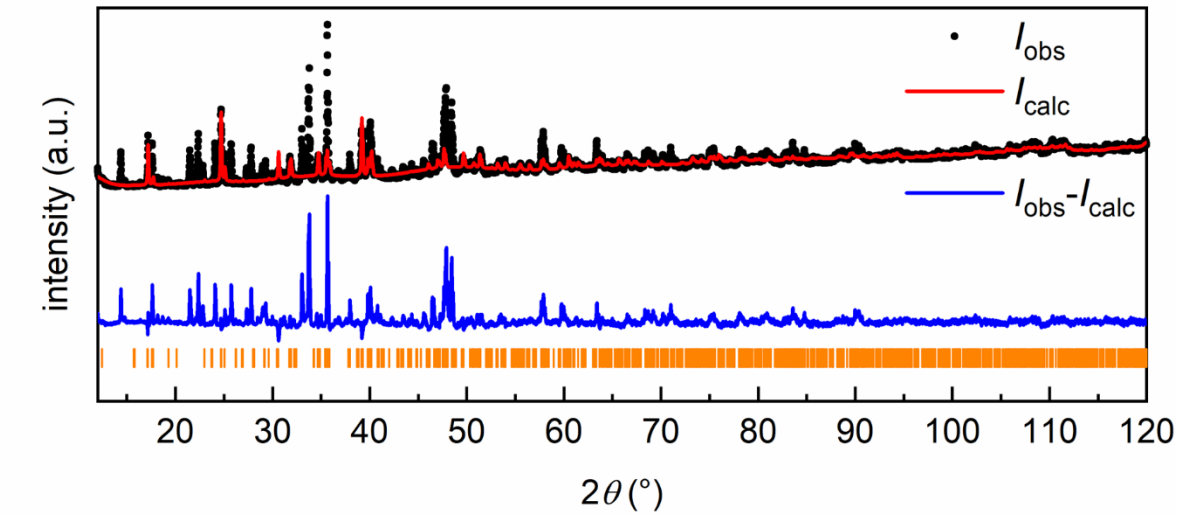

Figure 80. Powder X-ray diffraction pattern obtained after the reaction of $YbAl_2$ with four equivalents of sulfur annealed at 1273 K. Experimental data is shown as black dots, simulated diffraction patterns from refinements as red lines, the difference is shown as continuous blue lines. Bragg positions are shown as orange ($YbAl_2S_4$, space group *Fddd*) ticks. The remaining reflections could not be indexed.

Table 33. Lattice parameters for the compound $YbAl_2S_4$ synthesized in this work.

Compound	method	a / pm	b / pm	c / pm	Figure
$YbAl_2S_4$	powder*	1205.08(3)	2003.15(5)	2017.44(5)	Figure 79
$YbAl_2S_4$	SC*	1205.23(4)	1999.21(7)	2009.38(7)	
$YbAl_2S_4$	powder	602.0	1002.9	1004.5	[309], $

* This work; $ In this report no detailed structure description of $YbAl_2S_4$ is given, only unit cell parameters of an orthorhombic structure (likely to be the structure with space group *Cccm*, *vide infra*) were determined.

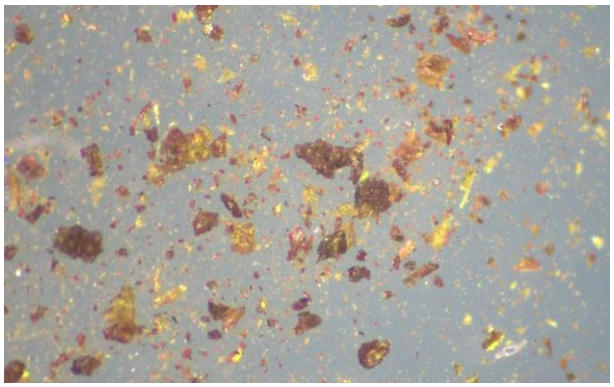

Figure 81. Picture of single crystals obtained after the reaction of $YbAl_2$ with four equivalents of sulfur annealed at 1272 K.

Table 34. Crystallographic data and structure refinement from single-crystal X-ray diffraction experiments for $YbAl_2S_4$.

Nominal composition		$YbAl_2S_4$
Refined composition		$YbAl_2S_4$
Structure type		$EuGa_2Se_4$ (*Fddd*)
Lattice parameters	*a* (pm)	1205.23(4)
	b (pm)	1999.21(7)
	c (pm)	2009.38(7)
	V (nm^3)	4.8416
Molar mass, g mol^{-1}		355.2
Density calc., g cm^{-3}		3.8988
Crystal size, µm		40×40×10
Detector distance, mm		31
Exposure time, s		10
Range in *hkl*		$-19 < h < 18$; $-26 < k < 31$; $-29 < l < 30$
θ_{min}, θ_{max}, deg		2.22, 34.83
Linear absorption coeff., mm^{-1}		16.977
No. of reflections		22052
R_{int} / R_σ		0.0215 / 0.0118
No. of independent reflections		2414
Reflections used [$I \geq 3\sigma(I)$]		1526
F(000), e		5120
*R*1 / *wR*2 for $I \geq 3\sigma(I)$		0.0134 / 0.0415
*R*1 / *wR*2 for all data		0.0260 / 0.0466
Data / parameters		2414 / 66
Goodness-of-fit on F^2		1.11
Extinction coefficient		–
Diff. Fourier residues /e^- $Å^{-3}$		+0.95 / –0.74

Table 35. Atom positions and equivalent isotropic displacement parameters (pm^2) for nominal $YbAl_2S_4$. U_{eq} is defined as one third of the trace of the orthogonalized U_{ij} tensor.

Atom	Wyckoff position	*x*	*y*	*z*	U_{eq}
Yb1	16*g*	1/8	1/8	0.37315(5)	53(1)
Yb2	8*b*	1/8	1/8	5/8	54(1)
Yb3	8*a*	1/8	1/8	1/8	55(1)
Al1	32*h*	0.16558(4)	0.30382(2)	0.00010(3)	56(2)
Al2	32*h*	0.37702(3)	0.01147(3)	0.00058(3)	61(2)
S1	32*h*	0.00114(12)	0.49973(5)	0.084386(19)	50(1)
S2	32*h*	0.25091(12)	-0.00006(5)	0.165111(19)	48(1)
S3	32*h*	0.25323(3)	0.094100(19)	0.00105(5)	59(1)
S4	32*h*	0.26429(3)	0.329643(19)	0.24913(5)	53(1)

Table 36. Interatomic distances (pm) for $YbAl_2S_4$. Standard deviations for the interatomic distances are ≤0.2 pm.

Yb1 (16*g*)	2	S3	300.0	Al2 (32*h*)	1	S3	222.6
	2	S4	300.2		1	S1	226.4
	2	S2	301.1		1	S1	226.5
	2	S1	304.3		1	S4	227.3
	2	Al2	372.5		1	Al2	300.0
	2	Al1	380.9	S1 (32*h*)	1	Al2	226.4
Yb2 (8*b*)	4	S4	300.0		1	Al2	226.5
	4	S1	302.7	S2 (32*h*)	1	Al1	225.7
	4	Al2	371.7		1	Al1	226.1
Yb3 (8*a*)	4	S3	299.6	S3 (32*h*)	1	Al2	222.6
	4	S2	303.3		1	Al1	226.3
	4	Al1	383.6	S4 (32*h*)	1	Al1	222.8
Al1 (32*h*)	1	S4	222.8		1	Al2	227.3
	1	S2	225.7				
	1	S2	226.1				
	1	S3	226.3				
	1	Al1	296.2				

5.5.3.3 Synthesis of MAl_2Se_4 (M = Ca, Eu, Yb) and $CaAl_2Se_4$

Expanding the investigations regarding the use of intermetallic precursors for the synthesis of chalcogenides, the following section deals with the selenization of intermetallic compounds. For initial experiments the compounds used before were tried as precursor materials. Table 37 summarizes the refined lattice parameters of the investigated compounds, namely the MAl$_2$Se$_4$ series with M = Ca, Eu and Yb, which will be discussed in the following.

Table 37. Lattice parameters for the compounds MAl$_2$Se$_4$ synthesized in this work alongside literature references.

Compound	method	*a* / pm	*b* / pm	*c* / pm	Figure
$CaAl_2Se_4$	powder*	1265.77(1)	2096.80(1)	2109.14(6)	Figure 84
$CaAl_2Se_4$	single crystal*	1265.48(4)	2096.13(7)	2108.58(7)	
$CaAl_2Se_4$	powder	633(1)	1048(1)	1053(1)	[167], §
$EuAl_2Se_4$	powder*	1258.80(2)	2146.07(3)	2169.42(4)	Figure 82
$EuAl_2Se_4$	–	1258(1)	2146(2)	2165.4(2)	[310]
$YbAl_2Se_4$	powder*	1266.01(4)	2096.17(6)	2109.53(4)	Figure 83

* This work; § In this report of $CaAl_2Se_4$ it was reported to crystallize in its own type (*Cccm*), with two Al split positions.

$EuAl_2Se_4$ has been synthesized before and is reported to be isostructural to the sulfur compound. This compound could be obtained phase pure based on X-ray powder analysis as can be seen in Figure 82. As for the synthetic conditions, the powders ($EuAl_2$ and elemental Se) were mixed, pressed to pellets and heated in graphitized silica ampoules. As a temperature program two dwelling periods at 973 and 1273 K for 10 hours were applied. Heating and cooling rates of 50 K h^{-1} were used. The structure model reported for $EuAl_2S_4$ was used to fit the X-ray powder pattern.

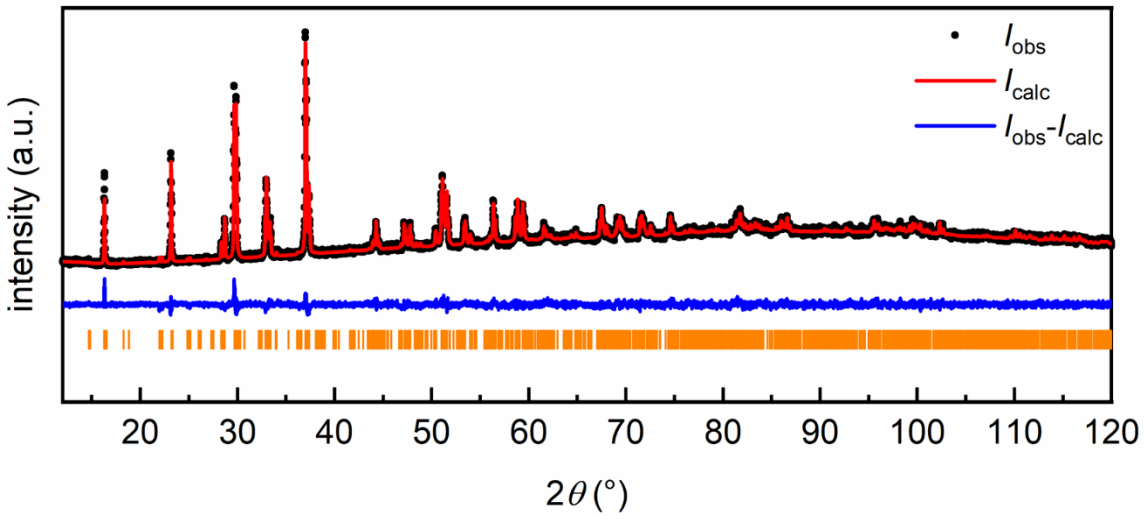

Figure 82. Powder X-ray diffraction pattern of the compound $EuAl_2Se_4$ synthesized by the reaction of $EuAl_2$ with four equivalents selenium. Experimental data is shown as black dots, simulated diffraction patterns from refinements as red lines, the difference is shown as continuous blue lines. Bragg positions are shown as orange ($EuAl_2Se_4$, space group *Fddd*) ticks.

In case of the Yb compound, the same temperature program was applied, leading to the X-ray powder pattern shown in Figure 83. The same structural model of $EuAl_2Se_4$ was used as a starting point and the powder pattern could be simulated quite well. However, another sample must be synthesized by applying slower cooling rates to yield single crystals for structural analysis.

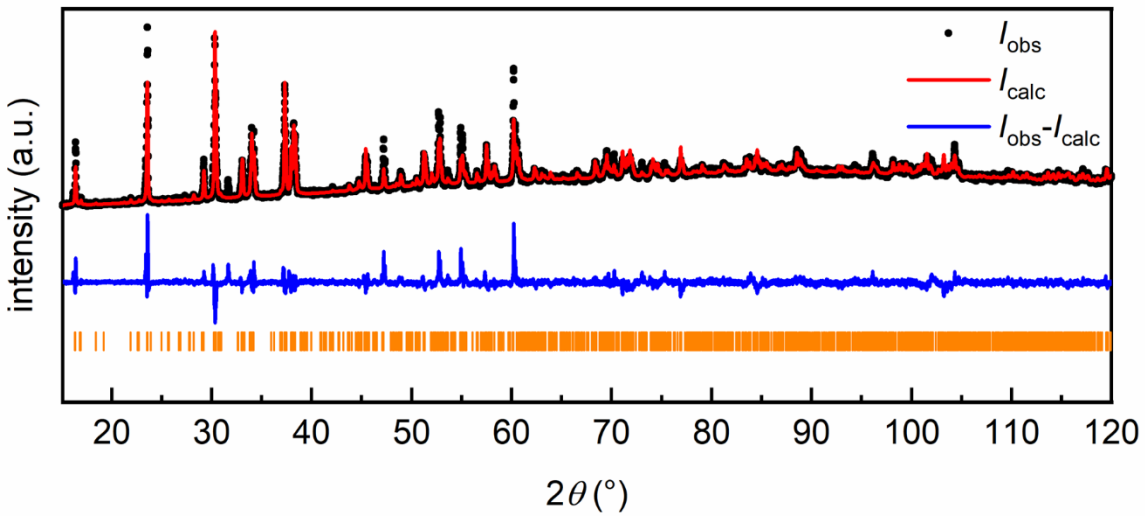

Figure 83. Powder X-ray diffraction pattern of the compound $YbAl_2Se_4$ synthesized by the reaction of $YbAl_2$ with four equivalents selenium. Experimental data is shown as black dots, simulated diffraction patterns from refinements as red lines, the difference is shown as continuous blue lines. Bragg positions are shown as orange ($YbAl_2Se_4$, space group *Fddd*) ticks.

Lastly, the Ca compound shall be discussed. It was synthesized as discussed before. The powder diffraction pattern is shown in Figure 84. The compound is described in literature to

crystallize in the orthorhombic crystal system with space group *Cccm* in an analogous way to the Sr compound. However, it is reported that the structure has two Al positions, which are given as partially occupied split positions, which seems incorrect.[167]

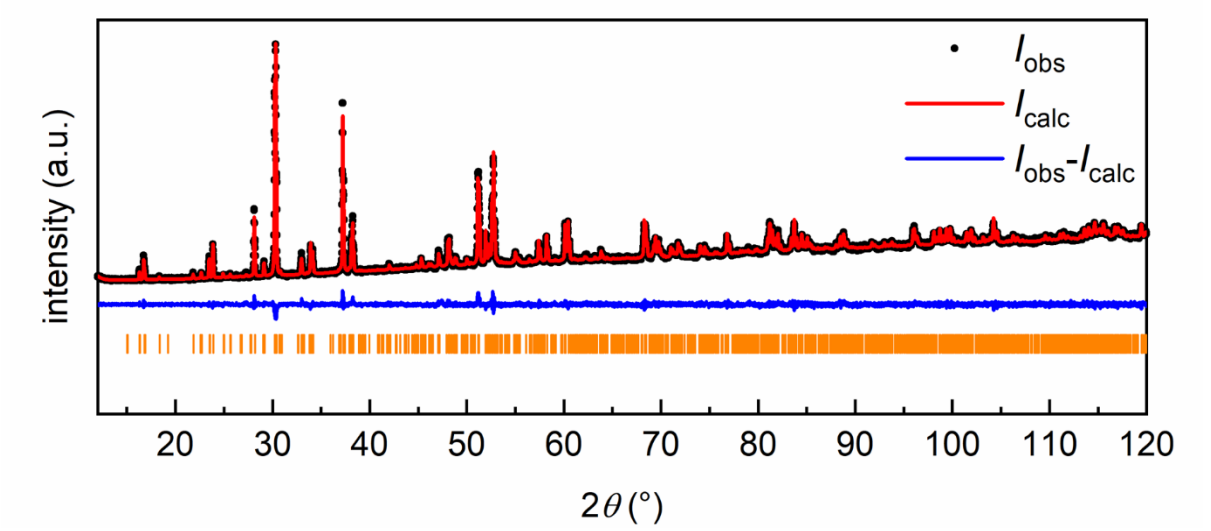

Figure 84. Powder X-ray diffraction pattern of the compound $CaAl_2Se_4$ synthesized by the reaction of $CaAl_2$ with four equivalents selenium. Experimental data is shown as black dots, simulated diffraction patterns from refinements as red lines, the difference is shown as continuous blue lines. Bragg positions are shown as orange ($CaAl_2Se_4$, space group *Fddd*) ticks.

Figure 85 shows an enlarged section of the powder diffraction pattern with two different structure types for the refinement. The top picture clearly reveals that some superstructure reflections are visible in the diffractogram, which can only be refined if the already discussed structure of $EuAl_2S_4$ with space group *Fddd* is used. The smaller unit cell with space group *Cccm* does not describe all observed reflections properly.

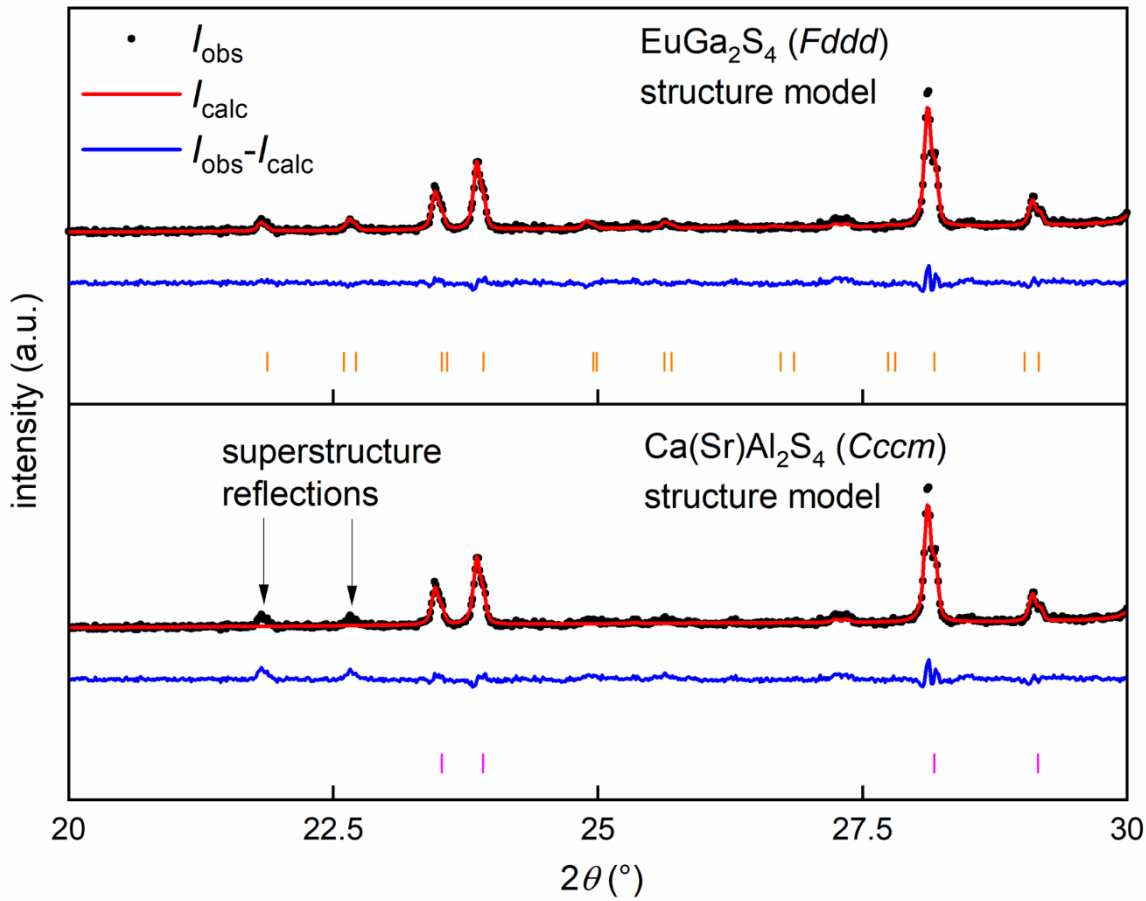

Figure 85. Zoomed in region of the X-ray powder pattern of $CaAl_2Se_4$ simulated using two different space groups (structure types), namely (*top*) *Fddd* and (*bottom*) *Cccm*. Experimental data is shown as black dots, simulated diffraction patterns from refinements as red lines, the difference is shown as continuous blue lines. Bragg positions are shown as orange ($CaAl_2Se_4$, space group *Fddd*) and pink ($CaAl_2Se_4$, space group *Cccm*) ticks.

For confirmation of the findings of the powder diffraction analysis, single crystals of $CaAl_2Se_4$ were grown by applying slow cooling rates. Pictures of the reddish crystals are shown in Figure 86. Details of the refinement are found in Table 38 - Table 40. It is also possible to find a structural relationship expressed by a Bärnighausen formalism[45-48] shown in Figure 87, indicating that the enlarged unit cell with space group *Fddd* originates from the unit cell described with space group *Cccm*, leading to a splitting of the atomic positions. With these structures being so similar, it could be speculated that the weak superstructure reflections could not be observed when the crystal structure was investigated back in 1978 on a Stoe Stadi II. A detailed description of the structure will not be given, since it is reported in literature and has been discussed several times. Figure 87 shows the unit cells for both structure types. On the left, the smaller unit cell (space group *Cccm*) is shown, while on the right the enlarged unit cell is depicted showing the movement of the Al and Se atoms.

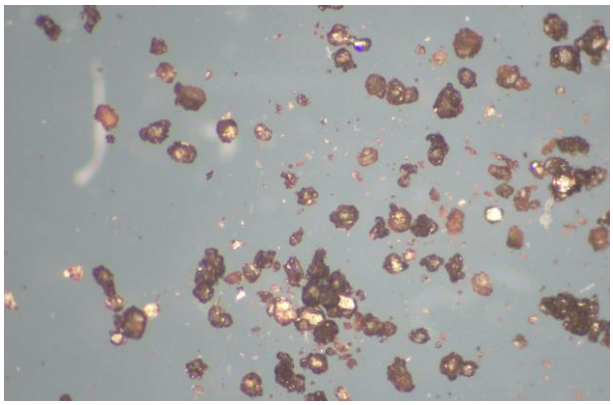

Figure 86. Picture of single crystals obtained after the reaction of $CaAl_2$ with four equivalents of selenium.

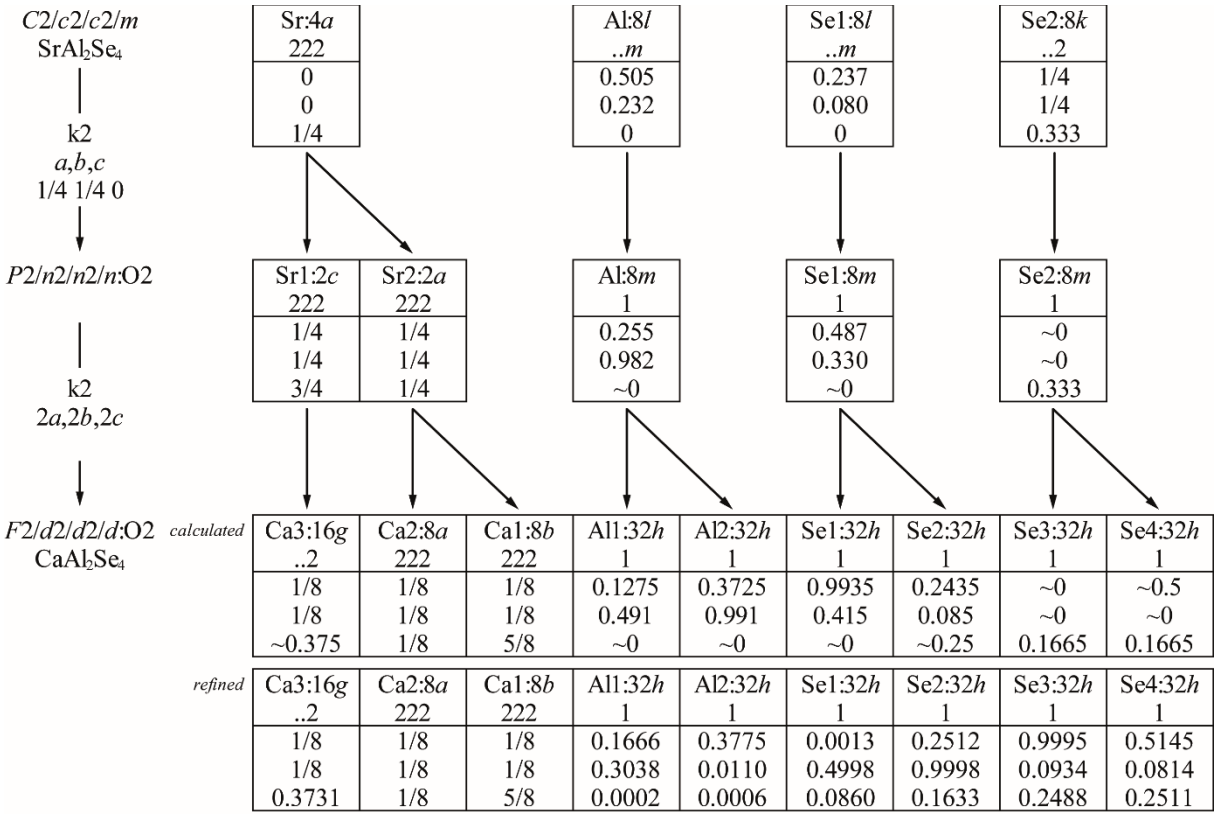

Figure 87. Bärnighausen formalism[45-48] indicating the structural relationship of the structure of $Ca(Sr)Al_2S_4$ found in literature and the identified structure for $CaAl_2Se_4$ adopting the $EuGa_2S_4$ structure type with space group *Fddd*.

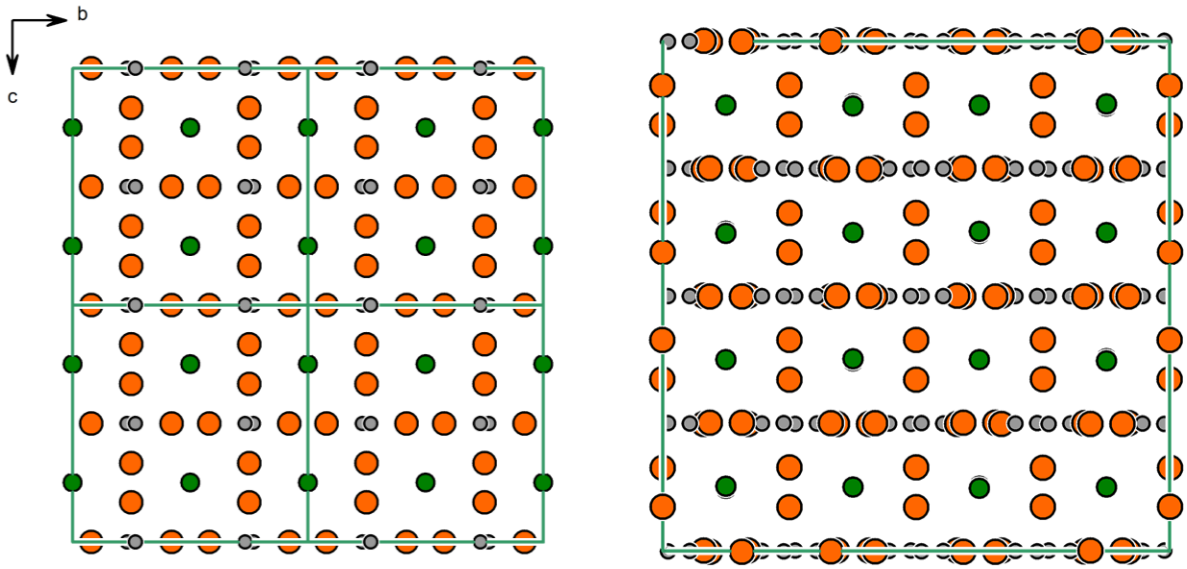

Figure 88. (*left*) Unit cell of $CaAl_2Se_4$, described in literature, adopting the $SrAl_2Se_4$ type structure (space group *Cccm*) and (*right*) the observed unit cell of the 2×2×2 superstructure adopting the $EuGa_2S_4$ type structure (space group *Fddd*). Ca, Al and Se are depicted as green, grey and orange spheres.

Table 38. Crystallographic data and structure refinement from single-crystal X-ray diffraction experiments for $CaAl_2Se_4$.

Nominal composition		$CaAl_2Se_4$
Refined composition		$CaAl_2Se_4$
Structure type		$EuGa_2Se_4$ (*Fddd*)
Lattice parameters	*a* (pm)	1265.48(4)
	b (pm)	2096.13(7)
	c (pm)	2108.58(7)
	V (nm^3)	5.5932
Molar mass, g mol^{-1}		409.9
Density calc., g cm^{-3}		3.894
Crystal size, μm		50×30×25
Detector distance, mm		40
Exposure time, s		10
Range in *hkl*		$h \pm 19$, $k \pm 32$, $l \pm 32$
θ_{min}, θ_{max}, deg		2.11, 33.16
Linear absorption coeff., mm^{-1}		21.848
No. of reflections		54144
R_{int} / R_σ		0.0468 / 0.0166
No. of independent reflections		2686
Reflections used [$I \geq 3\sigma(I)$]		1593
F(000), e		5824
*R*1 / *wR*2 for $I \geq 3\sigma(I)$		0.0223 / 0.0254
*R*1 / *wR*2 for all data		0.0515 / 0.0293
Data / parameters		2686 / 67
Goodness-of-fit on F^2		1.27
Extinction coefficient		280(40)
Diff. Fourier residues /e^- $Å^{-3}$		+1.01 / –1.30

Table 39. Atom positions and equivalent isotropic displacement parameters (pm^2) for $CaAl_2Se_4$. U_{eq} is defined as one third of the trace of the orthogonalized U_{ij} tensor.

Atom	Wyckoff position	*x*	*y*	*z*	U_{eq}
Ca1	16*g*	1/8	1/8	0.37315(4)	162(4)
Ca2	8*b*	1/8	1/8	5/8	199(5)
Ca3	8*a*	1/8	1/8	1/8	196(5)
Al1	32*h*	0.16657(5)	0.30384(3)	0.00014(5)	131(2)
Al2	32*h*	0.37750(5)	0.01099(3)	0.00062(5)	131(2)
Se1	32*h*	0.00129(4)	0.499750(19)	0.086024(11)	131(1)
Se2	32*h*	0.25120(4)	-0.000229(18)	0.163344(11)	127(1)
Se3	32*h*	0.250523(17)	0.093389(12)	0.00126(2)	139(1)
Se4	32*h*	0.264492(19)	0.331406(11)	0.24890(2)	127(1)

Table 40. Interatomic distances (pm) for $CaAl_2Se_4$. Standard deviations for the interatomic distances are ≤0.2 pm.

Ca1(16*g*)	2	Se4	313.3	Al2	1	Se3	235.9
	2	Se3	313.9		1	Se1	239.6
	2	Se2	314.4		1	Se1	239.9
	2	Se1	318.3		1	Se4	240.8
	2	Al2	389.9		1	Al2	313.5
	2	Al1	399.0	Se1	1	Al2	239.6
Ca2(8*b*)	2	Se4	314.0		1	Al2	239.9
	2	Se4	314.1	Se2	1	Al1	239.1
	4	Se1	316.6		1	Al1	239.6
	4	Al2	389.1	Se3	1	Al2	235.9
Ca3(8*a*)	4	Se3	312.5		1	Al1	239.6
	4	Se2	317.8	Se4	1	Al1	236.3
	4	Al1	401.8		1	Al2	240.8
Al1(32*h*)	1	Se4	236.3				
	1	Se2	239.1				
	1	Se3	239.6				
	1	Se2	239.6				
	1	Al1	309.1				

5.5.4 The obscure oxidation behavior of $HfAl_2$ – A high temperature in situ study

The work on Hf_4VAl_7 and especially the solid solution $Hf(V_{1-x}Al_x)_2$ did not only inspire the work on intermetallic compounds described in section 5.2.1. It also posed the questions what happens if the endmembers $HfAl_2$ and HfV_2 are oxidized and if the ternary compounds such as nominal HfVAl ($Hf(V_{0.5}Al_{0.5})_2$) show a totally different oxidation behavior.

In comparison to the topics before, it must be mentioned that for Hf and Al no ternary oxide is known. It is therefore expected that the oxidation of $HfAl_2$ leads to the phase segregation into HfO_2 and Al_2O_3.[24] For the first experiments, the oxidation reactions were performed in an STA system at 1273 K with a dwelling time of 5 h. Corresponding STA data are summarized in the appendix (Figure S60 - Figure S63).

For nominal HfVAl, a mixture of all three oxides, namely Al_2O_3 (corundum, $R\bar{3}c$), V_2O_5 (own type $Pmmn$)[311] and HfO_2 (ZrO_2 type $P2_1/c$)[312] is visible, and the powder X-ray diffraction pattern can be refined nicely, as can be seen in Figure 89.

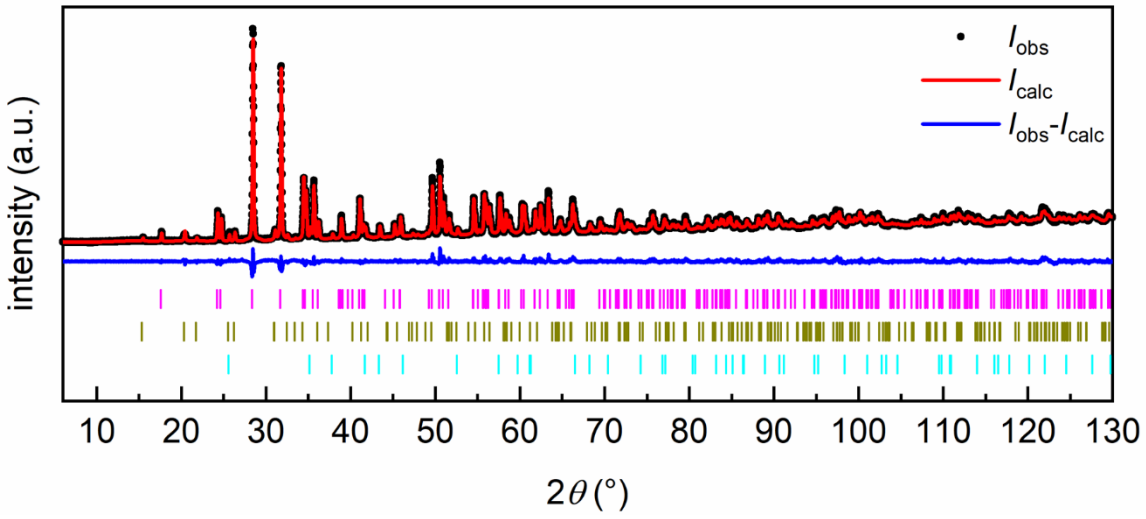

Figure 89. Powder X-ray diffraction pattern obtained after the reaction of $Hf(V_{0.5}Al_{0.5})_2$ in an STA setup at 1273 K for 5 h. Experimental data is shown as black dots, simulated diffraction patterns from refinements as red lines, the difference is shown as continuous blue lines. Bragg positions are shown as pink (HfO_2, space group $P2_1/c$, 56(1) mass%), dark yellow (V_2O_5, space group $Pmmn$, 23(1) mass%) and cyan (Al_2O_3, space group $R\bar{3}c$, 21(1) mass%) ticks.

For HfV_2, the powder X-ray pattern (Figure 90) of the oxidation product shows HfO_2 and V_2O_5. The reflections, however, could not be matched to the only existing ternary oxide HfV_2O_7 (SiP_2O_7 type, $Pa\bar{3}$).[313] Some minor undescribed reflections could not be matched to an existing phase so far.

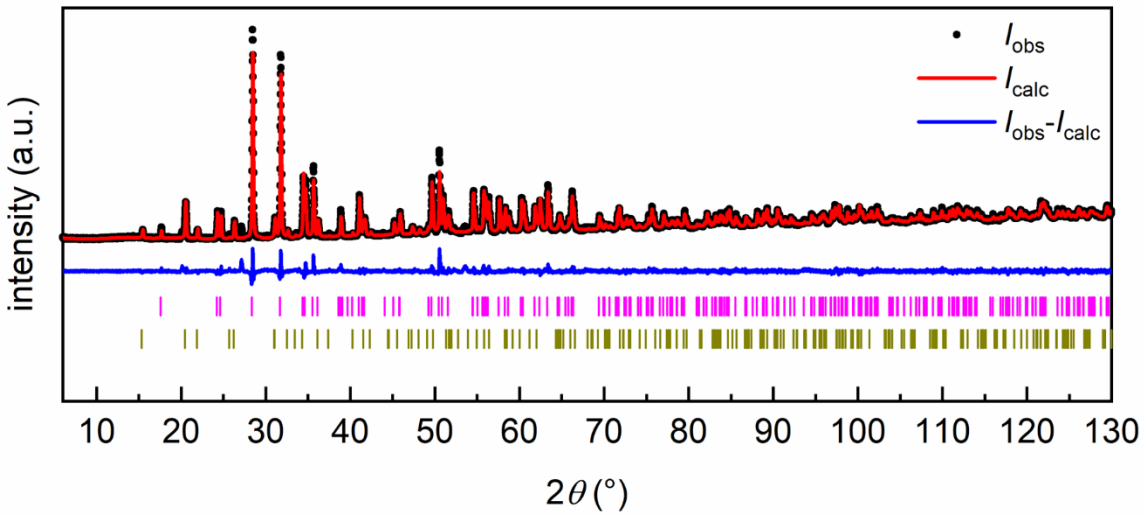

Figure 90. Powder X-ray diffraction pattern obtained after the reaction of HfV_2 in an STA setup at 1273 K for 5 h. Experimental data is shown as black dots, simulated diffraction patterns from refinements as red lines, the difference is shown as continuous blue lines. Bragg positions are shown as pink (HfO_2, space group $P2_1/c$, 61(1) mass%) and dark yellow (V_2O_5, space group *Pmmn*, 39(1) mass%) ticks.

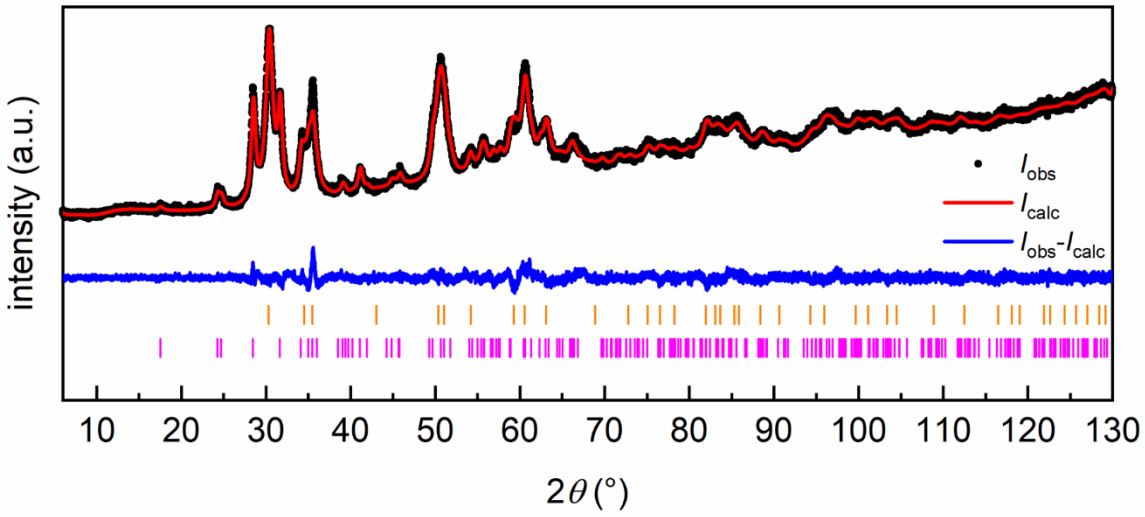

Figure 91. Powder X-ray diffraction pattern obtained after the reaction of $HfAl_2$ in an STA setup at 1273 K for 5 h. Experimental data is shown as black dots, simulated diffraction patterns from refinements as red lines, the difference is shown as continuous blue lines. Bragg positions are shown as orange (HfO_2, space group $P4_2/nmc$, 55(1) mass%) and pink (HfO_2, space group $P2_1/c$, 45(1) mass%) ticks.

The oxidation of $HfAl_2$ resulted in the powder X-ray diffractogram shown in Figure 91. In contrast to the data shown before, the sample shows extremely broad reflections. The reflections could be fitted to a mixture of HfO_2 in the already mentioned monoclinic ambient temperature (and pressure) phase. The other reflections could be matched to a phase described as a high temperature phase.[314] For HT-HfO_2, a cubic and tetragonal phase, which are related, are reported. Due to the quality of the data, it cannot be clarified which one is present here. It can only be concluded that the obtained powder pattern highly differs from the ambient temperature

phase. This mixture of the two polymorphs is puzzling, since this observation was not made for the oxidation of the other two phases.

This system deserved further investigation. One problem with the investigations in the STA system available here, is that the product formation seems quite inconsistent, which means that in the repetition of the experiment above with the same temperature program, the following powder pattern (Figure 92) was obtained, showing only the monoclinic phase of HfO_2. It is therefore likely that the phase formation within this system is not easy to understand. One reason could be slight changes in the reaction pathway.

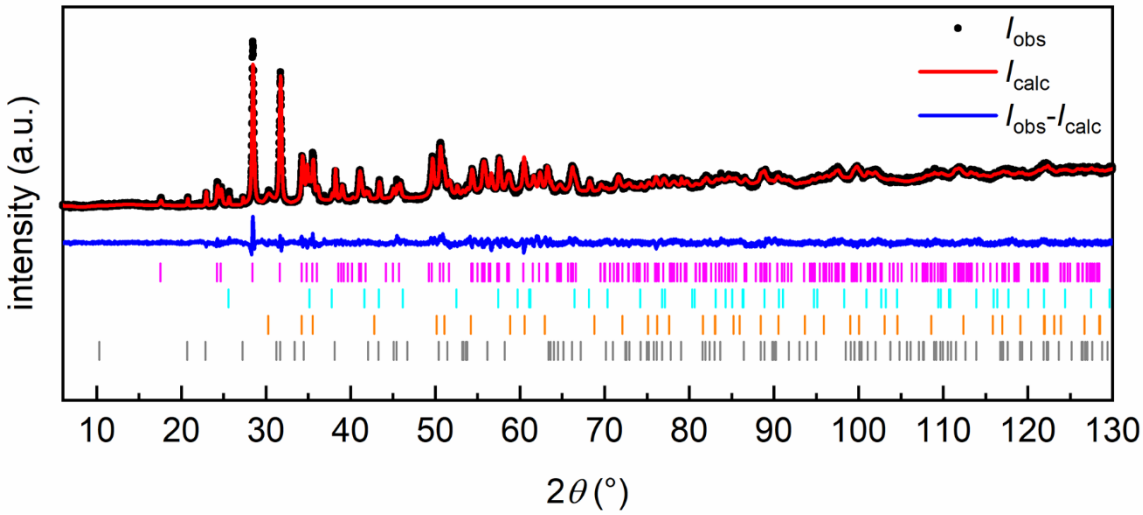

Figure 92. Powder X-ray diffraction pattern obtained after the reaction of $HfAl_2$ in an STA setup at 1273 K for 5 h. Experimental data is shown as black dots, simulated diffraction patterns from refinements as red lines, the difference is shown as continuous blue lines. Bragg positions are shown as pink (HfO_2, space group $P2_1/c$, 58(1) mass%), cyan (Al_2O_3, space group $R\bar{3}c$, 29(1) mass%), orange (HfO_2, space group $P4_2/nmc$, 8(1) mass%) and grey ($HfAl_3$, space group $I4/mmm$, 5(1) mass%) ticks.

A repetition of the experiments within the tube furnace operating at pure oxygen gave more insight. Figure 93 shows the diffractograms obtained after initial reaction of $HfAl_2$ at 1273 K for 1 and 24 hours. Oxidation of only one hour shows broadened reflections matching the cubic (or tetragonal) HT-HfO_2. After 24 hours of dwelling, the monoclinic polymorph of HfO_2 is found as the main phases, however, the reflections are still broadened. To further investigate this obscure behavior an in-situ study using an XRK900 was applied. A sample of $HfAl_2$ was heated at 100 K steps, dwelled there for 10 minutes. Afterwards, a measurement was started. The data recorded at 303, 1073 and 1173 K (maximum temperature of the system) are shown in Figure 94. One can see that oxidation happens between the last two steps. However, a mass fraction increase of $HfAl_3$ is seen, probably due to the beginning of the oxidation of $HfAl_2$, with

the Hf oxidizing before the Al. The occurrence of the intermetallic "intermediate" $HfAl_3$ is comparable to the findings of $ScAl_3$ and $YbAl_3$ described before.

In summary, it can be said that the results regarding the oxidation behavior of $HfAl_2$ cannot be explained conclusively. Synthetic conditions as well as probably the exact composition of the precursors seem to play a crucial role. The formation of two different polymorphs could depend on different amounts of Al^{3+} which are incorporated into the structure and might stabilize the high-temperature polymorph. To clarify these results, future investigations and a more detailed analysis are necessary.

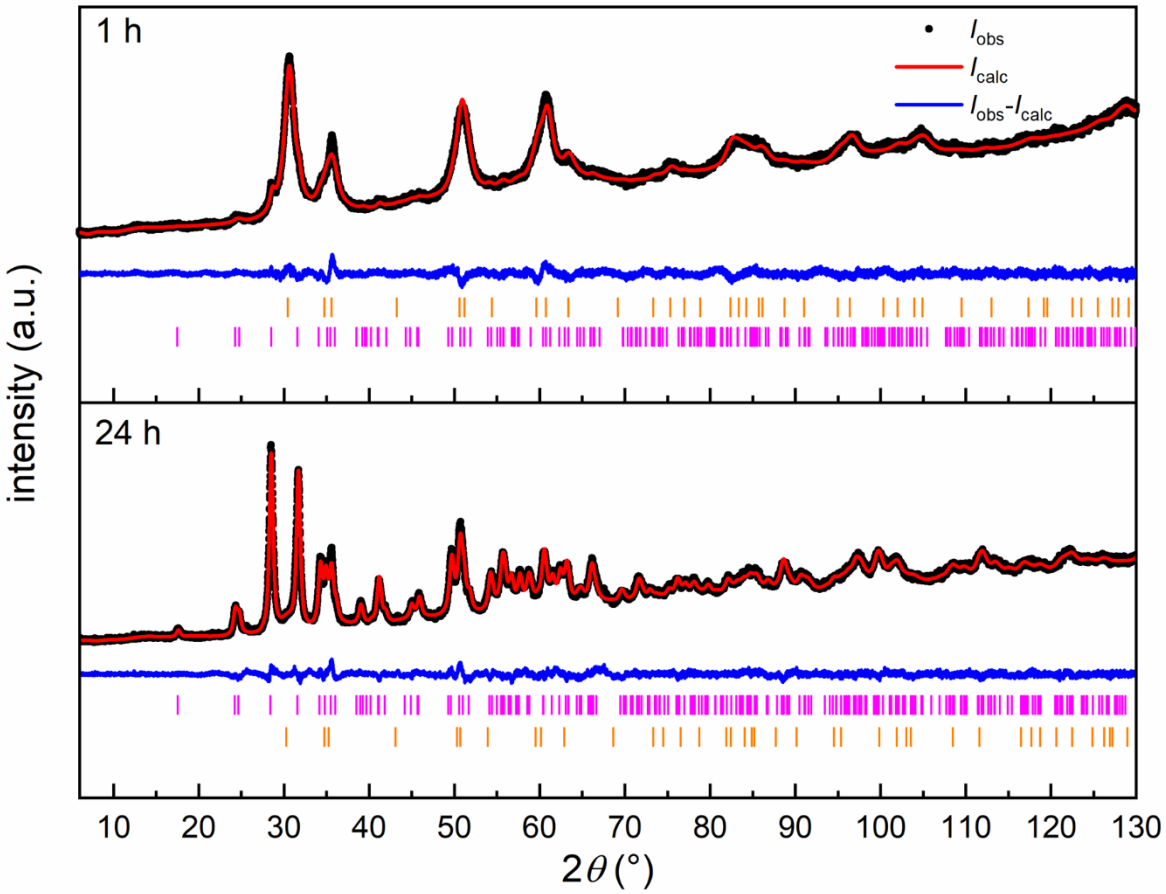

Figure 93. Powder X-ray diffraction pattern obtained after the reaction of $HfAl_2$ in a tube furnace setup operated at pure oxygen at 1273 K with dwelling times of (*top*) one and (*bottom*) 24 hours. Experimental data is shown as black dots, simulated diffraction patterns from refinements as red lines, the difference is shown as continuous blue lines. Bragg positions are shown as orange (HfO_2, space group $P4_2/nmc$, (*top*) 86(1) mass%, (bottom) 10(1) mass%) and pink (HfO_2, space group $P2_1/c$, (*top*) 14(1) mass%, (*bottom*) 90(1) mass%) ticks.

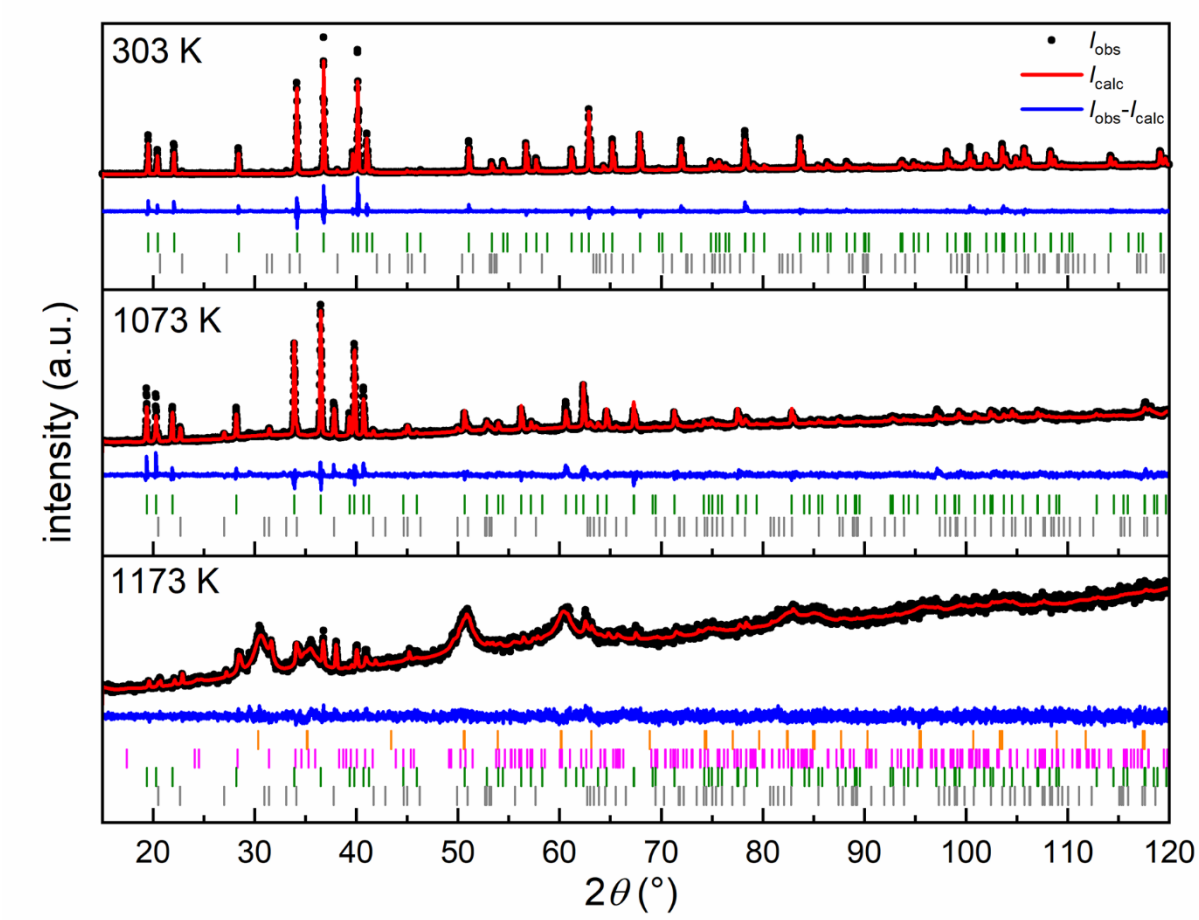

Figure 94. Powder X-ray diffraction pattern obtained after the reaction of $HfAl_2$ in an XRK setup: Diffratograms shown are recorded at (*top*) 303, (*middle*) 1073 and (*bottom*) 1173 K in the first heating cycle. Experimental data is shown as black dots, simulated diffraction patterns from refinements as red lines, the difference is shown as continuous blue lines. Bragg positions are shown as green ($HfAl_2$, space group $P6_3/mmc$, (*top*) 97(1) mass%, (*middle*) 82(1) mass%, (*bottom*) 8(1) mass%), dark grey ($HfAl_3$, space group $I4/mmm$, (*top*) 3(1) mass%, (*middle*) 18(1) mass%, (*bottom*) 6(1) mass%), orange (HfO_2, space group $P4_2/nmc$, (*top*) 0 mass%, (*middle*) 0 mass%, (*bottom*) 67(1) mass%) and pink (HfO_2, space group $P2_1/c$, (*top*) 0 mass%, (*middle*) 0 mass%, (*bottom*) 18(1) mass%) ticks.

5.6 Cooperation work

During this thesis, in which solid state nuclear resonance spectroscopy was used as a major part, cooperation work on other systems have been carried out. In the following section the publications that were published are presented. For further information, the reader is referred to the publications.

5.6.1 Structure, physical and ^{27}Al NMR-spectroscopic properties of the equiatomic compounds of the type *RE*AlRh (*RE* = Sm, Tb, Dy, Er, and Lu)

Published as an article

Mathis Radzieowski, Elias C. J. Gießelmann, Stefan Engel and Oliver Janka, *Z. Naturforsch. B* **2024**, *79*, 459.

https://doi.org/10.1515/znb-2024-0053

Within the series of the equiatomic *RE*AlRh compounds, the representatives with *RE* = Y, La–Nd, Gd, Ho, Tm and Yb have been synthesized and reported before. The members in between with *RE* = Sm, Tb, Dy, Er and Lu, however, were not reported yet. The missing members of this series have been synthesized and structurally as well as magnetically and NMR spectroscopically characterized. All members crystallize isostructurally in the orthorhombic TiNiSi type structure, similar to most of the known *RE*AlRh series. The evolution of their unit cell volumes exhibits the expected decrease due to the lanthanide contraction. While LuAlRh shows Pauli-paramagnetic behavior, SmAlRh, TbAlRh, DyAlRh, ErAlRh and TmAlRh exhibit antiferromagnetic ground states with Néel temperatures between T_N = 45 and 4 K. ^{27}Al MAS-NMR investigations have been conducted on YAlRh and LuAlRh, additional quantum-chemical calculations support the NMR study and enable to address the charge distribution in these intermetallic aluminum metallides.

5.6.2 Synthesis, magnetic and NMR spectroscopic properties of the MAl$_5$Pt$_3$ series (M = Ca, Y, La–Nd, Sm–Er)

Published as an article

Stefan Engel, Elias C. J. Gießelmann, Lars Schumacher, Yuemei Zhang, Frank Müller and Oliver Janka, *Dalton Trans.* **2024**, *53*, 12176.

https://doi.org/10.1039/D4DT01296H

Following recent investigation in the ternary system Sr–Al–Pt led to the discovery of SrAl$_5$Pt$_3$, which crystallizes in the orthorhombic YNi$_5$Si$_3$ type (*Pnma*) structure. Interestingly, only two more aluminum representatives, CeAl$_5$Pt$_3$ and EuAl$_5$Pt$_3$, have been reported to adopt this structure type. Therefore, the existence range of compounds adopting the YNi$_5$Si$_3$ type structure was investigated. Besides the already known Sr, Ce and Eu members, the series could be extended to Ca, Y and La-Nd as well as Sm-Er. All compounds were synthesized from the elements and characterized by powder X-ray diffraction. While for CaAl$_5$Pt$_3$ and LaAl$_5$Pt$_3$ also the respective M_2Al$_{16}$Pt$_9$ members were observed, the other compounds could be obtained either as X-ray pure materials or with small amounts of Al$_3$Pt$_2$ as side phase. The structure of ErAl$_5$Pt$_3$ could be refined from single-crystal data, verifying that also the small rare-earth elements adopt the YNi$_5$Si$_3$ type structure. Selected members of the series were furthermore characterized by magnetization and susceptibility measurements. Since YAl$_5$Pt$_3$ could be obtained as phase pure material and exhibits no paramagnetic behavior it was investigated by ^{27}Al MAS NMR investigations. Also, XPS measurements were conducted on this compound to gain an insight into the charge distribution. Finally, quantum-chemical calculations supported the NMR measurements and gave an insight into the chemical bonding and the charge distribution.

5.6.3 Black Titania and Niobia within Ten Minutes – Mechanochemical Reduction of Metal Oxides with Alkali Metal Hydrides

Published as an article

Anna Michaely, Oliver Janka, Elias C. J. Gießelmann, Robert Haberkorn, Haakon T. A. Wiedemann, Christopher W. M. Kay, and Guido Kickelbick, *Chem. Eur. J.* **2023**, *29*, e202300223.

https://doi.org/10.1002/chem.202300223

Summary

Partially or fully reduced transition metal oxides show extraordinary electronic and catalytic properties but are usually prepared by high temperature reduction reactions. This study reports the systematic investigation of the fast mechanochemical reduction of rutile-type TiO_2 and H-Nb_2O_5 to their partially reduced black counterparts applying NaH and LiH as reducing agents. Milling time and oxide to reducing agent ratio show a large influence on the final amount of reduced metal ions in the materials. For both oxides LiH shows a higher reducing potential than NaH. An intercalation of Li^+ into the structure of the oxides was proven by PXRD and subsequent Rietveld refinements as well as ^{6}Li solid-state NMR spectroscopy. The products showed a decreased band gap and the presence of unpaired electrons as observed by EPR spectroscopy, proving the successful reduction of Ti^{4+} and Nb^{5+}. Furthermore, the developed material exhibits a significantly enhanced photocatalytic performance towards the degradation of methylene blue compared to the pristine oxides. The presented method is a general, time efficient and simple method to obtain reduced transition metal oxides.

5.6.4 Mechanochemical Defect Engineering of Nb_2O_5: Influence of $LiBH_4$ and $NaBH_4$ Reduction on Structure and Photocatalysis

Manuscript submitted to Solids

Anna Michaely, Elias C. J. Gießelmann and Guido Kickelbick, *Solids* **2025**, *6*, 26.

https://doi.org/10.3390/solids6020026

Summary

Partial reduction of transition metal oxides via defect engineering is a promising strategy to enhance their electronic and photocatalytic properties. In this study, the mechanochemical reduction of Nb_2O_5 using $LiBH_4$ and $NaBH_4$ as reducing agents was systematically explored. Electron paramagnetic resonance (EPR) spectroscopy confirms a successful partial reduction of the oxide, as seen by the presence of unpaired electrons. Interestingly, larger hydride concentrations do not necessarily enable a higher degree of reduction as large amounts of the boron hydrides act as a buffer material and thus hinder the effective transfer of mechanical energy. Powder X-ray diffraction (PXRD) and ^7Li solid-state NMR spectroscopy indicate the intercalation of Li^+ into the Nb_2O_5 lattice. Raman spectroscopy further reveals the increased structural disorder, while optical measurements show a decreased band gap compared to pristine Nb_2O_5. The partially reduced samples show significantly enhanced photocatalytic performance for methylene blue degradation relative to the unmodified oxides.

5.6.5 A lithium–aluminium heterobimetallic dimetallocene

Published as an article

Inga-Alexandra Bischoff, Sergi Danés, Philipp Thoni, Bernd Morgenstern, Diego M. Andrada, Carsten Müller, Jessica Lambert, Elias C. J. Gießelmann, Michael Zimmer and André Schäfer,
Nat. Chem. **2024**, *16*, 1093.

https://doi.org/10.1038/s41557-024-01531-y

Summary

Homobimetallic dimetallocenes exhibiting two identical metal atoms sandwiched between two η^5 bonded cyclopentadienyl rings is a narrow class of compounds, with representative examples being dizincocene and diberyllocene. The synthesis and structural characterization of a heterobimetallic dimetallocene, accessible through heterocoupling of lithium and aluminylene fragments with pentaisopropylcyclopentadienyl ligands could be described in this publication. The Al–Li bond features a high ionic character and profits from attractive dispersion interactions between the isopropyl groups of the cyclopentadienyl ligands. A key synthetic step is the isolation of a cyclopentadienylaluminylene monomer, which also enables the structural characterization of this species. In addition to their structural authentication by single-crystal X-ray diffraction analysis, both compounds were characterized by multinuclear NMR spectroscopy in solution and in the solid state. Furthermore, reactivity studies of the lithium–aluminium heterobimetallic dimetallocene with an N-heterocyclic carbene and different heteroallenes were performed and show that the Al–Li bond is easily cleaved.

5.7 Review articles

Besides research articles three review articles were published on different topics of the structural chemistry of intermetallic compounds during this thesis. In two articles compounds containing either Yb or Eu were summarized about their different crystal structures and physical properties. A focus was set on the different valence states of Yb, which is known to show many examples of di- and trivalent states. In contrast to that, compounds with trivalent Eu are significantly scarce in intermetallic compounds. They were discussed as well. Another work that inspired many of the already discussed publications was the third review summarizing the structures of the Laves phases as well as superstructures, distortion and coloring variants of binary and multinary compounds that can be derived from them. The respective publications together with the respective abstract are given in the following in chronological order or their release. The interested reader is referred to the original publication.

5.7.1 Trivalent europium – a scarce case in intermetallics

Published as an article

Stefan Engel, Elias C. J. Gießelmann, Rainer Pöttgen and Oliver Janka, *Rev. Inorg. Chem.* **2023**, *43*, 571.

https://doi.org/10.1515/revic-2023-0003

Summary

In most intermetallic europium compounds, the Eu atoms exhibit a divalent oxidation state with a high effective magnetic moment since Eu^{2+} is isoelectronic with Gd^{3+}. Trivalent intermetallic Eu compounds, in contrast, are extremely scarce and under 20 examples are known to literature. The mini-review summarizes the known binary and ternary examples along with their crystal-chemical peculiarities as well as their magnetic and ^{151}Eu Mössbauer spectroscopic behavior. Additionally, compounds that exhibit valence phase transitions are summarized.

5.7.2 Laves phases: superstructures induced by coloring and distortions

Published as an article

Elias C. J. Gießelmann, Rainer Pöttgen and Oliver Janka, *Z. Allg. Anorg. Chem.* **2023**, *649*, e202300109.

https://doi.org/10.1002/zaac.202300109

Summary

The structural chemistry of Laves phases, especially with respect to their superstructures induced by coloring and distortions, is discussed. Starting from the three classical Laves phases $MgCu_2$, $MgZn_2$ and $MgNi_2$, the more complex Komura phases are derived. Different possibilities of their description are summarized. In the second part, the superstructures are discussed based on their respective prototypes. The crystal chemical relationships are illustrated based on group-subgroup descriptions using the Bärnighausen formalism.

5.7.3 On the Ytterbium Valence and the Physical Properties in Selected Intermetallic Phases

Published as an article

Stefan Engel, Elias C. J. Gießelmann, Maximilian K. Reimann, Rainer Pöttgen and Oliver Janka, *ACS Organic & Inorganic Au* **2024**, *4*, 188.

https://doi.org/10.1021/acsorginorgau.3c00054

Summary

This review article summarizes important aspects of the crystal chemistry of ytterbium-based intermetallic compounds along with a selection of their outstanding physical properties. These originate in many cases from the ytterbium valence. Different valence states are possible here, divalent ($4f^{14}$), intermediate-valent, or trivalent ($4f^{13}$) ytterbium, resulting in simple diamagnetic, Pauli or Curie−Weiss paramagnetic, or valence fluctuating behavior. Especially, some of the Yb^{3+} intermetallics have gained deep interest due to their Kondo or heavy Fermion ground states. The property investigations using magnetic and transport measurements, specific heat data, NMR, ESR, and Mössbauer spectroscopy, elastic and inelastic neutron scattering, and XAS data as well as detailed thermoelectric measurements are summarized.

6 Summary and Outlook

The work presented extends the knowledge on spectroscopic approaches of binary series of aluminides, the search for superstructures of the Laves phases and the larger group of Frank-Kasper phases as well as the oxidation behavior of intermetallic aluminum compounds as a synthetic tool to obtain valence-precise compounds such as oxides, sulfides or selenides.

It was possible to investigate two isostructural series of binary aluminides towards their electronic structure combining multiple methods such as solid state NMR and Raman spectroscopy as well as DFT calculations using the VASP followed by LOBSTER analysis. General trends could be observed generating insights into the situation within these compounds, however, transferring the results to compounds adopting different structure types remains challenging up to impossible since too many effects come together determining the differences of these compounds.

The structural chemistry of Laves phases could be extended by the series RE_2TiAl_3 adopting the Mg_2Ni_3Si structure type, labelling them the first aluminum compounds of this structure type. The superstructure Hf_4VAl_7 could be identified, while simultaneously showing the potential of systematic investigations concerning Laves phases combined with spectroscopic methods. Based on these findings, multiple systems such as Zr–V–Al as well as Hf–*T*–Al were investigated. This led to compounds, which do not adopt the Laves phase structures or related ones leading to the larger family of Frank-Kasper phases found within these systems. Here, the synthesis and structural analysis of a new binary compound Hf_6Al_7 is worth mentioning. Moreover, the compound ZrV_2Al_4 could be identified as the first structurally characterized ternary compound in the system Zr–V–Al. However, the synthesis of other homologues remains challenging and obtaining suitable single crystals was not possible yet. Overall, it can be said that a combination of diffraction and spectroscopic methods such as solid state NMR is crucial for identifying ordered or disordered structures.

Diving into the world of oxidation chemistry, the finding of the sub-oxide $Sc_4Au_2O_{1-x}$ must inspire more targeted synthesis on compounds adopting these structure types, especially when looking at possible sub-sulfides, which are not reported yet. The sub-oxide was observed during systematic investigations of the solid solution $Sc_2Au_{1-x}Al_x$. The endmembers could be analyzed using ^{27}Al and ^{45}Sc solid state NMR.

The question of whether intermetallic aluminides could be used as precursor materials for oxidation reactions with the chalcogenides the second large chapter investigated. In case of the reaction with oxygen, the approach is not straightforward and only in the case of nominal "$BaAl_2$" the expected (based on the composition of the intermetallic) phase pure product was obtained. For other examples, mixtures of many ternary and/or the binary oxides were found. The most outstanding example is the formation of the mayenite phase $Ca_{12}Al_{14}O_{33}$ when oxidizing $CaAl_2$. However, the results, being disappointing from a synthetic point of view, give many insights into the kinetic stability of the formed products on the surface of the intermetallic compounds. In detailed investigations, it was shown that ball milling of the precursor can highly affect reactivity and product formation. Other aspects that play a crucial role are the atmosphere (oxygen content), temperature and dwelling times. The situation is different for the heavier chalcogenides sulfur and selenium. Here, reactions leading to phase pure products can be performed readily (as was partially reported before). Aluminum sulfides of divalent metals such as Ca, Sr and Eu were synthesized by the sulfidation of intermetallic starting materials and further investigated using spectroscopic techniques. More compounds like $YbAl_2S_4$, $CaAl_2Se_4$, $EuAl_2Se_4$ and $YbAl_2Se_4$ could also be synthesized and structurally characterized. For another set of isostructural compounds, namely the $AEAl_4S_7$ (*AE* = Ca, Sr, Ba) series, it was shown that only the Ba compound could be obtained as a phase pure sample.

The playground for future investigations in all fields of research captured in this work is overwhelming. Many aspects of the systems described here deserve further investigations: the structural chemistry of the Frank-Kasper phases, for example. One can think e.g. of the combination of multiple main group elements and leaving the composition range of main group rich compounds, which was rarely done within this thesis. Concerning the field of oxidation reactions performed with intermetallic compounds, the impact of high-energy ball milling of the precursor when using sulfur or selenium powder is one of the most promising experiments that can be done in a follow-up study. For the oxidation behavior, it would be highly interesting to test aluminum poor intermetallic compounds. Here, all compounds investigated had an Al-content > 65%. However, in the oxidation process of e.g. $ScAl_2$ and $YbAl_2$ intermetallic intermediates could be isolated. Therefore, it would be highly interesting if the use of transition metal or rare earth metal rich precursors can lead to other intermetallic compounds.

7 References

[1] B. T. Matthias, T. H. Geballe, S. Geller, E. Corenzwit, *Phys. Rev.* **1954**, *95*, 1435.
[2] K. Strnat, G. Hoffer, J. Olson, W. Ostertag, J. J. Becker, *J. Appl. Phys.* **1967**, *38*, 1001.
[3] A. Ray, K. Strnat, *IEEE Trans. Magn.* **1972**, *8*, 516.
[4] J. J. Croat, J. F. Herbst, R. W. Lee, F. E. Pinkerton, *Appl. Phys. Lett.* **1984**, *44*, 148.
[5] K. A. Gschneidner, V. K. Pecharsky, *Annu. Rev. Mater. Res.* **2000**, *30*, 387.
[6] S. R. Brown, S. M. Kauzlarich, F. Gascoin, G. J. Snyder, *Chem. Mater.* **2006**, *18*, 1873.
[7] D. Shechtman, I. Blech, D. Gratias, J. W. Cahn, *Phys. Rev. Lett.* **1984**, *53*, 1951.
[8] R. Pöttgen, D. Johrendt, *Intermetallics - Synthesis, Structure, Function*, De Gruyter, Berlin, Boston, **2014**.
[9] O. Janka, R. Pöttgen, *Intermetallic compounds* in *Rare Earth Chemistry* (Eds.: R. Pöttgen, T. Jüstel, C. A. Strassert), De Gruyter, Berlin, **2020**, pp. 163.
[10] P. Gille, Y. Grin, *Crystal Growth of Intermetallics*, De Gruyter, Berlin, Boston, **2019**.
[11] Y. Grin, *Crystal Structure and Bonding in Intermetallic Compounds* in *Comprehensive Inorganic Chemistry II (Second Edition): Transition elements, lanthanides and actinides, Vol. 2* (Eds.: J. Reedijk, K. Poeppelmeier), Elsevier, Amsterdam, **2013**, pp. 359.
[12] W. Steurer, J. Dshemuchadse, *Intermetallics*, Union of Crystallography, Oxford University Press, Oxford, **2016**.
[13] O. Janka, R. Pöttgen, *Z. Naturforsch. B* **2020**, *75*, 421.
[14] R. Pöttgen, O. Janka, B. Chevalier, *Z. Naturforsch. B* **2016**, *71*, 165.
[15] O. Janka, O. Niehaus, R. Pöttgen, B. Chevalier, *Z. Naturforsch. B* **2016**, *71*, 737.
[16] R. Pöttgen, B. Chevalier, *Z. Naturforsch. B* **2015**, *70*, 289.
[17] S. Engel, E. C. J. Gießelmann, M. K. Reimann, R. Pöttgen, O. Janka, *ACS Org. Inorg. Au* **2024**, *4*, 188.
[18] M. Shatruk, *J. Solid State Chem.* **2019**, *272*, 198.
[19] G. Kresse, M. Schmid, E. Napetschnig, M. Shishkin, L. Köhler, P. Varga, *Science* **2005**, *308*, 1440.
[20] J. Doychak, M. Rühle, *Oxid. Met.* **1989**, *31*, 431.
[21] J. W. Fergus, *Mater. Sci. Eng. A* **2002**, *338*, 108.
[22] C. Kammer, *Aluminium-Taschenbuch 1: Grundlagen und Werkstoffe*, Aluminium-Zentrale, Düsseldorf, Germany, **1995**.
[23] O. Janka, *Metallic light-weight alloys: Al, Ti, Mg* in *Applied Inorganic Chemistry* (Eds.: R. Pöttgen, T. Jüstel, C. Strassert), De Gruyter, Berlin, Germany, **2022**, pp. 158.
[24] P. Villars, K. Cenzual, release 2024/25 ed., ASM International®, Materials Park, Ohio, USA, **2023**.
[25] F. Ostermann, *Anwendungstechnologie Aluminium*, Springer Vieweg, Berlin, Heidelberg, Germany, **2014**.
[26] W. Fischer, *Z. Kristallogr.* **2006**, *221*, 305.
[27] E. Parthé, *Z. Kristallogr.* **2006**, *221*, 301.
[28] J. B. Friauf, *J. Am. Chem. Soc.* **1927**, *49*, 3107.
[29] J. B. Friauf, *Phys. Rev.* **1927**, *29*, 34.
[30] L. Tarschisch, A. T. Titow, F. K. Garjanow, *Phys. Z. Sowjetunion* **1934**, *5*, 503.
[31] F. Laves, H. Witte, *Metallwirtsch.* **1935**, *14*, 645.
[32] K. H. Lieser, H. Witte, *Z. Metallkd.* **1952**, *43*, 396.
[33] F. Stein, A. Leineweber, *J. Mater. Sci.* **2021**, *56*, 5321.
[34] E. C. J. Gießelmann, R. Pöttgen, O. Janka, *Z. Anorg. Allg. Chem.* **2023**, *649*, e202300109.

[35] S. Kal, E. Stoyanov, J.-P. Belieres, T. L. Groy, R. Norrestam, U. Häussermann, *J. Solid State Chem.* **2008**, *181*, 3016.
[36] B. K. Godwal, V. Vijaykumar, S. K. Sikka, R. Chidambaram, *J. Phys. F: Metal Phys.* **1986**, *16*, 1415.
[37] L.-E. Edshammar, S. Andersson, *Acta Chem. Scand.* **1960**, *14*, 223.
[38] C. Wilson, *Acta Crystallogr.* **1959**, *12*, 660.
[39] D. Akhtar, R. Gopalan, T. P. Rajasekharan, *Int. J. Mater. Res.* **1987**, *78*, 201.
[40] H. Fukui, N. Hirao, Y. Ohishi, A. Q. R. Baron, *J. Phys.: Condens. Matter* **2010**, *22*, 095401.
[41] J. Emsley, *The Elements*, Clarendon Press, Oxford University Press, Oxford, New York, **1998**.
[42] R. P. Elliott, W. Rostoker, *Trans. ASM* **1958**, *50*, 617.
[43] V. Sadagopan, E. Pollard, H. C. Gatos, *Solid State Commun.* **1965**, *3*, 97.
[44] Y. Zhao, F. Chu, R. B. Von Dreele, Q. Zhu, *Acta Crystallogr. B* **2000**, *56*, 601.
[45] U. Müller, *Symmetry Relationships between Crystal Structures*, Oxford University Press, Oxford, New York, **2013**.
[46] U. Müller, *Z. Anorg. Allg. Chem.* **2004**, *630*, 1519.
[47] H. Bärnighausen, U. Müller, *Symmetriebeziehungen zwischen den Raumgruppen als Hilfsmittel zur straffen Darstellung von Strukturzusammenhängen in der Kristallchemie*, Universität Karlsruhe und Universität-Gh Kassel, Germany, **1996**.
[48] H. Bärnighausen, *MATCH, Commun. Math. Comput. Chem.* **1980**, *9*, 139.
[49] H. Witte, *Z. Angew. Mineral.* **1938**, *1*, 255.
[50] T. Mishra, R.-D. Hoffmann, C. Schwickert, R. Pöttgen, *Z. Naturforsch. B* **2011**, *66*, 771.
[51] Z. Blazina, Z. Ban, *Z. Naturforsch. B* **1981**, *35*, 1162.
[52] F. Eustermann, F. Stegemann, S. Gausebeck, O. Janka, *Z. Naturforsch. B* **2018**, *73*, 819.
[53] A. V. Zelinskii, A. O. Fedorchuk, O. Y. Zelinska, *Visn. Lviv. Derzh. Univ., Ser. Khim.* **2013**, *54*, 92.
[54] O. Sichevych, Y. Prots, W. Schnelle, M. Schmidt, Y. Grin, *Z. Kristallogr. NCS* **2006**, *221*, 263.
[55] Y. B. Kuz'ma, E. I. Gladyshevskii, *Dopov. Akad. Nauk Ukr. RSR* **1963**, *A25*, 205.
[56] D. Noréus, L. Eriksson, L. Göthe, P. E. Werner, *J. Less-Common Met.* **1985**, *107*, 345.
[57] A. E. Dwight, C. W. Kimball, *Acta Crystallogr. B* **1974**, *30*, 2791.
[58] S. Seidel, O. Janka, C. Benndorf, B. Mausolf, F. Haarmann, H. Eckert, L. Heletta, R. Pöttgen, *Z. Naturforsch. B* **2017**, *72*, 289.
[59] A. Lipatov, A. Gribanov, A. Grytsiv, S. Safronov, P. Rogl, J. Rousnyak, Y. Seropegin, G. Giester, *J. Solid State Chem.* **2010**, *183*, 829.
[60] D. Kaczorowski, A. Lipatov, A. Gribanov, Y. Seropegin, *J. Alloys Compd.* **2011**, *509*, 6518.
[61] I. Doverbratt, S. Ponou, S. Lidin, *J. Solid State Chem.* **2013**, *197*, 312.
[62] W. Jeitschko, H. Nowotny, F. Benesovsky, *Monatsh. Chem.* **1963**, *94*, 247.
[63] F. Stegemann, C. Benndorf, Y. Zhang, M. Bartsch, H. Zacharias, B. P. T. Fokwa, H. Eckert, O. Janka, *Inorg. Chem.* **2017**, *56*, 1919.
[64] A. I. Tursina, N. G. Bukhan'ko, A. V. Gribanov, V. A. Shchelkunov, Y. V. Nelyubina, *Acta Crystallogr. E* **2005**, *61*, i285.
[65] S. Engel, E. C. J. Gießelmann, L. Schumacher, Y. Zhang, F. Müller, O. Janka, *Dalton Trans.* **2024**, *53*, 12176.
[66] F. Stegemann, T. Block, S. Klenner, Y. Zhang, B. P. T. Fokwa, C. Doerenkamp, H. Eckert, O. Janka, *Eur. J. Inorg. Chem.* **2021**, *2021*, 3832.
[67] B. Hatt, *Acta Crystallogr.* **1961**, *14*, 119.

[68] N. Pavlyuk, I. Chumak, V. Pavlyuk, H. Ehrenberg, S. Indris, V. Hlukhyy, R. Pöttgen, *Z. Naturforsch. B* **2022**, *77*, 727.
[69] N. Pavlyuk, G. Dmytriv, V. Pavlyuk, I. Chumak, S. Indris, H. Ehrenberg, *J. Phase Equilib. Diffus.* **2022**, *43*, 458.
[70] A. F. Deutz, R. B. Helmholdt, A. C. Moleman, D. B. De Mooij, K. H. J. Buschow, *J. Less-Common Met.* **1989**, *153*, 259.
[71] R. Cywinski, S. H. Kilcoyne, C. A. Scott, *J. Phys.: Condens. Matter* **1991**, *3*, 6473.
[72] A. C. Lawson, J. L. Smith, J. O. Willis, J. A. O'Rourke, J. Faber, R. L. Hitterman, *J. Less-Common Met.* **1985**, *107*, 243.
[73] O. Osters, T. Nilges, M. Schöneich, P. Schmidt, J. Rothballer, F. Pielnhofer, R. Weihrich, *Inorg. Chem.* **2012**, *51*, 8119.
[74] F. Eustermann, F. Stegemann, M. Radzieowski, O. Janka, *Inorg. Chem.* **2019**, *58*, 16211.
[75] S. Seidel, R. Pöttgen, *Z. Anorg. Allg. Chem.* **2017**, *643*, 261.
[76] R. Horyń, *J. Less-Common Met.* **1977**, *56*, 103.
[77] A. Provino, D. Paudyal, M. L. Fornasini, I. Dhiman, S. K. Dhar, A. Das, Y. Mudryk, P. Manfrinetti, V. K. Pecharsky, *Acta Mater.* **2013**, *61*, 2236.
[78] E. I. Gladyshevskii, P. I. Krypyakevych, M. Y. Teslyuk, *Dokl. Akad. Nauk. SSSR* **1952**, *85*, 81.
[79] V. I. Zaremba, V. M. Baranyak, Y. M. Kalychak, *Visn. Lviv. Derzh. Univ., Ser. Khim.* **1984**, *25*, 18.
[80] I. Felner, *Solid State Commun.* **1977**, *21*, 267.
[81] A. E. Dwight, *J. Less-Common Met.* **1975**, *43*, 117.
[82] T. Takeshita, S. K. Malik, W. E. Wallace, *J. Solid State Chem.* **1978**, *23*, 225.
[83] V. Keimes, A. Mewis, *Z. Naturforsch. B* **1992**, *47*, 1351.
[84] F. C. Frank, J. S. Kasper, *Acta Crystallogr.* **1959**, *12*, 483.
[85] F. C. Frank, J. S. Kasper, *Acta Crystallogr.* **1958**, *11*, 184.
[86] S. Samson, *Acta Crystallogr.* **1965**, *19*, 401.
[87] M. Feuerbacher, C. Thomas, J. P. A. Makongo, S. Hoffmann, W. Carrillo-Cabrera, R. Cardoso, Y. Grin, G. Kreiner, J. M. Joubert, T. Schenk, J. Gastaldi, H. Nguyen-Thi, N. Mangelinck-Noël, B. Billia, P. Donnadieu, A. Czyrska-Filemonowicz, A. Zielinska-Lipiec, B. Dubiel, T. Weber, P. Schaub, G. Krauss, V. Gramlich, J. Christensen, S. Lidin, D. Fredrickson, M. Mihalkovic, W. Sikora, J. Malinowski, S. Brühne, T. Proffen, W. Assmus, M. de Boissieu, F. Bley, J. L. Chemin, J. Schreuer, W. Steurer, *Z. Kristallogr.* **2007**, *222*, 259.
[88] C. G. Wilson, D. K. Thomas, F. J. Spooner, *Acta Crystallogr.* **1960**, *13*, 56.
[89] H. Boller, H. Nowotny, A. Wittmann, *Monatsh. Chem.* **1960**, *91*, 1174.
[90] H. Arnfelt, A. Westgren, *Jernkontorets Ann.* **1935**, *119*, 185.
[91] C. R. Hunt, A. Raman, *Mater. Res. Bull.* **1968**, *3*, 489.
[92] P. Kripyakevich, E. Gladyshevskii, E. Pylaeva, *Kristallografiya* **1962**, *7*, 212.
[93] Y. V. Verbovytsky, *Chem. Met. Alloys* **2012**, *5*, 142.
[94] J. Braun, M. Ellner, *J. Alloys Compd.* **2000**, *309*, 118.
[95] C. Suryanarayana, S. K. Tiwari, T. R. Anantharaman, *Int. J. Mater. Res.* **1978**, *69*, 155.
[96] G. Nagorsen, H. Posch, H. Schäfer, A. Weiss, *Z. Naturforsch. B* **1969**, *24*, 1191.
[97] S. Amerioun, T. Yokosawa, S. Lidin, U. Häussermann, *Inorg. Chem.* **2004**, *43*, 4751.
[98] O. Pecher, B. Mausolf, V. Peters, K. Lamberts, A. Korthaus, F. Haarmann, *Chem. Eur. J.* **2016**, *22*, 17833.
[99] H. Nowotny, H. Wesenberg, *Z. Metallkd.* **1939**, *31*, 363.
[100] J. H. N. Van Vucht, K. H. J. Buschow, *Philips Res. Rep.* **1964**, *19*, 319.
[101] K. R. Andress, E. Alberti, *Z. Metallkd.* **1935**, *27*, 126.
[102] G. J. Miller, F. Li, H. F. Franzen, *J. Am. Chem. Soc.* **1993**, *115*, 3739.

[103] A. H. Gomes de Mesquita, K. H. J. Buschow, *Acta Crystallogr.* **1967**, *22*, 497.
[104] C. H. Johansson, J. O. Linde, *Ann. Phys.* **1925**, *78*, 439.
[105] D. A. Edwards, W. E. Wallace, R. S. Craig, *J. Am. Chem. Soc.* **1952**, *74*, 5256.
[106] Y. Ma, C. Rømming, B. Lebech, J. Gjønnes, J. Taftø, *Acta Crystallogr. B* **1992**, *48*, 11.
[107] G. Brauer, *Naturwissenschaften* **1938**, *26*, 710.
[108] O. Schob, E. Parthé, *Acta Crystallogr.* **1965**, *19*, 214.
[109] C. Bècle, R. Lemaire, *Acta Crystallogr.* **1967**, *23*, 840.
[110] M. B. Manyako, I. V. Rozhdestvenskaya, O. S. Zarechnyuk, T. I. Yanson, *Kristallografiya* **1985**, *30*, 484.
[111] J. V. Florio, R. E. Rundle, A. I. Snow, *Acta Crystallogr.* **1952**, *5*, 449.
[112] P. I. Krypyakevych, O. S. Zarechnyuk, *Dopov. Akad. Nauk Ukr. RSR, Ser. A* **1968**, *238*, 364.
[113] S. Niemann, W. Jeitschko, *Z. Metallkd.* **1994**, *85*, 345.
[114] R. Pöttgen, O. Janka, *Rev. Inorg. Chem.* **2023**, *43*, 357.
[115] S. Samson, *Acta Crystallogr.* **1961**, *14*, 1229.
[116] S. Samson, *Acta Crystallogr.* **1958**, *11*, 851.
[117] Y. Grin, I. S. Gavrilenko, V. Y. Markyiv, Y. P. Yarmolyuk, *Dopov. Akad. Nauk Ukr. RSR, Ser. A:* **1980**, *8*, 73.
[118] H. K. Fun, H. C. Lin, T. J. Lee, B. C. Yip, *Acta Crystallogr. C* **1994**, *50*, 661.
[119] Q. Luo, Q.-F. Gu, J.-Y. Zhang, S.-L. Chen, K.-C. Chou, Q. Li, *Sci. Rep.* **2015**, *5*, 15385.
[120] V. M. T. Thiede, W. Jeitschko, S. Niemann, T. Ebel, *J. Alloys Compd.* **1998**, *267*, 23.
[121] M. L. Fornasini, A. Palenzona, *J. Less-Common Met.* **1976**, *45*, 137.
[122] Y. N. Hryn, P. Rogl, *Visn. Lviv. Derzh. Univ., Ser. Khim.* **1986**, *27*, 38.
[123] G. Cordier, E. Czech, H. Ochmann, H. Schäfer, *J. Less-Common Met.* **1984**, *99*, 173.
[124] V. M. T. Thiede, W. Jeitschko, *Z. Naturforsch. B* **1998**, *53*, 673.
[125] E. Ganglberger, H. Nowotny, F. Benesovsky, *Monatsh. Chem.* **1965**, *96*, 1658.
[126] O. Kurylo, Y. V. Verbovytsky, O. R. Myakush, I. V. Koval'chuck, B. Y. Kotur, *Visn. Lviv. Derzh. Univ., Ser. Khim.* **2009**, *20*, 126.
[127] A. Raman, *Int. J. Mater. Res.* **1966**, *57*, 535.
[128] V. Y. Markyiv, N. N. Bjelyavyina, *Dopov. Akad. Nauk. Ukr. RSR, Ser. B* **1986**, *4*, 43.
[129] Y. P. Yarmolyuk, J. Loub, E. I. Gladyshevskii, *Dopov. Akad. Nauk Ukr. RSR, Ser. A* **1973**, *10*, 943.
[130] M. C. J. Marker, H. S. Effenberger, K. W. Richter, *Solid State Sci.* **2009**, *11*, 1475.
[131] A. V. Morozkin, *J. Alloys Compd.* **1999**, *289*, 10.
[132] M. M. Koza, A. Leithe-Jasper, E. Sischka, W. Schnelle, H. Borrmann, H. Mutka, Y. Grin, *Phys. Chem. Chem. Phys.* **2014**, *16*, 27119.
[133] B. Y. Kotur, *Inorg. Mater.* **1987**, *23*, 493.
[134] H. W. S. Arachchige, W. R. Meier, M. Marshall, T. Matsuoka, R. Xue, M. A. McGuire, R. P. Hermann, H. Cao, D. Mandrus, *Phys. Rev. Lett.* **2022**, *129*, 216402.
[135] S. Niemann, W. Jeitschko, *J. Solid State Chem.* **1995**, *114*, 337.
[136] S. Niemann, W. Jeitschko, *J. Solid State Chem.* **1995**, *116*, 131.
[137] G. H. Meier, F. S. Pettit, *Mater. Sci. Eng. A* **1992**, *153*, 548.
[138] A. Rahmel, M. Schütze, W. J. Quadakkers, *Mater. Corros.* **1995**, *46*, 271.
[139] M. Steinhorst, H. J. Grabke, *Mater. Sci. Eng. A* **1989**, *120-121*, 55.
[140] G. Geramifard, C. Gombola, P. Franke, H. J. Seifert, *Corros. Sci.* **2020**, *177*, 108956.
[141] F. Appel, U. Brossmann, U. Christoph, S. Eggert, P. Janschek, U. Lorenz, J. Müllauer, M. Oehring, J. D. H. Paul, *Adv. Eng. Mater.* **2000**, *2*, 699.
[142] R. Pflumm, S. Friedle, M. Schütze, *Intermetallics* **2015**, *56*, 1.
[143] P. A. Loginov, G. M. Markov, N. V. Shvyndina, G. V. Smirnov, E. A. Levashov, *Ceramics* **2022**, *5*, 389.

[144] R. Hoppe, H.-J. Röhrborn, *Naturwissenschaften* **1961**, *48*, 453.
[145] R. Hoppe, H.-J. Röhrborn, *Z. Anorg. Allg. Chem.* **1964**, *327*, 199.
[146] R. Hoppe, *J. Solid State Chem.* **1986**, *65*, 127.
[147] H. D. Wasel-Nielen, R. Hoppe, *Z. Anorg. Allg. Chem.* **1968**, *359*, 36.
[148] P. J. Yvon, R. B. Schwarz, C. B. Pierce, L. Bernardez, A. Conners, R. Meisenheimer, *Phys. Rev. B* **1989**, *39*, 6690.
[149] B. Cogel, H. U. Schuster, *Z. Anorg. Allg. Chem.* **1993**, *619*, 1765.
[150] W. Schauerte, H. U. Schuster, N. Knauf, R. Müller, *Z. Anorg. Allg. Chem.* **1992**, *616*, 186.
[151] P. Moser, W. Jung, H. U. Schuster, *Z. Anorg. Allg. Chem.* **1997**, *623*, 1781.
[152] P. Moser, W. Jung, *Z. Anorg. Allg. Chem.* **1998**, *624*, 1251.
[153] P. Moser, H. M. Schwunck, W. Jung, *Z. Anorg. Allg. Chem.* **1998**, *624*, 1256.
[154] H. M. Schwunck, P. Moser, W. Jung, *Z. Anorg. Allg. Chem.* **1999**, *625*, 463.
[155] H. M. Schwunck, P. Moser, W. Jung, *Z. Anorg. Allg. Chem.* **1998**, *624*, 1262.
[156] H. M. Schwunck, P. Moser, W. Jung, *Z. Anorg. Allg. Chem.* **1999**, *625*, 407.
[157] P. Moser, V. Cirpus, W. Jung, *Z. Anorg. Allg. Chem.* **1999**, *625*, 714.
[158] P. Moser, W. Jung, *Z. Anorg. Allg. Chem.* **2000**, *626*, 1421.
[159] A. Panahandeh, W. Jung, *Z. Anorg. Allg. Chem.* **2003**, *629*, 1651.
[160] M. Tampier, D. Johrendt, R. Pöttgen, G. Kotzyba, H. Trill, B. D. Mosel, *Z. Anorg. Allg. Chem.* **2002**, *628*, 1243.
[161] I. Antonyshyn, O. Sichevych, K. Rasim, A. Ormeci, U. Burkhardt, S. Titlbach, S. A. Schunk, M. Armbrüster, Y. Grin, *Eur. J. Inorg. Chem.* **2018**, *2018*, 3933.
[162] J. Sappl, F. Jung, C. Hoch, *Chem. Mater.* **2020**, *32*, 866.
[163] H. Watanabe, N. Kijima, *J. Ceram. Soc. Jpn.* **2009**, *117*, 115.
[164] B. Eisenmann, M. Jakowski, W. Klee, H. Schäfer, *Rev. Chim. Miner.* **1983**, *20*, 255.
[165] B. Eisenmann, M. Jakowski, H. Schafer, *Mat. Res. Bull.* **1982**, *17*, 1169.
[166] B. Eisenmann, M. Jakowski, H. Schafer, *Rev. Chim. Miner.* **1983**, *20*, 329.
[167] W. Klee, H. Schäfer, *Z. Naturforsch. B* **1978**, *33*, 829.
[168] W. Massa, *Kristallstrukturbestimmung*, Teubner, Stuttgart, **1994**.
[169] A. R. West, *Solid State Chemistry and its Applications*, Second Edition ed., John Wiley & Sons Inc., Hoboken, USA, **2022**.
[170] H. Wondratschek, U. Müller, *International Tables for Crystallography, Volume A1: Symmetry relations between space groups, Vol. A1*, John Wiley & Sons, Chichester, Großbritannien, **2011**.
[171] H. M. Rietveld, *J. Appl. Crystallogr.* **1969**, *2*, 65.
[172] H. M. Rietveld, *Acta Crystallogr.* **1967**, *22*, 151.
[173] Bruker AXS Inc., Version 5 ed., Karlsruhe (Germany), **2014**.
[174] F. Stegemann, C. Benndorf, T. Bartsch, R. S. Touzani, M. Bartsch, H. Zacharias, B. P. T. Fokwa, H. Eckert, O. Janka, *Inorg. Chem.* **2015**, *54*, 10785.
[175] T. Hirose, Y. Okamoto, J.-i. Yamaura, Z. Hiroi, *J. Phys. Soc. Jpn.* **2015**, *84*, 113701.
[176] Bruker AXS Inc., Version 6.02; includes XPREP and SADABS ed., Madison, WI (USA), **1999**.
[177] Agilent, Agilent Technologies Ltd., Yarnton, Oxfordshire, England, **2014**.
[178] L. Palatinus, G. Chapuis, *J. Appl. Crystallogr.* **2007**, *40*, 786.
[179] V. Petříček, M. Dušek, L. Palatinus, *Z. Kristallogr.* **2014**, *229*, 345.
[180] V. Petříček, M. Dušek, L. Palatinus, Institute of Physics, Praha (Czech Republic), **2006**.
[181] G. Sheldrick, *Acta Crystallogr.* **2015**, *A71*, 3.
[182] G. Sheldrick, *Acta Crystallogr.* **2015**, *C71*, 3.
[183] G. M. Sheldrick, *Acta Crystallogr.* **2008**, *A64*, 112.
[184] C. B. Hübschle, G. M. Sheldrick, B. Dittrich, *J. Appl. Crystallogr.* **2011**, *44*, 1281.

[185] K. Brandenburg, Crystal Impact, Version 4.6.8 ed., Bonn (Germany), **2022**.
[186] D. D. Laws, H.-M. L. Bitter, A. Jerschow, *Angew. Chem. Int. Ed.* **2002**, *41*, 3096.
[187] C. Benndorf, H. Eckert, O. Janka, *Acc. Chem. Res.* **2017**, *50*, 1459.
[188] H. Eckert, R. Pöttgen, *Z. Anorg. Allg. Chem.* **2010**, *636*, 2232.
[189] H. Eckert, *Z. Naturforsch. B* **2020**, *75*, 441.
[190] L. Schaffer, D. Preiss, R. S. Palani, N. Wiesner, J. Liu, S. Strymish, S. Bahri, S. Linse, N. Gershenfeld, R. G. Griffin, *J. Magn. Reson.* **2025**, *379*, 107909.
[191] Bruker Corp., Version 2.1 ed., Karlsruhe, **2008**.
[192] D. Massiot, F. Fayon, M. Capron, I. King, S. Le Calvé, B. Alonso, J.-O. Durand, B. Bujoli, Z. Gan, G. Hoatson, *Magn. Reson. Chem.* **2002**, *40*, 70.
[193] C. C. Yuan, Y. F. Yang, X. K. Xi, J. Cui, J. F. Xiang, *Solid State Nucl. Magn. Reson.* **2012**, *41*, 28.
[194] M. Radzieowski, F. Stegemann, C. Doerenkamp, S. F. Matar, H. Eckert, C. Dosche, G. Wittstock, O. Janka, *Inorg. Chem.* **2019**, *58*, 7010.
[195] S. Engel, E. C. J. Gießelmann, R. Pöttgen, O. Janka, *Rev. Inorg. Chem.* **2023**, *43*, 571.
[196] G. K. Shenoy, F. E. Wagner, *Mössbauer Isomer Shifts*, North-Holland Publishing, Amsterdam, **1978**.
[197] P. Gütlich, *Z. Anorg. Allg. Chem.* **2012**, *638*, 15.
[198] P. Gütlich, E. Bill, A. X. Trautwein, *Mössbauer Spectroscopy and Transition Metal Chemistry*, Springer, Berlin, Heidelberg, **2011**.
[199] N. N. Greenwood, T. C. Gibb, *Mössbauer Spectroscopy*, Chapman and Hall Ltd., London, **1971**.
[200] M. Radzieowski, F. Stegemann, T. Block, J. Stahl, D. Johrendt, O. Janka, *J. Am. Chem. Soc.* **2018**, *140*, 8950.
[201] G. Güntherodt, A. Jayaraman, G. Batlogg, M. Croft, E. Melczer, *Phys. Rev. Lett.* **1983**, *51*, 2330.
[202] J. Su, C. Zhu, *Mater. Res. Bull.* **2003**, *38*, 2025.
[203] W. J. Brya, *Solid State Commun.* **1971**, *9*, 2271.
[204] L.-S. Hsu, M. A. Tischler, *Phys. Status Solidi B* **1999**, *214*, 419.
[205] Y. Zhu, X. Ouyang, F. Yin, M. Zhao, J. Lou, *Metall. Mater. Trans. A* **2018**, *49*, 1859.
[206] C. Benndorf, F. Stegemann, H. Eckert, O. Janka, *Z. Naturforsch. B* **2015**, *70*, 101.
[207] H. Lueken, *Magnetochemie*, B. G. Teubner, Stuttgart, Leipzig, **1999**.
[208] J. Jensen, A. R. Mackintosh, *Rare earth magnetism: Structures and excitations*, Clarendon Press, Oxford, **1991**.
[209] H. Endres, *Chemische Aspekte der Festkörper-Physik*, Springer Verlag, Berlin, Heidelberg, **1984**.
[210] D. van Delft, P. Kes, *Europhys. News* **2011**, *42*, 21.
[211] J. Hafner, *J. Comput. Chem.* **2008**, *29*, 2044.
[212] V. L. Deringer, J. George, R. Dronskowski, U. Englert, *Acc. Chem. Res.* **2017**, *50*, 1231.
[213] R. Dronskowski, *Chemical Bonding*, Walter de Gruyter GmbH, Berlin/Boston, **2023**.
[214] P. E. Blöchl, *Phys. Rev. B* **1994**, *50*, 17953.
[215] G. Kresse, D. Joubert, *Phys. Rev. B* **1999**, *59*, 1758.
[216] G. Kresse, J. Furthmüller, *Comput. Mater. Sci.* **1996**, *6*, 15.
[217] G. Kresse, J. Furthmüller, *Phys. Rev. B* **1996**, *54*, 11169.
[218] P. Giannozzi, O. Andreussi, T. Brumme, O. Bunau, M. Buongiorno Nardelli, M. Calandra, R. Car, C. Cavazzoni, D. Ceresoli, M. Cococcioni, N. Colonna, I. Carnimeo, A. Dal Corso, S. de Gironcoli, P. Delugas, R. A. DiStasio, A. Ferretti, A. Floris, G. Fratesi, G. Fugallo, R. Gebauer, U. Gerstmann, F. Giustino, T. Gorni, J. Jia, M. Kawamura, H. Y. Ko, A. Kokalj, E. Küçükbenli, M. Lazzeri, M. Marsili, N. Marzari, F. Mauri, N. L. Nguyen, H. V. Nguyen, A. Otero-de-la-Roza, L. Paulatto, S. Poncé, D.

Rocca, R. Sabatini, B. Santra, M. Schlipf, A. P. Seitsonen, A. Smogunov, I. Timrov, T. Thonhauser, P. Umari, N. Vast, X. Wu, S. Baroni, *J. Phys.: Condens. Matter* **2017**, *29*, 465901.
[219] F. Bloch, *Z. Phys.* **1929**, *52*, 555.
[220] H. J. Monkhorst, J. D. Pack, *Phys. Rev. B* **1976**, *13*, 5188.
[221] H. P. Beck, M. Zhou, P. Hasanovic, E. Gießelmann, M. Springborg, *J. Chem. Educ.* **2021**, *98*, 3207.
[222] A. A. Emery, C. Wolverton, *Sci. Data* **2017**, *4*, 170153.
[223] N. J. Stone, *At. Data Nucl. Data Tables* **2016**, *111–112*, 1.
[224] E. Sanville, S. D. Kenny, R. Smith, G. Henkelman, *J. Comput. Chem.* **2007**, *28*, 899.
[225] W. Tang, E. Sanville, G. Henkelman, *J. Phys.: Condens. Matter* **2009**, *21*, 084204.
[226] G. Henkelman, A. Arnaldsson, H. Jónsson, *Comput. Mater. Sci.* **2006**, *36*, 354.
[227] A. Savin, R. Nesper, S. Wengert, T. F. Fässler, *Angew. Chem.* **1997**, *109*, 1892.
[228] R. Dronskowski, P. E. Blöchl, *J. Phys. Chem.* **1993**, *97*, 8617.
[229] R. Nelson, C. Ertural, J. George, V. L. Deringer, G. Hautier, R. Dronskowski, *J. Comput. Chem.* **2020**, *41*, 1931.
[230] S. Maintz, V. L. Deringer, A. L. Tchougréeff, R. Dronskowski, *J. Comput. Chem.* **2016**, *37*, 1030.
[231] S. Maintz, V. L. Deringer, A. L. Tchougréeff, R. Dronskowski, *J. Comput. Chem.* **2013**, *34*, 2557.
[232] V. L. Deringer, A. L. Tchougréeff, R. Dronskowski, *J. Phys. Chem. A* **2011**, *115*, 5461.
[233] C. Ertural, S. Steinberg, R. Dronskowski, *RSC Adv.* **2019**, *9*, 29821.
[234] P. C. Müller, C. Ertural, J. Hempelmann, R. Dronskowski, *J. Phys. Chem. C* **2021**, *125*, 7959.
[235] R. Pöttgen, T. Gulden, A. Simon, *GIT Labor-Fachz.* **1999**, *43*, 133.
[236] R. Pöttgen, A. Lang, R.-D. Hoffmann, B. Künnen, G. Kotzyba, R. Müllmann, B. D. Mosel, C. Rosenhahn, *Z. Kristallogr.* **1999**, *214*, 143.
[237] M. Radzieowski, *Darstellung, Kristallchemie, physikalische und spektroskopische Eigenschaften intermetallischer Aluminiumverbindungen sowie bi- und ternärer Zintl-Phasen*, Dissertation, Westfälische Wilhelms-Universität Münster (Münster), **2020**.
[238] M. J. Parsons, P. J. Brown, J. Crangle, K. U. Neumann, B. Ouladdiaf, T. J. Smith, N. K. Zayer, K. R. A. Ziebeck, *J. Phys.: Condens. Matter* **1998**, *10*, 8523.
[239] D. F. Barros, C. Nabil, J. C. P. d. Santos, D. A. Abreu, C. S. Barros, V. M. Silveira, C. A. Nunes, G. C. Coelho, *Calphad* **2024**, *84*, 102663.
[240] E. C. J. Gießelmann, S. Engel, J. Baldauf, J. Kösters, S. F. Matar, G. Kickelbick, O. Janka, *Inorg. Chem.* **2024**, *63*, 8180.
[241] E. C. J. Gießelmann, L. Ruck, S. Engel, B. Morgenstern, L. Schumacher, G. Kickelbick, O. Janka, *Z. Anorg. Allg. Chem.* **2025**, *651*, e202500044.
[242] M. A. Fedorova, V. V. Byrnashova, E. M. Sokolovskaya, P. I. Krypyakevych, *Tezizy Dokl. Vses. Konf. Kristallokhim. Intermet. Soeden.* **1974**, *2*, 18.
[243] K. Schubert, T. R. Anantharaman, H. O. K. Ata, H. G. Meissner, M. Pötzschke, W. Rossteutscher, E. Stolz, *Naturwissenschaften* **1960**, *47*, 512.
[244] Y. Verbovytskyy, *J. Alloys Compd.* **2016**, *666*, 440.
[245] G. Brauer, *Z. Anorg. Allg. Chem.* **1939**, *242*, 1.
[246] A. W. Hull, *Phys. Rev.* **1917**, *10*, 661.
[247] H. Müller, K. Weymann, *J. Less-Common Met.* **1986**, *119*, 115.
[248] H. Oesterreicher, W. E. Wallace, *J. Less-Common Met.* **1967**, *13*, 91.
[249] H. Oesterreicher, *J. Less-Common Met.* **1971**, *25*, 341.
[250] J. H. Wernick, S. Geller, *Trans. Metall. Soc. AIME* **1960**, *218*, 866.
[251] K. H. J. Buschow, R. P. van Stapele, *J. Appl. Phys.* **1970**, *41*, 4066.

[252] M. Mansmann, W. E. Wallace, *J. Chem. Phys.* **1964**, *40*, 1167.
[253] E. W. Lee, J. F. D. Montenegro, *J. Magn. Magn. Mater.* **1981**, *22*, 282.
[254] A. T. Tyvanchuk, T. I. Yanson, B. Y. Kotur, O. S. Zarechnyuk, M. L. Kharakterova, *Russ. Metal.* **1988**, *4*, 190.
[255] K. Remschnig, T. Le Bihan, H. Noel, P. Rogl, *J. Solid State Chem.* **1992**, *97*, 391.
[256] C. Kranenberg, A. Mewis, *Z. Anorg. Allg. Chem.* **2000**, *626*, 1448.
[257] T. I. Yanson, O. S. Zarechnyuk, *Visn. Lviv. Derzh. Univ., Ser. Khim.* **1984**, *25*, 11.
[258] A. M. Cardinale, D. Macciò, A. Saccone, *J. Therm. Anal. Calorim.* **2012**, *108*, 817.
[259] M. J. Kangas, D. C. Schmitt, A. Sakai, S. Nakatsuji, J. Y. Chan, *J. Solid State Chem.* **2012**, *196*, 274.
[260] E. C. J. Gießelmann, S. Engel, W. Kostusiak, Y. Zhang, P. Herbeck-Engel, G. Kickelbick, O. Janka, *Dalton Trans.* **2023**, *52*, 3391.
[261] E. C. J. Gießelmann, S. Engel, S. Pohl, M. Briesenick, L. P. Rüthing, C. Kloos, A. Koldemir, L. Schumacher, J. Wiethölter, J. Schmedt auf der Günne, G. Kickelbick, O. Janka, *Chem. Mater.* **2024**, *37*, 97.
[262] T. Shishido, S. Nojima, M. Tanaka, H. Horiuchi, T. Fukuda, *J. Alloys Compd.* **1995**, *227*, 175.
[263] S. Geller, V. B. Bala, *Acta Crystallogr.* **1956**, *9*, 1019.
[264] C. de Rango, G. Tsoucaris, C. Zelwer, *Acta Crystallogr.* **1966**, *20*, 590.
[265] S. Geller, E. A. Wood, *Acta Crystallogr.* **1956**, *9*, 563.
[266] P. Radhakrishna, J. Hammann, M. Ocio, P. Pari, Y. Allain, *Solid State Commun.* **1981**, *37*, 813.
[267] N. L. Ross, J. Zhao, R. J. Angel, *J. Solid State Chem.* **2004**, *177*, 3768.
[268] H. S. Yoder, M. L. Keith, *Am. Mineral.* **1951**, *36*, 519.
[269] F. Euler, J. A. Bruce, *Acta Crystallogr.* **1965**, *19*, 971.
[270] A. Nakatsuka, A. Yoshiasa, T. Yamanaka, *Acta Crystallogr. B* **1999**, *55*, 266.
[271] W. O. Milligan, L. W. Vernon, H. A. Levy, S. W. Peterson, *J. Phys. Chem.* **1953**, *57*, 535.
[272] L. Pauling, S. B. Hendricks, *J. Am. Chem. Soc.* **1925**, *47*, 781.
[273] G. J. Lehr, D. T. Morelli, *Intermetallics* **2013**, *32*, 225.
[274] A. F. Reid, A. E. Ringwood, *J. Geophys. Res.* **1975**, *80*, 3363.
[275] H. Lehnert, H. Boysen, P. Dreier, Y. Yu, *Z. Kristallogr.* **2000**, *215*, 145.
[276] M. G. Paton, E. N. Maslen, *Acta Crystallogr.* **1965**, *19*, 307.
[277] G. Will, *Aust. J. Phys.* **1988**, *41*, 283.
[278] K. Tezuka, Y. Tokuhara, M. Wakeshima, Y. J. Shan, H. Imoto, Y. Hinatsu, *Inorg. Chem.* **2013**, *52*, 12972.
[279] Y. Pelovsky, V. Raynova, I. Gruncharov, I. Dombalov, *J. Therm. Anal.* **1991**, *37*, 841.
[280] C. D. Brandle, H. Steinfink, *Inorg. Chem.* **1969**, *8*, 1320.
[281] M. L. Fornasini, G. Bruzzone, *J. Less-Common Met.* **1975**, *40*, 335.
[282] S. Engel, E. C. J. Gießelmann, L. E. Schank, G. Heymann, K. Brix, R. Kautenburger, H. P. Beck, O. Janka, *Inorg. Chem.* **2023**, *62*, 4260.
[283] G. Bruzzone, F. Merlo, *J. Less-Common Met.* **1975**, *39*, 1.
[284] D. K. Das, D. T. Pitman, *JOM* **1957**, *9*, 1175.
[285] J. Zhao, X. Zhang, H. Liu, Y. Xiao, H. Jiang, J. Zhang, *Cryst. Res. Technol.* **2018**, *53*, 1700201.
[286] X. Zhang, Q. Feng, J. Zhao, H. Liu, J. Li, Y. Xiao, F. Li, Q. Lu, *Curr. Appl. Phys.* **2020**, *20*, 96.
[287] J. A. Alonso, I. Rasines, J. L. Soubeyroux, *Inorg. Chem.* **1990**, *29*, 4768.
[288] B. C. Chakoumakos, G. A. Lager, J. A. Fernandez-Baca, *Acta Crystallogr. C* **1992**, *48*, 414.

[289] P. Sehrawat, Dayawati, P. Boora, R. K. Malik, S. P. Khatkar, V. B. Taxak, *Ceram. Int.* **2021**, *47*, 5432.
[290] A.-R. Schulze, H. Müller-Buschbaum, *Z. Anorg. Allg. Chem.* **1981**, *475*, 205.
[291] J. Li, E. A. Medina, J. K. Stalick, A. W. Sleight, M. A. Subramanian, *Z. Naturforsch. B* **2016**, *71*, 475.
[292] J. Terada, *J. Phys. Soc. Jpn.* **1953**, *8*, 158.
[293] W. Hörkner, H. Müller-Buschbaum, *Z. Anorg. Allg. Chem.* **1979**, *451*, 40.
[294] R. H. Arlett, J. G. White, M. Robbins, *Acta Crystallogr.* **1967**, *22*, 315.
[295] P. A. Franken, A. E. Hill, C. W. Peters, G. Weinreich, *Phys. Rev. Lett.* **1961**, *7*, 118.
[296] E. Boyko, L. G. Wisnyl, *Acta Crystallogr.* **1958**, *11*, 444.
[297] M. Capron, A. Douy, *J. Am. Ceram. Soc.* **2002**, *85*, 3036.
[298] M. Allix, S. Alahrache, F. Fayon, M. Suchomel, F. Porcher, T. Cardinal, G. Matzen, *Adv. Mater.* **2012**, *24*, 5570.
[299] W. Büssem, *Z. Kristallogr.* **1936**, *95*, 175.
[300] H. Bartl, T. Scheller, *Neues Jahrb. Mineral., Monatsh.* **1970**, 547.
[301] T. Sakakura, K. Tanaka, Y. Takenaka, S. Matsuishi, H. Hosono, S. Kishimoto, *Acta Crystallogr B* **2011**, *67*, 193.
[302] W. Hörkner, H. Müller-Buschbaum, *J. Inorg. Nucl. Chem.* **1976**, *38*, 983.
[303] E. Aruja, *Acta Crystallogr.* **1957**, *10*, 337.
[304] D. Mei, J. Jiang, F. Liang, S. Zhang, Y. Wu, C. Sun, D. Xue, Z. Lin, *J. Mater. Chem. C* **2018**, *6*, 2684.
[305] P. C. Donohue, *J. Solid State Chem.* **1970**, *2*, 6.
[306] K.-J. Range, H.-J. Hübner, *Z. Naturforsch. B* **1973**, *28*, 353.
[307] H. Schäfer, G. Schäfer, A. Weiss, *Z. Anorg. Allg. Chem.* **1963**, *325*, 77.
[308] H. Haeuseler, A. Cansiz, H. D. Lutz, *Z. Naturforsch. B* **1981**, *36*, 532.
[309] P. C. Donohue, J. E. Hanlon, *J. Electrochem. Soc.* **1974**, *121*, 137.
[310] O. Gorochov, V. V. Tien, N. H. Dung, E. Barthelemey, J. Flahaut, *Colloq. Int. Centre Natl. Rech. Sci.* **1970**, *2*, 157.
[311] A. Byström, K.-A. Wilhelmi, O. Brotzen, *Acta Chem. Scand.* **1950**, *4*, 1119.
[312] C. E. Curtis, L. M. Doney, J. R. Johnson, *J. Am. Ceram. Soc.* **1954**, *37*, 458.
[313] Y. Yamamura, A. Horikoshi, S. Yasuzuka, H. Saitoh, K. Saito, *Dalton Trans* **2011**, *40*, 2242.
[314] Q.-J. Hong, S. V. Ushakov, D. Kapush, C. J. Benmore, R. J. K. Weber, A. van de Walle, A. Navrotsky, *Sci. Rep.* **2018**, *8*, 14962.

8 Appendix

8.1 The first ternary ordered compound in the system Zr-V-Al adopting the $YbMo_2Al_4$ structure type

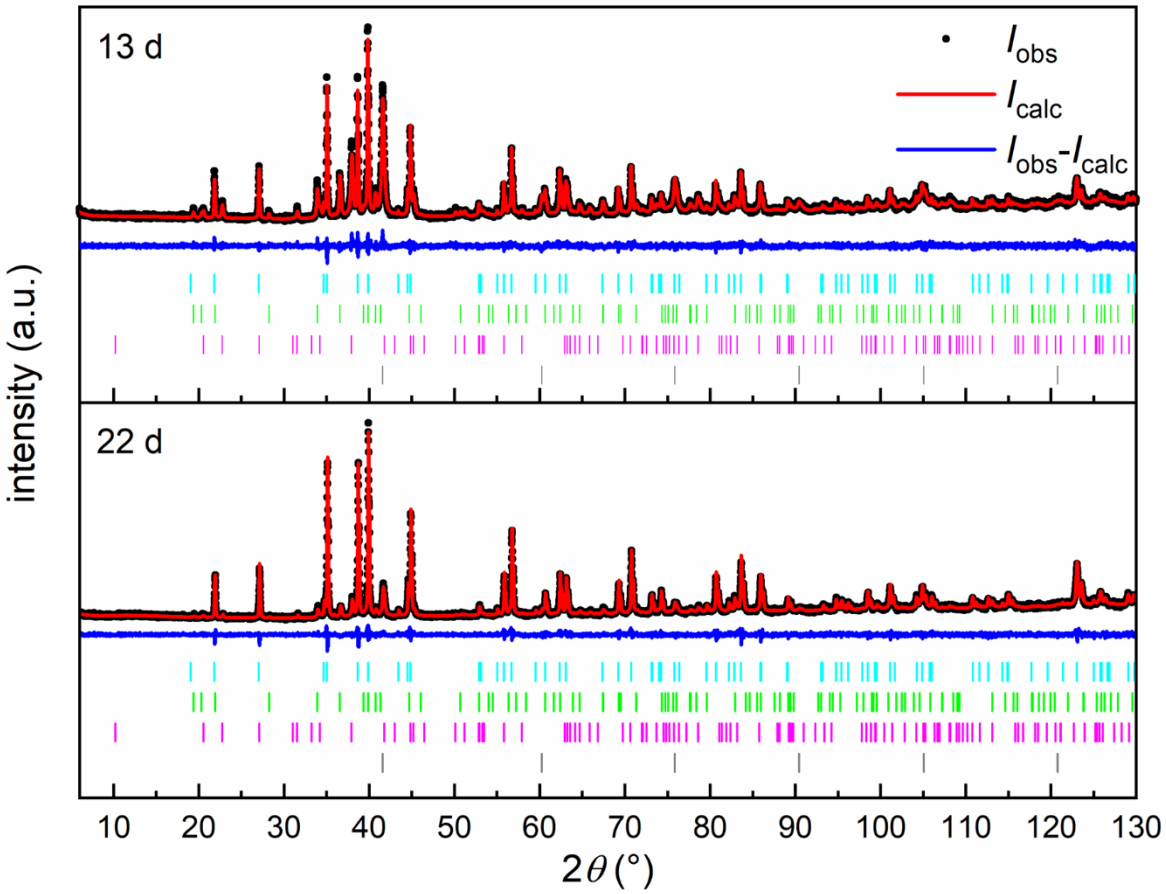

Figure S1. Powder X-ray diffraction pattern of the sample with the nominal composition ZrV_2Al_4 after arc-melting and subsequent annealing at 1073 K for (*top*) 13 and (*bottom*) 22 days followed by quenching. Experimental data is shown as black dots, simulated diffraction patterns from refinements as red lines, the difference is shown as continuous blue lines. Bragg positions are shown as cyan (ZrV_2Al_4, space group *I*4/*mmm*, (*top*) 44(1) mass%, (*bottom*) 82(1) mass%), green ($MgZn_2$ type $Zr(V_{1-x}Al_x)_2$, space group $P6_3/mmc$, (*top*) 16(1) mass%, (*bottom*) 6(1) mass%), pink ($ZrAl_3$, space group *I*4/*mmm*, (*top*) 18(1) mass%, (*bottom*) 5(1) mass%) and dark grey (elemental V, space group $Im\bar{3}m$, (*top*) 22(1) mass%, (*bottom*) 7(1) mass%) ticks.

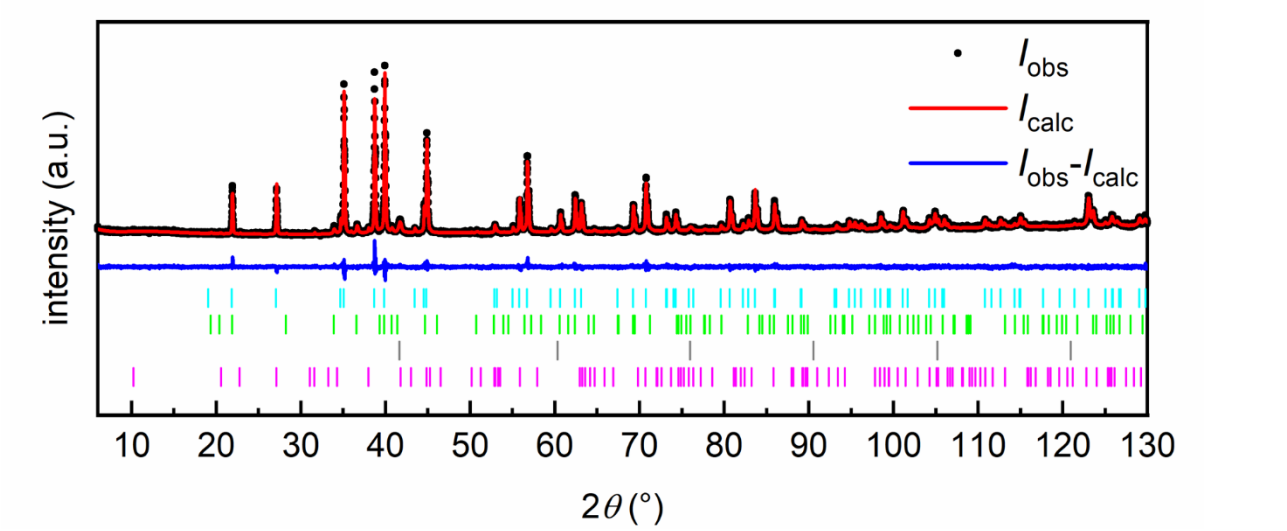

Figure S2. Powder X-ray diffraction pattern with nominal composition ZrV_2Al_4 after arc-melting and subsequent annealing at 1123 K for 39 d followed by slowly cooling the sample. Experimental data is shown as black dots, simulated diffraction patterns from refinements as red lines, the difference is shown as continuous blue lines. Bragg positions are shown as cyan (ZrV_2Al_4, space group *I*4/*mmm*, 89(1) mass%), green ($MgZn_2$ type $Zr(V_{1-x}Al_x)_2$, space group $P6_3/mmc$, 6(1) mass%), dark grey (elemental V, space group $Im\bar{3}m$, 4(1) mass%) and pink ($ZrAl_3$, space group *I*4/*mmm*, 1(1) mass%) ticks.

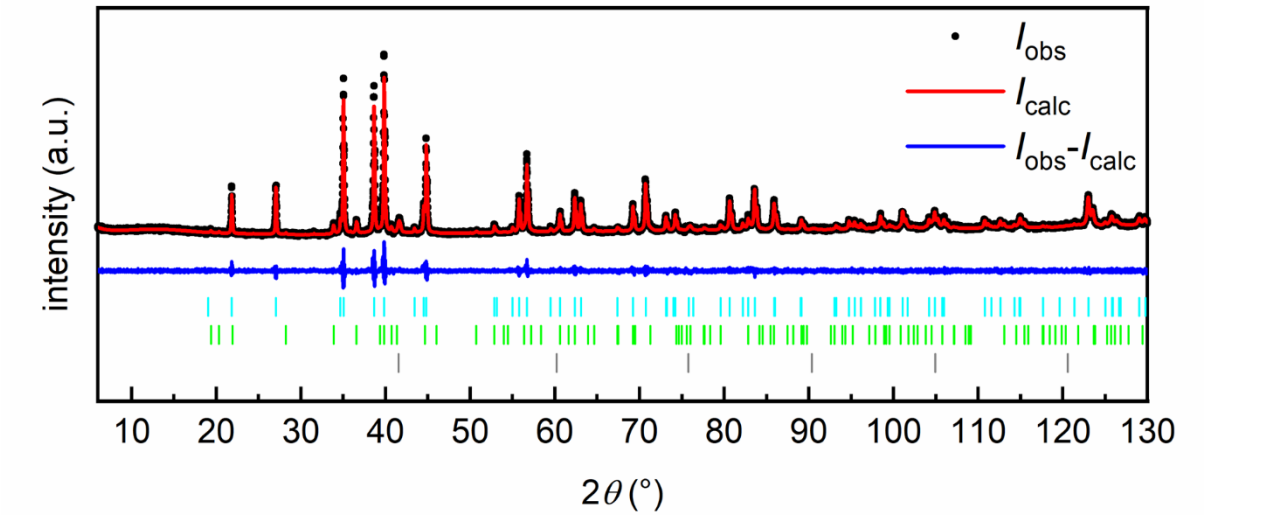

Figure S3. Powder X-ray diffraction pattern with nominal composition ZrV_2Al_4 after arc-melting and subsequent annealing at 1123 K for 39 d followed by quenching in liquid nitrogen. Experimental data is shown as black dots, simulated diffraction patterns from refinements as red lines, the difference is shown as continuous blue lines. Bragg positions are shown as cyan (ZrV_2Al_4, space group *I*4/*mmm*, 89(1) mass%), green ($MgZn_2$ type $Zr(V_{1-x}Al_x)_2$, space group $P6_3/mmc$, 7(1) mass%) and dark grey (elemental V, space group $Im\bar{3}m$, 4(1) mass%) ticks.

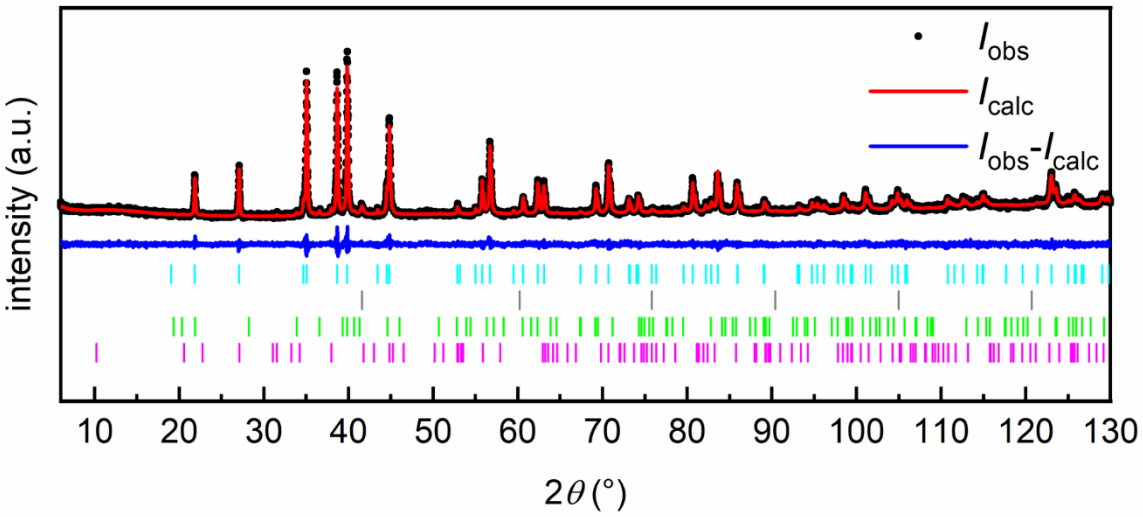

Figure S4. Powder X-ray diffraction pattern with nominal composition ZrV_2Al_4 after arc-melting and subsequent annealing at 1173 K for 39 d followed by slowly cooling the sample. Experimental data is shown as black dots, simulated diffraction patterns from refinements as red lines, the difference is shown as continuous blue lines. Bragg positions are shown as cyan (ZrV_2Al_4, space group *I*4/*mmm*, 94(1) mass%), green ($MgZn_2$ type $Zr(V_{1-x}Al_x)_2$, space group $P6_3/mmc$, 2(1) mass%), dark grey (elemental V, space group $Im\bar{3}m$, 3(1) mass%) and pink ($ZrAl_3$, space group *I*4/*mmm*, 1(1) mass%) ticks.

8.2 Synthesis and magnetic characterization of the solid solution $Gd(Fe_{1-x}Al_x)_2$

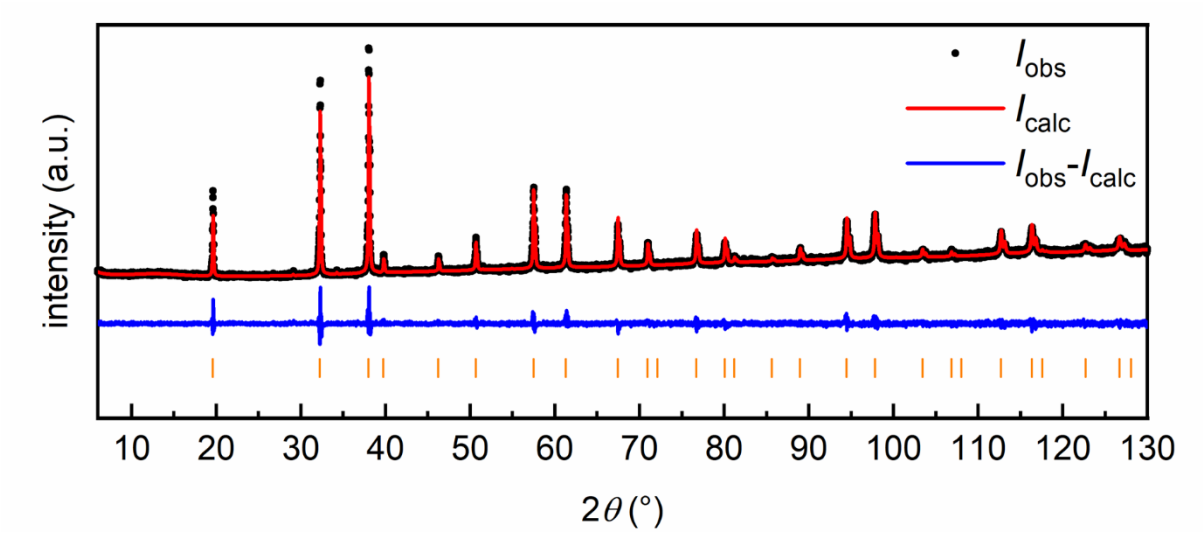

Figure S5. Powder X-ray diffraction pattern of nominal $Gd(Fe_{0.125}Al_{0.875})_2$ annealed at 1123 K. Experimental data is shown as black dots, simulated diffraction patterns from refinements as red line, the difference is shown as continuous blue line. Bragg positions are shown as orange ($MgCu_2$ type $Gd(Fe_{1-x}Al_x)_2$, space group $Fd\bar{3}m$) ticks.

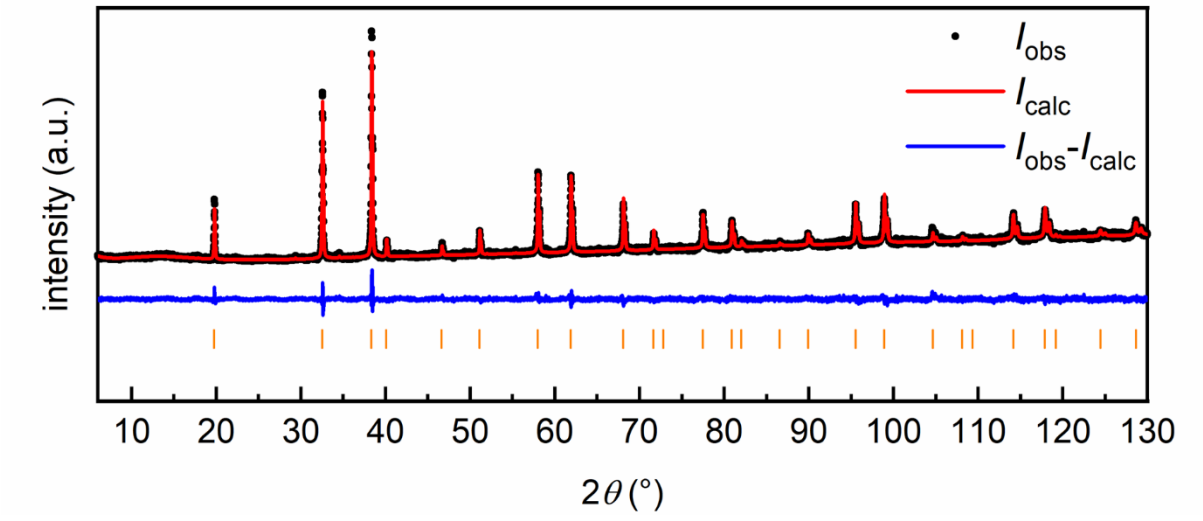

Figure S6. Powder X-ray diffraction pattern of nominal $Gd(Fe_{0.25}Al_{0.75})_2$ annealed at 1123 K. Experimental data is shown as black dots, simulated diffraction patterns from refinements as red lines, the difference is shown as continuous blue lines, and the Bragg positions are shown as orange ($MgCu_2$ type $Gd(Fe_{1-x}Al_x)_2$, space group $Fd\bar{3}m$) ticks.

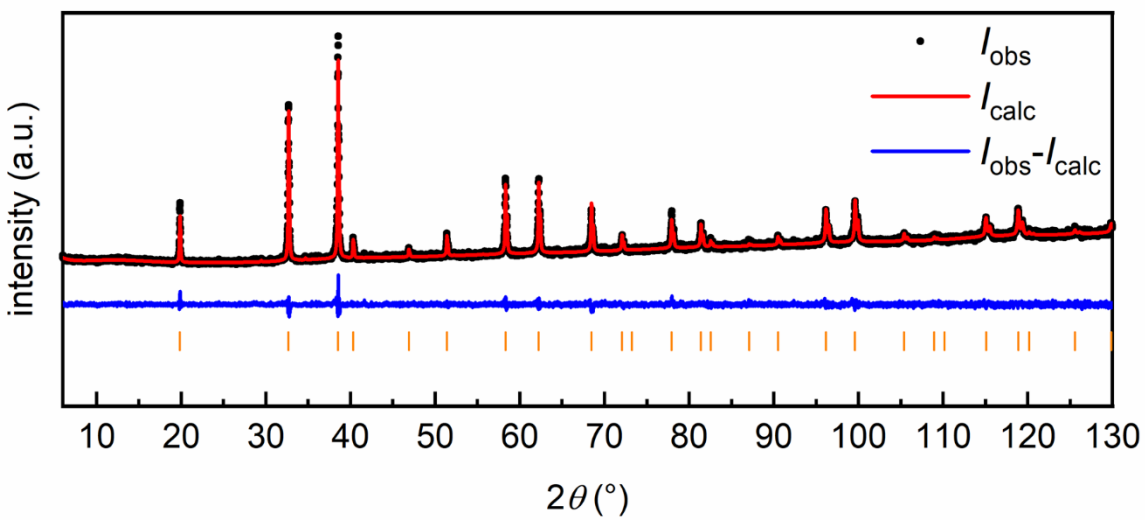

Figure S7. Powder X-ray diffraction pattern of nominal $Gd(Fe_{0.33}Al_{0.67})_2$ annealed at 1123 K. Experimental data is shown as black dots, simulated diffraction patterns from refinements as red lines, the difference is shown as continuous blue lines. Bragg positions are shown as orange ($MgCu_2$ type $Gd(Fe_{1-x}Al_x)_2$, space group $Fd\bar{3}m$) ticks.

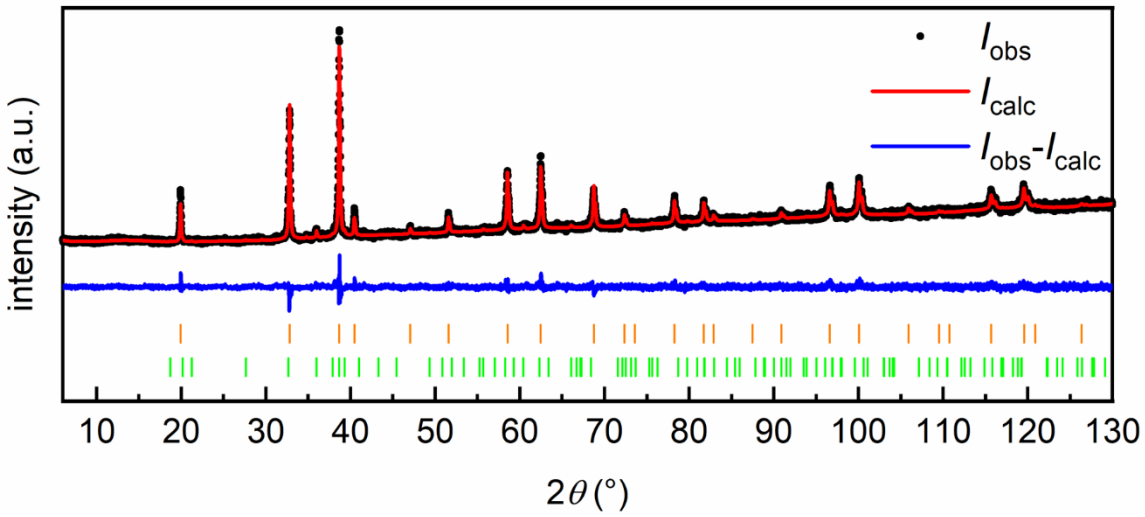

Figure S8. Powder X-ray diffraction pattern of nominal $Gd(Fe_{0.4}Al_{0.6})_2$ annealed at 1123 K. Experimental data is shown as black dots, simulated diffraction patterns from refinements as red lines, the difference is shown as continuous blue lines. Bragg positions are shown as orange ($MgCu_2$ type $Gd(Fe_{1-x}Al_x)_2$, space group $Fd\bar{3}m$) and green ($MgZn_2$ type $Gd(Fe_{1-x}Al_x)_2$, space group $P6_3/mmc$) ticks. The refined mass% are given in Table 14.

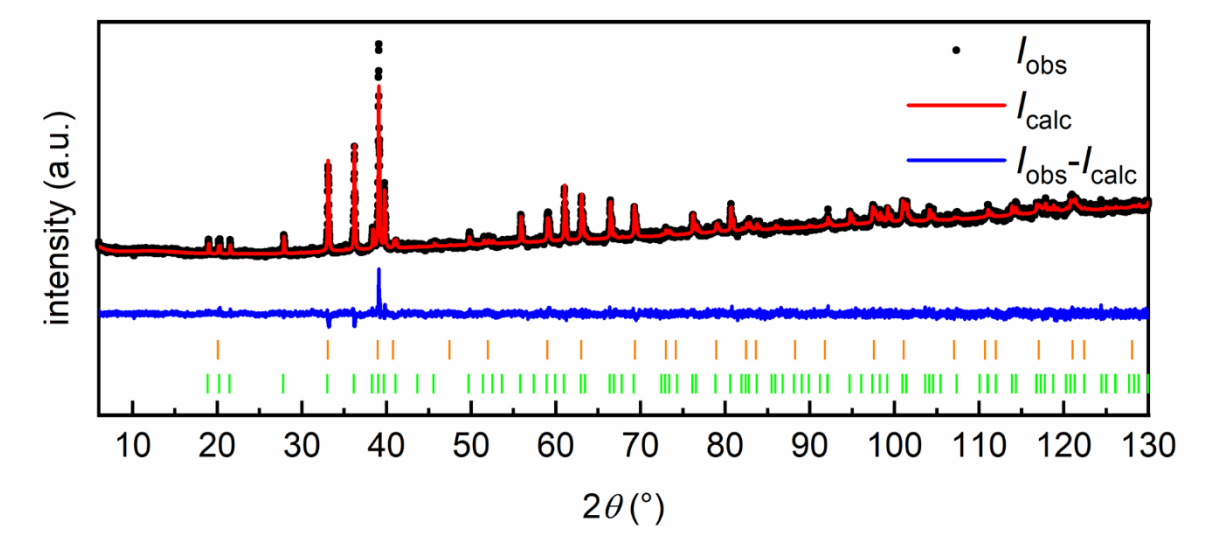

Figure S9. Powder X-ray diffraction pattern of nominal $Gd(Fe_{0.5}Al_{0.5})_2$ annealed at 1123 K. Experimental data is shown as black dots, simulated diffraction patterns from refinements as red lines, the difference is shown as continuous blue line. Bragg positions are shown as orange ($MgCu_2$ type $Gd(Fe_{1-x}Al_x)_2$, space group $Fd\bar{3}m$) and green ($MgZn_2$ type $Gd(Fe_{1-x}Al_x)_2$, space group $P6_3/mmc$) ticks. The refined mass% are given in Table 14.

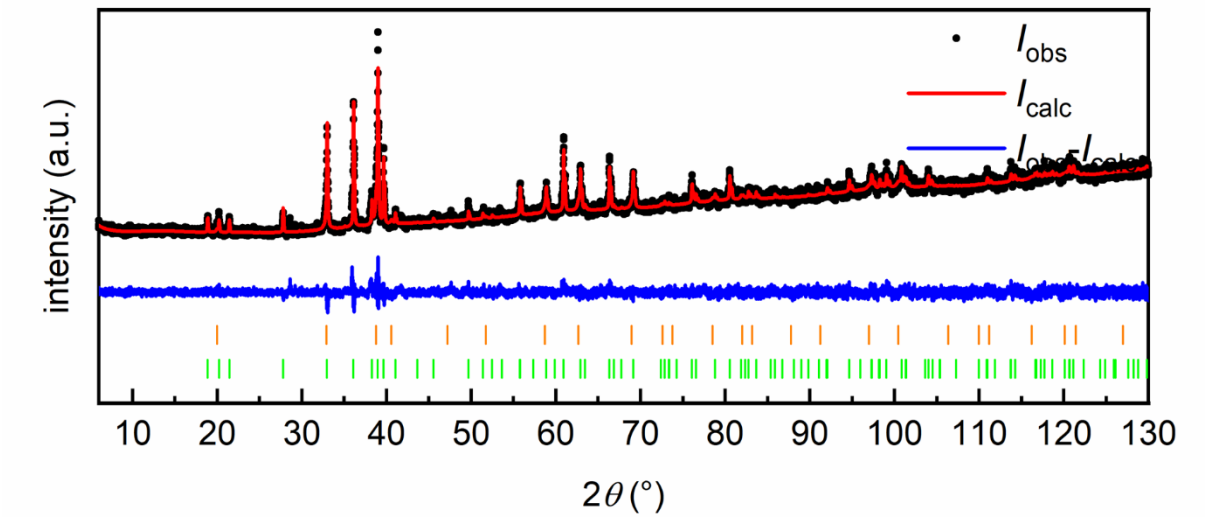

Figure S10. Powder X-ray diffraction pattern of nominal $Gd(Fe_{0.5}Al_{0.5})_2$ annealed at 1273 K. Experimental data is shown as black dots, simulated diffraction patterns from refinements as red lines, the difference is shown as continuous blue line. Bragg positions are shown as orange ($MgCu_2$ type $Gd(Fe_{1-x}Al_x)_2$, space group $Fd\bar{3}m$) and green ($MgZn_2$ type $Gd(Fe_{1-x}Al_x)_2$, space group $P6_3/mmc$) ticks. The refined mass% are given in Table 14.

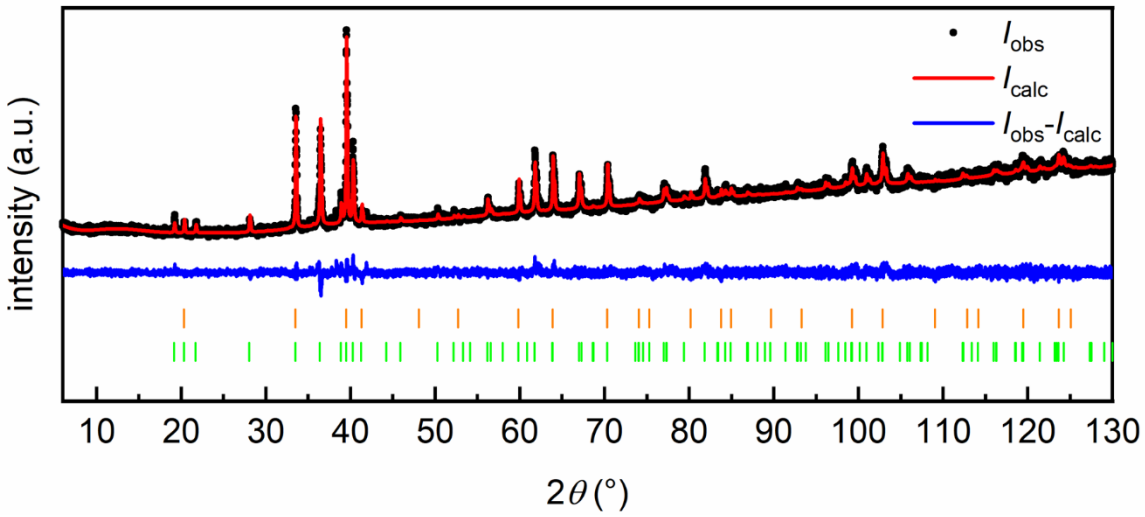

Figure S11. Powder X-ray diffraction pattern of nominal $Gd(Fe_{0.67}Al_{0.33})_2$ annealed at 1123 K. Experimental data is shown as black dots, simulated diffraction patterns from refinements as red lines, the difference is shown as continuous blue line. Bragg positions are shown as orange ($MgCu_2$ type $Gd(Fe_{1-x}Al_x)_2$, space group $Fd\bar{3}m$) and green ($MgZn_2$ type $Gd(Fe_{1-x}Al_x)_2$, space group $P6_3/mmc$) ticks. The refined mass% are given in Table 14.

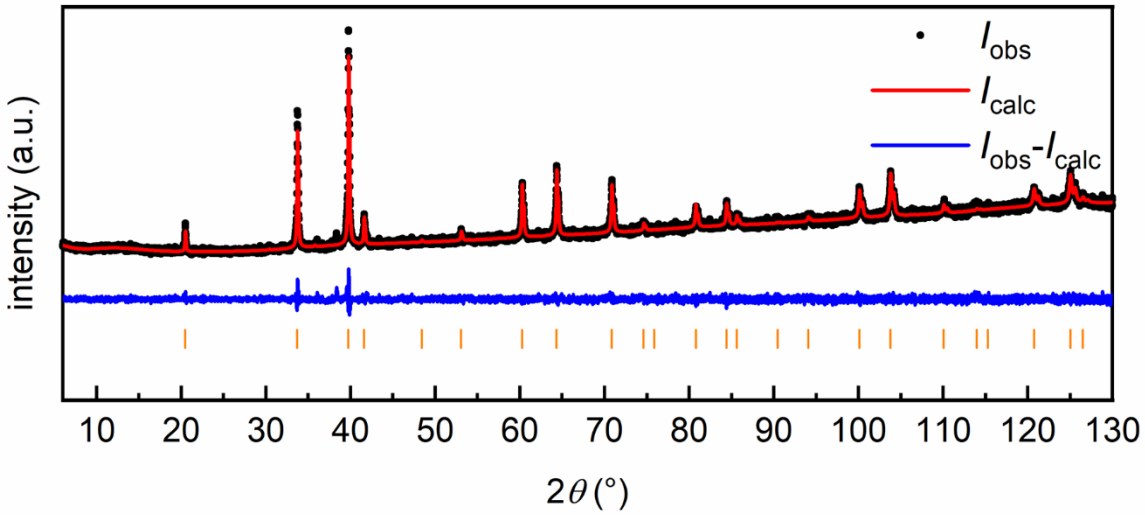

Figure S12. Powder X-ray diffraction pattern of nominal $Gd(Fe_{0.75}Al_{0.25})_2$ annealed at 1123 K. Experimental data is shown as black dots, simulated diffraction patterns from refinements as red lines, the difference is shown as continuous blue lines. Bragg positions are shown as orange ($MgCu_2$ type $Gd(Fe_{1-x}Al_x)_2$, space group $Fd\bar{3}m$) ticks.

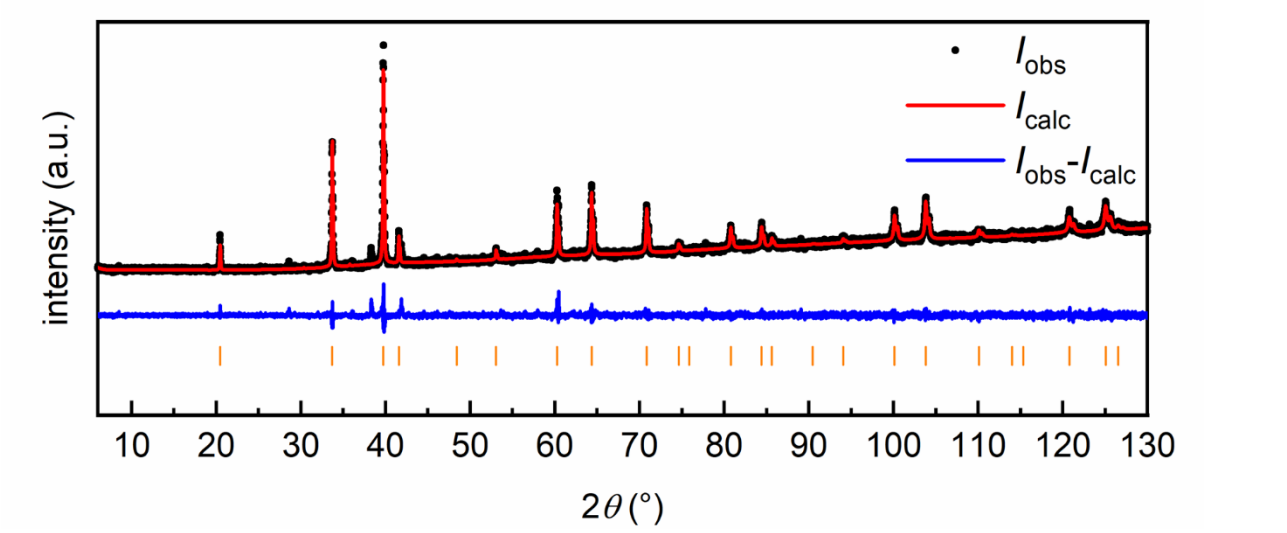

Figure S13. Powder X-ray diffraction pattern of nominal $Gd(Fe_{0.75}Al_{0.25})_2$ annealed at 1273 K. Experimental data is shown as black dots, simulated diffraction patterns from refinements as red lines, the difference is shown as continuous blue line. Bragg positions are shown as orange ($MgCu_2$ type $Gd(Fe_{1-x}Al_x)_2$, space group $Fd\bar{3}m$) ticks.

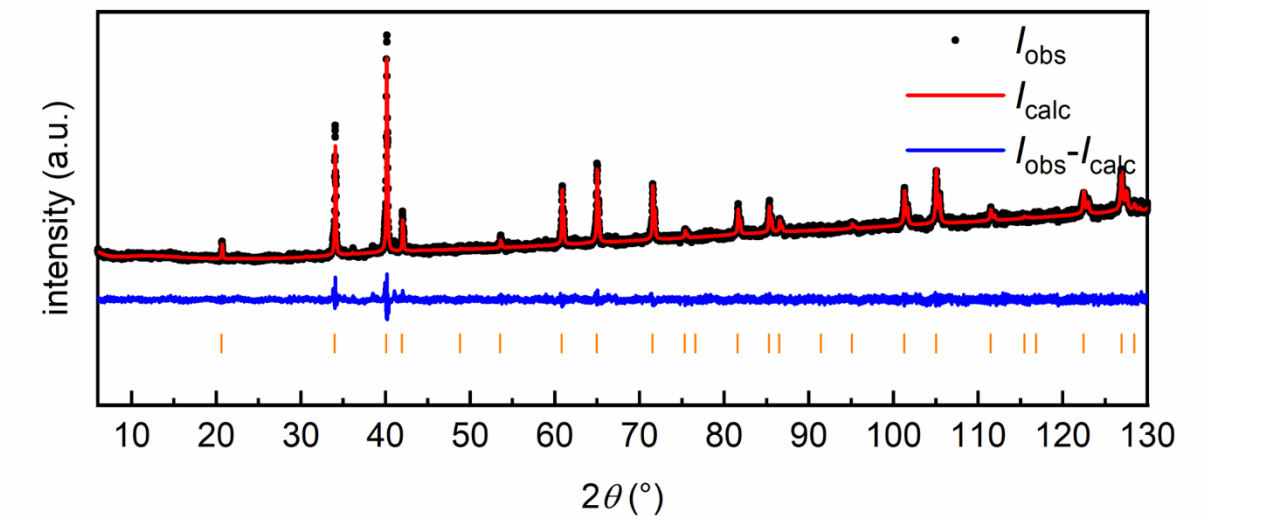

Figure S14. Powder X-ray diffraction pattern of nominal $Gd(Fe_{0.875}Al_{0.125})_2$ annealed at 1123 K. Experimental data is shown as black dots, simulated diffraction patterns from refinements as red lines, the difference is shown as continuous blue line. Bragg positions are shown as orange ($MgCu_2$ type $Gd(Fe_{1-x}Al_x)_2$, space group $Fd\bar{3}m$) ticks.

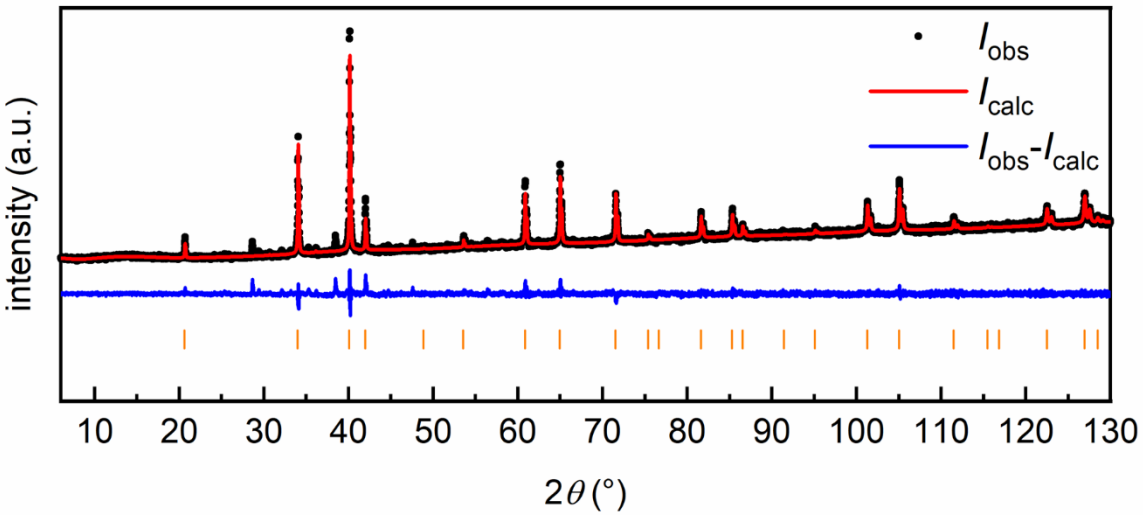

Figure S15. Powder X-ray diffraction pattern of nominal $Gd(Fe_{0.875}Al_{0.125})_2$ annealed at 1273 K. Experimental data is shown as black dots, simulated diffraction patterns from refinements as red lines, the difference is shown as continuous blue line. Bragg positions are shown as orange ($MgCu_2$ type $Gd(Fe_{1-x}Al_x)_2$, space group $Fd\bar{3}m$) ticks.

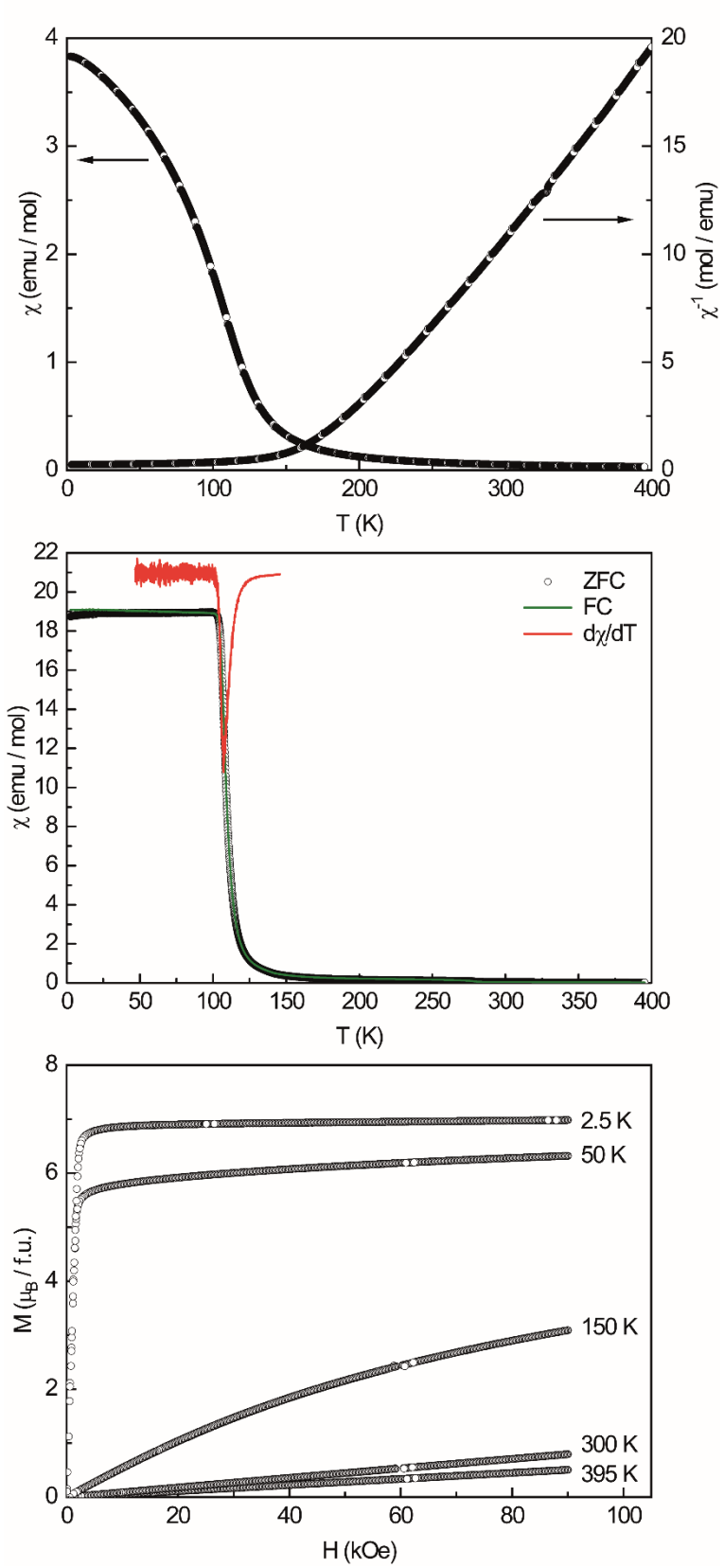

Figure S16. Magnetic data of nominal $Gd(Fe_{0.125}Al_{0.875})_2$. (*top*) Temperature dependence of the magnetic and inverse magnetic susceptibility (χ and $\chi-1$ data) measured with an applied external field of 10 kOe; (*middle*) zero-field-cooled/field-cooled (ZFC/FC) measurements measured with an applied external field of 100 Oe; (*bottom*) magnetization isotherms recorded at 2.5, 50, 150, 300 and 395 K.

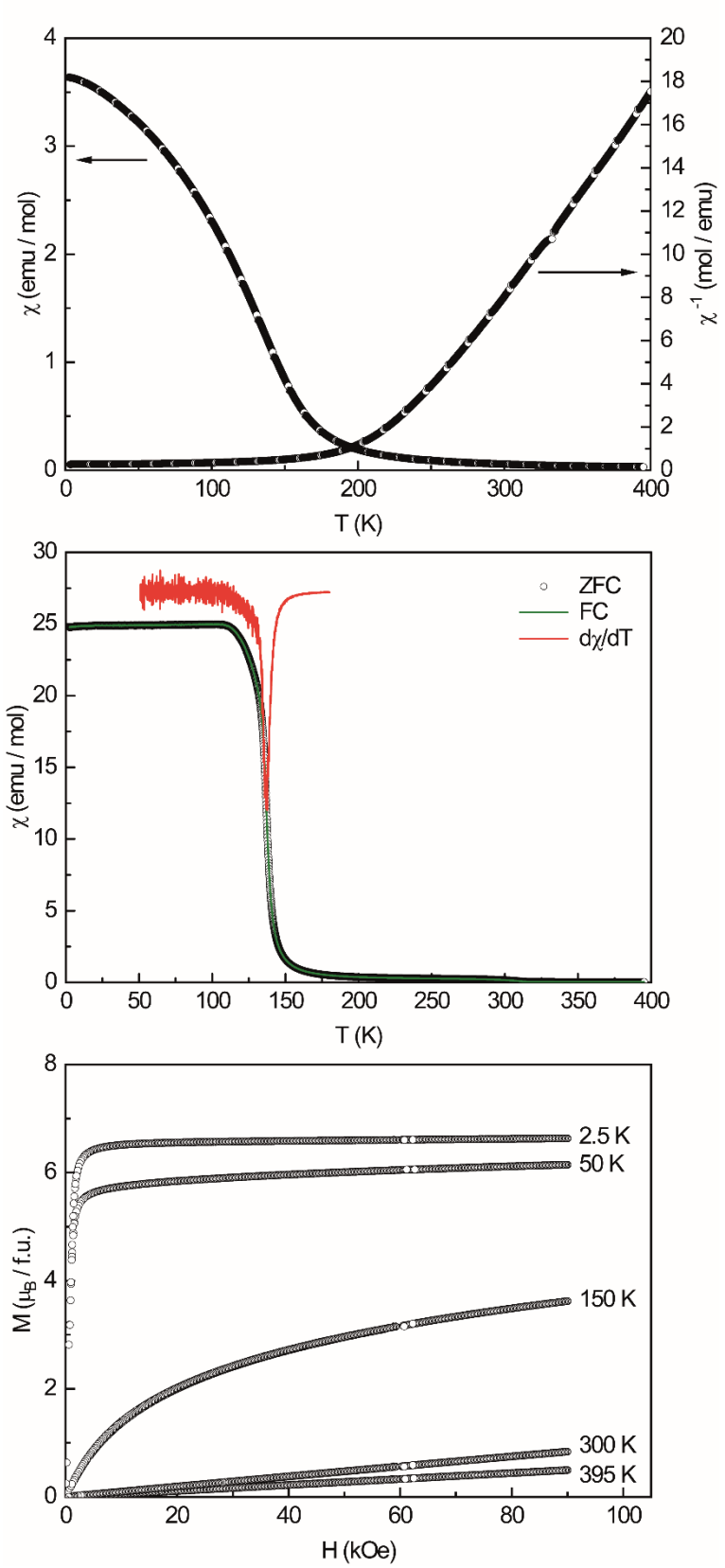

Figure S17. Magnetic data of nominal $Gd(Fe_{0.25}Al_{0.75})_2$. (*top*) Temperature dependence of the magnetic and inverse magnetic susceptibility (χ and $\chi-1$ data) measured with an applied external field of 10 kOe; (*middle*) zero-field-cooled/field-cooled (ZFC/FC) measurements measured with an applied external field of 100 Oe; (*bottom*) magnetization isotherms recorded at 2.5, 50, 150, 300 and 395 K.

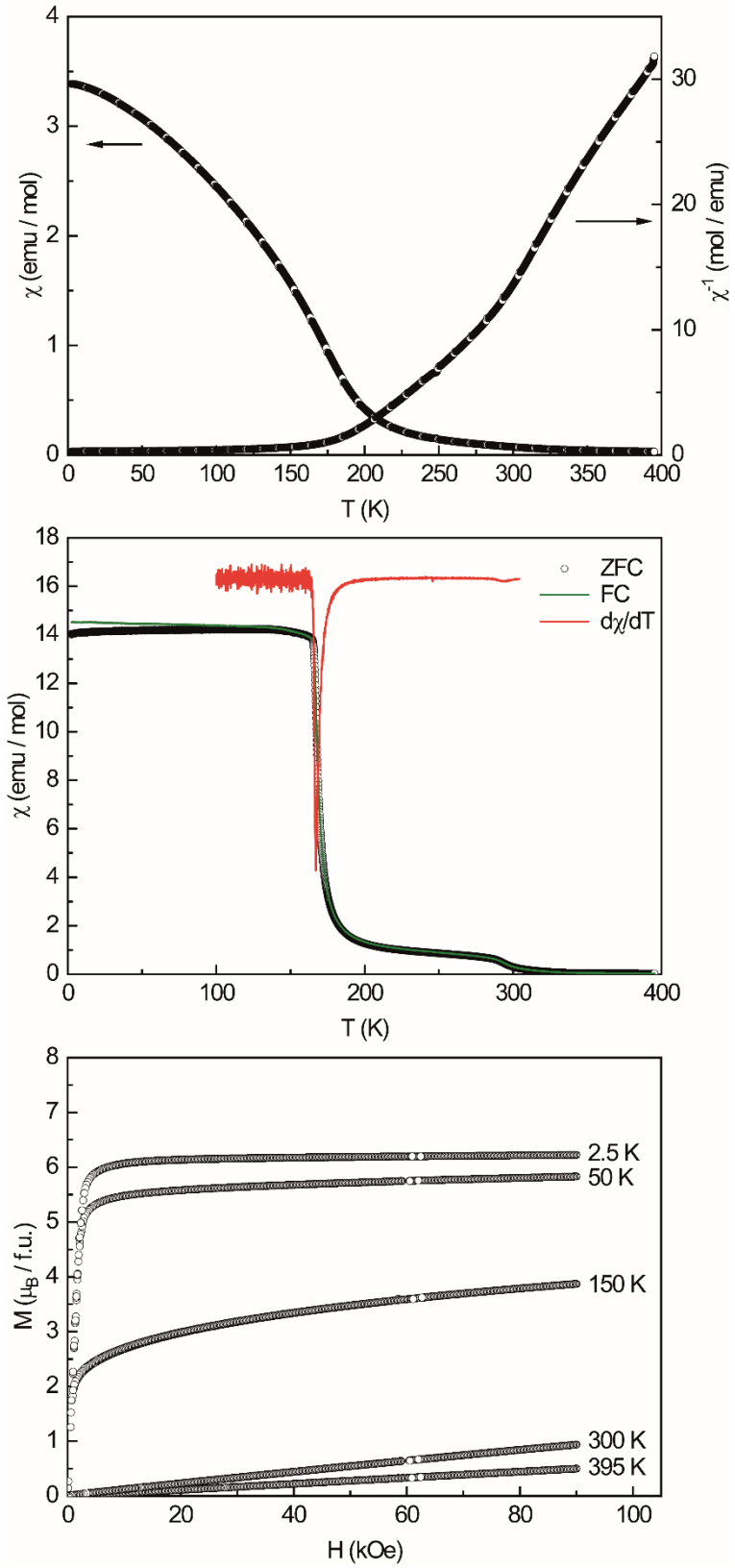

Figure S18. Magnetic data of nominal $Gd(Fe_{0.33}Al_{0.67})_2$. (*top*) Temperature dependence of the magnetic and inverse magnetic susceptibility (χ and χ−1 data) measured with an applied external field of 10 kOe; (*middle*) zero-field-cooled/field-cooled (ZFC/FC) measurements measured with an applied external field of 100 Oe; (*bottom*) magnetization isotherms recorded at 2.5, 50, 150, 300 and 395 K.

8.3 Differences in the oxidation behavior of the cubic rare earth Laves phases REAl$_2$ (RE = Sc, Y, La, Eu, Yb)

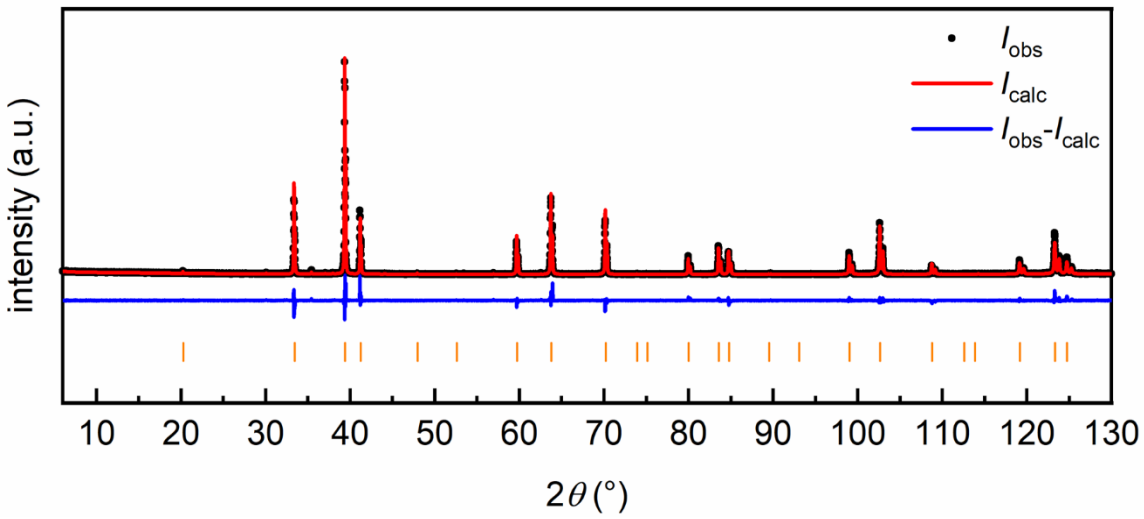

Figure S19. Powder X-ray diffraction pattern of ScAl$_2$. Experimental data is shown as black dots, simulated diffraction patterns from refinements as red lines, the difference is shown as continuous blue lines. Bragg positions are shown as orange (ScAl$_2$, space group $Fd\bar{3}m$) ticks.

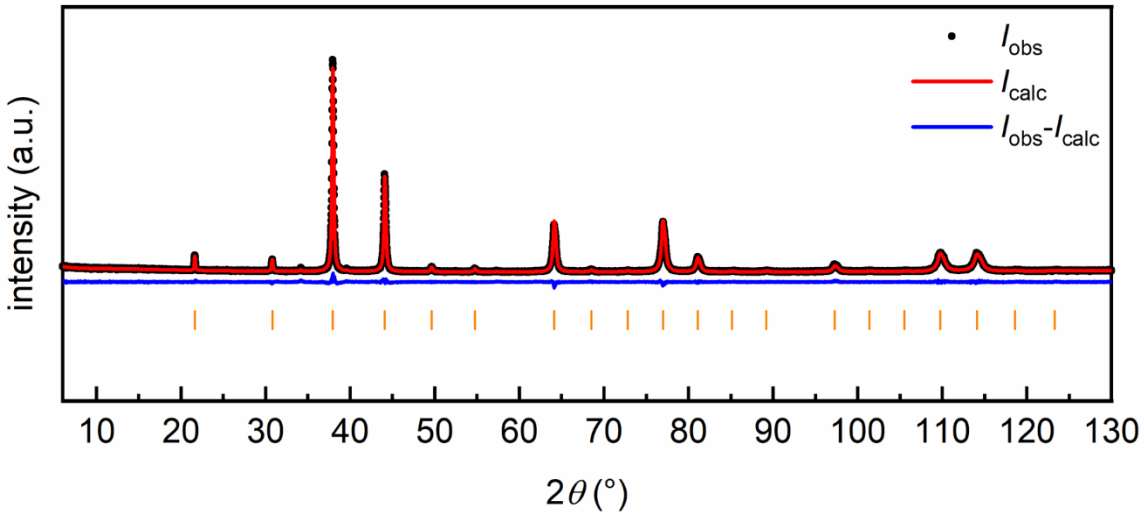

Figure S20. Powder X-ray diffraction pattern of ScAl$_3$. Experimental data is shown as black dots, simulated diffraction patterns from refinements as red lines, the difference is shown as continuous blue lines. Bragg positions are shown as orange (ScAl$_3$, space group $Fm\bar{3}m$) ticks.

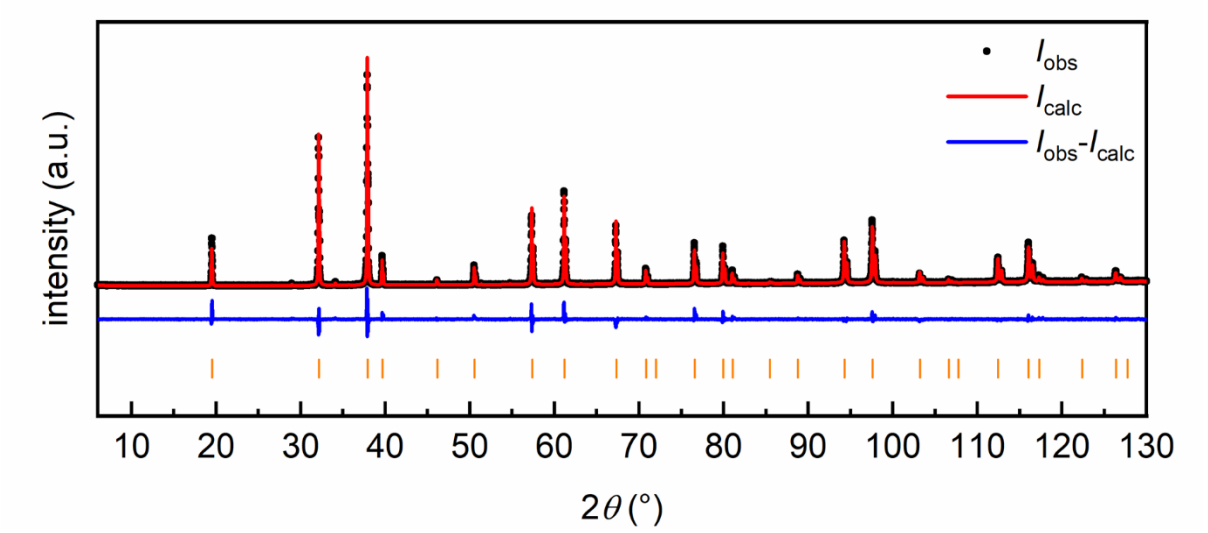

Figure S21. Powder X-ray diffraction pattern of YAl_2. Experimental data is shown as black dots, simulated diffraction patterns from refinements as red lines, the difference is shown as continuous blue lines. Bragg positions are shown as orange (YAl_2, space group $Fd\bar{3}m$) ticks.

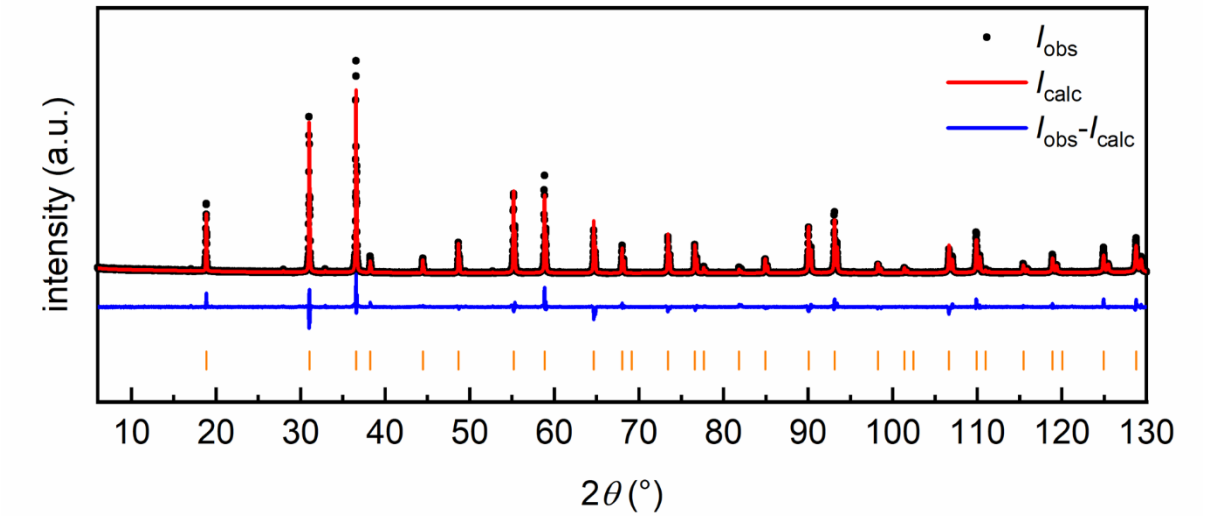

Figure S22. Powder X-ray diffraction pattern of $LaAl_2$. Experimental data is shown as black dots, simulated diffraction patterns from refinements as red lines, the difference is shown as continuous blue line. Bragg positions are shown as orange ($LaAl_2$, space group $Fd\bar{3}m$) ticks.

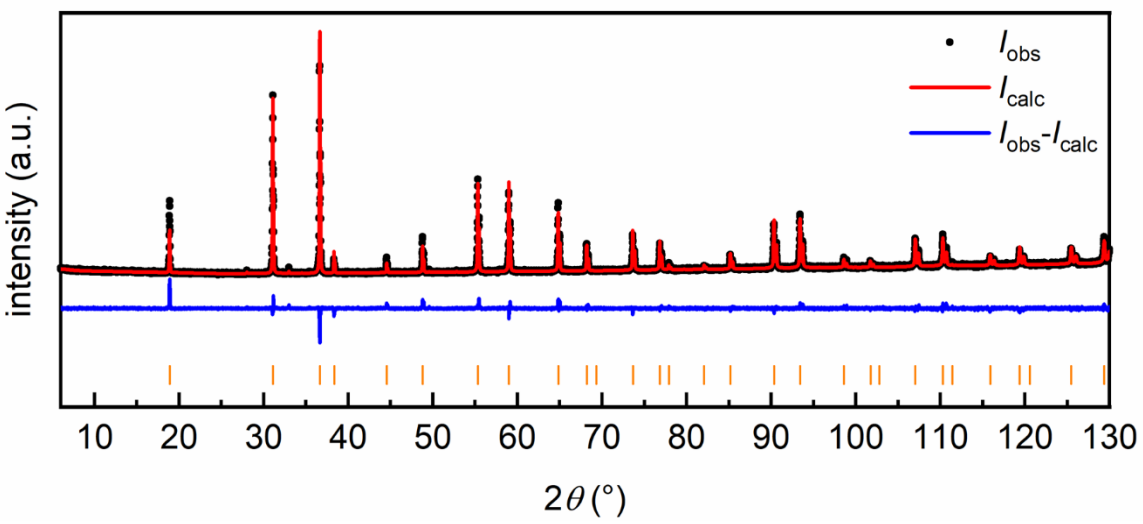

Figure S23. Powder X-ray diffraction pattern of $EuAl_2$. Experimental data is shown as black dots, simulated diffraction patterns from refinements as red lines, the difference is shown as continuous blue line. Bragg positions are shown as orange ($EuAl_2$, space group $Fd\bar{3}m$) ticks.

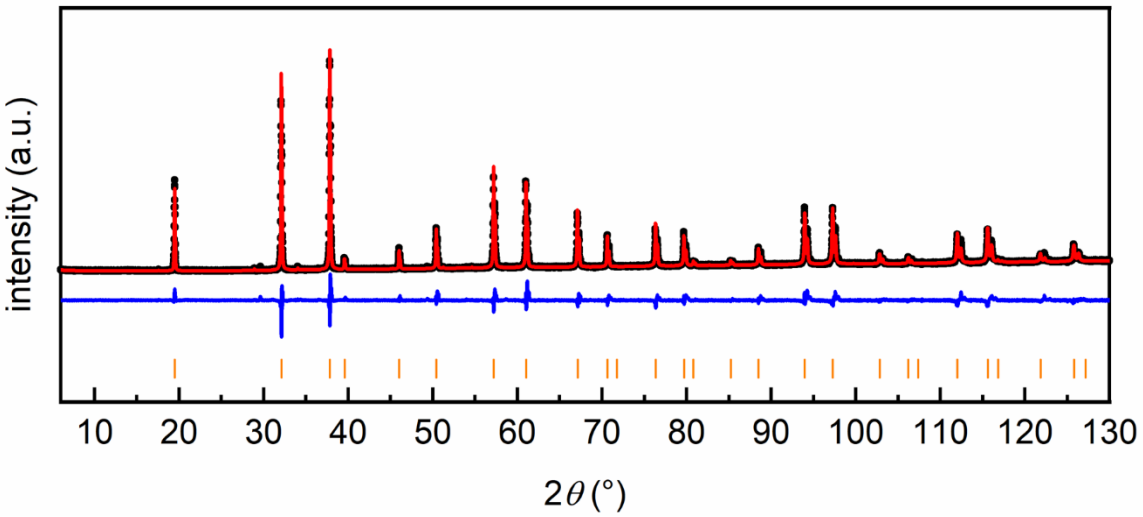

Figure S24. Powder X-ray diffraction pattern of $YbAl_2$. Experimental data is shown as black dots, simulated diffraction patterns from refinements as red lines, the difference is shown as continuous blue lines Bragg positions are shown as orange ($YbAl_2$, space group $Fd\bar{3}m$) ticks.

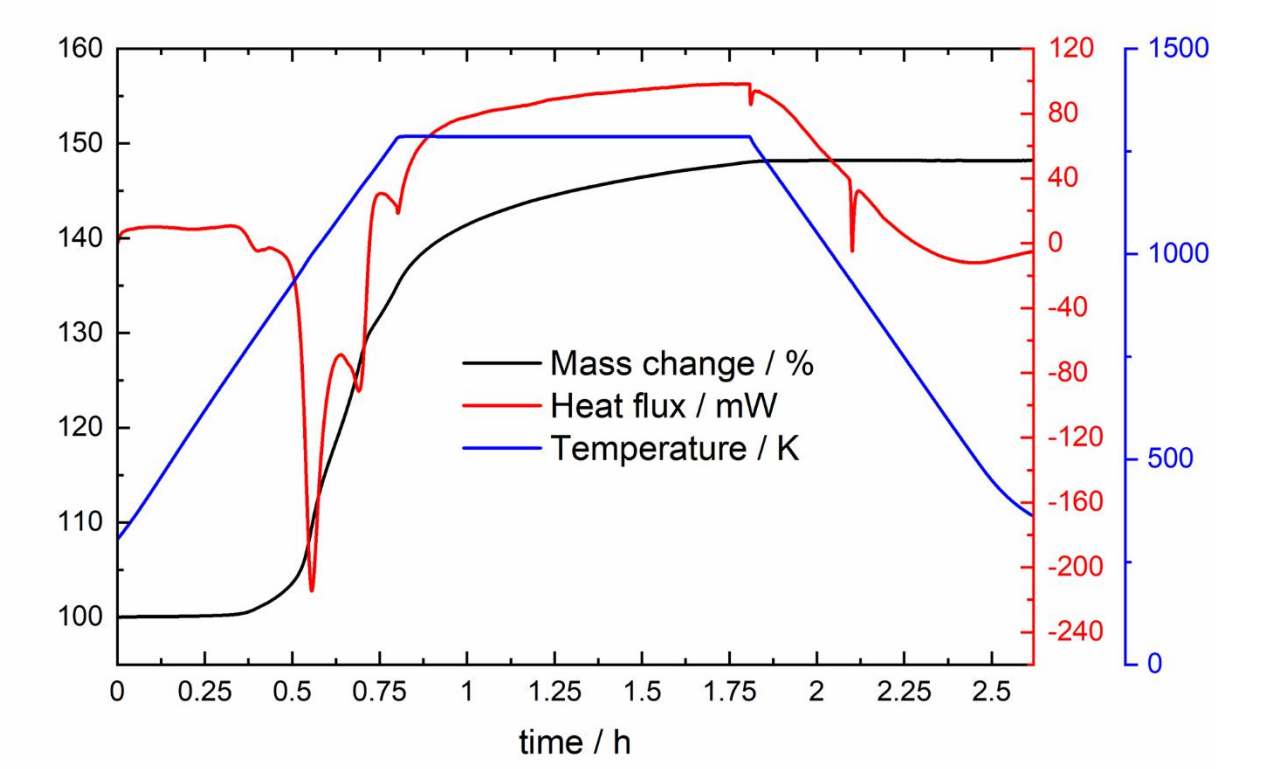

Figure S25. STA experiment for the oxidation reaction of $ScAl_2$ (mass change in black, heat flux in red and temperature program in blue).

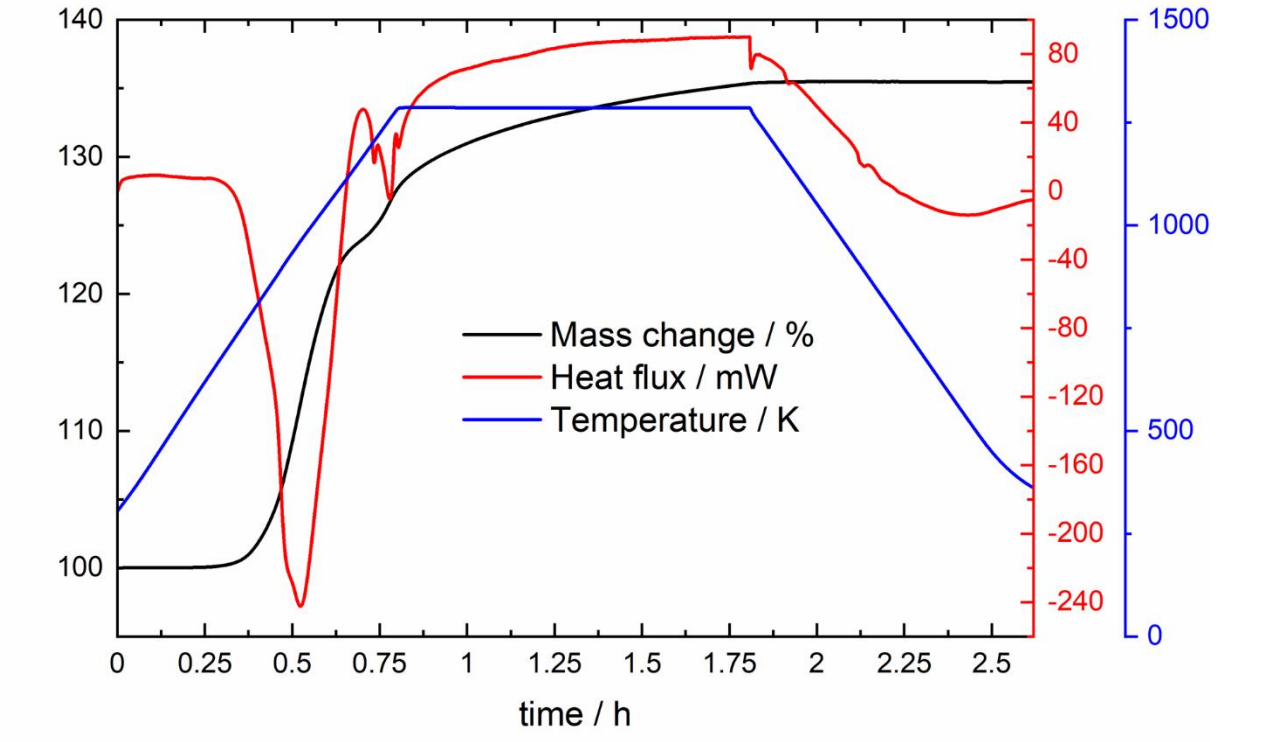

Figure S26. STA experiment for the oxidation reaction of YAl_2 (mass change in black, heat flux in red and temperature program in blue).

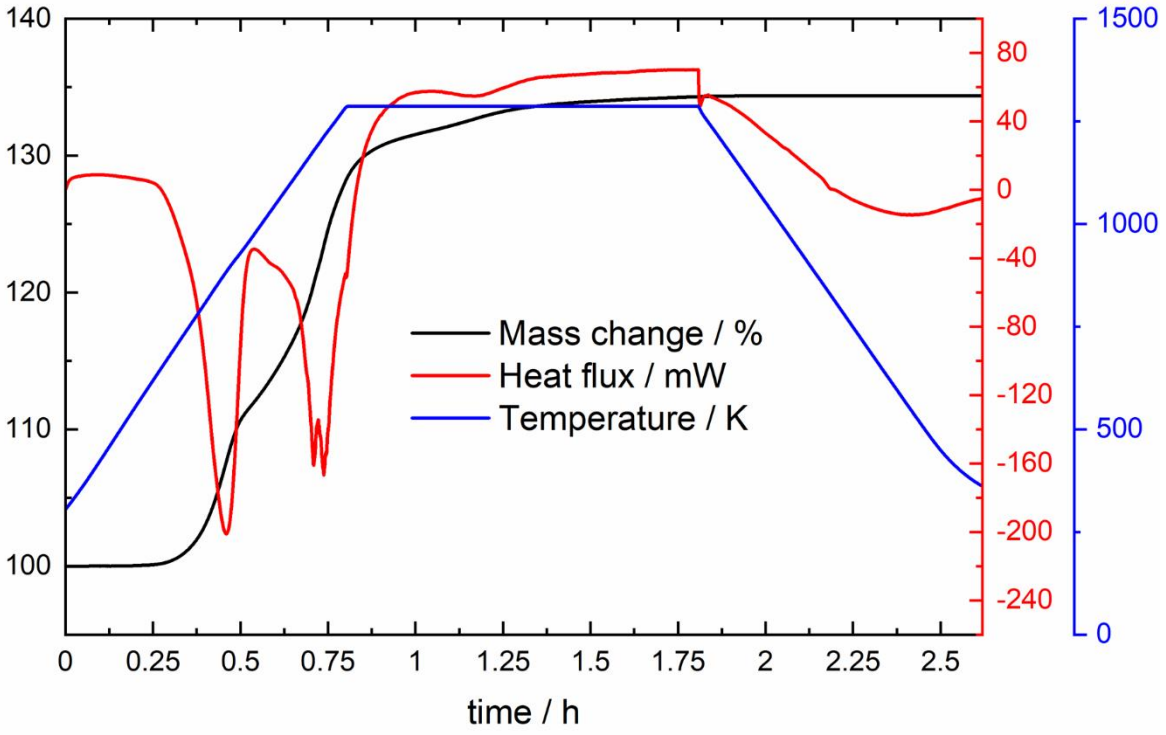

Figure S27. STA experiment for the oxidation reaction of $LaAl_2$ (mass change in black, heat flux in red and temperature program in blue).

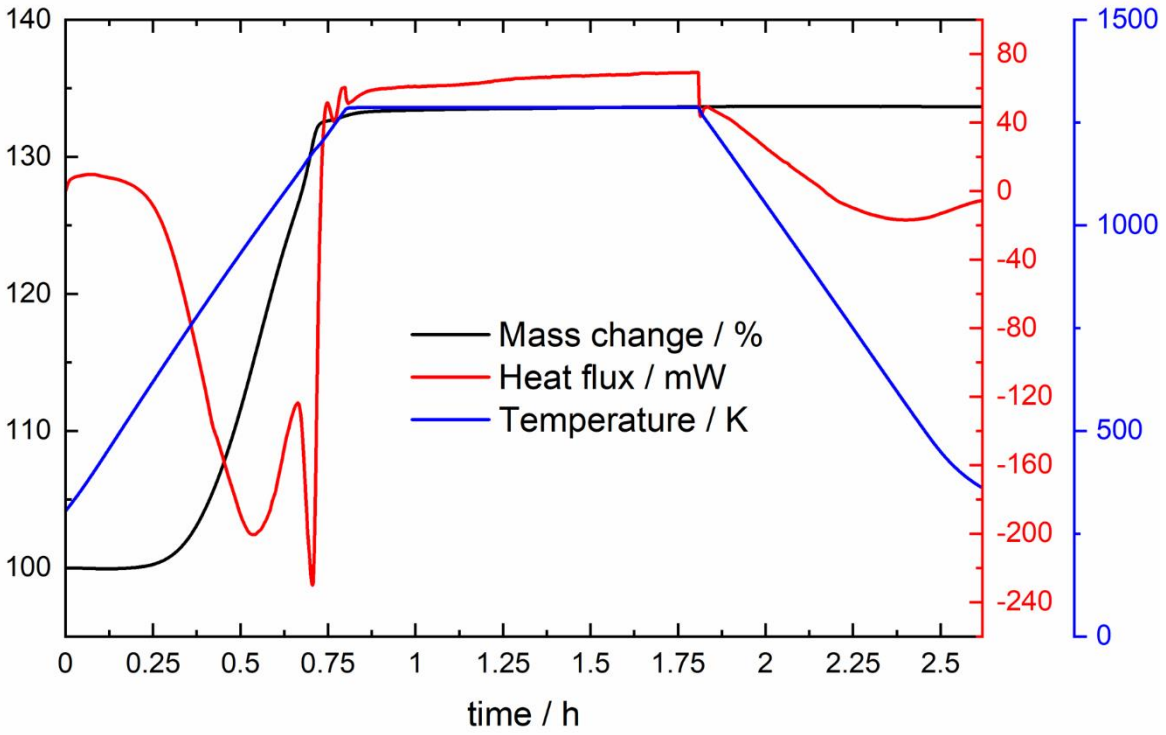

Figure S28. STA experiment for the oxidation reaction of $EuAl_2$ (mass change in black, heat flux in red and temperature program in blue).

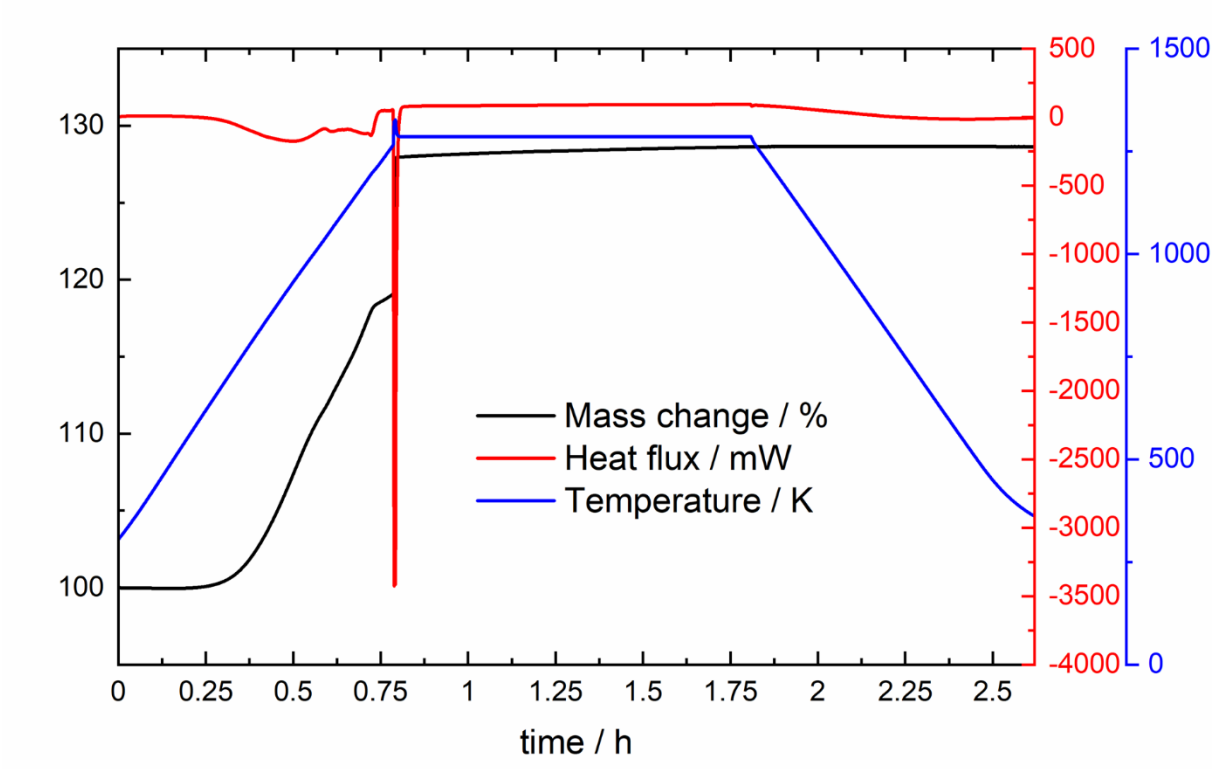

Figure S29. STA experiment for the oxidation reaction of $YbAl_2$ (mass change in black, heat flux in red and temperature program in blue).

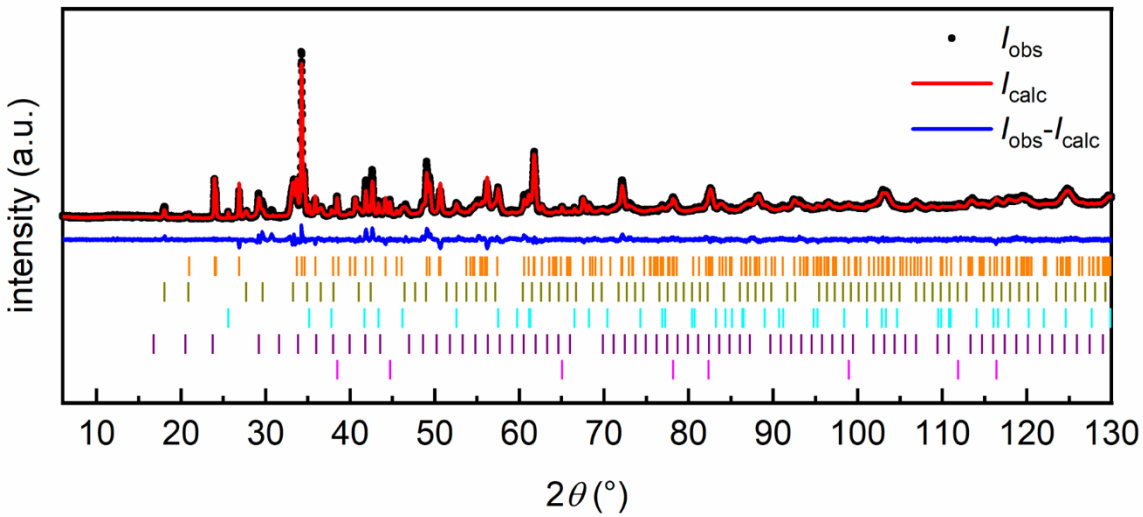

Figure S30. Powder X-ray diffraction pattern of oxidzized YAl_2 in a tube furnace with 100 % oxygen (1273 K, 5 h). Experimental data is shown as black dots, simulated diffraction patterns from refinements as red lines, the difference is shown as continuous blue lines. Bragg positions are shown as orange ($YAlO_3$, space group *Pnma*), dark yellow ($Y_3Al_5O_{12}$, space group $Ia\bar{3}d$), cyan (Al_2O_3, space group $R\bar{3}c$), purple (Y_2O_3, space group $Ia\bar{3}$) and pink (elemental Al, space group $Fm\bar{3}m$) ticks. The refined mass% are given in Table 24.

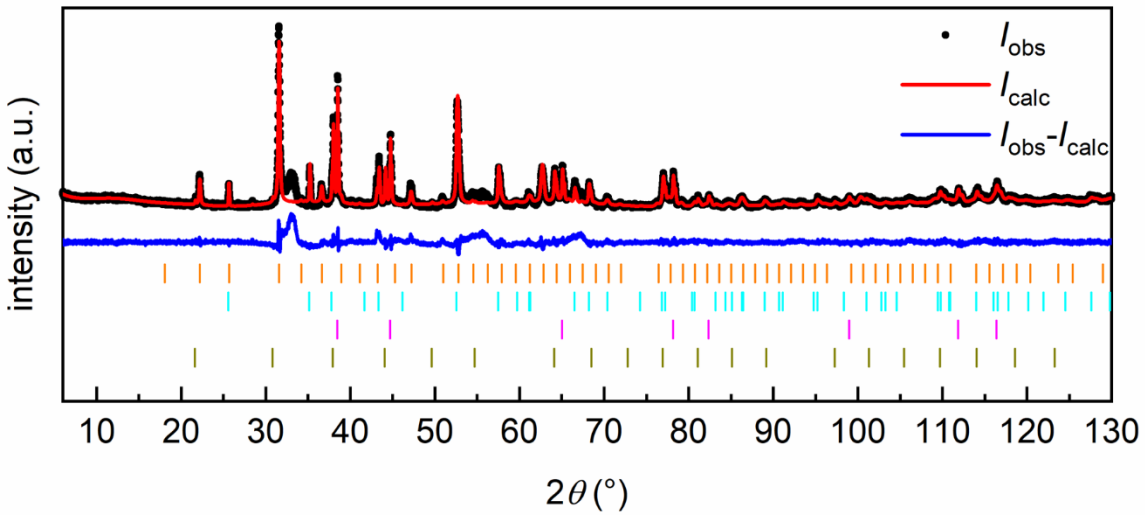

Figure S31. Powder X-ray diffraction pattern of $ScAl_2$ oxidized at 1273 K without dwelling time. Experimental data is shown as black dots, simulated diffraction patterns from refinements as red line, the difference is shown as continuous blue line. Bragg positions are shown as orange (Sc_2O_3, space group $Ia\bar{3}$), cyan (Al_2O_3, space group $R\bar{3}c$), pink (elemental Al, space group $Fm\bar{3}m$) and dark yellow ($ScAl_3$, space group $Pm\bar{3}m$) ticks. The refined mass% are given in Table 25.

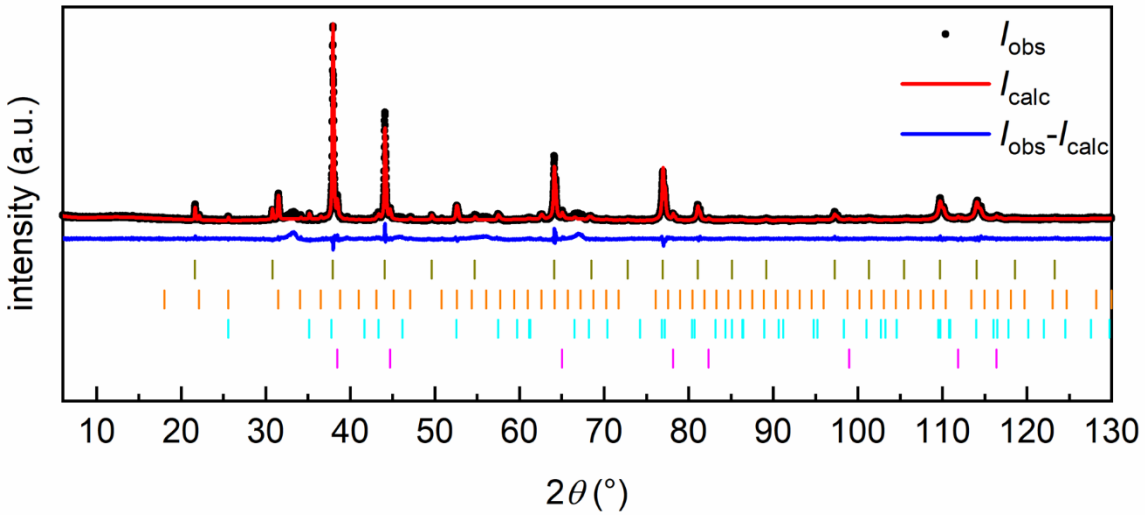

Figure S32. Powder X-ray diffraction pattern of $ScAl_3$ oxidized at 1273 K without dwelling time. Experimental data is shown as black dots, simulated diffraction patterns from refinements as red line, the difference is shown as continuous blue line. Bragg positions are shown as dark yellow ($ScAl_3$, space group $Pm\bar{3}m$), orange (Sc_2O_3, space group $Ia\bar{3}$), cyan (Al_2O_3, space group $R\bar{3}c$) and pink (elemental Al, space group $Fm\bar{3}m$) ticks. The refined mass% are given in Table 25.

8.4 A systematic study on the oxidation behavior of the alkaline earth aluminides $AEAl_4$ (AE = Ca, Sr, Ba), $SrAl_2$ and Ba_7Al_{13}

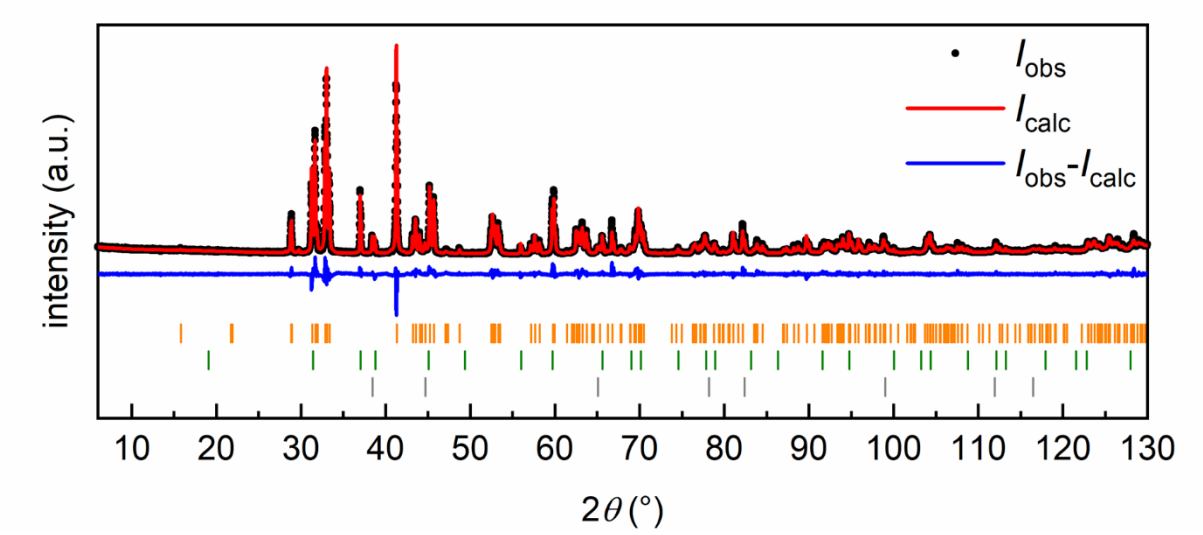

Figure S33. Powder X-ray diffraction pattern of nominal $CaAl_4$. Experimental data is shown as black dots, simulated diffraction patterns from refinements as red lines, the difference is shown as continuous blue lines. Bragg positions are shown as orange ($CaAl_4$, space group $C2/m$, 91(1) mass%), green ($CaAl_2$, space group $Fd\bar{3}m$, 6(1) mass%) and grey (elemental Al, space group $Fm\bar{3}m$, 3(1) mass%) ticks.

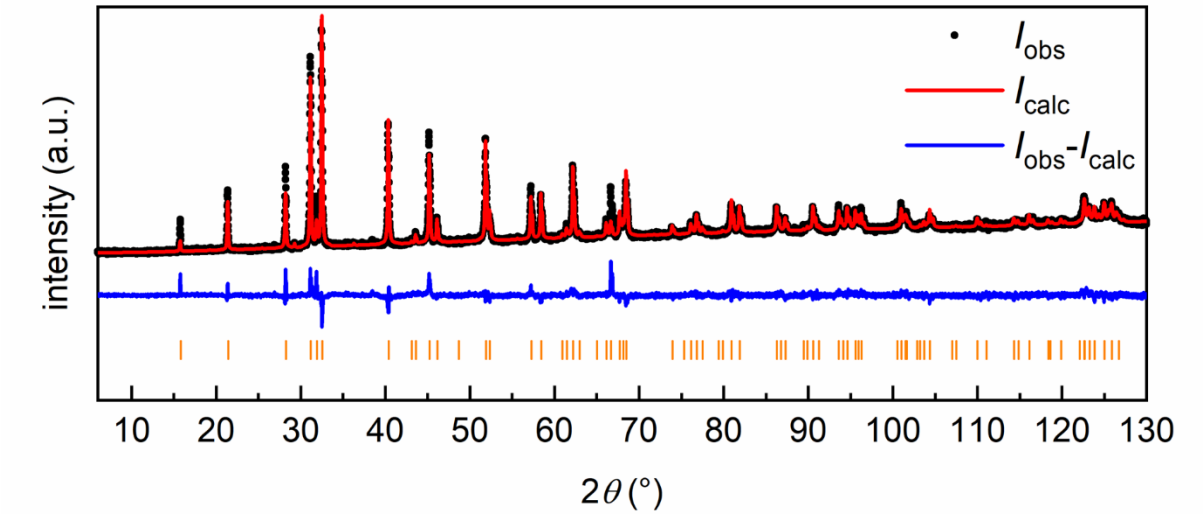

Figure S34. Powder X-ray diffraction pattern of nominal $SrAl_4$. Experimental data is shown as black dots, simulated diffraction patterns from refinements as red lines, the difference is shown as continuous blue lines. Bragg positions are shown as orange ($SrAl_4$, space group $I4/mmm$) ticks.

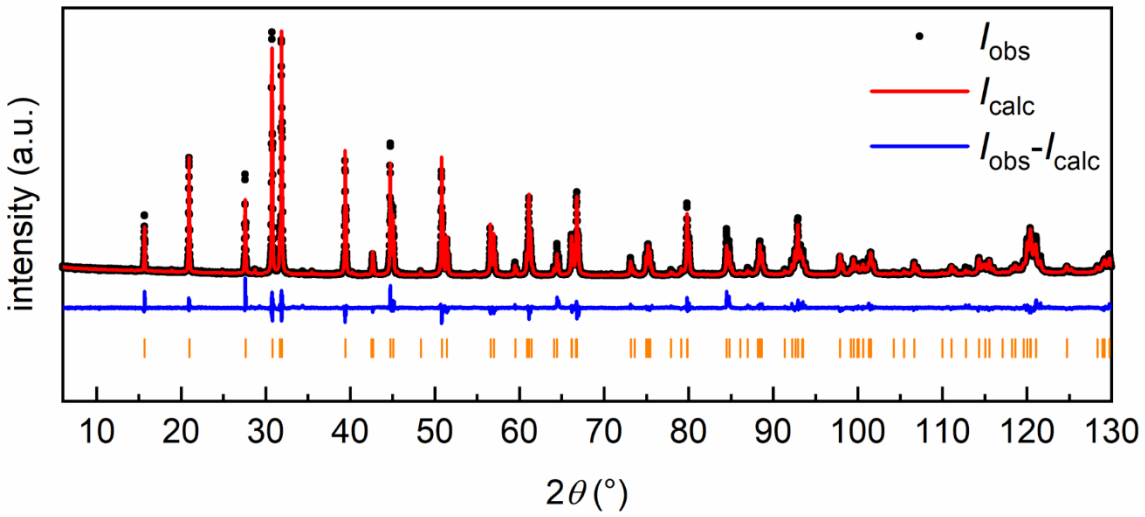

Figure S35. Powder X-ray diffraction pattern of nominal $BaAl_4$. Experimental data is shown as black dots, simulated diffraction patterns from refinements as red lines, the difference is shown as continuous blue lines. Bragg positions are shown as orange ($BaAl_4$, space group *I*4/*mmm*) ticks.

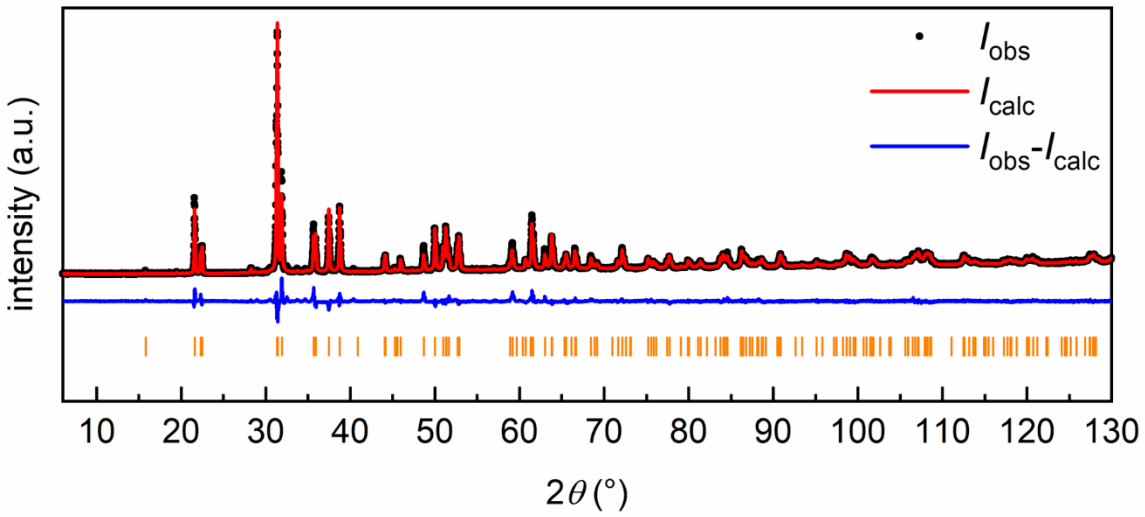

Figure S36. Powder X-ray diffraction pattern of nominal $SrAl_2$. Experimental data is shown as black dots, simulated diffraction patterns from refinements as red lines, the difference is shown as continuous blue lines. Bragg positions are shown as orange ($SrAl_2$, space group *Imma*) ticks.

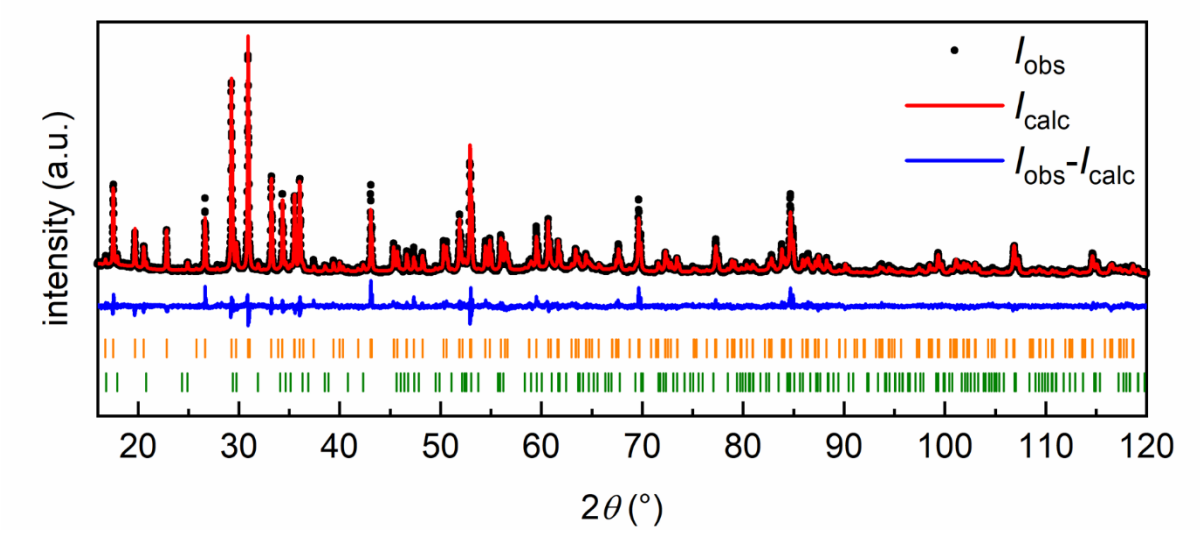

Figure S37. Powder X-ray diffraction pattern of nominal Ba_7Al_{13} ($Ba_{21}Al_{40}$). Experimental data is shown as black dots, simulated diffraction patterns from refinements as red lines, the difference is shown as continuous blue lines. Bragg positions are shown as orange (Ba_7Al_{13}, space group $P\bar{3}m1$, 90(1) mass%) and green (Ba_3Al_5, space group $P6_3/mmc$, 10(1) mass%) ticks.

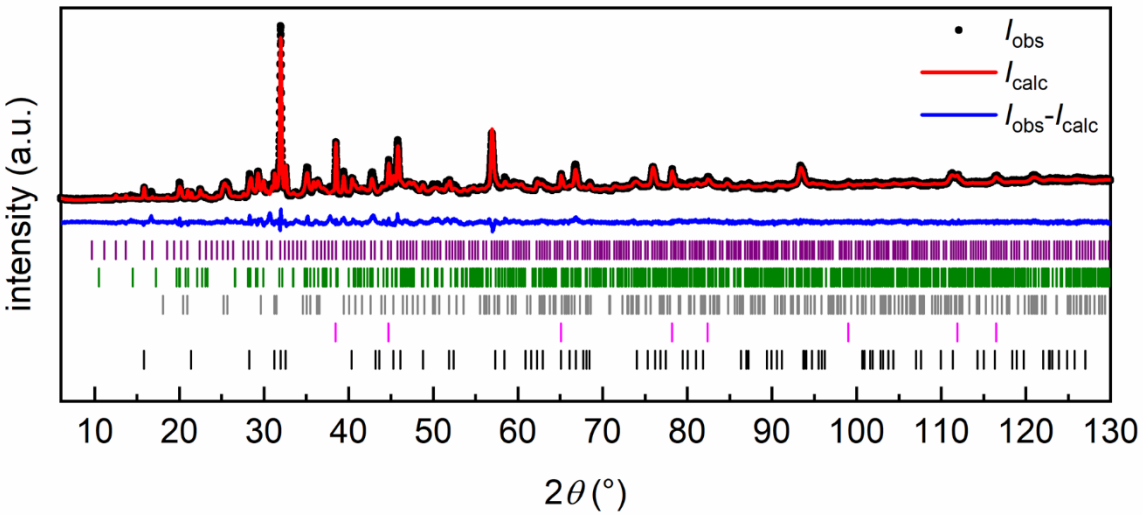

Figure S38. Powder X-ray diffraction pattern of $SrAl_2$ oxidized at 1273 K in an STA without dwelling time. Experimental data is shown as black dots, simulated diffraction patterns from refinements as red line, the difference is shown as continuous blue line. Bragg positions are shown as purple ($Sr_3Al_2O_6$, space group $Pa\bar{3}$), green ($SrAl_2O_4$, space group $P2_1$), dark grey ($SrCO_3$, space group *Pnma*), pink (elemental Al, space group $Fm\bar{3}m$) and black ($SrAl_4$, space group $I4/mmm$) ticks. The refined mass% are given in Table 28.

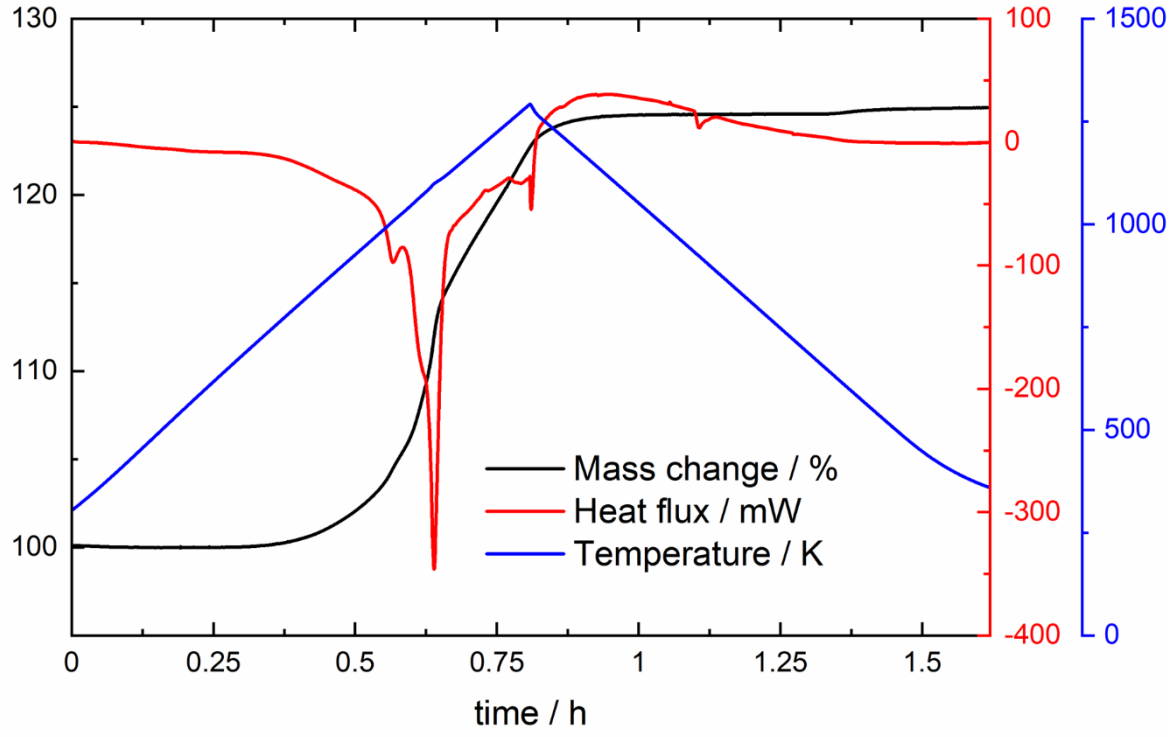

Figure S39. STA experiment for the oxidation reaction of $SrAl_2$ without dwelling time (mass change in black, heat flux in red and temperature program in blue).

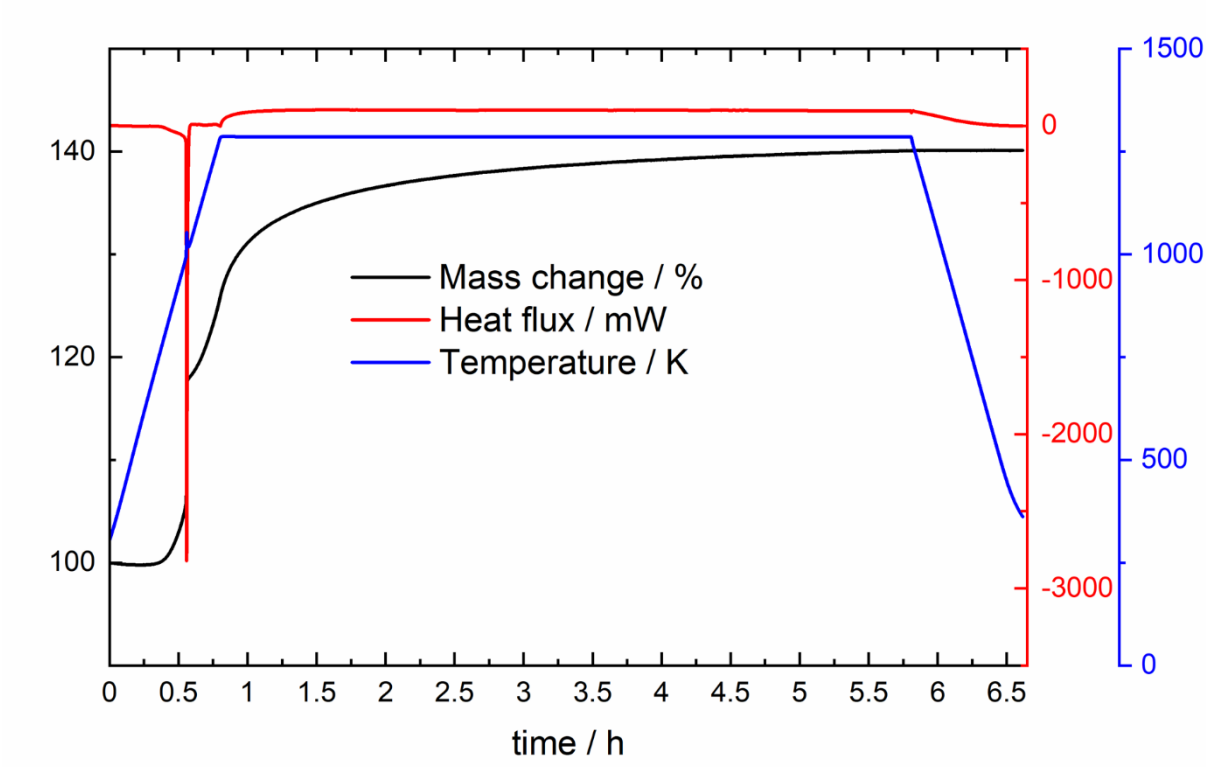

Figure S40. STA experiment for the oxidation reaction of $SrAl_2$ with 5 hours dwelling time (mass change in black, heat flux in red and temperature program in blue).

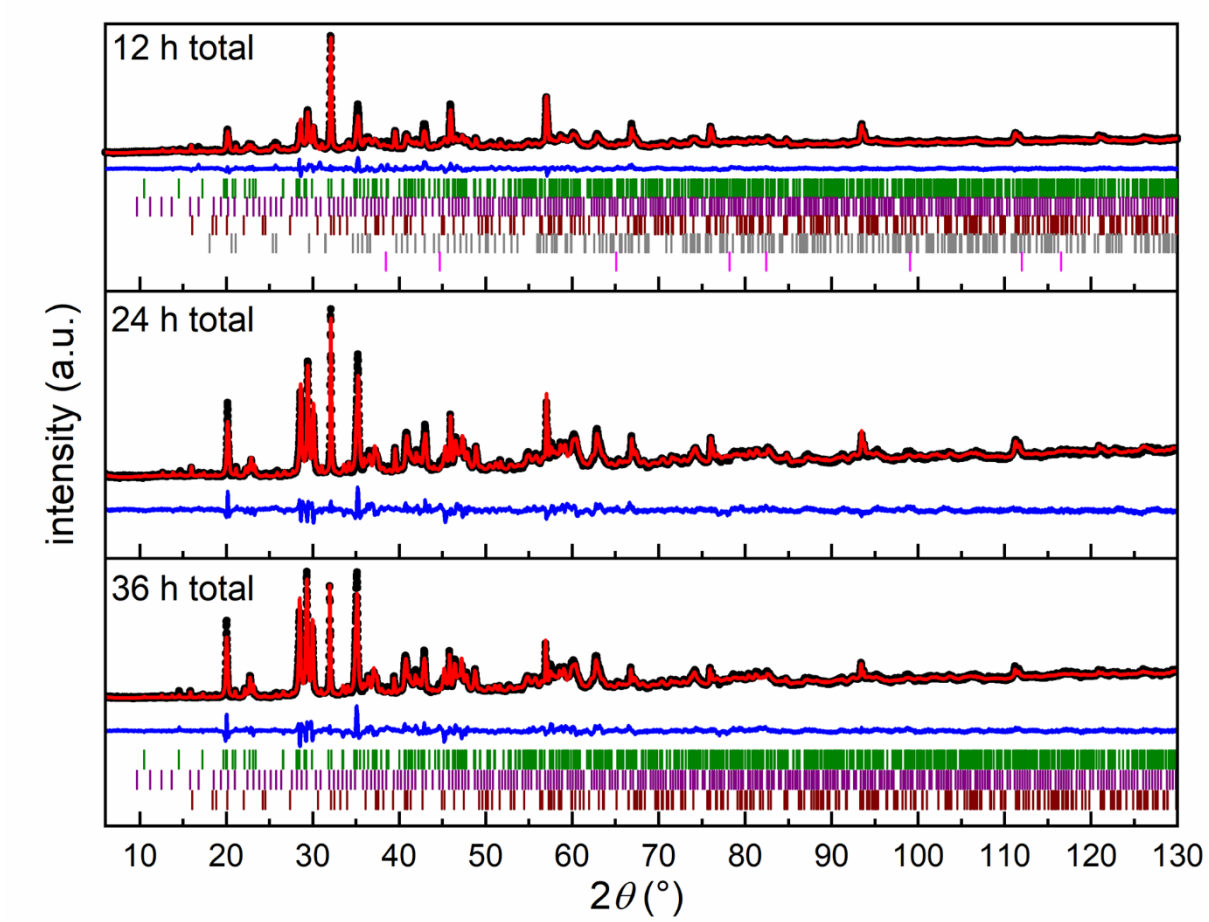

Figure S41. Powder X-ray diffraction patterns of $SrAl_2$ oxidized at 1273 K in a tube furnace operating with pure oxygen flow for (*top*) initial 12 hours, followed by grinding and additional annealing for 12 hours, resulting in total (*middle*) 24 and (*bottom*) 36 hours. Experimental data is shown as black dots, simulated diffraction patterns from refinements as red line, the difference is shown as continuous blue line. Bragg positions are shown as green ($SrAl_2O_4$, space group $P2_1$) purple ($Sr_3Al_2O_6$, space group $Pa\bar{3}$), brown ($SrAl_{12}O_{19}$, space group $P6_3/mmc$), dark grey ($SrCO_3$, space group *Pnma*) and pink (elemental Al, space group $Fm\bar{3}m$) ticks. The refined mass% are given in Table 29.

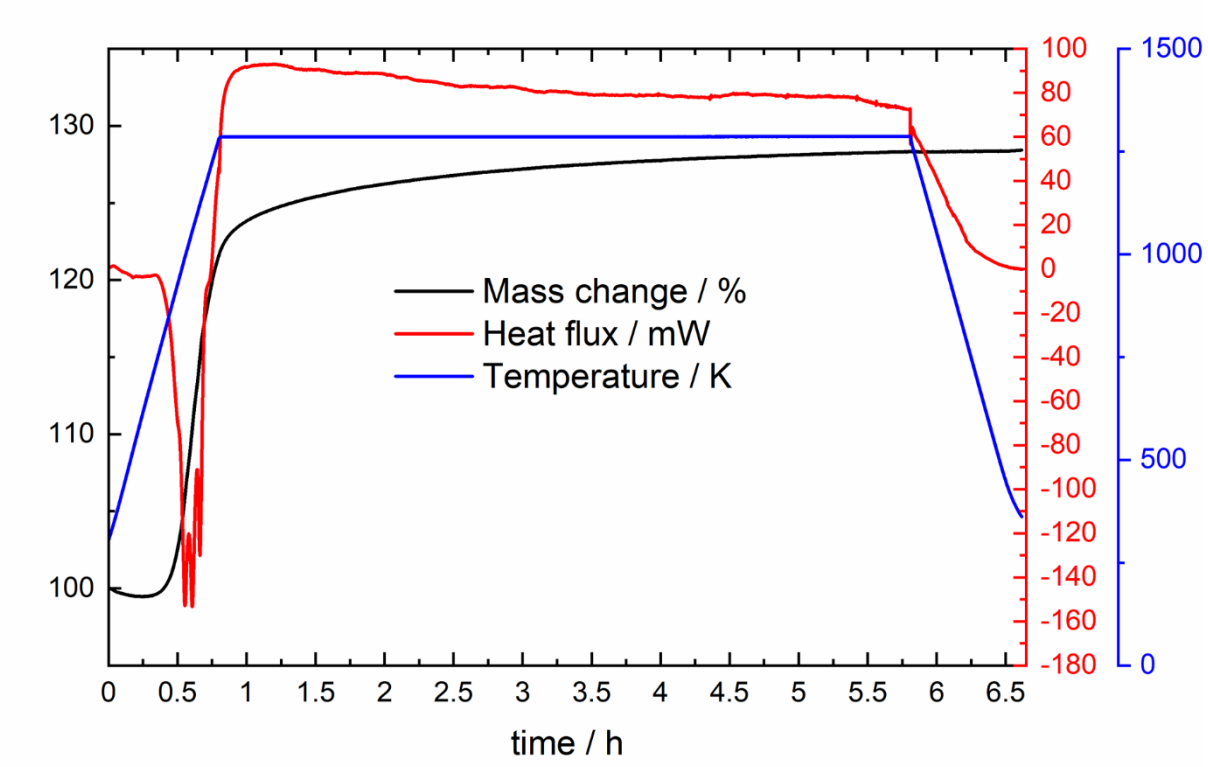

Figure S42. STA experiment for the oxidation reaction of "$BaAl_2$" with 5 hours dwelling time (mass change in black, heat flux in red and temperature program in blue).

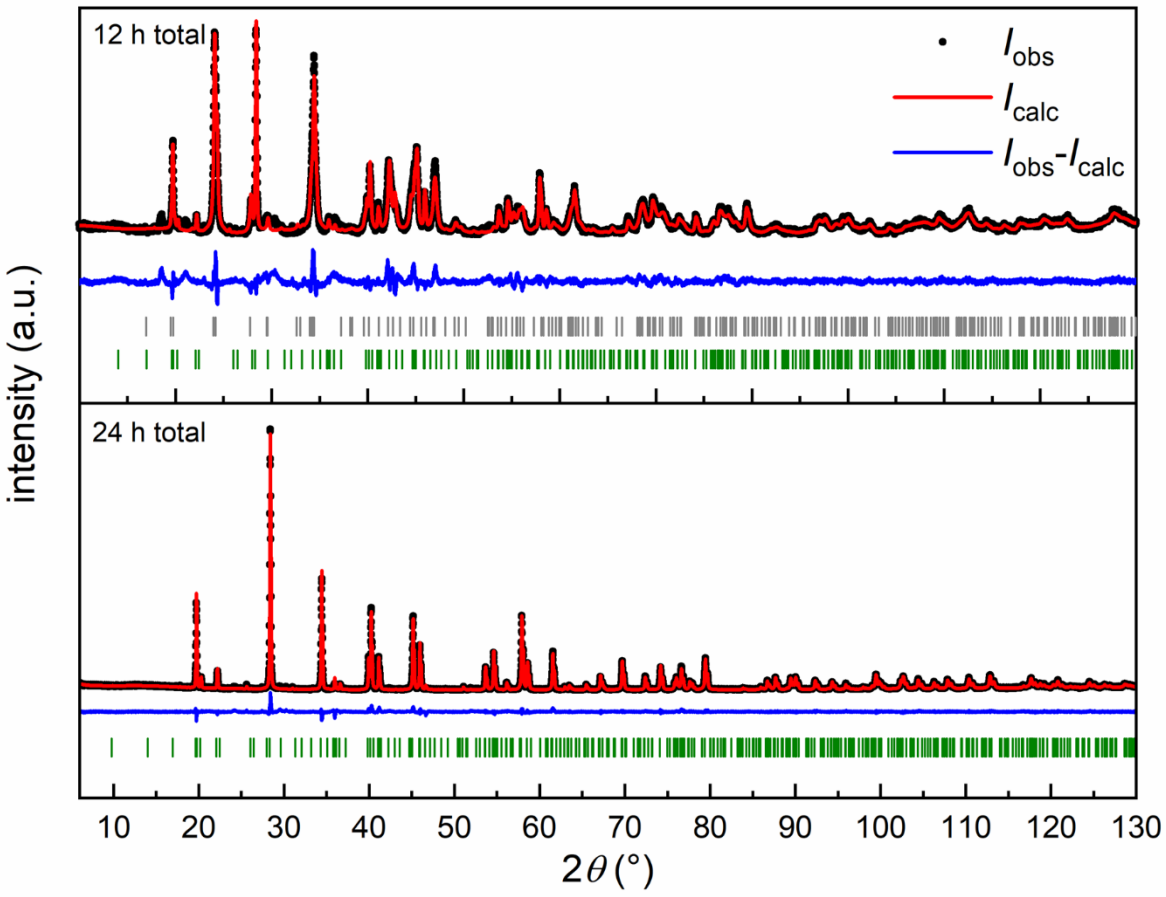

Figure S43. Powder X-ray diffraction patterns of "$BaAl_2$" oxidized at 1273 K in a tube furnace operating with pure oxygen flow for initial (*top*) 12 hours, followed by grinding and additional annealing for 12 hours, resulting in total times of (*bottom*) 24 hours. Experimental data is shown as black dots, simulated diffraction patterns from refinements as red line, the difference is shown as continuous blue line. Bragg positions are shown as green ($BaAl_2O_4$, space group $P6_3$, (*top*) 36(1) mass%, (*bottom*) 100 mass%) and dark grey ($BaCO_3$, space group *Pnma*, (*top*) 64(1) mass%) ticks.

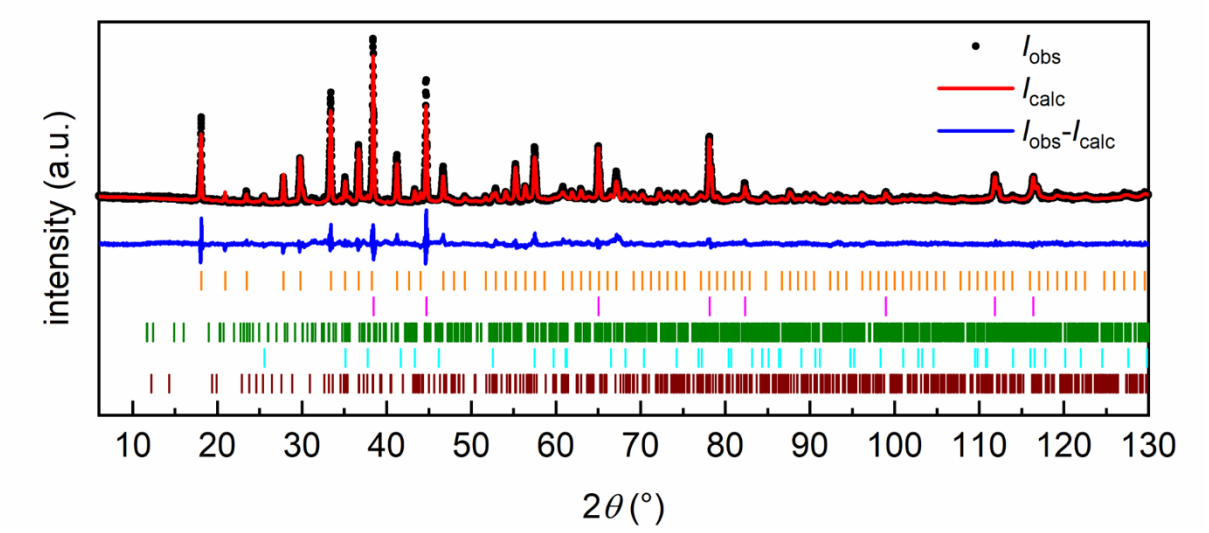

Figure S44. Powder X-ray diffraction pattern of $CaAl_4$ oxidized in an STA setup at 1273 K without dwelling times. Experimental data is shown as black dots, simulated diffraction patterns from refinements as red line, the difference is shown as continuous blue line. Bragg positions are shown as orange ($Ca_{12}Al_{14}O_{33}$, space group $I\bar{4}3d$), pink (elemental Al, space group $Fm\bar{3}m$), green ($CaAl_2O_4$, space group $P2_1/c$), cyan (Al_2O_3, space group $R\bar{3}c$) and brown ($CaAl_4O_7$, space group $C2_1/c$) ticks. The refined mass% are given in Table 30.

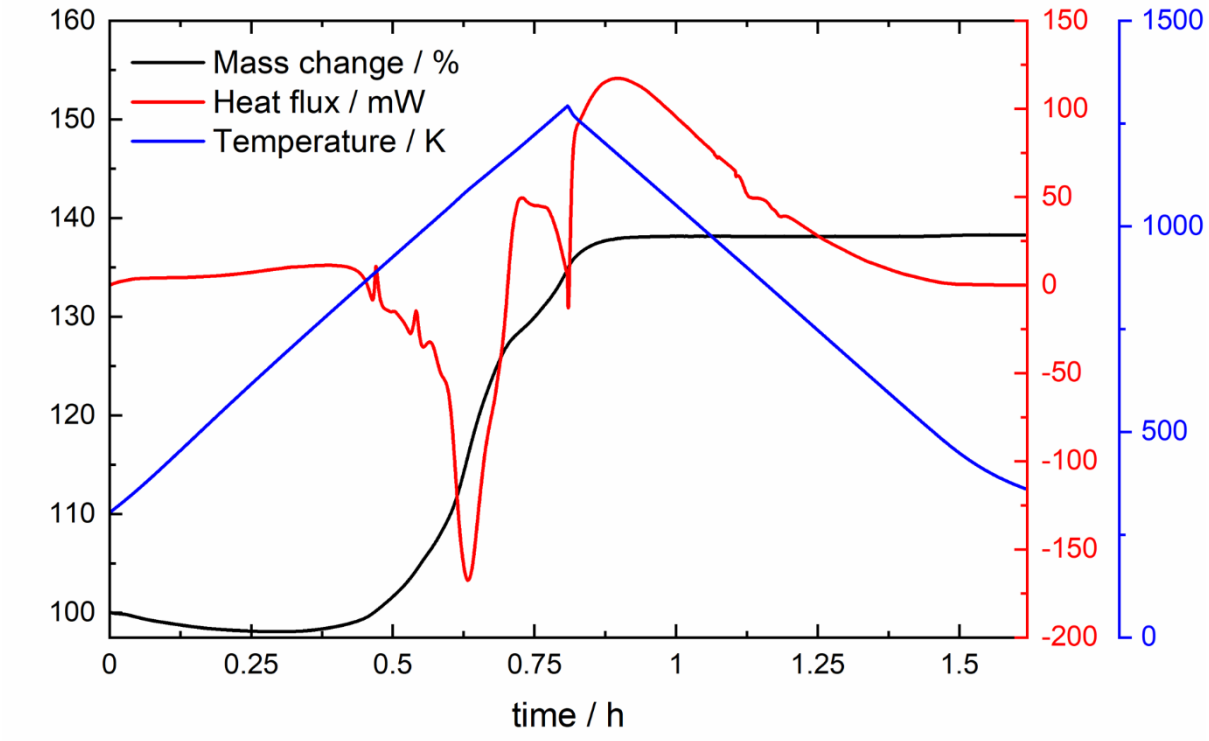

Figure S45. STA experiment for the oxidation reaction of $CaAl_4$ without dwelling time (mass change in black, heat flux in red and temperature program in blue).

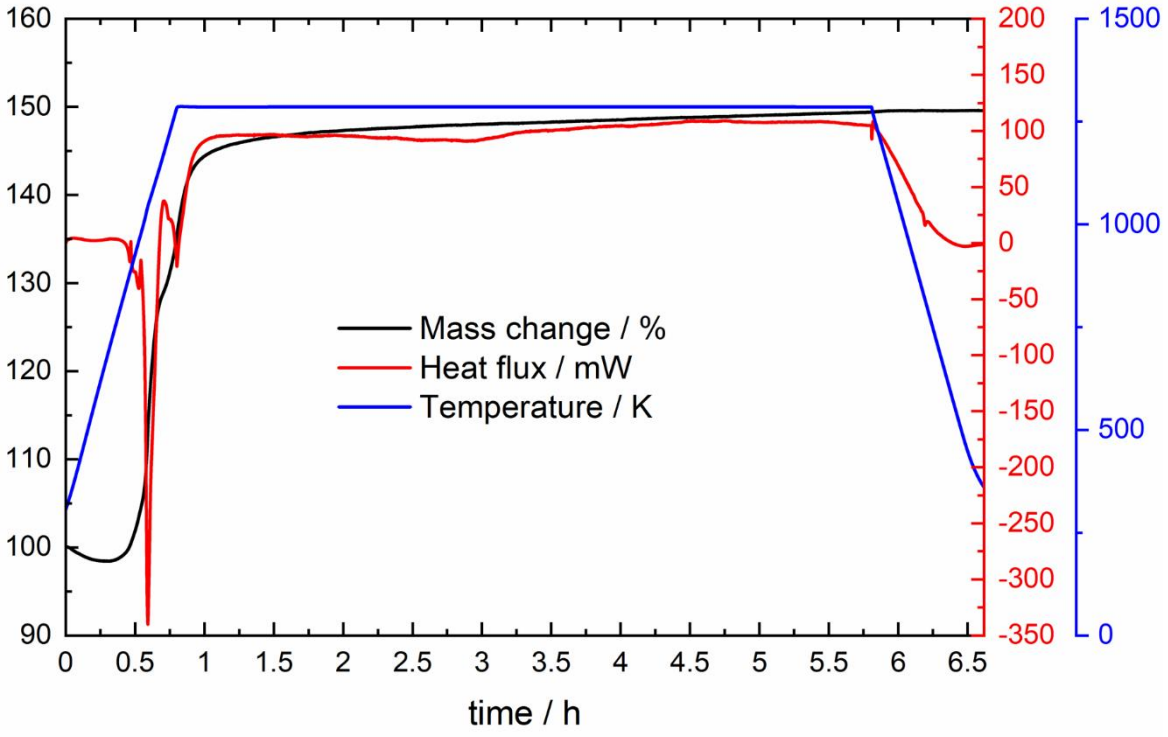

Figure S46. STA experiment for the oxidation reaction of $CaAl_4$ with 5 hours dwelling time (mass change in black, heat flux in red and temperature program in blue).

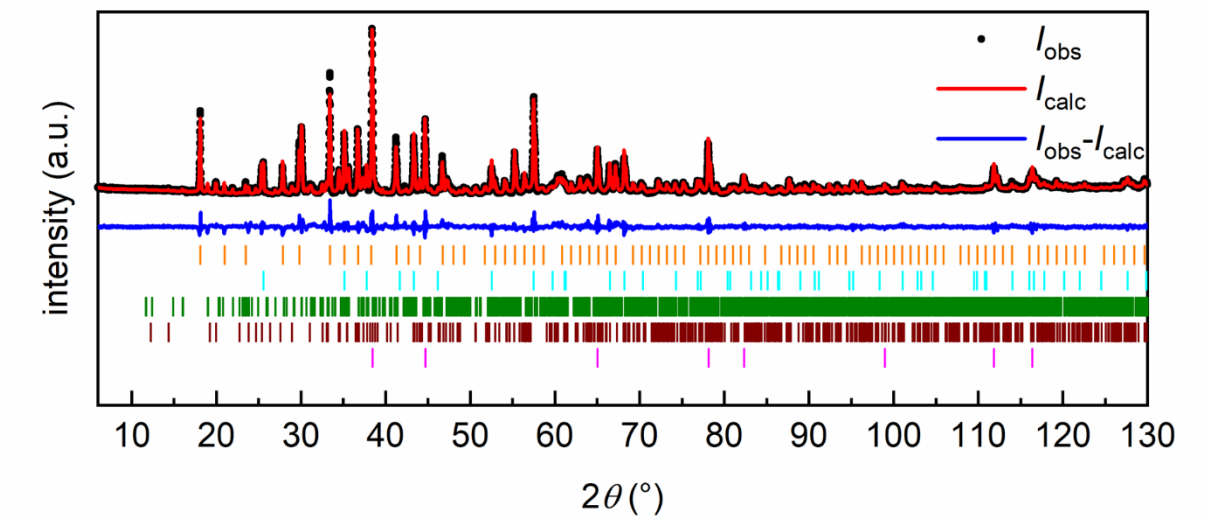

Figure S47. Powder X-ray diffraction patterns of $CaAl_4$ oxidized at 1273 K in a tube furnace operating with pure oxygen flow for initial 5 hours. Experimental data is shown as black dots, simulated diffraction patterns from refinements as red line, the difference is shown as continuous blue line. Bragg positions are shown as orange ($Ca_{12}Al_{14}O_{33}$, space group $I\bar{4}3d$), cyan (Al_2O_3, space group $R\bar{3}c$), green ($CaAl_2O_4$, space group $P2_1/c$), brown ($CaAl_4O_7$, space group $C2_1/c$) and pink (elemental Al, space group $Fm\bar{3}m$) ticks. The refined mass% are given in Table 30.

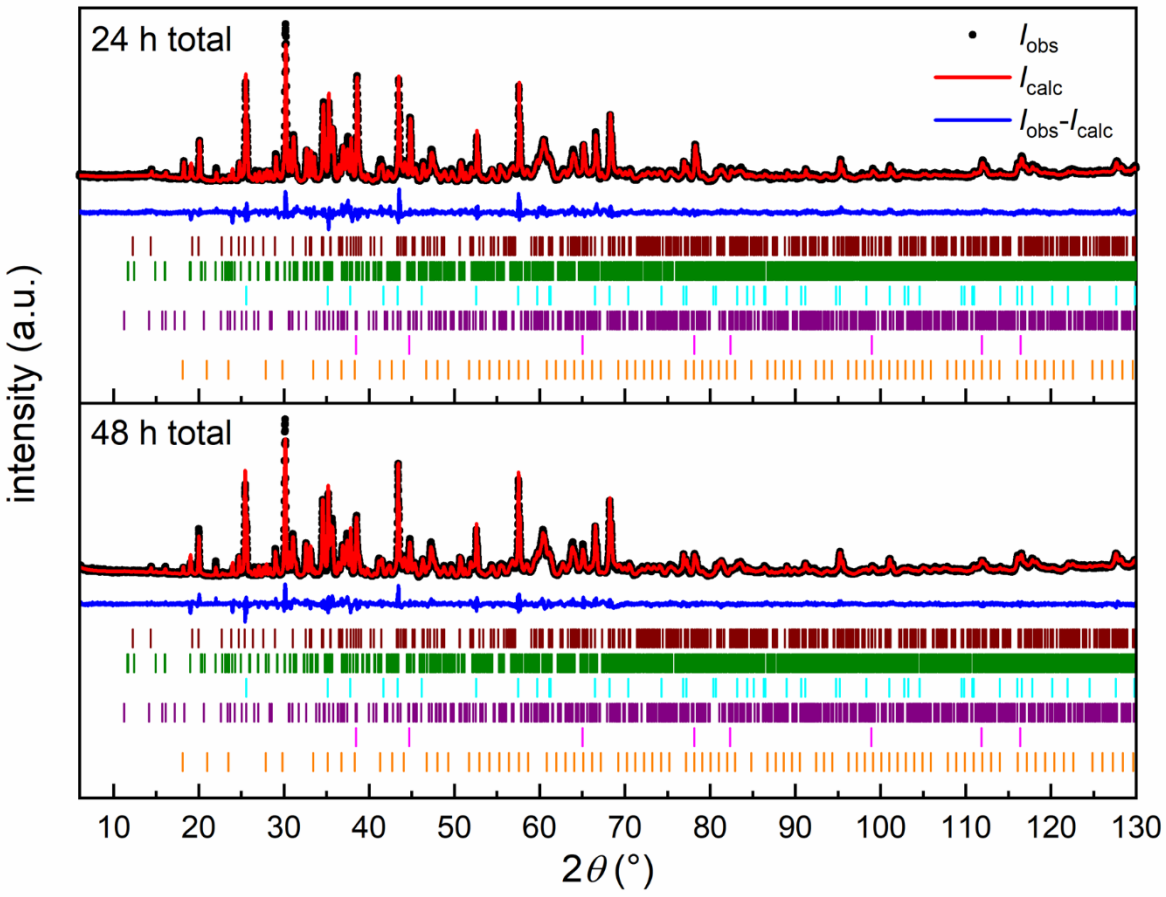

Figure S48. Powder X-ray diffraction patterns of $CaAl_4$ oxidized at 1273 K in a tube furnace operating with pure oxygen flow for (*top*) initial 24 hours, followed by grinding and additional annealing for 24 hours, resulting in total time of (*bottom*) 48. Experimental data is shown as black dots, simulated diffraction patterns from refinements as red line, the difference is shown as continuous blue line. Bragg positions are shown as brown ($CaAl_4O_7$, space group $C2_1/c$), green ($CaAl_2O_4$, space group $P2_1/c$), cyan (Al_2O_3, space group $R\bar{3}c$), purple ($Ca_5Al_6O_{14}$, space group $Cmc2_1$), pink (elemental Al, space group $Fm\bar{3}m$) and orange ($Ca_{12}Al_{14}O_{33}$, space group $I\bar{4}3d$) ticks. The refined mass% are given in Table 30.

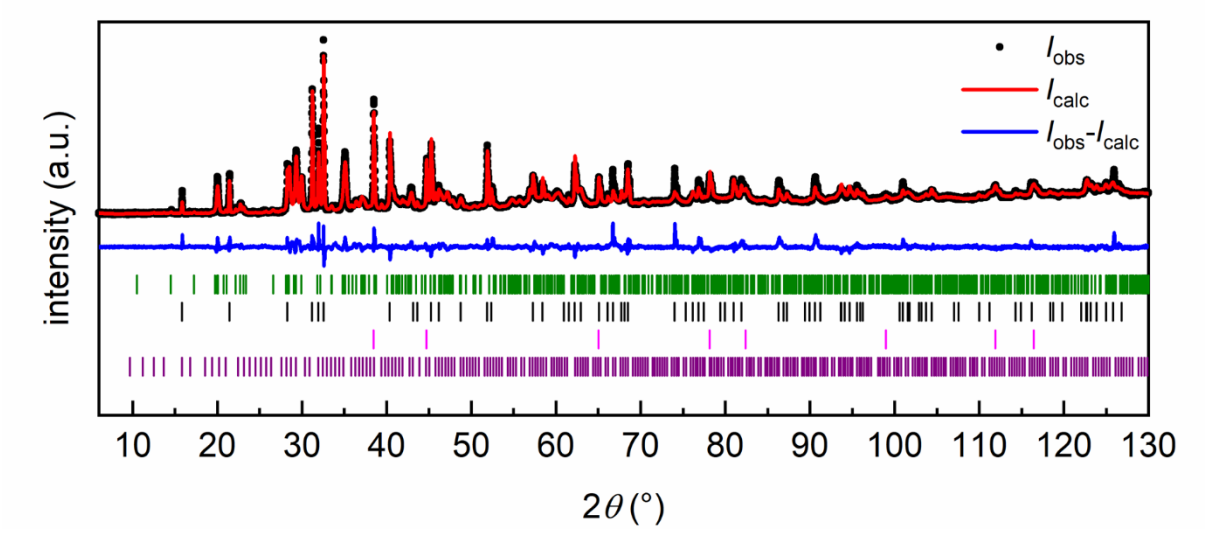

Figure S49. Powder X-ray diffraction pattern of $SrAl_4$ oxidized at 1273 K in an STA setup without dwelling time. Experimental data is shown as black dots, simulated diffraction patterns from refinements as red line, the difference is shown as continuous blue line. Bragg positions are shown as green ($SrAl_2O_4$, space group $P2_1$), black ($SrAl_4$, space group $I4/mmm$), pink (elemental Al, space group $Fm\bar{3}m$) and purple ($Sr_3Al_2O_6$, space group $Pa\bar{3}$) ticks. The refined mass% are given in Table 31.

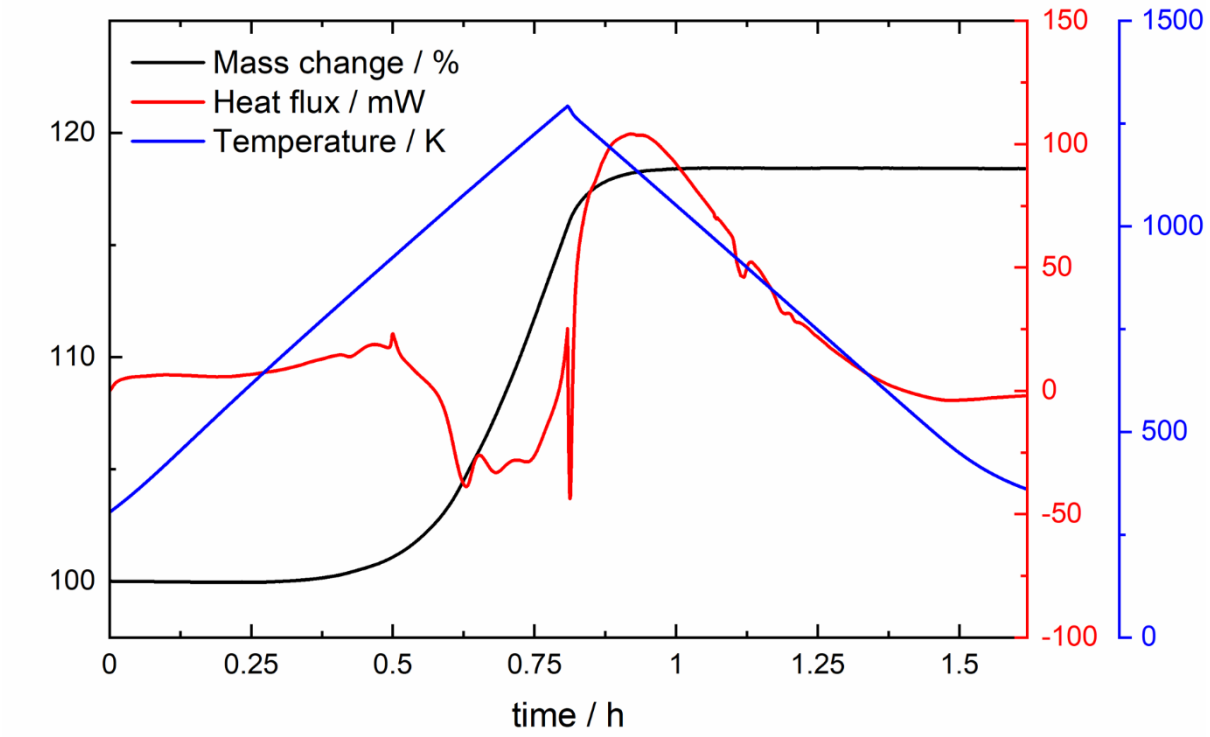

Figure S50. STA experiment for the oxidation reaction of $SrAl_4$ without dwelling time (mass change in black, heat flux in red and temperature program in blue).

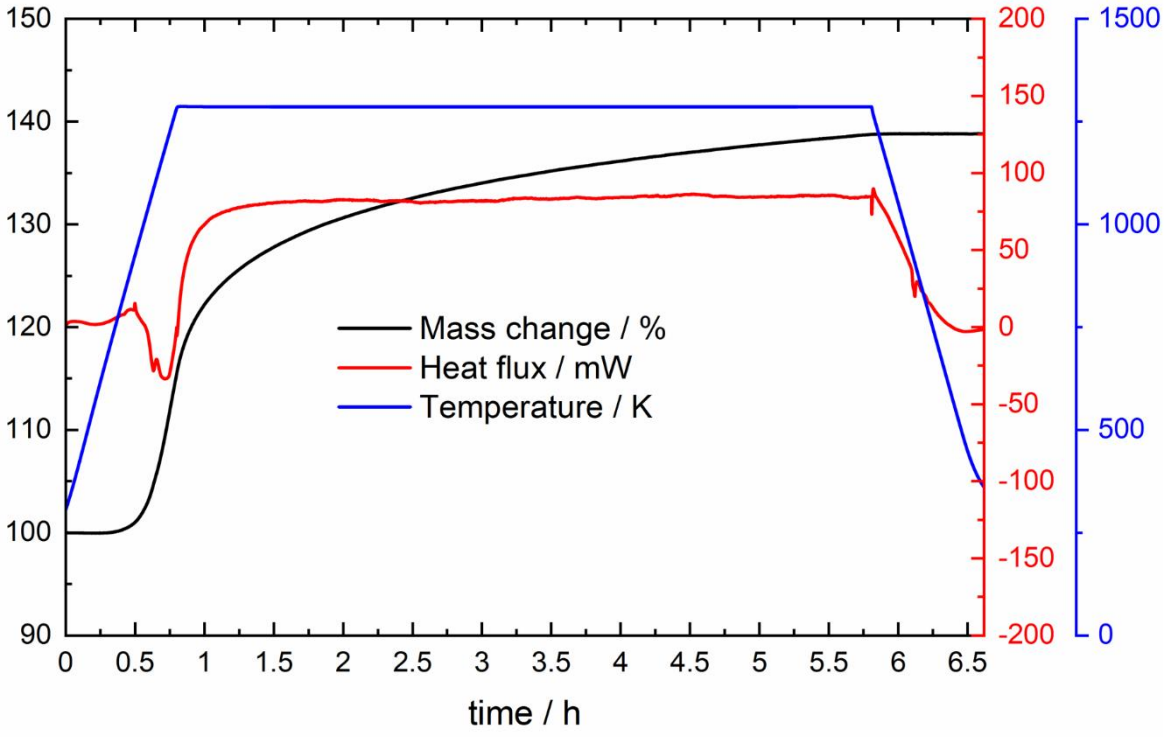

Figure S51. STA experiment for the oxidation reaction of $SrAl_4$ with 5 hours dwelling time (mass change in black, heat flux in red and temperature program in blue).

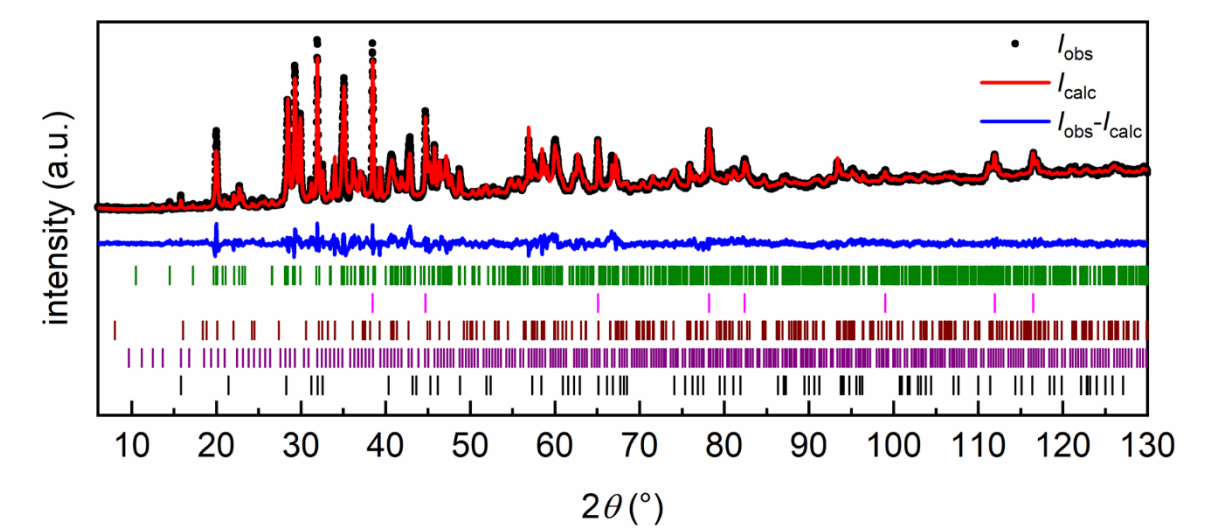

Figure S52. Powder X-ray diffraction patterns of $SrAl_4$ oxidized at 1273 K in a tube furnace operating with pure oxygen flow for 5 hours. Experimental data is shown as black dots, simulated diffraction patterns from refinements as red line, the difference is shown as continuous blue line. Bragg positions are shown as green ($SrAl_2O_4$, space group $P2_1$), pink (elemental Al, space group $Fm\bar{3}m$), brown ($SrAl_{12}O_{19}$, space group $P6_3/mmc$), purple ($Sr_3Al_2O_6$, space group $Pa\bar{3}$) and black ($SrAl_4$, space group $I4/mmm$) ticks. The refined mass% are given in Table 31.

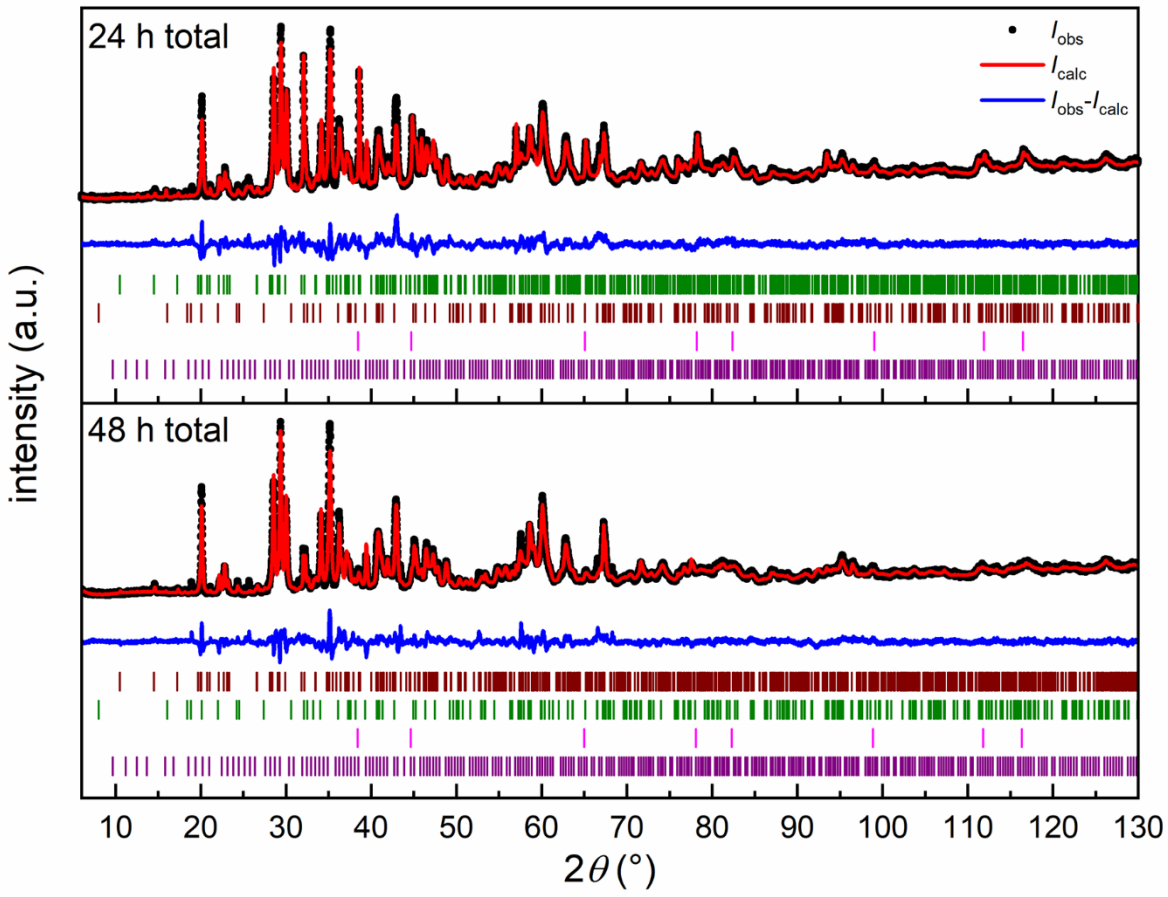

Figure S53. Powder X-ray diffraction patterns of $SrAl_4$ oxidized at 1273 K in a tube furnace operating with pure oxygen flow for (*top*) initial 24 hours, followed by grinding and additional annealing for 24 hours, resulting in total time of (*bottom*) 48 hours. Bragg positions are shown as green ($SrAl_2O_4$, space group $P2_1$), brown ($SrAl_{12}O_{19}$, space group $P6_3/mmc$), pink (elemental Al, space group $Fm\bar{3}m$) and purple ($Sr_3Al_2O_6$, space group $Pa\bar{3}$) ticks. The refined mass% are given in Table 31.

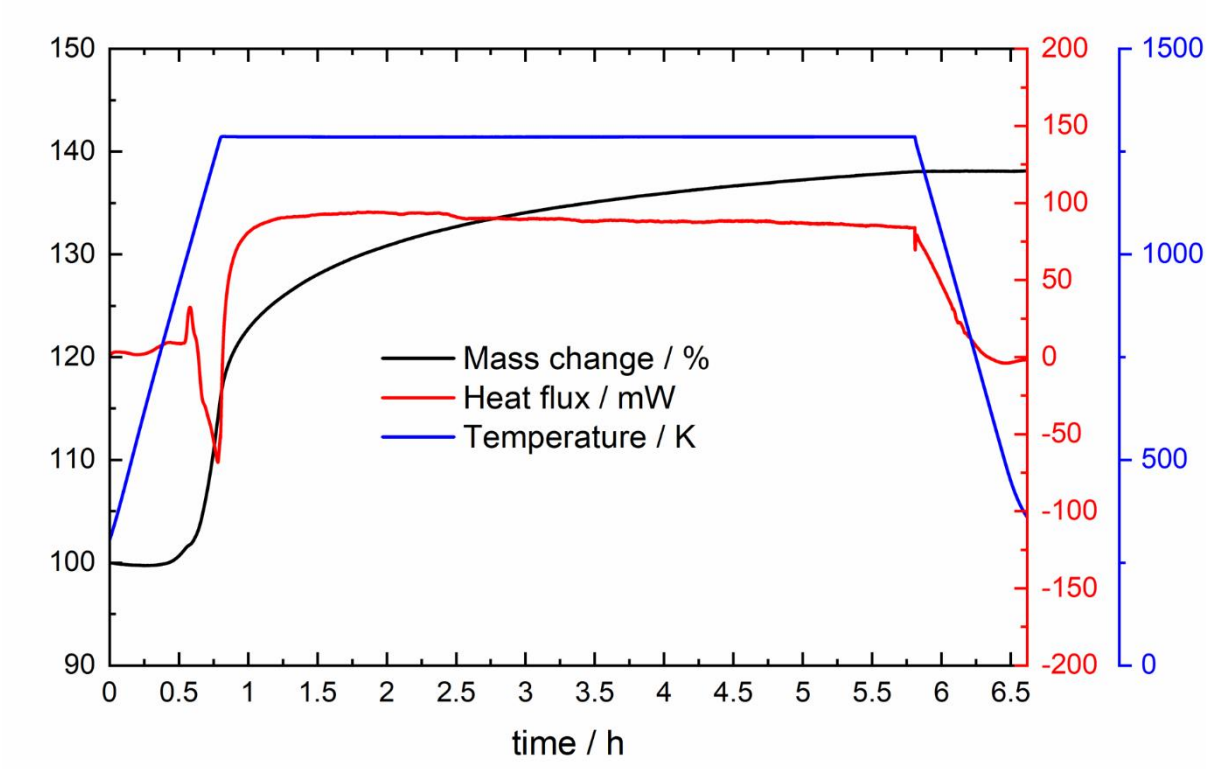

Figure S54. STA experiment for the oxidation reaction of $BaAl_4$ with 5 hours dwelling time (mass change in black, heat flux in red and temperature program in blue).

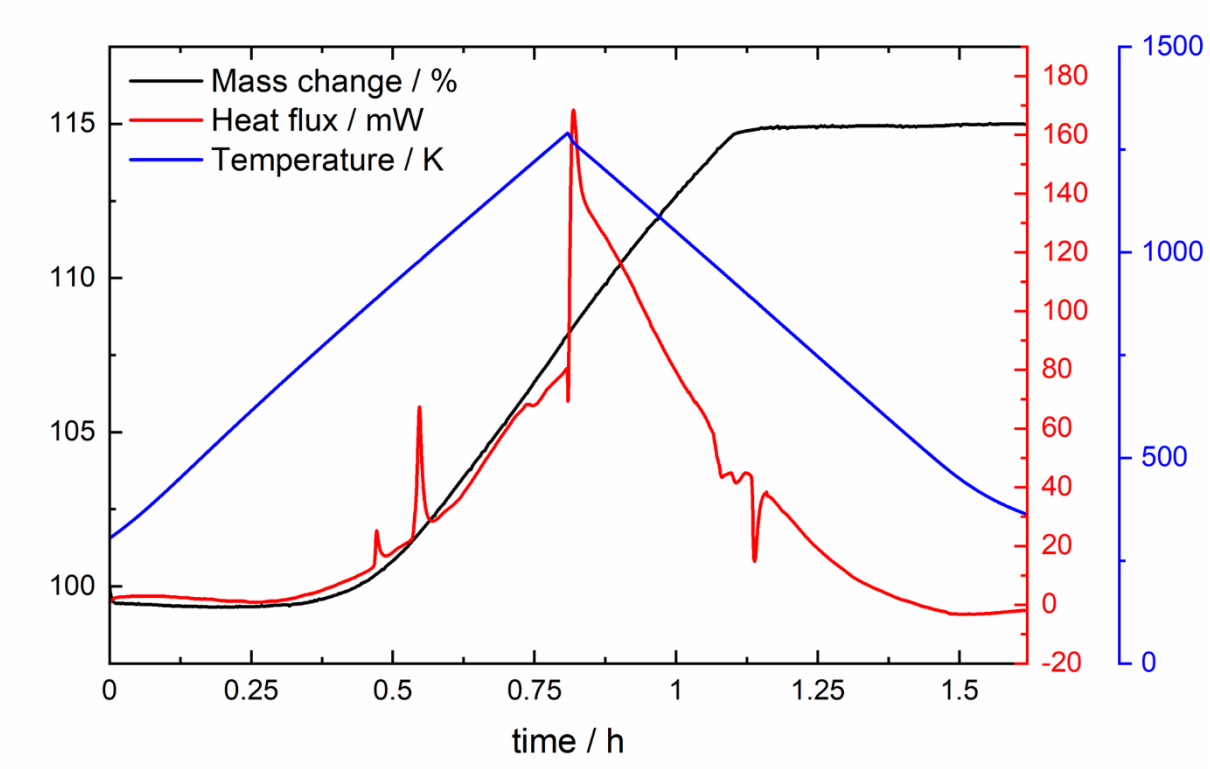

Figure S55. STA experiment under "inert atmosphere" $CaAl_4$ without dwelling time (mass change in black, heat flux in red and temperature program in blue).

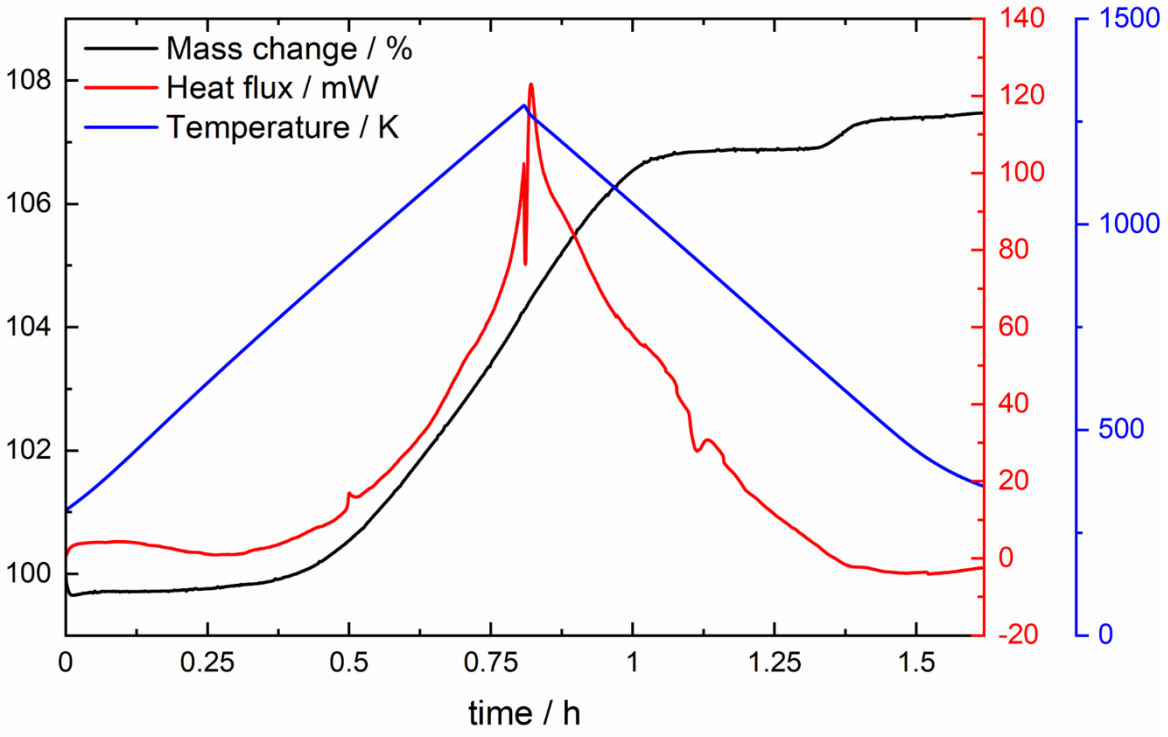

Figure S56. STA experiment under "inert atmosphere" $SrAl_4$ without dwelling time (mass change in black, heat flux in red and temperature program in blue).

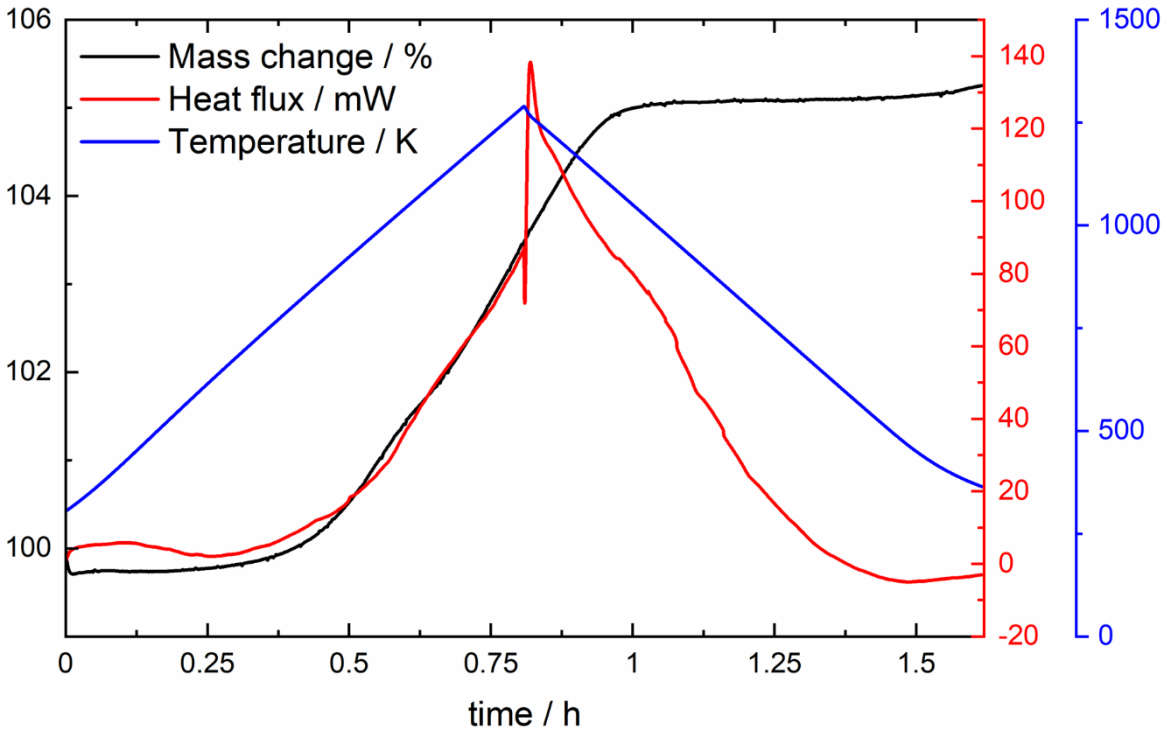

Figure S57. STA experiment under "inert atmosphere" $BaAl_4$ without dwelling time (mass change in black, heat flux in red and temperature program in blue).

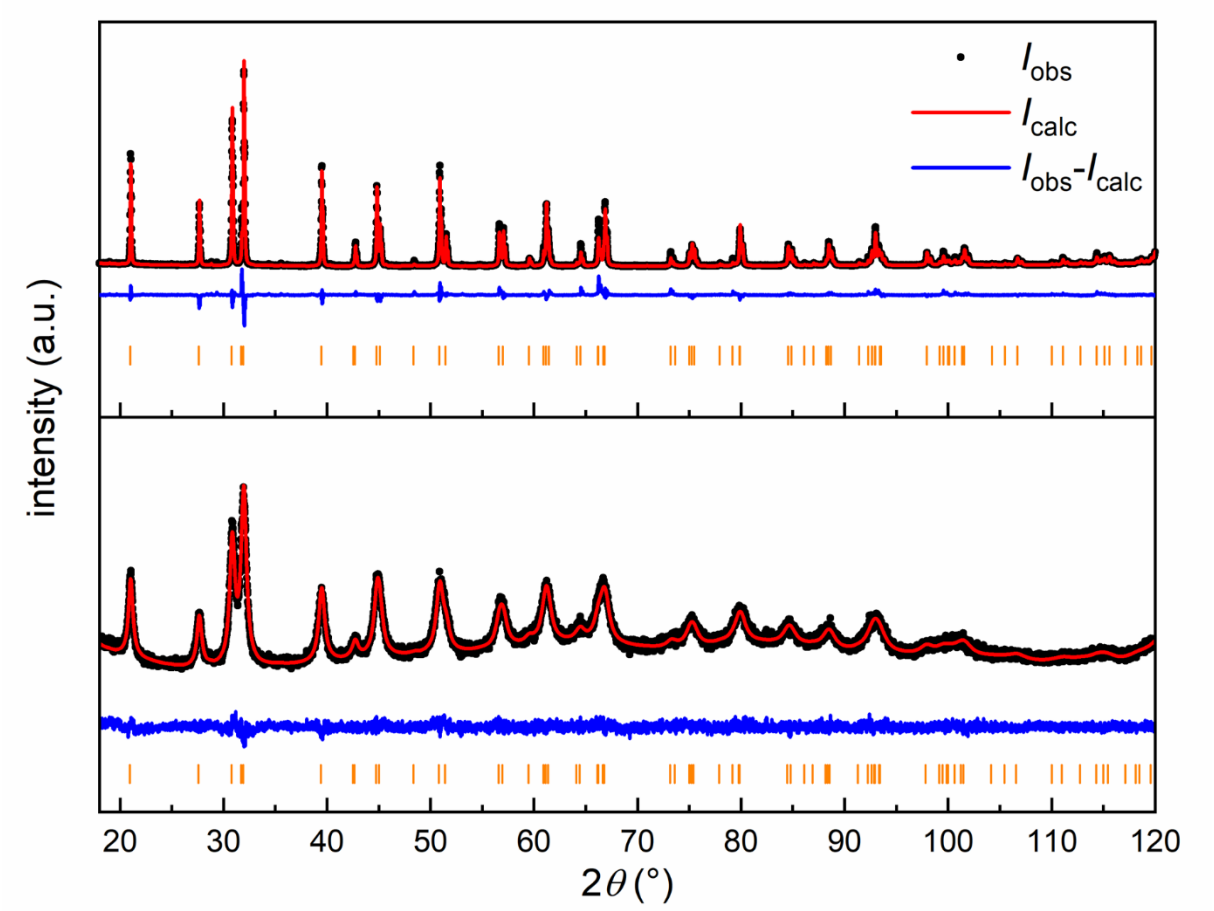

Figure S58. Powder X-ray diffraction pattern of (*top*) pristine $BaAl_4$ and (*bottom*) a ball milled sample after 180 minutes. Experimental data is shown as black dots, simulated diffraction patterns from refinements as red lines, the difference is shown as continuous blue lines. Bragg positions are shown as orange ($BaAl_4$, space group *I*4/*mmm*) ticks.

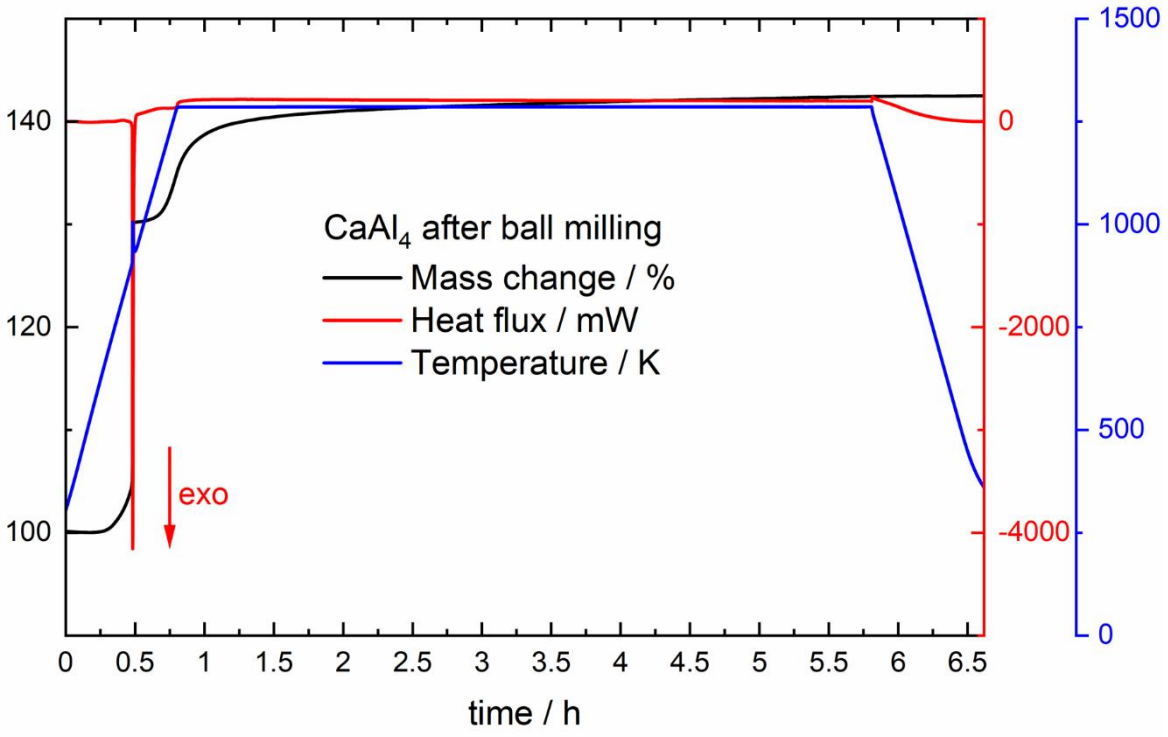

Figure S59. STA experiment for the ball-milled $CaAl_4$ (after 180 minutes) with five hours of dwelling time (mass change in black, heat flux in red and temperature program in blue).

8.5 The obscure oxidation behavior of $HfAl_2$ – A high temperature in situ study

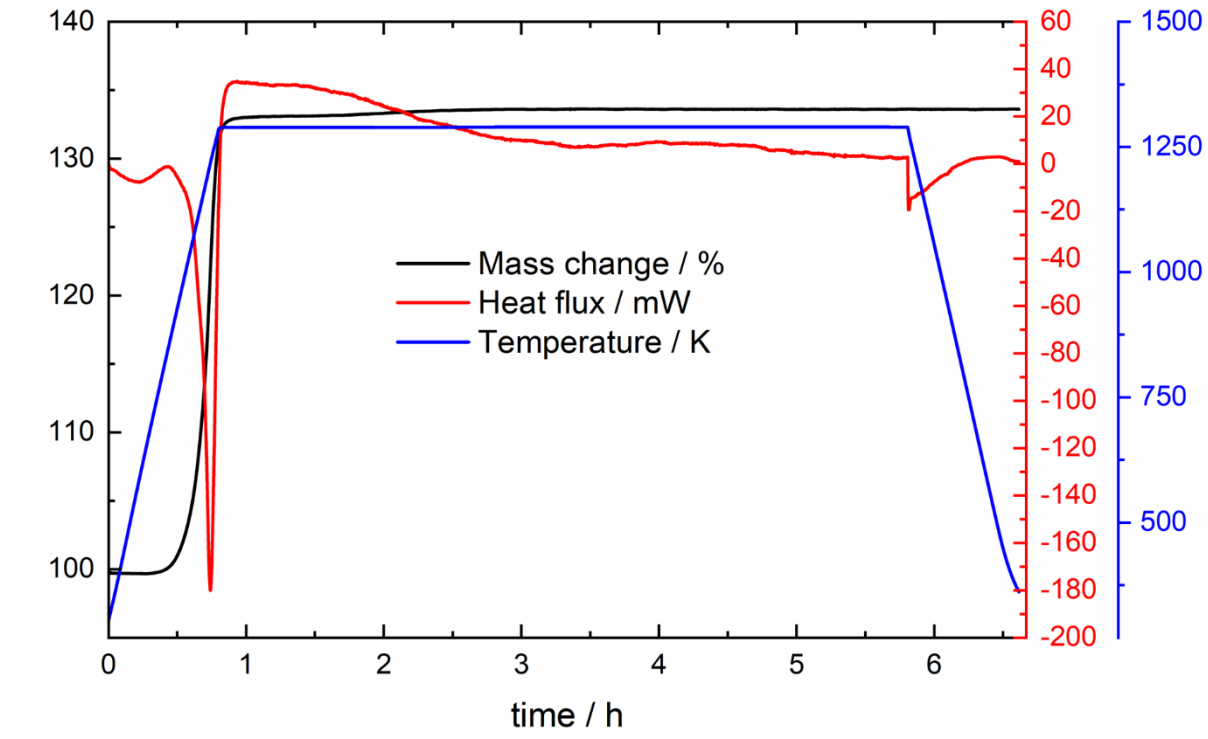

Figure S60. STA experiment for the oxidation reaction of $HfAl_2$ with 5 hours dwelling time (mass change in black, heat flux in red and temperature program in blue).

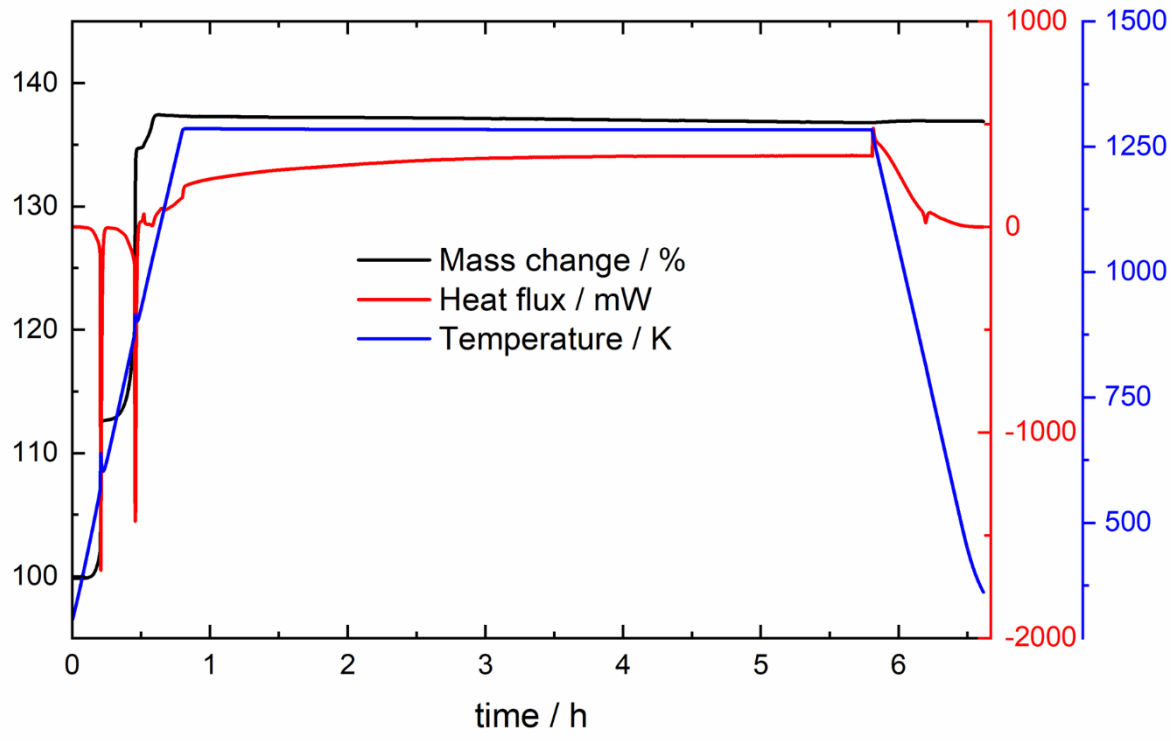

Figure S61. STA experiment for the oxidation reaction of HfV_2 with 5 hours dwelling time (mass change in black, heat flux in red and temperature program in blue).

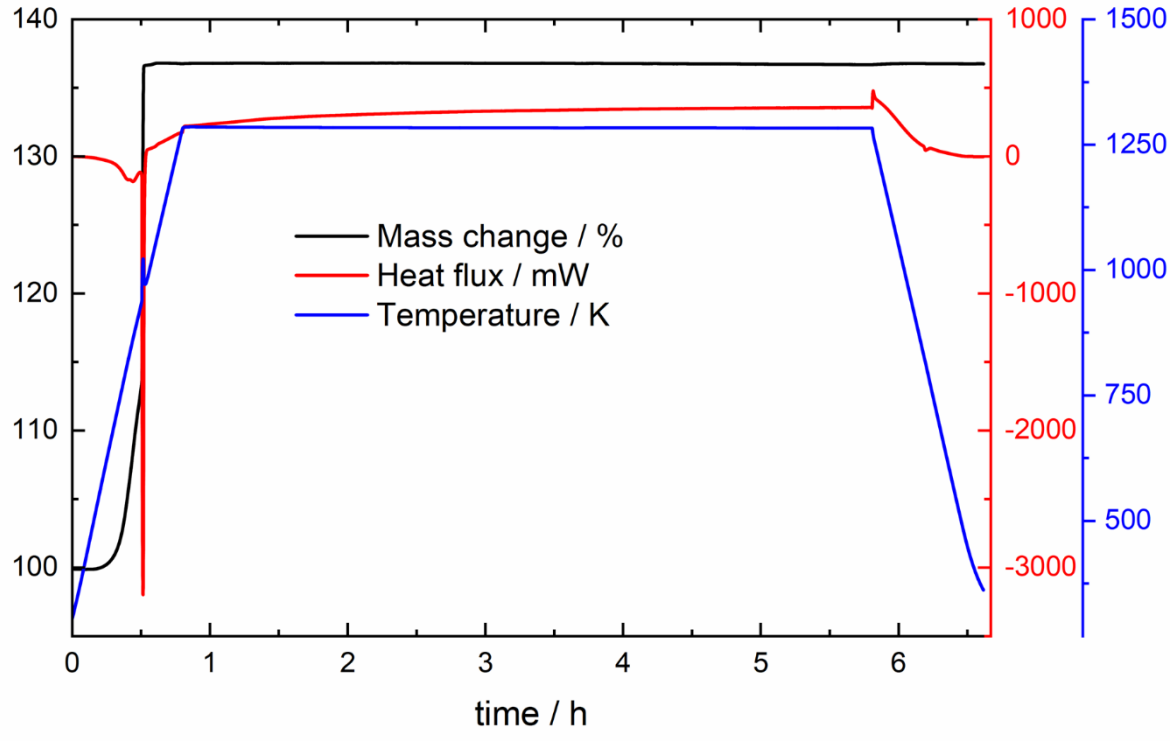

Figure S62. STA experiment for the oxidation reaction of $Hf(V_{0.5}Al_{0.5})_2$ with 5 hours dwelling time (mass change in black, heat flux in red and temperature program in blue).

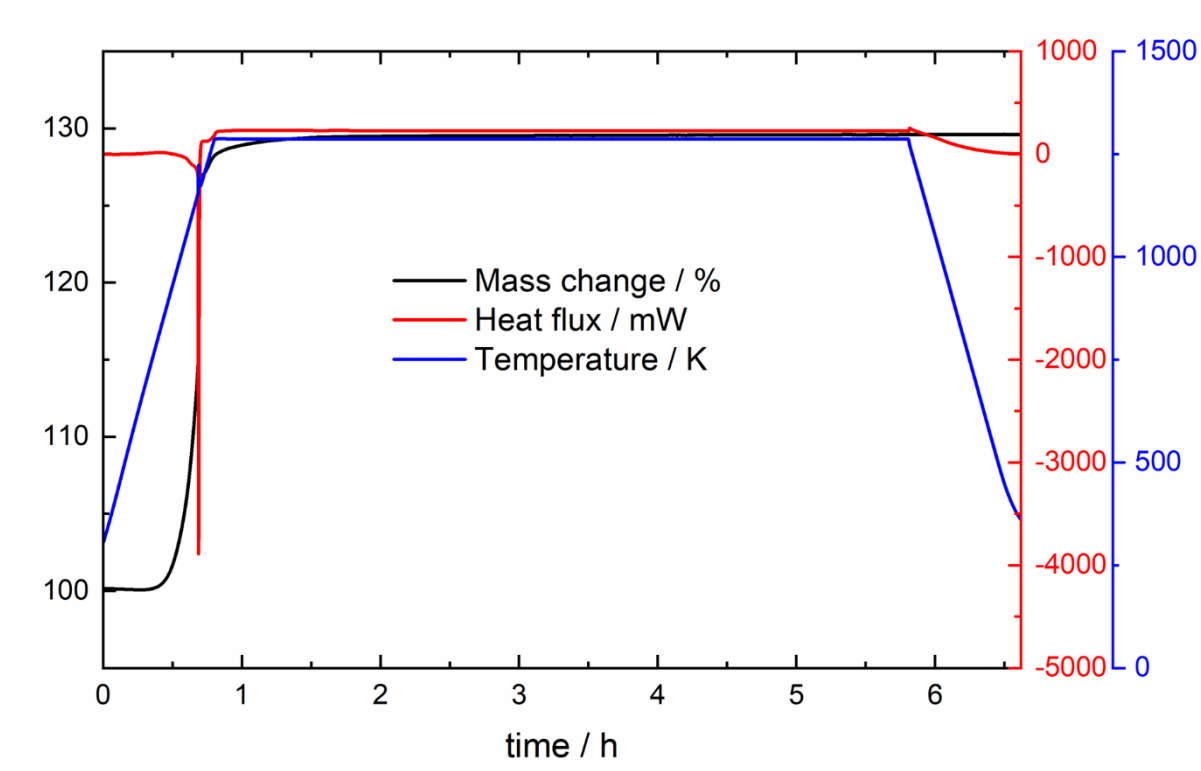

Figure S63. STA experiment for the oxidation reaction of $HfAl_2$ with 5 hours dwelling time (mass change in black, heat flux in red and temperature program in blue).